Universitat de Girona

COMPUTATIONAL STUDIES ORIENTED TOWARDS THE DEVELOPMENT OF A GREENER CHEMISTRY

Jesús Antonio Luque Urrutia

Per citar o enllaçar aquest document:
Para citar o enlazar este documento:
Use this url to cite or link to this publication:
http://hdl.handle.net/10803/672181

http://creativecommons.org/licenses/by/4.0/deed.ca

Aquesta obra està subjecta a una llicència Creative Commons Reconeixement

Esta obra está bajo una licencia Creative Commons Reconocimiento

This work is licensed under a Creative Commons Attribution licence

Universitat
de Girona

Computational Studies Oriented Towards the Development of a Greener Chemistry

Jesús Antonio Luque Urrutia

Doctoral Thesis

2021

Doctoral Thesis

Computational Studies Oriented Towards the Development of a Greener Chemistry

JESÚS ANTONIO LUQUE URRUTIA
2021

Doctoral Programme in Chemistry

Supervised by:

Dr. Albert Poater i Teixidor
Prof. Miquel Solà i Puig

Tutor:

Dr. Albert Poater i Teixidor

Presented in fulfillment of the requirements for a doctoral degree
from the University of Girona

Universitat de Girona

Dr. Albert Poater i Teixidor and Prof. Dr. Miquel Solà i Puig, from Universitat de Girona,

WE DECLARE:

That the thesis entitled " Computational Studies Oriented Towards the Development of a Greener Chemistry," presented by Jesús Antonio Luque Urrutia to obtain a doctoral degree, has been completed under our supervision and meets the requirements to opt for an International Doctorate.

For all intents and purposes, we hereby sign this document.

Signature

Dr. Albert Poater Teixidor

Prof. Dr. Miquel Solà Puig

Girona, January 27, 2021

Author's note:

Dear reader, before starting, I want to let you know that this thesis tries to be as accessible as possible for everyone, as I believe that science should be exciting and enjoyable to read. Therefore, you may find humorous sentences and some over-explaining so that anyone could follow the thesis.

I hope that you enjoy it

Acknowledgments

Esta tesis ha sido posible gracias a la financiación recibida de la beca de doctorado IFUdG2017 y la MOB2018 de la Universitat de Girona. Quiero agradecer a mis dos directores de tesis, Albert Poater i Teixidor i Miquel Solà i Puig, en primer lugar, por escogerme para realizar esta tesis, pero sobre todo por lo que he aprendido gracias a vosotros estos años. He de decir que, al inicio de la tesis, me faltaban muchas cosas, entre ellas entender el esfuerzo y dedicación que requiere la investigación científica y, aunque aún me falte mucho por recorrer, he podido mejorar mucho gracias a vosotros. Siempre me habéis ayudado tanto en el desarrollo de los proyectos, como en la búsqueda de becas o congresos donde poder ir a divulgar los resultados que íbamos obteniendo. Incluso cosas como el material de trabajo (cables, pantallas, ordenador…) que a veces puede parecer que es algo obvio, me lo habéis proporcionado cuando ha sido necesario, por lo que creo que es importante recordarlo. Gracias a vuestra experiencia, que espero haber captado aunque sea en parte, he crecido como investigador pero también como persona. Muchas gracias por haberme guiado durante la tesis.

Aunque una tesis es mucho trabajo, esfuerzo y dedicación, también es importante rodearte de gente que comparta la ilusión de investigar, por ello quiero agradecer a toda la gente de la Universitat de Girona que no solo me ha soportado todos estos años, sino que también me ha enseñado cosas. Me gustaría empezar por los compañeros de despacho. To my partners in the office; Óscar Belman, Maria Voccia, Sílvia Escayola, Martí Gimferrer, Massimo Christiano, Alessandra Cicolella, David Holgado, Gerard Pareres, Eric Casals, Judit Masdemont, Dandan Chen, and even all the people that came for shorter amounts of time, I want to thank you for your company, as well as your help and insight. I was the first on the office, and the periods when I had nobody to share opinions and laughs were tough, but all of you made working a bit easier every day. The memories I have with everyone there are really precious to me.

Quiero continuar con los compañeros “de bar” o de la hora de comer, en los cuales se incluyen también los compañeros de despacho y directores de la tesis, pero también el resto del IQCC. Gracias a Pau Besalú, Martí Gimferrer, Silvia Escayola, Steven Roldan, Dani Masó, Germano Giuliani, Silvia Simón, Pedro Salvador, Montse Rodríguez, Josep Mª Lluís, Lluís Blancafort, Albert Poater i Miquel Solà. Poder hablar de temas diversos, desde ciencia a política, ciclismo o de los proyectos de cada uno siempre no solo me ayudó a despejarme un poco del trabajo, también pude aprender mucho de vosotros. Además, de vez en cuando nos poníamos retos en grupo como el de quien hacía más flexiones, pero mi favorito sin duda alguna es el de traer pasteles caseros. Siempre es bueno engordar en grupo, ¿no?

En el transcurso de la tesis, he tenido el placer de poder viajar a varios sitios alrededor del mundo, por lo que he podido conocer a mucha gente que me ha ayudado por el camino. I want to thank everyone from the Roscoff institute; I enjoyed the stay and the company. Thanks to Guillaume, Maud, Quentin, Gianluca, Marcin, Wang, Jack, Winnie, Karol, and of course, everyone else (sorry, my memory is not that good with names, I am afraid) for a great stay there. We had lots of fun exploring that lovely village and its

surroundings, as well as learning the mathematical depths of quantum chemistry. I also want to thank the teachers Felix Aviat, Benoit Braida, Eric Cancès, Julia Contreras, Geneviève Dusson, Emanuel Giner, Nohad Gresh, Laura Grigori, Louis Lagardere, Tony, Lelièvre, Eleonora Luppi, Yvon Maday, Pierre Monmarché, Jean Philip Piquemal and Peter Reinhardt for their lessons. They were very inspiring and exciting for me.
I was able to travel to Saudi Arabia last year. It was an excellent experience for me, shattering all my possible views and prejudices I could have, and that is thanks to all the people I met there. I want to thank my supervisor Luigi Cavallo for letting me go there and teaching me a project that I did not even know. I did not even think about data analysis, but I learned it thanks to your guidance. Even more, you showed Massimo and me an excellent seafood cuisine, which I will fondly remember. I also want to thank all the people I met there, Didier, Zhen, Mohit, Christina, Sandra, Busra, Mona, Laura, Sheikha, and Rafia. I can only say that all of you were very nice, even to give me a birthday cake! I am fortunate to have met you all, and it would be great to meet with you again. The stay would have been entirely different without you there, so thank you very much!

Me gustaría agradecer como mención especial, a mis profesoras de química y física del instituto, Asunció Ferrer i Dolors Montserrat, ya que fue gracias al empujón que me dieron ellas, que me gustó tanto la ciencia. Sin vuestra pasión por enseñar, puede que hubiera hecho otra cosa. Muchas gracias, de verdad.

Quiero agradecer también a todos mis amigos por el apoyo que me habéis dado, Alex, Esperanza, Carlos, Christian, Isaac, Dani, Eric, Adrià, Sara, Ricard, María, Carla y Sergi. No todo es trabajo, y por ello todos vosotros habéis ayudado enormemente tanto a desconectar, como a hacer un poco de brainstorming de vez en cuando, para que negarlo. Se necesita mucha cooperación tanto como para quedar para hacer una cena con 14 pizzas, como para jugar a rol de mesa. Quiero agradecer también a mi pareja Clara Muñoz, que en estos últimos meses tu apoyo ha sido muy importante para mí. Siempre me has dado fuerzas y ánimos para seguir apretando hasta poder acabar, y bueno, ¡ya lo ves!

Y por último, pero no por ello menos importante, quiero agradecer todo el apoyo que mi familia me ha dado. A mi madre Maite Urrutia y mi padre Antonio Luque por criarme, cuidarme y preocuparse tanto de mi bienestar, como de mi trabajo. Sé que muchas veces era difícil de entenderme, pero aprecio mucho que lo intentarais. A mis hermanas Ana Mari, Carmen, Silvia, Sandra y Marimar, que, aunque no nos veamos muy seguido, siempre me preguntabais sobre cómo me iba el doctorado, y siempre me habéis cuidado como el pequeño de la familia que soy. Obviamente también a mis sobrinos/as Eric, Joel, Giseva, Sayoa y el pequeño Izan; espero que podáis llegar tan lejos como os lo propongáis.

Para todos vosotros, y también aquellos a los que no os he mencionado y aun así me habéis apoyado, muchas, muchísimas gracias a todos.

Full List of publications

This thesis is presented as a compendium of publications.

Published articles included in the thesis:

1. Luque-Urrutia, J. A.; Poater, A. **The Fundamental Noninnocent Role of Water for the Hydrogenation of Nitrous Oxide by PNP Pincer Ru-based Catalysts.** *Inorg. Chem.* **2017**, *56*, 23, 14383-144387. DOI: 10.1021/acs.inorgchem.7b02630.
   JCR Impact Factor= 4.70; SJR position 5/45 in FECYT ranking, 1st quartile.

2. Masdemont, J.; Luque-Urrutia, J. A.; Gimferrer, M.; Milstein, D.; Poater, A. **Mechanism of Coupling of Alcohols and Amines to Generate Aldimines and H_2 by a Pincer Manganese Catalyst.** *ACS Catal.* **2019**, *9*, 3, 1662-1669. DOI: 10.1021/acscatal.8b04175
   JCR Impact Factor = 12.35; SJR position 12/159 in FECYT ranking, 1st quartile.

3. Luque-Urrutia, J. A.; Solà, M.; Milstein, D.; Poater, A. **Mechanism of the Manganese-Pincer-Catalyzed Acceptorless Dehydrogenative Coupling of Nitriles and Alcohols**. *J. Am. Chem. Soc.* **2019**, *141*, 6, 2398-2403. DOI: 10.1021/jacs.8b11308
   JCR Impact Factor = 14.61; SJR position 13/177 in FECYT ranking, 1st quartile.

4. Luque-Urrutia, J. A.; Solà, M.; Poater, A. **The Influence of the pH on the Reaction Mechanism of Water Oxidation by a Ru(bda) catalyst.** *Catal. Today,* **2020**, *358*, 278-283. DOI: 10.1016/j.cattod.2019.12.005.
   JCR Impact Factor = 5.83; SJR position 8/71 in FECYT ranking, 1st quartile.

5. Luque-Urrutia, J. A.; Kamdar, J. M.; Grotjahn, D. B.; Solà, M.; Poater, A. **Understanding the Performance of a Bisphosphonate Ru catalyst for Water Oxidation Catalysis.** *Dalton Trans.* **2020**, *49*, 14052-14060. DOI: 10.1039/d0dt02253e.
   JCR Impact Factor = 4.17; SJR position 5/45 in FECYT ranking, 1st quartile.

6. Natongchai, W.; Luque-Urrutia, J. A.; Phungpanya, C.; Solà, M.; D'Elia, V.; Poater, A.; Zipse, H. **Cycloaddition of CO_2 to epoxides by highly nucleophilic 4-aminopyridines: establishing a relationship between carbon basicity and catalytic performance by experimental and DFT investigations.** *Org. Chem. Front.*, **2021**, Advance Article. DOI: 10.1039/d0qo01327g
   JCR Impact Factor = 5.16; SJR position 7/57 in FECYT ranking, 1st quartile.

7. Luque-Urrutia, J. A.; Poater, A.; Solà, M. **Do Carbon Nano-Onions Behave as Nanoscopic Faraday Cages? A Comparison of the Reactivity of C_{60}, C_{240}, $C_{60}@C_{240}$, $Li^+@C_{60}$, $Li^+@C_{240}$, and $Li^+@C_{60}@C_{240}$.** *Chem. Eur. J.,* **2020**, *26*, 804-808. DOI: 10.1002/chem.201904650.
   JCR Impact Factor = 4.86; SJR position 44/177 in FECYT ranking, 1st quartile.

Other published articles not included in the thesis:

8. Meconi, G. M., Vummaleti, S. V. C.; Luque-Urrutia, J. A.; Belanzoni, P.; Nolan, S. P.; Jacobsen, H.; Cavallo, L.; Solà, M.; Poater, A. **Mechanism of the Suzuki-Miyaura Cross-Coupling Reaction Mediated by [Pd](NHC)(allyl)Cl] Precatalysts.** *Organometallics,* **2017**, *36*, 2088-2095. DOI: 10.1021/acs.organomet.7b00114.
   JCR Impact Factor = 4.05; SJR position 11/57 in FECYT ranking, 1st quartile.

9. Luque-Urrutia, J. A.; Gimferrer, M.; Casals-Cruañas, E.; Poater, A. **In Silico Switch from Second- to First-Row Transition Metals in Olefin Metathesis: From Ru to Fe and from Rh to Co**. *Catalysts* **2017**, *7*, 12, 389-400. DOI: 10.3390/catal7120389
   JCR Impact Factor = 3.47; SJR position 55/146 in FECYT ranking, 2nd quartile.

Table of Contents

List of Abbreviations **_5_**

List of Figures **_7_**

List of Tables **_13_**

Abstract **_15_**

Resum **_19_**

Resumen **_23_**

Chapter 1. Introduction **29**

1.1. Environmental crisis 29
  1.1.1. Global pollution 29
  1.1.2. Climate change 30
    1.1.2.1. CO_2 and Global Warming 31
    1.1.2.2. N_2O, SO_2, and the acid rain 32
    1.1.2.3. CFCs and the ozone layer 33
  1.1.3. Energy dependence 33
1.2. Catalysts 36
  1.2.1. Hydrogen production 36
    1.2.1.1. Water-splitting 37
    1.2.1.2. Water Oxidation Catalysis 39
      1.2.1.2.1. I2M *vs*. WNA 39
      1.2.1.2.2. Reproducing the PSII activity 40
    1.2.1.3. Acceptorless dehydrogenative coupling 42
  1.2.2. Reusing atmospheric gases for waste management 44
    1.2.2.1. N_2O recycling 44
    1.2.2.2. CO_2 recycling 45
1.3. Future of energy production 46
  1.3.1. Solar cells 47
  1.3.2. Dye-sensitized solar cells 49
    1.3.2.1. Fullerenes and CNOs 50

Chapter 2. Methodology and Computational Chemistry Tools **53**

2.1. Quantum chemistry 53
  2.1.1. A look into Quantum Mechanics 53
    2.1.1.1. The Hartree-Fock method 57
    2.1.1.2. Basis sets and atomic orbitals 58
    2.1.1.3. Density Functional Theory (DFT) 61
    2.1.1.4. How to choose the optimal functional and basis set 64

2.2. Geometry optimization and transition states 64
  2.2.1. Potential Energy Surface (PES) 65
    2.2.1.1. Gibbs energy 66
    2.2.1.2. Energy corrections 67
    2.2.1.3. Relevant measurements 70
      2.2.1.3.1. Calculation of pK_a 70
      2.2.1.3.2. Calculation of electropotentials 71
      2.2.1.3.3. Mayer Bond Orders (MBO) 74
      2.2.1.3.4. Effective Oxidation State (EOS) 74

Chapter 3. Objectives 77

Chapter 4. Hydrogen production as a clean energy source 83
4.1. The Influence of the pH on the reaction mechanism of water oxidation by a Ru(bda) catalyst 83
4.2. Understanding the Performance of a Bisphosphonate Ru catalyst for Water Oxidation Catalysis 91
4.3. Mechanism of the Manganese-Pincer-Catalyzed Acceptorless Dehydrogenative Coupling of Nitriles and Alcohols 103
4.4. Mechanism of Coupling of Alcohols and Amines To Generate Aldimines and H_2 by a Pincer Manganese Catalyst 111

Chapter 5. Recycling of atmospheric gases 123
5.1. The Fundamental Noninnocent Role of Water for the Hydrogenation of Nitrous Oxide by PNP Pincer Ru-based Catalysts 123
5.2. Cycloaddition of CO_2 to epoxides by highly nucleophilic 4-aminopyridines: establishing a relationship between carbon basicity and catalytic performance by experimental and DFT investigations 131

Chapter 6. Clean energy production through solar cells 149
6.1. Do Carbon Nano-onions Behave as Nanoscopic Faraday Cages? A Comparison of the Reactivity of C_{60}, C_{240}, $C_{60}@C_{240}$, $Li^+@C_{60}$, $Li^+@C_{240}$, and $Li^+@C_{60}@C_{240}$ 149

Chapter 7. Results and discussion 157
7.1. Highlights of hydrogen production for a clean energy source 157
  7.1.1. Water Oxidation Catalysis: carboxylates, phosphonates, and pH157
  7.1.2. Acceptorless Dehydrogenative Coupling: industrial processes refining 166

7.2. Atmospheric gas recycling 173
  - 7.2.1. Energy production through N_2O recycling 173
  - 7.2.2. CO_2 recycling as a building block for other carbon-based compounds 176

7.3. Highlights of clean energy production through solar cells 179
  - 7.3.1. Third-generation solar cells: are nano onions a future possibility? 179

Chapter 8. Conclusions 185

8.1. Hydrogen production as a clean energy source 185
  - 8.1.1. Water Oxidation Catalysis 185
  - 8.1.2. Acceptorless Dehydrogenative Coupling 186

8.2. Atmospheric gas recycling 186

8.3. Clean energy production through solar cells 187

Chapter 9. Bibliography 189

Chapter 10. Annex 203

10.1. Section 4.1 SI 203

10.2. Section 4.2 SI 205

10.3. Section 4.4 SI 215

10.4. Section 5.1 SI 219

10.5. Section 5.2 SI 220

10.6. Section 6.1 SI 227

List of Abbreviations

Abbreviation	Description
ADC	Acceptorless Dehydrogenative Coupling
ATP	Adenosine TriPhosphate
bda	2,2’-Bipyridine-6,6’-Dicarboxylic Acid
CFC	ChloroFluoroCarbons
CNO	Carbon Nano Onion
DFT	Density Functional Theory
EOS	Effective Oxidation State
E_{xc}	Exchange potential
FCI	Full Configuration Interaction
FNR	Ferredoxin NADP Reductase
GGA	Generalized Gradient Approximation
I2M	Interaction between 2 Metal-oxo centers
IUPAC	International Union of Pure and Applied Chemistry
LDA	Local Density Approximation
MBO	Mayer Bond Order
NADP	Nicotinamide Adenine Dinucleotide Phosphate
NADPH	Hydrogenated NADP
NOAA	National Oceanic and Atmospheric Administration
OEP	Optimized Effective Potential
OS	Oxidation State
PCET	Proton Coupled Electron Transfer
PCM	Polarizable Continuum Model
PES	Potential Energy Surface
PNP	Phosphorous-Nitrogen-Phosphorous
PSII	Photosystem II
r.d.s.	Rate-determining step
RI	Reliability Index
SCRF	Self-Consistent Reaction Field
SHE	Standard Hydrogen Electrode
SI	Supporting Information
SMD	Solvation Model Density
STO	Slater-Type Orbital
T_{elec}	Kinetic energy of electrons
T_{nuc}	Kinetic energy of nuclei
TOF	TurnOver Frequency
TON	TurnOver Number
TS	Transition State
UV	UltraViolet
V_c	Coulombic repulsion
V_{ee}	Potential energy electron-electron
V_{en}	Potential energy electron-nuclei
V_{ex}	External potential energy from nuclei
V_{nn}	Potential energy nuclei-nuclei
WNA	Water Nucleophilic Attack
WOC	Water Oxidation Catalysis
ZPE	Zero Point Energy

List of Figures

Figure 1. *a) Air pollution in Shanghai, China. b) Red mud lake in Mandeville, Louisiana. c) Part of the Pacific Ocean garbage patch.* 29

Figure 2. *Global warming effect. The addition of significant amounts of CO_2 to the atmosphere increases the radiation bouncing back to Earth, heating it more than it should.* 30

Figure 3. *Annual global emission of CO_2 in million tons throughout 200 years.* 31

Figure 4. *Annual temperature in Celsius recorded by NASA, NOAA, the Berkeley Earth research group, the Met Office Hadley Centre (UK), and the Cowtan and Way analysis from 1880 to 2019.*[17] 32

Figure 5. *Satellite observations of the Ozone layer by the NASA until 2013.* 33

Figure 6. *Global fossil fuel consumption between 1800 and 2016.* 34

Figure 7. *Photo of a group of wind turbines that represent visual pollution.* 34

Figure 8. *Nuclear fission of ^{235}U* 35

Figure 9. *Effect of a catalyst in the PES of a reaction.* 36

Figure 10. *Representation of the photosynthesis mechanism in a thylakoid membrane.*[1] 38

Figure 11. *Intermolecular vs. Intramolecular I2M.* 39

Figure 12. *WNA and subsequent deprotonation.* 40

Figure 13. *The general mechanism for a catalyst that can perform both I2M and WNA.* 40

Figure 14. *Structure representation of the blue dimer for WOC.* 41

Figure 15. *3D view of the Ru(bda)(pic)$_2$ catalyst. Colored atoms: C grey, H white, N blue, O red, Ru yellow.* 41

Figure 16. *WOC catalysts A (with dicarboxylate ligand) and B (with diphosphonate ligand)* 42

Figure 17. *General cross-coupling reaction of arenes with alkenes.* 42

Figure 18. *General ADC reaction of arenes with alkenes.* 43

Figure 19. *Proposed mechanism for the efficient production of acrylonitriles with a Mn based ADC catalyst. P stands for P^iPr and Mn stands for $Mn(CO)_2$ for clarity.* 43

Figure 20. *PNP pincer catalyst with a Mn metal center able to perform ADC to produce aldimines.* 43

Figure 21. *Hydrogenation of N_2O by the PNP-pincer Ru based catalyst* 44

Figure 22. *The general mechanism for CO_2 cycloaddition to epoxides. The CO_2 block is highlighted in red.* 45

Figure 23. *Target nucleophiles for epoxide opening.* 46

Figure 24. *Formation of positive and negatives bands through the interaction of the electron orbitals in a given material.* 48

Figure 25. *Solar cell electron-hole movement.* 48

Figure 26. *Dye-sensitized solar cell general mechanism.* 49

Figure 27. *Structure of C_{60} fullerene.* 50

Figure 28. *Diels-Alder reaction.* 51

Figure 29. *Example of a transition state of a Diels-Alder reaction between $Li^+@C_{60}@C_{240}$ CNO and cyclopentadienyl. Inner fullerene highlighted in green, and lithium cation shown in red.* 51

Figure 30. *Difference between reflection and refraction of light. n_1 and n_2 refer to different media such as air and water.* 53

Figure 31. *Huygens's wavelet and wavefront representation.* 54

Figure 32. *Double slit experiment with the resulting interferences.* 54

Figure 33. *Black body radiation according to classical physics (black line) and Planck's approach (colored lines).* 55

Figure 34. *Bohr atom model showing the different n levels. Radii according to n^2.* 59

Figure 35. *Atomic orbital wavefunctions of the H atom. X-axis shows l, Y-axis shows n quantum numbers.* 59

Figure 36. *Orbitals of subshell p.* 60

Figure 37. *Observable electron density of aniline.* 61

Figure 38. *Jacob's ladder of chemical accuracy.* 63

Figure 39. *Example of a PES comparing an angle, a length and the energy of each conformation.* 65

Figure 40. *Representation of the ZPE of a system.* 65

Figure 41. *TS between two minima in a given system.* 66

Figure 42. *3D view of a saddle point. This is where a TS is located.* 66

Figure 43. *Correction between experimental and computational data.* 71

Figure 44. *PCET sample mechanism. Extracted from one of the articles in this thesis.* 72

Figure 45. *$E_{1/2}$ vs. pH diagrams for the $Ru^{IV/III}$ and $Ru^{III/II}$ couples of cis-$[Ru^{II}(bpy)_2(py)(H_2O)]^{2+}$. The Figure is taken from Meyer and Huynh.[203] Dashed vertical lines show the pK_a of $Ru^{III}OH_2^{3+}$ (0.85) and $Ru^{II}OH_2^{2+}$ (10.6).* 73

Figure 46. *3D view of the $Ru(bda)(pic)_2$ catalyst. Colored atoms: C grey, H white, N blue, O red, Ru yellow.* 77

Figure 47. *WOC catalysts A (with dicarboxylate ligand) and B (with diphosphonate ligand).* 78

Figure 48. *Proposed mechanism for the efficient production of acrylonitriles with a Mn based ADC catalyst. P means $P^{i}Pr$ and Mn means $Mn(CO)_2$ for clarity.* 78

Figure 49. *PNP pincer catalyst. Mn in pink, P in green, N in blue, C in grey and H in white.* 78

Figure 50. *Hydrogenation of N_2O by the PNP-pincer Ru based catalyst ($P = P(iPr)_2$).* 79

Figure 51. *Mechanism of the CO_2 cycloaddition to epoxides for cyclic carbonate synthesis, and the N-based nucleophiles to study.* 79

Figure 52. *$Li^+@C_{60}@C_{240}$ CNO. Inner fullerene recolored in green for clarity. Li^+ shown in red.* 80

Figure 53. *Proposed water oxidation mechanism for $[Ru(bda)(pic)_2]$ at pH = 8.* 158

Figure 54. *Mechanism for the Ru-bda catalyst at pH = 1; PCETs in green; Gibbs energy barriers in orange; reduction potentials in light blue; Gibbs reaction energies in grey. Energies are given in kcal/mol and oxidation potentials in V. Arrows in blue denote oxidation processes and in green proton-coupled electron transfers.* 158

Figure 55. *The carboxylate catalyst mechanism at pH = 8; Gibbs energy barriers in orange; reduction potentials in light blue; pK_a in purple; Gibbs reaction energies in grey. Energies are given in kcal/mol and reduction potentials in V. Main path represented with bold arrows. Arrows in blue denote oxidation processes, in purple proton transfers, in green proton-coupled electron transfers, and pink for dashed disproportion processes.* 159

Figure 56. *Electrochemical reaction mechanism catalyzed by **Ru(bpa)** (= $^{1}\mathbf{0}^{+0}$) at pH = 8. Favored pathways highlighted with thick arrows. Green = PCET, blue = oxidation, purple = deprotonation. Species are labeled $^{\mathbf{X}}\mathbf{Y}^{\mathbf{q}}$, where **X** indicates a spin state, and q is the total charge of species **Y**.* 160

Figure 57. *General mechanism for **Ru(bpa)** at pH = 1. Green arrows for PCETs, blue for OSs, and purple for pK_a. Species are labeled $^{\mathbf{X}}\mathbf{Y}^{q}$, where **X** indicates the spin state, and **q** is the total charge of species **Y**.* 161

Figure 58. *Monoprotonated phosphonate mechanism for **Ru(bpa)** at pH = 1. Species are labeled $^{\mathbf{X}}\mathbf{Y}^{\mathbf{q}}$, where **X** indicates the spin state, and **q** is the total charge of species **Y**.* 162

Figure 59. *I2M and WNA mechanisms pathways (with 1 or 2 assisting water molecules) for the deprotonated (bpa at pH = 8) and protonated ($bpaH_2$ at pH = 1) phosphonate catalyst (axial ligands and non-interacting hydrogens removed for clarity). Gibbs energy barriers (kcal/mol) in orange.* 163

Figure 60. *Liberation of O_2 through WNA for the $bpaH_2$ catalyst at pH = 1. Gibbs reaction energy (kcal/mol) in grey, pK_a for deprotonations in purple.* 163

Figure 61. *PCET test showing the formation of a Ru^{V}-OO complex that could not regenerate the catalyst.* 164

Figure 62. *Cerium Ammonium Nitrate electropotential study (in blue, the reduction potentials; in black, the Gibbs energies of the successive substitution of NO_3^- by H_2O in the CAN structure).* 165

Figure 63. *Proposed final mechanisms at both pH for $bpaH_2$/bpaH and bpa catalysts. Green arrows for PCETs, and purple for pKa. Species are labeled $^{\mathbf{X}}\mathbf{Y}^{\mathbf{q}}$, where **X** indicates the spin state, and **q** is the total charge of species **Y**. Blue values represent redox potentials, grey values represent Gibbs reaction energies and purple values represent pK_a.* 166

Figure 64. *Dehydrogenative coupling of arenes and alkenes with the aid of a hydrogen acceptor in a palladium-catalyzed reaction.* 167

Figure 65. *Catalytic ADC reported by Milstein et al.[87] with the catalyst structure.* 167

Figure 66. *Full mechanism of the manganese catalyzed ADC for the synthesis of acrylonitriles starting from alcohols and nitriles. All values shown are Gibbs energies in kcal/mol. TS highlighted in purple. ..168*
Figure 67. *First cycle of the ADC catalysis for aldehyde formation (energies in kcal/mol). 169*
Figure 68. *Isomerization assisted by explicit water or alcohol molecules (energies in kcal/mol). 170*
Figure 69. *Second cycle for ADC catalysis showing acrylonitrile formation (energies in kcal/mol). 171*
Figure 70. *The full reaction mechanism for the ADC of benzyl alcohols with benzyl amines (in blue the steps assisted by water and in green by the alcohol; R_1 = CH_2-Ph; in black (minima) and in orange (TSs). Solvent Gibbs energies in kcal/mol and referred to catalyst **1**, except for the metal-free reaction pathway included in the box that refers to aldehyde **5**). 172*
Figure 71. *Hydrogenation of N_2O by the PNP-pincer Ru-based catalyst **1** (P = $P(iPr)_2$). 174*
Figure 72. *Full mechanism for the hydrogenation of N_2O. Isopropyl ligand represented. Tert-butyl and phenyl ligands energy shown as well (green and pink energies respectively). (Gibbs energies in kcal/mol, and referred to the catalyst **1**). 174*
Figure 73. *Percentage of the occupied volume of the ligands in respect to the metal center ($\%V_{bur}$) and steric maps (XY plane) for the PNP pincer ligands, including iPr, Ph, and tBu substituents on the phosphorous atoms of catalyst **1** (Mn is placed in the center and the closest N atom is on the x-axis, while both hydrides are on the z-axis, curves are given in Å). 175*
Figure 74. *A hypothesis of the PNP catalysis for greener chemistry. 176*
Figure 75. *Mechanism of the epoxide cyclization. Path A depicted on the right side mechanism, and Path B is depicted on the left side. 176*
Figure 76. *Path A of CO_2 cyclization 177*
Figure 77. *Path B of CO_2 cyclization 178*
Figure 78. *The optimized mechanism for CO_2 and epoxide cyclization. Values shown represent Gibbs energies in kcal/mol. In blue, with DMAP, and in red, with [4]. 178*
Figure 79. *Experimental conditions for the epoxide cyclization. 179*
Figure 80. *Schlegel diagram for a C_{240} fullerene with the five different bonds highlighted, $[5,6]_D$ in red, $[6,6]_B$ in grey, $[6,6]_{C1}$ in green, $[6,6]_{C2}$ in pink, and $[6,6]_{C3}$ in blue. The 12 pentagons of the fullerene are also marked in red. 180*
Figure 81. *Representation of the different bonds found in a C_{240} cage. 180*
Figure 82. *Effect of a charge inside a Faraday cage. The charge (cation) polarizes the cage (fullerene) and can polarize the outside in the same intensity while being unaffected by external fields. 183*
Figure S1. *Plot of the DFT (x-axis) and experimental (y-axis) pK_a of the different acids. 207*
Figure S2. *The bisphosphonate Ru catalyst B's mechanism according to the two phosphonate ligands' protonation at pH = 8. Species $^{1}\mathbf{0}^{-2}$ is **B** deprotonated twice at pH 8; the superscripts left and right signify spin multiplicity (here, singlet) and overall charge, respectively. For reaction arrows, red = less favorable, blue = oxidation, green = PCET, and purple = deprotonation. For numbered species, green indicates deprotonated diphosphonate ligand, whereas red indicates doubly deprotonated ligand. Numbers near arrows in blue indicate the reduction potential in V; purple numbers indicate pK_a, and grey numbers (minima) indicate Gibbs free energy in kcal/mol. 209*
Figure S3. *The mechanism for the bisphosphonate Ru catalyst **B** with retention of ligand protons at pH 1. For reaction arrows, red = less favorable, blue = oxidation, green = PCET, and purple = deprotonation. For numbered species, green indicates deprotonated diphosphonate ligand, whereas red indicates doubly deprotonated ligand. Numbers near arrows indicate the reduction potential in V; purple numbers indicate pK_a, and grey numbers (minima) indicate Gibbs free energy in kcal/mol. 210*
Figure S4. *The mechanism for the bisphosphonate Ru catalyst **B** with retention of ligand protons at pH 1. For reaction arrows, red = less favorable, blue = oxidation, green = PCET, and purple = deprotonation. For numbered species, green indicates deprotonated diphosphonate ligand, whereas red indicates doubly deprotonated ligand. Numbers near arrows indicate the reduction potential in V; purple numbers indicate pK_a, and grey numbers (minima) indicate Gibbs free energy in kcal/mol. 210*
Figure S5. *pK_a for each molecule going from Biprotonated to Monoprotonated and Deprotonated phosphonates. 211*
Figure S6. *Cyclic voltammetry of Ru(bpa) at pH=1 (Blue). 212*
Figure S7. *Cyclic voltammetry of Ru(bpa) at pH=7 (blue). 212*

Figure S8. *Differential pulse voltammetry comparing* ***2*** *(blue) and* ***3*** *(red). [Note:* ***2*** *is the bpa catalyst subject of our computational studies] Top: pH 7 (0.1 M potassium phosphate buffer). Bottom: pH 1 (0.1 M CF3SO3H). Dashed lines highlight relative peak heights. Catalyst concentration: 0.5 mM. 212*

Figure S9. *Pourbaix diagrams and square wave voltammograms for* $[Ru^{II}(bpaH_2)(pic)_2]$ ***(A,C)****;* $[Ru^{II}(bpaH_2)(isq)_2]$ ***(B,D)****. 213*

Figure S10. *Cerium Ammonium Nitrate electropotential study. 214*

Figure S11. *Full reaction mechanism at the level M06-D3/cc-pVTZ~sdd//BP86-D3BJ/SVP~sdd for the ADC of benzyl alcohols with benzyl amines (in blue the steps assisted by water and in green by the alcohol; in black (minima) and in orange (TSs) Gibbs free energies in the solvent in kcal/mol and referred to catalyst* ***1****, whereas to the aldehyde* ***5*** *in the metal-free reaction pathway included in the box). 218*

Figure S12. *Reaction barriers (kcal/mol) for the ring-opening of epoxide* ***5a*** *by several nucleophiles. ...222*

Figure S13. *Reaction barriers (kcal/mol) for the cycloaddition of* CO_2 *to propylene oxide catalyzed by pyridine according to two different pathways. 223*

Figure S14. *According to two different pathways, reaction barriers (kcal/mol) for the cycloaddition of* CO_2 *to propylene oxide are catalyzed by DMAP. 224*

Figure S15. *Reaction barriers (kcal/mol) for the cycloaddition of* CO_2 *to propylene oxide catalyzed by nucleophile* ***4*** *according to two different pathways. 225*

Figure S16. *Reaction barriers (kcal/mol) for the cycloaddition of* CO_2 *to propylene oxide catalyzed by TBD according to two different pathways. 226*

Figure S17. *Structure comparison between PBEPBE/3-21G(d) and PBEPBE/6-311G(d,p) with the root-mean-square deviation of atomic positions (RMSD). 229*

Figure S18. *Electrostatic potential surface for* $Li^+@C_{240}$ *optimized (top left) and non-optimized with the* Li^+ *at the center (top right) and* $Li^+@C_{60}@C_{240}$ *(bottom). 230*

Figure S19. *Non-covalent interactions in the* $Li^+@C_{60}@C_{240}$*. 230*

List of Tables

Table 1. *Experimental, calculated, and corrected pK_a values for different acids.* 71
Table 2. *Catalytic investigation of N-nucleophiles for the cycloaddition of CO_2 to epoxides* ***5a*** *and* ***5b*** *under atmospheric CO_2 pressure.*[a] 179
Table 3. *Reaction enthalpies (ΔH_r, enthalpy difference between adduct and reactants) and enthalpies barriers ($\Delta H^{\ddagger}$, enthalpy difference between TS and reactant complex) in kcal/mol of the Diels-Alder reaction between fullerenes and Cp, with toluene as solvent.* 181
Table 4. *Summarized [6-6] bond energies (in kcal/mol) extracted from Table 3.* 181
Table 5. *The energy of the LUMO for the different fullerenes studied in this work (in a.u.).* 182
Table S1. *Experimental, DFT, and corrected pK_a values for different acids.* 207
Table S2. *pK_a for the conversion of the two phosphonates in the catalyst: biprotonated, monoprotonated, and deprotonated.* 211
Table S3. *Multiplicity and Spin density for all the relevant structures.* 212
Table S4. *Benchmark study of all the computed species included in Figure 2 and Scheme 2 (Gibbs free energies in the solvent, in kcal/mol), using the optimized geometries at the BP86-D3BJ/SVP~sdd level.* 216
Table S5. *Benchmark study of all the computed species included in Figure 2 and Scheme 2 (Gibbs free energies in the solvent, in kcal/mol).* 217
Table S6. *Benchmarking for the fullerene calculations.* 230

Abstract

According to Dr. Paul Anastas quote:

> *"We are all in the same boat, and we only have one boat."*
>
> Minnesota Green Chemistry Forum, 2013

In this thesis, we emphasize this thought. For a long time, we have believed that everything is profitable, that resources are unlimited, and there are no consequences. However, reality is often disappointing. The use of non-renewable resources, the excessive waste production, and forfeiting the task of recycling has led us to walk over a fragile thread that, once broken, may never restore itself. Metaphors aside, we are talking about our planet, the Earth, and its unique characteristic of harboring life, including ourselves. Our world has its equilibrium; when the wind erodes a mountain, a beach appears, or when a fire devastates an area, eventually, new life rises from the ashes. However, humans have been distorting this balance for decades now. Our evolving way of living has increased the number of resources every person consumes, as either food, shelter, or energy; we overworked everything until exhaustion. We even have the Earth Overshoot Day, which has the "honor" of remembering the day we have consumed all the planet's resources created over a year. Right now, this day is located on July 29, meaning that to supply every human being, we need the resources of 1.75 Earths at the standard recovery rate of the natural resources. However, this is just one problem lurking in the back of our minds like a bad omen: our planet is dying.

Scientists worldwide have already said actively and passively that we have in front of us one of the most significant problems we have ever faced: climate change. For many people, it just means that it will be a bit hotter in summer and a bit warmer in winter, but this is far from reality. Every living thing in this world has acclimated to its environment, like polar bears with their transparent fur to retain the most heat or elephants with their large ears to release it. However, this occurred through the evolution of several thousand years, and every being was able to adapt to it or die trying. Now, we are changing the climate at an alarming rate. The global surface temperature rose from +0.2 ºC approximately from 1970 until 2000, then +0.6 ºC until 2015, and close to +0.8 ºC in 2020. This temperature rise means that, in 100 years, we could see an increase in the global surface temperature between +2 ºC and +6 ºC. It is unsustainable, and we should try to revert it, or, if we are too late, to slow it down as much as possible. For that to happen, there are many possible ways to help. In this thesis, we research catalysts to use water as a source of energy and recycle gases like CO_2 and N_2O, but we also look towards non-catalytic ways of generating energy through solar cell production.

Starting from the catalysis of water to produce hydrogen, we look at the best catalyst involved in water oxidation catalysis (WOC) that we could find: Ru(bda)(pic)$_2$. This catalyst performs as well as photosystem II (PSII), involved in the photosynthesis of a leaf, and the trick to its efficiency is the equatorial ligand bda. It includes carboxylates fixed around the Ru atom, leaving an opening angle large enough for a water molecule to react, converting an octahedral Ru into a reactive hepta-coordinated Ru. While this catalyst was experimentally tested, the full mechanism was still missing. Thus, we wanted to fill in this gap to understand it better. There were discrepancies among several researchers on how the mechanism works, making us want to study all the possibilities available. Knowing why and how it works makes it possible to introduce modifications and upgrade the catalyst into a better one. We demonstrate this catalysis's entire mechanism, analyze the different proposals of other research papers, and study the system's pH influence. We found that the mechanism varies slightly according to the pH since there are deprotonations involved, but it occurs only on intermediates with short life spans, and the overall reaction looks utterly unaffected by these changes. Following this work, we performed a second project modifying this catalyst; more precisely, we changed the carboxylate groups in the bda ligands for phosphonate groups, forming the new ligand bpaH$_2$. Previous studies had shown that the bda outperforms the bpaH$_2$ and its different protonation states, but the reason was still unknown.

Furthermore, the bpaH$_2$ required Ceric Ammonium Nitrate (CAN) at pH=1 because otherwise, no reaction could occur. All these pieces were missing; thus, we developed the full mechanism of bpaH$_2$ at pH=1 and pH=8. Thanks to that, we could observe the different protonation states of the bpaH$_2$ in each pH and revealed the potentials needed to deprotonate water into an oxo ligand. Nevertheless, we also found out that the catalysis could not proceed through either known mechanisms, a dimerization that releases O$_2$ (I2M), or a nucleophilic attack of water that deprotonates a water molecule again before removing the oxygen (WNA). The reason behind this is that in the case of the I2M, experimental results from other authors had shown that it is a first-order reaction according to the catalyst, meaning that the rate-determining step (r.d.s.) could not be a dimer between catalyst, but while the other choice, *i.e.* WNA, should have been confirmed, we found out it was not possible. As we looked into the second water deprotonation, the hydrogens' pK$_a$ was too high for our given pH; therefore, the hydroperoxy ligand (-OOH$_2$) could not deprotonate. Since neither WNA nor I2M could proceed, it left us with the last choice by elimination, *i.e.* an I2M between the catalyst and the CAN oxidant (Ru-CAN). The problem here lies in CAN, as the structure in the solvent phase is unknown. While we tried to find a suitable geometry, we decided that since we did not have a solid ground on this structure, we would stop this research as it could shift the study's target towards the definition of this CAN structure.

The next projects present a dehydrogenative reaction with a new manganese catalyst that enabled it to become acceptorless since this type of reaction usually requires a sacrificial molecule, or acceptor, to accept the free hydrogens. By eliminating this acceptor, we thoroughly dispose of the waste. Thus, we found it as an excellent example of avoiding waste, and since it was still a new research, it lacked the full mechanism. Even more, this catalyst is one of the most researched types of catalyst nowadays, *i.e.* a PNP pincer catalyst which, as its name implies, has two phosphorous atoms and one nitrogen atom bound to the metal center, as a single ligand. The original theorized mechanism pales in comparison to the complete mechanism we discovered. Not only were we able to locate the r.d.s. of the process, but we also found out the relationship between two experimental isomers that were able to convert one into the other if left alone long enough at room temperature or by heating the mixture for 30 min.

Furthermore, we found that the initial mechanism had an ionic mixture as a possible intermediate, but actually, it is a bond between the Mn center and the substrate's CN ligand. Next, we wanted to delve further into the PNP pincer catalysis, as it shows promising and diversified reactivity; thus, we looked into a second catalyst. This time, we chose a similar catalyst, with an identical reaction temperature, but instead of forming imines like the previous one, it produced aldimines. We were expecting a similar mechanism; even though after several tries, we found out that the catalyst's only job was to transform the reactant alcohol into an aldehyde, which in turn united with the amine to form the aldimines. This last step happens without the catalyst's help, being this the r.d.s. of the reaction.

Continuing with green chemistry, we wanted to study processes related to recycling the waste already generated, such as N_2O and CO_2. We decided to follow up with a PNP pincer catalyst for the first gas, just like the previous projects, since the N_2O converting reaction was tested experimentally with a very similar catalyst that we studied previously. We have determined the full mechanism of this reaction, including a suitable catalyst poisoning, which appears if the environment is dry, revealing that water is a great help as an assistant molecule. A volumetric study of the phosphonate ligands (isopropyl, phenyl, and *tert*-butyl) hinted into which one is optimal for this catalysis and, only through the help of a bond analysis we were able to determine that isopropyl is the best of the three. Additionally, after testing three different PNP pincer ligand catalysts, we propose to combine the three for future research based on the various researched mechanisms' properties.

The last project is about waste recycling and it involves CO_2, the gas most responsible for climate change. To recycle the atmospheric CO_2, we looked into the cyclization of epoxides to obtain a cyclic carbonate. The experimental conditions are already promising since they require 100 ºC but 1 atm of CO_2, meaning that we could reach optimal temperatures if tuned properly while not needing tremendous pressure. In this study, we tested the possibility of removing the commonly used halides as epoxide openers, since they create CO_2 when produced, into N-labile ligands such as DMAP or pyridine. Even more, two possible mechanistic pathways were tested and determined that only one of them is viable. The results show that some ligands precipitate when in contact with CO_2, while in other cases, the r.d.s. are too high in energy. Thankfully, there were two ligands, namely [4] and DMAP, which could perform the reaction and give hope to this research path, where [4] was found to be the best option for halide substitution.

Finally, yet importantly, we wanted to test a different perspective in green chemistry, such as solar cells' production. Solar cells differ significantly in types, so we focused on a fullerene-based cell, which uses the fullerenes as a surface where the photosensitive dyes transfer the electrons through the surface, but we went deeper than that. Instead of using fullerenes, we tested fullerenes inside other fullerenes, also known as carbon nano-onions (CNOs). As solar cells rely on electron movement, we wanted to see if it would be possible to affect them by doping or trapping ions into de nano-onions, as they could emit an electronic field. For that to happen, the CNOs should be perfect Faraday cages. If we trap an ion inside, the outer fullerene should have the same charge as the ion, creating the field we wanted. Unfortunately, our study shows partial charge shielding, which means that these endohedral fullerenes are not perfect Faraday cages for the proposed role.

Overall, we tested several mechanisms and properties towards green chemistry, and we demonstrate that it is possible to improve their related industrial processes to save our planet.

Resum

Segons la cita del Dr. Paul Anastas:

"Tots estem en el mateix vaixell i només tenim un vaixell".

Fòrum de Química Verda de Minnesota, 2013

En aquesta tesi, emfatitzem en aquest pensament. Durant molt de temps hem cregut que tot és rendible, que els recursos són il·limitats i que això no té conseqüències. No obstant això, la realitat és decebedora. L'ús de recursos no renovables, la producció excessiva de residus i la renúncia a la tasca de reciclar-los, ens ha portat a caminar sobre un fil molt fi que, un cop trencat, pot ser que mai es recuperi. Deixant de banda les metàfores, estem parlant del nostre planeta, la Terra, i la seva característica única d'albergar vida, incloent-nos a nosaltres mateixos. El nostre planeta té el seu propi equilibri, quan el vent erosiona una muntanya, apareix una platja, o quan un incendi devasta una àrea, sorgeix nova vida de les cendres. No obstant això, els humans han estat tractant de distorsionar aquest equilibri durant dècades. La nostra forma de vida en evolució ha augmentat la quantitat de recursos que consumeix cada persona, ja sigui com a aliment, refugi o energia; tot s'ha treballat en excés fins a l'esgotament. Fins i tot tenim ara el que es coneix com el Dia de la Sobrecàrrega de la Terra, que té "l'honor" de recordar el dia en què s'han consumit tots els recursos que el planeta crea al llarg d'un any. Ara mateix, aquest dia se situa en el 29 de juliol, la qual cosa significa que per a abastir a cada ésser humà, necessitem els recursos de 1.75 Terres, al ritme normal de recuperació dels recursos naturals. No obstant això, aquest és només un dels problemes que amenacen en el fons de les nostres ments com un mal presagi: el nostre planeta es mor.

Científics de tot el món ja han dit activa i passivament que tenim davant nostre un dels majors problemes que hem enfrontat: el canvi climàtic. Per a moltes persones, només vol dir que farà una mica més de calor a l'estiu i una mica més de calor a l'hivern, res no s'allunya més de la realitat. Tots els éssers vius d'aquest món s'han aclimatat al seu entorn, com els óssos polars amb el seu pelatge transparent per retenir la major part de la calor o els elefants amb les seves grans orelles per alliberar-lo. No obstant això, això s'ha fet al llarg de l'evolució de diversos milers d'anys, i cada ésser va poder adaptar-se o morir en l'intent. Ara estem canviant el clima a un ritme alarmant. La temperatura global de la superfície ha anat augmentant de +0.2 ºC aproximadament des de 1970 fins al voltant de l'any 2000, +0.6 ºC fins al 2015, i ara en el 2020 estem a prop de +0.8 ºC. Això vol dir que en 100 anys, podríem veure una temperatura superficial superior entre +2 ºC i +6 ºC. Això és clarament insostenible i hauríem d'intentar revertir-ho, o si ja no hi ha marxa enrere, frenar-ho tant com sigui possible. Per fer-ho, hi ha moltes formes

possibles d'ajudar. En aquesta tesi, investiguem catalitzadors per utilitzar l'aigua com a font d'energia i per reciclar gasos com el CO_2 i el N_2O, però també busquem formes no catalítiques de generar energia a través de la producció de cèl·lules solars.

Partint de la catàlisi de l'aigua per produir hidrogen, observem el millor catalitzador involucrat en la catàlisi d'oxidació de l'aigua que vam poder trobar: $Ru(bda)(pic)_2$. Aquest catalitzador funciona tan bé com el fotosistema II involucrat en la fotosíntesi d'una fulla, i el secret per a la seva eficiència és el lligand equatorial bda. Inclou carboxilats que es fixen al voltant de l'àtom de Ru, deixant un angle d'obertura prou gran com perquè reaccioni una molècula d'aigua, convertint un Ru octaèdric en un Ru hepta-coordinat, molt més reactiu. Si bé aquest catalitzador es va provar experimentalment, encara faltava el mecanisme complet, de manera que volíem omplir aquests buits per comprendre-ho millor. Més encara, existien discrepàncies entre varis investigadors sobre com funciona el mecanisme, el que ens va fer voler estudiar totes les possibilitats disponibles. Al saber per què i com funciona, és possible introduir modificacions i actualitzar el catalitzador a un de millor. Vam demostrar el mecanisme complet d'aquesta catàlisi, analitzant les diferents propostes d'altres treballs d'investigació, i estudiem la influència del pH sobre el sistema. Vam descobrir que el mecanisme varia lleugerament d'acord amb el pH, ja que hi ha desprotonacions involucrades, però passa només a intermedis amb períodes de vida curts i la reacció general sembla no veure's afectada per aquests canvis. Arran d'aquest treball, vam realitzar un segon projecte modificant aquest catalitzador; més precisament, vam canviar els grups carboxilat en els lligands bda per grups fosfonat, formant el nou lligand $bpaH_2$. Estudis anteriors havien demostrat que el bda supera el $bpaH_2$ i els seus diferents estats de protonació, però la raó encara es desconeix. A més, el $bpaH_2$ requeria nitrat d'amoni cèric (CAN) a pH = 1 perquè en cas contrari no podria passar cap reacció. Moltes d'aquestes peces faltaven, de manera que hem desenvolupat el mecanisme complet de $bpaH_2$ a pH = 1 i pH = 8. Gràcies a això, vam poder observar els diferents estats de protonació de l'$bpaH_2$ que ocorrien en cada pH, i vam revelar els potencials necessaris per desprotonar l'aigua en un lligant oxo. No obstant això, També vam descobrir que la catàlisi no podia procedir a través de cap dels dos mecanismes coneguts, una dimerització que allibera O_2 (I2M) o un atac nucleofílic de l'aigua que havia de desprotonar una molècula d'aigua novament abans d'alliberar l'oxigen (WNA). La raó darrere d'això és que en el cas de l'I2M, els resultats experimentals d'altres autors havien demostrat que es tracta d'una reacció de primer ordre segons el catalitzador, el que significa que el pas limitant de la reacció (r.d.s.) no podria ser un dímer entre catalitzadors, però mentre que la altra opció, WNA, hauria d'haver estat confirmada, vam descobrir que no era possible. Quan analitzem la segona desprotonació d'aigua, el pK_a dels hidrògens era massa alt donat el nostre pH, per tant, el lligant de hidroperòxid ($-OOH_2$) no podia desprotonar. Això ens va deixar una última opció per eliminació, un I2M entre el catalitzador i l'oxidant CAN (Ru-CAN). El problema aquí rau en el CAN, ja que es desconeix l'estructura en fase solvent. Mentre intentàvem trobar una estructura adequada, a la fi vam decidir que, com que no teníem una base sòlida sobre aquesta estructura, aturaríem aquesta investigació ja que podria canviar l'objectiu de l'estudi cap a la definició d'aquesta estructura CAN.

Els següents projectes d'aquest treball, presenten una reacció deshidrogenant amb un nou catalitzador de manganès que li va permetre funcionar sense un acceptor, ja que aquest tipus de reacció sol requerir una molècula de sacrifici, o acceptor, per acceptar els hidrògens alliberats. Al eliminar aquest acceptor, els subproductes no desitjats s'eliminen per complet, de manera que el trobem com un gran exemple per evitar el malbaratament de material, i com encara era una investigació nova, no tenia el mecanisme complet. És més, aquest catalitzador és un dels tipus de catalitzador més investigats en l'actualitat, un catalitzador tipus pinça PNP, que com el seu nom ho indica, té dos àtoms de fòsfor i un àtom de nitrogen unit al metall com un sol lligand. El mecanisme teoritzat original empal·lideix en comparació amb el mecanisme complet que vam descobrir. No només vam poder localitzar el pas limitant del procés, també vam descobrir la relació entre dos isòmers experimentals que es podien convertir un en l'altre si es deixaven sols el temps suficient a temperatura ambient o escalfant la mescla durant 30 minuts.

A més, hem trobat que el mecanisme inicial tenia una barreja iònica com a possible intermedi però, en realitat, és un enllaç entre el centre de Mn i el lligand CN de el substrat. A continuació, volíem aprofundir més en la catàlisi de pinça PNP, ja que mostra una reactivitat diversa i prometedora, de manera que busquem un segon catalitzador. Aquest cop vam triar un catalitzador similar, amb idèntica temperatura, però en lloc de formar imines com l'anterior, va produir aldimines. Encara que esperàvem un mecanisme similar després de diversos intents, vam descobrir que l'únic treball del catalitzador era transformar l'alcohol inicial en un aldehid, que al seu torn s'unia amb l'amina per formar les aldimines. Aquest últim pas es va realitzar sense l'ajuda del catalitzador i és el pas limitant de la reacció.

Continuant amb la química verda, volíem estudiar processos relacionats amb el reciclatge dels residus ja generats, com el N_2O i el CO_2. Per al primer gas, vam decidir seguir amb un catalitzador de pinça PNP, a l'igual que els projectes anteriors, ja que la reacció de conversió de N_2O es va provar experimentalment amb un catalitzador molt similar a què estudiem anteriorment. Hem pogut determinar el mecanisme complet d'aquesta reacció, inclòs un enverinament per catalitzador que apareix si l'ambient està completament sec, el que significa que l'aigua és de gran ajuda com a molècula assistent. Un estudi volumètric dels lligands de fosfonat (isopropil, fenil i *tert*-butil) va insinuar quin és l'òptim per a aquesta catàlisi, tot i que només amb l'ajuda d'una anàlisi dels enllaços vam poder determinar que l'isopropil és el millor dels tres. A més, després de provar 3 catalitzadors de lligand de pinça PNP diferents, proposem aquí una combinació dels tres per a futures investigacions, basats en les diferents propietats dels mecanismes investigats.

L'últim projecte sobre reciclatge de residus involucra el CO_2, el gas més responsable del canvi climàtic. Per reciclar el CO_2 atmosfèric, analitzem la ciclació d'epòxids per obtenir un carbonat cíclic. Les condicions experimentals ja són prometedores, ja que requereixen 100 ºC, però 1 atm de CO_2, el que vol dir que si s'optimitza correctament, podríem arribar a temperatures òptimes sense necessitat d'una gran pressió. En aquest estudi, vam provar la possibilitat d'eliminar els halurs d'ús comú com obridors de l'epòxid, ja que creen CO_2 al produir-los, a lligands N-làbils com DMAP o piridina. És més, es van provar dues possibles vies mecanístiques i es va determinar que només una d'elles és viable. Els resultats mostren que per a alguns lligands, quan entren en contacte amb el CO_2, precipiten, mentre que en altres casos, el pas limitant requereix massa energia. Afortunadament, hi havia dos lligands, [4] i DMAP, que van poder realitzar la reacció i donar esperances a aquest camí d'investigació amb [4] com la millor opció per substituir els halurs.

Per últim, però no menys important, volíem provar un punt de vista diferent en química verda, com la producció de cel·les solars. Les cel·les solars difereixen molt en tipus, pel que ens enfoquem en una cel·la basada en ful·lerens, que fa servir els ful·lerens com una superfície on els tints fotosensibles transfereixen els electrons a través de la superfície, però vam anar més enllà d'això. En lloc d'utilitzar ful·lerens, vam provar els ful·lerens dins d'altres ful·lerens, també coneguts com nano cebes de carboni. Com les cel·les solars depenen del moviment dels electrons, volíem saber si seria possible afectar la transferència, dopant o atrapant ions en nano cebes, ja que podrien emetre un camp electrònic. Perquè això succeeixi, les nano cebes de carboni haurien de ser gàbies de Faraday perfectes. Si atrapem un ió a l'interior, el ful·lerè exterior hauria de tenir la mateixa càrrega que l'ió, creant el camp que volíem. Desafortunadament, el nostre estudi mostra que hi ha un blindatge de càrrega parcial, el que significa que aquests ful·lerens endoèdrics no són gàbies de Faraday perfectes per al paper proposat.

En resum, hem provat diferents mecanismes i propietats dirigides cap a la química verda, i demostrem que és possible millorar els processos industrials involucrats per salvar el nostre planeta.

Resumen

Según la cita del Dr. Paul Anastas:

"Todos estamos en el mismo barco y solo tenemos un barco".

Foro de Química Verde de Minnesota, 2013

En esta tesis, enfatizamos en este pensamiento. Durante mucho tiempo hemos creído que todo es rentable, que los recursos son ilimitados y que eso no tiene consecuencias. Sin embargo, la realidad es decepcionante. El uso de recursos no renovables, la producción excesiva de residuos y la renuncia a la tarea de reciclarlos, nos ha llevado a caminar sobre un hilo muy fino que, una vez roto, puede que nunca se recupere. Dejando de lado las metáforas, estamos hablando de nuestro planeta, la Tierra, y su característica única de albergar vida, incluyéndonos a nosotros mismos. Nuestro planeta tiene su propio equilibrio, cuando el viento erosiona una montaña, aparece una playa, o cuando un incendio devasta un área, surge nueva vida de las cenizas. Sin embargo, los humanos han estado distorsionando este equilibrio durante décadas. Nuestra forma de vida en evolución ha aumentado la cantidad de recursos que consume cada persona, ya sea como alimento, refugio o energía; todo se ha trabajado en exceso hasta el agotamiento. Incluso tenemos ahora lo que se conoce como el Día de la Sobrecarga de la Tierra, que tiene el “honor” de recordar el día en el que se han consumido todos los recursos que el planeta crea a lo largo de un año. Ahora mismo, este día se ubica en el 29 de julio. Esto significa que, para abastecer a cada ser humano, necesitamos los recursos de 1.75 Tierras, al ritmo normal de recuperación de los recursos naturales. Sin embargo, este es solo uno de los problemas que acechan en el fondo de nuestras mentes como un mal presagio: nuestro planeta se muere.

Científicos de todo el mundo ya han dicho activa y pasivamente que tenemos frente a nosotros uno de los mayores problemas que hemos enfrentado: el cambio climático. Para muchas personas, solo significa que hará un poco más de calor en verano y un poco más de calor en invierno, nada más lejos de la realidad. Todos los seres vivos de este mundo se han aclimatado a su entorno, como los osos polares con su pelaje transparente para retener la mayor parte del calor o los elefantes con sus grandes orejas para liberarlo. Sin embargo, esto se ha hecho a lo largo de la evolución de varios miles de años, y cada ser pudo adaptarse o morir en el intento. Ahora estamos cambiando el clima a un ritmo alarmante. La temperatura global de la superficie ha ido aumentando, +0.2ºC aproximadamente desde 1970 hasta alrededor del año 2000, +0.6ºC en 2015 y ahora +0.8ºC en 2020. Esto significa que, en 100 años, podríamos ver una temperatura superficial superior, entre +2ºC y +6ºC. Esto es claramente insostenible y deberíamos intentar revertirlo, o si ya no hay vuelta atrás, frenarlo tanto como sea posible. Para

hacerlo, hay muchas formas posibles de ayudar. En esta tesis, investigamos catalizadores para utilizar el agua como fuente de energía y para reciclar gases como el CO_2 y el N_2O, pero también buscamos formas no catalíticas de generar energía a través de la producción de células solares.

Partiendo de la catálisis del agua para producir hidrógeno, observamos el mejor catalizador involucrado en la catálisis de oxidación del agua que pudimos encontrar: $Ru(bda)(pic)_2$. Este catalizador funciona tan bien como el fotosistema II involucrado en la fotosíntesis de una hoja, y el truco para su eficiencia es el ligando ecuatorial bda. Incluye carboxilatos que se fijan alrededor del átomo de Ru, dejando un ángulo de apertura lo suficientemente grande como para que reaccione una molécula de agua, convirtiendo un Ru octaédrico en un Ru hepta-coordinado, mucho más reactivo. Si bien este catalizador se probó experimentalmente, aún faltaba el mecanismo completo, por lo que queríamos llenar esos vacíos para comprenderlo mejor. Más aún, existían discrepancias entre diversos investigadores sobre cómo funciona el mecanismo, lo que nos hizo querer estudiar todas las posibilidades disponibles. Al saber por qué y cómo funciona, es posible introducir modificaciones y actualizar el catalizador a uno mejor. Demostramos el mecanismo completo de esta catálisis, analizando las diferentes propuestas de otros trabajos de investigación, y estudiamos la influencia del pH sobre el sistema. Descubrimos que el mecanismo varía ligeramente de acuerdo con el pH, ya que hay desprotonaciones involucradas, pero ocurre solo en intermedios con períodos de vida cortos y la reacción general parece no verse afectada por estos cambios. A raíz de este trabajo, realizamos un segundo proyecto modificando este catalizador; más precisamente, cambiamos los grupos carboxilato en los ligandos bda por grupos fosfonato, formando el nuevo ligando $bpaH_2$. Estudios anteriores habían demostrado que el bda supera al $bpaH_2$ y sus diferentes estados de protonación, pero la razón aún se desconoce. Además, el $bpaH_2$ requería nitrato de amonio cérico (CAN) a pH = 1 porque de lo contrario no podría ocurrir ninguna reacción. Muchas de estas piezas faltaban, por lo que desarrollamos el mecanismo completo de $bpaH_2$ a pH = 1 y pH = 8. Gracias a ello, pudimos observar los diferentes estados de protonación del $bpaH_2$ que ocurrían en cada pH, y revelaron los potenciales necesarios para desprotonar el agua en un ligando oxo. Sin embargo, También descubrimos que la catálisis no podía proceder a través de ninguno de los dos mecanismos conocidos, una dimerización que libera O_2 (I2M) o un ataque nucleofílico del agua que debía desprotonar una molécula de agua nuevamente antes de liberar el oxígeno (WNA). La razón detrás de esto es que en el caso del I2M, los resultados experimentales de otros autores habían demostrado que se trata de una reacción de primer orden según el catalizador, lo que significa que el paso limitante de la reacción (r.d.s.) no podría ser un dímero entre catalizador, pero mientras que la otra opción, WNA debería haber sido confirmada, descubrimos que no era posible. Cuando analizamos la segunda desprotonación de agua, el pK_a de los hidrógenos era demasiado alto dado nuestro pH, por lo tanto, el ligando de hidroperóxido ($-OOH_2$) no podía desprotonar. Esto nos dejó una última opción por eliminación, un I2M entre el catalizador y el oxidante CAN (Ru-CAN). El problema aquí radica en el CAN, ya que se desconoce la estructura en fase solvente. Mientras intentábamos encontrar una estructura adecuada, al final decidimos que, dado que no teníamos una base sólida sobre esta estructura, detendríamos esta investigación, ya que podría cambiar el objetivo del estudio hacia la definición de esta estructura CAN.

Los siguientes proyectos de este trabajo presentan una reacción deshidrogenante con un nuevo catalizador de manganeso que le permitió funcionar sin un aceptor, ya que este tipo de reacción suele requerir una molécula de sacrificio, o aceptor, para aceptar los hidrógenos liberados. Al eliminar este aceptor, los subproductos no deseados se eliminan por completo, por lo que lo encontramos como un gran ejemplo para evitar el desperdicio de material, y como aún era una investigación nueva, carecía del mecanismo completo. Es más, este catalizador es uno de los tipos de catalizador más investigados en la actualidad, un catalizador tipo pinza PNP, que como su nombre lo indica, tiene dos átomos de fósforo y un átomo de nitrógeno unido al metal como un solo ligando. El mecanismo teorizado original palidece en comparación con el mecanismo completo que descubrimos. No solo pudimos localizar el r.d.s. del proceso, también descubrimos la relación entre dos isómeros experimentales que podían convertir uno en el otro si se dejaban solos el tiempo suficiente a temperatura ambiente o calentando la mezcla durante 30 minutos.

Además, vimos que el mecanismo inicial tenía una mezcla iónica como posible intermedio, pero en realidad es un enlace entre el centro de Mn y el ligando CN del sustrato. A continuación, queríamos profundizar más en la catálisis de pinza PNP, ya que muestra una reactividad diversa y prometedora, por lo que buscamos un segundo catalizador. Esta vez elegimos un catalizador similar, con idéntica temperatura, pero en lugar de formar iminas como el anterior, produjo aldiminas. Aunque esperábamos un mecanismo similar después de varios intentos, descubrimos que el único trabajo del catalizador era transformar el alcohol inicial en un aldehído, que a su vez se unía con la amina para formar las aldiminas. Este último paso se realizó sin la ayuda del catalizador y es el paso limitante de la reacción.

Continuando con la química verde, queríamos estudiar procesos relacionados con el reciclaje de los residuos ya generados, como el N_2O y el CO_2. Para el primer gas, decidimos seguir con un catalizador de pinza PNP, al igual que los proyectos anteriores, ya que la reacción de conversión de N_2O se probó experimentalmente con un catalizador muy similar al que estudiamos anteriormente. Hemos podido determinar el mecanismo completo de esta reacción, incluido un envenenamiento por catalizador que aparece si el ambiente está completamente seco, lo que significa que el agua es de gran ayuda como molécula asistente. Un estudio volumétrico de los ligandos de fosfonato (isopropilo, fenilo y terbutilo) insinuó cuál es el óptimo para esta catálisis, aunque solo con la ayuda de un análisis de los enlaces pudimos determinar que el isopropilo es el mejor de los tres. Además, después de probar tres catalizadores de ligando de pinza PNP diferentes, proponemos aquí una combinación de los tres para futuras investigaciones, basados en las diferentes propiedades de los mecanismos investigados.

El último proyecto sobre reciclaje de residuos involucra al CO_2, el gas más responsable del cambio climático. Para reciclar el CO_2 atmosférico, analizamos la ciclación de epóxidos para obtener un carbonato cíclico. Las condiciones experimentales ya son prometedoras, ya que requieren 100 ºC, pero 1 atm de CO_2. Esto significa que, si se optimiza correctamente, podríamos alcanzar temperaturas óptimas sin necesidad de una gran presión. En este estudio, probamos la posibilidad de eliminar los haluros de uso común como abridores del epóxido, ya que crean CO_2 al producirlos, en ligandos N-lábiles como DMAP o piridina. Es más, se probaron dos posibles mecanismos y se determinó que solo uno de ellos es viable. Los resultados muestran que, para algunos ligandos, cuando entran en contacto con el CO_2, precipitan, mientras que, en otros casos, el paso limitante requiere demasiada energía. Afortunadamente, había dos ligandos, [4] y DMAP, que pudieron realizar la reacción y dar esperanzas a este camino de investigación, siendo [4] la mejor opción para la substitución de haluros.

Por último, pero no menos importante, queríamos probar un punto de vista diferente en química verde, como la producción de células solares. Las células solares difieren mucho en tipos, por lo que nos enfocamos en una célula basada en fullereno, que usa los fullerenos como una superficie donde los tintes fotosensibles transfieren los electrones a través de la superficie, pero fuimos más allá de eso. En lugar de usar fullerenos, probamos los fullerenos dentro de otros fullerenos, también conocidos como nanocebollas de carbono. Como las células solares dependen del movimiento de los electrones, queríamos saber si sería posible afectarlas dopando o atrapando iones en nanocebollas, ya que podrían emitir un campo electrónico. Para que eso suceda, las nanocebollas de carbono deberían ser jaulas de Faraday perfectas. Si atrapamos un ion en el interior, el fullereno exterior debería tener la misma carga que el ion, creando el campo que queríamos. Desafortunadamente, nuestro estudio muestra que hay un blindaje de carga parcial, lo que significa que estos fullerenos endoédricos no son jaulas de Faraday perfectas para el rol propuesto.

En resumen, hemos probado diferentes mecanismos y propiedades dirigidos a la química verde, demostrando que es posible mejorar los procesos industriales estudiados, para salvar nuestro planeta.

Chapter 1. Introduction

1.1. Environmental crisis

The Earth is about 4.5 billion years old, and the oldest known fossil is about 3.8 billion years old. This gives a rough estimate of when life began. Our ancestors have proliferated for only 6 million years, and our species, the Homo Erectus, evolved around 2 million years ago. Throughout our existence, civilization began 6000 years ago, followed by the industrialization of humankind which started in the 18th century, barely 260 years ago. Despite having existed on our planet for such a short time, we have been able to modify the entire ecosystem for ourselves in this short period of 220 years.

Currently, we have many global problems that have arisen due to our negligence, and the only way to solve them before it is too late is to try to combine all humanity's efforts.

1.1.1. Global pollution

We need industrial processes such as food factories, vehicle production, IT businesses, and many more. They require the use of all our needs, such as clean air, water, and soil, every day. We pollute the air due to the tons of CO_2, N_2O, and other harmful gases that we release, resulting from all our motorized vehicles and production plants' exhaust pipes without any environmental concern (***Figure 1a***).[2] Our soil is absorbing all the waste material generated by the industry, such as red mud; an iron-containing mud formed by the extraction of the aluminum in bauxite, which currently has no useful utility, creates vast wastelands, and leaks its iron contents into the soil, leaving it sterile (***Figure 1b***).[3] We also contaminate our water due to accidental spillages like the Kuwaiti Oil Fires,[4] which leaked 136 million tons of crude oil into the Persian Gulf Sea in the year 2000.

Moreover, the enormous amounts of plastics dumped into the ocean are enough to create the Great Pacific garbage patch.[5] It is an island made entirely of plastic waste that has a size of around 1.6 million square kilometers, 2.6 times the whole length of the

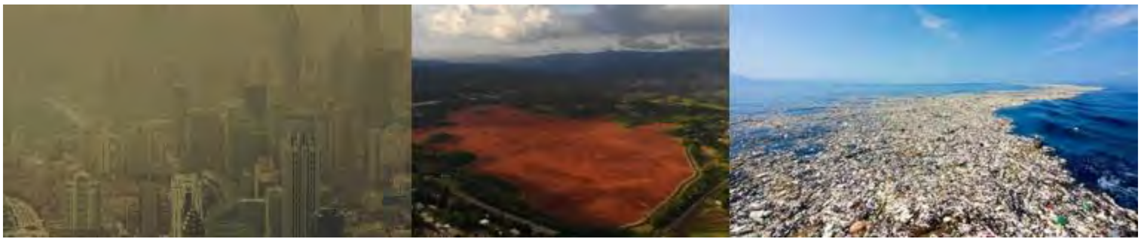

Figure 1. a) Air pollution in Shanghai, China. b) Red mud lake in Mandeville, Louisiana. c) Part of the Pacific Ocean garbage patch.

Iberian Peninsula (***Figure 1c***). These problems arose to cater to the people's needs, but there are more than 7 billion humans on Earth, and the number is growing, which projects a dangerous future.

1.1.2. Climate change

With such an impact on our planet, it is evident that all the mentioned issues entwine, developing into global problems that affect everyone simultaneously, not only to the nearest group of each polluting site. Together, we have developed the most remarkable and notorious problem that gains the most recognition: climate change.

To explain what climate change is, we have first to define the climate: a set of weather patterns related to a specific location that will remain the same for extended periods (thousands of years). The atmosphere obtains most of its energy from the Sun and a small part from the Earth's core. The energy balance is simple; if the energy taken from the Sun and the Earth is greater than the heat going out to the outer space, we obtain a Global Warming effect (***Figure 2***), while if it is the opposite, a Global Cooling effect. Overall, we define climate change as the change in weather patterns (climate) of a specified region, in this case, the whole planet itself, depending on the biosphere's energy input and output.

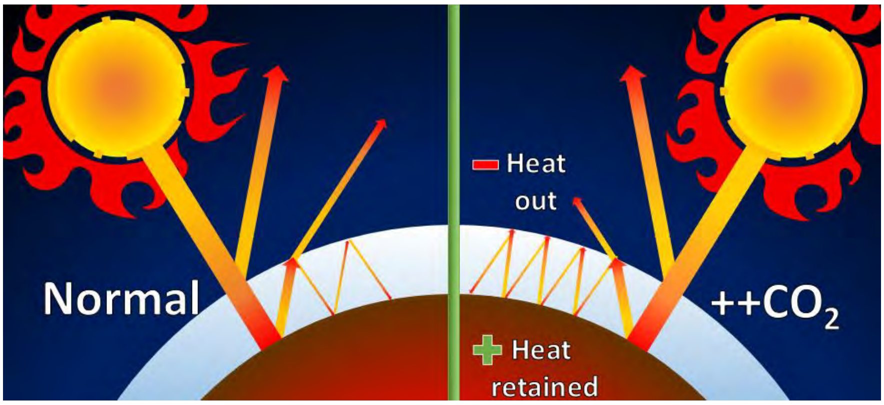

Figure 2. Global warming effect. The addition of significant amounts of CO_2 to the atmosphere increases the radiation bouncing back to Earth, heating it more than it should.

According to these data, while climate change occurs since the beginning, as individuals, we barely should be able to see it or not see it at all, as the climate has been stable for periods longer than our lifespan. However, we must take into account humankind's work. The reason for the Earth to be able to harbor life is because first, it orbits in the habitable zone of our solar system, and second, it was able to create an atmosphere, which is a gas distribution of the different elements that are part of the air (H_2, O_2, CO_2…). The planet retains these components thanks to its gravity, and one of the essential works they do is insulate the Sun's radiation.

As stated above, the vast majority of the planet's energy comes from the Sun in the form of radiation. Without an atmosphere, all the radiation would hit the ground, a tiny part would get absorbed, and then the rest would bounce off to outer space. This phenomenon would not be enough to heat the planet, and it would become an icy rock. Thanks to the atmosphere, we do not receive all the radiation on the Earth's surface, such as most UV radiation that is dangerous for life, as it can damage cells. Furthermore, the atmosphere acts as a radiation mirror that bounces it off to the surface, so that it heats the surface again instead of losing the energy at once. Humankind industrialization can alter the amounts and composition of the atmosphere to extraordinary limits. Fossil fuel burning and other industrial processes have increased the ratio of carbon dioxide (CO_2), nitrous oxide(N_2O), sulfur oxide (SO_2), and other gases such as chlorofluorocarbons (CFCs) considerably.[6] These changes in composition create different problems, some of which we explain in the following sections.

1.1.2.1. CO_2 and Global Warming

The gas with more significant amounts spilled towards the atmosphere is CO_2. Any burning process like using fossil fuels or breathing produces it (***Figure 3***).[7] CO_2 is a very inert gas that is not directly harmful to life, though the daily anthropogenic contribution is astronomical.[7-8] One of these gas's particularities is that it is an excellent infrared reflector, or in other terms, it is a heat mirror.[9] Instead of letting the radiation leave the planet, only a fraction does, and the rest comes back to the Earth to reheat it again. With more significant quantities of CO_2, more radiation is sent to reheat the planet. This process name is the Greenhouse effect.[10] As a reference, according to the National Oceanic and Atmospheric Administration, NOAA, if we did not have any greenhouse effect gases, the temperature of our planet would average -18 ºC, while thanks to them, we can be comfortable at 20 ºC in our daily lives.[11]

Abuse of our production and consumption methods has led us to higher temperatures that steadily increase each year. In September 2019, the average surface temperature was 0.95 ºC above the whole 20th century (***Figure 4***). Almost 1 ºC may not appear to be much, but should we put it into perspective, in the past 150 years, we have been heating the oceans about a thousand times the worldwide annual energy consumption, or 1.5 Hiroshima nuclear bombs per second.[12-13] The temperature will keep rising between 1.4 to 5.6 ºC in the current century.[14]

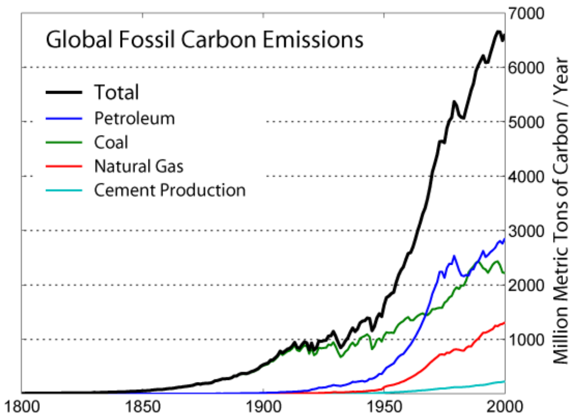

Figure 3. Annual global emission of CO_2 in million tons throughout 200 years.

Besides going further to less optimal temperatures for sustainable life, we observe problems that depend on Global Warming. We see anomalies nowadays and natural disasters, such as hurricane Dorian, category 5, which struck the Bahamas in September 2019,[15] or the melting of the ice caps, which if they disappeared entirely, the water level would rise approximately 70 meters.[16] In that case, we also have to consider that the amount of freshwater introduced to the ocean could change our oceans' sea currents, altering the whole planet's weather drastically.[18-19]

With everything said, the actual worldwide topic lies in abandoning fossil fuel burning and CO_2 recycling or storage to avoid the worst possible outcome.

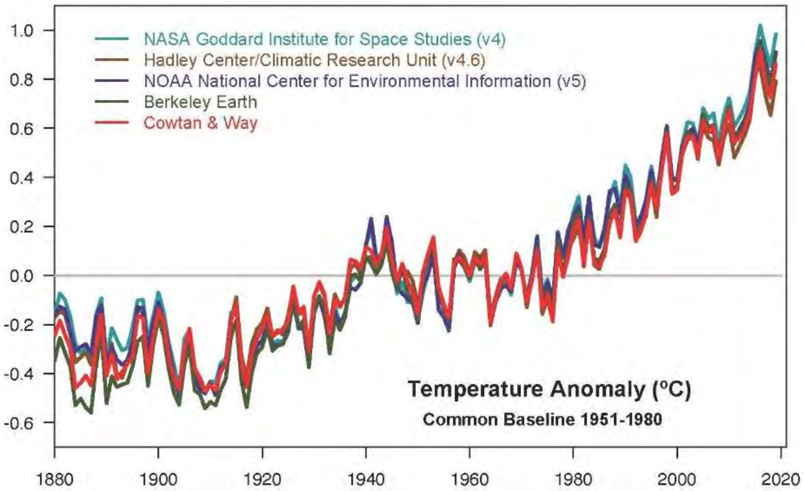

Figure 4. Annual temperature in Celsius recorded by NASA, NOAA, the Berkeley Earth research group, the Met Office Hadley Centre (UK), and the Cowtan and Way analysis from 1880 to 2019.[17]

1.1.2.2. N_2O, SO_2, and the acid rain

CO_2 is undoubtedly one of the most notorious gases we produce every day, responsible for over 60% of the Greenhouse effect, but others to consider like N_2O and SO_2, when combined with water, create acid rain.

N_2O has a steady-state lifetime of 120 years, which means that it has been accumulating in the air over the past decades.[18] The Environmental Protection Agency of the United States (EPA) recorded in 2010 that out of the 29.5 tons emitted of N_2O to the atmosphere, 36% is humankind's responsibility.[19] Due to the proportionally low amount emitted of N_2O compared to the amount of CO_2, we could consider it as a minor problem. Nevertheless, N_2O has three hundred times the efficiency of CO_2 at reflecting the infrared radiation.[20] This means that the only reason CO_2 is the primary problem for the Greenhouse effect is the massive amounts produced. Several developments and research helped control the CFCs;[24] thus, N_2O is one of the principal causes of the ozone layer hole (see section 1.2.2).

We can find another critical gas, sulfur dioxide, at atmospherical concentrations of 1 ppm and a life span of days to weeks. Nonetheless, concentrated emission can occur, mainly due to volcanic activity that releases around 20 million tons of SO_2.[21] Luckily, in an industrial process such as coal burning, where we find high amounts of sulfur, we have already found solutions to avoid the creation of this gas. The Claus process[22] can produce sulfur as a byproduct, while the Stretford process can remove it from the fuel before burning. Furthermore, we have retained most of the SO_2 formed in power plants that burn sulfur-containing coal thanks to calcium oxide (CaO) filters.[23] When both react, we obtain calcium sulfite ($CaSO_3$) to recover, after oxidation, calcium sulfate ($CaSO_4$).

Acid rain is the combination of both gases in the atmosphere with water droplets. Sulfur dioxide converts to sulfuric acid, while N_2O (and any other nitrogen oxide) converts into nitric or nitrous acid.[24] This rain can be highly acidic, like in the Poás Volcano in Costa Rica or the Kilauea in Hawaii (pH = 2), and affect its surroundings.[25-26] Such acidic conditions are killing most, if not all, fish species and microbiological life that live in lakes or rivers affected by the rain. While animals can be irritated or even burnt from the rain's exposure, they are struck indirectly due to the soil pH. The plants feeding on the soil nutrients can die due to nutrients leaching and the mobilization of toxic ions such as aluminum to the surface,[27-28] and the acid's prolonged exposition.

With everything we said, while the sulfur dioxide is controlled and monitored, the impact of the N_2O we emit may not be evident, but the potential risks are there. Therefore, it is in our primary interest to find ways for the use of this gas.

1.1.2.3. CFCs and the ozone layer

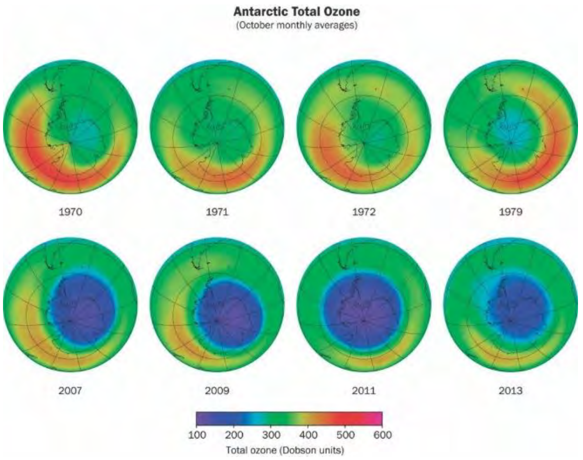

Figure 5. Satellite observations of the Ozone layer by the NASA until 2013.

As for the last gases, the CFCs, we know them for their usefulness in creating bubbles in rigid plastics, grease or glue cleaners, or as vaporizers for pesticides, spray paint, and many more.[29] However, once these gases release into the atmosphere, they perform a photometric reaction, which gives a chloride radical. This radical has an excellent affinity for Ozone (O_3), and to make things worse, it undergoes a catalytic reaction, which means that a single chlorine radical can break up to 100.000 O_3 molecules. Ozone is the best UV radiation absorber enveloping the Earth, giving us protection, and, for this reason, we denominate it as the Ozone layer. Without it, we would surely perish. Thankfully, we have stopped most of these CFCs' usage that created a hole in the Ozone layer and began the required environmental repairs.[30-31]

1.1.3. Energy dependence

The environmental impact discussed in the previous section involves many different variables, such as factory production. Nevertheless, one of the most outstanding issues, the excessive CO_2 production, is society's energy needs. With innovation and technology, we require more energy to power up our vehicles, phones, and computers and create an increasing energy demand. Energy production in a power plant needs either fossil fuels or renewable resources to work.

Fossil fuels are a source of non-renewable energy generated over millions of years of organic matter buried in the ground where we can distinguish mainly three different sources: natural gas, crude oil, and coal. All the sources contain carbon atoms in varying amounts, which, if burnt, generate CO_2. They are a good source of money, as we need only to collect, refine, and burn to produce tremendous amounts of energy. Even if they are non-renewable, there are massive deposits globally; however, we have steadily depleted them during our industrialization process that began 260 years ago.

The scientific community estimated that in 2042 we would run out of crude oil, in 2044 of natural gas, and in 2112 of coal.[32] We may have underestimated these values, as there are factors such as the industrialization of developing countries or the increase in population that could quickly reduce the amount we have left (***Figure 6***).[33-35]

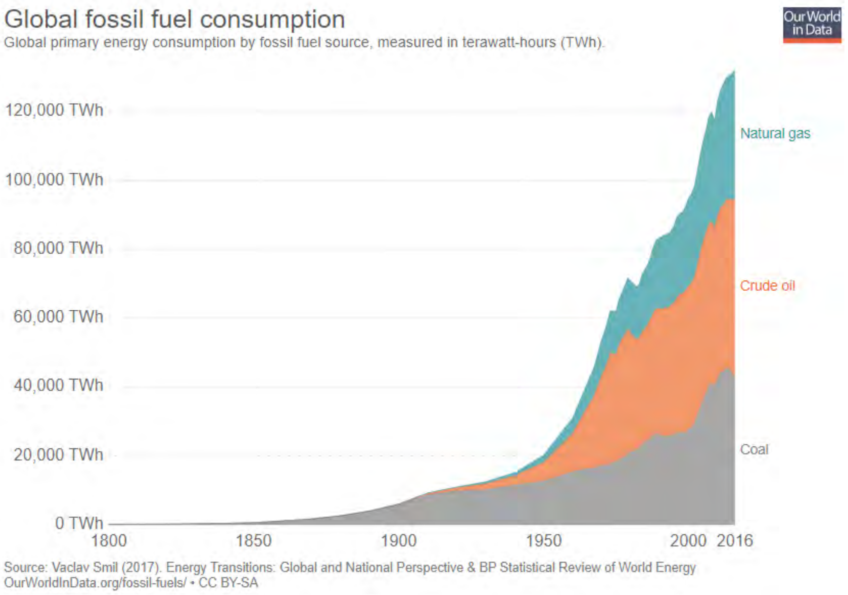

Figure 6. Global fossil fuel consumption between 1800 and 2016.

This means that at best, we currently have between 20 and 25 years before we will be not able to drive diesel or gas cars, as there will not be any fuel left. Even earlier, the price it would reach near their depletion would become astronomical, so it is clear that the less wealthy already have less time than the rest. Looking optimistically, if we end up burning every non-renewable source of our planet, and we are still able to live in it, at least we will no longer have the power to harm/affect our atmosphere as much as now.

The best choice right now is to use renewable energy sources. These sources should be clean, unlimited, and rich in energy. We are developing the technology to do it efficiently; thus, they are more expensive and less profitable than fossil fuels. Still, we have different choices to look for, like harnessing water's kinetic energy in hydroelectric plants. This power plant is built in large rivers or dams, holding vast amounts of water that passes through a set of turbines, creating electricity when released.

Nevertheless, it has a crucial flaw: water needs to go through the turbine; therefore, this is not a reliable energy income as one can expect dry seasons; thus, there might not be enough water to power up the plant. Another choice is wind turbines that can harvest the wind's kinetic energy, as their name implies. Once again, these have the same problem as the hydroelectric power plants: it might not have enough wind to fill our energy quota. Furthermore, they have other issues like wind direction. As they are huge fans, only the wind that is parallel to the blades will move them. They also contribute to the so-called visual pollution, as the size and amount of wind turbines needed to make enough energy usually transform the landscape, leaving a fearful sight for Don Quixote (***Figure 7***).

Figure 7. Photo of a group of wind turbines that represent visual pollution.

These two previous sources are not reliable enough (yet) to use them as our primary energy source because they are neither constant nor energy-rich. Nevertheless, there is a prosperous and reliable source: nuclear power. In nuclear power plants, we use the heat produced in nuclear fission (***Figure 8***) to heat water, convert it into steam, and make it go through a turbine. Technically, it is clean energy because we do not produce CO_2; however, nuclear fission requires radioactive materials. To perform nuclear fission, we have a set of neutron-enriched uranium put together on the reactor. We profit from their radioactivity to release free neutrons that will hit nearby enriched atoms, splitting them into two. By doing so, we get an incredible amount of energy from this exothermic reaction that gets converted into kinetic energy for the particles involved and thermic energy that will heat water to convert it to steam. While this is a highly energetic process, the result is that we consume this radioactive material until radioactive isotopes which we can no longer use for energy production appear. Those radioactive isotopes are what we call nuclear waste. Once again, there is a catch: it will continue to be radioactive for up to tens of thousands of years. Thus, we cannot only store it. To decrease the radiation's impact, we seal the waste in huge lead barrels and then bury them deep in the ground, creating nuclear cemeteries. Of course, that is not flawless. Over the years, the radioactive material will start emitting into the soil and permeate its surroundings. Additionally, the safety risks involved include long-lasting radiation that will damage the affected zone such as Fukushima[36] or Chernobyl,[37] and points towards the fear of the population and possible future damages to the ecosystem.

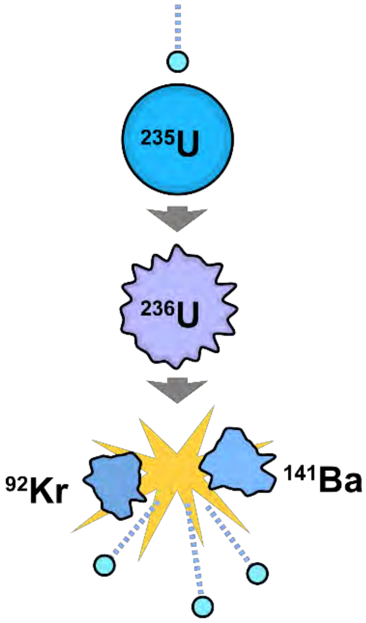

Figure 8. Nuclear fission of ^{235}U

The ideal solution would be to have something as energetic as a nuclear reaction without dealing with all the waste and risks involved. Luckily, we have been using it since the very beginning: an everlasting self-sustainable nuclear reactor, which is so far away that the problems described are non-existent: the Sun. It fulfills its role as an unlimited source, as we want to use the radiation emitted by its reactions, and should the Sun ever deplete; we would no longer need the energy. It is clean and highly energetic, ideal for our needs. The main issue now is how to harvest its energy for our consumption.

There are two possible approaches; one is direct: convert the radiation we receive directly into electricity. A clear example is solar cells, which scientists develop using different materials like fullerenes.[38-40] The other is indirect: create clean fuels using this radiation, like hydrogen production from the water oxidation reaction for its posterior consumption.

1.2. Catalysts

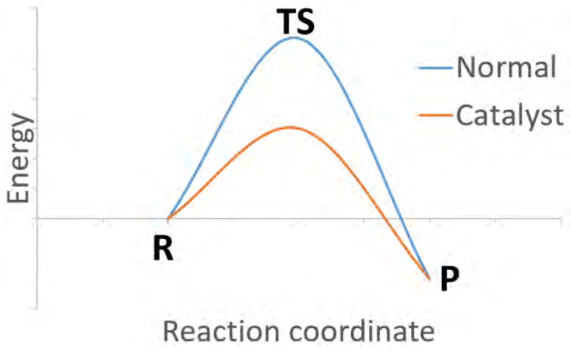

Figure 9. Effect of a catalyst in the PES of a reaction.

Before going into further details and considering that we want to be more efficient, we need to connect the solar radiation with a specific reaction. If we use water oxidation as an example, it happens slowly. If it occurred naturally at the required speed, water would be a very scarce resource. It is not the case, though, so we need something that speeds it up. This "something" should be selective to our target reaction; it should be able to do it as many times as possible before decomposing, it should be as environmentally friendly as possible, and most importantly, it should be able to decrease the energy demands of our target reaction and perform it at our desired speed. This desired molecule is known as a catalyst.

Tailoring catalysts to specific needs is an art. In our case, we want to take advantage of solar radiation. Thus, we need to connect them with photons, yet, it is unnecessary to entangle catalyst efficiency with them; photons can become an electron source in our media, and those electrons will later get involved in the catalyst mechanism. For instance, in a chlorophyll pigment's chloroplast stroma, located on a leaf, we can observe Photosystems I and II (see section 1.2.1.1). These systems can capture a photon and use it to excite an electron to a higher energy level, which is transferred to an electron-acceptor molecule, pheophytin. Once we have promoted the electron, a chain of reactions occurs towards the chloroplast's light-dependent reactions. These chain reactions are nature's answer to light conversion into chemical energy. Therefore, the aim is to reproduce its effects with a human-made light acceptor that can release excited electrons. Therefore, it is possible to focus on catalyst design and optimization while thinking about light to obtain the required electrons.

1.2.1. Hydrogen production

From an indirect approach of sunlight conversion into a useful chemical, choosing what to produce is mandatory. It must be highly energetic and easy to produce, and when it burns to produce energy, it must not generate CO_2 in the process. This ideal implies discarding all carbon-based fuels. A fine choice is molecular hydrogen (H_2), in the sense that its combustion will only produce water ((1).

$$2\ H_2{}^{gas} + O_2{}^{gas} \rightarrow 2\ H_2O^{gas} \tag{1}$$

Compared to hydrocarbon fuels, 1 Kg of hydrogen produces the same amount of energy as 2.8 Kg of gasoline.[41] This appears to be ideal, as with less fuel, we obtain the same energy, and the combustion products are non-toxic; however, that is far from reality. It is imperative to understand this statement to know the properties of hydrogen.[42] First, hydrogen is a gas, which means that it fills the entire container available and, to increase the amount stored, it must be pressurized. The hydrogen density under ambient temperature and pressure is 0.00009 Kg/L; thus, storing 1 Kg of hydrogen needs a container of over 10 thousand liters, which is not practical. If the hydrogen is pressurized to 700atm, its density becomes 0.038 Kg/L, so that we could use a 26 L tank for 1 Kg. Another option is to liquefy it by cooling it to temperatures lower than 20 K, obtaining thus a density of 0.07 Kg/L, where a 14 L tank would suffice.[43-44] Overall, we obtain the same amount of energy from a 14 L liquefied H_2 tank at 20 K than a 3.8 L tank of gasoline at room temperature. Besides, there are further problems with hydrogen, such as the liquid's boil-off, which increases the tank's pressure and loses 1% of its contents per day,[45] or the high risk of explosion, as it is extremely flammable.[46] One of the most remarkable hydrogen accidents in history is the Hindenburg disaster, New Jersey 1937, where the German zeppelin LZ 129 Hindenburg ignited, causing 36 victims. If hydrogen must become a reliable energy source, developing better-storing conditions is a must-have for safer fuel storage in our vehicles. Many materials ranging from carbon nanotubes,[47] glass arrays,[48] and activated carbons[49] have been tested for their storage, but they suffer from either low absorption (requiring more material for storage) or too high absorption (not possible to recover the H_2).

Nevertheless, there is still one option; to produce hydrogen *in situ* according to our needs. With this approach, storage would not be a problem if the source of hydrogen was safe. Fortunately, water is a source of hydrogen. It is often safer to store water in a deposit than compressed or liquefied hydrogen; furthermore, if we use water as a source, we obtain water due to H_2 combustion; it is the definition of a renewable source of energy. There are two main pathways to obtain hydrogen from water: water splitting and water oxidation.

1.2.1.1. Water-splitting

We define the water-splitting reaction as water breaking down into both hydrogen and oxygen:

$$2\,H_2O \rightarrow 2\,H_2 + O_2 \tag{2}$$

This reaction is also present in the photosynthesis at PSII (***Figure 10***).[50] On the light-dependent phase, a photon is absorbed into the PSII, which excites an electron, starting an electron chain reaction that will convert CO_2 into sugars and oxygen gas. Water dissociates into oxygen gas and protons to recover the excited electron in the PSII. This reaction loads the inner part of the membrane with protons and creates a gradient. The ATP synthase uses such a gradient and releases the protons to the outside. Once at the outer part of the membrane, the protons react at the ferredoxin- NADP reductase (FNR), where they convert NADP into NADPH.

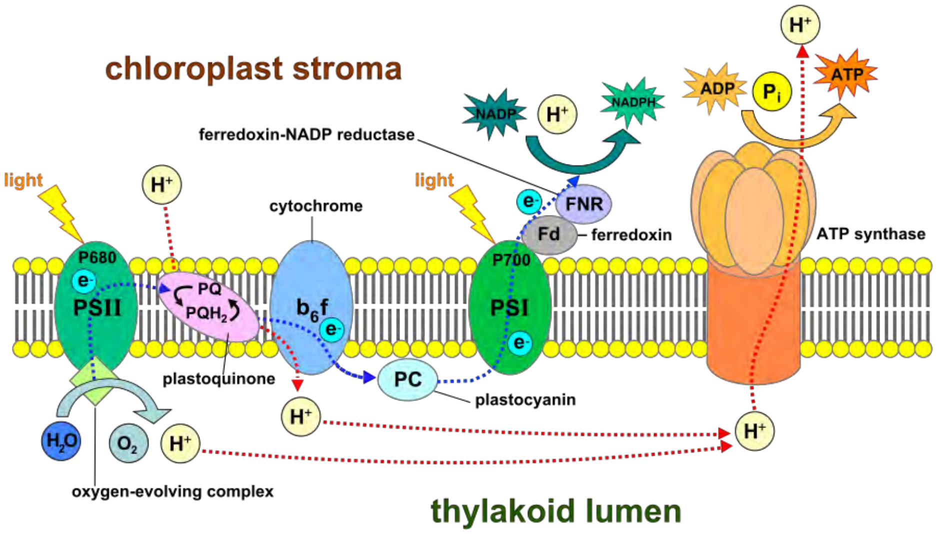

Figure 10. Representation of the photosynthesis mechanism in a thylakoid membrane.[1]

They also return to the plastoquinone to reduce it into plastoquinol, thus restarting the whole process.

Photosynthesis is a refined multi-step process that we would like to reproduce, more precisely, the water dissociation through light. Nevertheless, scaling it for commercial use has its flaws. There are several ways to produce water splitting such as electrolysis, radiolysis, and thermal decomposition.[51-53]

Water electrolysis occurs once we apply an electric current of at least 1.23 V into the water through two electrodes. This energy can separate water into H_2 and O_2 gas, and it is pH-independent. However, the energy needed to produce the H_2 gas is more valuable than the one produced by burning the hydrogen obtained, and since the efficiency of the reaction is not 100%, it needs even more. The right approach would be attaching solar panels that produce electricity, which we want to store as chemical power, but still, neither the electrolysis nor the solar cells are very efficient, which translates into a net energy loss. A production plant for hydrogen storage could be the right choice if we needed the gas for synthesis, nonetheless.

Radiolysis benefits from nuclear radiation, more precisely from alpha radiation (He^{+2} nuclei emitted from a larger radioactive material). When using alpha radiation to split water, it converts into different radicals and ions (Eq. 3).[54]

$$H_2O \xrightarrow{\alpha} e^-_{aq}, HO\cdot, H\cdot, HO_2\cdot, H_3O^+, OH^-, H_2O_2, H_2 \qquad (3)$$

As seen above, water radiolysis gives both ions, radicals, and hydrogen. Even if the possible combinations could lead towards water or ozone, it is possible to recover and reuse them until the desired hydrogen production increases. Since it bases on alpha radiation, it could be a possible solution for nuclear waste (section 1.1.3), producing hydrogen while containing the waste, with all risks considered. Even if this can be an efficient choice for producing and storing hydrogen, as an *in situ* production, it is not the best.

Thermal decomposition of water involves high temperatures to dissociate it into a combination of hydrogen and oxygen gas and H, O, and OH radicals. There is a solar-thermal hydrogen producer in Almeria, Spain that concentrates sun rays using mirrors to reach 1000K that combines gas diffusion gradients optimizations to produce ~1 Kg of H_2 per hour, which is roughly 33.3 Kw/h.[55]

Water splitting requires significant amounts of energy to occur. Nevertheless, there is still one possibility: to use catalysts, or even better, photocatalysts. These catalysts focus on the reduction and oxidation of water, hydrogen, and oxygen. The main goal is to mimic the PSII (***Figure 10***) efficiency and use light to promote the electron displacement through the media. We show the target reaction below:

$$2\,H_2O \rightarrow O_2 + 4\,H^+ + 4\,e^- \tag{4}$$

This reaction is just the half-reaction of water splitting since we obtain protons and electrons separately, and it combines with the second half-reaction as follows:

$$4\,H^+ + 4\,e^- \rightarrow 2H_2 \tag{5}$$

Therefore, we aim to split water through two redox processes, oxidation of water and proton reduction. Eq. 4 shows what water oxidation is, one of the main themes of this work.

1.2.1.2. Water Oxidation Catalysis

As stated in the previous section (Eq. 4 and Eq. 5), WOC separates the water-splitting reaction into its half-reactions that consist of the oxidation of water and the reduction of protons into hydrogen.[56]

There is a step where two water molecules must combine to form the oxygen molecule. Depending on how they interact and the catalyst's design, the reaction goes either through the Interaction of two Metal-oxide centers (I2M) or through a Water Nucleophilic Attack (WNA).

1.2.1.2.1. I2M *vs*. WNA

First, to have either I2M or WNA, the catalyst must interact with one water molecule and deprotonate it to generate the reaction center where the other water molecule attaches.

According to the I2M mechanism, it needs two reactive centers, as the name implies. The typical procedure is that a water molecule attacks the catalyst's metal center, and then it releases both protons and electrons from the water into the media. This procedure is repeated twice in order to have the two necessary M=O units that will react later. The design of the catalysts that rely on this mechanism can either be monometallic,[57] which means that the I2M mechanism is intermolecular, or bimetallic;[58] thus, the mechanism is intramolecular (***Figure 11***).

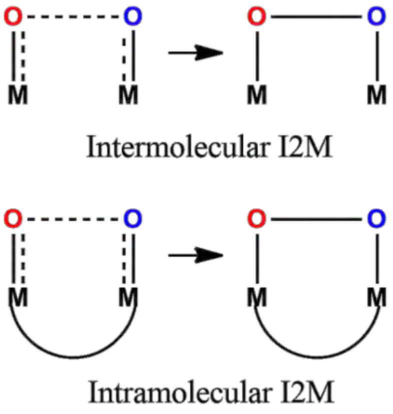

Figure 11. Intermolecular *vs.* Intramolecular I2M.

On the other hand, there is the WNA mechanism. As its name implies, it occurs when one water molecule reacts nucleophilically due to oxygen polarization. This means that an electrophilic counterpart must be present, and since we want an O-O bond, another water molecule must become that electrophilic reagent. As water interacts with the metal center, it releases protons and electrons, which means that it transitions from a neutral H_2O to a hydroxyl (-OH) and then towards an oxide (=O). To do so, the metal center oxidizes to high oxidation states (OS) (for Ru, it reaches a +5 OS).

This electron deficiency in the metal tightens all the surrounding bonds' electrons and translates into electrophilic oxygen, perfect for the WNA. Once the water attacks the metal oxide center, the deprotonation continues, creating hydroperoxide (-OOH) and finally peroxide (-OO) bonds, which in the end releases oxygen (***Figure 12***).

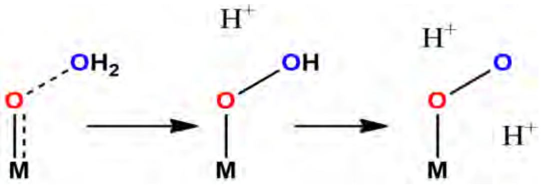

Figure 12. WNA and subsequent deprotonation.

Of course, having either I2M or WNA does not preclude the other. Some catalysts can perform both mechanisms simultaneously since both rely on the same M=O bond (***Figure 13***). There are many ways to distinguish between mechanisms and to know which one rules water oxidation. Monometallic catalysts can attach them to a surface and try to perform the reaction. If there are no results, or the reaction barely occurs, but it works when the catalyst is free in the media, it would show a clear preference towards I2M. Distinguishing between mechanisms is more difficult for bimetallic catalysts or if both I2M and WNA occur in a given catalyst. Overall, research should tailor the catalysts according to their efficiency and pathways.

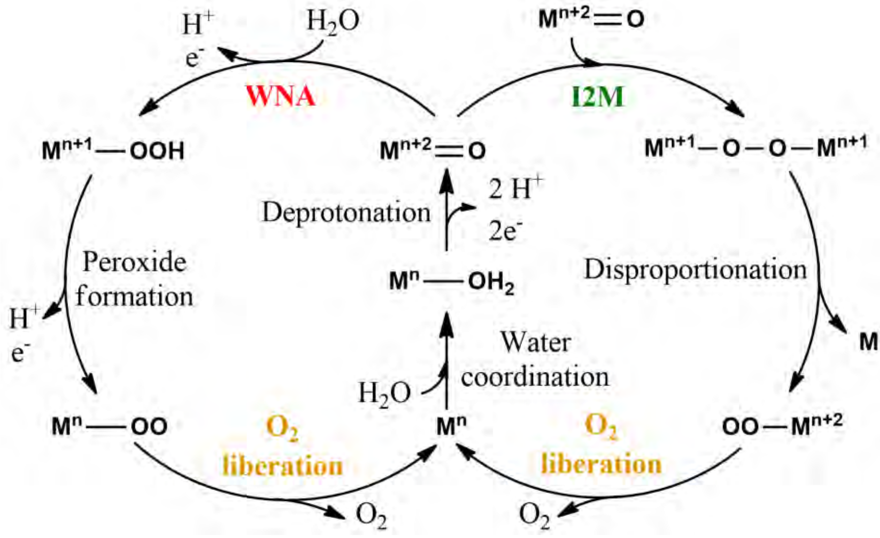

Figure 13. The general mechanism for a catalyst that can perform both I2M and WNA.

1.2.1.2.2. Reproducing the PSII activity

As previously mentioned, nature is the first reference to reproduce. In this case, the water oxidation of the PSII is the target mechanism. Between 1982 and 1985, Meyer and coworkers[59-60] reported the first catalyst to perform WOC, known as "the blue dimer," due to its color (***Figure 14***).

This catalyst was the starting line for the development of further water oxidation catalysts with different metal centers such as Ru,[61] Mn,[62-63] or Ir.[57, 64] Unfortunately, the TurnOver Numbers (TON) and TurnOver Frequencies (TOF) of those catalysts was not enough. The blue dimer had a TON of 13 and a TOF of 0.004s^{-1}, which means that it was slow and had a short life. Until 2005, the catalysts were bimetallic,[65-66,] but Thummel and Zong[67] were able to report a monometallic catalyst. In 2009, carboxylate ligands were introduced to the Ru catalysts[68] increasing ten-fold the TONs obtained until that moment, while also increasing the TOFs to 41 s^{-1}. [69] In 2012, Sun and coworkers reported a colossal leap in WOC, a Ru catalyst with a TON of 8360, and a TOF of 303 s^{-1} (***Figure 15***).[70] This is indeed comparable to the PSII, with a TOF between 100-400 s^{-1}.

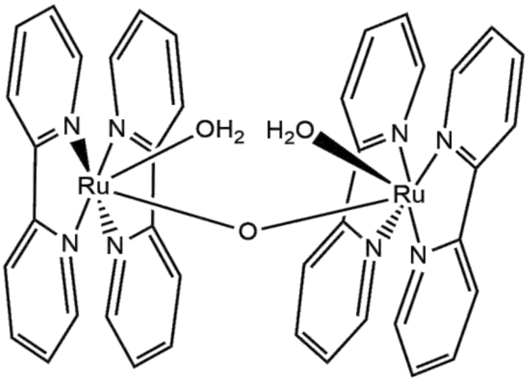

Figure 14. Structure representation of the blue dimer for WOC.

So, why is this new catalyst so good? Which is the reason for this efficiency leap? The revolutionary step was to use Bipyridine-6,6'-dicarboxylate, or bda in short, as a ligand. This bda ligand binds to the Ru metal center through the two carboxylates' oxygens and the pyridine's nitrogen, forming a tetradentate chelate. This ligand's most crucial characteristic is that the angle O-Ru-O formed is wider than in a standard octahedral compound (123º *vs*. 90º respectively). This larger angle allows a water molecule to interact with the metal center, creating a 7-coordinated Ru. This geometry creates a very reactive metal oxide center, which develops into the fast catalysis stated above. While this is indeed a great discovery, this catalyst's mechanism had yet to be fully comprehended. Thus, this thesis's first objective is to determine the mechanism of the best catalyst for WOC known to date.

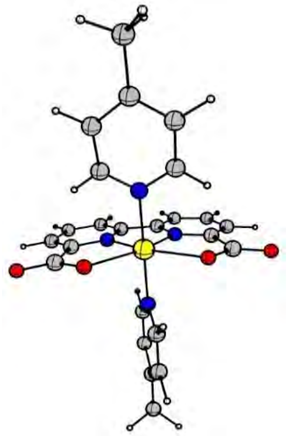

Figure 15. 3D view of the Ru(bda)(pic)$_2$ catalyst. Colored atoms: C grey, H white, N blue, O red, Ru yellow.

Still, there is a good ground for improving the catalyst, and there are already several articles that try to do so.[71-73] Since the most remarkable feature is the 7-coordinated Ru center, some researchers have focused on swapping the axial ligands.[74] Their research shows that including more π-π interactions increases the dimers' stability formed through the I2M mechanism and improve the TON of the catalyst. Other reports have changed the carboxylates to phosphonates,[75] which are quite similar and include a fascinating property to the catalyst; *i.e.* the pH dependence. This dependence is available thanks to the phosphonate ligands' protonation, which translates into different catalytic activities according to the pH. In 2016, Concepcion *et al.*[76] and Grotjahn *et al.*[77] reported a phosphonated catalyst (B), Ru(2,2'-bipyridine-6,6'-diphosphonate)(picoline)$_2$, and compared it with the carboxylated one (A) (***Figure 16***). Other researchers have also studied this catalyst.[78-79]

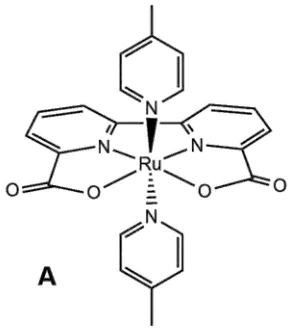

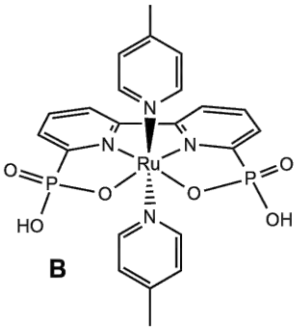

Figure 16. WOC catalysts A (with dicarboxylate ligand) and B (with diphosphonate ligand)

The computational analysis determined that B had lower barriers in the known r.d.s., either the dimerization of the I2M or the second water attacking through WNA, which should translate into faster reactions, but the experimental results pointed otherwise; the phosphonated catalyst had worse activity than the carboxylated one. Is this difference related to the pH dependence, or is it due to the mechanism's oxidant? Understanding this difference is vital, as the r.d.s. may not be the same depending on the ligand yet; no reports include a full overview of the mechanism at different pH able to explain it. Since this thesis's first objective was to develop the carboxylated catalyst (A) mechanism, it would be possible to replicate it with the phosphonated ligands and include all possible pathways, achieving a meaningful result. Therefore, this thesis's second objective is to determine the full mechanism at different pH for the phosphonated catalyst (B), compare it with the mechanism of the carboxylated counterpart (A), and find an answer to the disparity of the experimental and computational results.

1.2.1.3. Acceptorless dehydrogenative coupling

Besides water oxidation, there are other possible pathways to create hydrogen-like refining industrial processes. With some changes, they may produce H_2 for either storage or to help power the factory. An exciting reaction that may fulfill this role is the dehydrogenative cross-coupling (***Figure 17***). [80]

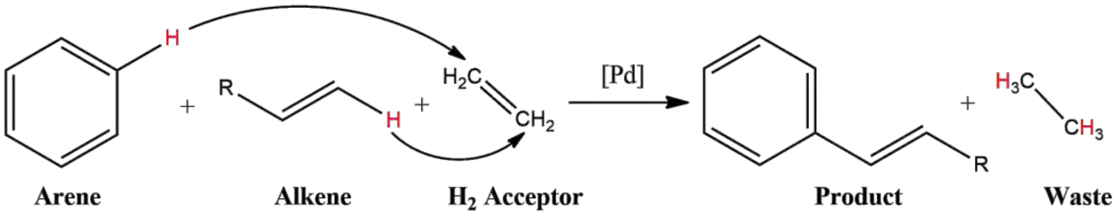

Figure 17. General cross-coupling reaction of arenes with alkenes.

This reaction forms C-C bonds between reagents. The hydrogens attached to the involved carbon atoms must be removed through an H_2 acceptor. This acceptor is usually an alkene that hydrogenates, ending up as a side-product or waste that must be isolated from the main product, causing efficiency drops due to the additional steps required. A significant improvement for this reaction was the Acceptorless Dehydrogenative Coupling (ADC),[81-82] which can perform a dehydrogenative step without needing an acceptor. Thus, it produces hydrogen gas as a side-product, without any additional steps to separate it from the target product (***Figure 18***).

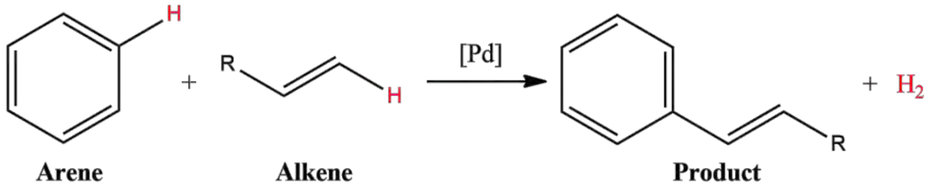

Figure 18. General ADC reaction of arenes with alkenes.

While this is a good improvement towards green chemistry, the ADC catalysts usually contain heavy transition metals, such as Rh,[83] Ir,[84] or Pd,[85] that are both expensive and scarce. In 2017, Milstein *et al*. reported[86-87] an unprecedented efficient α olefination of nitriles through the ADC of nitriles and alcohols. They compared several tests with up-to-date catalysts, and one of them stood out from the rest: an Mn-based catalyst, which they further researched for a hypothetical mechanism (***Figure 19***).

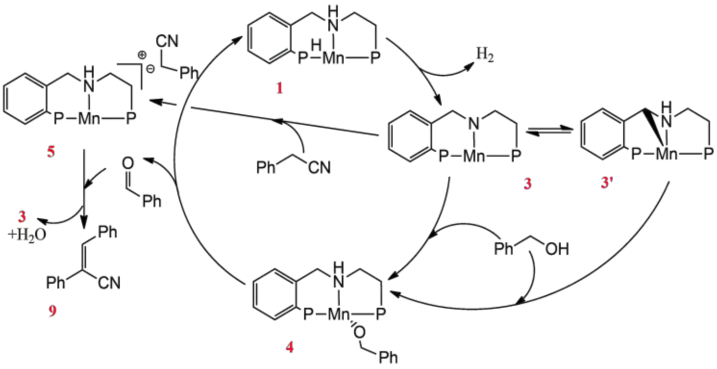

Figure 19. Proposed mechanism for the efficient production of acrylonitriles with a Mn based ADC catalyst. P stands for $\mathrm{P^iPr}$ and Mn stands for $\mathrm{Mn(CO)_2}$ for clarity.

The Mn center is an excellent upturn as it is the third most abundant metal resource on Earth. It lowers the catalyst's production cost, and the impact for its extraction is lower than the scarce metals like Pd. The initial mechanism proposition appears in ***Figure 19*** but lacks analytical depth, as there is no kinetic data nor clear pathways that lead towards the product.

Nevertheless, this is a great discovery: a catalyst that produces acrylonitriles while also generating hydrogen in the process. As a remark, acrylonitriles are widely used in different areas, mainly as precursors for the synthesis of pyrroles,[88] benzonitriles,[89] or medical treatments like malaria,[90] produced in significant quantities. Therefore, aspiring towards production with less waste and more abundant metals like Mn is a necessity. Due to the need for eco/cost-friendly catalysts involving this reaction that produces hydrogen for its storage or *in situ* production, the third goal of this thesis is to find all the mechanistic data, both thermodynamic and kinetic, to serve as the baseline for further development with earth-abundant metals like Mn.

This catalyst is included in a group of high performing catalysts, which share a particularity: its phosphorous-nitrogen-phosphorous (PNP) pincer ligand. PNP pincer ligands have been a hot topic for many years[91-94] since they have multiple metal center activation or catalysis uses. It is possible to tune the PNP ligands as preferred, as we can functionalize the ligand's backbone to obtain different reactivity. Following the work mentioned above with the Mn metal center PNP catalyst, and to look towards its diverse functionality, a second hydrogen-producing catalyst was considered (***Figure 20***).[95]

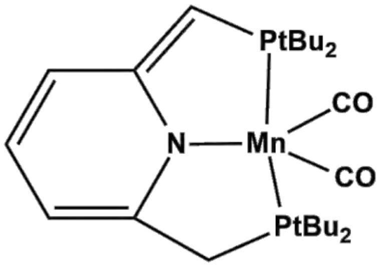

Figure 20. PNP pincer catalyst with a Mn metal center able to perform ADC to produce aldimines.

Compared to the catalyst in ***Figure 19***, the PNP pincer ligand is similar, and actually, they both produce H_2 through an ADC, but their reactivity is different. The previous catalyst needed alcohols and nitriles to produce acrylonitriles, and this catalyst uses alcohols and amines to produce aldimines. Interestingly, they even share the temperature needed for their respective reactions, 135ºC, and they both are the first of their kind to be reported; an Mn catalyst for ADC synthesis of acrylonitriles (***Figure 19***) and in this case, an Mn catalyst for ADC synthesis of aldimines (***Figure 20***). Besides, aldimines also have a great interest in the industry, as they are precursors for dyes, pesticides, pharmaceuticals, and more.[96] Overall, the similarity between catalysts, yet the different reactivity that can go towards environmentally benign production of different but essential compounds, is remarkable. Therefore, to see the similarities and differences between both mechanisms, this thesis's fourth goal involves studying the aldimine catalyst (***Figure 20***) and its comparison with the acrylonitrile catalyst (***Figure 19***).

1.2.2. Reusing atmospheric gases for waste management

1.2.2.1. N_2O recycling

Section 1.2.1 has covered hydrogen production as a target fuel for its clean combustion and chemical energy storage. Nevertheless, there are more issues to tackle in green chemistry. As stated in section 1.1.2.2, N_2O is a growing problem, mostly due to its steady-state life of 120 years, which indicates that even if its production relies on appearing as a byproduct in small quantities, over the last decades, it has become a problem. One of the known ways of getting rid of N_2O is to hydrogenate it:

$$N_2O + H_2 \rightarrow N_2 + H_2O \qquad (6)$$

It is a simple reaction where N_2O is converted into water and nitrogen, environmentally neutral gases that serve different purposes like the synthesis of ammonia in the Haber Bosch process.[97] Now, to make this reaction fast and viable, it is time to choose a catalyst. Fortunately, one type of catalyst is obtaining an impact in all-round catalysis due to their flexibility and selectivity, which coincidentally, have been discussed in this thesis already: PNP pincer ligand catalysts. While researching the H_2 production in the previous section, a very similar catalyst to ***Figure 20*** demonstrated high TON and efficiency towards N_2O hydrogenation (***Figure 21***).

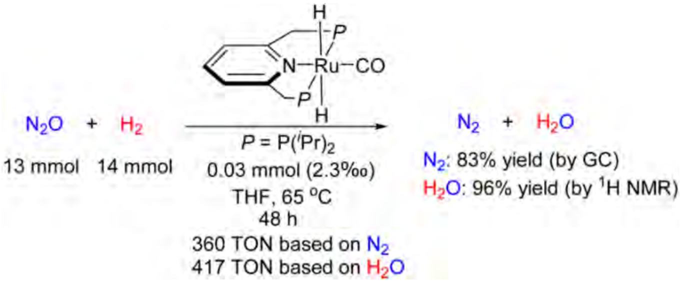

Figure 21. Hydrogenation of N_2O by the PNP-pincer Ru based catalyst

Milstein's group[98] reported a set of catalysts with ligand variations that could perform such hydrogenation. Thanks to their extensive experimental work, they defined a hypothetical mechanism, but some parts were obscure; thus, they labeled them as a "complicated mixture." Furthermore, in their experimental tests, they compared different phosphorous ligands owing isopropyl, *tert*-butyl, and phenyl substituents, and according to their data on the other catalysts, isopropyl was the best choice from those three, as the TON increased ten-fold. Despite not having apparent involvement with the metal center, it is evident that the ligands played an essential role in this catalysis, yet there was no explanation for this phenomenon.

These issues, followed by the lack of kinetic data, enticed us to work towards a full mechanism development for this catalyst, not only with isopropyl ligands but also with the *tert*-butyl and phenyl ones. Therefore, this thesis's fifth goal is to define a proper mechanism for another member of the family of PNP pincer ligands, not only to prove their wide range of applications but also to empower further catalytic research in N_2O recycling and give further insight on phosphorous ligands.

1.2.2.2. CO_2 recycling

It is almost mandatory to tackle one of the most problematic gases in green chemistry: CO_2. Generally, CO_2 is an inert gas that we produce massively due to organic material combustion like fossil fuels or other breathing processes. Thanks to the CO_2, the planet can heat up by retaining the infrared rays within the atmosphere (see ***Figure 2*** in section 1.1.1 for more details), and it is also a carbon building block for plants, as they collect it in photosynthesis to grow. While CO_2 is vital to life, we produce vaster amounts than what can be recycled by nature; thus, the quantity of CO_2 in the atmosphere is increasing rapidly. As mentioned before, this accumulation causes the already Greenhouse effect, where the planet keeps heating up, and changes to the climate become apparent. Should that continue, we might reach a point of no return, where life may become unsustainable all over the globe. This point of no return is the main reason for CO_2 recycling to be one of the hottest topics in science, and among all the possibilities, epoxides are one of the most researched.[99-102] Due to this fact, we will see one type of recycling with epoxides: using CO_2 as a carbon source for cyclic carbonate synthesis.

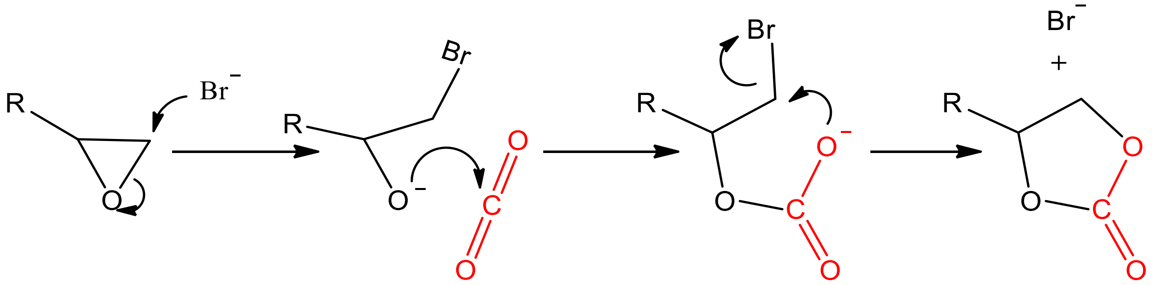

Figure 22. The general mechanism for CO_2 cycloaddition to epoxides. The CO_2 block is highlighted in red.

There has been some development in CO_2 recycling in environmental conditions,[103-106] since we want to reuse the CO_2 in the atmosphere with metal/halogen-free procedures. The last two procedures are usually required because CO_2 is so stable that it will remain unchanged unless we provide enough force. Therefore, the halogen helps to open the epoxide and provides a nucleophilic attack through the oxygen, while the metal helps to stabilize the negative charge; thus, CO_2 remains within the carbonate. The problem with this procedure is that we need a nucleophilic leaving group that can open the epoxide, but the halogens can corrode the reactor where the reaction occurs,[107-108] and their

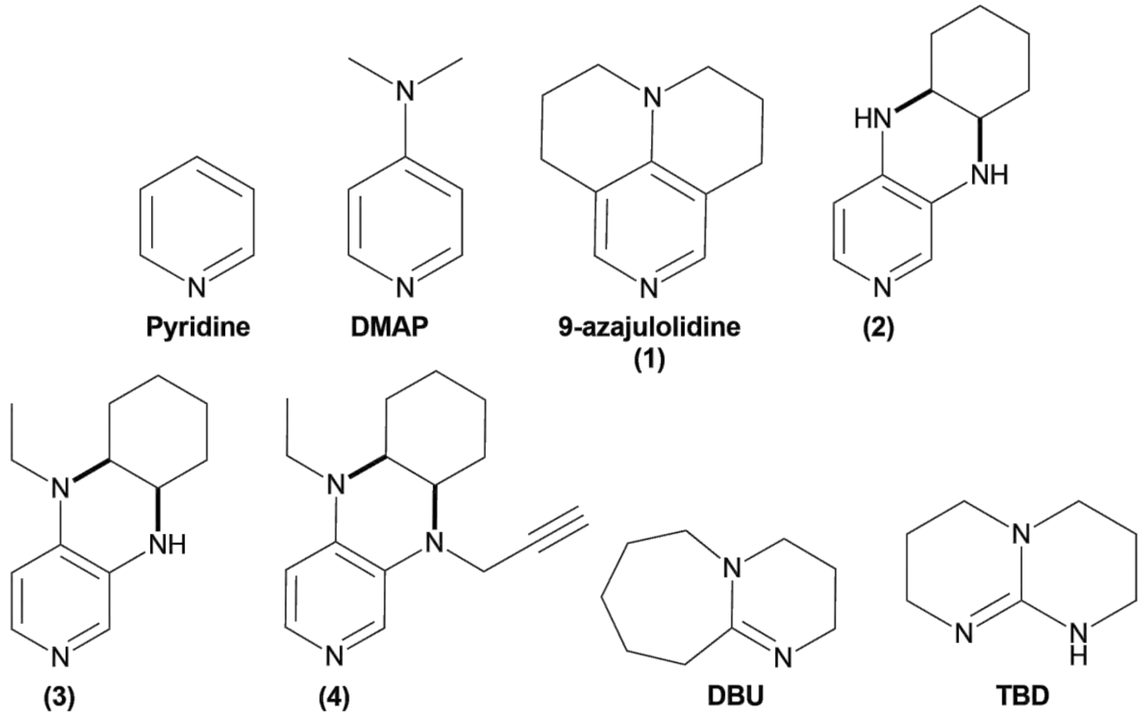

Figure 23. Target nucleophiles for epoxide opening.

production creates a huge carbon footprint.[109] Therefore, we aim to find a suitable nucleophile that can substitute the halogen's work. Based on several articles,[110-114] we will use nitrogen-based nucleophiles, as it is possible to tune their nucleophilicity and fixation (***Figure 23***).

The variety of nucleophiles aims to unveil their reactivity with propylene epoxide as the main building block for CO_2 cyclization. This project combines computations and experiments, yet only the former is discussed in this thesis.

This thesis's sixth goal is to research several nitrogen-based nucleophiles for the CO_2 cycloaddition to epoxides to recycle CO_2.

1.3. Future of energy production

The previous sections have focused on using catalysts to synthesize clean fuels like hydrogen and derived them onto the catalytic recycling of both N_2O and CO_2. According to the clean fuel production section, hydrogen is the fuel of the future. Even with its flaws, it can store ample amounts of energy, reused through combustion. However, let us talk about the elephant in the room: converting power into chemical storage and back to power is inefficient. It is well-known that all chemical reactions have different yields, either due to side-products forming or, in this case, energy loss.

Let us assume that we obtain an efficient catalyst that can produce hydrogen like the ones previously explained. It obtains the electron transfers it needs through sunlight. Even if we get the best catalyst possible, there is a net energy loss in the process, either because of the required energy overpotential to perform redox reactions,[115] due to side-products, or conversion of part of the energy into heat, known as heat dissipation. Overall, chemical reactions involve energy loss. A reasonable point of view would be:

why bother designing complicated mechanisms and catalysis to create chemical compounds that we want to convert into energy if we could directly transform the sunlight into energy through other technology like solar cells? This reasoning usually leads to using batteries to store the energy to not lose as much energy as in the chemical process. To answer this, another question appears: How do we produce those batteries? As the technology level increases, the energy needs become not only more extensive but also constant. Almost all everyday tasks need batteries: mobile phones, laptops, TVs, cars, and of course, power reserves to distribute between the population. Newer technologies also tend to demand more energy; in 1946, the first cellphone had a battery life of 30 min[116] yet in 2019, with more energy-demanding gadgets with internet, apps, videos, and so on, the battery lasts from a full day if used extensively, to several if it is not.

Those batteries increase their capacity thanks to material engineering and a particular small alkali metal: lithium. It has a wide variety of applications, but the most known is that it is in cell batteries. Unfortunately, working with lithium is a challenging task; its extraction is too polluting as it can poison underground water supplies, permanently damage the soil and produce air pollution.[117] Furthermore, even if all these problems were solved and included automation to avoid human damage, there is still a finite amount of lithium, between 20 and 40 million tons.[118] Considering such a vast amount, it could last for another 365 years, but when it runs out, what is the plan? The last 250 years of fossil fuel non-stop burning showed that it is not a good idea to exhaust resources until it is too late. Therefore, while it is crucial to develop other technologies that depend on lithium or other metals, it is vital to have a backup plan. Hydrogen production is available in power plants that do not use all their capacity, which means it can store energy automatically. When the demand is low, we could direct all the energy excess produced into hydrogen production; thus, less energy loss in the meantime. Hydrogen is just another type of “battery” like lithium ones, but renewable.

The take-home message is that it is essential to look for as many energy production ways as possible. In this thesis, we research a promising direct solar energy conversion to electricity: solar cells.

1.3.1. Solar cells

Solar cells are an exciting technology for creating energy, based entirely on the materials and their disposition. To build a solar cell, we need different materials depending on their conductivity. There are three types of materials according to their conductivity: conductor, semiconductor, and insulator. They differ only in the energy gap between the highest occupied energy state of their valence electrons, which forms due to the combination of all the bonding orbitals of the material. The lowest unoccupied energy states result from the combination of all the anti-bonding orbitals (***Figure 24***).

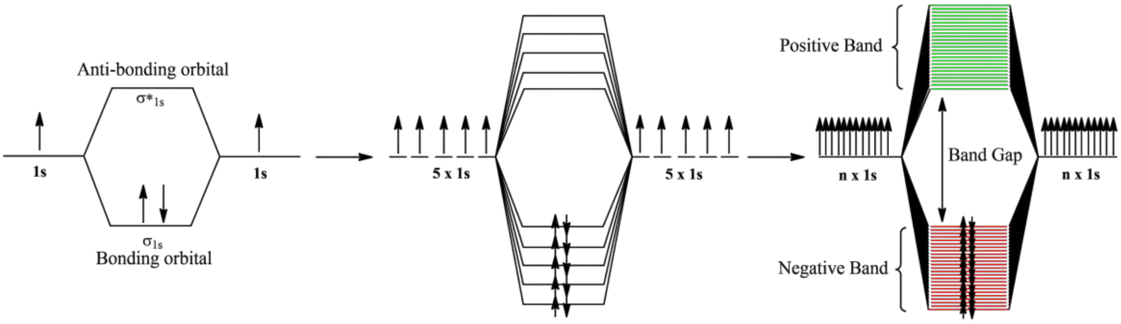

Figure 24. Formation of positive and negatives bands through the interaction of the electron orbitals in a given material.

The difference in conductivity depends on the bandgap size. If the negative and the positive bands overlap, it is a conductor, as the electrons are free to move from one band to the other. If the bandgap does not overlap, then it is either a semiconductor or an insulator. In this situation, it needs an external energy source to promote electrons from the Negative (N)-band towards the Positive (P)-band. The insulator or semiconductor property depends on the energy applied. If it can promote the electron, it becomes a semiconductor; whereas if the energy were not enough, it would be an insulator. A common insulator is cork produced from tree bark, but it is just an insulator for the voltage used at home since applying high enough voltages, like lightning, would allow the electrons to cross the band gap.

Solar cells work with this feature but through two different layers of materials. One layer is rich in electrons, the N-layer, while the other layer is lacking, the P-layer. Combined, they have a bandgap small enough so that a photon can excite an electron; thus, they are semiconductors. Once they make contact, electrons from the N-band of the N-layer rush to fill the gaps in the P-band of the P-layer until equilibrium at the junction. The junction's opposing charges create an electric field that acts as a diode, allowing only electron movement from the P-layer to the N-layer, making the electron flow stop. Now, sunlight comes into play in the form of photons. When a photon reaches an electron close to this electric field, it has enough energy for its excitation and creates a free electron and a hole. The electric field between layers will push this free electron towards the N-layer, and the hole will go towards the P-layer. Neither layer is no longer in equilibrium, so they will try to recombine both electron and hole, but now the N-layer cannot give this electron back to the P-layer due to the junction electric field. By providing a passage in the form of a cable through one layer to another, it is possible to benefit from the electron gradient and move electrons through the cable. This current, combined with the generated electric field's voltage, gives useful electrical power (***Figure 25***).

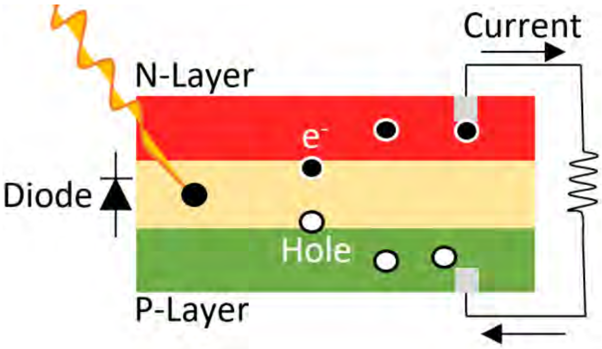

Figure 25. Solar cell electron-hole movement.

As solar cells depend on the gap between layers, they rely on their materials' properties. There are three categories, starting from the first generation of solar cells,[119] based in crystalline silicones like polycrystalline silicon. They are very expensive to produce since their production is based on growth controlled silicon crystals, yet they are the most sold worldwide as their research was the first.[120] Second-generation solar cells[121] are also called thin-layer solar cells due to their technology, which consists of micrometer-thick layers of material that function as a complete solar cell. However, even if they are much cheaper than the first generation, their efficiencies pale in comparison. The latest technology in solar cells is the third generation,[122] consisting mainly of organic materials such as dyes,[123] polymers,[124] and quantum dots.[125] They are very cheap to mass-produce as the target is to print them like paper, while also having the best efficiency of all generations (up to 47.1%).[126] Unfortunately, they are still in research and have not yet been commercially available. This thesis delves deeper into one type of third-generation solar cells: Dye-sensitized solar cells.

1.3.2. Dye-sensitized solar cells

As stated above, these third-generation cells are still under research. A particular type is the dye-sensitized solar cells, not because of their efficiency (12.0~12.5%), but due to their physical properties.[127] They are flexible and semi-transparent, allowing for diverse applications, including printing them through conventional roll-printing techniques. These properties imply that their cost is minimum and mass production possible, meaning that they are perfect candidates to compete with fossil fuels due to their reduced price.

They work similarly to silicon-based solar cells, yet they have a significant difference. While the silicon acts as both electron carrier and donor, these roles separate in the dye-sensitized solar cell. The first layer includes a dye, a material that can absorb a photon and excite it to enable its transfer. This electron is not transferred through the same dye; instead, a charge separation process occurs between the dye and a semiconductor. A set of titanium oxide (TiO_2) particles acts as both scaffold and semiconductor. Once the electron has moved unto the TiO_2, it diffuses towards the desired circuit. When the electron returns, it comes back through a platinum electrode, and here occurs the most significant difference between silicon and dye-based solar cells; the platinum and the TiO_2 are not in contact; in fact, they connect through an I^-/I_3^- electrolyte. The triiodide ion takes the electrons from the platinum cathode and reduces to iodide. This iodide oxidizes to the triiodide when in contact with the dye that was initially photoexcited, completing the circuit (***Figure 26***).

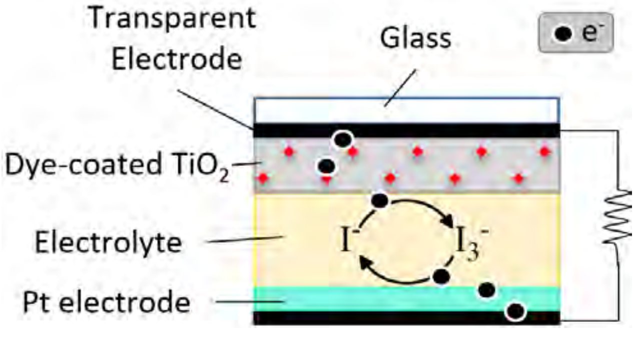

Figure 26. Dye-sensitized solar cell general mechanism.

Despite requiring expensive metals like platinum for the electrode or ruthenium for the dyes,[128] the amount needed is minimal. Besides, since these cells do not need complex assembly or materials like silicon cells, they are one of the cheapest choices for the future. These cells have technical problems, though; the charge transfer between dye and scaffold is inferior; one of their low-efficiency reasons. Furthermore, the electrolyte is a liquid; thus, high and low temperatures may expand or freeze it, respectively, potentially damaging the cell or further reducing its efficiency. As a critical remark, the dyes are usually in the nanometer spectrum; thus, to absorb as many photons as possible, their density through the surface has to be high. It needs scaffolds with large surface areas, being this the reason for the TiO_2 nanoparticles. Different nanoparticles can vary the efficiency of the process, depending on their charge transfer capabilities. With this in mind, there is an up-and-coming field: carbon nanostructures and, in particular, fullerenes.

1.3.2.1. Fullerenes and CNOs

Fullerenes are an allotrope of carbon like graphite or diamond. The first discovered fullerene in 1985 was C_{60},[129] which resembles a soccer ball (***Figure 27***). Fullerenes consist of twelve pentagons and a varying number of hexagons depending on the number of C atoms, which gives them a large surface area and different reactivity depending on the bonds. Their structure contains an extended π-conjugation that enables them to absorb visible light and photoexcite electrons.

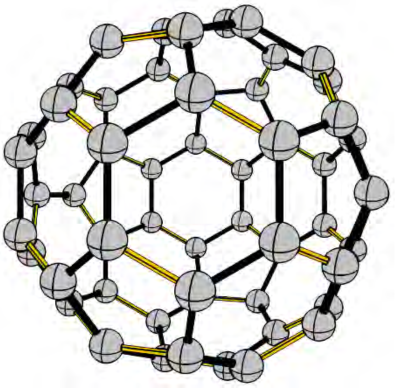

Figure 27. Structure of C_{60} fullerene.

Following the last section, the need for better surfaces for dyes and better charge transfer between the surface and the electrode is apparent. Fullerenes could replace the TiO_2 layer to increase the solar cell's efficiency, but some requirements exist.

First, the charge transfer needs to be better than with the TiO_2 nanostructures. Fullerenes research demonstrated that they can transfer charges close to the range of TiO_2, but they may not be enough yet.[130-131] Nevertheless, their functionalization is rich, and many research papers focus on fullerene functionalization and the different bond reactivity.[132-134] Even more, the addition of ions inside the fullerenes provides further depth into their reactivity, thus considering them as dyes and scaffolds simultaneously. Fullerenes have the current spotlight in dye-synthesized solar cell development for these reasons. While they are an exciting topic to research, there is an even more exciting structure tightly related: CNOs.

A Carbon-Nano Onion (CNO) definition is a fullerene inside another fullerene, *i.e.,* a C_{60} inside a C_{240}, also named $C_{60}@C_{240}$. CNO's research on their electronic properties is promising, but the large atom count has made computational studies difficult. Nevertheless, they have proven a better charge transfer than fullerenes, but also than TiO_2.[135-137] Therefore, CNO's seem to be an enhanced version of fullerenes in charge transfer, but their reactivity lacks computational research, mainly due to their size and control synthesis for lab results. Nevertheless, their bonds' reactivity studies are still relevant and demanded precisely due to their charge transfer capabilities. Since fullerenes include many formal double bonds, an excellent approach to study their reactivity is the Diels-Alder reaction (***Figure 28***).[138]

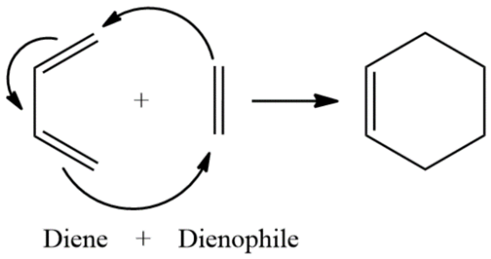

Figure 28. Diels-Alder reaction.

This reaction is fundamental yet straightforward in organic chemistry. It consists of the formation of rings through a compound with two conjugated bonds (diene) and another molecule with a double bond. Due to fullerenes' natural composition, rich in double bonds, it is possible to use them as dienophiles. As for the diene, cyclopentadiene is optimal since it can give depth to the study as the methylene can point towards one bond or another while not increasing the atom count much.

Overall, this thesis's last objective is to study the smallest CNO reactivity, $C_{60}@C_{240}$, using a Diels-Alder reaction, and compare it with its reactivity when including a Li^+ cation in the inner fullerene, $Li^+@C_{60}@C_{240}$ (***Figure 29***). The Li^+ ion adds depth to the study as its presence helps to understand both the reactivity and the CNO shielding capabilities in charge transfer processes, such as a Faraday Cage.[139]

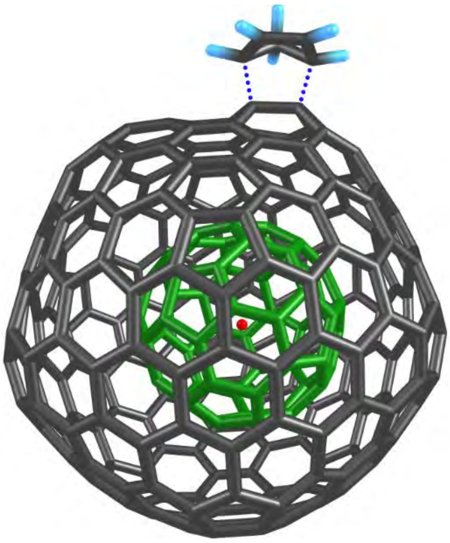

Figure 29. Example of a transition state of a Diels-Alder reaction between $Li^+@C_{60}@C_{240}$ CNO and cyclopentadienyl. Inner fullerene highlighted in green, and lithium cation shown in red.

Chapter 2. Methodology and Computational Chemistry Tools

2.1. Quantum chemistry

Whenever someone hears about quantum chemistry, the first thing that usually comes to mind is Schrödinger's cat or the Heisenberg uncertainty principle. The first one is a narrative story about a cat inside a box containing a device with a radioactive particle with a 50% probability of disintegrating and a bottle of poisonous gas that will open if the particle disintegrates, killing the cat. Since this is only a matter of probability, it is mandatory to open the box to know what happened to the cat; thus, it is both dead and alive simultaneously until we observe it to determine its state. The second one refers to the concept of measuring the velocity and the position of a particle. For a simplified explanation, to measure any, we must interact with the particle, making it impossible to know both parameters at once precisely. To clarify, when we look at the particle's position, we do not know its exact speed, while if we observe its speed, we cannot know its exact position. These two theories relate to particles' quantum properties, but they are not the leading cause of quantum chemistry development. Nevertheless, they constitute an essential piece of knowledge developed thanks to what is known as quantum mechanics. The following sections will try to explain quantum chemistry's development in a simple, yet exciting way, for all the readers that may be new to this concept.

2.1.1. A look into Quantum Mechanics

Around the 17th and 18th centuries, scientists noticed some characteristic effects not easily explained using classical physics. A known example relates to light. In 1670, following Descartes[140] work in 1637, Newton started its corpuscular theory of light.[141] This theory focuses on light refraction, which is the bending of light crossing two media of different density (water and air, for example), and light reflection, which occurs when light bounces off a surface at the same angle (***Figure 30***).

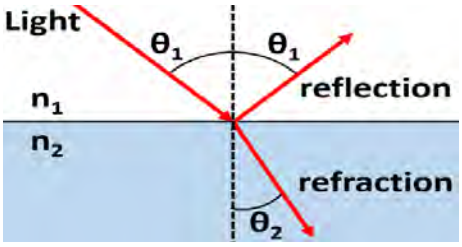

Figure 30. Difference between reflection and refraction of light. n_1 and n_2 refer to different media such as air and water.

Newton stated that light had to be composed of little particles or corpuscles, infinitely small particles with properties because only physical particles would move in straight lines. On the other hand, Hooke[142] proposed in 1672 a pulse theory that stated that light propagates like waves in water, and in 1678 Huygens[143] proposed the mathematical view, his wave theory of light waves (***Figure 31***). This theory defended that light is composed of waves and that each one was a wavefront, a source of spheric wavelets (or wave origins) that moved through a media called ether, which envelops all space. The combination of the new waves generates more wavefronts that, at the same time, produce more wavelets and so on. Both theories tried to describe light, and while Newton can describe reflection, Huygens can describe both reflection and refraction, but none can explain the diffraction and interference observed in light. In the early 19th century, Young[144] proposed a set of reasons supporting the wave theory of light. He used a ripple tank, a device to generate waves in water, and demonstrated that with two wave origins, there were some places where both waves collided destructively, thus not showing any wave. After this experiment, he also developed what we know as the double-slit experiment. To understand it, let us think first about what would happen if a beam of light crossed a single slit. If the light consisted of particles, we would observe a pattern according to the shape of the slit it crossed. However, should we experiment, the conclusion is a spread-out form of the slit pattern, which is already a good indicator that light is a wave instead of a corpuscle.

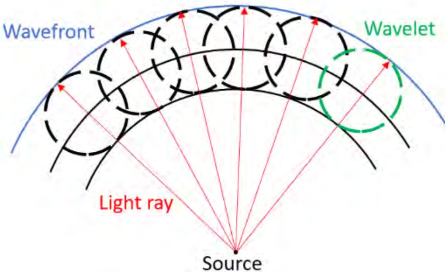

Figure 31. Huygens's wavelet and wavefront representation.

Now, returning to the double-slit experiment, if we shoot a single beam of light through two identical slits, we observe the same spread pattern, but now there are shadow bands along with the pattern. These are the result of destructive interference between both waves (***Figure 32***). In 1818, Fresnel[145] demonstrated that with his mathematical principle of interference, together with the Huygens wave theory of light and Young's experimental support, they could demonstrate reflection, refraction, diffraction, and interference; thus, they made the Huygens-Fresnel principle. Altogether, this was the beginning of the acceptance of the wave theory of light.

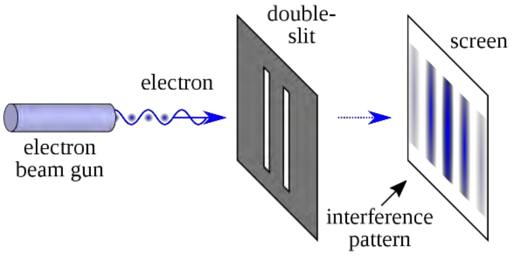

Figure 32. Double slit experiment with the resulting interferences.

For the next century, new problems involving radiation arose, such as the black body radiation,[146] which tried to explain, in very rough terms, the relationship between the increase of temperature in a black body (an object that absorbs all radiation, thus it can also emit all radiation as well) and the emitted radiation of this body due to the heat. Using classical physics, Rayleigh and Jeans[147] defined experimental results related to the radiation (energy) that an ideal black body would emit, increasing when the frequency increases as well, but only up to 10^5 GHz. According to classical physics, higher frequencies implied energy emissions that could be infinite, which means that any given object could radiate infinite energy, thus leading everything to a temperature close to the absolute zero. This phenomenon is known as the Ultraviolet catastrophe. Luckily, this is not the case, which indicates that classical physics cannot define this, so a new model was necessary.

Planck's approach[148] to this problem resulted in another giant leap in quantum mechanics. In 1901 he proposed that there were individuals in the matter that vibrated at a given frequency with a given energy level. This definition means that if a black body absorbed an infrared light as an example, it would emit the same infrared light at another given time, but not a higher one because the energy is quantified. This new concept became the widely known Planck's Law:

$$E = n \cdot h \cdot f \qquad (7)$$

Where *E* is energy emitted by a black body, *n* is the number of vibrating individuals at a given frequency *f,* and *h* is a constant able to transform frequency units into energy units, also known as Planck's constant.

Thanks to this proposal, quantum mechanics emerged and considered Max Planck as the quantum theory's father.

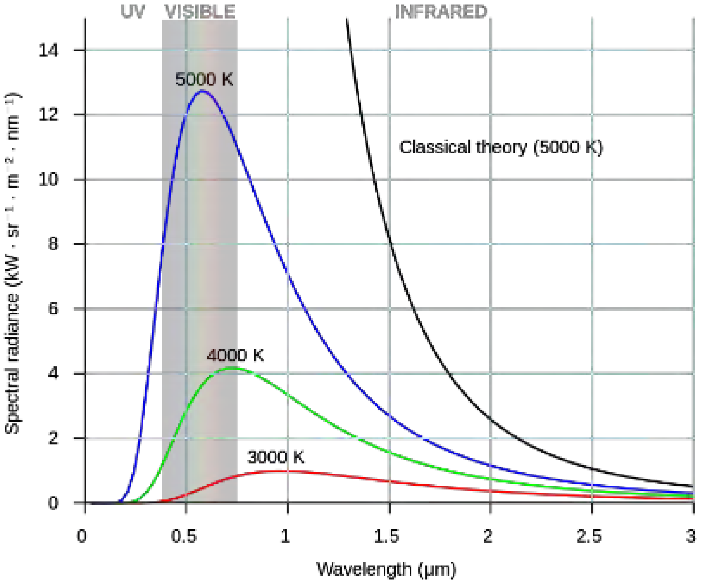

Figure 33. Black body radiation according to classical physics (black line) and Planck's approach (colored lines).

Going back to the black body problem, Planck described the radiation emission according to the heat of a black body compared to the classical view (***Figure 33***), but an intrinsic "problem" arose from this deduction. Light has a defined frequency determined by the speed of light and its wavelength:

$$f = \frac{c}{\lambda} \qquad (8)$$

Therefore, a given wavelength will only have a specific frequency, and this frequency will emit light only when it has a given energy. For a 500 nm wavelength:

$$f = \frac{c}{\lambda} = \frac{3 * 10^{8}}{5 * 10^{-7}} = 0.6 * 10^{15} Hz \qquad (9)$$

$$E = n * 6.6 * 10^{-34} * 0.6 * 10^{15} = n * 3.96 * 10^{-19} J \qquad (10)$$

Eq. 10 means that a 500 nm light wave can give an integer multiple of energy packets of $3.96 \cdot 10^{-19}$ J, but not in between, implying that energy is not continuous; therefore, if this is true, then light cannot be a wave, because the energy of waves is continuous.
Continuing the time scale, in 1905, Einstein[149] published his view on the photoelectric effect. When a light package hits a material, it will emit electrons. The classical view of this effect is that all materials could emit electrons when hit with a light beam independent of its frequency. If anyone wanted to increase the electron emission speed, increasing the intensity of the beam of light was enough to make it happen, and accordingly, a dim light could emit electrons, but since it was not intense enough, there would be a time lag Eqin order to build up the energy required. However, experimental results showed that the electron emission only occurred when reaching or surpassing certain frequency thresholds. Using Planck's previous work that explained that light travels in packages of determined energy and frequency, Einstein demonstrated that light is not a single wave but a sum of discrete wave packets. He also stated the importance of momentum's transfer during emission and absorption of radiation since the radiation that resulted in these processes always had a specific direction and velocity. With energy and momentum, light once again behaved as a particle, but also as a wave simultaneously. This finding is the first report for the quantum effect called wave-particle duality, and it attributes to the light packages, also known as photons. Einstein was awarded the Nobel Prize in 1921 for this discovery.[150]
In 1924, de Broglie[151] hypothesized that it was not only light that had this duality, but also all matter behaved as both a wave and a particle. Derived from rearranging the equations of Planck and Einstein:

$$E = h \cdot f \qquad \text{Planck's Law} \qquad (11)$$

$$p = \frac{E}{c} = \frac{hf}{\lambda f} = \frac{h}{\lambda} \qquad \text{Einstein's momentum} \qquad (12)$$

$$\lambda = \frac{h}{p} = \frac{h}{m \cdot v} \qquad \text{de Broglie equation} \qquad (13)$$

Eq. 13 implies that any particle with a mass *m* and a velocity *v* has an associated wavelength. Davisson, Germer, and Thomson[152-153] confirmed their hypothesis three years later, where they found the diffraction of an electron, a feature only found in waves.
In 1927, Schrödinger's[154] equation paved the way for modern quantum mechanics. All scientists struggled to define both a particle and a wave correctly, yet not simultaneously. De Broglie described the electron as a particle with wave-like properties but only considered electrons in a plane, not as a tridimensional particle. Schrödinger's approach was to consider the electron in a potential well caused by the atom's protons. We show the time-independent formula that he devised and reproduced the Bohr model's energy levels in Eq. 14.

$$\hat{\mathrm{H}}\,|\Psi\rangle = E|\Psi\rangle \qquad (14)$$

The Ψ refers to the wavefunction, which describes the probable position, momentum, time and spin of all particles that define our system (quantum-state), and $\hat{H}$ refers to the

Hamiltonian operator, which correspond to the sum of all the kinetic and potential energies for all the particles in the quantum system. Overall, Schrödinger's time-independent equation describes a given stationary quantum state.

In an atomic system, we consider both the electrons and the nuclei for a given quantum state. Max Born and Robert Oppenheimer[155] proposed that it was better to treat the nuclei's and electrons' movement separately due to the difference in both particles' mass. Namely, the electrons orbit the nuclei much faster than the nuclei move. Next, due to this movement's imparity, one can approximate the nuclei to be stationary concerning the system's electrons. By doing so, we neglect the nuclei's kinetic contribution, and the potential energy of the nuclei becomes constant. Effort-wise, for each particle in a given system, there are three variables (x, y, z coordinates), and the complexity of the equation dictates that, at best, the necessary power to solve the equation increases to the square of the number of coordinates in a given system. Therefore, with this approximation, the resolution effort is significantly reduced.

In 1927 Heisenberg[156-157] introduced the uncertainty principle already explained in the previous section, and from 1930 onwards, more specialized subjects developed such as quantum chemistry, quantum electronics, quantum optics, and more. While it seems that thanks to the Schrödinger equation, we can define any given system, which is true, it is also apparent that the required calculations increase exponentially both in size and difficulty, even with the Born-Oppenheimer approximation. A hydrogen atom needs the potential and kinetic energy between proton and electron, which is simple enough. The next more straightforward system would be a helium atom with two protons and two electrons. In this case, it needs proton-proton interaction, electron-electron interaction, two proton-electron interactions (one for each different electron), and the kinetic energy of each particle, and this is just a simplified approach to show that the more particles involved, the greater the complexity. Nevertheless, the most crucial issue with the Schrödinger equation is that it cannot precisely explain systems with more than one electron due to the Coulomb electron-electron repulsion dielectronic term. This repulsion means that interacting with one electron will affect the other as well.

2.1.1.1. The Hartree-Fock method

In 1928, Hartree[158-160] published a way to approximate Schrödinger's equation for multi-electronic systems, the self-consistent method. In a system with two or more electrons, we use a multi-electronic wavefunction to solve the Schrödinger equation, where one wavefunction defines each electron's position, momentum, and spin while depending on each one of the others (repulsion between electrons). Defining one of the electrons' position affects the whole system, needing to redefine the rest of them, but now the new positions of the other electrons disturb the initial one; thus, the mathematical effort increases rapidly. Hartree's solution was to consider each electron individually: for each electron, one spin-orbital, and one wavefunction. The variational principle[161] dictates that the optimal spin-orbitals are those that minimize the energy of the system. Still, the field seen by one electron depends on the other electrons; thus, we must provide an initial guess of the spin-orbitals. This initial guess serves to solve the Schrödinger equation, which will give new spin-orbitals (each electron is affected by the average repulsion of the other ones) and gives the system's energy. With these new spin-orbitals, the process is repeated iteratively until the energy calculated changes by a predefined amount (hence an approximation) of the previous cycle. When this happens, it implies that the last energy found for the system is equal or approximate to the previous iteration, so the system is now said to be self-consistent. Overall, it converts a multi-electronic wavefunction into the product of single-electron wavefunctions as follows:

$$\psi(\mathrm{r}_1, \mathrm{r}_2, \cdots, \mathrm{r}_i) \approx \varphi_1(\mathrm{r}_1)\varphi_2(\mathrm{r}_2) \cdots \varphi_i(\mathrm{r}_i) \tag{15}$$

Then it minimizes the energy of the system, also known as the energy of the ground state:

$$E_0 = \langle \psi_0 | \hat{\mathrm{H}} | \psi_0 \rangle \tag{16}$$

All this explanation summarizes as follows: with an initial spin-orbital, we can obtain the system's optimal spin-orbitals, and their associated optimal energy, also known as the ground-state energy.

Although it seems a good approximation, there is a fatal flaw in its design: the Pauli Exclusion Principle is disobeyed.[162] This principle dictates that two or more identical fermions (particles with half-integer spin), in our case electrons, cannot be located in the same quantum state simultaneously. More precisely, if two electrons coexisted within the same orbital, the spin must be different from each other. This statement also implies that the exchange of two electrons must be antisymmetric to exchanging space and spin. Slater[163] and Fock[164] demonstrated that Hartree's method did not fulfill it in 1930. Later on, in 1935, Hartree reformulated the mathematical method to correct it using Fock's work. Thus the Hartree-Fock method[165] was born, and the mathematical tool that Slater developed, also known as Slater determinants, complied with the antisymmetry principle. As this method relies on iteration, and the cycles grow exponentially according to the number of electrons present in our quantum system, the work required to solve the Schrödinger's equation for medium-sized atoms was large. It was not until 1950 that computers reached a resource threshold beyond what handwriting could reach.[166] This was the turning point in quantum mechanics to delve deeper into the computing world.

2.1.1.2. Basis sets and atomic orbitals

Reading the previous section, we can have a general grasp on how to treat wavefunctions in a quantum state, but the information regarding the atomic orbitals is still lacking. Right now, with these atomic orbitals put into the Hartree-Fock functional, it should be possible to obtain a reasonable solution for the Schrödinger's equation; therefore, let us see what they are.

First, atomic orbitals are a mathematical function that can define the electron and its wave properties in an atom. These orbitals enable calculating the probability of an electron being located in a specific spatial region. In other words, the orbitals describe "electron clouds" that surround the atom and indicate the most likely position of an electron. These electron clouds are defined using four quantum numbers: the principal quantum number (n), the azimuthal quantum number (l), and the magnetic quantum number (m_l), thus defining the spatial orbital, and if we include the fourth quantum number, the spin quantum number (s), then we have the complete spin-orbital (a combination of spatial orbital and spin). In general terms, these numbers are sets of numerical values that give acceptable solutions to Schrödinger's equation for the hydrogen atom (single electron wavefunction).

The principal quantum number (*n*) defines the energy of an electron. It can go from 1 to any integer number. The higher the quantum number, the less attached to the nucleus of the atom. This definition fulfills the quantization of energy, as every electron defined will have a specific energy level. This number appears first in the Bohr atomic model, which described an atom like a small solar system, where the nucleus would be the sun and the electrons the surrounding planets, but instead of gravity pulling everything together, that would be the role of electrostatic forces (***Figure 34***). This number derived from the values of orbital angular momentum, L, in the Bohr model. This equation, however, was originated from a 2D atomic model, but the Schrödinger wave equation describes the energy using this quantum number in a 3D model:

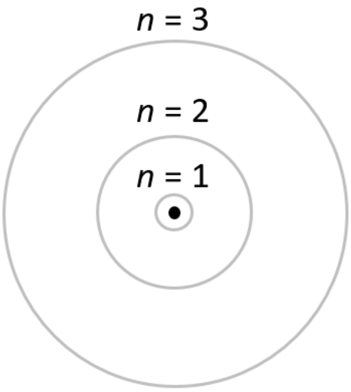

Figure 34. Bohr atom model showing the different n levels. Radii according to n^2.

$$L = n \cdot \hbar = n \cdot \frac{h}{2\pi} \qquad \text{Bohr's orbital angular momentum} \qquad (17)$$

$$E_n = \frac{E_1}{n^2} \qquad \text{Schrödinger's bound state energies} \qquad (18)$$

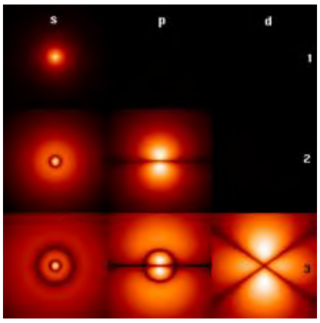

Figure 35. Atomic orbital wavefunctions of the H atom. X-axis shows l, Y-axis shows n quantum numbers.

Where n is the principal quantum number. Overall, the principal quantum number allows for the quantization of energy, but it fails to define complex systems where the energy levels are degenerate. The azimuthal quantum number (*l*) defines the electron's angular momentum in a given quantum state. To simplify, it gives the shape of the orbitals. The quantum number *l* correlates with the quantum number *n* as follows:

$$l = 0 \rightarrow n - 1 \qquad (19)$$

An integer defines n, so it defines *l* as well. As each azimuthal quantum number has a given shape, the first four are named as *s* (*l* = 0) for sharp, *p* (*l* = 1) for principal, *d* (*l* = 2) for diffuse and *f* (*l* = 3) for fundamental. The following ones continue the alphabetical order except for the letter *j*, avoided as not to get confused with the letter *i* (*s, p, d, f, g, h, i, k,* …).

While the principal quantum number defines the energy level, the azimuthal quantum number defines the subshells inside the energy level. Still, there is missing information, such as the number of orbitals in a tridimensional space. The magnetic quantum number (m_l) appears to tackle this issue. It originates from breaking down the wavefunction expressed in spherical coordinates (as it is a tridimensional space) into a product of the radii, the polar angle (angle between Z-axis and Y-axis), and the azimuthal angle (angle between X-axis and Y-axis):

$$\psi(r,\theta,\phi) = R(r)P(\theta)F(\phi) \tag{20}$$

By solving the differential equation, one can find that values greater than the azimuthal quantum number do not allow a solution for the polar angle, and in the end, the magnetic number can be any integer between –l and l, with the zero included. This magnetic number determines how many orbitals are in a subshell, so let us suppose a subshell of l = 1 (p subshell). The subshell includes three orbitals with magnetic quantum number -1, 0, and 1. These are also known as the orbitals p_x, p_y, and p_z (***Figure 36***).[167]

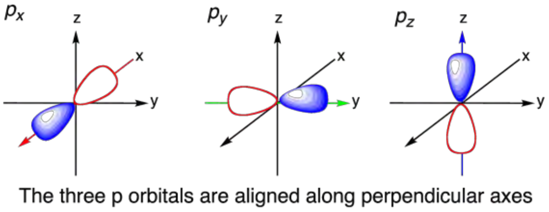

Figure 36. Orbitals of subshell p.

Finally, the spin quantum number (*s*) appears to define that the electrons are spinning while also fulfilling Pauli's exclusion principle. The Stern-Gerlach experiment[168-169] proved the existence of electron spin in 1920, even before it was formulated. The experiment consisted of evaporating silver atoms in a vacuum, and using thin slits, a magnetic beam with a homogeneous magnetic field guided the atoms, colliding with a metallic plate. Classical physics determines that the atoms should have formed a thin line in the beam's shape; instead, two lines were formed. This occurred since silver has an unpaired electron in its valence shell; thus, we determine the spin. Since it is either positive or negative, the electron behaves like a small magnet, going towards the magnetic beam if negative while going away if positive. In 1928, the Dirac equation[170] was able to predict all four quantum numbers naturally, not only the spin quantum number. Pauli's exclusion principle states that two fermions (electrons) cannot share the same quantum numbers in the same quantum state. Since the spin quantum number can be either +1/2 or -1/2, if *n*, *l,* and m_l are the same, only two electrons can occupy the same spatial orbital, each with a different spin quantum number. Now that the atomic orbitals are defined, it is possible to describe a given quantum state. It is possible to use all orbitals, to describe our quantum state. Nevertheless, this is very costly, even in computational terms, and for some systems with many atoms it can be hard to accomplish. This is where basis sets come into play.

A basis set is a set of functions that will define each of our atomic orbitals of our quantum state. They transform the differential equations into algebraic equations for an efficient computational implementation. As an example, a carbon atom has six electrons spread in the orbitals $1s2s2p_x2p_y2p_z$. The bare minimum amount of basis sets needed to define the carbon atom are two *s* basis sets and one *p* basis set (STO basis set, for instance). Typically, this gives poor results, but it is the cheapest reasonable calculation. For the same carbon atom, it is also possible to use more functions to define it, emphasizing the valence electrons and giving them more flexibility since they are responsible for the bonding. A basis set where the valence electrons have the flexibility to go a level beyond their valence level (increase the n quantum number by 1), also called valence double-zeta basis set, increases the accuracy of the calculation. This basis set would use one *s* orbital set for the inner orbital (n=1), one *s* and one *p* orbital sets for the valence orbital (n = 2) and one *s*, one *p* sets, and one *d* orbital set if it also includes polarizable functions for the next available energy level (n = 3). By doing so, the five orbital sets (double-zeta valence polarized) represent better the valence electrons than with three orbital sets (minimal).

2.1.1.3. Density Functional Theory (DFT)

With all the information collected so far, we can calculate a given quantum state's wavefunction if there is enough computational power. However, the computing power is limited, and the difficulty of solving the wavefunction increases rapidly with the number of electrons. As stated previously, the wavefunction depends on 3N variables (x, y, and z for each electron) + 1N variable (spin of each electron) for a total of 4N variables where N is the number of electrons. A water molecule has 10 electrons, which means that it needs 40 variables, yet it is a very simple molecule. Therefore, it was imperative to find a better way to compute the wavefunction to reduce the number of coordinates, so scientists decided to use the electron density.[171]

This electron density is the probability density of finding an electron in a region of space. In mathematical terms, the electron density [ρ(r)] is a function of the spatial coordinates (r). By making this approximation, we assume that it is impossible to know the precise location of an electron; instead, we tackle the problem by attributing them to the regions of space they will most likely occupy. The 4N variables convert into only three variables by treating the electrons as indistinguishable, independently of the number of electrons. In a one-electron system, the electron density is proportional to the square of its wavefunction.[156] Electron density is a measurable trait, as X-ray diffraction can detect it (***Figure 37***).

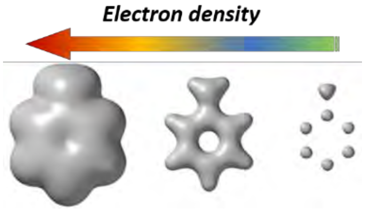

Figure 37. Observable electron density of aniline.

In a density plot, the maxima represent the nuclei's position, as it is where we locate the electrons, and the valleys between maxima are the bonds of the molecule. However, to be useful to solve Schrödinger's equation, this density must represent the system's energy. Pierre Hohenberg and Walter Kohn[172] demonstrated that the electron density correlates to the system's energy through a reduction to the absurd method. In a given system with electrons and nuclei, we can consider the Hamiltonian operator as follows:

$$H = T_{elec} + T_{nuc} + V_{en} + V_{nn} + V_{ee} \qquad (21)$$

Using the Born Oppenheimer approximation, we neglect the kinetic energy of the nuclei (T_{nuc}), and the potential energy between nuclei (V_{nn}) is constant. Meaning that we describe the system by the number of electrons and the nuclei's potential, which also means that they also give the wavefunction and electron density. The first Hohenberg-Kohn theorem assumes that two external potentials (V_{ex1} and V_{ex2}) that can originate from nuclei have the same electron density. Since the potentials are different, the Hamiltonians should be different and thus, their corresponding wavefunctions as well, unless the difference between V_{ex1} and V_{ex2} is a constant. If one applies this to the ground-state energy associated with each wavefunction:

$$E^1 = \langle \psi_1 | \hat{\mathrm{H}}_1 | \psi_1 \rangle \text{ and } E^2 = \langle \psi_2 | \hat{\mathrm{H}}_2 | \psi_2 \rangle \qquad (22)$$

Since the difference resides in the nuclei potential:

$$E^1 = \langle \psi_1 | \hat{\mathrm{H}}_1 | \psi_1 \rangle < \langle \psi_2 | \hat{\mathrm{H}}_1 | \psi_2 \rangle = \langle \psi_2 | \hat{\mathrm{H}}_2 + V_{ex1} - V_{ex2} | \psi_2 \rangle \tag{23}$$

$$E^1 < E^2 + \int [v_1(r) - v_2(r)] \rho(r) dr \tag{24}$$

Swapping the indexes 1 and 2:

$$E^2 < E^1 + \int [v_2(r) - v_1(r)] \rho(r) dr \tag{25}$$

Finally, adding Eq. 24 to Eq. 25, we obtain:

$$E^1 + E^2 < E^1 + E^2 \tag{26}$$

This equation shows that the assumption that both potentials were not equal is wrong, which determines that the potential *V*(*r*) is unique to the functional of *ρ*(*r*). Since the potential also fixes the Hamiltonian, then the electron density can determine all properties of the system:

$$\rho(r) \rightarrow V_{ext}(r) \rightarrow \hat{\mathrm{H}} \tag{27}$$

$$\rho_0 \rightarrow \{N, Z_A, R_A\} \rightarrow \hat{\mathrm{H}} \rightarrow \psi_0 \rightarrow E_0 \tag{28}$$

This finding goes by the hand of the second theorem of Hohenberg-Kohn that states that the functional responsible for a given quantum state's ground state energy gives the lowest energy if and only if the density is the correct ground state density, which means that any density that is not the ground state density will give higher energy than the ground state. Hohenberg-Kohn developed their functional F_{HK}, which can minimize any starting density until reaching the density of the ground state:

$$F_{HK}[\rho] = \underset{\psi \rightarrow \psi_{\rho_0}}{\mathrm{Min}} \langle \psi | \hat{T} + \widehat{V_{ee}} | \psi \rangle \tag{29}$$

Nevertheless, the exact expression to correlate F_{HK} and the electron density is unknown because the exact form of *T*[*ρ*] is unknown, deriving into errors that led to preferring one-electron wavefunctions due to their higher accuracy. It was until 1965 when Walter Kohn and Lu Jeu Sham[173] suggested that we approach the system's kinetic energy (*T*[*ρ*]) through an alternate set of molecular orbitals from a reference system of non-interacting electrons. By doing so, they demonstrated that it is possible to calculate the electron density as follows:

$$\rho(\vec{r}) = \sum_{i=1}^{N} |\chi_i(\vec{r})|^2 \tag{30}$$

Where χ_i are the Kohn-Sham spin-orbitals. Thanks to this expression, using an initial set of molecular orbitals, one can obtain an initial electron density guess. This density will enable the F_{HK} solution, which, in turn, will give a new set of orbitals. There is an outstanding flaw in this process: by adding a set of non-interacting one-electron orbitals, the function now depends again on 3N variables, instead of 3. Still, since these orbitals are not correlated, it is much easier to compute than the fully correlated HF method. Speaking of HF, this process also iterates until the energy converges. If one compares HF and DFT, there are apparent differences. In HF, the Hamiltonian is exact, but due to a Slater determinant's use as a multi-electron wavefunction, the solution is always approximate. On the other hand, in DFT, the Hamiltonian is approximate, but the final electron density can be exact. The general formula obtained through this process:

$$E[\rho] = T_s[\rho] + V_{ne}[\rho] + V_C[\rho] + E_{xc} \tag{31}$$

Where E is the total energy, T_s is the kinetic energy of the reference system, V_{ne} is the nuclei-electron interaction, and V_c is the Coulombic repulsion between electrons. At this point, the exchange-correlation energy between electrons, plus the difference in kinetic energy between the set of non-interacting electrons and the real interacting ones, compiles into the E_{xc} term, which is unknown. This new term is responsible for DFT flaws, like not describing intermolecular interactions such as van der Waals forces, charge transfer excitations, transition states, potential energy surfaces, and others. Overall, DFT methods exist in a wide variety just to try to describe this E_{xc} term. According to the degree of parameters to consider in this E_{xc} calculation, we can divide DFT functionals into LDA, GGA, Meta-GGA, Hybrids, and hybrid meta-GGA, increasing in accuracy according to Jacob's Ladder[174] (***Figure 38***).

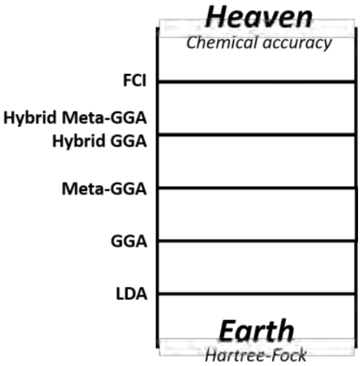

Figure 38. Jacob's ladder of chemical accuracy.

In summary, LDA means Local Density Approximation, a method that depends exclusively on the density.[175] It runs well in systems where the electron density is constant, but it cannot describe weak interactions nor thermochemical predictions, and even more, they usually overestimate the bond strength. The next step corresponds to the Generalized Gradient Approximations or GGA.[176] This approach takes the LDA and improves it by adding the density gradient into the functional. It corrects LDA's overbinding, has more real magnetic properties, and better energy barriers yet, Van der Waals forces are not present, and for some metals, GGA is worse than LDA. Following GGA comes meta-GGA functionals.[177] These functionals also include kinetic energy density. Some qualities improve compared to the GGA, but adding the kinetic energy, which depends on the Kohn-Sham orbitals, implies further calculations and longer computational times. Hybrid methods[178] include the exact HF exchange, or at least, a part of it through a mixing parameter. This approach calculates the HF exchange and adds it to get closer to the system's exact energy; thus, the problem with these methods is that since we calculate HF, we have to deal with 4N variables, not like the 3N previous methods. Therefore, it is much more time-consuming. The ladder's final step would be the Full Configuration Interaction, or FCI,[179], where we have the exact exchange and the exact correlation. It is the most time consuming and the most expensive one as it requires all possible electron configurations. Due to the depth of this method, it is often used for small molecules or atoms only.

2.1.1.4. How to choose the optimal functional and basis set

Considering the number of available functionals and basis sets, choosing which is best appropriate for our target work can be difficult. There are three main possibilities for choosing the right methodology based on each given project and the available bibliography.

Let us assume three cases: one where there is no information available for our project (new research topic or experimental data without computational info); one that is similar to other computational works on the bibliography, and a last one where the project is new, but some target data (such as pK_a) are relevant to the project. In the first case, without any computational background, the best choice is to do a benchmark. Benchmarking serves to study different functional/basis combination and compare a particular step with the available experimental data. Usually, it is better to choose the methodology that most closely resembles the experimental data; however, there are some specific cases where accuracy must be set aside for the project's sake. As a clear example of such a case, there is a project on a multi-layered fullerene (or CNO) consisting of over three hundred atoms in this thesis. For quantum mechanical calculations, this implies a high cost since, as stated previously, the power needed increases in an N^3 fashion, leading to long-lasting calculations for each molecule. Thus, the benchmark served to verify experimental data and find the most time-efficient functional/basis set combination.

If neither experimental nor computational data are available for our project, benchmarking does not help as there are no experiments to compare; thus, the methodology must be chosen based on the most similar molecules from other works. In the second case, where published papers focus on similar compounds as our target project, an optimal approach is to mimic their procedure, with their same molecules, to verify that we can reproduce their data. The methodology should be proven as it was published in a previous article, while also allowing the comparison between both papers, should that be a topic of interest.

For the last option, a project without predecessors that targets measurements like electropotentials or pK_a should aim to reproduce these measurements of already published computational works. As stated above, this ensures the validity of the procedure and helps to identify human errors. Once we reproduce the measurements, it is possible to import their methodology into the new project. When looking for methodology, it is advisable to search for the whole target process (equations, regressions, and everything useful) to help in the upcoming project.

Once we choose the functional and the basis set, it is possible to include corrections to define our target system better. A clear example would be a reaction in the gas phase, in ethanol, or water. While it is the same reaction, the media changes experimentally, so it must change in the computational work, hence the corrections.

2.2. Geometry optimization and transition states

Before making any corrections, it is crucial to view what we should try to correct clearly. The most critical data in computational chemistry is energy. This energy relates to the stability of a given compound or the likeability of one reaction to occur or not. It can also show whether a reaction path is possible at any given condition. This energy will determine the outcome of the analysis, and it must reflect the experimental behavior; thus, it is crucial to understand if it is correct or if it needs adjustments and why. The very first thing one must know is the Potential Energy Surface (PES) and its meaning.

2.2.1. Potential Energy Surface (PES)

The PES is the relationship between a molecule (or a set of molecules) geometry and its energy (***Figure 39***). This concept originates thanks to the Born-Oppenheimer approximation since it considers the nuclei as static, thus enabling the molecule to take a specific structure.

As shown in the 3D PES view in ***Figure 39***, we can see the relationship between different coordinates such as bond length, angles, or dihedral angles and relate them to the molecule's energy at those specific parameters. The PES can take any shape depending on the studied system; however, it shares some particularities. As visual training, imagine a surface with any shape, then put a marble in the spot where the initial guess structure would be located and let it go. The marble would slide across the surface, back and forth, until it rested at a minimum. This effect occurs as well with molecules, with the subtle difference that unless it is a system at the absolute zero (0K) where all the particles are stationary, it will never completely stop moving across the surface, but most of the time, it will take the shape of the minima. We can explain reactivity through the PES and the system moving through the surface.

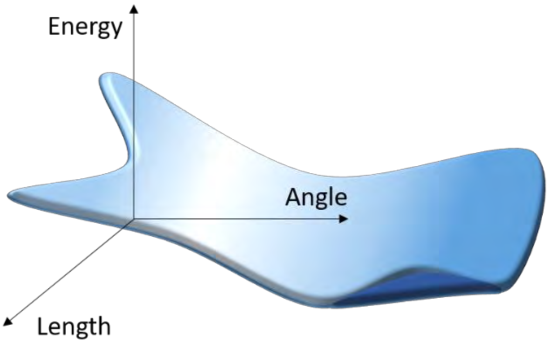

Figure 39. Example of a PES comparing an angle, a length and the energy of each conformation.

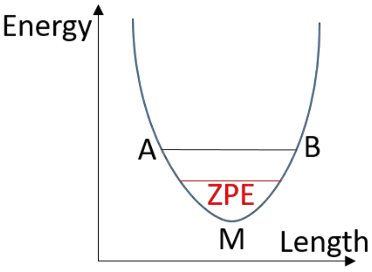

Figure 40. Representation of the ZPE of a system.

In ***Figure 40***, a 2D PES involves the length of a bond and the system's energy. Considering the previous example, the molecule will never stay at the minima M, but it will go from A to B, passing through M steadily due to the bond's vibration. The more energy we give to the system, the higher point A and point B would locate. The lowest line drawn by A and B at any given condition is known as the zero-point energy or ZPE, and it represents the movement of the nuclei. In mathematical terms, there is a known expression to search for minima: Newton-Raphson's method.[180-182] Using the energy E(x) function, we can find the minimum through the Hessian matrix (Eq. 32). This method takes an initial guess of the energy function, which derives from the guess of the spin-orbitals we design, and then iterates until it converges into a minimum. This method is better than others (*i.e.*, gradient descent[183-184]) since it uses the slope's tangent at each point to find the next variable until the slope is approximately zero.

$$\vec{x}_{n+1} = \vec{x}_n - H_k^{-1}\vec{g}_k \tag{32}$$

Where H_k^{-1} is the Hessian matrix and $\vec{g}_k$ is the gradient vector.

Let us assume now that there is a reaction between two molecules (***Figure 41***). Once again, the energy is useful for this task. In this case, however, a maximum can be observed that connects two minima. This maximum is known as a transition state (TS), though in 3D, it is a bit more complicated than that (***Figure 42***).

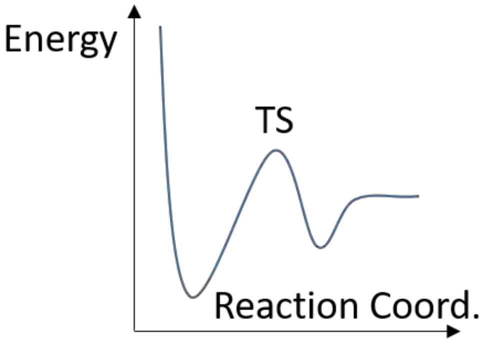

Figure 41. TS between two minima in a given system.

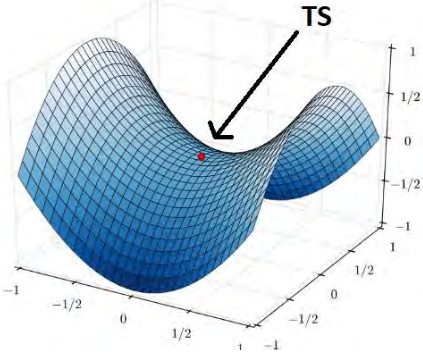

Figure 42. 3D view of a saddle point. This is where a TS is located.

TSs are points in the PES representing the lowest energy point in the path between two minima. They are the critical point for kinetic studies as they dictate the speed of the reaction. Assuming a PES that represents all possible geometries of a given system versus their energy, the TS is a maximum in the path from one minimum to another, yet it is a minimum through the rest of the coordinates. This particularity is known as a saddle point, and with it, one understands why the reaction goes through there, as it is the optimal path.

TSs are impossible to track experimentally as they are so unstable that they will instantaneously go towards one of the minima. In this sense, quantum mechanics is a valuable tool for locating the TS of any reaction and obtaining its information. Nevertheless, it is not an easy task due to its nature. In a ground-state calculation, we try to find a minimum in all directions; thus, it should be relatively simple to obtain it with a good starting point. Nevertheless, to locate a TS, we must start from a geometry close to the TS.

2.2.1.1. Gibbs energy

Between 1875 and 1878, Josiah Williard Gibbs[185] reported what is known as the basis of thermodynamics: enthalpy, defined as the heat of a reaction at constant pressure, and free enthalpy, which informs us if the reaction can occur spontaneously at constant temperature and pressure. The latter is known as the Gibbs free energy in its honor.

$$G(P,T) = H - TS \qquad (33)$$

Eq. 33 is the general representation of the Gibbs energy. Looking deeper into the formula, the enthalpy represents the following:

$$H = U + ZPE + C_vT + P \cdot V \qquad (34)$$

This enthalpy comprises the internal electronic energy (U), the nuclei energy at 0 K (ZPE), the change of the internal energy when going from 0 K to T K (C_v), and the product $P{\cdot}V$ at any given conditions by the law of the ideal gases ($PV = nRT$). The Gibbs energy

assumes that the system is at constant pressure, temperature, and isolated without heat transfer between mass, only with the environment.
To calculate C_v, we must rely on mechanical statistics to partition the energy according to their function (vibrations, rotations, *etc.*). For a more specific understanding:

$$C_v = k_B N \left[2T \cdot \left(\frac{\partial \ln(q)}{\partial T} \right)_{V,N} + T^2 \cdot \left(\frac{\partial^2 \ln(q)}{\partial T^2} \right)_{V,N} \right] \tag{35}$$

where "*q*" is the product of all the partition functions:

$$q = q_n q_e q_v q_r q_t \tag{36}$$

Such functions (nuclei, electronic, vibrational, rotational, and translational) allow an accurate representation of the system's energy; thus, it is possible to use the Gibbs energy as a measure of spontaneity. The entropy (*S*) of the Gibbs formula also relies on this energy partition. In a given reaction, we want to measure how the Gibbs energy evolves; thus, we represent it as:

$$\Delta G = \Delta H - T\Delta S \tag{37}$$

$$S = N k_B \ln(q) - k_B (N \ln N - N) + N k_B T \left(\frac{\partial \ln(q)}{\partial T} \right)_{V,N} \tag{38}$$

Where Eq. 37 is the most used form. According to Gibbs, any reaction with a $\Delta G < 0$ implies that the reaction is spontaneous (exergonic reaction), a $\Delta G = 0$ means that it is at equilibrium, and a $\Delta G > 0$ means that the reaction will not occur without external interference (endergonic reaction). It is important to remark that while a reaction can be spontaneous, we may not observe it if it does not occur fast enough. Human combustion (oxidation) is spontaneous, but it is also so slow that we can live for another day. The aforementioned TSs determine the speed at which reactions occur. Due to these properties, the Gibbs energy is an optimal choice to study mechanistic pathways. Once the energy has been established as the main target to study, it is time to adjust it using the appropriate corrections.

2.2.1.2. Energy corrections

As stated in the previous section, the methodology chosen for each project is vital and determines the results we obtain. Nevertheless, those results may not reflect the experiments, thus the need to correct them. We have used the following corrections in one or more papers presented in this thesis.

Thermal correction

A straightforward adjustment is to specify the temperature at which the experiment occurs. This modification can heavily affect energy, as seen in Eq. 34, 37, and 38. Furthermore, the temperature is considered additional energy for the system, and it can significantly affect the population of the vibrational levels and the energy barriers of the TSs.

Pressure correction

Usually, all calculations consider a standard pressure of 1 atm; however, there is an adjustment of P = 1354 atm in the water oxidation articles. At first glance, it shocks to see this number since the experiments do not occur at this pressure. Martin, Hay, and Pratt[183] first used this correction because in gas calculations, at P = 1 atm, water has a very low density, far from the experimental one of *ca.* 1gr/cm^3. If water is a solvent and a reactant, it has more freedom before complexation than after; thus, this adjustment tries to reflect water's behavior in such a circumstance. This correction affects the translation entropy of the system. In order to obtain this value of 1354 atm, the following procedure applies:

$$PV = nRT \tag{39}$$

$$P = \frac{nRT}{V} \tag{40}$$

$$d = \frac{m}{V} \qquad m = M_w \cdot n \tag{41}$$

$$d = \frac{M_w \cdot n}{V} \tag{42}$$

$$n = \frac{d \cdot V}{M_w} \tag{43}$$

$$P = \frac{d \cdot R \cdot T}{M_w} \tag{44}$$

Using the ideal gas formula and the seen adjustments, one can use the liquid's density, in this case, water, to reproduce the media. We can obtain the P = 1354 atm by using the density of water at 25 ºC (d = 0.997 g/cm^3), the gas constant (R = 82.06 $cm^3 \cdot atm/_{K \cdot mol}$), the temperature (T = 298.15 K) and the molecular weight (Mw = 18.015 g/mol). As a remark, when the solvent is not water, the pressure must vary according to the solvent (*i.e.,* for methanol P = 605 atm)

Dispersion correction

There is a set of electron correlation effects that occur at long distances in molecules. These become relevant for larger molecules (*i.e.,* protein). Kohn-Sham DFT does not include this kind of relationship between electrons, and it is currently one of the main targets to solve for DFT. These long-distance [induced dipole]-[induced dipole] interactions are the London Dispersion Forces,[186] the weakest of the attractive van der Waals[187] dispersion forces. In tiny molecules, they might not be significant enough to alter the geometry, but they are a force to reckon with as the size increases. Grimme[188] developed an equation that considers these forces:

$$E = \sum_{AB} \sum_{n=6,8,10,\ldots} s_n \frac{C_n^{AB}}{r_{AB}^{r}} f_{d,n}(r_{AB}) \tag{45}$$

In simple terms, they consider the sum of all the atom pairs of the system through these dispersion coefficients C_n to account for them and the f_{dn} damping functions to avoid double counting forces or short-distance correlation. This operation is known as DFT-D3 dispersion correction. Even though this was tested throughout thousands of articles, deeming it as a robust dispersion correction, it appears that it overemphasizes the dispersion effect in some cases. In 2006, Becke and Johnson proposed[189] a finite damping for their model, which bases on the Optimized Effective Potential (OEP) of Sharp and Horton,[190] and Talman and Shadwick.[191] They introduced some approximations to the model in order to simplify it for computational efficiency. Their procedure was so good that Grimme introduced it into its model. This damping significantly improves non-bonded distances and has better intramolecular dispersion overall when coupled with Grimme's model, also known as the DFT-D3BJ dispersion correction.[192]

Solvent correction

Most geometry optimization calculations are done in the gas phase. However, it does not reflect the media of the reaction, which is usually in a solution. To handle this, there are two basic ways to represent the media: include as many solvent molecules as possible (explicit model), or emulate the environment that the solvent would create (implicit model). It is useful for the first one to make molecular mechanics calculations since it relies entirely on several approximations (*i.e.,* nuclei are masses and bonds are springs) that do not need a lot of computing power for each atom; thus, we can compute a more considerable amount of them. On the other hand, quantum mechanics allow for more precision and give better overall energies, but due to its immense power consumption since it takes into account all the quantum properties, the more atoms, the longer the calculations. If we want to stick using quantum mechanics, a suitable correction is to emulate the solvent as a polarizable continuum and make a cavity where we locate the target molecule. This method is known as Self-Consistent Reaction Field (SCRF).[193] There are two approaches to this topic: the Polarizable Continuum Model (PCM)[194] and the Solvation Model Density (SMD).[195] The first one relies on defining a cavity with the shape of the target molecule; then, it represents the solvent as a dielectric constant that interacts with the molecule. A simple interpretation:

$$\Delta G_{solv} = \Delta G_{cav} + \Delta G_{disp} + \Delta G_{elec} + \Delta G_{h-b} \tag{46}$$

Where the first term accounts for the Gibbs energy required to make the cavity, the second one accounts for the van der Waals dispersion forces between the solvent and the solute, the third for the electrostatic component (polarization and charge distribution), and the fourth accounts for the hydrogen bonds that may or may not occur. The second approach, SMD, is based on the same principle, but it is parametrized to work optimally with the Minnesota functionals (M06, M06L, M06-2X, *etc.*).[196-197]

Integration grid correction

As previously stated, DFT has several approximations; thus, it is challenging to pinpoint inherent flaws to the calculations. One of them is that depending on the integration grid used to calculate the Schrödinger equation; we can find differences of 5 kcal/mol or greater due to the molecule's orientation. The need for integration grids arises from the exchange-correlation functionals calculations, where analytical solutions are impossible; thus, we apply a numerical quadrature named integration grid. Of course, varying the energy depending on the orientation should not occur. In 2019, Bootsma and Wheeler[198] detected this flaw while testing the Gibbs energies of molecules with low-frequency modes, and thankfully, they found a solution. It is as simple as asking the computing program to increase the grid of calculation from the standard 75302 to denser 99590 grid or even higher. We can avoid most of the energy fluctuations due to the low-frequency vibrations, and the results become reliable.

2.2.1.3. Relevant measurements

In some cases, there are specific measurements of interest, such as electropotentials or pK_a. Due to the computational methodology, these values require the utmost care to reflect the experiments. While the experiments should give similar results every time, the computational results can vary depending on the functional and basis set chosen and the different corrections that each author may use. Therefore, it is imperative to give proper reasoning behind the procedure and corrections that one uses on its work. We explain the pK_a and electropotential calculations alongside Mayer Bond Orders (MBO) and Effective Oxidation States (EOS) in the following sections.

2.2.1.3.1. Calculation of pK_a

In this thesis's projects, we use the pK_a to determine a given molecule's protonation state. Once we have the pK_a, we can compare it with the pH of the media. If the pH is higher than the pK_a, then the molecule deprotonates, while if it is the opposite, pH < pK_a, then the molecule remains protonated. In order to calculate the pK_a, we begin with a general reaction:

$$AOH \rightarrow AO^- + H^+ \tag{47}$$

The Gibbs energy (ΔG) of this reaction in a solution can be used in the pK_a calculation as follows:

$$\Delta G = \left(G_{AO^-} + G_{H^+}^{exp.}\right) - G_{AOH} \tag{48}$$

$$\Delta G = -R \cdot T \cdot \ln(K_a) \tag{49}$$

$$pK_a = \log\left(e^{\frac{\Delta G}{RT}}\right) \tag{50}$$

This set of equations is how we obtain our calculated pK_a. To have a better approximation, we follow the same procedure as Concepcion *et al.*[76] have calculated different pK_a and compared them with known experimental values, as seen in their Supporting Information (SI). To adjust our results, we plot the calculated pK_a *vs.* the experimental pK_a and use the obtained linear regression to correct the computational results, giving more accurate data:

Table 1. Experimental, calculated, and corrected pK_a values for different acids.

Acid	**pK_a**		
	Experimental	**Calculated**	**Corrected**
CF_3-COOH	0.23	3.05	0.17
CHF_2-COOH	1.34	5.34	1.08
CH_2F-COOH	2.60	9.06	2.56
CH_3-COOH	4.76	14.22	4.61
H-PO(OH)$_2$	1.30	6.43	1.52
H_3C-PO(OH)$_2$	2.38	9.30	2.66

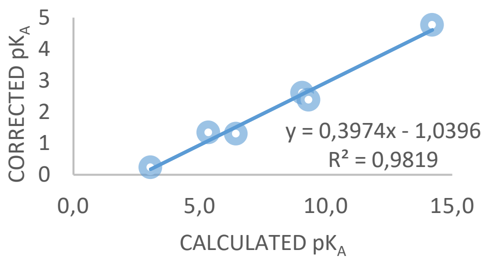

Figure 43. Correction between experimental and computational data.

It is important to remark that we must apply this correction for every change in the computational methodology. The same linear regression is not valid for combinations of different functionals and basis sets.

While this is the standard approach towards pK_a calculation, there are alternatives. According to one of our target compounds, an organometallic hydroxy acid compound, it is possible to use another pK_a formula, such as the one developed by Durrant and Gilson.[199] In their work, they report a set of organometallic hydroxy acid compounds that got their pK_a measured. They found a linear regression that correlated 26 different compounds, which derived in Eq. 51.

$$pKa = 0.275 \cdot \Delta E - 4.20 \tag{51}$$

In this case, ΔE refers to the electronic energy in solution rather than the Gibbs energy. Thus, one must consider that the solvated proton's value for this equation is $\Delta E_{H+} = -258.4$ kcal/mol since they developed their formula with this value. There can be more types of pK_a calculations, such as regressions with experimental data or other kinds of corrections but, which one should we use? The answer is simple: choose the one that resembles the most the experimental data, which is what we want to simulate and correlate. In different articles reported in this thesis, the pK_a calculation we used changes between Eq. 51 and the correction of ***Figure 43*** to reproduce a given experimental pK_a better.

2.2.1.3.2. Calculation of electropotentials

There are two types of electropotentials in the articles of this thesis. The first one refers to the redox potentials, which determine whether a compound is oxidized or reduced, while the second one refers to the simultaneous transfer of protons and electrons, known as Proton Coupled Electron Transfers (PCET). For the redox potentials, the calculation is straightforward:

$$A^{+} + e^{-} \rightarrow A \tag{52}$$

$$\varepsilon^{o}{}_{red} = -\frac{\Delta G_{reaction}}{nF} - SHE \tag{53}$$

Where the "n" refers to the number of electrons transferred, the "F" is the Faraday constant, and the SHE refers to the Standard Hydrogen Electrode (4.28 V).[200] For the second type of potentials, the PCET is a bit more complicated. For the sake of understanding the procedure, let us use the example of ***Figure 44***. As one can see, there are two options to transform $Ru^{II}OH_2$ to $Ru^{III}OH$; first, oxidation followed by deprotonation, and second, deprotonation followed by oxidation. The key point to understand why PCET is different from a normal redox process is the proton presence in the reaction.

This proton will be included in the Gibbs energy of the reaction as follows:

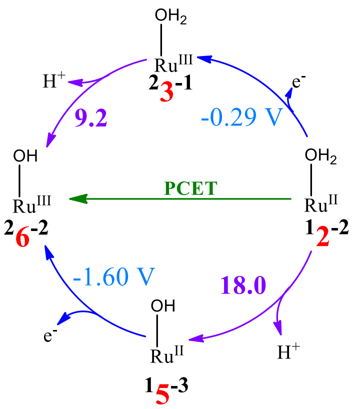

Figure 44. PCET sample mechanism. Extracted from one of the articles in this thesis.

$$Ru^{III}(OH) + H^{+} + e^{-} \rightarrow Ru^{II}(OH_2) \tag{54}$$

$$\Delta G_{reaction} = \Delta G_{Ru^{II}(OH_2)} - \Delta G_{Ru^{III}(OH)} - \Delta G_{H^{+}} \tag{55}$$

In order to address the new proton term, which does not appear in a redox reaction, we consider the SHE reaction:

$$H^{+}{}_{solv} + e^{-} \rightarrow \frac{1}{2} \cdot H_{2\,gas} \tag{56}$$

From which we can obtain the ΔG_{SHE}:

$$\Delta G_{SHE} = \frac{1}{2}\Delta G_{H_2} - \Delta G_{H^{+}} \tag{57}$$

$$-\Delta G_{H^{+}} = -\frac{1}{2}\Delta G_{H_2} + \Delta G_{SHE} \tag{58}$$

This $-\Delta G_{H^{+}}$ term can be now substituted in Eq. 58 and use it in Eq. 53:

$$\varepsilon^{\underline{o}}{}_{red} = -\frac{\Delta G_{Ru^{II}(OH_2)} - \Delta G_{Ru^{III}(OH)} - \frac{1}{2}\Delta G_{H_2} + \Delta G_{SHE}}{nF} - SHE \tag{59}$$

$$\varepsilon^{\underline{o}}{}_{red} = -\frac{\Delta G_{Ru^{II}(OH_2)} - \Delta G_{Ru^{III}(OH)} - \frac{1}{2}\Delta G_{H_2}}{nF} + SHE - SHE \tag{60}$$

$$\varepsilon^{\underline{o}}{}_{red} = -\frac{\Delta G_{Ru^{II}(OH_2)} - \Delta G_{Ru^{III}(OH)} - \frac{1}{2}\Delta G_{H_2}}{nF} \tag{61}$$

Comparing this methodology with the $\Delta G_{reaction}$ that uses the experimental value of $\Delta G_{H^{+}} = -270.3$ kcal/mol,[201] we have tested both and obtained the same potentials; thus, both procedures are correct. Despite this, since this is a computational study, we have chosen to use Eq. 61 since it does not rely on experimental values. While this is just a simplification of the formula, we still have to tackle the fact that according to the media's pH, which involves the protons (H^+), the reaction could be more or less favorable. In order to consider this, we use the Nernst equation:

$$\varepsilon_{red} = \varepsilon^{o}{}_{red} + 0.059 \cdot (pH - pKa) \qquad (62)$$

Following the example of ***Figure 44***, we have to determine when to apply it. To do so, we followed Meyer and coworkers works[202-203] that studied similar $RuOH_2$ complexes experimentally. In their works, they present different redox reactions according to the media pH (***Figure 45***).

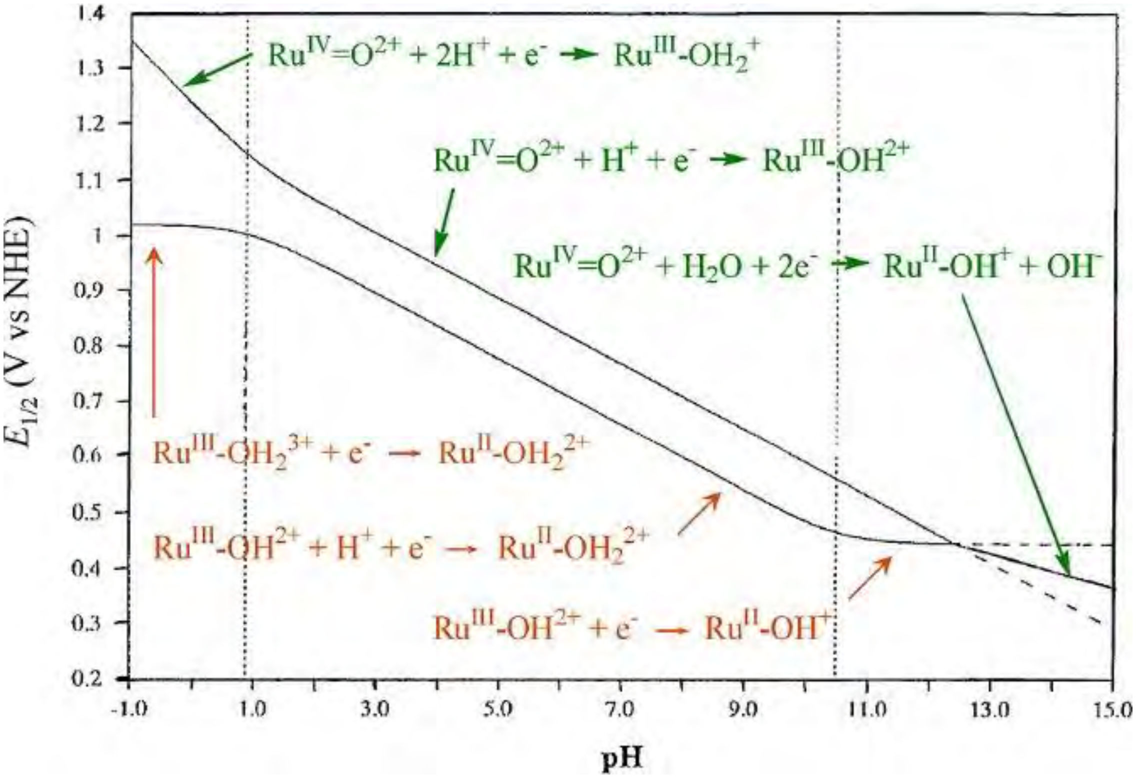

Figure 45. $E_{1/2}$ *vs*. pH diagrams for the $Ru^{IV/III}$ and $Ru^{III/II}$ couples of cis-$[Ru^{II}(bpy)_2(py)(H_2O)]^{2+}$. The Figure is taken from Meyer and Huynh.[203] Dashed vertical lines show the pK_a of $Ru^{III}OH_2^{3+}$ (0.85) and $Ru^{II}OH_2^{2+}$ (10.6).

Following their results, we applied the same principles to our mechanism in ***Figure 44*** as follows:

$$Ru^{III}(OH_2)^{-1}: pKa^{I} \quad \& \quad Ru^{II}(OH_2)^{-2}: pK_a^{II} \qquad (63)$$

First of all, we define the target compounds; in this case, it is a $Ru^{III/II}$ redox reaction. Each one of them has a given pK_a that we define as pKa^{I} and pKa^{II}. In all cases, $pKa^{I} < pKa^{II}$ moreover, we assume that the potential in the media is enough to perform all oxidations. If $pH < pKa^{I}$ we consider a $0H^+/1e^-$ pH-independent reaction:

$$Ru^{III}(OH_2)^{-1} + e^- \rightarrow Ru^{II}(OH_2)^{-2} \qquad (64)$$

Thus, no pH correction is applied. This is the step from **2** to **3**. *If* $pKa^{I} < pH < pKa^{II}$ we consider a $1H^+/1e^-$ pH-dependent reaction:

$$Ru^{III}OH^{-2} + e^{-} + H^{+} \rightarrow Ru^{II}(OH_2)^{-2} \tag{65}$$

Here, we apply the Nernst equation. The pK_a used in the equation is pK_a^I. This is the step of **2** to **6**. If $pKa^{II} < pH$ then we consider a 0H$^+$/1e$^-$ pH-independent reaction:

$$Ru^{III}OH^{-2} + e^{-} \rightarrow Ru^{II}OH^{-3} \tag{66}$$

Thus, no correction is applied. This is the step from **5** to **6**. Doing this correction for the molecules shown in ***Figure 44*** gives a PCET potential of 1.43 V at pH = 8 and a potential of 1.84 V at pH = 1.
We can now define the solvated proton properly and apply the Nernst equation accordingly with all the above considerations.

2.2.1.3.3. Mayer Bond Orders (MBO)

Depending on the target system to study, the reactivity varies according to the atoms and their bonding. It is common to have weak intermolecular bonds, hydrogen bonds, or even allylic or agostic bonds. Each of them defines a different interaction in a mechanism; thus, it is crucial to identify them. To do so, one can use the MBO.[204] By definition; the MBO uses two matrixes: the density matrix (P) and the overlap matrix (S):

$$P_{st} = \sum_{i}^{occupied} n_i c_{is} c_{it} \tag{67}$$

$$S_{st} = \int \psi_s^* \cdot \psi_t \, d\tau \tag{68}$$

As Eq. 67 shows, we can obtain the density matrix using the occupation numbers (n_i), and the coefficients of the two involved atoms (c_{rs} and c_{rt}), which refer to their respective atomic orbitals (s and t). The overlap matrix in Eq. 68 describes the overlap of the atomic orbitals basis sets through each atom's orbital wavefunction. Combining both, one can obtain the mathematical explanation of the MBO as follows:

$$B_{AB}^{Mayer} = \sum_{s}^{on\ A} \sum_{t}^{on\ B} (PS)_{st}(PS)_{ts} \tag{69}$$

Eq. 69 dictates that the MBO between two atoms A and B (B_{AB}^{Mayer}) is the sum over the orbitals (s for atom A, t for atom B), for the product of the density and overlap matrices (PS). The most important thing about MBO is that it can reflect the bond’s strength; therefore, we can use it to determine each molecular bond's character in the target system.

2.2.1.3.4. Effective Oxidation State (EOS)

In some of the works presented in this thesis, we targeted catalysts known for their high OS, such as a Ru^V metal center. Indeed, this is not common for Ru, as for it to achieve such a highly oxidized state, it should have a very stabilizing environment. Knowing that, some predicted compounds could be misplaced as Ru^{V} when, in fact, they could be a $\mathrm{Ru}^{\mathrm{IV}}$ or a $\mathrm{Ru}^{\mathrm{III}}$. To tackle this problem, we decided to use the EOS developed by Salvador *et al.*,[205] which focuses exclusively on the OS's proper determination. EOS work originates from the lack of continuity throughout scientific reports, as the IUPAC definition appeared to be ambiguous. In 2015, a new IUPAC definition[206] for the OS was defined as "the atom's charge after ionic approximation of its heteronuclear bonds." By definition, one should approach the OS through a Lewis structure that assigns bonds and then uses a fundamental chemical concept such as electronegativity to define the OS.

Nevertheless, in the field of quantum chemistry, there was not a proper calculation method. Salvador's group reported the EOS methodology to fill this gap. To begin with, they developed the method with effective atomic orbitals. These orbitals are distorted hybrid orbitals created from the molecule's electron density function for each atom, which means that these effective atomic orbitals consider their environment by definition. Each of these orbitals has an occupation number ($\lambda_{\mu}^{A,\sigma}$) that can either contain an electron, thus $\lambda_{\mu}^{A,\sigma} \to 1$ or not, thus $\lambda_{\mu}^{A,\sigma} \to 0$. Furthermore, the orbitals are divided between alfa and beta electrons for deeper analysis. Their method assigns values to the occupation number and tries to fill them with electrons, starting from the $\lambda_{\mu}^{A,\sigma} \to 1$ and going towards the $\lambda_{\mu}^{A,\sigma} \to 0$. Once every electron is assigned, the last occupied (LO) orbital is compared to the first unoccupied (FU) orbital following the formula in Eq. 70:

$$R^{\sigma} = 100 \cdot \min\left(1, \lambda_{LO}^{\sigma} - \lambda_{FU}^{\sigma} + \frac{1}{2}\right) \text{ where } \lambda_{LO}^{\sigma} \geq \lambda_{FU}^{\sigma} \tag{70}$$

Eq. 70 refers to the Reliability Index (RI), which, as its name implies, states how reliable the EOS assignation is. It compares the frontier orbitals according to their occupation number; the greater the difference, the higher the RI. Worst-case scenario, $\lambda_{LO}^{\sigma} = \lambda_{FU}^{\sigma}$ thus the RI = 50%. As a remark, it relies on the wavefunction, not on a Lewis structure, which means that it gives the most likely result for molecules with multiple Lewis structures. Additionally, it is possible to separate the molecules into fragments to study them individually, such as the metal center on one side and each of the different ligands on the other.

Closing up the methodology chapter, we used the following programs for the elaboration of the articles in this thesis: for optimization, frequency, solvent calculations, as well as MBOs, Gaussian09,[207] and Gaussian16;[208] for the EOSs, APOST-3D; for chemical visualization of the molecules, Chemcraft 1.8[209] and GaussView;[210] for Lewis structure and mechanism drawings, ChemDraw Ultra 12.0.[211]

Chapter 3. Objectives

This brief chapter aims to enumerate the different objectives for this thesis. Even if Chapter 1 already states them, here they are reorganized with a summary.
First, the thesis's primary goal is to work towards environmentally friendly chemistry, known as green chemistry. The reasoning behind this is improving both the quality of life and better managing and maintaining our planet. Since this is a broad topic, it needs more concrete objectives. Thus, three objectives become the main focus: hydrogen production as a clean energy source, atmospheric gas recycling, and clean energy production of solar cells.

First, we already have defined that hydrogen is one of the most promising fuels to produce, as its combustion produces only steam while other fossil fuels produce CO_2 and other gases like nitrous and sulfurous oxide. Catalysis is also one of the required aspects of green chemistry as it needs trace amounts of materials to produce significant quantities of the desired products. Altogether, we have chosen to study some catalytic reactions that produce hydrogen catalytically, which we set as objectives.

As mentioned in section 1.2.1.2**¡Error! No se encuentra el origen de la referencia.**, WOC is a promising way to produce hydrogen gas *in situ*, using solar power as the driving force. The best catalyst for this procedure is the one shown in ***Figure 46***. Knowing the whole mechanism for any procedure enables smart modifications to the catalyst to lower TS barriers. Thus, this project aims to learn about its mechanism for future updates.

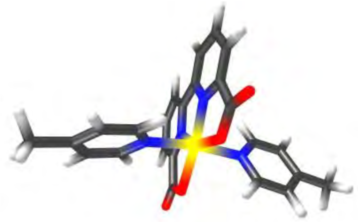

Figure 46. 3D view of the Ru(bda)(pic)$_2$ catalyst. Colored atoms: C grey, H white, N blue, O red, Ru yellow.

Since the first objective bases on the catalyst in ***Figure 46*** for future updates, we wanted to test and compare it with a similar catalyst, but with meaningful modifications to change the reactivity. This change involves the equatorial carboxylates, which we replace with phosphonates. The change is meaningful, but experimental data can help corroborate the mechanism of both catalysts. Adding phosphonate ligands (bpa) instead of carboxylate ligands (bda), we add three new possibilities depending on the pH: $[bpaH_2]^0$, $[bpaH]^{-1}$, and $[bpa]^{-2}$. We include both catalysts to be compared (carboxylated and phosphonated) in ***Figure 47***.

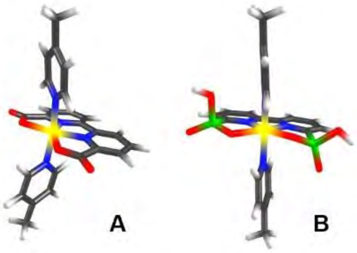

Figure 47. WOC catalysts A (with dicarboxylate ligand) and B (with diphosphonate ligand).

Going towards greener chemistry, the procedures in our industry should be revised as we make discoveries. One of the most remarkable innovations for any industry in greener productions is to stop producing waste. Of course, several processes could improve, but we chose the ADC as it also falls within the main objective of hydrogen production. The acrylonitrile production serves as the precursor of many medical treatments, but its production generates side-products that do not have enough demand and become waste. One of these non-desired products is a hydrogen acceptor that, as its name suggests, accepts the hydrogen atoms generated in the procedure into its structure. The ADC mechanism still produces the acrylonitrile; however, it does not need the acceptor.

We significantly reduce the products and the reagents, but now the hydrogen atoms are combined to create a hydrogen molecule. This acceptorless mechanism has just been discovered for a specific catalyst, and even though the experimental results are precise, the mechanism is still blurry. Therefore, one of the thesis projects will determine this mechanism according to the experimental results shown in ***Figure 48***.

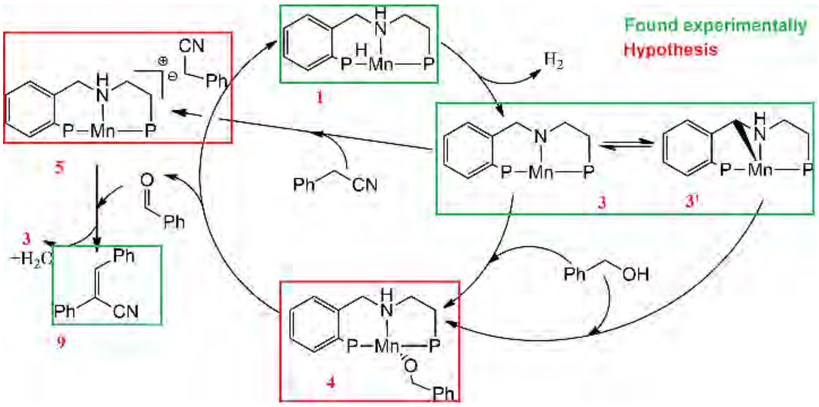

Figure 48. Proposed mechanism for the efficient production of acrylonitriles with a Mn based ADC catalyst. P means P^iPr and Mn means $Mn(CO)_2$ for clarity.

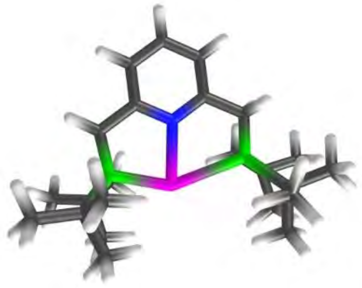

Figure 49. PNP pincer catalyst. Mn in pink, P in green, N in blue, C in grey and H in white.

Like objectives 1 and 2, we wanted to delve further into this acceptorless dehydrogenative mechanism with a second catalyst. Interestingly, the chosen catalyst falls into the same category as the previous one, known as PNP pincer catalysts due to their PNP bonds with the metal center. It shares similar experimental conditions with the previous catalyst yet, instead of acrylonitriles, it produces aldimines. Since it still produces hydrogen and shares the ADC procedure and structure with the previous ADC catalyst, but it has different reactivity, we decided to study the mechanism that involves the catalyst shown in ***Figure 49***.

While it is vital to have better-optimized catalysis toward environmentally friendly chemistry, it is also necessary to use the industry's undesired products that we already have as raw material to avoid waste. To address global pollution, one of the causes of climate change is N_2O, which is not as present as CO_2 but has a much more significant impact. The reason why CO_2 is more relevant than N_2O is the colossal difference in quantity between them. If we swap the amounts of CO_2 and N_2O, Global Warming could be considered the Global Boiling. Jokes aside, even if it does not have a significant impact right now, as it is not as present as CO_2, we cannot afford to let it grow steadily either. Therefore, following the above leads, we aim to develop a mechanism to recycle this N_2O based on an experimental catalyst related to the PNP pincer ligands, as mentioned above (***Figure 50***).

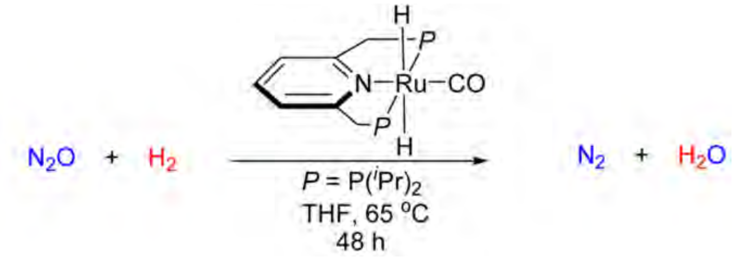

Figure 50. Hydrogenation of N_2O by the PNP-pincer Ru based catalyst (P = P(*i*Pr)$_2$).

The giant of Global Warming, CO_2, is a growing problem that we must face head-on. While there are many ways of reusing it, they often require high temperatures and pressures or use reactants that produce high amounts of CO_2 to obtain them. Therefore, we want to confront a relevant procedure: the cycloaddition of epoxides into cyclic carbonates. This process uses halides as a reactant and, consequently, requires producing CO_2 to generate the halide used for CO_2 recycling. Overall, we want to remove the initial CO_2 production by changing the halides for a different nucleophile. To do so, we will study several N-based labile ligands that may replace halide's role. We display the target mechanism and ligands in ***Figure 51***.

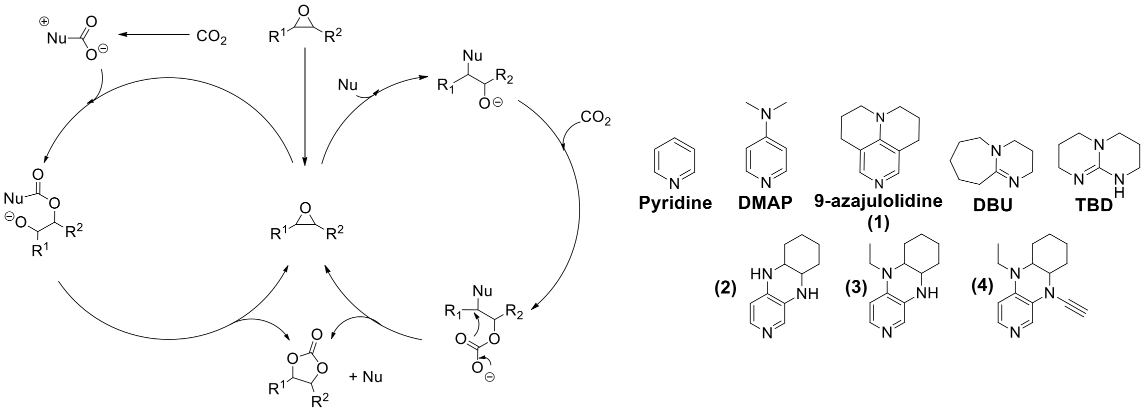

Figure 51. Mechanism of the CO_2 cycloaddition to epoxides for cyclic carbonate synthesis, and the N-based nucleophiles to study.

In the third main focus, we decided to deviate from the homogeneous catalysis towards another field of green chemistry. One of them is the solar cells, which collect light and transform it into energy for our consumption. Based on recent compounds used in solar cells, such as fullerenes, we decided on the thesis's ultimate objective.

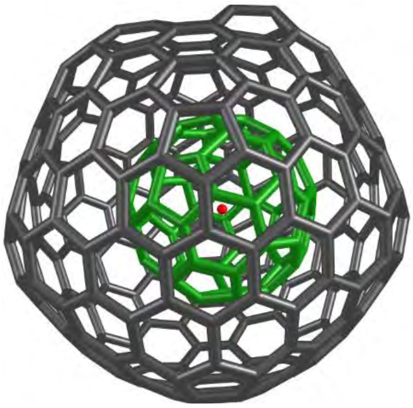
Figure 52. $Li^+@C_{60}@C_{240}$ CNO. Inner fullerene recolored in green for clarity. Li^+ shown in red.

As explained in section 1.3, these dye-synthesized solar cells can be mass-produced for light collection. They use mainly a surface made of TiO_2 with light-collecting dyes attached to it. This layout means that the charge transfer between materials is difficult. A way of improving this is by using functionalized fullerenes that combine surface and dye into a single molecule. A reasonable take is to use nano-onions, encapsulated fullerenes within another fullerene since experimental data shows that they have improved charge transfer compared to single fullerenes.[212-214] Accordingly, we decided to study one of the possible properties that involve this encapsulation: Faraday cages. It is just a way of testing these nano-onions' reactivity since, to include them in solar cells, we need to functionalize them. A simple known reaction for C_{60} is the Diels-Alder reaction, and it improves when encapsulating Li^+ cations; thus, we will study the same reaction for these nano-onions. Additionally, Faraday cages are related to electronic properties; thus, it might be relevant for future development in charge-transfer studies, though we do not delve further into this topic. Overall, we decided to test several nano-onions' reactivity and compared them with the same nano-onions with a Li^+ cation inside. ***Figure 52*** shows one of these nano-onions studied in this thesis.

Chapter 4. Hydrogen production as a clean energy source

4.1. The Influence of the pH on the reaction mechanism of water oxidation by a Ru(bda) catalyst

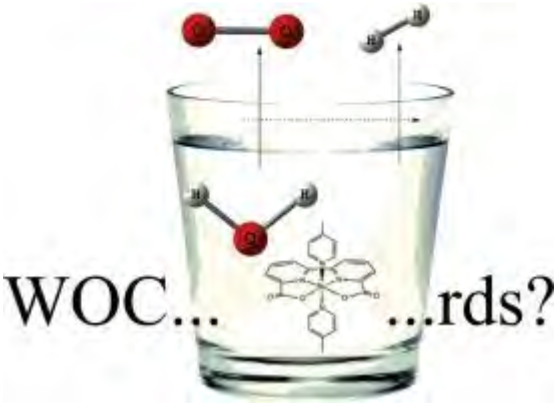

Luque-Urrutia, J. A.; Solà, M.; Poater, A. **The Influence of the pH on the Reaction Mechanism of Water Oxidation by a Ru(bda) catalyst.** *Catal. Today,* **2020**, *358*, 278-283.
DOI: 10.1016/j.cattod.2019.12.005

This thesis author has contributed to the DFT calculations, data analysis, writing, and revisions of the article.

Reproduced with permission from:

Luque-Urrutia, J. A.; Solà, M.; Poater, A. **The Influence of the pH on the Reaction Mechanism of Water Oxidation by a Ru(bda) catalyst.** *Catal. Today,* **2020**, *358*, 278-283.

https://doi.org/10.1016/j.cattod.2019.12.005

Copyright © 2019 Elsevier B.V. All rights reserved.

Catalysis Today 358 (2020) 278–283

Contents lists available at ScienceDirect

Catalysis Today

journal homepage: www.elsevier.com/locate/cattod

The influence of the pH on the reaction mechanism of water oxidation by a Ru(bda) catalyst

Jesús A. Luque-Urrutia, Miquel Solà*, Albert Poater*

Institut de Química Computacional i Catàlisi and Departament de Química, Universitat de Girona, C/ Maria Aurèlia Capmany, 69, 17003, Girona, Catalonia, Spain

ARTICLE INFO

Keywords:
Water oxidation catalysis
Ruthenium complex
DFT
Redox potential
O_2 formation
Reaction mechanism
Dicarboxylate

ABSTRACT

Recent results of Concepcion's group (*Chem. Com*51 (2015) 4105) on water oxidation catalysis (WOC) by a ruthenium complex suggest that, at pH = 8, O_2 release takes place after formation of a rhomboid bis(μ-oxo)-Ru_2^V species and not after generation of the typical μ-η^1:η^1-peroxo-Ru_2^{IV} intermediate, coming from the coupling of two Ru^V=O moieties (I2M mechanism), which is widely accepted to be formed at pH = 1. To analyze the differences between the reaction mechanisms of this WOC at different pHs, we performed DFT calculations of the full mechanism at pH = 1 and 8 of the WOC process catalyzed by the 2,2′-bipyridine-6,6′-dicarboxylate Ru complex. At pH = 8, we found that barriers leading to the hypothetic formation of rhombic $Ru_2^VO_2$ species are higher than those involved in the canonical I2M mechanism. The rate determining step at the latter pH is found to be the dimer formation while the bond cleavage for the O_2 liberation process is barrierless. The computational results confirm that the most common I2M mechanism is preferred at both pHs, as the new proposal comprising formation of bis(μ-oxo)-Ru_2^V species involves higher energy barriers.

1. Introduction

The production of hydrogen has become one of the main modern research focus due to its potential as energy source. Since it is costly and dangerous to maintain tanks of pressurized hydrogen for our daily use, *in situ* production is currently under investigation [1–3]. Ideally, H_2 is obtained from water because of its abundance, low risk and cost for its storage and manipulation [4]. But more importantly, it represents a carbon-free production of energy, and does not make use of fossil fuel sources.

In 2012, Sun, Llobet, Privalov et al. designed the 2,2′-bipyridine-6,6′-dicarboxylate Ru catalyst, [Ru(bda)(pic)$_2$] (Fig. 1) [5]. This, and other Ru catalysts [6–8], mimic the Photosystem II catalytic activity, showing a great efficiency in water oxidation catalysis (WOC). This catalyst is able to undertake proton coupled electron transfer (PCET) reactions like other ruthenium complexes [9,10]. In most cases, these Ru complexes initiate their catalytic activity rearranging from 6- to 7-coordination [11].

Two possible mechanisms for O—O bond formation in WOC have been proposed, namely, water nucleophilic attack (WNA) [12–14] and coupling between 2 M-O centers (I2M) (Fig. 2) [15–19]. Several studies have shown that the I2M pathway is the preferred mechanism for this catalyst [16,20,21]. Even though previous works suggested that there might be a sort of equilibrium between both mechanisms, as previously described for Ru(bda) complexes [22], the WNA was found energetically disfavored [16]. Despite the rather good efficiency of the [Ru(bda)(pic)$_2$] catalyst [23], further research is needed to fully understand the reaction mechanism of this seven coordinated molecular ruthenium water oxidation catalyst [24,25]. Usually, the reaction follows an I2M between two monomers, forming a Ru-O-O-Ru bond [26,27]. However, Concepcion et al. [28,29] suggested another route at pH = 8 involving the formation of a Ru-O-Ru central motif followed by a bis(μ-oxo)-Ru_2^V species with a rhomboid metal core (see Scheme 1).

Since two different mechanisms for the two pHs were proposed, in this work, we aim to unveil the reaction mechanism of the WOC catalyzed by [Ru(bda)(pic)$_2$] at pH 1 and 8 to confirm whether the Concepcion et al. proposal at pH = 8 is competitive with the widely accepted I2M mechanism. Additionally, comprehending the reaction mechanism on a molecular scale may help to diminish the byproducts of the reaction and to improve the current turnover number (TON) and turnover frequency (TOF) of this reaction [30,31].

Abbreviations: CAN, cerium ammonium nitrate; I2M, interaction between 2 M-O sites; PCET, proton coupled electron transfer; rds, rate determining step; WNA, water nucleophilic attack; WOC, water oxidation catalysis; OS, oxidation state; EO, Seffective oxidation state

* Corresponding authors.
E-mail addresses: miquel.sola@udg.edu (M. Solà), albert.poater@udg.edu (A. Poater).

https://doi.org/10.1016/j.cattod.2019.12.005
Received 5 March 2019; Received in revised form 14 November 2019; Accepted 2 December 2019
Available online 03 December 2019
0920-5861/ © 2019 Elsevier B.V. All rights reserved.

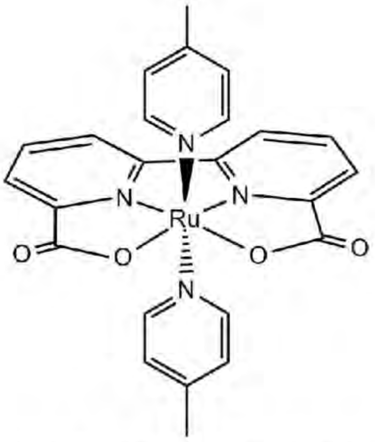

Fig. 1. The $[Ru^{II}(bda)(pic)_2]$ catalyst studied in this work.

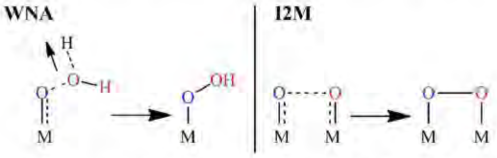

Fig. 2. WNA and I2M mechanisms for the O–O bond formation.

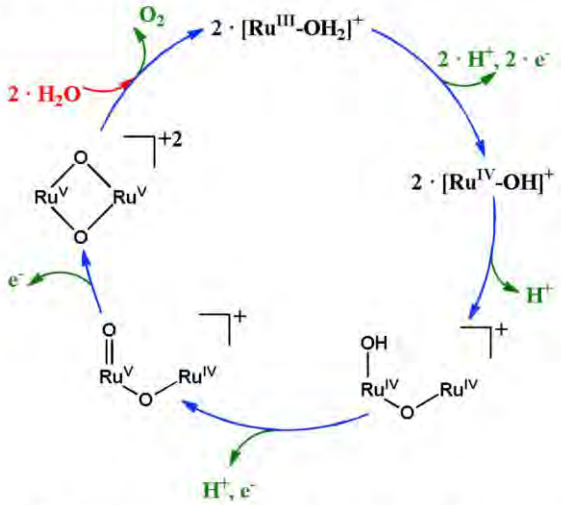

Scheme 1. Proposed water oxidation mechanism for $[Ru(bda)(pic)_2]$ (abbreviated as Ru) at pH = 8. Adapted from Concepcion et al. [28].

2. Computational details

All DFT calculations were performed with the Gaussian09 set of programs [32] using the M06-L functional [33,34]. The electronic configuration of the molecular systems was described with the standard split-valence basis set with a polarization function of Ahlrichs and co-workers for H, C, N, O, P (SVP keyword in Gaussian09) [35]. Ruthenium was described by the small-core quasi-relativistic Stuttgart/Dresden effective core potential, with an associated valence basis set (standard SDD keyword in Gaussian09) [36]. The geometry optimizations were performed without symmetry constraints, and the characterization of the local stationary points was carried out by analytical frequency calculations. These frequencies were used to calculate unscaled zero-point energies (ZPEs) as well as thermal corrections and entropy effects at 298.15 K and 1354 atm [37] by using the standard statistical mechanics relationships for an ideal gas. The pressure of 1354 atm was considered in our calculations based on the work of Martin et al. [37], who determined that this pressure simulates the experimental density of liquid water for the ideal water gas including the deformations performed by the surrounding water solvent in aqueous media [38]. We obtained the solvent energies by single-point calculations on the optimized geometries with the triple-ζ basis set of Weigend and Ahlrichs for main-group atoms (TZVP keyword in Gaussian09) [39], whereas for ruthenium the SDD basis set was employed. Solvent effects were included with the polarizable continuous solvation model PCM using H_2O as a solvent [40,41]. The reported Gibbs energies in this work are electronic energies obtained at the M06-L/TZVP ~ sdd//M06-L/SVP ~ sdd level of theory corrected with zero-point energies, thermal corrections, and entropy effects evaluated at 298.15 K and 1354 atm at the M06-L/SVP ~ sdd level and including solvation Gibbs energies calculated with the M06-L/TZVP ~ sdd//M06-L/SVP ~ sdd method.

To evaluate the pK_a values of our transition metal complexes, we used the scheme of Durrant and Gilson [42]. In particular, pK_a values in this work were obtained through their formula for hydroxy acids (Eq. (1)):

$$AOH \rightarrow AO^- + H^+$$
$$pK_a = 0.275 \cdot \Delta E - 4.20 \tag{1}$$

where ΔE refers to the reaction energy in kcal/mol obtained from the electronic energies in solution. Application of Eq. (1) to the related 2,2′-bipyridine-6,6′-diphosphonate Ru catalyst yields a pK_a of 4.13 and 4.30 (protons of different phosphonate groups) not far from the experimental value of ~4.1 for the double deprotonation of the phosphonate group [43]. For the energy of the solvated proton H_3O^+ we used -258.4 kcal/mol [42].

We represent redox reactions [44] using the following equation:

$$A^+ + e^- \rightarrow A$$
$$\varepsilon^0_{red} = \frac{\Delta G}{-nF} - \varepsilon^0_{SHE} \tag{2}$$

Where ΔG is the Gibbs energy of the reaction. The *SHE* refers to the absolute potential of the Standard Hydrogen Electrode (4.28 V) [45] in water, *n* refers to the number of electrons transferred and *F* is the Faraday constant. Energies are given in kcal/mol and the reduction potential ε^0_{red} in V.

Since PCET reactions include ΔG_{H^+}, we used the following formula to determine its reduction potential:

$$Ru^nOH + e^- + H^+ \rightarrow Ru^{n-1}OH_2$$
$$\varepsilon^0_{red} = \frac{\Delta G_{Ru^{n-1}OH_2} - \Delta G_{Ru^nOH} - 0.5 \cdot \Delta G_{H_2}}{-nF} \tag{3}$$

Where we used the Gibbs energy of the calculated solvated hydrogen molecule. Additionally, since the reduction potentials of PCET reactions are dependent on the pH, we included the 0.059 · pH correction obtained at 298.15 K [46]. For a more detailed description, see the SI.

Since the formal charges on ruthenium are in some cases arguable, we undertook an Effective Oxidation State (EOS) analysis to assign the oxidation state (OS) of the Ru atom in intermediates and transition states, via the in-house software APOST-3D [47]. Using the Topological Fuzzy Voronoi Cells (TFVC) 3D-space partitioning method and a 70 × 434 atomic grid for the numerical integration, we obtained the Reliability index ($R_\sigma(\%)$) calculated using the occupancies of the last occupied (λ^σ_{LO}) and first unoccupied (λ^σ_{FU}) effective atomic orbitals as shown in Eq. (4):

$$R_\sigma(\%) = 100 \cdot \min(1,\ \max(0, \lambda^\sigma_{LO} - \lambda^\sigma_{FU} + 1/2))$$

This index reveals the reliability of the oxidation states assigned to the chosen atoms or molecular fragments. For R > 65–70 %, the oxidation state can be assigned with confidence.

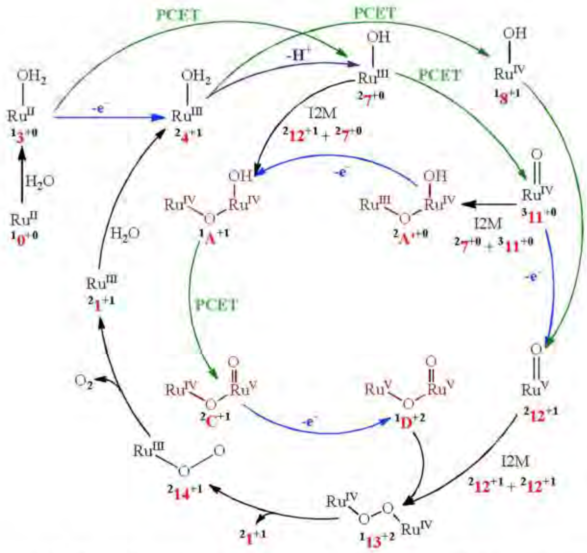
PCET
PCET
-H⁺
-e⁻
PCET
-e⁻
I2M
I2M
I2M
H₂O
H₂O
O₂
-e⁻
PCET
-e⁻
RuII 1₀⁺⁰
RuII 1₃⁺⁰
RuIII 2₄⁺¹
RuIII 2₇⁺⁰
RuIV 1₈⁺¹
RuIV 3₁₁⁺⁰
RuV 2₁₂⁺¹
RuIII 2₁⁺¹
1A⁺¹
2A'⁺⁰
2C⁺¹
1D⁺²
2₁₄⁺¹
2₁⁺¹
1₁₃⁺²
2₁₂⁺¹ + 2₇⁺⁰
2₇⁺⁰ + 3₁₁⁺⁰
2₁₂⁺¹ + 2₁₂⁺¹

Scheme 2. General reaction mechanism for the water oxidation catalysis by 2,2′-bipyridine-6,6′-dicarboxylate Ru catalyst. Arrows in blue denote oxidation processes, in purple deprotonation, and in green proton-coupled electron transfers. (For interpretation of the references to colour in this figure legend, the reader is referred to the web version of this article).

3. Results and discussion

In Scheme 2, we report all possible routes for the WOC mechanism catalyzed by the 2,2′-bipyridine-6,6′-dicarboxylate Ru catalyst. Further details are given in Scheme 3 (pH = 1) and Scheme 4 (pH = 8). Throughout this work, we named our complexes as $^{2S+1}\mathbf{X}^{+q}$, where S is the spin and q the charge of species **X**. It is worth noting that for all species with even number of electrons we have computed the closed-shell singlet, the open-shell singlet, the triplet, and the quintuplet electronic states. We found that in all cases the closed-shell singlet is favored, except for the TS of the I2M coupling between two Ru^{V}O units ($^{2}\mathbf{12}^{+1}+{}^{2}\mathbf{12}^{+1}$ in Scheme 3), for which the open-shell singlet state is lower in energy, and for the Ru^{IV}=O species, for which the triplet is the ground state in agreement with the calculations done by Concepcion and coworkers [12]. Further, for species with odd number of electrons, we tested both the doublet and quadruplet electronic states, the latter being higher in energy in all cases. In this work, we represent only the lowest energy electronic states for the sake of clarity.

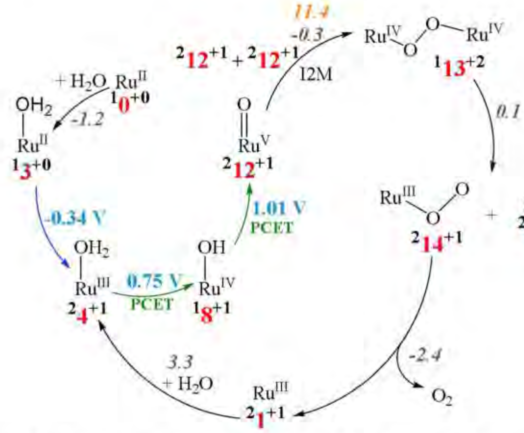
11.4
-0.3
2₁₂⁺¹ + 2₁₂⁺¹
I2M
RuIV O O RuIV
1₁₃⁺²
+ H₂O RuII
1₀⁺⁰
-1.2
OH₂ RuII 1₃⁺⁰
O RuV 2₁₂⁺¹
0.1
RuIII O O
+ RuIII 2₁⁺¹
2₁₄⁺¹
-0.34 V
1.01 V
PCET
OH₂ RuIII 2₄⁺¹
0.75 V
PCET
OH RuIV 1₈⁺¹
3.3
+ H₂O
RuIII 2₁⁺¹
-2.4
O₂

Scheme 3. Mechanism for the Ru-bda catalyst at pH = 1; PCETs in green; Gibbs energy barriers in orange; reduction potentials in light blue; Gibbs reaction energies in grey. Energies are given in kcal/mol and oxidation potentials in V. Arrows in blue denote oxidation processes and in green proton-coupled electron transfers. (For interpretation of the references to colour in this figure legend, the reader is referred to the web version of this article).

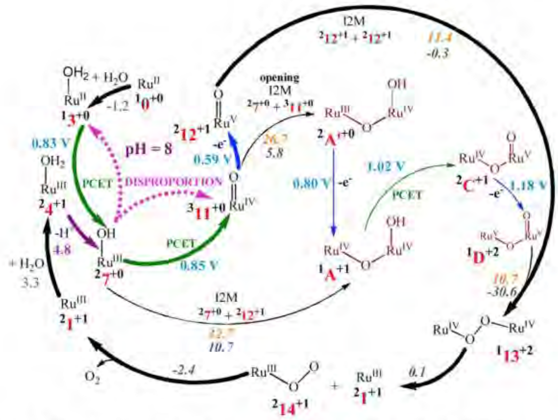
I2M
2₁₂⁺¹ + 2₁₂⁺¹
11.4
-0.3
OH₂ + H₂O RuII
RuII 1₃⁺⁰
-1.2 1₀⁺⁰
opening
I2M
2₇⁺⁰ + 3₁₁⁺⁰
2₁₂⁺¹ RuV
pH = 8
-e⁻
0.59 V
26.7
5.8
2A'⁺⁰
0.83 V
OH₂ RuIII 2₄⁺¹
PCET
DISPROPORTION
3₁₁⁺⁰ RuIV
0.80 V
-e⁻
1.02 V
PCET
2C⁺¹
1.18 V
-e⁻
-H⁺
4.8
OH RuIII 2₇⁺⁰
PCET
0.85 V
1A⁺¹
1D⁺²
10.7
-30.6
+ H₂O
3.3
RuIII 2₁⁺¹
I2M
2₇⁺⁰ + 2₁₂⁺¹
32.7
10.7
RuIV O O RuIV
1₁₃⁺²
O₂
-2.4
RuIII O O
+ RuIII 2₁⁺¹
2₁₄⁺¹
0.1

Scheme 4. Mechanism for the carboxylate catalyst at pH = 8; PCETs potentials in green; Gibbs energy barriers in orange; reduction potentials in light blue; pK$_a$s in purple; Gibbs reaction energies in grey. Energies are given in kcal/mol and reduction potentials in V. Main path represented with bold arrows. Arrows in blue denote oxidation processes, in purple proton transfers, in green proton-coupled electron transfers and in pink and dashed disproportion processes. (For interpretation of the references to colour in this figure legend, the reader is referred to the web version of this article).

We have chosen intermediate $^{2}\mathbf{4}^{+1}$ as the catalyst while $^{1}\mathbf{0}^{+0}$ and $^{1}\mathbf{3}^{+0}$ (represented in Fig. 1) have been defined as precatalysts. Comparing our structural data with those given in the Supporting Information (SI) by Concepcion et al. [28] we determined that bond lengths of our structures are similar to theirs, the biggest absolute error being 0.066 Å. Two experiments were performed by Concepcion's group at pH = 1, one was the addition of excess CAN (Cerium Ammonium Nitrate), *i.e.* the oxidant in the media at pH = 1, we ensure a minimal reduction potential of 1.72 V [48,49]; and the other was the cyclic voltammetry. For the sake of clarity, we define the CAN potential as the maximum to perform the different oxidation reactions thus; we do not consider reactions with higher potentials. We have tried many different pathways and possibilities, and we represent in Scheme 3 the most likely reaction mechanism at pH = 1. A full account of all different reaction paths can be found in the SI.

The oxidation state on ruthenium atoms (for all studied complexes in this work) ranges from II to V as we show in Table 1 with their respective reliability indexes. As we can see, $^{3}\mathbf{11}^{+0}$, $^{2}\mathbf{12}^{+1}$, $^{2}\mathbf{A'}^{+0}$, $^{2}\mathbf{C}^{+1}$ and $^{1}\mathbf{D}^{+2}$ are the most problematic since their R% are not high enough to determine with total confidence the OS of their Ru atoms. This is due to the close proximity in energy between the occupied and unoccupied orbitals, *i.e.* molecule $^{2}\mathbf{12}^{+1}$ λ^{σ}_{LO} has an assigned occupancy of 0.440 e^{-} while the λ^{σ}_{FU} an occupancy of 0.448 e^{-}. This difference implies that it is not possible to determine with total certainty whether the oxo group fragment OS is considered -2 (thus Ru fragment +5) or -1 (thus Ru fragment +4). It is worth noting that out of these five complexes, only complexes $^{3}\mathbf{11}^{+0}$ and $^{2}\mathbf{12}^{+1}$ are relevant in the reaction mechanisms found to be operative (*vide infra*).

Moving to the mechanism discussion (Scheme 3), starting from $^{1}\mathbf{0}^{+0}$, first, a water molecule interacts with $^{1}\mathbf{0}^{+0}$ in the second coordination sphere to form $^{1}\mathbf{3}^{+0}$ and releasing 1.2 kcal/mol. The same energy value was reported by Concepcion et al. [12] for the coordination of water to Ru^{II}. In the experiments by their group, they observed that at pH = 1 there were two oxidation steps at 0.85 V and 1.10 V [50]. Our calculations indicate that these two steps are two PCET processes at 0.75 V and 1.01 V. We also considered the oxidations and deprotonations separately, but due to the low pH, the intermediates found would re-protonate. Comparing the proposal by Concepcion et al.

Table 1
Oxidation states (OS) and their corresponding Reliability indexes (R%) for some the molecules represented in this work.

Mol.	0	1	4	7	8	11	12	A
OS	II	III	III	III	IV	IV	V	IV&IV
R%	90.4	86.0	87.0	92.8	85.7	59.8	50.9	78.1
Mol.	A'	C	D	13	14	7 + 12 TS	7 + 11 TS	12 + 12 TS
OS	III&IV	IV&V	IV&IV	IV&IV	III	IV&IV	III&IV	IV&IV
R%	63.9	60.3	63.3	81.1	85.0	75.3	78.3	73.6

[12] and our work, we obtained similar results up to the formation of $^{2}\mathbf{12}^{+1}$. Furthermore, the calculations are in agreement with the detection of this type of intermediate by Copéret, Pushkar et al. [51].

Once we form $^{2}\mathbf{12}^{+1}$, a coupling between 2 M-O sites occurs. Formation of $^{1}\mathbf{13}^{+2}$, Ru^{IV}-O-O-Ru^{IV}, through an I2M mechanism is exergonic by 0.3 kcal/mol and has an estimated Gibbs energy barrier of 11.4 kcal/mol. The corresponding transition state displays an open-shell singlet character and indeed, it is a bimolecular oxyl radical coupling of two [Ru^{V}=O]$^{+}$ species as Concepcion et al. [28] and Sun et al. [5] groups reported. The highest in energy structure used to estimate the energy barrier for an O—O frozen bond distance of 1.90 Å was obtained with a linear transit procedure by changing the O—O distance with steps of 0.1 Å. We used this estimate, as we were unable to locate the exact transition state. It is worth noting that the same linear transit procedure leads to an error of less than 0.1 kcal/mol for similar transition states with a Ru-bda complex [52]. Moreover, the barrier fits into the expected energy range at our given conditions [53]. The interaction between two $^{2}\mathbf{12}^{+1}$ monomers giving the dimer $^{1}\mathbf{13}^{+2}$ turns out to be the rate determining step (rds) of the process at pH = 1 [54]. Following the mechanism, we studied the dimer cleavage. From the linear transit carried out following the same procedure as for the search of the I2M transition state, we concluded that the $^{1}\mathbf{13}^{+2} \rightarrow {}^{2}\mathbf{14}^{+1} + {}^{2}\mathbf{1}^{+1}$ transformation is a barrierless dissociative process. Once the Ru^{V}-η^{1}-O$_2$ compound $^{2}\mathbf{14}^{+1}$ is obtained, the release of molecular oxygen, again barrierless and exergonic by 2.4 kcal/mol, leads to compound $^{2}\mathbf{1}^{+1}$, which then hydrates to regenerate the active catalyst $^{2}\mathbf{4}^{+1}$.

At pH = 8 (Scheme 4), the mechanism shows some differences. The transformation from $^{1}\mathbf{0}^{+0}$ to $^{2}\mathbf{4}^{+1}$ does not occur. Instead, the water coordination leads to $^{1}\mathbf{3}^{+0}$, and then via a PCET directly to $^{2}\mathbf{7}^{+0}$. This compound $^{2}\mathbf{7}^{+0}$ was characterized using X-ray cristallography by Sun and coworkers [55], who also stated that at pH 7 and above, two molecules of $^{2}\mathbf{7}^{+0}$ disproportionate into $^{3}\mathbf{11}^{+0}$ and $^{1}\mathbf{3}^{+0}$. Reported Pourbaix diagram by Concepcion's group [28] show that at pH > 6, the line of the pH dependent reaction of $^{1}\mathbf{3}^{+0}$ to $^{3}\mathbf{11}^{+0}$ crosses below the line of the pH independent reaction of $^{1}\mathbf{3}^{+0}$ to $^{2}\mathbf{4}^{+1}$. As a consequence, they observed a 2e^{-}/2H^{+} step in their experiments. Actually, this step could be considered to gather the two PCETs discussed above from the calculations: from $^{1}\mathbf{3}^{+0}$ to $^{2}\mathbf{7}^{+0}$, and from $^{2}\mathbf{7}^{+0}$ to $^{3}\mathbf{11}^{+0}$. Finally, the oxidation of $^{3}\mathbf{11}^{+0}$ to $^{2}\mathbf{12}^{+1}$ with a potential of − 0.59 V enables the same $^{2}\mathbf{12}^{+1} + {}^{2}\mathbf{12}^{+1}$ path as found at pH = 1. We have also studied the possible formation of the compound $^{1}\mathbf{A}^{+1}$ as proposed in the work by Concepcion and coworkers [28], as well as a possible species $^{2}\mathbf{A'}^{+0}$. Gibbs energy barriers for the formation of compound $^{1}\mathbf{A}^{+1}$ of 32.7 kcal/mol ($^{2}\mathbf{7}^{+0} + {}^{2}\mathbf{12}^{+1}$) was found, whereas generation of $^{2}\mathbf{A'}^{+0}$ from $^{2}\mathbf{7}^{+0} + {}^{3}\mathbf{11}^{+0}$ has to overcome a Gibbs energy barrier of 26.7 kcal/mol, all these barriers to be compared with the barrier of 11.4 kcal/mol found for the $^{2}\mathbf{12}^{+1} + {}^{2}\mathbf{12}^{+1}$ coupling. All these alternative reaction paths have barriers higher in energy than the $^{2}\mathbf{12}^{+1} + {}^{2}\mathbf{12}^{+1}$ path, the rds at pH = 1. Moreover, the $^{2}\mathbf{12}^{+1} + {}^{2}\mathbf{12}^{+1}$ path is also the one showing a more favorable thermodynamics among the different I2M processes studied. Therefore, we conclude that these new proposals are less likely to be operative than the common I2M path. Therefore, our results indicate that the $^{2}\mathbf{12}^{+1} + {}^{2}\mathbf{12}^{+1}$ bimolecular step is the rds at both pHs. Furthermore, we also tried to locate the rhomboid bis(μ-oxo)-Ru$_2^{V}$ species (Scheme 1) but all our attempts lead to compound $^{1}\mathbf{13}^{+2}$. We concluded that the bis(μ-oxo)-Ru$_2^{V}$ species does not exist in the potential energy surface, probably because the sterically hindered metal center prefers an μ-η^{1}:η^{1}-peroxo-Ru$_2^{IV}$ structure rather than a bis(μ-oxo)-Ru$_2^{V}$ arrangement. Finally, the proposed reaction mechanism at pH = 8 is base-assisted in the sense that formation of $^{3}\mathbf{11}^{+0}$ is favored at this pH.

4. Conclusions

We have explored the full mechanism for the 2,2′-bipyridine-6,6′-dicarboxylate Ru WOC catalyst at pH = 1 and 8. The most important difference in the reaction mechanisms at these two pH is the appearance of compounds $^{2}\mathbf{7}^{+0}$ and $^{3}\mathbf{11}^{+0}$ at pH = 8. This occurs because the basic pH enables the deprotonation of species $^{2}\mathbf{4}^{+1}$. Furthermore, experiments show that at basic pHs there is only one 2e^{-}/2H^{+} step. We propose that this 2e^{-}/2H^{+} step is the sum of the two PCETs from $^{1}\mathbf{3}^{+0}$ to $^{2}\mathbf{7}^{+0}$ and $^{2}\mathbf{7}^{+0}$ to $^{3}\mathbf{11}^{+0}$. The compounds $^{2}\mathbf{7}^{+0}$ and $^{3}\mathbf{11}^{+0}$ open new paths that may lead to the Concepcion et al. proposed compound $^{1}\mathbf{A}^{+1}$. We studied all possible dimerization processes between species involved in the mechanism and we found that the I2M $^{2}\mathbf{7}^{+0} + {}^{3}\mathbf{11}^{+0}$ to obtain $^{2}\mathbf{A'}^{+0}$ is lower in energy than $^{2}\mathbf{7}^{+0} + {}^{2}\mathbf{12}^{+1}$ I2M, yet both involve energy barriers higher than the $^{2}\mathbf{12}^{+1} + {}^{2}\mathbf{12}^{+1}$ I2M. Overall, we believe that at room temperature the Concepcion et al. proposal at pH = 8 that requires formation of $^{2}\mathbf{A'}^{+0}$ or $^{1}\mathbf{A}^{+1}$, is not possible or, at least, the reaction will be much slower than the already known path corresponding to the coupling between two Ru^{V}=O moieties.

Associated Content

Computational details, reaction pathways, Cartesian coordinates and energies of all species studied. This material is available free of charge via the Internet.

Declaration of Competing Interest

The authors declare no competing financial interest.

Acknowledgments

J.A.L.U. thanks Universitat de Girona for a IFUdG2017 PhD fellowship. A.P. is a Serra Húnter Fellow. A.P. and M.S. thank the Spanish MINECO for projects CTQ2014-59832-JIN and CTQ2017-85341, respectively. M.S. thanks the Generalitat de Catalunya for project 2017SGR39, the Xarxa de Referència en Química Teòrica i Computacional, and ICREA Academia 2014 prize. We thank Dr. Verònica Postils, Martí Gimferrer, Prof. Dr. Antoni Llobet, and Prof. Dr. Etsuko Fujita for helpful comments.

Appendix A. Supplementary data

Supplementary material related to this article can be found, in the online version, at doi:https://doi.org/10.1016/j.cattod.2019.12.005.

References

[1] C. Wang, S. Cao, W. Fu, A stable dual-functional system of visible-light-Driven Ni(II) reduction to a nickel nanoparticle catalyst and robust in situ hydrogen production, Chem. Commun. 49 (2013) 11251–11253.

[2] J. Morris, M. Radu, In situ produced hydrogen (hydrogen on demand), Int. J. Hydrogen Energy 35 (2010) 7021–7023.

[3] J.M. Silva, M.A. Soria, L.M. Madeira, Thermodynamic analysis of glycerol steam reforming for hydrogen production with in situ hydrogen and carbon dioxide separation, J. Power Sources 273 (2015) 423–430.

[4] T. Liu, B. Zhang, L. Sun, Iron-based molecular water oxidation catalysts: abundant, cheap, and promising, Chem. Asian J. 14 (2019) 31–43.

[5] L. Duan, F. Bozoglian, S. Mandal, B. Stewart, T. Privalov, A. Llobet, L. Sun, A molecular ruthenium catalyst with water-oxidation activity comparable to that of photosystem II, Nat. Chem. 4 (2012) 418–423.

[6] M. Schulze, V. Kunz, P.D. Frischmann, F. Würthner, A supramolecular ruthenium macrocycle with high catalytic activity for water oxidation that mechanistically mimics photosystem II, Nat. Chem. 8 (2016) 576–583.

[7] R. Matheu, M.Z. Ertem, C. Gimbert-Suriñach, X. Sala, A. Llobet, Seven coordinated molecular ruthenium–water oxidation catalysts: a coordination chemistry journey, Chem. Rev. 119 (2019) 3453–3471.

[8] L. Sun, L. Hammarström, B. Åkermark, S. Styring, Towards artificial photosynthesis: ruthenium-manganese chemistry for energy production, Chem. Soc. Rev. 30 (2001) 36–49.

[9] G.F. Manbeck, E. Fujita, J.J. Concepcion, Proton-coupled electron transfer in a strongly coupled photosystem II-Inspired chromophore-imidazole-phenol complex: stepwise oxidation and concerted reduction, J. Am. Chem. Soc. 138 (2016) 11536–11549.

[10] (a) M.V. Sheridan, B.D. Sherman, Z. Fang, K.-R. Wee, M.K. Coggins, T.J. Meyer, Electron transfer mediator effects in the oxidative activation of a ruthenium dicarboxylate water oxidation catalyst, ACS Catal. 5 (2015) 4404–4409;
(b) Y. Tsubonouchi, S. Lin, A.R. Parent, G.W. Brudvig, K. Sakai, Light-induced water oxidation catalyzed by an oxido-bridged triruthenium complex with a Ru-O-Ru-O-Ru motif, Chem. Commun. 52 (2016) 8018–8021.

[11] Q. Daniel, P. Huang, T. Fan, Y. Wang, L. Duan, L. Wanga, F. Li, Z. Rinkevicius, F. Mamedov, M.S.G. Ahlquist, S. Styring, L. Sun, Rearranging from 6- to 7-coordination initiates the catalytic activity: an EPR study on a Ru-bda water oxidation catalyst, Coord. Chem. Rev. 346 (2017) 206–215.

[12] J.J. Concepcion, M.-K. Tsai, J.T. Muckerman, T.J. Meyer, Mechanism of water oxidation by single-site ruthenium complex catalysts, J. Am. Chem. Soc. 132 (2010) 1545–1557.

[13] I. López, M.Z. Ertem, S. Maji, J. Benet-Buch, A. Keidel, U. Kuhlmann, P. Hildebrandt, C.J. Cramer, V.S. Batista, Llobet, a. A self-improved water-oxidation catalyst: is one site really enough? Angew. Chem. Int. Ed. 53 (2014) 205–209.

[14] L. Vigara, M.A. Ertem, N. Planas, F. Bozoglian, N. Leidel, H. Dau, M. Haumann, L. Gagliardi, C.J. Cramer, A. Llobet, Experimental and quantum chemical characterization of the water oxidation cycle catalysed by $[Ru^{II}(damp)(bpy)(H_2O)]^{2+}$, Chem. Sci. 3 (2012) 2576–2586.

[15] S.W. Gersten, G.J. Samuels, T.J. Meyer, Catalytic oxidation of water by an oxo-bridged ruthenium dimer, J. Am. Chem. Soc. 104 (1982) 4029–4030.

[16] R. Kang, K. Chen, J. Yao, S. Shaik, H. Chen, Probing ligand effects on O-O bond formation of Ru-Catalyzed water oxidation: a computational survey, Inorg. Chem. 53 (2014) 7130–7136.

[17] S. Neudeck, S. Maji, I. López, S. Meyer, F. Meyer, A. Llobet, New powerful and oxidatively rugged dinuclear Ru water oxidation catalyst: control of mechanistic pathways by tailored ligand design, J. Am. Chem. Soc. 136 (2014) 24–27.

[18] R.-Z. Liao, M.D. Kärkäs, T.M. Laine, B. Åkermark, P.E.M. Siegbahn, On the mechanism of water oxidation catalyzed by a dinuclear ruthenium complex: a quantum chemical study, Catal. Sci. Technol. 6 (2016) 5031–5041.

[19] F.A. Pasha, A. Poater, S.V.C. Vummaleti, T. de Bruin, J.-M. Basset, L. Cavallo, Revisiting O–O bond formation through outer-sphere water molecules versus bimolecular mechanisms in water-oxidation catalysis (WOC) by Cp*Ir based complexes, Eur. J. Inorg. Chem. (2019) 2093–2100.

[20] R. Staehle, L. Tong, L. Wang, L. Duan, A. Fischer, M.S.G. Ahlquist, L. Sun, S. Rau, Water oxidation catalyzed by mononuclear ruthenium complexes with a 2,2'-Bipyridine-6,6'-dicarboxylate (bda) ligand: how ligand environment influences the catalytic behavior, Inorg. Chem. 53 (2014) 1307–1319.

[21] (a) Y. Xie, D.W. Shaffer, J.J. Concepcion, O – O radical coupling: from detailed mechanistic understanding to enhanced water oxidation catalysis, Inorg. Chem. 57 (2018) 10533–10542;
(b) S. Zhan, M.S.G. Ahlquist, Dynamics and reactions of molecular Ru catalysts at carbon nanotube–water interfaces, ACS Catal. 8 (2018) 8642–8648.;
(c) S. Zhan, M.S.G. Ahlquist, Dynamics and reactions of molecular Ru catalysts at carbon nanotube-water interfaces, J. Am. Chem. Soc. 140 (2018) 7498–7503..

[22] D. Scherrer, M. Schilling, S. Luber, T. Fox, B. Spingler, R. Alberto, C.J. Richmond, Ruthenium water oxidation catalysts containing the non-planar tetradentate ligand, biisoquinoline dicarboxylic acid ($biqaH_2$), Dalton Trans. 45 (2016) 19361–19367.

[23] L. Tong, L. Duan, Y. Xu, T. Privalov, L. Sun, Structural modifications of mononuclear ruthenium complexes: a combined experimental and theoretical study on the kinetics of ruthenium catalyzed water oxidation, Angew. Chem. Int. Ed. 50 (2011) 445–449.

[24] R. Matheu, M.Z. Ertem, M. Pipelier, J. Lebreton, D. Dubreuil, J. Benet-Buchholz, X. Sala, A. Tessier, A. Llobet, The role of seven-coordination in Ru-catalyzed water oxidation, ACS Catal. 8 (2018) 2039–2048.

[25] B. Zhang, L. Sun, Ru-bda: unique molecular water-oxidation catalysts with distortion induced open site and negatively charged ligands, J. Am. Chem. Soc. 141 (2019) 5565–5580.

[26] X. Sala, I. Romero, M. Rodríguez, L. Escriche, A. Llobet, Molecular catalysts that oxidize water to dioxygen, Angew. Chem. Int. Ed. 48 (2009) 2842–2852.

[27] N. Govindarajan, A. Tiwari, B. Ensing, E.J. Meijer, Impact of the ligand flexibility and solvent on the O–O bond formation step in a highly active ruthenium water oxidation catalyst, Inorg. Chem. 57 (2018) 13063–13066.

[28] J.J. Concepcion, D.K. Zhong, D.J. Szalda, J.T. Muckerman, E. Fujita, Mechanism of water oxidation by $[Ru(bda)(L)_2]$: the return of the blue dimer, Chem. Commun. 51 (2015) 4105–4108.

[29] J.T. Muckerman, M. Kowalczyk, Y.M. Badiei, D.E. Polyansky, J.J. Concepcion, R. Zong, R.P. Thummel, E. Fujita, New water oxidation chemistry of a seven-coordinate ruthenium complex with a tetradentate polypyridyl ligand, Inorg. Chem. 53 (2014) 6904–6913.

[30] S. Zhan, D. Martensson, M. Purg, S.C.L. Kamerlin, M.S.G. Ahlquist, Capturing the role of explicit solvent in the dimerization of Ru^V(bda) water oxidation catalysts, Angew. Chem. Int. Ed. 56 (2017) 6962–6965.

[31] D.W. Shaffer, Y. Xie, J.J. Concepcion, O–O bond formation in ruthenium-catalyzed water oxidation: single-site nucleophilic attack vs. O–O radical coupling, Chem. Soc. Rev. 46 (2017) 6170–6193.

[32] Gaussian 09, Revision E.01, M. J. Frisch, G. W. Trucks, H. B. Schlegel, G.E. Scuseria, M.A. Robb, J.R. Cheeseman, G. Scalmani, V. Barone, B. Mennucci, G.A. Petersson, H. Nakatsuji, M. Caricato, X. Li, H.P. Hratchian, A.F. Izmaylov, J. Bloino, G. Zheng, J.L. Sonnenberg, M. Hada, M. Ehara, K. Toyota, R. Fukuda, J. Hasegawa, M. Ishida, T. Nakajima, Y. Honda, O. Kitao, H. Nakai, T. Vreven, J.A. Montgomery, Jr., J.E. Peralta, F. Ogliaro, M. Bearpark, J.J. Heyd, E. Brothers, K.N. Kudin, V.N. Staroverov, R. Kobayashi, J. Normand, K. Raghavachari, A. Rendell, J.C. Burant, S. S. Iyengar, J. Tomasi, M. Cossi, N. Rega, N.J. Millam, M. Klene, J.E. Knox, J.B. Cross, V. Bakken, C. Adamo, J. Jaramillo, R. Gomperts, R.E. Stratmann, O. Yazyev, A.J. Austin, R. Cammi, C. Pomelli, J.W. Ochterski, R.L. Martin, K. Morokuma, V.G. Zakrzewski, G.A. Voth, P. Salvador, J.J. Dannenberg, S. Dapprich, A.D. Daniels, Ö. Farkas, J.B. Foresman, J.V. Ortiz, J. Cioslowski, D.J. Fox, Gaussian, Inc., Wallingford CT, 2009.

[33] Y. Zhao, D.G. Truhlar, The M06 suite of density functionals for main group thermochemistry, thermochemical kinetics, noncovalent interactions, excited states, and transition elements: two new functionals and systematic testing of four M06-class functionals and 12 other functionals, Theor. Chem. Acc. 120 (2008) 215–241.

[34] Y. Zhao, D.G. Truhlar, A new local density functional for main-group thermochemistry, transition metal bonding, thermochemical kinetics, and noncovalent interactions, J. Chem. Phys. 125 (194101) (2006) 1–18.

[35] A. Schäfer, H. Horn, R. Ahlrichs, Fully optimized contracted gaussian basis sets for atoms Li to Kr, J. Chem. Phys. 97 (1992) 2571–2577.

[36] U. Haeusermann, M. Dolg, H. Stoll, H. Preuss, Accuracy of energy-adjusted quasirelativistic ab initio pseudopotentials, Mol. Phys. 78 (1993) 1211–1224.

[37] R.L. Martin, P.J. Hay, L.R. Pratt, Hydrolysis of ferric ion in water and conformational equilibrium, J. Phys. Chem. A 102 (1998) 3565–3573.

[38] (a) M. García-Melchor, M.C. Pacheco, C. Nájera, A. Lledós, G. Ujaque, Mechanistic exploration of the Pd-Catalyzed copper-free sonogashira reaction, ACS Catal. 2 (2012) 135–144;
(b) A. Poater, E. Pump, S.V.C. Vummaleti, L. Cavallo, The right computational recipe for olefin metathesis with Ru-Based catalysts: the whole mechanism of ring-closing olefin metathesis, J. Chem. Theory Comput. 10 (2014) 4442–4448;
(c) L. Falivene, V. Barone, G. Talarico, Unraveling the role of entropy in tuning unimolecular vs. bimolecular reaction rates: the case of olefin polymerization catalyzed by transition metals, Mol. Catal. 452 (2018) 138–144.

[39] F. Weigend, R. Ahlrichs, Balanced basis set of split valence, triple zeta valence and quadruple zeta valence quality for H to Rn: design and assessment of accuracy, Phys. Chem. Chem. Phys. 7 (2005) 3297–3305.

[40] V. Barone, M. Cossi, Quantum calculation of molecular energies and energy gradients in solution by a conductor solvent model, J. Phys. Chem. A 102 (1998) 1995–2001.

[41] J. Tomasi, M. Persico, Molecular interactions in solution: an overview of methods based on continuous distributions of the solvent, Chem. Rev. 94 (1994) 2027–2094.

[42] M.C. Durrant, R. Gilson, Estimation of the pK_a values of water ligands in transition metal complexes using density functional theory with polarized continuum model solvent corrections, Dalton Trans. (2009) 10223–10230.

[43] J.M. Kamdar, D.C. Marelius, C.E. Moore, A.L. Rheingold, D.K. Smith, D.B. Grotjahn, Ruthenium complexes of 2,2'-bipyridine-6,6'-diphosphonate ligands for water oxidation, ChemCatChem 8 (2016) 3045–3049.

[44] F. Acuña-Parés, Z. Codolà, M. Costas, J.M. Luis, J. Lloret-Fillol, Unraveling the mechanism of water oxidation catalyzed by nonheme Iron complexes, Chem. Eur. J. 20 (2014) 5696–5707.

[45] C.P. Kelly, C.J. Cramer, D.G. Truhlar, Single-ion solvation free energies and the normal hydrogen electrode potential in methanol, acetonitrile, and dimethyl sulfoxide, J. Phys. Chem. B 111 (2007) 408–422.

[46] (a) W. Nernst, The New Heat Theorem, Dover, New York, 1969;
(b) A.-S. Feiner, A.J. McEvoy, The nernst equation, J. Chem. Educ. (1994), pp. 493–494.

[48] (a) M.Z. Ertem, L. Gagliardi, C.J. Cramer, Quantum chemical characterization of the mechanism of an iron-based water oxidation catalyst, Chem. Sci. 3 (2012) 1293–1299;
(b) A. Bucci, G. Menendez Rodriguez, G. Bellachioma, C. Zuccaccia, A. Poater, L. Cavallo, A. Macchioni, An alternative reaction pathway for iridium-catalyzed water oxidation driven by cerium ammonium nitrate (CAN), ACS Catal. 6 (2016) 4559–4563.

[49] E. Wadsworth, F.R. Duke, C.A. Goetz, Present status of cerium(IV)-cerium(III)

potentials, Anal. Chem. 29 (1957) 1824–1825.

[50] D.W. Shaffer, Y. Xie, D.J. Szalda, J.J. Concepcion, Manipulating the rate-limiting step in water oxidation catalysis by ruthenium bipyridine – dicarboxylate complexes, Inorg. Chem. 55 (2016) 12024–12035.

[51] D. Lebedev, Y. Pineda-Galvan, Y. Tokimaru, A. Fedorov, N. Kaeffer, C. Copéret, Y. Pushkar, The key $Ru^{V}=O$ intermediate of site-isolated mononuclear water oxidation catalyst detected by in situ X-ray absorption spectroscopy, J. Am. Chem. Soc. 140 (2018) 451–458.

[52] C.J. Richmond, S. Escayola, A. Poater, Axial ligand effects of Ru-BDA complexes in the O–O bond formation via the I2M bimolecular mechanism in water oxidation catalysis, Eur. J. Inorg. Chem. (2019) 2093–2100.

[53] (a) C.J. Richmond, R. Matheu, A. Poater, L. Falivene, J. Benet-Buchholz, X. Sala, L. Cavallo, A. Llobet, Supramolecular water oxidation with Ru-bda-Based catalysts, Chem. Eur. J. 20 (2014) 17282–17286;
(b) R. Matheu, A. Ghaderian, L. Francàs, P. Chernev, M.Z. Ertem, J. Benet-Buchholz, V.S. Batista, M. Haumann, C. Gimbert-Suriñach, X. Sala, A. Llobet, Behavior of Ru–bda water-oxidation catalysts in low oxidation states, Chem. Eur. J. 24 (2018) 12838–12847.

[54] D.W. Shaffer, Y. Xie, D.J. Szalda, J.J. Concepción, Manipulating the rate-limiting step in water oxidation catalysis by ruthenium bipyridine – dicarboxylate complexes, Inorg. Chem. 55 (2016) 12024–12035.

[55] B. Zhang, F. Li, R. Zhang, C. Ma, L. Chen, L. Sun, Characterization of a trinuclear ruthenium species in catalytic water oxidation by $Ru(bda)(pic)_2$ in neutral media, Chem. Commun. 52 (2016) 8619–8622.

4.2. Understanding the Performance of a Bisphosphonate Ru catalyst for Water Oxidation Catalysis

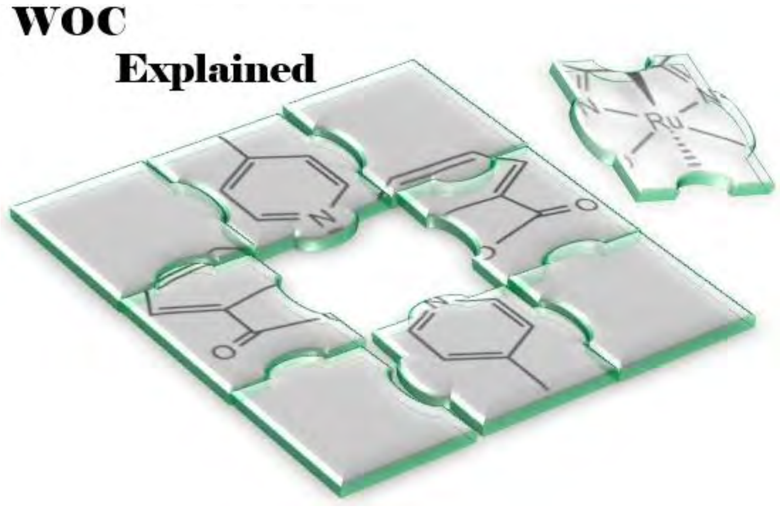

Luque-Urrutia, J. A.; Kamdar, J. M.; Grotjahn, D. B.; Solà, M.; Poater, A. **Understanding the Performance of a Bisphosphonate Ru catalyst for Water Oxidation Catalysis.** *Dalton Trans.* **2020**, *49*, 14052-14060.
DOI: 10.1039/D0DT02253E.

This thesis author has contributed to the DFT calculations, data analysis, writing, and revisions of the article.

Reproduced with permission from:

Luque-Urrutia, J. A.; Kamdar, J. M.; Grotjahn, D. B.; Solà, M.; Poater, A. **Understanding the Performance of a Bisphosphonate Ru catalyst for Water Oxidation Catalysis.** *Dalton Trans.* **2020**, *49*, 14052-14060.

https://doi.org/10.1039/D0DT02253E

Reproduced by permission of The Royal Society of Chemistry.

Dalton Transactions

PAPER

Cite this: *Dalton Trans.*, 2020, **49**, 14052

Understanding the performance of a bisphosphonate Ru water oxidation catalyst†

Jesús A. Luque-Urrutia, [a] Jayneil M. Kamdar,[b] Douglas B. Grotjahn, *[b] Miquel Solà *[a] and Albert Poater *[a]

Received 25th June 2020,
Accepted 1st September 2020

DOI: 10.1039/d0dt02253e

rsc.li/dalton

Water oxidation catalysts (WOCs) create electrons that allow generating H_2 from water and sunlight, a promising process for the production of clean energy. The mechanism of water oxidation mediated by Ru(2,2′-bipyridine-6,6′-diphosphonato)(4-picoline)$_2$ has been studied computationally to comprehend the results obtained in the experiments performed by the Concepcion and Grotjahn groups. Our study was performed at pH = 8 and 1. At pH = 8, the phosphonates are fully deprotonated and the catalysis, which is shown to be more energetically costly than that of the dicarboxylato Ru catalyst counterpart, takes place through a mechanism that involves a bimolecular interaction between two metal-oxo units (I2M). At pH = 1, only one of the phosphonates of the catalyst can deprotonate. After testing all possible pathways and comparing with experimental data, we conclude that the catalysis proceeds neither through a water nucleophilic attack nor *via* I2M, but rather we hypothesize that the rate-determining step involves both the catalyst and the ceric ammonium nitrate.

Introduction

In situ hydrogen generation has been a hot topic during recent years due to the increasing need for clean fuel production with a high energy output.[1–3] To reach a sustainable reaction for H_2 production, the use of cheap raw materials and catalysts has been the main focus of research. Accordingly, water as a reactant is an obvious choice due to its availability and its proton reduction and water oxidation reactions. Due to the harsh conditions required to perform the water oxidation process, researchers have been trying to develop different water oxidation catalysts (WOCs).[4,5] The first molecular WOC found by Meyer *et al.* known as the "blue dimer",[6,7] inspired many other researchers to perform this kind of catalysis with different transition metals, such as Ru[8–10] or Ir.[11,12] Many catalysts involving Ru have been developed, but one of the most interesting is the 2,2-bipyridine-6,6-dicarboxylic acid (bda) Ru catalyst (**A**), which was first explored by Sun,[13] Privalov,[14] and Llobet *et al.*[15] It performs WOC efficiently, partly due to the large O–Ru–O angle (~123°) that the bda infers to the catalyst. This angle provides a gap for a water molecule to interact with an octahedral Ru intermediate,[16] forming a hepta-coordinated compound.[17,18] This peculiar seven-coordinated structure appears to lower overpotentials required for the oxidative steps while emulating the activity of the WOC in Photosystem II.[19] Even though there are already some studies which focus on the exchange of axial ligands, such as pyridine, picoline or isoquinoline,[20] with the conclusion that the bda remains mostly unchanged,[21] the hepta-coordinated metal center[22–24] is fundamental for the stabilization of higher oxidation sates of the ruthenium.[17]

Towards the development of more efficient catalysts, in 2016 Grotjahn *et al.*[25] and Concepcion *et al.*[26] reported Ru(2,2′-bipyridine-6,6′-diphosphonato)(picoline)$_2$, **B**, a phosphorus analog of the Ru(bda) catalyst (Fig. 1) with the novel ligand

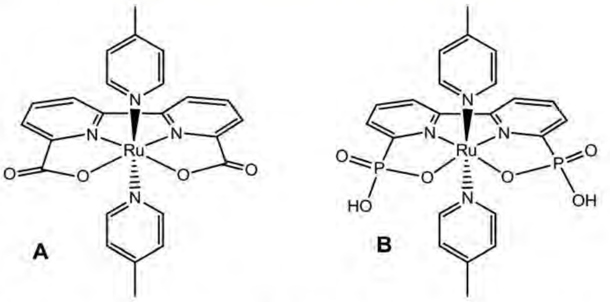

Fig. 1 WOC catalysts **A** (with dicarboxylato ligand (bda)) and **B** (with diphosphonato ligand (bpaH_2)) studied in this work.

---

[a] Institut de Química Computacional i Catàlisi and Departament de Química, Universitat de Girona, c/Mª Aurèlia Capmany 69, 17003 Girona, Catalonia, Spain. E-mail: albert.poater@udg.edu

[b] Department of Chemistry and Biochemistry, San Diego State University, 5500 Campanile Drive, San Diego, CA, 92182-1030, USA

† Electronic supplementary information (ESI) available: Computational details and all XYZ coordinates, energies and 3D structures of all species. See DOI: 10.1039/d0dt02253e

This journal is © The Royal Society of Chemistry 2020

$bpaH_2$. The largest difference between the bda (**A**) and $bpaH_2$ (**B**) ligands is that the $bpaH_2$ has phosphonate groups instead of carboxylate groups. Each of the phosphonates groups are monoanionic like the carboxylates but depending on the pH, they can become dianionic thanks to their hydroxyl group. In basic media, the doubly deprotonated bpa ligand results in four negative charges (as opposed to two negative charges with the biprotonated bpa at pH = 1 or the bda) that stabilize the higher oxidation states of the Ru center. Furthermore, the non-coordinated hydroxyl group is able to participate in proton transfer reactions.

From past studies,[17,24,27] two important conclusions were drawn in relation to the performance of the catalysts included in Fig. 1: the dicarboxylato catalyst **A** generally outperforms the diphosphonato catalyst **B** with lower overpotentials and higher TOFs, even though there is not a clear understanding of the reason. On the other hand, under acidic conditions (pH = 1), the phosphonate catalyst appears to need ceric ammonium nitrate (CAN) for the reaction to progress. It is worth noting that CAN works under mid to low pH, otherwise it precipitates.[28] At pH = 8 and pH = 1 without CAN, the catalytic activity of **B** is minimal if any.

WOC testing using sacrificial oxidants has been performed with sodium peroxodisulfate,[29] potassium peroxymonosulfate,[30] as well as many others.[31,32] However, one of the most used oxidants is the Ce^{IV} reagent CAN. It accepts one electron, forming Ce^{III},[33] a one-electron change that is relevant to operation of a photoelectrochemical cell. In many, but not all cases, it has been shown that the WOC catalysts that work with CAN also work electrochemically.[34] A notable exception observed by the Grotjahn group is that **B**, and a derivative with O^iPr groups in place of OH groups, at pH = 1 were active catalysts using CAN, but mostly inactive electrochemically, even when driven to 1.8 V potential. In CAN-driven reactions of **B**, Concepcion's group observed first-order dependence of reaction rate on both concentrations of **B** and CAN. Taken together, these findings strongly implicate a non-innocent role for CAN; Costas, Lloret-Fillol, *et al.*[35] have suggested with iron based catalysts that CAN interacts with the catalyst to reduce some barriers by making a dimer between two different metal complexes, and more recently, this has been also checked by Cavallo, Macchioni, *et al.*,[36] for iridium catalysts. Similarly, Sakai's group[37] has suggested Ce–OH–Ru interaction during CAN-driven WOC. Nevertheless, Ertem, Roth, Llobet *et al.*[38] reported that when testing the O–O bond formation through ^{18}O kinetic isotopic effects, the CAN does not intervene in the bond formation, but it can help to oxidize the catalyst prior to that.

Finally, there are two commonly proposed mechanistic pathways for WOC: a bimolecular interaction between two metal-oxo units (I2M) and a mononuclear water nucleophilic attack (WNA).[39–41] For the dicarboxylato catalyst **A**,[15] experiments performed by Ahlquist, Sun, *et al.*[42] have shown that while the majority of Ru catalysts operate by the WNA mechanism, **A** operates by the I2M mechanism.[43,44] In the case of the phosphonate catalyst **B**,[20a] available evidence suggests WNA mechanism operates; nevertheless here we will analyze both WNA and I2M mechanistic possibilities (Scheme 1).

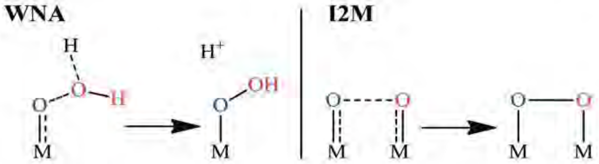

Scheme 1 O–O Bond formation for the WNA mechanism (left) and the I2M mechanism (right).

All in all, we wanted to delve deeper in understanding the behavior of this phosphonate catalyst, which is pH responsive due to the phosphonate ligands.

Computational details

All DFT calculations were performed with the Gaussian09 set of programs,[45] using the M06L functional.[46,47] The electronic configuration of the molecular systems was described with the standard split-valence basis set with a polarization function of Ahlrichs and co-workers for H, C, N, O and P (SVP keyword in Gaussian).[48] The small-core quasi-relativistic Stuttgart/Dresden effective core potential, with an associated valence basis set (standard SDD keywords in Gaussian09) was used for Ru.[49–51] The geometry optimizations were performed without symmetry constraints, and analytical frequency calculations were carried out to characterize the located stationary points. These frequencies were used to calculate unscaled zero-point energies (ZPEs) as well as thermal corrections and entropy effects at 298 K and 1354 atm to better simulate molecular proximity[52] by using the standard statistical mechanics relationships for an ideal gas. A pressure 1354 atm was considered in the calculations as recommended by Martin *et al.*,[52] who determined that this pressure defines the ideal water gas including the relative pressure performed by the surrounding water solvent in aqueous media.[53,54] Energies were obtained by single-point calculations on the optimized geometries with the triple-ζ basis set of Weigend and Ahlrichs for main-group atoms (TZVP keyword in Gaussian),[55] whereas for ruthenium the SDD basis set was employed. Solvent effects were included with the polarizable continuous solvation model PCM using H_2O as solvent.[56,57] The reported Gibbs energies in this work include energies obtained at the M06L/TZVP~SDD//M06L/SVP~SDD level of theory corrected with zero-point energies, thermal corrections, and entropy effects evaluated at 298 K and 1354 atm with the M06L/SVP~SDD method.

To evaluate the pK_a in transition metal complexes that hold ligands, we have used the following procedure:

$$AOH \rightarrow AO^- + H^+$$

$$pK_a = -\log\left(e^{-\frac{\Delta G}{RT}}\right) \quad (1)$$

Using experimental pK_a values *versus* our calculated results, we have adjusted a regression line that provides more reliable pK_a values that the direct use of eqn (1) (see ESI†). The proton energy used for the pK_a is $\Delta G = -270.3$ kcal mol^{-1}, which includes the translational entropy correction.[58]

We represent both proton coupled electron transfer (PCET) and redox reactions[59] with eqn (2) and (3):

$$A^+ + e^- \rightarrow A \tag{2}$$

$$\overset{\circ}{\varepsilon}_{\text{red}} = \frac{\Delta G}{-nF} - \text{SHE}, \tag{3}$$

where ΔG is the Gibbs energy of the reaction, SHE refers to the absolute potential of the Standard Hydrogen Electrode (4.28 V) in water,[60] n refers to the number of electrons and F is the Faraday constant. Energies are given in kcal mol^{-1} and the reduction potential ε in V.

Since PCET reactions include ΔG_{H^+}, we use eqn (4):

$$\overset{\circ}{\varepsilon}_{\text{red}} = \frac{\Delta G_{M^n OH_2} - \Delta G_{M^{n+1} OH} - 0.5 \cdot \Delta G_{H_2}}{-nF} \tag{4}$$

Using this methodology, we can determine the reduction potential for the PCET reactions without experimental values.[61] For more information, check the ESI.† Finally, due to the analysis of different pH conditions, we applied the Nernst equation approximation for the PCETs at 298 K and atmospheric pressure:

$$\varepsilon = \overset{\circ}{\varepsilon}_{\text{red}} - 0.0591 \cdot \text{pH} \tag{5}$$

ε is the corrected PCET reduction potential considered in the mechanisms at the given pH value.

Results and discussion

The reaction mechanisms depicted in Fig. 2 and 3 constitute a summary of the most relevant paths of the full reaction mechanisms that can be found in the ESI.† Molecular structures **Y** in the reaction mechanisms are labelled $^{X}\mathbf{Y}^{q}$, where X indicates spin state (1 = singlet, 2 = doublet, 3 = triplet, 4 = quadruplet) and q is the total charge of species **Y**.

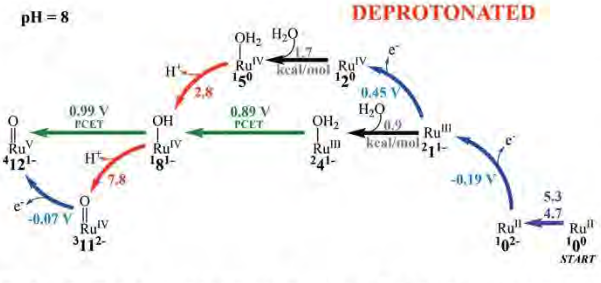

Fig. 2 Optimal electrochemical reaction mechanism catalyzed by **B** (=[Ru^{II}]^0) at pH = 8. Green = PCET, blue = oxidation, red = deprotonation. Species are labelled $^{X}Y^{q}$, where X indicates spin state and q is the total charge of species Y. Full figure in ESI.†

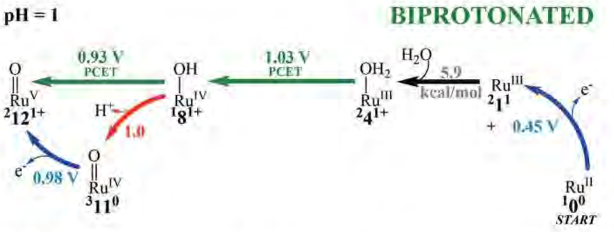

Fig. 3 Optimal mechanism for **B** at pH = 1. Green arrows for PCETs, blue for oxidation states, and red for pK_a. Species are labelled $^{X}Y^{q}$, where X indicates spin state and q is the total charge of species **Y**. Full figure in ESI.†

Mechanism at pH 8

The diagram in Fig. 2 outlines the most likely mechanistic scenarios at pH = 8 starting from the Ru^{II} species **B** (**[Ru^{II}]^0**) to the Ru^{V} species (**[Ru^{V}=O]$^{1-}$**) (see ESI† for the full figure). The Grotjahn and Concepcion groups independently measured a pK_a of approximately 4 for simultaneous deprotonation of both phosphonate moieties of **[Ru^{II}]^0**. As seen in Fig. 2, our estimates for the first and second deprotonation pK_a of **[Ru^{II}]^0** are 4.7 and 5.3. At pH = 8, the reaction mechanism starts with Ru^{II} species **[Ru^{II}]$^{2-}$**. From **[Ru^{II}]$^{2-}$**, either one-electron oxidation can lead to **[Ru^{III}]$^{1-}$** or water can coordinate the metal giving **[Ru^{II}–OH$_2$]$^{2-}$**, however, looking into previous work on similar catalysts[62] we assume that the oxidation step is preferred, reaching therefore **[Ru^{III}]$^{1-}$**.

Two paths for progression of species **[Ru^{III}]$^{1-}$** are possible: (i) stepwise oxidation to **[Ru^{IV}–OH$_2$]^0** and then a simple deprotonation to **[Ru^{IV}–OH]$^{1-}$** (pK_a = 2.8) and (ii) PCET from **[Ru^{III}–OH$_2$]$^{1-}$** to **[Ru^{IV}–OH]$^{1-}$** at 0.89 V. The first path, **[Ru^{II}]$^{2-}$** → **[Ru^{III}]$^{1-}$** → **[Ru^{IV}]^0** → **[Ru^{IV}–OH$_2$]^0** → **[Ru^{IV}–OH]$^{1-}$**, is the lowest potential pathway and involves two oxidation steps: oxidation from **[Ru^{II}]$^{2-}$** to **[Ru^{III}]$^{1-}$** creates the actual Ru^{III} catalyst ($\varepsilon = -0.19$ V), and the second oxidation with ε = 0.45 V leads to species **[Ru^{IV}]^0**. It interacts with water reaching **[Ru^{IV}–OH$_2$]^0** in a slightly endergonic process (ΔG = 1.7 kcal mol^{-1}), and finally it deprotonates towards **[Ru^{IV}–OH]$^{1-}$**.[63,64] In the second path, *i.e.*, **[Ru^{II}]$^{2-}$** → **[Ru^{III}]$^{1-}$** → **[Ru^{III}–OH$_2$]$^{1-}$** → **[Ru^{IV}–OH]$^{1-}$**, **[Ru^{IV}–OH]$^{1-}$** could be reached from **[Ru^{III}–OH$_2$]$^{1-}$** through a PCET at 0.89 V (p$K_{a\text{-IV}}$ = 2.8 and p$K_{a\text{-III}}$ = 9.2). It is quite likely that the two paths described above for the oxidation of H$_2$O–Ru^{III} species **[Ru^{III}]$^{1-}$** are operative. We cannot favor one or the other with only the thermodynamic data collected. Our findings match those of Concepcion *et al.*[20a] If we consider experimental data, such as the voltammograms from Grotjahn *et al.* (see ESI†), there is no peak at 0.45 V, thus the PCET is likely to be the preferred path. Finally, Ru^{V} species **[Ru^{V}=O]$^{1-}$** is reached through a PCET at 0.99 V or through a deprotonation (pK_a = 7.8) towards **[Ru^{IV}=O]$^{2-}$** followed by an oxidation at −0.07 V. Due to the similar values of pK_a and the medium pH, we cannot distinguish between these two routes to Ru^{V} species **[Ru^{V}=O]$^{1-}$**.[65] Since experiments were done at pH = 7, we believe that once again, the PCET prevailed over the deprotonation in these experiments. At higher pHs, however, the route through **$[Ru^{IV}{=}O]^{2-}$** could be operative.

Mechanism at pH 1

Turning now to acidic conditions, when CAN becomes the oxidant, the pH is either close to 1 (using CAN alone) or intentionally started at 1 (using acid media). We performed the same mechanistic analysis at pH = 1, where CAN is considered simply as a one electron redox agent providing an overall oxidizing potential of 1.6–1.7 V to the medium.

Fig. 3 shows that the switch from pH = 8 to pH = 1 forces some changes to the pathway. Importantly, the identity of the redox steps changes due to the lack of ligand deprotonation. Conversion of **$[Ru^{II}]^0$** to **$[Ru^{III}–OH_2]^{1+}$** can follow two routes: either oxidation to **$[Ru^{III}]^{1+}$** with a redox potential of 0.45 V followed by endergonic water binding (ΔG = 5.9 kcal mol^{-1}) or water binds **$[Ru^{II}]^0$** to form **$[Ru^{II}–OH_2]^0$** (ΔG = 2.5 kcal mol^{-1}) followed by oxidation (ε = 0.60 V). As previously stated, we believe that the catalyst first oxidizes, and then binds the water molecule following the **$[Ru^{II}]^0 \rightarrow [Ru^{III}]^{1+} \rightarrow [Ru^{III}–OH_2]^{1+}$** path. Next, two PCET steps lead to Ru^V oxo species **$[Ru^V{=}O]^{1+}$**. The first PCET step leading from Ru^{III} to Ru^{IV} is predicted to be more demanding: 1.03 V, 0.14 V higher than for the Ru^{IV} to Ru^V oxidation at pH = 8, and 0.28 V higher than for the similar step for the carboxylate counterpart.[66]

Subsequently, PCET from **$[Ru^{IV}–OH]^{1+}$** to Ru^V oxo species **$[Ru^V{=}O]^{1+}$** occurs at 0.93 V. Alternatively, **$[Ru^{IV}–OH]^{1+}$** can deprotonate first (pK_a = 1) and then by oxidation (0.98 V) species **$[Ru^V{=}O]^{1+}$** is reached. Due to the similarity between the pK_a and the pH of the medium, thus once more, we cannot distinguish between the two paths from **$[Ru^{IV}–OH]^{1+}$** to **$[Ru^V{=}O]^{1+}$** with computational data alone. Experimentally, cyclic voltammograms show activity at 1.4 V. This is far from the 1.03 V found computationally. An explanation to this difference can be found by looking at the pK_a of the phosphonates in each complex. We found that **$[Ru^{III}–OH_2]^{1+}$** has a pK_a for the deprotonation of one of the phosphonates of 0.2, **$[Ru^{IV}–OH]^{1+}$** has a pK_a of 0.8, and **$[Ru^V{=}O]^{1+}$** has a pK_a of 1.1. What this means is that compounds **$[Ru^{III}–OH_2]^{1+}$** and **$[Ru^{IV}–OH]^{1+}$** spontaneously become **$[Ru^{III}–OH_2]^0$** and **$[Ru^{IV}–OH]^0$** with one of their phosphonates deprotonated at pH = 1. If one looks at the PCETs of the monoprotonated phosphonate catalyst (Fig. 4), they are 1.26 V and 1.21 V, respectively, which are much closer to the experimental 1.4 V. We will come back to this issue later.

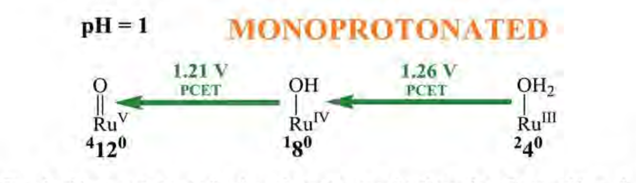

Fig. 4 Monoprotonated phosphonate mechanism for **B** at pH = 1. Species are labelled $^XY^q$, where X indicates spin state and q is the total charge of species **Y**. Full figure in ESI.†

Because the III/IV redox couple of cerium is in the range of 1.6–1.7 V, when CAN is used to drive water oxidation, the proposed PCET at 1.26 V can occur. However, we must consider kinetics. Predicting the speed of a redox process is not an easy task. A useful generalization is that redox couples driven with overpotentials that surpass 0.6 V, usually occur at a fast rate.[67] In our case, for the **$[Ru^{III}–OH_2]^0$** to **$[Ru^{IV}–OH]^0$** PCET reaction, we observe that we have an overpotential of >0.34 V (>1.60 V CAN – 1.26 V PCET). Formation of oxygen from water with CAN does occur experimentally. This can be explained through the difference between implementation of electrodes *vs.* CAN; the oxidizing equivalents provided by the polarization of the medium through the electrode surface may not be sufficient, while on the other hand with a large (>1000-fold) excess of CAN the reaction can proceed. Excesses of other stoichiometric oxidants with sufficient oxidation potential such as $[Co^{III}(H_2O)_6]^{3+}$ or $[Ru^{III}(bipy)_3]^{3+}$ can perform the same function as CAN.[68]

Again, we want to compare our redox potential results for the bda catalyst **A** at pH = 1 (two PCETs of 0.75 and 1.01 V),[65] with the results given in Fig. 4. The bda catalyst **A** requires less positive potentials than **B** (1.26 and 1.21 V), and furthermore, the PCET at most positive potential for **A** is Ru^{IV}–OH to $Ru^V{=}O$,[15] while in the case of **B** the highest potential PCET is the transition of $[Ru^{III}–OH_2]$ to $[Ru^{IV}–OH]$, which again is consistent with the more sluggish performance of **B** compared to that of **A**.

I2M *vs.* WNA pathways

Scheme 2 represents the comparison between pathways. Starting from the mechanism at pH = 8 and considering the O–O bond formation, I2M, approach of two molecules of intermediate **$[Ru^V{=}O]^{1-}$** to form **$[Ru^{III}–OO]^{2-}$** turns out to be the rate determining step (rds).[69] With a Gibbs energy barrier of 19.7 kcal mol^{-1}, this transition state (with an O–O distance of

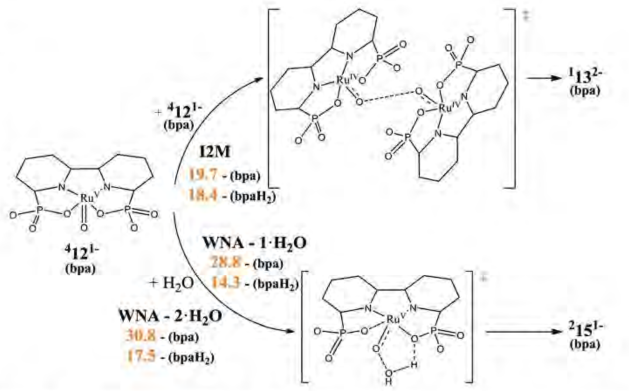

Scheme 2 I2M and WNA mechanisms pathways (with 1 or 2 assisting water molecules) for the deprotonated (bpa at pH = 8) and protonated (bpaH$_2$ at pH = 1) phosphonate catalyst (axial ligands and non-interacting hydrogens removed for clarity). Gibbs energy barriers (kcal mol^{-1}) in orange.

1.884 Å) is 7.3 kcal mol^{-1} more kinetically demanding than the corresponding one in the catalysis by Ru(bda), explaining the slower catalysis of the bisphosphonate Ru catalyst.[65] As a matter of fact, we have also tested whether an initial adduct is formed, but since the adduct is 13 kcal mol^{-1} higher than two **[Ru^{V}═O]$^{1-}$** units, we believe that this potential adduct is not a relevant species in the reaction mechanism. It is important to note that the I2M product **[Ru^{III}–OO]$^{2-}$** is disfavored by 5.7 kcal mol^{-1} whereas in the case of the Ru(bda) the analogous species is slightly favored by 0.3 kcal mol^{-1}.[65] We suggest that bonding of two negatively charged molecules of **[Ru^{V}═O]$^{1-}$** is particularly disfavored by coulombic repulsion in the bisphosphonate Ru catalyst because of the phosphonate oxygens, which are more negatively charged than the ones at the bda carboxylates.

Then, cleavage of one of the Ru(bpa) halves recovers **[Ru^{III}]$^{1-}$** and we obtain peroxide intermediate **[Ru^{III}–OO]$^{1-}$**, without a kinetic cost. Finally, **[Ru^{III}–OO]$^{1-}$** releases O_2 and regenerates species **[Ru^{III}]$^{1-}$** to complete the catalytic cycle. Considering a WNA pathway from **[Ru^{V}═O]$^{1-}$**, we tested Concepcion's proposal of phosphonate-assisted water nucleophilic attack, but we found the transition state (TS) for this interaction at 28.8 kcal mol^{-1}, 9.1 kcal mol^{-1} higher in energy than the TS for the I2M pathway. The barrier for the WNA does not decrease by the assistance of an additional second water molecule (Scheme 2, $\Delta G^{\ddagger} = 30.8$ kcal mol^{-1}), however, the phosphonate is dangling when a second water molecule is included. Neither the structures predicted by Concepcion *et al.*,[26] where both phosphonate ligands provided a Ru–O bond each one, could help here to decrease the energy barrier. Hence we conclude that the WNA pathway is not competitive at pH = 8. For further details of the I2M and WNA, mechanisms check the ESI.†

As to the mechanism at pH = 1, at the stage of Ru^{V} oxo species **[Ru^{V}═O]$^{1+}$**, we tested the hypothesis of water nucleophilic attack (WNA) that has been proposed by groups of Grotjahn and Concepcion. We calculate that WNA on Ru^{V} oxo species **[Ru^{V}═O]$^{1+}$** with one and two assisting water molecules displays Gibbs energy barriers of 14.3 and 17.5 kcal mol^{-1}, respectively, whereas in the I2M pathway increases to 18.4 kcal mol^{-1}. To point out that the transition state of the I2M process has a short O–O distance of 1.695 Å and displays a closed-shell singlet character already, like the next intermediate. This indicates that at pH = 1 the WNA is the preferred pathway. Nevertheless, the full WNA reaction mechanism requires the two deprotonation steps depicted in Fig. 5.

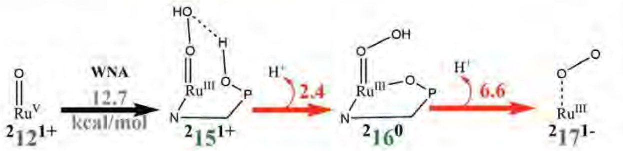

Fig. 5 Liberation of O_2 through WNA for the bpaH_2 catalyst at pH = 1. Gibbs reaction energy (kcal mol^{-1}) in grey, pK_a for deprotonations in red.

However, the pK_a of species **[Ru^{III}–OOH$_2$]$^{1+}$** and **[Ru^{III}–OOH]^{0}** are higher than the pH, and thus these species do not deprotonate. With this information, it is clear that while water may be able to bind to the Ru═O center, it will not deprotonate. Overall, experiments show that the I2M pathway cannot occur, yet, the computational data shows that it cannot undergo WNA either.

There is only one option left that fulfills the experimental results; interaction of one Ru═O catalyst molecule and one ceric ammonium nitrate molecule. Concepcion's group observed first order dependence of the reaction rate on both the concentration of **B** and CAN, and our suggestion is fully consistent with this experimental result. Second, the reaction progresses only with CAN and, to the best of our knowledge, no other oxidants were tested. Applying an external potential does not reproduce the catalytic activity with it, which indicates that the CAN plays an important role besides being an oxidant. This also explains why at more basic pH there is no catalytic activity; CAN is not suitable at neutral pH because it would precipitate.

Finally, let us mention that we tried to find a possible binuclear pathway involving the CAN. To do so, we searched for an initial structure of the CAN species. However, despite our efforts, we could not find an energetically accessible structure for CAN showing reduction potentials close to 1.6–1.7 V and, therefore, we were unable to explore a possible the formation of a Ru–Ce dimer (see Fig. S6 in the ESI†).

Computation *vs.* experiments

In this section, we perform a comparison between experimental and computational data. The first experimental data we can compare is the cyclic voltammetries given by Grotjahn *et al.*[25] and Concepcion *et al.*[26] (see ESI†) that shows the existence of two peaks: 0.28 V and 1.20 V at pH = 1 and −0.03 V and 1.05 V at pH = 7.[70] Starting from the pH = 1 mechanism, we can assign the experimental 0.28 V to the 0.45 V calculated oxidation that refers to **[Ru^{II}]^{0}** → **[Ru^{III}]$^{1+}$**. For the peak at 1.40 V, we have to consider the two PCETs that occur in the monoprotonated mechanism (bpaH, Fig. 4) at electropotentials close to 1.25 V, which we believe responsible for the experimental peak at 1.20 V. Last but not least, due to the close proximity for both PCET potentials, the experimental results show only one peak because they overlap. There is another possibility: the oxidation of **[Ru^{III}]$^{1-}$** → **[Ru^{IV}]^{0}** calculated at 0.45 V yet, there is no experimental peak at this potential. We believe that this oxidation does not occur due to kinetic reasons. Finally, at pH = 8, we can see experimentally two peaks at −0.03 V and 1.05 V. The first peak coincides with our calculated −0.19 V (Fig. 2). As for the second peak at 1.05 V we believe once again that the two PCETs **[Ru^{III}–OH$_2$]$^{1-}$** → **[Ru^{IV}–OH]$^{1-}$** and **[Ru^{IV}–OH]$^{1-}$** → **[Ru^{V}═O]$^{1-}$** are responsible for this peak.

As a whole, the proposed reaction mechanisms that agree with experimental evidences are depicted in Fig. 6.

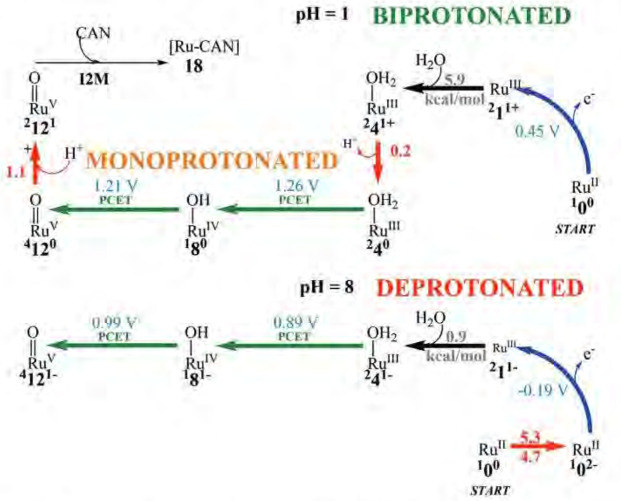

Fig. 6 Proposed final mechanisms at both pH for $bpaH_2$/bpaH and bpa catalysts.

Conclusions

We have computationally studied the water oxidation catalysis for the bisphosphonate bispyridine Ru catalyst **B** according to the experiments performed by the Grotjahn and Concepcion groups. The study is divided into two different pH regimes, basic (pH = 8) and acidic (pH = 1). For pH = 8, the reaction mechanism follows an I2M pathway that is the rds with a barrier of 19.7 kcal mol^{-1}. This Gibbs energy barrier is higher in energy than the one found at 11.4 kcal mol^{-1} for its carboxylate counterpart, studied previously by some of us.[66] The WNA is not competitive at pH = 8 due to a Gibbs barrier of 28.8 kcal mol^{-1}. At pH = 1, the WNA mechanism with a barrier of 14.3 kcal mol^{-1} is preferred over the I2M with a barrier of 18.4 kcal mol^{-1}. However, the WNA pathway at pH = 1 for the O_2 liberation involves two deprotonations that are not possible at pH = 1. This means that WNA cannot progress after binding the water molecule. Considering this, we hypothesize a third pathway; a bimolecular rate-determining step that involves the Ru catalyst and CAN. Despite several tries, we did not find a suitable structure for CAN to do a detailed study of this mechanism. Nevertheless, all the experimental and computational results lead us to believe that this is indeed the mechanism, since it fulfills experimental evidences. It has first-order kinetics to the Ru catalyst and it works at pH = 1 with CAN but not with external potentials.

Conflicts of interest

There are no conflicts to declare.

Acknowledgements

J. A. L. U. thanks Universitat de Girona for a IFUdG2017 PhD fellowship. A. P. is a Serra Húnter Fellow. A. P. and M. S. thank the Ministerio de Economía y Competitividad (MINECO) of Spain for projects CTQ2014-59832-JIN, PGC2018-097722-B-I00 and CTQ2017-85341-P; Generalitat de Catalunya for project 2017SGR39, Xarxa de Referència en Química Teòrica i Computacional, and ICREA Academia prize 2014 to M. S. and 2019 to A. P. D. B. G. and J. M. K. were supported during writing and editing by the U.S. Department of Energy, Office of Science, Office of Basic Energy Sciences, under Award DE-SC0018310. We thank Prof. Javier J. Concepcion for helpful discussions about the role of sacrificial oxidants and mechanism.

Notes and references

1 K. Wang, H. Chen, Y. Hua, Y. Tong, Y. Wang and S. Song, Layer-Stacking Porous WC_x Nanoparticles on Carbon Cloth as Self-Supported Integrated Electrode for Hydrogen Evolution Reaction, *Mater. Today Energy*, 2018, **10**, 343–351.

2 N. Guo, Y. Zeng, H. Li, X. Xu, H. Yu and H. Han, Novel Mesoporous TiO_2@g-C_3N_4 Hollow Core@Shell Heterojunction with Enhanced Photocatalytic Activity for Water Treatment and H_2 Production Undress Simulated Sunlight, *J. Hazard. Mater.*, 2018, **353**, 80–88.

3 E. R. López, F. Dorado and A. de Lucas-Consuegra, Electrochemical Promotion for Hydrogen Production via Ethanol Steam Reforming Reaction, *Appl. Catal., B*, 2019, **243**, 355–364.

4 (*a*) Y.-Y. Li, C. Gimbert, A. Llobet, P. E. M. Siegbahn and R.-Z. Liao, Quantum Chemical Study of the Mechanism of Water Oxidation Catalyzed by a Heteronuclear Ru_2Mn Complex, *ChemSusChem*, 2019, **12**, 1101–1110; (*b*) L. Vigara, M. Z. Ertem, N. Planas, F. Bozoglian, N. Leidel, H. Dau, M. Haumann, L. Gagliardi, C. J. Cramer and A. Llobet, Experimental and Quantum Chemical Characterization of the Water Oxidation Cycle Catalysed by $[Ru^{II}(damp)(bpy)(H_2O)]^{2+}$, *Chem. Sci.*, 2012, **3**, 2576–2586.

5 (*a*) L. Wang, D. W. Shaffer, G. F. Manbeck, D. E. Polyansky and J. J. Concepcion, High-Redox-Potential Chromophores for Visible-Light-Driven Water Oxidation at Low pH, *ACS Catal.*, 2019, **10**, 580–585; (*b*) D. Wang, L. Wang, M. D. Brady, C. J. Dares, G. J. Meyer, T. J. Meyer and J. J. Concepcion, Self-Assembled Chromophore–Catalyst Bilayer for Water Oxidation in a Dye-Sensitized Photoelectrosynthesis Cell, *J. Phys. Chem. C*, 2019, **123**, 30039–30045.

6 J. A. Gilbert, D. S. Eggleston, W. R. Murphy, D. A. Geselowitz, S. W. Gersten, D. J. Hodgson and T. J. Meyer, Structure and Redox Properties of the Water-Oxidation Catalyst $[(bpy)_2(OH_2)RuORu(OH_2)(bpy)_2]^{4+}$, *J. Am. Chem. Soc.*, 1985, **107**, 3855–3864.

7 S. W. Gersten, G. J. Samuels and T. J. Meyer, Catalytic Oxidation of Water by an Oxo-Bridged Ruthenium Dimer, *J. Am. Chem. Soc.*, 1982, **104**, 4029–4030.

8 L. Duan, C. M. Araujo, M. S. G. Ahlquist and L. Sun, Highly efficient and robust molecular ruthenium catalysts for

water oxidation, *Proc. Natl. Acad. Sci. U. S. A.*, 2012, **109**, 15584–15588.

9 J. J. Concepcion, J. W. Jurss, J. L. Templeton and T. J. Meyer, One Site is Enough. Catalytic Water Oxidation by $[Ru(tpy)(bpnm)(OH2)]^{2+}$ and $[Ru(tpy)(bpz)(OH2)]^{2+}$, *J. Am. Chem. Soc.*, 2008, **130**, 16462–16463.

10 S. Romain, F. Bozoglian, X. Sala and A. Llobet, Oxygen–Oxygen Bond Formation by the Ru-Hbpp Water Oxidation Catalyst Occurs Solely via an Intramolecular Reaction Pathway, *J. Am. Chem. Soc.*, 2009, **131**, 2768–2769.

11 J. F. Hull, D. Balcells, J. D. Blakemore, C. D. Incarvito, O. Eisenstein, G. W. Brudvig and R. H. Crabtree, Highly Active and Robust Cp* Iridium Complexes for Catalytic Water Oxidation, *J. Am. Chem. Soc.*, 2009, **131**, 8730–8731.

12 N. D. McDaniel, F. J. Coughlin, L. L. Tinker and S. Bernhard, Cyclometalated Iridium(III) Aquo Complexes: Efficient and Tunable Catalysis for the Homogeneous Oxidation of Water, *J. Am. Chem. Soc.*, 2008, **130**, 210–217.

13 L. Duan, A. Fischer, Y. Xu and L. Sun, Isolated Seven-Coordinate Ru(IV) Dimer Complex with $[HOHOH]^-$ Bridging Ligand as an Intermediate for Catalytic Water Oxidation, *J. Am. Chem. Soc.*, 2009, **131**, 10397–10399.

14 J. Nyhlén, L. Duan, B. Akermark, L. Sun and T. Privalov, Evolution of O_2 in a Seven-Coordinate Ru^{IV} Dimer Complex with a $[HOHOH]^-$ Bridge: A Computational Study, *Angew. Chem., Int. Ed.*, 2010, **49**, 1773–1777.

15 L. Duan, F. Bozoglian, S. Mandal, B. Stewart, T. Privalov, A. Llobet and L. Sun, A Molecular Ruthenium Catalyst with Water-Oxidation Activity Comparable to that of Photosystem II, *Nat. Chem.*, 2012, **4**, 418–423.

16 (*a*) A. Poater, J. Mola, A. Gallegos Saliner, I. Romero, M. Rodríguez, A. Llobet and M. Solà, Mechanistic Theoretical Insight of Ru(II) Catalysts with a Meridional-Facial Bpea Fashion Competition, *Chem. Phys. Lett.*, 2008, **458**, 200–204; (*b*) J. A. Luque-Urrutia and A. Poater, The Fundamental non Innocent Role of Water for the Hydrogenation of Nitrous Oxide by PNP pincer Ru-based catalysts, *Inorg. Chem.*, 2017, **56**, 14383–14387; (*c*) M. Gil-Sepulcre, J. C. Axelson, J. Aguiló, L. Solà-Hernández, L. Francàs, A. Poater, L. Blancafort, J. Benet-Buchholz, G. Guirado, L. Escriche, A. Llobet, R. Bofill and X. Sala, Synthesis and Isomeric Analysis of Ru^{II} Complexes Bearing 2 Pentadentate Scaffolds, *Inorg. Chem.*, 2016, **55**, 11216–11229; (*d*) S. Escayola, M. Solà and A. Poater, Mechanism of the Facile Nitrous Oxide fixation by Homogeneous Ruthenium Hydride Pincer Catalysts, *Inorg. Chem.*, 2020, **59**, 9374–9383.

17 R. Matheu, M. Z. Ertem, M. Pipelier, J. Lebreton, D. Dubreuil, J. Benet-Buchholz, X. Sala, A. Tessier and A. Llobet, The Role of Seven-Coordination in Ru-Catalyzed Water Oxidation, *ACS Catal.*, 2018, **8**, 2039–2048.

18 R. Matheu, S. Neudeck, F. Meyer, X. Sala and A. Llobet, Foot of the Wave Analysis for Mechanistic Elucidation and Benchmarking Applications in Molecular Water Oxidation Catalysis, *ChemSusChem*, 2016, **9**, 3361–3369.

19 (*a*) M. Schulze, V. Kunz, P. D. Frischmann and F. A. Würthner, Supramolecular Ruthenium Macrocycle with High Catalytic Activity for Water Oxidation that Mechanistically Mimics Photosystem II, *Nat. Chem.*, 2016, **8**, 576–583; (*b*) C. W. Cady, R. H. Crabtree and G. W. Brudvig, Functional Models for the Oxygen-Evolving Complex of Photosystem II, *Coord. Chem. Rev.*, 2008, **252**, 444–455.

20 (*a*) Y. Xie, D. W. Shaffer and J. J. Concepcion, O–O Radical Coupling: From Detailed Mechanistic Understanding to Enhanced Water Oxidation Catalysis, *Inorg. Chem.*, 2018, **57**, 10533–10542; (*b*) R. Matheu, A. Ghaderian, L. Francàs, P. Chernev, M. Z. Ertem, J. Benet-Buchholz, V. S. Batista, M. Haumann, C. Gimbert-Suriñach, X. Sala and A. Llobet, Behavior of Ru-bda Water-Oxidation Catalyst in Low Oxidation States, *Chem. – Eur. J.*, 2018, **24**, 12838–12847; (*c*) Q. Daniel, L. Wang, L. Duan, F. Li and L. Sun, Tailored Design of Ruthenium Molecular Catalyst with 2,2′-Bypyridine-6,6′-dicarboxylate and Pyrazole Based Ligands for Water Oxidation, *Dalton Trans.*, 2016, **45**, 14689–14696.

21 S. Zhan, D. Martensson, M. Purg, S. C. L. Kamerlin and M. S. G. Ahlquist, Capturing the Role of Explicit Solvent in the Dimerization of Ru^V(bda) Water Oxidation Catalysts, *Angew. Chem., Int. Ed.*, 2017, **56**, 6962–6965.

22 R. Matheu, M. Z. Ertem, C. Gimbert-Suriñach, X. Sala and A. Llobet, Seven Coordinated Molecular Ruthenium-Water Oxidation Catalysts: a Coordination Chemistry Journey, *Chem. Rev.*, 2019, **119**, 3453–3471.

23 B. Zhang and L. Sun, Ru-bda: Unique Molecular Water-Oxidation Catalysts with Distortion Induced Open Site and Negatively Charged Ligands, *J. Am. Chem. Soc.*, 2019, **141**, 5565–5580.

24 J. J. Concepcion, D. K. Zhong, D. J. Szalda, J. T. Muckerman and E. Fujita, Mechanism of Water Oxidation by [Ru(bda)(L)$_2$]: the Return of the "Blue Dimer", *Chem. Commun.*, 2015, **51**, 4105–4108.

25 J. M. Kamdar, D. C. Marelius, C. E. Moore, A. L. Rheingold, D. K. Smith and D. B. Grotjahn, Ruthenium Complexes of 2,2′-bipyridine-6,6′-diphosphonate Ligands for Water Oxidation, *ChemCatChem*, 2016, **8**, 3045–3049.

26 Y. Xie, D. W. Shaffer, A. Lewandowska-Andralojc, D. J. Szalda and J. J. Concepcion, Water Oxidation by Ruthenium Complexes Incorporating Multifunctional Bipyridil Diphosphonate Ligands, *Angew. Chem., Int. Ed.*, 2016, **55**, 8067–8071.

27 (*a*) R. Matheu, A. Ghaderian, L. Francàs, P. Chernev, M. Z. Ertem, J. Benet-Buchholz, V. S. Batista, M. Haumann, C. Gimbert-Suriñach, X. Sala and A. Llobet, Behavior of Ru–bda Water-Oxidation Catalysts in Low Oxidation States, *Chem. – Eur. J.*, 2018, **24**, 12838–12847; (*b*) C. J. Richmond, S. Escayola and A. Poater, Axial Ligand Effects of Ru–BDA Complexes in the O–O Bond Formation via the I2M Bimolecular Mechanism in Water Oxidation Catalysis, *Eur. J. Inorg. Chem.*, 2019, 2093–2100.

28 V. Sridharan and J. C. Menéndez, Cerium(IV) Ammonium Nitrate as a Catalyst in Organic Synthesis, *Chem. Rev.*, 2010, **110**, 3805–3849.

29 S. Tanaka, A. Masahiko and K. Sakai, Visible Light-induced Water Oxidation Catalyzed by Molybdenum-based Polyoxometalates with Mono and Dicobalt(III) Cores as Oxygen-evolving Centers, *Chem. Commun.*, 2012, **48**, 1653–1655.

30 J. Limburg, J. S. Vrettos, L. M. Liable-Sands, A. L. Rheingold, R. H. Crabtree and G. W. Brudvig, A Functional Model for O-O Bond Formation by the O_2-Evolving Complex in Photosystem II, *Science*, 1999, **283**, 1524–1527.

31 T. Kikuchi and K. Tanaka, Mechanistic Approaches to Molecular Catalysts for Water Oxidation, *Eur. J. Inorg. Chem.*, 2014, 607–618.

32 A. R. Parent, R. H. Crabtree and G. W. Brudvig, Comparison of Primary Oxidants for Water-Oxidation Catalysis, *Chem. Soc. Rev.*, 2013, **42**, 2247–2252.

33 Z. Codolà, I. Gamba, F. Acuña-Parés, C. Casadevall, M. Clémancey, J.-M. Latour, J. M. Luis, J. Lloret-Fillol and M. Costas, Design of Iron Coordination Complexes as Highly Active Homogenous Water Oxidation Catalysts by Deuteration of Oxidation-Sensitive Sites, *J. Am. Chem. Soc.*, 2019, **141**, 323–333.

34 A. Mills, Heterogeneous Redox Catalysts for Oxygen and Chlorine Evolution, *Chem. Soc. Rev.*, 1989, **18**, 285–316.

35 Z. Codolà, L. Gómez, S. T. Kleespies, L. Que Jr., M. Costas and J. Lloret-Fillol, Evidence for an Oxygen Evolving Iron-oxo-cerium Intermediate in Iron-catalysed Water Oxidation, *Nat. Commun.*, 2015, **6**, 5865.

36 A. Bucci, G. Menendez Rodriguez, G. Bellachioma, C. Zuccaccia, A. Poater, L. Cavallo and A. Macchioni, An Alternative Reaction Pathway for Iridium-Catalyzed Water Oxidation Driven by Cerium Ammonium Nitrate (CAN), *ACS Catal.*, 2016, **6**, 4559–4563.

37 M. Yoshida, S. Masaoka, J. Abe and K. Sakai, Catalysis of Mononuclear Aquaruthenium Ccomplexes in Oxygen Evolution from Water: A new Radical Coupling Path using Hydroxocerium(IV) Species, *Chem. – Asian J.*, 2010, **5**, 2369–2378.

38 A. M. Angeles-Boza, M. Z. Ertem, R. Sarma, C. H. Ibañez, S. Maji, A. Llobet, C. J. Cramer and J. P. Roth, Competitive Oxygen-18 Kinetic Isotope Effects Expose O–O Bond Formation in Water Oxidation Catalysis by Monomeric and Dimeric Ruthenium Complexes, *Chem. Sci.*, 2014, **5**, 1141–1152.

39 (*a*) S. Roeser, F. Bozoglian, C. J. Richmond, A. B. League, M. Z. Ertem, L. Francàs, P. Miró, J. Benet-Buchholz, C. J. Cramer and A. Llobet, Water Oxidation Catalysis with Ligand Substituted Ru-bpp Type Complexes, *Catal. Sci. Technol.*, 2016, **6**, 5088–5101; (*b*) A. Poater, Environmental Friendly Fe Substitutive of Ru in Water Oxidation Catalysis, *Catal. Commun.*, 2014, **44**, 2–5.

40 D. W. Shaffer, Y. Xie and J. J. Concepcion, O-O Bond Formation in Ruthenium-Catalyzed Water Oxidation: Single-Site Nucleophilic Attack Vs. O-O Radical Coupling, *Chem. Soc. Rev.*, 2017, **46**, 6170–6193.

41 M. Z. Ertem and J. J. Concepcion, Oxygen Atom Transfer as an Alternative Pathway for Oxygen-Oxygen Bond Formation, *Inorg. Chem.*, 2020, **59**, 5966–5974.

42 T. Fan, L. Duan, P. Huang, H. Chen, Q. Daniel, M. S. G. Ahlquist and L. Sun, The Ru-tpc Water Oxidation Catalyst and Beyond: Water Nucleophilic Attack Pathway Versus Radical Coupling Pathway, *ACS Catal.*, 2017, 7, 2956–2966.

43 I. López, M. Z. Ertem, S. Maji, J. Benet-Buchholz, A. Keidel, U. Kuhlmann, P. Hildebrandt, C. J. Cramer, V. S. Batista and A. Llobet, A Self-Improved Water-Oxidation Catalyst: is One Site Really Enough?, *Angew. Chem., Int. Ed.*, 2014, **53**, 205–209.

44 (*a*) S. Zhan and M. S. G. Ahlquist, Dynamics and Reactions of Molecular Ru Catalysts at Carbon Nanotube–Water Interfaces, *ACS Catal.*, 2018, **8**, 8642–8648; (*b*) S. Zhan and M. S. G. Ahlquist, Dynamics and Reactions of Molecular Ru Catalysts at Carbon Nanotube-Water Interfaces, *J. Am. Chem. Soc.*, 2018, **140**, 7498–7503.

45 M. J. Frisch, G. W. Trucks, H. B. Schlegel, G. E. Scuseria, M. A. Robb, J. R. Cheeseman, G. Scalmani, V. Barone, B. Mennucci, G. A. Petersson, H. Nakatsuji, M. Caricato, X. Li, H. P. Hratchian, A. F. Izmaylov, J. Bloino, G. Zheng, J. L. Sonnenberg, M. Hada, M. Ehara, K. Toyota, R. Fukuda, J. Hasegawa, M. Ishida, T. Nakajima, Y. Honda, O. Kitao, H. Nakai, T. Vreven, J. A. Montgomery Jr., J. E. Peralta, F. Ogliaro, M. Bearpark, J. J. Heyd, E. Brothers, K. N. Kudin, V. N. Staroverov, R. Kobayashi, J. Normand, K. Raghavachari, A. Rendell, J. C. Burant, S. S. Iyengar, J. Tomasi, M. Cossi, N. Rega, J. M. Millam, M. Klene, J. E. Knox, J. B. Cross, V. Bakken, C. Adamo, J. Jaramillo, R. Gomperts, R. E. Stratmann, O. Yazyev, A. J. Austin, R. Cammi, C. Pomelli, J. W. Ochterski, R. L. Martin, K. Morokuma, V. G. Zakrzewski, G. A. Voth, P. Salvador, J. J. Dannenberg, S. Dapprich, A. D. Daniels, Ö. Farkas, J. B. Foresman, J. V. Ortiz, J. Cioslowski and D. J. Fox. *Gaussian 09, Revision E.01*, Gaussian, Inc., Wallingford CT, 2009.

46 Y. Zhao and D. G. Truhlar, The M06 Suite of Density Functionals for Main Group Thermochemistry, Thermochemical Kinetics, Noncovalent Interactions, Excited States, and Transition Elements: Two New Functionals and Systematic Testing of Four M06-Class Functionals and 12 Other Functionals, *Theor. Chem. Acc.*, 2008, **120**, 215–241.

47 Y. Zhao and D. G. Truhlar, A New Local Density Functional for Main-Group Thermochemistry, Transition Metal Bonding, Thermochemical Kinetics, and Noncovalent Interactions, *J. Chem. Phys.*, 2006, **125**, 194101, 1–18.

48 A. Schäfer, H. Horn and R. Ahlrichs, Fully Optimized Contracted Gaussian Basis Sets for Atoms Li to Kr, *J. Chem. Phys.*, 1992, **97**, 2571–2577.

49 U. Haeusermann, M. Dolg, H. Stoll and H. Preuss, Accuracy of Energy-Adjusted Quasirelativistic ab initio Pseudopotentials, *Mol. Phys.*, 1993, **78**, 1211–1224.

50 W. Küchle, M. Dolg, H. Stoll and H. Preuss, Energy-Adjusted Pseudopotentials for the Actinides. Parameter

Sets and Test Calculations for Thorium and Thorium Monoxide, *J. Chem. Phys.*, 1994, **100**, 7535–7542.

51 T. Leininger, A. Nicklass, H. Stoll, M. Dolg and P. Schwerdtfeger, The Accuracy of the Pseudopotential Approximation. II. A Comparison of Various Core Sizes for Indium Pseudopotentials in Calculations for Spectroscopic Constants of InH, InF, and InCl, *J. Chem. Phys.*, 1996, **105**, 1052–1059.

52 R. L. Martin, P. J. Hay and L. R. Pratt, Hydrolysis of Ferric Ion in Water and Conformational Equilibrium, *J. Phys. Chem. A*, 1998, **102**, 3565–3573.

53 (*a*) A. Poater, E. Pump, S. V. C. Vummaleti and L. Cavallo, The Right Computational Recipe for Olefin Metathesis with Ru-Based Catalysts: the Whole Mechanism of Ring-Closing Olefin Metathesis, *J. Chem. Theory Comput.*, 2014, **10**, 4442–4448; (*b*) L. Falivene, E. Barone and G. Talarico, Unraveling the Role of Entropy in Tuning Unimolecular vs. Bimolecular Reaction Rates: The Case of Olefin Polymerization Catalyzed by Transition Metals, *Mol. Catal.*, 2018, **452**, 138–144.

54 (*a*) M. García-Melchor, M. C. Pacheco, C. Nájera, A. Lledós and G. Ujaque, Mechanistic Exploration of the Pd-Catalyzed Copper-Free Sonogashira Reaction, *ACS Catal.*, 2012, **2**, 135–144; (*b*) S. Coufourier, Q. Gaignard-Gaillard, J.-F. Lohier, A. Poater, S. Gaillard and J.-L. Renaud, Hydrogenation of CO_2, Hydrogenocarbonate, and Carbonate to Formate in Water using Phosphine Free Bifunctional Iron Complexes, *ACS Catal.*, 2020, **10**, 2108–2116; (*c*) A. Gómez-Suárez, Y. Oonishi, A. R. Martin, S. V. C. Vummaleti, D. J. Nelson, D. B. Cordes, A. M. Z. Slawin, L. Cavallo, S. P. Nolan and A. Poater, On the Mechanism of the Digold(I)-Hydroxide-Catalysed Hydrophenoxylation of Alkynes, *Chem. – Eur. J.*, 2016, **22**, 1125–1132.

55 F. Weigend and R. Ahlrichs, Comparative Study of the Chemical Reactivity of Helical Peptide Models for Protein Glycation, *Phys. Chem. Chem. Phys.*, 2005, **7**, 3297–3305.

56 V. Barone and M. Cossi, Quantum Calculation of Molecular Energies and Energy Gradients in Solution by a Conductor Solvent Model, *J. Phys. Chem. A*, 1988, **102**, 1995–2001.

57 J. Tomasi and M. Persico, Molecular Interactions in Solution: An Overview of Methods Based on Continuous Distributions of the Solvent, *Chem. Rev.*, 1994, **94**, 2027–2094.

58 R.-Z. Liao and P. E. M. Siegbahn, Quantum Chemical Modeling of Homogeneous Water Oxidation Catalysis, *ChemSusChem*, 2017, **10**, 4236–4263.

59 F. Acuña-Parés, Z. Codolà, M. Costas, J. M. Luis and J. Lloret-Fillol, Unraveling the Mechanism of Water Oxidation Catalyzed by Nonheme Iron Complexes, *Chem. – Eur. J.*, 2014, **20**, 5696–5707.

60 C. P. Kelly, C. J. Cramer and D. G. Truhlar, Single-Ion Solvation Free Energies and the Normal Hydrogen Electrode Potential in Methanol, Acetonitrile, and Dimethyl Sulfoxide, *J. Phys. Chem. B*, 2007, **111**, 408–422.

61 J. Schneider, R. E. Bangle, W. B. Swords, L. Troian-Gautier and G. J. Meyer, Determination of Proton-Coupled Electron Transfer Reorganization Energies with Application to Water Oxidation Catalysts, *J. Am. Chem. Soc.*, 2019, **141**, 9758–9763.

62 C. Gimbert-Suriñach, D. Moonshiram, L. Francàs, N. Planas, V. Bernales, F. Bozoglian, A. Guda, L. Mognon, I. López, M. A. Hoque, L. Gagliardi, C. J. Cramer and A. Llobet, Structural and Spectroscopic Characterization of Reaction Intermediates Involved in a Dinuclear Co-Hbpp Water Oxidation Catalyst, *J. Am. Chem. Soc.*, 2016, **138**, 15291–15294.

63 M. H. V. Huynh and T. J. Meyer, Proton-Coupled Electron Transfer, *Chem. Rev.*, 2007, **107**, 5004–5064.

64 T. J. Meyer and R. A. Binstead, Hydrogen Atom Transfer between Metal Complex Ions in Solution, *J. Am. Chem. Soc.*, 1987, **109**, 3287–3297.

65 D. Lebedev, Y. Pineda-Galvan, Y. Tokimaru, A. Fedorov, N. Kaeffer, C. Copéret and Y. Pushkar, The Key Ru^V=O Intermediate of Site-Isolated Mononuclear Water Oxidation Catalyst Detected by in Situ X-ray Absorption Spectroscopy, *J. Am. Chem. Soc.*, 2018, **140**, 451–458.

66 J. A. Luque-Urrutia, M. Solà and A. Poater, The Influence of the pH on the Reaction Mechanism of Water Oxidation by a Ru(bda) Catalyst, *Catal. Today*, 2020, DOI: 10.1016/j.cattod.2019.12.005.

67 (*a*) H. Ezaki, M. Morinaga and S. Watanabe, Hydrogen Overpotential for Transition Metals and Alloys, and its Interpretation Using an Electronic Model, *Electrochim. Acta*, 1993, **38**, 557–564; (*b*) G. T. Burstein, A Hundred Years of Tafel's Equation: 1905-2005, *Corros. Sci.*, 2005, **47**, 2858–2870.

68 (*a*) R. Kang, K. Chen, J. Yao, S. Shaik and J. Chen, Probing Ligand Effects on O–O Bond Formation of Ru-Catalyzed Water Oxidation: A Computational Survey, *Inorg. Chem.*, 2014, **53**, 7130–7136; (*b*) Prof. J. J. Concepcion, personal communication. .

69 (*a*) C. J. Richmond, R. Matheu, A. Poater, L. Falivene, J. Benet-Buchholz, X. Sala, L. Cavallo and A. Llobet, Supramolecular Water Oxidation with Ru-bda-Based Catalysts, *Chem. – Eur. J.*, 2014, **20**, 17282–17286; (*b*) D. W. Shaffer, Y. Xie, D. J. Szalda and J. J. Concepcion, Manipulating the Rate-Limiting Step in Water Oxidation Catalysis by Ruthenium Bipyridine-Dicarboxylate Complexes, *Inorg. Chem.*, 2016, **55**, 12024–12035.

70 The experimental values using the Ag/AgCl reference electrode were converted to the NHE electrode (V_{NHE} = 0.199 V + $V_{Ag/AgCl}$).

This journal is © The Royal Society of Chemistry 2020

4.3. Mechanism of the Manganese-Pincer-Catalyzed Acceptorless Dehydrogenative Coupling of Nitriles and Alcohols

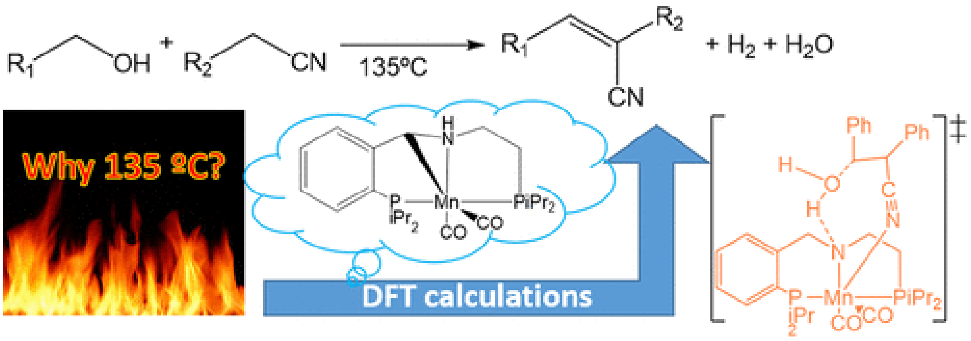
R1 OH + R2 CN
135ºC
R1 R2 CN + H2 + H2O
Why 135 ºC?
DFT calculations
H N
P Mn PiPr2
iPr2 CO CO
Ph Ph
H O
H C N
N
P Mn PiPr2
iPr2 CO CO
‡

Luque-Urrutia, J. A.; Solà, M.; Milstein, D.; Poater, A. **Mechanism of the Manganese-Pincer-Catalyzed Acceptorless Dehydrogenative Coupling of Nitriles and Alcohols.** *J. Am. Chem. Soc.* **2019**, *141*, 2398-2403.
DOI: 10.1021/jacs.8b11308.

This thesis author has contributed to the DFT calculations, writing, data analysis, and revisions of the article.

Reproduced with permission from:

Luque-Urrutia, J. A.; Solà, M.; Milstein, D.; Poater, A. **Mechanism of the Manganese-Pincer-Catalyzed Acceptorless Dehydrogenative Coupling of Nitriles and Alcohols.** *J. Am. Chem. Soc.* **2019**, *141*, 2398-2403.

https://doi.org/10.1021/jacs.8b11308

Copyright © 2019, American Chemical Society.

JOURNAL OF THE AMERICAN CHEMICAL SOCIETY

Article

Cite This: J. Am. Chem. Soc. 2019, 141, 2398–2403

pubs.acs.org/JACS

Mechanism of the Manganese-Pincer-Catalyzed Acceptorless Dehydrogenative Coupling of Nitriles and Alcohols

Jesús A. Luque-Urrutia,[‡] Miquel Solà,[*,‡] David Milstein,[*,§] and Albert Poater[*,‡]

[‡]Institut de Química Computacional i Catàlisi and Departament de Química, Universitat de Girona, C/Maria Aurèlia Capmany, 69, 17003 Girona, Catalonia, Spain

[§]Department of Organic Chemistry, The Weizmann Institute of Science, Rehovot, 76100, Israel

Supporting Information

ABSTRACT: A recent study showed that a Mn-pincer could catalyze the acceptorless dehydrogenative coupling of nitriles and alcohols to yield acrylonitriles. The reaction mechanism proposed in that work contained some intermediates that, in most of the cases, were not characterized. Moreover, one of the intermediates involved a charged separation, which is unlikely in apolar solvents. To clarify the reaction mechanism of this critical reaction, we decided to perform a DFT study. Our results prove the existence of a cooperative effect of the metal and the ligand in several steps of the catalytic cycle. We also find the presence of several equilibria between isomeric intermediates where water, or the same alcohol reagent, takes part in assisting the proton transfer. Furthermore, we have analyzed the charge-separated structure proposed experimentally and have found a nearly pure covalent bond between the two expected charged moieties. Finally, the Knoevenagel condensation step that generates the acrylonitrile is found to be the rate-determining step.

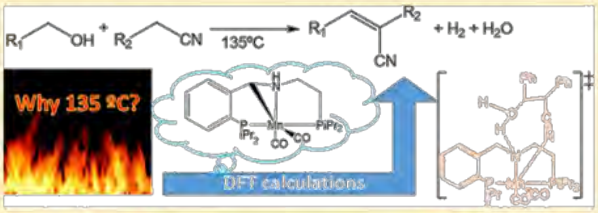

INTRODUCTION

Currently being researched by many authors, acrylonitriles are known to be a worthwhile resource in synthesis, including the formation of benzonitriles[1] and pyrroles[2] used as a treatment for malaria.[3] The SOHIO process,[4] which consists of the catalytic ammoxidation of propylene, is used to produce them on an industrial level. Another recognized way of producing acrylonitriles is to form a C=C bond using the Knoevenagel condensation.[5] This reaction involves the nucleophilic attack of an activated carbon, located between two electron-withdrawing groups, on a carbonyl, a ketone, or an aldehyde (see Scheme 1).

Scheme 1. Knoevenagel Condensation for the Formation of Unsaturated Acrylonitriles

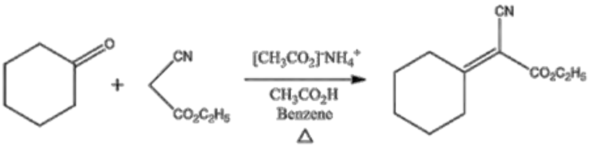

While this is a widely used synthetic strategy for many applications,[6] researchers nowadays are aiming to produce it using new methodologies involving less waste, greater productivity, and energy efficiency gain.[7] One of these approaches to produce acrylonitriles is the catalytic dehydrogenative cross-coupling reaction (CDC).[8] This procedure requires a sacrificial molecule to accept the liberated hydrogen atoms, thus generating stoichiometric amounts of waste where, ideally, waste should not be generated. To reduce this problem, an upgrade in the mechanism that involves the formation of H_2 instead of the hydrogenation of a sacrificial molecule, the so-called acceptorless dehydrogenative coupling (ADC)[9] reaction, was developed.[10] In this new procedure that significantly reduces waste, the formation of H_2 creates the possibility to synchronize the acrylonitrile synthesis with the controlled production of H_2 as a viable energy source.[11] A problem with this approach is, however, that it usually requires noble transition metal complexes, such as iridium or rhodium,[12] which are scarce and costly compared to earth-abundant metals such as iron, cobalt, or manganese.[13] In 2017, an experimental study by one of us (shown in Scheme 2) reported the (for any catalyst) unprecedented efficient α-olefination of nitriles by ADC of alcohols and nitriles, catalyzed by the recently developed Mn-pincer catalyst (**1**, see Figure 1).[14]

This work used various alcohols and nitriles as starting materials and compared the catalytic activity of **1** with that of

Scheme 2. Catalytic Acceptorless Dehydrogenative Coupling Reaction Reported by Milstein et al.[14]

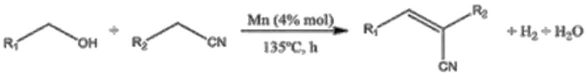

Received: October 19, 2018
Published: January 11, 2019

© 2019 American Chemical Society

DOI: 10.1021/jacs.8b11308
J. Am. Chem. Soc. 2019, 141, 2398–2403

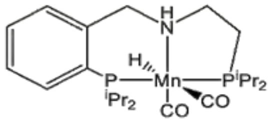

Figure 1. Mn catalyst **1** for acceptorless dehydrogenative coupling as reported by Milstein and co-workers.[14]

other recently reported metal pincer catalysts.[15] They found that using their Mn catalyst resulted in conversions of up to >99% and yields up to 91% (see Scheme 3).

Scheme 3. Proposed Mechanism by Milstein et al. of Acceptorless Dehydrogenative Coupling of Nitriles with Alcohols[a]

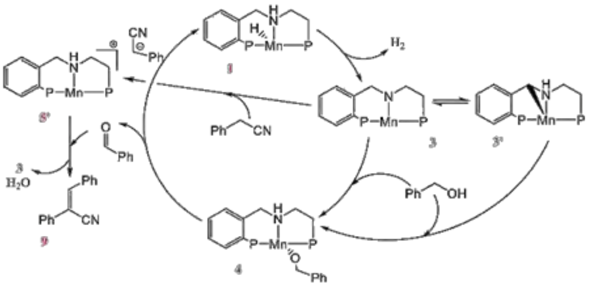

[a]We have removed both the carbonyl ligands coordinated to Mn and ^{i}Pr groups on the phosphorous atoms for the sake of clarity.[14].

The Mn catalyst represents a more promising possibility in the field of ADC and acrylonitrile synthesis. The production of molecular hydrogen and water as byproducts is but one of the key reasons behind the importance of this catalysis. As we believe that this catalyst is a ground-breaking development in its field, here we unravel the whole reaction mechanism using density functional theory (DFT) calculations. We start from the proposed reaction pathway, as shown in Scheme 3. Our primary goal is to better understand the recent experiments by Milstein and co-workers that provide substituted acrylonitrile synthesis by coupling alcohols and nitriles using a manganese pincer complex under mild reaction conditions,[14] i.e., a partial hydrogen-borrowing reaction that allows water and dihydrogen to be released as byproducts.

■ RESULTS AND DISCUSSION

The full reaction mechanism for the formation of substituted acrylonitriles from the coupling of alcohols with nitriles is depicted in Figure 2, starting from the well-characterized catalyst **1**.

In the first step, a H_2 molecule is formed with a relatively low energy barrier (22.0 kcal/mol). A water molecule assists the H−H bond formation from the hydride of the manganese and the hydrogen atom held by one of the N−H groups of the catalyst. The resulting H_2 coordination gives intermediate **2**, which is unstable by 16.1 kcal/mol in comparison to **1**. The rather low thermodynamic stability of **2** helps to understand the small energy barrier, only 3.6 kcal/mol, required to release the H_2 molecule and thus leading to the trigonal bipyramid **3**. Therefore, **2** is the intermediate required for the formation of the hydrogen molecule and its liberation. In the experiments, an isomer of compound **3** was found, **3′**, which is 5.5 kcal/mol more stable, and so their equilibrium needs further discussion. In the previous work,[14] **3′** was assigned as the thermodynamic isomer and **3** as the kinetic. Its interconversion involves a proton transfer to the nitrogen atom from its nearby methylene group in **3**, to generate the NH and CH moieties in **3′**. We found that the direct interconversion was unaffordable since it would require overcoming a 75.3 kcal/mol energy barrier. Moreover, adding a water molecule barely assisted this step, as it only decreased the energy barrier by a mere 5.4 kcal/mol. Nonetheless, we had to consider that complex **3′** had been determined using X-ray analysis and that it had been obtained using two different approaches: first by heating the media to 110 °C for 30 min and, second, by leaving the rest of the media for 12 h. This result implies that an alternative interconversion step, or sum of steps, had to be taken into account.

Figure 3 depicts the steps involved in the interconversion between **3** and **3′**. Results show that this interconversion takes place through complex **4**. The transformations of **3** → **4** and **4** → **3′** assisted by an alcohol molecule have Gibbs energy barriers of 23.7 and 25.2 kcal/mol, respectively, at 135 °C (see Figure 3). Therefore, **3** and **3′** can be interconverted using the alcohol in the media. Nevertheless, the experiments showed the formation of **3′** from **3** without alcohol, but only stoichiometrically.[14a] Thus, the same approach using water was studied. As we hypothesized, when using water we obtained Gibbs energy barriers at 135 °C for the steps **3** → **4** and **4** → **3′** of 15.4 and 27.9 kcal/mol, respectively. These energy barriers are surmountable at room temperature and could easily be sped up by heating. These results are in perfect agreement with the experiments carried out at 25 and 135 °C, respectively.[14]

The interconversion of **3** → **3′** via intermediate **4** would indeed be feasible with traces of water from a nondried solvent, acting as a proton transfer shuttle,[16] progressing in the equilibria toward the thermodynamically most stable isomer **3′** as Milstein et al. previously described.[14] Additionally, we also studied the possibility of the interconversion between −OH and $-OCH_2Ph$ ligands in molecule **4** to see whether they were interchangeable. With a barrier of 18.0 and 21.5 kcal/mol at 25 and 135 °C, respectively, to exchange the alkoxy ligand from the original alcohol by a hydroxo from a water molecule, we conclude that it is possible to exchange both ligands.

With regard to Figure 2, to close the catalytic cycle through **4**, the liberation of the aldehyde requires overcoming a transition state (TS) with an energy barrier placed 18.1 kcal/mol above **4**. **4** → **1** involves a proton transfer from the methylene group of the alkoxy ligand still bonded to the metal, to release the aldehyde together with the regeneration of the catalyst **1**. Thus, this is an inner shell process since the alkoxy group is bonded via its oxygen to the manganese, making a single molecule. It is important to remark that we were not able to find a TS with an assisting water or alcohol molecule for this **4** → **1** transformation, probably due to the steric constraints of the active site.

The alternative outer shell mechanism is represented in the step **3** → **1** with an energy barrier of 22.0 kcal/mol above **3** and 27.5 kcal/mol with respect to **3′**. In this process, the alcohol undertakes a concerted double hydrogen transfer to yield the expected aldehyde in a single step.[17] Comparing the mechanisms, both are possible but the outer shell mechanism is favored.[18] We also considered the transition from **3′** to **1** but with a barrier of 44.3 kcal/mol above **3′**, this step is not competitive.

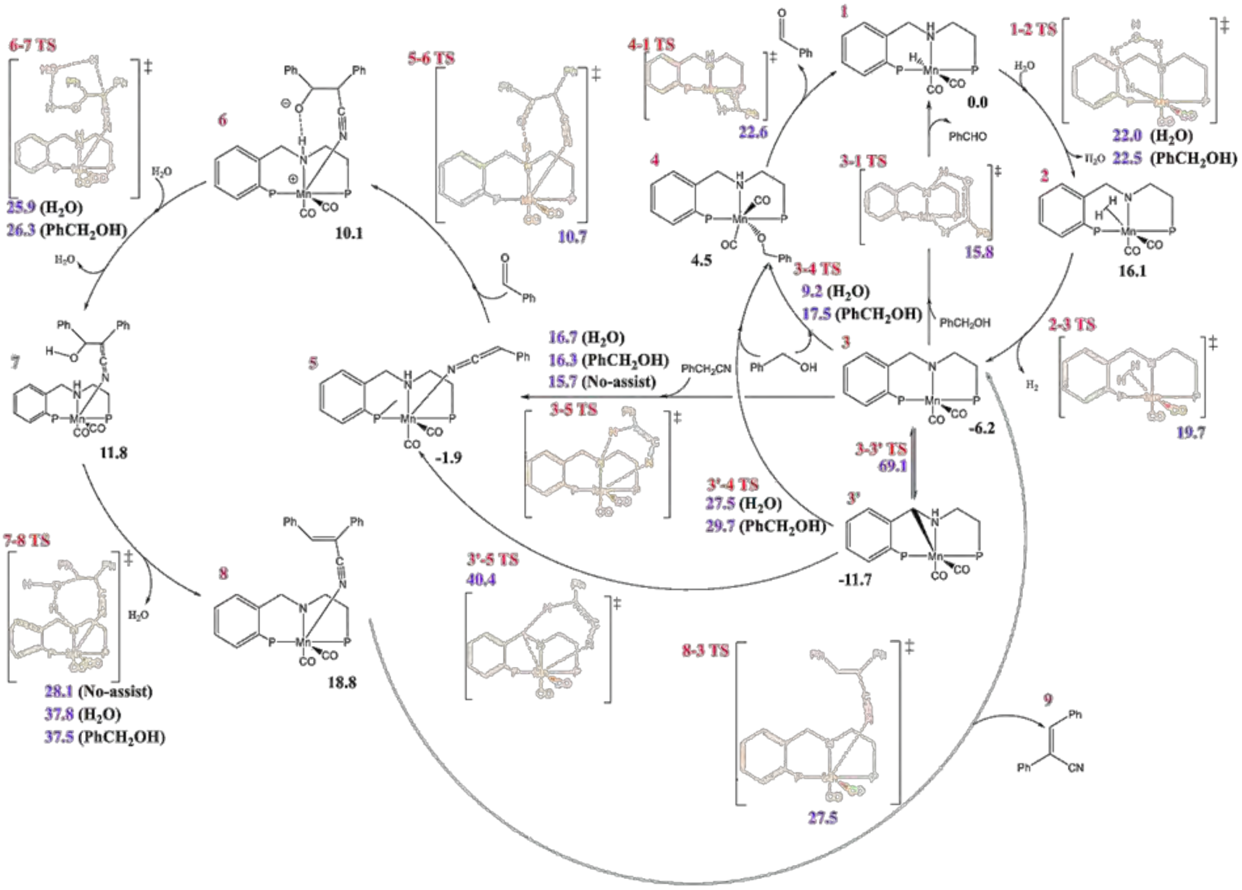
6-7 TS
25.9 (H2O)
26.3 (PhCH2OH)
6
10.1
5-6 TS
10.7
4-1 TS
22.6
1
0.0
PhCHO
1-2 TS
22.0 (H2O)
22.5 (PhCH2OH)
2
16.1
4
4.5
3-1 TS
15.8
3-4 TS
9.2 (H2O)
17.5 (PhCH2OH)
PhCH2OH
7
11.8
5
-1.9
16.7 (H2O)
16.3 (PhCH2OH)
15.7 (No-assist)
PhCH2CN
3-5 TS
3
-6.2
2-3 TS
19.7
H2
3-3' TS
69.1
3'-4 TS
27.5 (H2O)
29.7 (PhCH2OH)
3'
-11.7
7-8 TS
28.1 (No-assist)
37.8 (H2O)
37.5 (PhCH2OH)
8
18.8
3'-5 TS
40.4
8-3 TS
27.5
9

Figure 2. Full mechanism for the acceptorless dehydrogenative coupling of benzyl alcohols with nitriles (relative Gibbs energies for solvent media in kcal/mol and referred to catalyst **1**, and P = P^{i}Pr$_2$). For the sake of clarity, we have reported the missing Lewis structures for a few transition states in Figure 3. All data shown were calculated at T = 135 °C, mimicking the experiments.

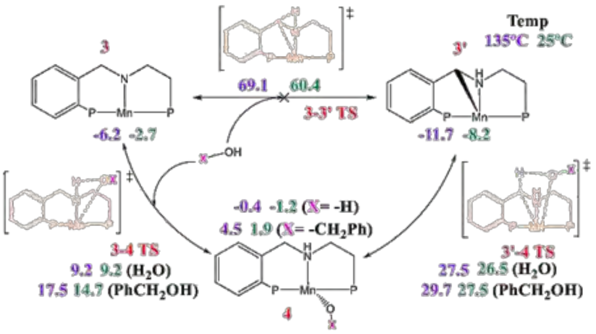
Temp
135°C 25°C
3
-6.2 -2.7
69.1 60.4
3-3' TS
3'
-11.7 -8.2
-0.4 -1.2 (X= -H)
4.5 1.9 (X= -CH2Ph)
3-4 TS
9.2 9.2 (H2O)
17.5 14.7 (PhCH2OH)
3'-4 TS
27.5 26.5 (H2O)
29.7 27.5 (PhCH2OH)
4

Figure 3. Formation of the thermodynamic isomer **3′** from the kinetic **3**, using either water or benzyl alcohol as a cocatalyst. Calculated at 25 and 135 °C (energy values in green and violet, respectively), relative Gibbs energy values (in kcal/mol) referred to catalyst **1**; P = P^{i}Pr$_2$ and CO ligands not included for the sake of clarity.

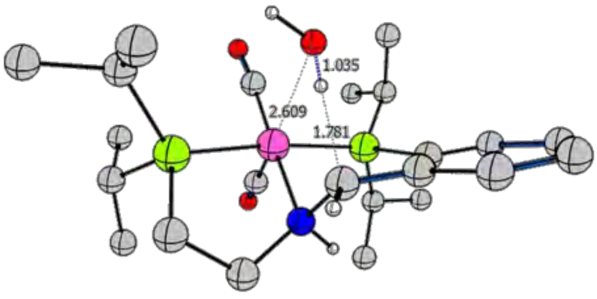
1.035
2.609
1.781

Figure 4. Structural geometry of the transition state for the step **4** → **3′**, assisted by water, with relevant distances shown in Å (most of the H atoms have been omitted for clarity).

Continuing along the acrylonitrile catalytic pathway from **3**, the reaction can also evolve to intermediate **5**, since the corresponding transition state is 21.9 kcal/mol above **3** and thus in perfect competition with **3** → **1** transformation, which step is only 0.1 kcal/mol higher in energy. The path from **3′** to **5** was also studied. This transformation has a 52.2 kcal/mol energy barrier above **3′**, which is too high to be surpassed at experimental conditions. The addition of a nitrile to **3** was analyzed, connecting Mn with the C atom in the CH group of the nitrile or with the N atom. None of the attempts to connect Mn with the C atom of the CH group resulted in the formation of stable intermediates. On the other hand, the interaction of the nitrile through the N atom leads to intermediate **5**. An alternative intermediate **5**, described in a similar way to species **5′** in Scheme 3, would lead to a nitrile ligand anion and a protonated catalyst cation which would stay together through an electrostatic interaction, but calculations have confirmed the covalent character of the Mn−N interaction in intermediate **5**. Moreover, the Mayer bond order[19] (MBO) of the formed Mn−N bond in complex **5** was found to be 0.55, not far from the typical values of Mn−N bonds.[20] Further, to check whether we had an ionic or a covalent bond, we analyzed the NPA charges of both moieties, which were −0.25 (nitrile) and 0.25 e⁻ (Mn complex), thus far away from the ca. +1 and −1 charges expected in an ionic complex. The values of the charges and bond order support the covalency of this bond and rule out the ionic nature of the Mn−N bond in complex **5**.

Once we reach molecule **5**, given the nucleophilic character of the nitrile ligand, the reaction pathway evolves to **6** with the formation of the C−C bond between the carbonyl of the aldehyde and the terminal CHPh moiety of the former nitrile. Intermediate **6** holds a favorable H-bond between the NH moiety and the oxygen of the carbonyl group. On the other hand, the relatively low negative charge on the oxygen atom (−0.402 e⁻) of intermediate **6** is consistent with a partial anionic character on it. Moreover, the new C−C bond is still rather weak, elongated by 1.748 Å, with an associated MBO of just 0.669 e⁻. We also tried to approach the C−C bond formation starting from **4** and adding the nitrile here, but without success.

The Gibbs energy barrier for the next step **6** → **7** is 15.8 kcal/mol above **6** using water as a proton transfer assistant (32.9 kcal/mol without H_2O or alcohol as proton shuttle). The formation of intermediate **8** from **7**, which consists of a concerted release of a water molecule through a condensation reaction, requires overcoming a 16.3 kcal/mol energy barrier. We also investigated if additional explicit water or alcohol molecules could play an assisting role in all the different proton transfer reactions present in the mechanism. An addition of a second water molecule in all the water-assisted steps did not decrease any energy barrier. The substitution of the assisting water molecule by an assisting alcohol molecule increased the energy barriers by a small amount. In the presence of alcohol all assisted steps are still possible, and therefore, the mechanism could be performed initially in a thoroughly dried media.

Finally, the regeneration of **3** and the release of the desired product **9**, closing the mechanistic cycle (**8** → **3**), occurs with an 8.7 kcal/mol barrier.

All in all, and considering the higher stability of molecule **3′**, we observe that the rate-determining step (rds) is located at the Knoevenagel condensation step **7** → **8** involving release of water and formation of the acrylonitrile product **9** coordinated to Mn. This **7** → **8** process has a global energy barrier of 39.8 kcal/mol from **3′** or 34.3 kcal/mol from **3**. It is also important to note that the Gibbs energy barriers for steps **3′** → **4** and **8** → **3** (both placed 39.2 kcal/mol above **3′**) have a difference of only 0.6 kcal/mol as compared to that of the rds, the latter processes being in clear competition with the described rds.[21]

CONCLUSIONS

We have described the full DFT mechanism for the Mn-catalyzed acceptorless dehydrogenative coupling of alcohols with nitriles. Our study indicates that the rate-determining step corresponds to the release of a water molecule that leads to the final product **9** (**7** → **8** step). For the equilibrium between **3** and **3′**, our results show the importance that a water molecule has in assisting the proton transfer to carry out the interconversion between the kinetic complex **3** and its thermodynamic isomer **3′**. The alcohol reagent can also adopt the same role, with an additional kinetic cost of only a few kcal/mol. We tested the coordination of the nitrile through the C atom alpha to the N atom in complex **3**, but only the N coordination leads to the stable complex **5**. Complex **5** was found to have the Mn metal center bonded covalently to the N atom of the nitrile ligand. A proton transfer assistant, like water, is needed in almost all proton transfer reactions except for the rds **7** → **8** and the **3** → **5** step. The reagent alcohol is also capable of undertaking the same proton transfer assistant role as water, although water performs better. It is worth emphasizing that the cooperative MnNH framework acts as both a platform for alcohol dehydrogenation and a kind of templating agent for the Knoevenagel intramolecular proton relay and H-bonding group. Finally, we confirmed that the catalytic mechanism is restarted when intermediate **8** released product **9** and yielded complex **3**.

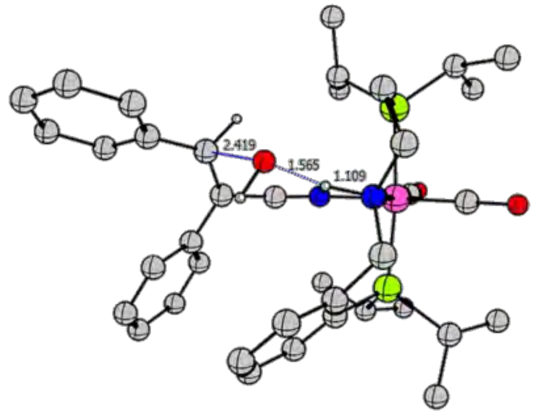

Figure 5. Structural geometry of the transition state that corresponds to the rds step **7** → **8**, with relevant distances shown in Å. Most of the H atoms have been omitted for clarity.

COMPUTATIONAL DETAILS

DFT calculations were performed with the Gausian09 set of programs,[22] using the BP86 functional of Becke and Perdew,[23−25] together with the Grimme D3BJ[26,27] correction term to the electronic energy. We described the electronic configuration of the molecular systems with the triple-ζ basis set of Weigend and Ahlrichs for all atoms (TZVP keyword in Gaussian).[28] We performed the geometry optimizations without symmetry constraints, and analytical frequency calculations were carried out to characterize the located stationary points. These frequencies were used to calculate unscaled zero-point energies (ZPEs) as well as thermal corrections and entropy effects at 25 and 135 °C. Single-point energy calculations were performed on the optimized geometries with the M06 functional[29] and the cc-pVTZ basis set.[30] The same functional and basis set were used to estimate solvent effects with the universal solvation model SMD of Cramer and Truhlar,[31] using toluene as the solvent. The reported Gibbs energies in this work include M06/cc-pVTZ//BP86-D3BJ/TZVP electronic energies with solvent effects obtained at the same level of theory, corrected with zero-point energies, thermal corrections, and entropy effects evaluated at 25 or 135 °C with the BP86-D3BJ/TZVP method.

ASSOCIATED CONTENT

Supporting Information

The Supporting Information is available free of charge on the ACS Publications website at DOI: 10.1021/jacs.8b11308.

Computational details and all XYZ coordinates, energies, and 3D structures of all species (XYZ)

AUTHOR INFORMATION

Corresponding Authors

*miquel.sola@udg.edu
*david.milstein@weizmann.ac.il
*albert.poater@udg.edu

ORCID

Miquel Solà: 0000-0002-1917-7450
David Milstein: 0000-0002-2320-0262
Albert Poater: 0000-0002-8997-2599

Notes

The authors declare no competing financial interest.

ACKNOWLEDGMENTS

J.A.L.U. thanks the Universitat de Girona for the IFUdG2017 Ph.D. fellowship. A.P. and M.S. are grateful to the Ministerio de Economía y Competitividad (MINECO) of Spain (projects CTQ2014-59832-JIN and CTQ2017-85341-P), the Generalitat de Catalunya (project 2017SGR39, Xarxa de Referència en Química Teòrica i Computacional, the ICREA Academia prize 2014 awarded to M.S.), and the European Fund for Regional Development (FEDER) grant UNGI10-4E-801. D.M. holds the Israel Matz Professorial Chair.

REFERENCES

(1) Zhu, C.-Z.; Wei, Y.; Shi, M. Base-Promoted Tandem Cyclization for the Synthesis of Benzonitriles by C-C Bond Construction. *Adv. Synth. Catal.* **2018**, *360*, 808–813.

(2) Guchhait, S. K.; Sisodiya, S.; Saini, M.; Shah, Y. V.; Kumar, G.; Daniel, D. P.; Hura, N.; Chaudhary, V. Synthesis of Polyfunctionalized Pyrroles via a Tandem Reaction of Michael Addition and Intramolecular Cyanide-Mediated Nitrile-to-Nitrile Condensation. *J. Org. Chem.* **2018**, *83*, 5807–5815.

(3) Sharma, K.; Shrivastava, A.; Mehra, R. N.; Deora, G. S.; Alam, M. M.; Zaman, M. S.; Akhter, M. Synthesis of Novel Benzimidazole Acrylonitriles for Inhibition of Plasmodium Falciparum Growth by Dual Target Inhibition. *Arch. Pharm.* **2018**, *351*, 1–13.

(4) Hanna, T. A. The Role of Bismuth in the SOHIO Process. *Coord. Chem. Rev.* **2004**, *248*, 429–440.

(5) Knoevenagel, E. Condensation von Malondiure mit Aromatiachen Aldehyden durch Ammoniak und Amine. *Ber. Dtsch. Chem. Ges.* **1898**, *31*, 2596–2619.

(6) (a) Lidström, P.; Tierney, J.; Wathey, B.; Westman, J. Microwave Assisted Organic Synthesis – A Review. *Tetrahedron* **2001**, *57*, 9225–9283. (b) Greaves, T. L.; Drummond, C. J. Protic Ionic Liquids: Properties and Applications. *Chem. Rev.* **2008**, *108*, 206–237. (c) Hasegawa, S.; Horike, S.; Matsuda, R.; Furukawa, S.; Mochizuki, K.; Kinoshita, Y.; Kitagawa, S. Three-Dimensional porous Coordination Polymer Functionalized with Amide Groups Based on Tridentate Ligand: Selective Sorption and Catalysis. *J. Am. Chem. Soc.* **2007**, *129*, 2607–2614.

(7) (a) Grasselli, R. K.; Trifirò, F. Acrylonitrile from Biomass: Still Far from Being a Sustainable Process. *Top. Catal.* **2016**, *59*, 1651–1658. (b) Guerrero-Pérez, M. O.; Bañares, M. A. Metrics of Acrylonitrile: From Biomass vs. Petrochemical Route. *Catal. Today* **2015**, *239*, 25–30.

(8) Li, C.-J. Cross-Dehydrogenative Coupling (CDC): Exploring C-C Bond Formations beyond Functional Group Transformations. *Acc. Chem. Res.* **2009**, *42*, 335–344.

(9) (a) Tsukada, N.; Hartwig, J. F. Intermolecular and Intramolecular, Platinum-Catalyzed, Acceptorless Dehydrogenative Coupling of Hydrosilanes with Aryl and Aliphatic Methyl C-H Bonds. *J. Am. Chem. Soc.* **2005**, *14*, 5022–5023. (b) Gunanathan, C.; Milstein, D. Metal-Ligand Cooperation by Aromatization-Dearomatization: A New Paradigm in Bond Activation and "Green" Catalysis. *Acc. Chem. Res.* **2011**, *44*, 588–602. (c) Borghs, J. C.; Azofra, L. M.; Biberger, T.; Linnenberg, O.; Cavallo, L.; Rueping, M.; El-Sepelgy, O. Manganese-Catalyzed Multicomponent Synthesis of Pyrroles through Acceptorless Dehydrogenation Hydrogen Autotransfer Catalysis: Experiment and Computation. *ChemSusChem* **2019**, DOI: 10.1002/cssc.201802416.

(10) Gunanathan, C.; Milstein, D. Applications of Acceptorless Dehydrogenation and Related Transformations in Chemical Synthesis. *Science* **2013**, *341*, 1229712.

(11) (a) Schlapbach, L.; Züttel, A. Hydrogen-Storage Materials for Mobile Applications. *Nature* **2001**, *414*, 353–358. (b) Huber, G. W.; Iborra, S.; Corma, A. Synthesis of Transportation Fuels from Biomass: Chemistry, Catalysts and Engineering. *Chem. Rev.* **2006**, *106*, 4044–4098. (c) Masdemont, J.; Luque-Urrutia, J. A.; Gimferrer, M.; Milstein, D.; Poater, A. *ACS Catal.* **2019**, 1662.

(12) (a) Li, J.-J.; Liu, Y.-X.; Tang, W.-J.; Xue, D.; Li, C.-Q.; Xiao, J.-L.; Wang, C. Atmosphere-Controlled Chemoselectivity: Rhodium-Catalyzed Alkylation and Olefination of Alkylnitriles with Alcohols. *Chem. - Eur. J.* **2017**, *23*, 14445–14449. (b) Qu, S.; Dang, Y.; Song, C.; Wen, M.; Huang, K.-W.; Wang, Z.-X. Catalytic Mechanisms of Direct Pyrrole Synthesis via Dehydrogenative Coupling Mediated by PNP-Ir or PNN-Ru Pincer Complexes: Crucial Role of Proton-Transfer Shuttles in the PNP-Ir System. *J. Am. Chem. Soc.* **2014**, *136*, 4974–4991.

(13) (a) Filonenko, G. A.; van Putten, R.; Hensen, E. J. M.; Pidko, E. A. Catalytic (De)Hydrogenation Promoted by Non-Precious Metals - Co, Fe and Mn: Recent Advances in an Emerging Field. *Chem. Soc. Rev.* **2018**, *47*, 1459–1483. (b) Kallmeier, F.; Kempe, R. Manganese Complexes for (De)Hydrogenation Catalysis: A Comparison to Cobalt and Iron Catalysts. *Angew. Chem., Int. Ed.* **2018**, *57*, 46–60.

(14) (a) Chakraborty, S.; Das, U. K.; Ben-David, Y.; Milstein, D. Manganese Catalyzed α-Olefination of Nitriles by Primary Alcohols. *J. Am. Chem. Soc.* **2017**, *139*, 11710–11713. (b) Chakraborty, S.; Gellrich, U.; Diskin-Posner, Y.; Leitus, G.; Avram, L.; Milstein, D. Manganese-Catalyzed N-Formylation of Amines by Methanol Liberating H_2: A Catalytic and Mechanistic Study. *Angew. Chem., Int. Ed.* **2017**, *56*, 4229–4233.

(15) Daw, P.; Ben-David, Y.; Milstein, D. Direct Synthesis of Benzimidazoles by Dehydrogenative Coupling of Aromatic Diamines and Alcohols Catalyzed by Cobalt. *ACS Catal.* **2017**, *7*, 7456–7460.

(16) Nguyen, D. H.; Trivelli, X.; Capet, F.; Paul, J.-F.; Dumeignil, F.; Gauvin, R. M. Manganese Pincer Complexes for the Base-Free, Acceptorless Dehydrogenative Coupling of Alcohols to Esters: Development, Scope, and Understanding. *ACS Catal.* **2017**, *7*, 2022–2032.

(17) Bauer, J. O.; Chakraborty, S.; Milstein, D. Manganese-Catalyzed Direct Deoxygenation of Primary Alcohols. *ACS Catal.* **2017**, *7*, 4462–4466.

(18) (a) Dub, P. A.; Gordon, J. C. Metal–Ligand Bifunctional Catalysis: The "Accepted" Mechanism, the Issue of Concertedness, and the Function of the Ligand in Catalytic Cycles Involving Hydrogen Atoms. *ACS Catal.* **2017**, *7*, 6635–6655. (b) Li, H.-X.; Wang, Z.-X. *Sci.* Computational Mechanistic Studies of Acceptorless Dehydrogenation Reactions Catalyzed by Transition Metal Complexes. *Sci. China: Chem.* **2012**, *55*, 1991–2008.

(19) (a) Mayer, I. Charge, Bond Order and Valence in the Ab Initio SCF Theory. *Chem. Phys. Lett.* **1983**, *97*, 270–274. (b) Mayer, I. Bond Order and Valence: Relations to Mulliken's Population Analysis. *Int. J. Quantum Chem.* **1984**, *26*, 151–154. (c) Bridgemann, A. J.; Cavigliasso, G.; Ireland, L. R.; Rothery, J. The Mayer Bond

Order as a Tool in Inorganic Chemistry. *J. Chem. Soc., Dalton Trans.* **2001**, 2095−2108. (d) Casitas, A.; Poater, A.; Solà, M.; Stahl, S. S.; Costas, M.; Ribas, X. Molecular Mechanism of Acid-Triggered Aryl-Halide Reductive Elimination in Well-Defined Aryl-Cu^{III}-Halide Species. *Dalton Trans* **2010**, *39*, 10458−10463.

(20) (a) Chen, X.-L.; Zhang, Y.; Zhang, M.-Y.; Zeng, M.-H. Bond Order Analysis, Packing Ratio, and Electronic Structures of Two Structural Polymorphs Based on Manganese Complexes. *Chin. J. Chem.* **2017**, *35*, 927−930. (b) Jurca, T.; Ouanounou, S.; Shih, W.-C.; Ong, T.-G.; Yap, G. P. A.; Korobkov, I.; Gorelesky, S.; Richeson, D. Structural and Electronic Trends for Five Coordinate 1st Row Transition Metal Complexes: Mn(II) to Zn(II) Captured in a Bis(IminoPyridine) Framework. *Dalton Trans* **2016**, *45*, 14327−14334.

(21) Kozuch, S.; Shaik, S. How to Conceptualize Catalytic Cycles? The Energetic Span Model. *Acc. Chem. Res.* **2011**, *44*, 101−110.

(22) Frisch, M. J.; Trucks, G. W.; Schlegel, H. B.; Scuseria, G. E.; Robb, M. A.; Cheeseman, J. R.; Scalmani, G.; Barone, V.; Mennucci, B.; Petersson, G. A.; Nakatsuji, H.; Caricato, M.; Li, X.; Hratchian, H. P.; Izmaylov, A. F.; Bloino, J.; Zheng, G.; Sonnenberg, J. L.; Hada, M.; Ehara, M.; Toyota, K.; Fukuda, R.; Hasegawa, J.; Ishida, M.; Nakajima, T.; Honda, Y.; Kitao, O.; Nakai, H.; Vreven, T.; Montgomery, J. A., Jr.; Peralta, J. E.; Ogliaro, F.; Bearpark, M.; Heyd, J. J.; Brothers, E.; Kudin, K. N.; Staroverov, V. N.; Kobayashi, R.; Normand, J.; Raghavachari, K.; Rendell, A.; Burant, J. C.; Iyengar, S. S.; Tomasi, J.; Cossi, M.; Rega, N.; Millam, N. J.; Klene, M.; Knox, J. E.; Cross, J. B.; Bakken, V.; Adamo, C.; Jaramillo, J.; Gomperts, R.; Stratmann, R. E.; Yazyev, O.; Austin, A. J.; Cammi, R.; Pomelli, C.; Ochterski, J. W.; Martin, R. L.; Morokuma, K.; Zakrzewski, V. G.; Voth, G. A.; Salvador, P.; Dannenberg, J. J.; Dapprich, S.; Daniels, A. D.; Farkas, Ö.; Foresman, J. B.; Ortiz, J. V.; Cioslowski, J.; Fox, D. J. *Gaussian 09*, Revision E.01; Gaussian, Inc.: Wallingford, CT, 2009.

(23) Becke, A. Density-Functional Exchange-Energy Approximation with Correct Asymptotic Behaviour. *Phys. Rev. A: At., Mol., Opt. Phys.* **1988**, *38*, 3098−3100.

(24) Perdew, J. P. Density-Functional Approximation for the Correlation Energy of the Inhomogeneous Electron Gas. *Phys. Rev. B: Condens. Matter Mater. Phys.* **1986**, *33*, 8822−8824.

(25) Perdew, J. P. Erratum: Density-functional Approximation for the Correlation Energy of the Inhomogeneous Electron Gas. *Phys. Rev. B: Condens. Matter Mater. Phys.* **1986**, *34*, 7406−7406.

(26) Johnson, E. R.; Becke, A. D. A Post-Hartree-Fock Model of Intermolecular Interactions: Inclusion of Higher-Order Corrections. *J. Chem. Phys.* **2006**, *124*, 174104−174113.

(27) (a) Grimme, S.; Antony, J.; Ehrlich, S.; Krieg, H. A Consistent and Accurate Ab Initio Parametrization of Density Functional Dispersion Correction (DFT-D) for the 94 Elements H-Pu. *J. Chem. Phys.* **2010**, *132*, 154104. (b) Grimme, S.; Ehrlich, S.; Goerigk, L. Effect of the Damping Function in Dispersion Corrected Density Functional Theory. *J. Comput. Chem.* **2011**, *32*, 1456−1465.

(28) Weigend, F.; Ahlrichs, R. Balanced Basis Sets of Split Valence, Triple Zeta Valence and Quadruple Zeta Valence Quality for H to Rn: Design and Assessment of Accuracy. *Phys. Chem. Chem. Phys.* **2005**, *7*, 3297−3305.

(29) Zhao, Y.; Truhlar, D. G. The M06 Suite of Density Functionals for Main Group Thermochemistry, Thermochemical Kinetics, Noncovalent Interactions, Excited States, and Transition Elements: Two New Functionals and Systematic Testing of Four M06-Class Functionals and 12 Other Functionals. *Theor. Chem. Acc.* **2008**, *120*, 215−241.

(30) Kendall, R. A.; Dunning, T. H., Jr.; Harrison, R. J. Electron Affinities of the First-Row Atoms Revisited. Systematic Basis Sets and Wave Functions. *J. Chem. Phys.* **1992**, *96*, 6796−6806.

(31) Marenich, A. V.; Cramer, C. J.; Truhlar, D. G. Universal Solvation Model Based on Solute Electron Density and a Continuum Model of the Solvent Defined by the Bulk Dielectric Constant and Atomic Surface Tensions. *J. Phys. Chem. B* **2009**, *113*, 6378−6396.

4.4. Mechanism of Coupling of Alcohols and Amines To Generate Aldimines and H_2 by a Pincer Manganese Catalyst

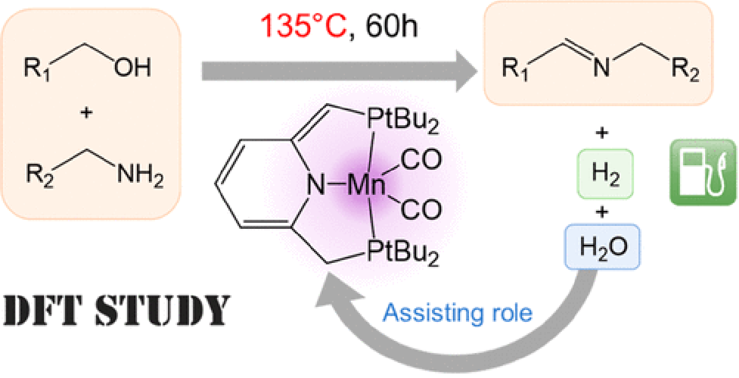
135°C, 60h
R1 OH
+
R2 NH2
PtBu2
CO
N–Mn
CO
PtBu2
R1 N R2
+
H2
+
H2O
DFT STUDY
Assisting role

Masdemont, J.; Luque-Urrutia, J. A.; Gimferrer, M.; Milstein, D.; Poater, A. **Mechanism of Coupling of Alcohols and Amines To Generate Aldimines and H_2 by a Pincer Manganese Catalyst.** *ACS Catal.* **2019**, *9*, 1662-1669.
DOI: 10.1021/acscatal.8b04175.

This thesis author has contributed to the DFT calculations, data analysis, writing, and revisions of the article.

Reproduced with permission from:

Masdemont, J.; Luque-Urrutia, J. A.; Gimferrer, M.; Milstein, D.; Poater, A. **Mechanism of Coupling of Alcohols and Amines To Generate Aldimines and H_2 by a Pincer Manganese Catalyst.** *ACS Catal.* **2019**, *9*, 1662-1669.

https://doi.org/10.1021/acscatal.8b04175

Copyright © 2019, American Chemical Society.

ACS Catalysis
Research Article
Cite This: *ACS Catal.* 2019, 9, 1662−1669
pubs.acs.org/acscatalysis

Mechanism of Coupling of Alcohols and Amines To Generate Aldimines and H_2 by a Pincer Manganese Catalyst

Judit Masdemont,[†] Jesús A. Luque-Urrutia,[†] Martí Gimferrer,[†] David Milstein,[‡] and Albert Poater*[,†]

[†]Institut de Química Computacional i Catàlisi and Departament de Química, Universitat de Girona, Campus Montilivi, 17003 Girona, Catalonia, Spain

[‡]Department of Organic Chemistry, The Weizmann Institute of Science, Rehovot 76100, Israel

Supporting Information

ABSTRACT: Acceptorless dehydrogenative coupling (ADC) of alcohols and amines using a manganese-based catalyst is able to produce aldimines, which have a wide reactivity, without underestimating the generation of a clean fuel, since as a result of this coupling, molecular hydrogen is also obtained. Therefore, the aldimine synthesis represents an interesting reaction from chemical and clean energy points of view. In this work, the computational study, via density functional theory (DFT) calculations, of a manganese-based catalyst for the acceptorless dehydrogenative coupling of alcohols and amines, together with the elucidation of its catalytic cycle using benzene as a solvent, is carried out. Calculations provided insight not only into the catalytic pathway but also into the noncatalyzed organic transformation to reach the desired aldimine, on the basis of the aldehyde generated in the catalytic cycle. The importance of the alternative isomers of the Mn-pincer complex, previously characterized experimentally, and the assisting role of alcohol or water are also described.

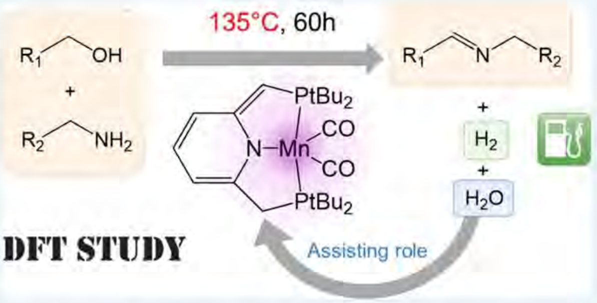

KEYWORDS: *aldimine, manganese, water assisted, catalysis, pincer ligand, green chemistry*

Downloaded via KING ABDULLAH UNIV SCI TECHLGY on November 25, 2019 at 10:25:14 (UTC).
See https://pubs.acs.org/sharingguidelines for options on how to legitimately share published articles.

INTRODUCTION

Aldimines are imines with the general formula R−CH=N−R′. The structure of an aldimine is analogous to that of an aldehyde, substituting the oxygen of the carbonyl group for a nitrogen, which enables a particular reactivity and, consequently, a wide range of applications; mainly as synthesis intermediates used for the production of pharmacological derivatives, colorants, and agrochemical products among many others.[1]

In a general recipe for the synthesis of imines, a mixture of an aldehyde or ketone with an amine in the presence of an acid catalyst is required. Recent routes to aldimines involve acceptorless dehydrogenative coupling (ADC) of alcohols and amines,[2,3] depicted in Scheme 1.

Scheme 1. Acceptorless Dehydrogenative Coupling (ADC) of Alcohols with Amines Using a Metal-Based Catalyst

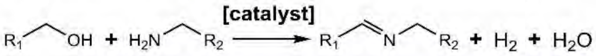

Interestingly, in this type of reaction, the involved hydrogen atoms do not hydrogenate the C=N double bond; instead, molecular hydrogen is generated as the only coproduct, resulting in an environmentally benign reaction.[3] Moreover, H_2 is a possible energy source that may be the main fuel in the future, as the only byproduct from its combustion. Since no carbon-based products are released from the combustion of H_2, the procedure becomes promising for green chemistry.[3−5] Furthermore, the possibility of using an alcohol as reactant increases the interest for this sustainable reaction, since alcohols can be obtained in high amounts at the industrial level, even from renewable resources such as lignocellulose biomass.[6,7]

In the first synthesis of imines by ADC of alcohols and amines, a Ru-based complex was used as catalyst.[8] Since 2011, other transition-metal complexes, mostly based on precious metals, have been used as catalysts for this reaction.[9] Currently, a strong interest in replacing these catalysts with complexes of cheaper and earth-abundant transition metals is taking hold.[10] Apart from iron[11] and cobalt,[12] there is interest in utilizing manganese as the transition metal for the development of new catalysts due to it being the third most abundant transition metal on earth.[13,14] In 2016, Milstein and co-workers described a Mn-pincer complex (Figure 1) which catalyzes the ADC of alcohols with amines.[15] Pincer complexes generally adopt a meridional geometry,[16,17] although the facial shape may be preferred in some cases.[18] The chelating nature and rigidity of pincer ligands generally confers high thermal stability to the resulting complexes, without hindering reactivity. Concurrently

Received: October 16, 2018
Revised: December 10, 2018
Published: January 11, 2019

© 2019 American Chemical Society

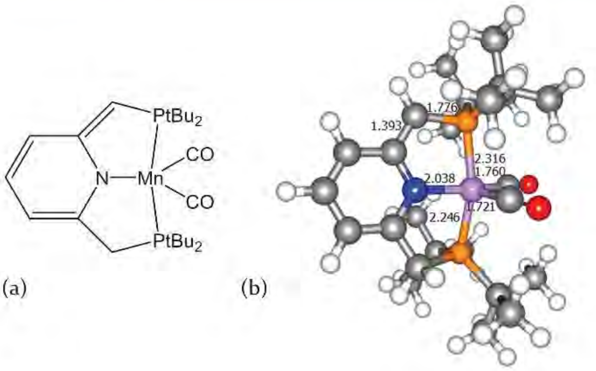

Figure 1. Manganese catalyst (**1**) used for the ADC of benzyl alcohols with benzylamines: (a) Lewis structure; (b) 3D view (selected bond distances given in Å).

Kirchner and co-workers showed that with Co^{II} catalysts featuring a PCP ligand holding a 1,3-diaminobenzene scaffold the alkylation of aromatic amines with primary alcohols did not lead to imines but amines.[19] Thus, there is a general trend: iron- and cobalt-based transition-metal catalysts tend to lead to amines, whereas manganese and cobalt catalysts lead to imines.[20]

In this work, we report a computational study starting from the mechanism proposed by Milstein et al.[15] using the Mn catalyst displayed in Figure 1; bearing a trigonal-bipyramidal geometry, constrained by its PNP pincer ligand.[21,22] The aldimine generation using benzene as solvent achieved conversions and yields of over 99% with substituted benzyl alcohols and/or amines and up to 92% with nonsubstituted reactants after 60 h at 135 °C. The structural and electronic properties have also been explored by density functional theory (DFT) calculations to unveil further mechanistic insights.

■ RESULTS AND DISCUSSION

First of all, we optimized complex **1** for the different possible spin states in order to check the multiplicity with the lowest energy, locating the triplet state 6.7 kcal/mol higher in energy in comparison to the singlet, followed by all of the remaining states. Thus, we determined that in all cases the singlet is the ground state. In Figure 2, we depicted the full reaction mechanism, trying to link all the structures experimentally characterized by Milstein and co-workers,[15] mimicking the past work of hydrogenation of nitriles and ketones by Beller and co-workers.[23]

Starting from **1**, we can observe three main steps: **1** → **1′**, **1** → **2**, and **1** → **4**. To form the required aldehyde **5** in a single step, we must overcome an energy barrier of 31.9 kcal/mol, reaching the hydride Mn complex **2** through **TS 1-2**. The complexity of this step is due to the protonation of a sp^2 carbon of the pincer ligand together with the geometrical rearrangement around the metal, going from a trigonal-bipyramidal to an octahedral geometry (see Figure 3a). This mechanism had already been described by Boncella et al. for an aliphatic PNP-pincer complex[24] using a water molecule instead of an alcohol. The incorporation of the alkoxy moiety to the metal center on **1**, combined with the protonation of the methine moiety of the pincer ligand, is a competing reaction that leads to species **1′** (see Figure 3b). This alternative step requires almost half the energy of the aldehyde formation path **1** → **2**, being kinetically preferred. Thermodynamically, **1′** is 1.0 kcal/mol above **1**, whereas **2** is 1.2 kcal/mol below in energy, thus **2** being favored. However, from **1′** it is possible to

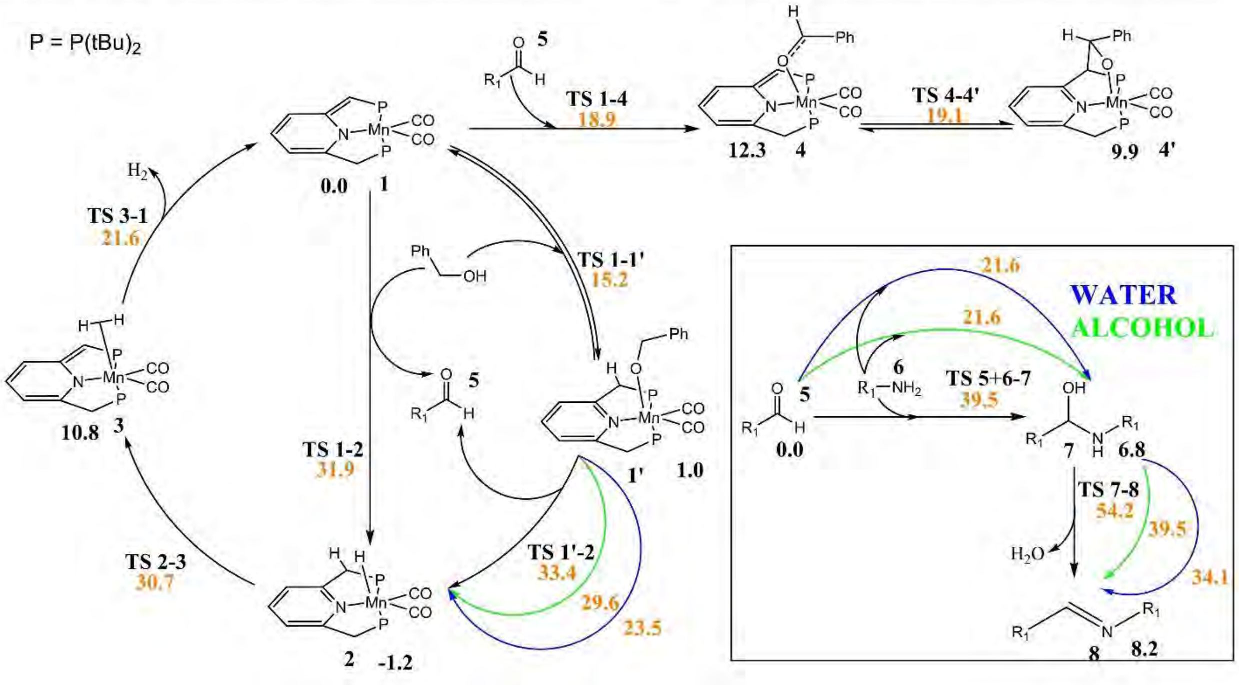

Figure 2. Full reaction mechanism for the ADC of benzyl alcohols with benzylamines. In blue are shown the steps assisted by water and in green those by the alcohol; in black (minima) and in orange (transition states) are shown Gibbs free energies in solvent in kcal/mol referenced to catalyst **1**, whereas they are referenced to the aldehyde **5** in the metal-free reaction pathway included in the box.

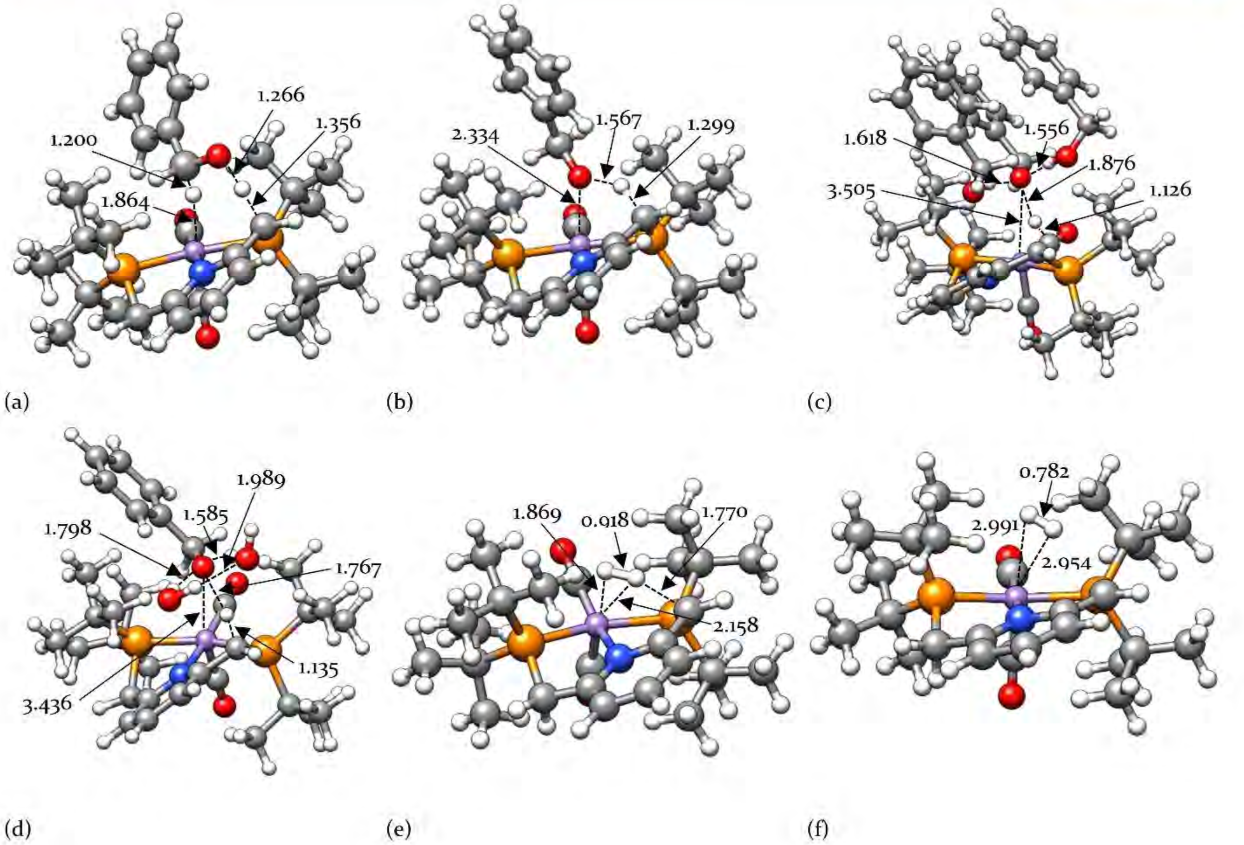

Figure 3. Transition states (a) **1** → **2**, (b) **1** → **1′**, (c) **1′** → **2** (assisted by alcohol), (d) **1′** → **2** (assisted by water), (e) **2** → **3**, and (f) **3** → **1** (selected distances given in Å).

reach the same intermediate **2**, overcoming an energy barrier of 32.4 kcal/mol. The assistance of an external water or alcohol molecule lowers this second energy barrier by 2.5 and 3.2 kcal/mol (see Figures 3c,d), respectively. According to this, at the initial step we might lose part of our active catalyst in such equilibria but, in the long term, the reaction will evolve through **1′**, especially with the additional formation of water as a byproduct (see Scheme 1).

From intermediate **2**, the formation of molecular hydrogen and the regeneration of catalyst **1** is straightforward; when both hydrogen atoms are held in a syn conformation, H_2 is formed but is still attached to the metal center, with an energy cost of 31.9 kcal/mol (see Figure 3e), leading to **3**. Finally, in the step that closes the catalytic cycle, the previously formed hydrogen molecule is released, via a transition state with an associated energy barrier of 10.8 kcal/mol (see Figure 3f). Kinetically, the formation of H_2 on Mn becomes the rate-determining step (rds), although it is still in competition with the previous step, isoenergetic, or only 1−2 kcal/mol less energetically demanding if it is assisted by an external water or alcohol molecule. Furthermore, previous work by Kirchner et al.[20] led also to nearly identical energy values for the last two transition states. Thus, both transition states must be taken into account.[25] On the other hand, the H_2 release from benzyl alcohol, prone to be undertaken without the presence of a metal catalyst, was reconsidered but with a huge energy barrier of 82.1 kcal/mol, almost 50 kcal/mol above the corresponding catalytic barrier: i.e. for step **1** → **2**. This unveils the fundamental role of the transition-metal complex in the kinetics. Moreover, the thermodynamics were also favored by the catalyst with an exergonic balance of 1.2 kcal/mol, whereas a destabilization of 4.9 kcal/mol without a metal catalyst was found, deeming the noncatalyzed reaction unviable once more.

Once the aldehyde **5** is formed, the mechanism might evolve through two possible ways. The noncatalyzed step **5** + **6** → **7**, where **5** reacts with the benzyl amine (**6**), requires more energy than the interaction of the aldehyde with the catalyst in **1** → **4**, even when this step is assisted externally by water or benzyl alcohol molecules. Kinetically, the formation of **7** is still 2.7 kcal/mol more expensive than the formation of **4**. Actually, this shows a preference toward the interaction of the aldehyde with the catalyst **1** instead of the direct reaction between amine and aldehyde, even though both are possible under our given conditions. The explanation for the stabilization achieved while the reaction is assisted by the water molecule is related to the constrained four-membered ring due to the four main atoms involved in such a step without water: two from the aldehyde and two from the amine. With water, the concerted transition state is more relaxed, presenting a nearly symmetrical six-membered ring (see Figure 4a). From the organic intermediate **7**, the generation of the desired aldimine **8** consists of a proton transfer and a C−O bond cleavage (see Figure 4b), releasing a water molecule as a byproduct. It requires overcoming an important energy barrier of 54.2 kcal/mol, which decreases

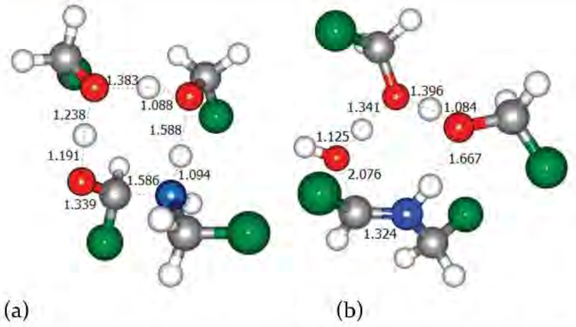

Figure 4. Transition states (a) 5 + 6 → 7 and (b) 7 → 8 assisted by one and two alcohol molecules, respectively (phenyl groups simplified for clarity as green balls; selected distances given in Å).

sharply to 39.5 or 34.1 kcal/mol when the reaction is assisted by two water or benzyl alcohol molecules, respectively. The latter transition state describes the rate-determining step (rds), and its associated energy barrier is completely reasonable bearing in mind the experimental temperature (135 °C), but only taking into account the aid of the alcohol reagent or the water as a cocatalyst, without which the barrier could not be overcome.[26] As the reaction itself generates water as a byproduct, even though in the first stages the alcohol will take the assisting role, the water will participate actively afterward. Thus, only a sort of preactivation would be necessary before facing the regular catalytic cycle assisted by water molecules from the same reaction. Moreover, the use of a solvent that is not thoroughly dried is a hint that traces of water are enough to activate the catalysis at the beginning. Furthermore, even though the most reasonable path to get intermediate 7 is directly from the aldehyde 5, in agreement with the proposed mechanism by Milstein et al.,[15] the metal-assisted step was also attempted. We found that the hemiaminal intermediate homologous to 7 was placed 14.9 kcal/mol above it.

Complex **4** can progress through intramolecular C−C bond formation between the former aldehyde and the nearby carbine moiety (**4** → **4′**). Even though kinetically the process is rather facile, with a low energy barrier of 6.8 kcal/mol, and even though **4′** is 3.4 kcal/mol more stable than **4**, the process is thermodynamically disfavored by 9.9 kcal/mol with respect to **1**. Consequently, this indicates that we use part of our catalyst in this equilibrium, slowing down the reaction, as occurs in the equilibria involved in the transformation of the initial **1** that leads to intermediate **2**.

Once we detailed the mechanism, we wanted to identify the influence of the amine in electronic terms. According to Milstein et al. an aryl imine with a methoxy group (OMe) in a para position leads to a 97% conversion with a 99% yield, while the same amine, but now with a fluoride ligand (F) instead of the methoxy group, has a poor 52% conversion with a 55% yield. To explain the experimental results, we undertook DFT calculations for the steps **5** + **6** → **7** and **7** → **8**, as shown in Scheme 2. In general, larger upper barriers were found for the fluoride-substituted amine, whereas for the methoxy-substituted the energy barriers were found to be nearly unmodified. However, the energy differences are extremely low (<1 kcal/mol), which do not allow us to extract robust conclusions as we are within the DFT error. Thus, the latter low energy differences forced characterization calculations in order to better understand the role of the substituents in the para position of the benzylamine. We extracted from a natural population analysis (NPA) and compiled in Table 1 the natural charges of the nitrogen atoms from the different species. We do not observe a remarkable change in the charge of the hydrogen, independently of the electron-donating (OMe) or electron-withdrawing (F) character of the functional group located in the para position of the aryl ring, in comparison with the H-substituted species. Therefore, we must conclude that the charge is not affected.

Scheme 2. Metal-Free Reaction Pathway between the Aldehyde and the Benzylamine, with H, OMe, or F Substituents in the Para Position[a]

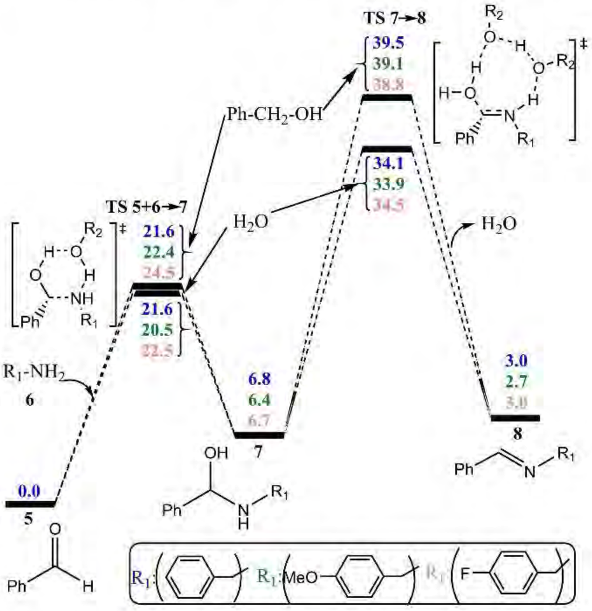

[a]Step **5** + **6** → **7** and **7** → **8** are assisted by either two water (R_2 = H) or benzyl alcohol molecules (R_2 = CH_2Ph) molecules; energies are given in kcal/mol.

Table 1. Natural Charge for the N Atom According to Different Substituents

	substituent		
	H	F (para)	MeO (para)
6	−0.873	−0.874	−0.872
5 + 6 → 7	−0.707	−0.707	−0.706
7	−0.720	−0.721	−0.719
7 → 8	−0.610	−0.609	−0.607
8	−0.453	−0.455	−0.453

Continuing with the electronic analysis of the benzylamines, we checked the aromaticity of the aryl group through the calculation of the nuclear independent chemical shift (NICS), defined by Schleyer et al.[27] This magnetic aromaticity index is defined as the negative value of the absolute shielding computed at the central point of a ring, even though it can be computed at any point of the system. The more negative the value, the higher the aromaticity.[28,29] In our case, we performed the calculation on the center of the aryl ring (NICS(0))[30] and 1 Å above and below it ($(NICS(1)_{in}$ and

NICS(1)$_{out}$, respectively). To properly interpret the results obtained, which are compiled in Table 2, the computation of a reference value is required. In our case, we used benzene as a reference for checking whether electron-donating or electron-withdrawing groups induce an increase or decrease in the intrinsic aromaticity of the ring. We observe that the aromaticity increases for the fluoride-substituted arene, which in combination with the higher energy barrier in comparison to the methoxy-substituted arene explains better the lower yields and conversion. To confirm the data, we performed a HOMA index calculation.[31,32] As a geometrical index, the closer to 1 the value obtained, the more similar our structure is to the reference structure (benzene, again, with equal C−C bond distances of 1.388 Å) and, thus, the more aromatic the molecule. The index provided values of 0.889 and 0.920 for the OMe- and F-substituted aryl, respectively, while the value is 0.907 (between those data) for the nonsubstituted aryl. Taking into account that greater aromaticity of the aryl ring leads to less reactivity, the geometrical index HOMA, together with the electronic index NICS(1)$_{out}$, confirmed that the OMe- and the F-substituted aryls will be more and less reactive species, respectively.

Table 2. NICS Analysis for the Para-Substituted Amine

	substituent		
	H	F (para)	MeO (para)
NICS(0)	−7.647	−9.310	−8.431
NICS(1)$_{out}$	−10.134	−9.944	−9.587
NICS(1)$_{in}$	−9.394	−9.657	−9.301

Last but not least, we performed conceptual DFT analyses[33] to evaluate the overall electronics of the benzylamine molecule, as they have allowed the study of the reactivity and regioselectivity of chemical reactions.[34,35] We used the highest occupied molecular orbital (HOMO) and the last occupied molecular orbital (LUMO), which correspond to the frontier molecular orbitals, to calculate the chemical hardness and the electrophilicity within the Koopmans theorem. The results obtained are compiled in Table 3. For both concepts the differences obtained are quantitatively small, but qualitatively the electrophilicity values show that the F-based amine becomes less nucleophilic, whereas the nucleophilicity with a methoxy group is maximum with respect to the nonsubstituted amine, in perfect agreement with Scheme 2, despite the low energy differences due to the para substituents.

Table 3. Chemical Hardness (η) and Electrophilicity (ω) for the Unsubstituted Amine and the Para-Substituted Amine

	substituent		
	H	F (*para*)	MeO (*para*)
η	0.160	0.153	0.149
ω	0.043	0.049	0.040

Finally, to emphasize the role of stabilization between aromatic rings, we plot the noncovalent interactions (NCI), calculated using the NCIplot program developed by Contreras-Garcia,[36] on the transition state 7 → 8 for the differently substituted aryl rings (see Figure 5).

The NCI plots allow observation and qualitative evaluation and depiction, in the tridimensional space, of the strength of the noncovalent interactions between the different regions of the molecular system: in our case, between the several aryl rings in this particular condensation step.[37] In Figure 5, we represent the results obtained for the three differently substituted amines studied, plotting the isocontour obtained with a value of 0.4 of the reduced density gradient. For a correct interpretation of the results, we selected, for the color scale, the interval from −0.05 (red and repulsive) to 0.05 (blue and attractive) of the second density Hessian eigenvalue. Qualitatively, taking into consideration the interaction between aryl rings, we distinguish a trend that unveils more attractive regions for the OMe substituent in comparaison to that with F. This is in perfect agreement with experimental findings.

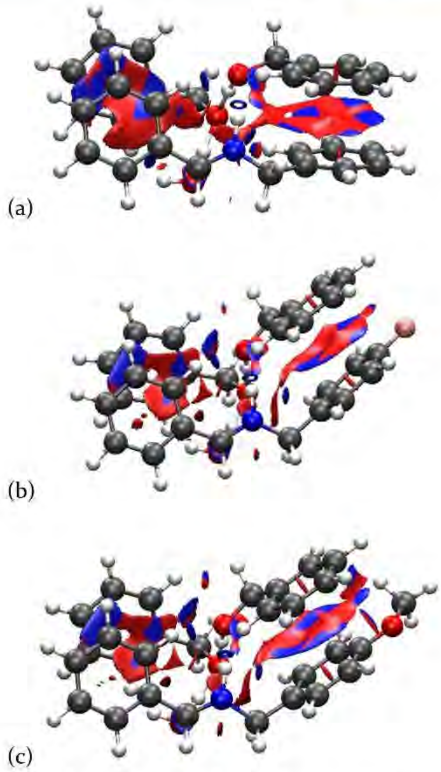

Figure 5. NCIplots of **7** → **8**, substituted with (a) H, (b) F, and (c) OMe and assisted by two benzyl alcohol molecules. The isosurface represents a value of 0.4 with a color scale for the reduced density gradient from −0.05 (red) to 0.05 (blue).

■ CONCLUSIONS

We determined the full mechanism of the aldimine formation reaction, undertaking calculations using a manganese-based catalyst. The catalyst is necessary in the generation of aldimines starting from amines and alcohols, as the formation of the aldehyde from the alcohol requires its assistance. Still, the presence of the reagent benzyl alcohol is necessary to undertake the step that leads to the intermediate between the aldehyde and the desired aldimine, when there are no traces of water. The last step that leads to the aldimine must be again assisted by water or alcohol. The cocatalyst role of those protic agents is due to the formation of at least six-membered rings more stable than the four-membered rings in both transition states (**5** + **6** → **7** and **7** → **8**). As the reaction evolves, water is generated as a byproduct and the alcohol is no longer necessary for the last two pure organic steps, because the formation of this intermediate is easily water-assisted with a lower energy barrier. Overall, the effect of water/alcohol was demonstrated for both the Mn-catalyzed and the metal-free sides of the reaction. In the former part (Figure 2), the major effect applies to lowering the energy barrier corresponding to the step **1′** → **2**. Nevertheless, this was not the case for the rest of the catalytic cycle: i.e., the energies associated with the other steps are not solvent-dependent.

Furthermore, other forms of the catalyst can be formed (as **1′** and **4′**), since they are kinetically facile, but they are less stable thermodynamically than **1**; thus, the formation of the product **8** is always favored. Nonetheless, those equilibria are considered as a possible drawback of the reaction because they may reduce the quantity of available catalyst and force an increase in the catalyst loading.

On the other hand, to show the importance of the nature of the amine reagent, we added a substituent in a para position of the aryl group of the amine, with consequent changes in the energy barrier of the formation of **7** and **8**. Actually, when the substituent is a fluoride, the energy barrier increases with respect to the amine without substituents, and the situation is similar when the substituent is a methoxide group. However, the step **5** + **6** → **7** is kinetically easier to overcome with the latter electron donor methoxy substituent. For this reason, yields are higher when there is a methoxide in the para position of the aryl group of the amine, on the basis of the higher nucleophilicity.

COMPUTATIONAL DETAILS

DFT static calculations were performed with the Gausian09 set of programs,[38] using the BP86 functional of Becke and Perdew,[39−41] together with the Grimme D3BJ correction term to the electronic energy.[42] The electronic configuration of the molecular systems was described with the double-ζ basis set with Ahlrichs polarization for main-group atoms (SVP keyword in Gaussian).[43] The geometry optimizations were performed without symmetry constraints, and analytical frequency calculations performed the characterization of the located stationary points. These frequencies were used to calculate unscaled zero-point energies (ZPEs) as well as thermal corrections and entropy effects at 298 K. Energies were obtained by single-point calculations on the optimized geometries with the M06 functional[44] and the cc-pVTZ basis set[45] and estimation of solvent effects with the universal solvation model SMD of Cramer and Truhlar,[46] using benzene as solvent. The reported free energies in this work include energies obtained at the M06/cc-pVTZ~sdd level of theory corrected with zero-point energies, thermal corrections, and entropy effects evaluated at 135 °C, achieved at the BP86-D3BJ/SVP~sdd level. Further, the approach of Martin et al. was used to exclude the potential overestimation of the entropy contribution (further details in the Supporting Information).[47,48]

Frontier molecular orbitals (HOMO and LUMO) have been used in the framework of conceptual DFT, thanks to the Koopmans approximation,[49] such as chemical harness (η) and electrophilicity (ω),[50] which describe the stability of the system and the affinity of the system to interact with a nucleophile. Electrophilicity is calculated by eq 1, using the chemical potential (eq 2) and the chemical hardness values (eq 3).

$$\omega = \frac{\mu^2}{2\eta} \tag{1}$$

$$\mu \cong \frac{1}{2}(\varepsilon_{\mathrm{L}} + \varepsilon_{\mathrm{H}}) \tag{2}$$

$$\eta \cong \frac{1}{2}(\varepsilon_{\mathrm{L}} + \varepsilon_{\mathrm{H}}) \tag{3}$$

In addition, the changes in local aromaticity have been quantified using two probes of local aromaticity, based on the structure and the magnetic properties, respectively. As a measure for the aromaticity structure, the harmonic oscillator model of the aromaticity index (HOMA) was used, defined by Kruszewski and Krygowski in eq 4[31]

$$\mathrm{HOMA} = 1 - \frac{\alpha}{n}\sum_{i=1}^{n} (R_{\mathrm{opt}} - R_i)^2 \tag{4}$$

where n is the number of bonds considered and α is an empirical constant (for C−C bonds α = 257.7) fixed to give HOMA = 0 for a model nonaromatic system and HOMA = 1 for a system with all bonds equal to an optimal value R_{opt}, which is 1.388 Å for C−C bonds, assumed to be achieved for fully aromatic systems. R_i stands for a running bond length. As a magnetic aromaticity index, NICS (nucleus-independent chemical shift) calculations have been undertaken, using the GIAO (gauge-including atomic orbital method) model,[51] calculated at the level BP86-D3BJ/6-311+G(d,p)//BP86-D3BJ/SVP.

ASSOCIATED CONTENT

Ⓢ Supporting Information

The Supporting Information is available free of charge on the ACS Publications website at DOI: 10.1021/acscatal.8b04175.

Benchmarks with the tested computational methods (PDF)

XYZ coordinates with the energies of all computed species (XYZ)

AUTHOR INFORMATION

Corresponding Author

*E-mail for A.P.: albert.poater@udg.edu.

ORCID

David Milstein: 0000-0002-2320-0262
Albert Poater: 0000-0002-8997-2599

Notes

The authors declare no competing financial interest.

ACKNOWLEDGMENTS

J.A.L.-U. thanks the Universitat de Girona for a IFUdG2017 Ph.D. fellowship. M.G. thanks the Generalitat de Catalunya for an FI2018 predoctoral fellowship. A.P. thanks the Spanish MINECO for the project CTQ2014-59832-JIN and the EU for a FEDER fund (UNGI08-4 × 10^{-003}). A.P. thanks the Generalitat de Catalunya (project number 2017SGR39, Xarxa de Referència en Química Teòrica i Computacional). D.M. holds the Israel Matz Professorial Chair. We thank the reviewers for helpful comments.

REFERENCES

(1) (a) Kumar, R.; Kumar, S.; Bala, M.; Ratnam, A.; Singh, U. P.; Ghosh, K. Unprecedented Oxidation of Aldimine to Carboxamido Function During Reactivity Studies on Ruthenium Complex with Acidified Nitrite Solution: Synthesis of Ruthenium Nitrosyl Complex Having {RuNO}(6) Moiety and Photorelease of Coordinated NO. *J. Organomet. Chem.* **2018**, *863*, 77−83. (b) Wang, L.-Y.; Gong, C.-C.; Shen, Y.; Xu, M.-L.; He, G.-H.; Wang, L.; Song, Y.-H. Conjugated Schiff Base Polymer Foam/Macroporous Carbon Integrated Electrode for Electrochemical Sensing. *Sens. Actuators, B* **2018**, *265*, 227−233. (c) Wang, C.-F.; Yang, G.-Y.; Zao, Z.-S.; Tao, J. Monitoring the Spin States of Ferrous Ions by Fluorescence Spectroscopy in Spin-Crossover-Fluorescent Hybrid Materials. *Chem. - Eur. J.* **2018**, *24*, 3218−3224.

(2) Crabtree, R. H. Homogeneous Transition Metal Catalysis of Acceptorless Dehydrogenative Alcohol Oxidation: Applications in Hydrogen Storage and to Heterocycle Synthesis. *Chem. Rev.* **2017**, *117*, 9228−9246.

(3) Gunanathan, C.; Milstein, D. Applications of Acceptorless Dehydrogenation and Related Transformations in Chemical Synthesis. *Science* **2013**, *341*, 1229712.

(4) Chakraborty, S.; Gellrich, U.; Diskin-Posner, Y.; Leitus, G.; Avram, L.; Milstein, D. Manganese-Catalyzed N-Formylation of Amines by Methanol Liberating H_2: A Catalytic and Mechanistic Study. *Angew. Chem., Int. Ed.* **2017**, *56*, 4229−4233.

(5) Chakraborty, S.; Kumar Das, U.; Ben-David, Y.; Milstein, D. Manganese Catalyzed α-Olefination of Nitriles by Primary Alcohols. *J. Am. Chem. Soc.* **2017**, *139*, 11710−11713.

(6) Barta, K.; Ford, P. C. Catalytic Conversion of Nonfood Woody Biomass Solids to Organic Liquids. *Acc. Chem. Res.* **2014**, *47*, 1503−1512.

(7) Vispute, T. P.; Zhang, H.; Sanna, A.; Xiao, R.; Huber, G. W. Renewable Chemical Commodity Feedstocks From Integrated Catalytic Processing of Pyrolysis Oils. *Science* **2010**, *330*, 1222−1227.

(8) Gunanathan, C.; Milstein, D. Metal-Ligand Cooperation by Aromatization-Dearomatization: A New Paradigm in Bond Activation and "Green" Catalysis. *Acc. Chem. Res.* **2011**, *44*, 588−602.

(9) (a) Zhang, J.; Balaraman, E.; Leitus, G.; Milstein, D. Electron-Rich PNP- and PNN-Type Ruthenium(II) Hydrido Borohydride Pincer Complexes. Synthesis, Structure, and Catalytic Dehydrogenation of Alcohols and Hydrogenation of Esters. *Organometallics* **2011**, *30*, 5716−5724. (b) Jin, H.; Xie, J.; Pan, C.; Zhu, Z.; Cheng, Y.; Zhu, C. Rhenium-Catalyzed Acceptorless Dehydrogenative Coupling via Dual Activation of Alcohols and Carbonyl Compounds. *ACS Catal.* **2013**, *3*, 2195−2198.

(10) van der Vlugt, J. I. Cooperative Catalysis with First-Row Late Transition Metals. *Eur. J. Inorg. Chem.* **2012**, *2012*, 363−375.

(11) Poater, A.; Vummaleti, S. V. C.; Pump, E.; Cavallo, L. Comparing Ru and Fe-Catalyzed Olefin Metathesis. *Dalton Trans* **2014**, *43*, 11216−11220.

(12) Luque-Urrutia, J. A.; Gimferrer, M.; Casals-Cruañas, E.; Poater, A. In Silico Switch from Second- to First-row Transition Metals in Olefin Metathesis: From Ru to Fe and From Rh to Co. *Catalysts* **2017**, *7*, 389.

(13) Bryndza, H. E.; Fong, L. K.; Paciello, R. A.; Tam, W.; Bercaw, J. Relative metal-hydrogen, -oxygen, -nitrogen, and -carbon bond strengths for organoruthenium and organoplatinum compounds; equilibrium studies of Cp*(PMe3)2RuX and (DPPE)MePtX systems. *J. Am. Chem. Soc.* **1987**, *109*, 1444−1456.

(14) Schneider, S.; Meiners, J.; Askevold, B. Cooperative Aliphatic PNP Amido Pincer Ligands − Versatile Building Blocks for Coordination Chemistry and Catalysis. *Eur. J. Inorg. Chem.* **2012**, *2012*, 412−429.

(15) Mukherjee, A.; Nerush, A.; Leitus, G.; Shimon, L. J. W.; David, Y. B.; Jalapa, N. A. E.; Milstein, D. Manganese-Catalyzed Environmentally Benign Dehydrogenative Coupling of Alcohols and Amines to Form Aldimines and H_2: A Catalytic and Mechanistic Study. *J. Am. Chem. Soc.* **2016**, *138*, 4298−4301.

(16) Jensen, C. M. Iridium PCP Pincer Complexes: Highly Active and Robust Catalysts For Novel Homogeneous Aliphatic Dehydrogenations. *Chem. Commun.* **1999**, 2443−2449.

(17) van Koten, G. Tuning the Reactivity of Metals held in a Rigid Ligand Environment. *Pure Appl. Chem.* **1989**, *61*, 1681−1694.

(18) (a) van Koten, G.; Milstein, D. *Organometallic Pincer Chemistry*; Springer-Verlag: Berlin-Heidelberg, 2013. (b) Peris, E.; Crabtree, R. H. Key Factors in Pincer Ligand Design. *Chem. Soc. Rev.* **2018**, *47*, 1959−1968.

(19) Mastalir, M.; Tomsu, G.; Pittenauer, E.; Allmaier, G.; Kirchner, K. Co(II) PCP Pincer Complexes as Catalysts for the Alkylation of Aromatic Amines with Primary Alcohols. *Org. Lett.* **2016**, *18*, 3462−3465.

(20) Mastalir, M.; Glatz, M.; Gorgas, N.; Stöger, B.; Pittenauer, E.; Allmaier, G.; Veiros, L. F.; Kirchner, K. Divergent Coupling of Alcohols and Amines Catalyzed by Isoelectronic Hydride MnI and FeII PNP Pincer Complexes. *Chem. - Eur. J.* **2016**, *22*, 12316−12320.

(21) (a) Yu, H.; Jia, G.; Lin, Z. Theoretical Studies on O-Insertion Reactions of Nitrous Oxide with Ruthenium Hydride Complexes. *Organometallics* **2008**, *27*, 3825−3833. (b) Zhang, J.; Balaraman, E.; Leitus, G.; Milstein, D. Electron-Rich PNP- and PNN-Type Ruthenium(II) Hydrido Borohydride Pincer Complexes. Synthesis, Structure, and Catalytic Dehydrogenation of Alcohols and Hydrogenation of Esters. *Organometallics* **2011**, *30*, 5716−5724. (c) Zell, T.; Ben-David, Y.; Milstein, D. Highly Efficient, General Hydrogenation of Aldehydes Catalyzed by PNP Iron Pincer Complexes. *Catal. Sci. Technol.* **2015**, *5*, 822−826.

(22) Qu, S.; Dang, Y.; Song, C.; Wen, M.; Huang, K.-W.; Wang, Z.-X. Catalytic Mechanisms of Direct Pyrrole Synthesis via Dehydrogenative Coupling Mediated by PNP-Ir or PNN-Ru Pincer Complexes: Crucial Role of Proton-Transfer Shuttles in the PNP-Ir System. *J. Am. Chem. Soc.* **2014**, *136*, 4974−4991.

(23) Elangovan, S.; Topf, C.; Fischer, S.; Jiao, H.; Spannenberg, A.; Baumann, W.; Ludwig, R.; Junge, K.; Beller, M. Selective Catalytic Hydrogenations of Nitriles, Ketones, and Aldehydes by Well-Defined Manganese Pincer Complexes. *J. Am. Chem. Soc.* **2016**, *138*, 8809−8814.

(24) Tondreau, A. M.; Michalczyk, R.; Boncella, J. M. Reversible 1,2-Addition of Water To Form a Nucleophilic Mn(I) Hydroxide Complex: A Thermodynamic and Reactivity Study. *Organometallics* **2017**, *36*, 4179−4183.

(25) Kozuch, S.; Shaik, S. How to Conceptualize Catalytic Cycles? The Energetic Span Model. *Acc. Chem. Res.* **2011**, *44*, 101−110.

(26) (a) Luque-Urrutia, J. A.; Poater, A. The Fundamental Noninnocent Role of Water for the Hydrogenation of Nitrous Oxide by PNP Pincer Ru-based Catalysts. *Inorg. Chem.* **2017**, *56*, 14383−14387. (b) Luque-Urrutia, J. A.; Solà, M.; Milstein, D.; Poater, P. Mechanism of the Manganese-Pincer Catalyzed Acceptorless Dehydrogenative Coupling of Nitriles and Alcohols. *J. Am. Chem. Soc.* **2019**, DOI: 10.1021/jacs.8b11308.

(27) Schleyer, P. v. R.; Maerker, C.; Dransfeld, A.; Jiao, H.; van Eikema Hommes, N. J. R. Nucleus-Independent Chemical Shifts: a Simple and Efficient Aromaticity Probe. *J. Am. Chem. Soc.* **1996**, *118*, 6317−6318.

(28) Corminboeuf, C.; Heine, T.; Seifert, G.; Schleyer, P. v. R.; Weber, J. Induced Magnetic Fields in Aromatic [n]-Annulenes-Interpretation of NICS Tensor Components. *Phys. Chem. Chem. Phys.* **2004**, *6*, 273−276.

(29) Schleyer, P. v. R.; Manoharan, M.; Jiao, H. J.; Stahl, F. The Acenes: is there a Relationship Between Aromatic Stabilization and Reactivity? *Org. Lett.* **2001**, *3*, 3643−3646.

(30) Poater, J.; Duran, M.; Solà, M.; Silvi, B. Theoretical Evaluation of Electron Delocalization in Aromatic Molecules by Means of Atoms in Molecules (AIM) and Electron Localization Function (ELF) Topological Approaches. *Chem. Rev.* **2005**, *105*, 3911−3947.

(31) (a) Kruszewski, J.; Krygowski, T. M. Definition of Aromaticity Basing on the Harmonic Oscillator Model. *Tetrahedron Lett.* **1972**, *13*, 3839−3842. (b) Krygowski, T. M. Crystallographic Studies of Inter-

and Intramolecular Interactions Reflected in Aromatic Character of π-Electron Systems. *J. Chem. Inf. Model.* **1993**, *33*, 70−78.

(32) (a) Krygowski, T. M.; Cyránski, M. K. Structural Aspects of Aromacity. *Chem. Rev.* **2001**, *101*, 1385−1419. (b) Schleyer, P. v. R. Introduction: Aromacity. *Chem. Rev.* **2001**, *101*, 1115−1117.

(33) (a) Parr, R. G.; Donnelly, R. A.; Levy, M.; Palke, W. E. Electronegativity: The Density Funcional Viewpoint. *J. Chem. Phys.* **1978**, *68*, 3801−3807. (b) Parr, R. G.; Pearson, R. G. Absolute Hardness: Companion Parameter to Absolute Electronegativity. *J. Am. Chem. Soc.* **1983**, *105*, 7512−7516. (c) Geerlings, P.; De Proft, F.; Langenaeker, W. Conceptual Density Functional Theory. *Chem. Rev.* **2003**, *103*, 1793−1873.

(34) Poater, A.; Gallegos Saliner, A.; Carbó, R.; Poater, J.; Solà, M.; Cavallo, L.; Worth, A. P. Modelling the Structure-Property Relationships of Nanoneedles: a Journey Towards Nanomedicine. *J. Comput. Chem.* **2009**, *30*, 275−284.

(35) Ayers, P. W.; Parr, R. G. Variational Principles for Describing Chemical Reactions: The Fukui Function and Chemical Hardness Revisited. *J. Am. Chem. Soc.* **2000**, *122*, 2010−2018.

(36) (a) Johnson, E. R.; Keinan, S.; Mori-Sanchez, P.; Contreras-Garcia, J.; Cohen, A. J.; Yang, W. Revealing Noncovalent Interactions. *J. Am. Chem. Soc.* **2010**, *132*, 6498−6506. (b) Contreras-Garcia, J.; Johnson, E.; Keinan, S.; Chaudret, R.; Piquemal, J. P.; Beratan, D.; Yang, W. NCIPLOT: A Program for Plotting Noncovalent Interaction Regions. *J. Chem. Theory Comput.* **2011**, *7*, 625−632.

(37) Poater, J.; Gimferrer, M.; Poater, A. Covalent and Ionic Capacity of MOFs To Sorb Small Gas Molecules. *Inorg. Chem.* **2018**, *57*, 6981−6990.

(38) Frisch, M. J.; Trucks, G. W.; Schlegel, H. B.; Scuseria, G. E.; Robb, M. A.; Cheeseman, J. R.; Scalmani, G.; Barone, V.; Mennucci, B.; Petersson, G. A.; Nakatsuji, H.; Caricato, M.; Li, X.; Hratchian, H. P.; Izmaylov, A. F.; Bloino, J.; Zheng, G.; Sonnenberg, J. L.; Hada, M.; Ehara, M.; Toyota, K.; Fukuda, R.; Hasegawa, J.; Ishida, M.; Nakajima, T.; Honda, Y.; Kitao, O.; Nakai, H.; Vreven, T.; Montgomery, J. A., Jr.; Peralta, J. E.; Ogliaro, F.; Bearpark, M.; Heyd, J. J.; Brothers, E.; Kudin, K. N.; Staroverov, V. N.; Kobayashi, R.; Normand, J.; Raghavachari, K.; Rendell, A.; Burant, J. C.; Iyengar, S. S.; Tomasi, J.; Cossi, M.; Rega, N.; Millam, N. J.; Klene, M.; Knox, J. E.; Cross, J. B.; Bakken, V.; Adamo, C.; Jaramillo, J.; Gomperts, R.; Stratmann, R. E.; Yazyev, O.; Austin, A. J.; Cammi, R.; Pomelli, C.; Ochterski, J. W.; Martin, R. L.; Morokuma, K.; Zakrzewski, V. G.; Voth, G. A.; Salvador, P.; Dannenberg, J. J.; Dapprich, S.; Daniels, A. D.; Farkas, Ö.; Foresman, J. B.; Ortiz, J. V.; Cioslowski, J.; Fox, D. J. *Gaussian 09, Revision E.01*; Gaussian, Inc., Wallingford, CT, 2009.

(39) Becke, A. Density-Functional Exchange-Energy Approximation with Correct Asymptotic Behaviour. *Phys. Rev. A: At., Mol., Opt. Phys.* **1988**, *38*, 3098−3100.

(40) Perdew, J. P. Density-Functional Approximation for the Correlation Energy of the Inhomogeneous Electron Gas. *Phys. Rev. B: Condens. Matter Mater. Phys.* **1986**, *33*, 8822−8824.

(41) Perdew, J. P. Erratum: Density-functional Approximation for the Correlation Energy of the Inhomogeneous Electron Gas. *Phys. Rev. B: Condens. Matter Mater. Phys.* **1986**, *34*, 7406−7406a.

(42) (a) Grimme, S.; Antony, J.; Ehrlich, S.; Krieg, H. A Consistent and Accurate Ab Initio *Parametrization* of Density Functional Dispersion Correction (DFT-D) for the 94 Elements H-Pu. *J. Chem. Phys.* **2010**, *132*, 154104. (b) Grimme, S.; Ehrlich, S.; Goerigk, L. Effect of the Damping Function in Dispersion Corrected Density Functional Theory. *J. Comput. Chem.* **2011**, *32*, 1456−1465.

(43) Schäfer, S.; Horn, H.; Ahlrichs, R. Fully Optimized Contracted Gaussian Basis Sets for Atoms Li to Kr. *J. Chem. Phys.* **1992**, *97*, 2571−2577.

(44) Zhao, Y.; Truhlar, D. G. The M06 Suite of Density Functionals for Main Group Thermochemistry, Thermochemical Kinetics, Noncovalent Interactions, Excited States, and Transition Elements: Two New Functionals and Systematic Testing of Four M06-Class Functionals and 12 Other Functionals. *Theor. Chem. Acc.* **2008**, *120*, 215−241. (b) Zhao, Y.; Truhlar, D. G. A New Local Density Functional for Main-Group Thermochemistry, Transition Metal Bonding, Thermochemical Kinetics, and Noncovalent Interactions. *J. Chem. Phys.* **2006**, *125*, 194101.

(45) Kendall, R. A.; Dunning, T. H., Jr.; Harrison, R. J. Electron Affinities of the First-Row Atoms Revisited. Systematic Basis Sets and Wave Functions. *J. Chem. Phys.* **1992**, *96*, 6796−806.

(46) Marenich, A. V.; Cramer, C. J.; Truhlar, D. G. Universal Solvation Model Based on Solute Electron Density and a Continuum Model of the Solvent Defined by the Bulk Dielectric Constant and Atomic Surface Tensions. *J. Phys. Chem. B* **2009**, *113*, 6378−6396.

(47) Martin, R. L.; Hay, P. J.; Pratt, L. R. Hydrolysis of Ferric Ionvin Water and Conformational Equilibrium. *J. Phys. Chem. A* **1998**, *102*, 3565−3573.

(48) (a) Sieffert, N.; Bühl, M. Ruthenium-Triphenylphosphine Complexes: Multiple Reaction Pathways. *J. Am. Chem. Soc.* **2010**, *132*, 8056−8070. (b) Manzini, S.; Poater, A.; Nelson, D. J.; Cavallo, L.; Slawin, A. M. Z.; Nolan, S. P. Insights into the Decomposition of Olefin Metathesis Pre-Catalysts. *Angew. Chem., Int. Ed.* **2014**, *53*, 8995−8999. (c) Poater, A.; Pump, E.; Vummaleti, S. V. C.; Cavallo, L. The Right Computational Recipe for Olefin Metathesis with Ru-Based Catalysts: the Whole Mechanism of Ring-Closing Olefin Metathesis. *J. Chem. Theory Comput.* **2014**, *10*, 4442−4448.

(49) Koopmans, T. Über die Zuordnung von Wellenfunktionen und Eigenwerten zu den Einzelnen Elektronen Eines Atoms. *Physica* **1934**, *1*, 104−113.

(50) Parr, R. G.; von Szentpaly, L.; Liu, S. Electrophilicity Index. *J. Am. Chem. Soc.* **1999**, *121*, 1922−1924.

(51) Wolinski, K.; Hilton, J. F.; Pulay, P. Efficient Implementation of the Gauge-Independent Atomic Orbital Method for NMR Chemical Shift Calculations. *J. Am. Chem. Soc.* **1990**, *112*, 8251−8260.

DOI: 10.1021/acscatal.8b04175
ACS Catal. 2019, 9, 1662−1669

Chapter 5. Recycling of atmospheric gases

5.1. The Fundamental Noninnocent Role of Water for the Hydrogenation of Nitrous Oxide by PNP Pincer Ru-based Catalysts

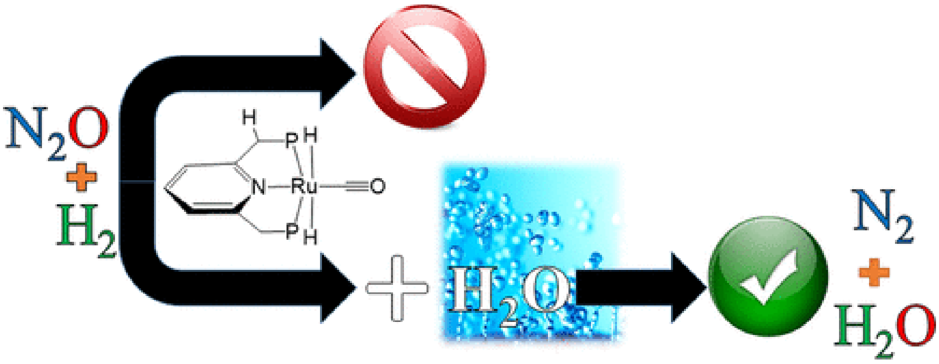

Luque-Urrutia, J. A.; Poater, A. **The Fundamental Noninnocent Role of Water for the Hydrogenation of Nitrous Oxide by PNP Pincer Ru-based Catalysts.** *Inorg. Chem.* **2017**, *56*, 14383-14387.
DOI: 10.1021/acs.inorgchem.7b02630.

This thesis author has contributed to the DFT calculations, data analysis, writing, and revisions of the article.

Reproduced with permission from:

Luque-Urrutia, J. A.; Poater, A. **The Fundamental Noninnocent Role of Water for the Hydrogenation of Nitrous Oxide by PNP Pincer Ru-based Catalysts.** *Inorg. Chem.* **2017**, *56*, 14383-14387.

https://doi.org/10.1021/acs.inorgchem.7b02630

Copyright © 2017, American Chemical Society.

Inorganic Chemistry

Communication

pubs.acs.org/IC

The Fundamental Noninnocent Role of Water for the Hydrogenation of Nitrous Oxide by PNP Pincer Ru-based Catalysts

Jesús A. Luque-Urrutia[‡] and Albert Poater[*,‡]

[‡]Institut de Química Computacional i Catàlisi and Departament de Química, Universitat de Girona, Campus Montilivi, 17003 Girona, Catalonia, Spain

Supporting Information

ABSTRACT: The hydrogenation of nitrous oxide by PNP pincer ruthenium complexes supposes a promising way to functionalize a hazardous gas and reduce the greenhouse effect, generating dinitrogen and water. Here, by DFT calculations we describe not only the whole mechanism for such a green transformation but we unravel the fundamental role of water, without which the reaction could not go forward. Water assists mandatorily in the H transfer to generate the hydroxyl group together with the release of dinitrogen.

Scheme 1. Hydrogenation of N_2O by the PNP-pincer Ru based catalyst 1 ($P = P(iPr)_2$)

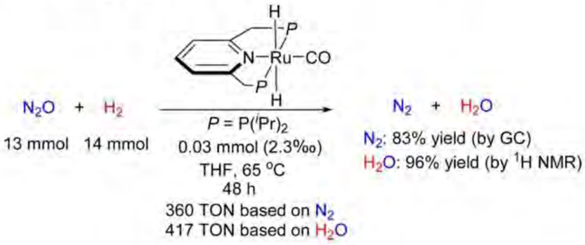

The greenhouse effect (GE) has become a worldwide problem that keeps on affecting the world climate and the beings that live in it. The main perpetrators for this phenomenon are the greenhouse gases: carbon dioxide (CO_2), methane (CH_4), ozone-depleting substances (ODS), hydrofluorocarbons (HFCs), sulfur hexafluoride (SF_6), perfluorocarbons (PFCs), and nitrous oxide (N_2O).[1,2] The gas with the most impact right now is CO_2, being over 60% of the GE cause; however, the other ones should not be overlooked. N_2O has been making ground over the years due to the increase in nitrogenized substances for our daily life,[3] such as fertilizers and pesticides or burning fossil fuels.[4] These processes add N_2O to the atmosphere, and due to its steady-state lifetime (120 years), it has been increasing for decades.[5,6]

The reductive process that consists of the hydrogenation of N_2O by means of H_2 to generate innocuous N_2 and H_2O has turned out to be feasible by heterogeneous[7] and homogeneous[8,9] catalytic systems. For the latter systems, the reaction was indeed not catalytic, but simply stoichiometric,[8] and further, computationally, this reaction was scarcely studied. Thus, key mechanistic insights are missing. In order to address these drawbacks, and following the recent Milstein et al. catalytic work,[9] we have focused our efforts on unveiling the full mechanism for catalyst **1** in Scheme 1. The latter catalyst displayed the highest TON for the reaction that converts N_2O and H_2 into innocuous N_2 and H_2O. This catalyst bears a PNP pincer ligand,[10,11,12] which consists of an equatorial tridentate ligand that binds to the ruthenium center by two phosphorus atoms and one nitrogen atom.[13−15] Recently, the computational studies by Gonçalves and Huang turned out to be fundamental for the rationalization of the reactivity of pincer based complexes from an aromatic point of view.[16] These pincer type ligands have shown many experimental applications such as the formation of NH_3 starting from N_2[17] and what could be its counterpart, the cleavage of the N−H bond in NH_3[18] as well as many others. In terms of transition metal centers, Fe,[19,20] Ru,[21,22] Ir,[23,24] Mo,[25,26] Ni,[27,28] W,[29,30] and Pd[31,32] have been studied, showing a growing interest in this kind of pincer ligands and a high applicability to many areas.[15]

From the initial catalyst **1**, i.e., a nearly symmetrical species, a N_2O molecule is added by the attack of its oxygen to the Ru−H moiety, the bond of which breaks at the same time, and consequently the former hydride protonates the terminal nitrogen atom (see Figure 1).[33] Overall, the transition state that defines this concerted attack of the entering N_2O turns out to be the highest energy barrier, with 26.7 kcal/mol. The next step implies the formation of the hydroxo ligand on ruthenium with the concerted release of a N_2 molecule. However, this step is again not trivial. It requires an energy amount of 33.5 kcal/mol (see Figure 2a), whereas when assisted by a water molecule, the energy barrier decreases to 25.5 kcal/mol (see Figure 2b). This means that in order to go forward, traces of water in the solvent used, THF, are mandatory.[34,35] THF was found to not assist this step, even not facilitating it. Anyway, the barrier corresponding to the **I → I−II + H_2O** step represents the rate-determining step (rds) since it describes the upper energy point of the whole reaction pathway, even though the previous energy barrier corresponding to the step **1 → 1−I** is slightly higher in energy by 1.2 kcal/mol.[36] Once the hydroxo species **II** is formed, any of both methylidene moieties of the pincer ligand provides a proton, generating the aqua complex **III**, overcoming a facile transition state. Then, the H_2O liberation means the generation of catalyst **2**.

From **2**, the coordination of H_2 to the vacant position of the ruthenium center, followed by a H-transfer to the close

Received: October 13, 2017
Published: November 17, 2017

© 2017 American Chemical Society

DOI: 10.1021/acs.inorgchem.7b02630
Inorg. Chem. 2017, 56, 14383−14387

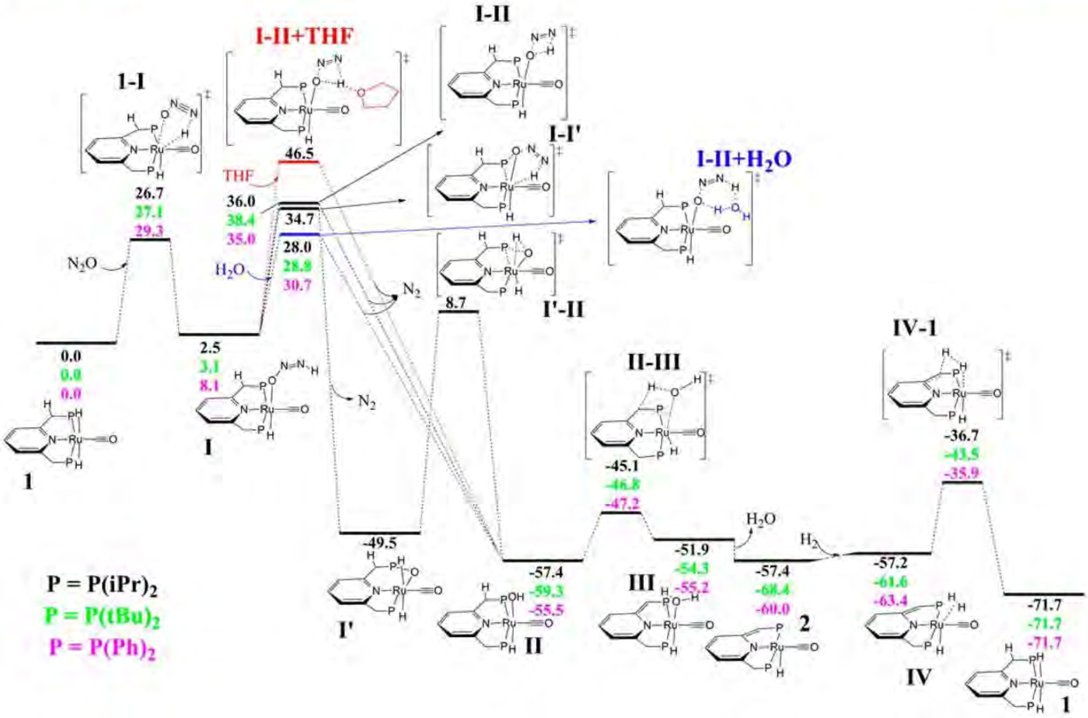

Figure 1. Full mechanism for the hydrogenation of N_2O. Isopropyl ligand represented. tert-Butyl and phenyl ligands' energy shown as well (green and pink energies respectively). (Gibbs free energies in kcal/mol, and referred to catalyst **1**.)

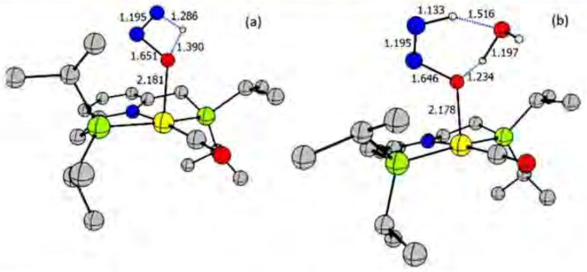

Figure 2. Transition states **I** → **II** (a) not assisted or (b) assisted by a water molecule (most of hydrogens omitted for clarity, selected distances given in Å).

methylylidene of the pincer ligand, generates the dihydride species **1**, thus closing the catalytic cycle, in a strongly exergonic manner (71.7 kcal/mol). Here, the first thing that should be remarked is that the thermodynamic equilibrium between catalysts **1** and **2** with intermediate **IV** in between is strongly displaced toward **1**, by 14.3 kcal/mol. This was unexpected since the same equilibrium for complex **3** of Wang et al. (see Scheme 2),[37] which resembles our catalyst, was found to be only slightly displaced to the hydrogenated species, by only 2.2 kcal/mol.

Scheme 2. Catalyst Screening for Hydrogenation of N_2O

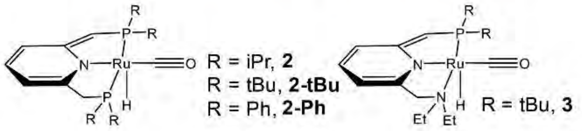

For the sake of a direct comparison, after replicating their calculations (M05-2*X*/6-311++G(2d,p) ~ sdd //M05-2*X*/6-31G(d,p) ~ sdd) with the computational scheme used here (M06/aug-cc-PVTZ ~ sdd//M06/TZVP ~ sdd), we obtained an energy difference of 4.7 kcal/mol. We attribute the increase of the preference for **1** with respect to **3** to the increased flexibility of the pincer ligand that bears **1**, thanks to the second P atom, over a N atom of **3**. This is explained due to the increased preference for the sp^3 hybridization of the phosphorus over the nitrogen atom, together with the smaller size of the latter atom (98 pm for P vs 65 pm for N in Bohr's atomic radius model).[38]

Alternative pathways were also tested. First, instead of coordination to the ruthenium center of N_2O via the O atom, it was done via the terminal N atom, which turns out to be 12.9 kcal/mol more expensive. Then, without the presence of traces of water, the formation of the isomer **I′** is favored by 1.4 kcal/mol with respect to the direct formation of **II** (see Figure 1). This step has to be considered as a possible catalyst death since it leads to a peculiar Ru−P bond cleavage, where the oxygen atom is inserted between both atoms (see Figure 3). Once we achieve this undesired species **I′**, the energy required to reorder the atoms in order to generate **II** is 58.2 kcal/mol, which is an energy barrier too high bearing the experimental conditions. Thus, this confirms that at an initial stage, traces of water must assist the mechanism development before water molecules formed as a byproduct of the hydrogenation of N_2O are released. Furthermore, the assistance of either more water or THF molecules was tested. Among the computed data, for the hydrogenation step **IV** → **1**, a water molecule increased the energy barrier by 25.9 kcal/mol, while a second water molecule also increased the energy barrier of steps **I** → **II** and **II** → **III** by 9.1 and 2.0 kcal/mol, respectively. Actually, going into detail,

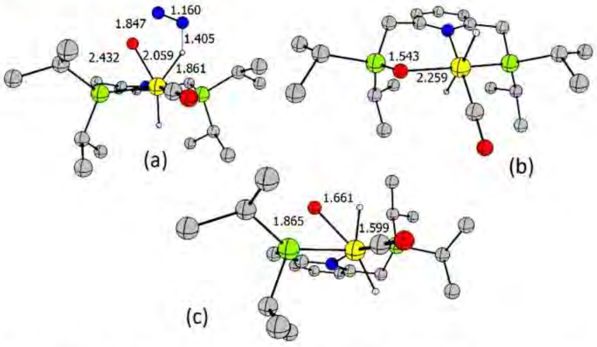

Figure 3. Alternative pathway through intermediate **I′**: (a) transition state **I** → **I′**, (b) intermediate **I′** and (c) transition state **I′** → **II** (most of hydrogens omitted for clarity, selected distances given in Å).

the six-membered cycle of the water assisted transition state **I** → **II** displayed in Figure 2b is fundamental to explaining its relative high stability.

To understand the nature of the pincer ligand and its role in the catalytic studied reaction here, we have also performed an analysis of catalyst **1** replacing the iPr ligands bonded to the phosphorus atoms of the pincer ligand by tert-butyl (tBu) groups (**1-tBu**) and phenyl (Ph) ligands (**1-Ph**). The results for both latter catalysts, with poorer catalytic performance with respect to **1**, are compared in Figure 1, as well.

According to our data, we have found that, just as Milstein et al. found, the isopropyl ligands are better than the tert-butyl and phenyl ligands. Looking into the energy data in Figure 1, we can see that **1-tBu** and **1-Ph** are both higher in energy in all cases (except **III** for **1-Ph**, vide infra) going up to a maximum energy difference of 12.9 kcal (**I**–**II**) for **1-tBu** and 7.7 kcal/mol (**I**) for **1-Ph**. Even though the iPr and the Ph ligands quite resemble one another, for the tBu there are increased differences with respect to the other ligands, which is caused by the higher steric hindrance of the latter ligand.

As we can see in Figure 4, the steric hindrance of the tBu groups is remarkable compared to the Ph and the iPr ones; therefore, we can correlate this increase in bulkiness to its poorer catalytic performance. However, we noticed that system **2-Ph** is indeed less hindered than **2**, yet it is slightly worse. This poorer performance bearing phenyls may be due to the stronger C–P double bond that exists between the phosphorus moiety and the pyridine of the PNP pincer in **2-Ph** that later must be hydrogenated to regenerate the catalytic hydride species **1**. According to the Mayer bond order data for the bond between the P atom and the methylylidene fragment that gets hydrogenated, we observed a clear difference: for **2** being 1.079, while for **2-Ph** it is 1.131, whereas upon hydrogenation of the CH moiety, MBOs for species **1** are 0.894 for the Ph and 0.881 for iPr.

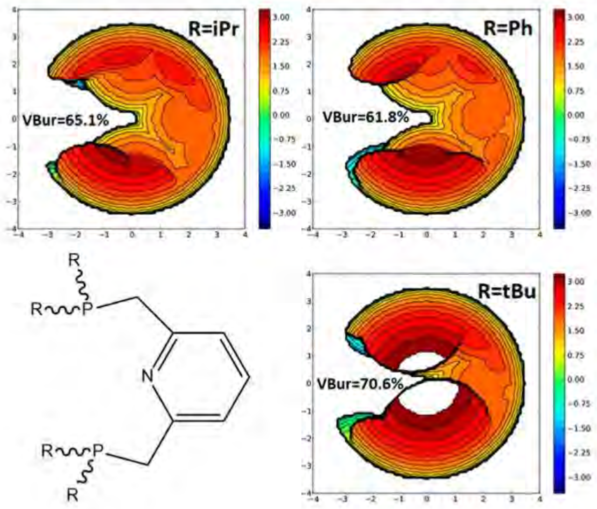

Figure 4. Steric maps for the pincer ligands of the catalysts **1**, **1-tBu**, **1-Ph**. Ru metal center and CO ligand omitted for clarity (tBu center is out of scale).

We have determined the whole reaction mechanism for the pincer based catalyst **1**. The possibility of a water autocatalysis at the initial stages of the reaction was determined, while it would be hindered as time progresses and water is formed as a product of the hydrogenation of N_2O. In complete absence of water, a peculiar bond cleavage of any of the Ru–P bonds in order to form a Ru–O–P moiety has been computationally highly stable, and we consider it a plausible catalyst poisoning due to the high energy required in order to continue the mechanism and close the catalytic cycle. Between the three studied ligands on P atoms, iPr is indeed the best one, with tBu having increased bulkiness and Ph gaining some conjugation between the phenyls and the pyridine, thus, requiring more energy to overcome the upper barrier of the whole mechanism. Further studies are planned to in silico predict a modified PNP pincer Ru-based catalyst that does not need the presence of any water molecule, together with the control of the potential Ru–P bond cleavage that here has been demonstrated to lead toward the decomposition of the catalyst.

■ ASSOCIATED CONTENT

Supporting Information

The Supporting Information is available free of charge on the ACS Publications website at DOI: 10.1021/acs.inorgchem.7b02630.

Computational details and all XYZ coordinates, energies and 3D structures of all species (PDF)

■ AUTHOR INFORMATION

Corresponding Author

*E-mail: albert.poater@udg.edu.

ORCID

Albert Poater: 0000-0002-8997-2599

Notes

The authors declare no competing financial interest.

■ ACKNOWLEDGMENTS

J.A.L.-U. thanks Universitat de Girona for a IFUdG2017 predoctoral fellowship. A.P. thanks the Spanish MINECO for a project CTQ2014-59832-JIN, and the EU for a FEDER fund (UNGI08-4E-003)). We thank Profs. David Milstein and Rong Zheng for helpful comments.

■ REFERENCES

(1) Freedman, B.; Frost, R. *Gale Encyclopedia of Science;* Gale Group, 1995; pp 1875–1880.

(2) Rodhe, H. A Comparison of the Contribution of Various Greenhouse Gases to the Greenhouse Effect. *Science* **1990**, *248*, 1217–1219.

(3) (a) Konsolakis, M. Recent Advances on Nitrous Oxide (N_2O) Decomposition over Non-Noble-Metal Oxide Catalysts: Catalytic Performance, Mechanistic Considerations, and Surface Chemistry Aspects. *ACS Catal.* **2015**, *5*, 6397−6421. (b) Severin, K. Synthetic Chemistry with Nitrous Oxide. *Chem. Soc. Rev.* **2015**, *44*, 6375−6386. (c) Parmon, V. N.; Panov, G. I.; Uriarte, A.; Noskov, A. S. Nitrous Oxide in Oxidation Chemistry and Catalysis: Application and Production. *Catal. Today* **2005**, *100*, 115−131. (d) Tolman, W. B. *Angew. Chem., Int. Ed.* **2010**, *49*, 1018−1024.

(4) López, J. C.; Quijano, G.; Souza, T. S. O.; Estrada, J. M.; Lebrero, R.; Muñoz, R. Biotechnologies for Greenhouse Gases (CH_4, N_2O, and CO_2) Abatement: State of the Art and Challenges. *Appl. Microbiol. Biotechnol.* **2013**, *97*, 2277−2303.

(5) Hsu, J.; Prather, M. J. Global Long-Lived Chemical Modes Excited in a 3-D Chemistry Transport Model: Stratospheric N_2O, NO_y, O_3 and CH_4 Chemistry. *Geophys. Res. Lett.* **2010**, *37*, L07805.

(6) Montzka, S. A.; Dlugokencky, E. J.; Butler, J. H. Non-CO_2 Greenhouse Gases and Climate Change. *Nature* **2011**, *476*, 43−50.

(7) (a) Benton, A. F.; Thacker, C. M. The Kinetics of Reaction between Nitrous Oxide and Hydrogen at a Silver Surface. *J. Am. Chem. Soc.* **1934**, *56*, 1300−1304. (b) Dixon, J. K.; Vance, J. E. The Reaction between Nitrous Oxide and Hydrogen on Platinum. *J. Am. Chem. Soc.* **1935**, *57*, 818−821. (c) Miyamoto, A.; Baba, S.; Mori, M.; Murakami, Y. Ion-Solvent Molecule Interactions in the Gas Phase. The Potassium Ion and Benzene. *J. Phys. Chem.* **1981**, *85*, 3117−3122. (d) Delahay, G.; Mauvezin, M.; Guzmán-Vargas, A.; Coq, B. Effect of the Reductant Nature on the Catalytic Removal of N_2O on Fe-Zeolite-β Catalysts. *Catal. Commun.* **2002**, *3*, 385−389. (e) Nobukawa, T.; Yoshida, M.; Okumura, K.; Tomishige, K.; Kunimori, K. Effect of Reductants in N_2O Reduction Over Fe-MFI Catalysts. *J. Catal.* **2005**, *229*, 374−388.

(8) (a) Kaplan, A. W.; Bergman, R. G. Nitrous Oxide Mediated Oxygen Atom Insertion into a Ruthenium−Hydride Bond. Synthesis and Reactivity of the Monomeric Hydroxoruthenium Complex $(DMPE)_2Ru(H)(OH)$. *Organometallics* **1997**, *16*, 1106−1108. (b) Lee, J.-H.; Pink, M.; Tomaszewski, J.; Fan, H.; Caulton, K. G. Facile Hydrogenation of N_2O by an Operationally Unsaturated Osmium Polyhydride. *J. Am. Chem. Soc.* **2007**, *129*, 8706−8707. (c) Doyle, L. E.; Piers, W. E.; Borau-Garcia, J. Ligand Cooperation in the Formal Hydrogenation of N_2O Using a $PC_{sp2}P$ Iridium Pincer Complex. *J. Am. Chem. Soc.* **2015**, *137*, 2187−2190. (d) Gianetti, T. L.; Annen, S. P.; Santiso-Quinones, G.; Reiher, M.; Driess, M.; Grützmacher, H. Nitrous Oxide as a Hydrogen Acceptor for the Dehydrogenative Coupling of Alcohols. *Angew. Chem., Int. Ed.* **2016**, *55*, 1854−1858. (e) Gianetti, T. L.; Rodríguez-Lugo, R. E.; Harmer, J. F.; Trincado, M.; Vogt, M.; Santiso-Quinones, G.; Grützmacher, H. Zero-Valent Amino-Olefin Cobalt Complexes as Catalysts for Oxygen Atom Transfer Reactions from Nitrous Oxide. *Angew. Chem., Int. Ed.* **2016**, *55*, 15323−15328.

(9) Zeng, R.; Feller, M.; Ben-David, Y.; Milstein, D. Hydrogenation and Hydrosilylation of Nitrous Oxide Homogeneously Catalyzed by a Metal Complex. *J. Am. Chem. Soc.* **2017**, *139*, 5720−5723.

(10) Yu, H.; Jia, G.; Lin, Z. Theoretical Studies on O-Insertion Reactions of Nitrous Oxide with Ruthenium Hydride Complexes. *Organometallics* **2008**, *27*, 3825−3833.

(11) Zhang, J.; Balaraman, E.; Leitus, G.; Milstein, D. Electron-Rich PNP- and PNN-Type Ruthenium(II) Hydrido Borohydride Pincer Complexes. Synthesis, Structure, and Catalytic Dehydrogenation of Alcohols and Hydrogenation of Esters. *Organometallics* **2011**, *30*, 5716−5724.

(12) Zell, T.; Ben-David, Y.; Milstein, D. Highly Efficient, General Hydrogenation of Aldehydes Catalyzed by PNP Iron Pincer Complexes. *Catal. Sci. Technol.* **2015**, *5*, 822−826.

(13) Schneider, S.; Meiners, J.; Askevold, B. Cooperative Aliphatic PNP Amido Pincer Ligands − Versatile Building Blocks for Coordination Chemistry and Catalysis. *Eur. J. Inorg. Chem.* **2012**, *2012*, 412−429.

(14) van der Vlugt, J. I. Cooperative Catalysis with First-Row Late Transition Metals. *Eur. J. Inorg. Chem.* **2012**, *2012*, 363−375.

(15) Qu, S.; Dang, Y.; Song, C.; Wen, M.; Huang, K.; Wang, Z. Catalytic Mechanisms of Direct Pyrrole Synthesis via Dehydrogenative Coupling Mediated by PNP-Ir or PNN-Ru Pincer Complexes: Crucial Role of Proton-Transfer Shuttles in the PNP-Ir System. *J. Am. Chem. Soc.* **2014**, *136*, 4974−4991.

(16) Gonçalves, T. P.; Huang, K. Metal-Ligand Cooperative Reactivity in the (Pseudo)-Dearomatized $PN_x(P)$ Systems: The Influence of the Zwitterionic Form in Dearomatized Pincer Complexes. *J. Am. Chem. Soc.* **2017**, *139*, 13442−13449.

(17) Kuriyama, S.; Arashiba, K.; Nakajima, K.; Tanaka, H.; Kamaru, N.; Yoshizawa, K.; Nishibayashi, Y. Catalytic Reduction of Dinitrogen to Ammonia by Use of Molybdenum−Nitride Complexes Bearing a Tridentate Triphosphine as Catalysts. *J. Am. Chem. Soc.* **2014**, *136*, 9719−9731.

(18) Chang, Y.; Nakajima, Y.; Tanaka, H.; Yoshizawa, K.; Ozawa, F. Facile N−H Bond Cleavage of Ammonia by an Iridium Complex Bearing a Noninnocent PNP-Pincer Type Phosphaalkene Ligand. *J. Am. Chem. Soc.* **2013**, *135*, 11791−11794.

(19) Fillman, K. L.; Bielinski, E. A.; Schmeier, T. J.; Nesvet, J. C.; Woodruff, T. M.; Pan, C. J.; Takase, M. K.; Hazari, N.; Neidig, M. L. Flexible Binding of PNP Pincer Ligands to Monomeric Iron Complexes. *Inorg. Chem.* **2014**, *53*, 6066−6072.

(20) Mellone, I.; Gorgas, N.; Bertini, F.; Peruzzini, M.; Kirchner, K.; Gonsalvi, L. Selective Formic Acid Dehydrogenation Catalyzed by Fe-PNP Pincer Complexes Based on the 2,6-Diaminopyridine Scaffold. *Organometallics* **2016**, *35*, 3344−3349.

(21) Nakajima, Y.; Okamoto, Y.; Chang, Y.; Ozawa, F. Synthesis, Structures, and Reactivity of Ruthenium Complexes with PNP-pincer Type Phosphaalkene Ligands. *Organometallics* **2013**, *32*, 2918−2925.

(22) Alberico, E.; Lennox, A. J. J.; Vogt, L. K.; Jiao, H.; Baumann, W.; Drexler, H.; Nielsen, M.; Spannenberg, A.; Checinski, M. P.; Junge, H.; Beller, M. Unravelling the Mechanism of Basic Aqueous Methanol Dehydrogenation Catalyzed by Ru−PNP Pincer Complexes. *J. Am. Chem. Soc.* **2016**, *138*, 14890−14904.

(23) Cheng, C.; Kim, B. G.; Guironnet, D.; Brookhart, M.; Guan, C.; Wang, D. Y.; Krogh-Jespersen, K.; Goldman, A. S. Synthesis and Characterization of Carbazolide-Based Iridium PNP Pincer Complexes. Mechanistic and Computational Investigation of Alkene Hydrogenation: Evidence for an Ir(III)/Ir(V)/Ir(III) Catalytic Cycle. *J. Am. Chem. Soc.* **2014**, *136*, 6672−6683.

(24) Feller, M.; Ben-Ari, E.; Diskin-Posner, Y.; Carmieli, R.; Weiner, L.; Milstein, D. O_2 Activation by Metal−Ligand Cooperation with Ir^I PNP Pincer Complexes. *J. Am. Chem. Soc.* **2015**, *137*, 4634−4637.

(25) Öztopcu, Ö.; Holzhacker, C.; Puchberger, M.; Weil, M.; Mereiter, K.; Veiros, L. F.; Kirchner, K. Synthesis and Characterization of Hydrido Carbonyl Molybdenum and Tungsten PNP Pincer Complexes. *Organometallics* **2013**, *32*, 3042−3052.

(26) Wei, Z.; Junge, K.; Beller, M.; Jiao, H. Hydrogenation of Phenyl-Substituted C ≡ N, C = N, C ≡ C, C = C and C = O Functional Groups by Cr, Mo and W PNP Pincer Complexes − a DFT Study. *Catal. Sci. Technol.* **2017**, *7*, 2298−2307.

(27) Vogt, M.; Rivada-Wheelaghan, O.; Iron, M. A.; Leitus, G.; Diskin-Posner, Y.; Shimon, L. J. W.; Ben-David, Y.; Milstein, D. Anionic Nickel(II) Complexes with Doubly Deprotonated PNP Pincer-type Ligands and Their Reactivity Toward CO_2. *Organometallics* **2013**, *32*, 300−308.

(28) Kreye, M.; Freytag, M.; Jones, P. G.; Williard, P. G.; Bernskoetter, W. H.; Walter, M. D. Homolytic H_2 Cleavage by a Mercury-Bridged Ni(i) Pincer Complex $[\{(PNP)Ni\}_2\{\mu\text{-Hg}\}]$. *Chem. Commun.* **2015**, *51*, 2946−2949.

(29) Moha, V.; Leitner, W.; Hölscher, M. Hölscher M. H_3 Synthesis in the N_2/H_2 Reaction System using Cooperative Molecular Tungsten/Rhodium Catalysis in Ionic Hydrogenation: A DFT Study. *Chem. - Eur. J.* **2016**, *22*, 2624−2628.

(30) Arashiba, K.; Sasaki, K.; Kuriyama, S.; Miyake, Y.; Nakanishi, H.; Nishibayashi, Y. Synthesis and Protonation of Molybdenum− and Tungsten−Dinitrogen Complexes Bearing PNP-Type Pincer Ligands. *Organometallics* **2012**, *31*, 2035−2041.

(31) Bailey, W. D.; Kaminsky, W.; Kemp, R. A.; Goldberg, K. I. Synthesis and Characterization of Anionic, Neutral, and Cationic PNP Pincer Pd^{II} and Pt^{II} Hydrides. *Organometallics* **2014**, *33*, 2503−2509.

(32) Yang, Z.; Xia, C.; Liu, D.; Liu, Y.; Sugiya, M.; Imamoto, T.; Zhang, W. P-Stereogenic PNP Pincer-Pd Catalyzed Intramolecular Hydroamination of Amino-1,3-dienes. *Org. Biomol. Chem.* **2015**, *13*, 2694−2702.

(33) DFT static calculations were performed with Gaussian09 using the BP86-D3BJ functional, and the SDD basis set for ruthenium and the TZVP basis set for the other atoms. Single-point calculations on the optimized geometries with M06 functional and the aug-cc-PVTZ basis set. Solvent effects were included by PCM using THF as a solvent.

(34) Values at a pressure of 1354 atm using the approach of Martin and co-workers, excluding the potential overestimation of the entropy contribution, confirm the message of the paper since the barrier assisted by a water molecule in step I→II is again 8.0 kcal/mol exactly lower in energy, whereas the undesired step I→I′ is still favored by 1.3 kcal/mol without the assistance of a water molecule. Further, the no reversibility character of the 2→1 step is confirmed, since the energy difference increases 4.6 kcal/mol.

(35) (a) Martin, R. L.; Hay, P. J.; Pratt, L. R. Hydrolysis of Ferric Ion in Water and Conformational Equilibrium. *J. Phys. Chem. A* **1998**, *102*, 3565−3573. (b) Manzini, S.; Poater, A.; Nelson, D. J.; Cavallo, L.; Slawin, A. M. Z.; Nolan, S. P. Insights into the Decomposition of Olefin Metathesis Pre-Catalysts. *Angew. Chem., Int. Ed.* **2014**, *53*, 8995−8999. (c) Poater, A.; Pump, E.; Vummaleti, S. V. C.; Cavallo, L. The Right Computational Recipe for Olefin Metathesis with Ru-Based Catalysts: the Whole Mechanism of Ring-Closing Olefin Metathesis. *J. Chem. Theory Comput.* **2014**, *10*, 4442−4448.

(36) Kozuch, S.; Shaik, S. How to Conceptualize Catalytic Cycles? The Energetic Span Model. *Acc. Chem. Res.* **2011**, *44*, 101−110.

(37) Lu, G.; Li, H.; Zhao, L.; Huang, F.; Schleyer, P.; Wang, Z.-X. v. R.; Wang, Z. Designing Metal-Free Catalysts by Mimicking Transition-Metal Pincer Templates. *Chem. - Eur. J.* **2011**, *17*, 2038−2043.

(38) Bohr, N. On the Constitution of Atoms and Molecules. *Phys. Mag.* **1913**, *26*, 1−25.

DOI: 10.1021/acs.inorgchem.7b02630
Inorg. Chem. 2017, 56, 14383−14387

5.2. Cycloaddition of CO_2 to epoxides by highly nucleophilic 4-aminopyridines: establishing a relationship between carbon basicity and catalytic performance by experimental and DFT investigations

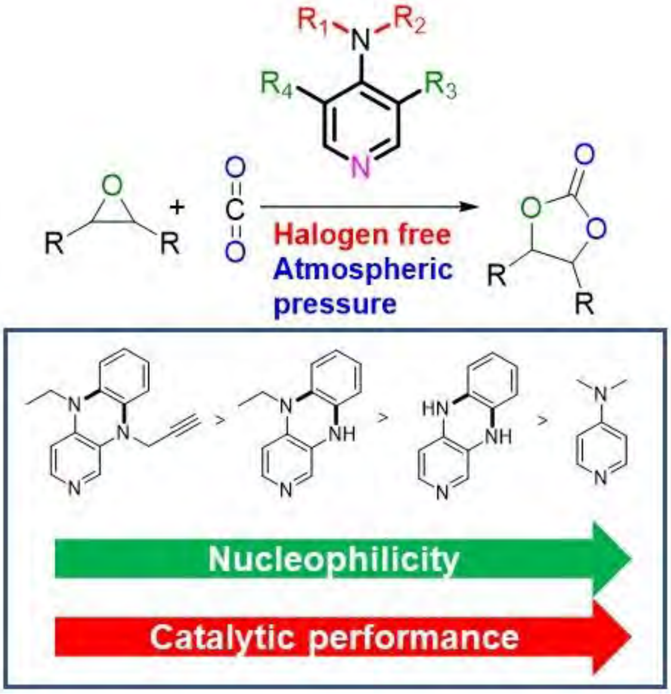
Halogen free
Atmospheric pressure
Nucleophilicity
Catalytic performance

Natongchai, W.; Luque-Urrutia, J. A.; Phungpanya, C.; Solà, M.; D'Elia, V.; Poater, A.; Zipse, H. **Cycloaddition of CO_2 to epoxides by highly nucleophilic 4-aminopyridines: establishing a relationship between carbon basicity and catalytic performance by experimental and DFT investigations.** *Org. Chem. Front.* **2021**, Advance Article
DOI: 10.1039/d0qo01327g.

This thesis author has contributed to the DFT calculations, data analysis, writing, and revisions of the article.

Reproduced with permission from:

Natongchai, W.; Luque-Urrutia, J. A.; Phungpanya, C.; Solà, M.; D'Elia, V.; Poater, A.; Zipse, H. **Cycloaddition of CO_2 to epoxides by highly nucleophilic 4-aminopyridines: establishing a relationship between carbon basicity and catalytic performance by experimental and DFT investigations.** *Org. Chem. Front.* **2020**, Advance Article.

https://doi.org/10.1039/d0qo01327g

Reproduced by permission of The Royal Society of Chemistry.

ORGANIC CHEMISTRY
FRONTIERS

CHINESE CHEMICAL SOCIETY

ROYAL SOCIETY OF CHEMISTRY

RESEARCH ARTICLE

View Article Online
View Journal

Check for updates

Cite this: DOI: 10.1039/d0qo01327g

Cycloaddition of CO_2 to epoxides by highly nucleophilic 4-aminopyridines: establishing a relationship between carbon basicity and catalytic performance by experimental and DFT investigations†

Wuttichai Natongchai,[a] Jesús Antonio Luque-Urrutia,[b] Chalida Phungpanya,[a] Miquel Solà,[b] Valerio D'Elia,*[a] Albert Poater*[b] and Hendrik Zipse[c]

Received 29th October 2020,
Accepted 6th December 2020

DOI: 10.1039/d0qo01327g

rsc.li/frontiers-organic

The development of single-component halogen-free organocatalysts in the highly investigated cycloaddition of CO_2 to epoxides is sought-after to enhance the sustainability of the process and reduce costs. In this context, the use of strongly nucleophilic single-component catalysts has been generally restricted to a limited selection of *N*-nucleophiles. In this study, predictive calculations of epoxide-specific carbon basicities suggested that highly nucleophilic 3,4-diaminopyridines possess suitable basicity to serve as active single-component catalysts for the cycloaddition of CO_2 to epoxides. Indeed, experimentally, the most active compounds of this class performed efficiently for the conversion of epoxides to carbonates under atmospheric pressure outperforming the catalytic activity of traditional *N*-nucleophiles. Importantly, the 3,4-diaminopyridino scaffold could be easily supported on polystyrene and used as a recyclable heterogeneous catalyst under atmospheric CO_2 pressure. Finally, the mechanism of the cycloaddition reaction catalyzed by several *N*-nucleophiles was investigated highlighting the importance of the 3,4-diaminopyridine nucleophilicity in competently promoting the crucial initial step of epoxide ring-opening without the addition of nucleophiles or hydrogen bond donors.

Introduction

Cyclic organic carbonates are a class of compounds with multiple remarkable applications, for example as solvents[1–4] and chemical intermediates for the synthesis of fine chemicals[5–7] and polymers.[8–12] Importantly, the synthesis of cyclic carbonates *via* cycloaddition reaction of CO_2 to epoxides offers the highly sought-after opportunity to recycle CO_2 as a C1 source for the synthesis of commodity chemicals[13–19] under mild conditions. A vast amount of literature has been produced in recent years on the development of efficient catalytic systems for the latter reaction as highlighted in several reviews.[20–26] Current focus on the catalytic synthesis of cyclic carbonates from epoxides has recently strongly diversified to include several environmentally-conscious areas of research such as the carbonation of bio-based epoxides for the valorization of renewable building blocks,[27–30] the use of impure sources of CO_2,[31–33] the conversion of CO_2 to cyclic carbonates under ambient conditions[23,34–36] and the development of metal-[37–45] and/or halogen-free catalytic systems.[46–48] Concerning the latter two aspects, significant advances have been reported in the development of attractive metal-free catalysts able to efficiently carry out the cycloaddition of CO_2 to carbonates with some catalytic systems employing inexpensive and bio-based hydrogen bond donors (HBDs) such as cellulose,[49] pentaerythritol,[50] ascorbic acid,[29,51] tannic acid,[52] *etc.*[25,41] However, the actual sustainability of this catalytic strategy is still limited by the need for halogen-based catalytic components such as ammonium or phosphonium halide salts that serve to provide anions acting as nucleophiles and as leaving groups in different steps of the well-established cycloaddition mechanism.[53,54] The presence of halides can lead to reactor corrosion;[46,55] moreover, it is known that the production of halogens is an energy intensive process with a significant carbon footprint.[56] There is, therefore, high interest in developing more

---

[a] *Department of Materials Science and Engineering, School of Molecular Science and Engineering, Vidyasirimedhi Institute of Science and Technology (VISTEC), 555 Moo 1, 21210, Payupnai, WangChan, Rayong, Thailand. E-mail: valerio.delia@vistec.ac.th*

[b] *Institut de Química Computacional i Catàlisi and Departament de Química, Universitat de Girona, C/M. Aurèlia Capmany, 69, 17003 Girona, Catalonia, Spain*

[c] *Department Chemie, Ludwig-Maximilians-Universität München, Butenandtstraße 5–13, Haus F, 81377 München, Germany*

† Electronic supplementary information (ESI) available. See DOI: 10.1039/d0qo01327g

This journal is © the Partner Organisations 2020

sustainable halogen-free organocatalysts.[57] Seminal work on binary catalytic systems employing HBDs in the presence of halogen-free nucleophiles were reported such as DMAP/*p*-methoxyphenol[58] (DMAP: 4-dimethylaminopyridine), DBU/cellulose[59] (DBU: 1,8-diazabicyclo[5.4.0]undec-7-ene) and DBU-histidine.[60] However, the use of these catalytic systems required relatively harsh reaction conditions (120 °C, 20–36 bar CO_2 pressure) and, often, high loadings (up to 10 mol%) of bases. Moreover, in the prospect of heterogeneous catalysts design, it should be considered that the different components of binary catalytic systems are generally difficult to co-immobilize, making the use of single catalytic moieties more desirable.

In 2007, Shiels and Jones reported the DMAP-catalyzed synthesis of propylene carbonate from propylene oxide (PO) reaching high PO conversion at 120 °C and 34 bar CO_2.[61] More recently, some single-component halogen- and metal-free homogeneous catalysts were reported to operate under slightly milder conditions (T: 100–120 °C, P_{CO_2}: 10–20 bar) based on Schiff bases,[62,63] tertiary amines,[64–66] ammonium salts[67] and N-heterocyclic compounds (triazoles, azolates, 2-aminopyridines, DBU, adducts of imidazolium compounds).[68–73] Similarly, metal- and halogen-free heterogeneous catalysts were recently reported that operate efficiently in the 120–140 °C temperature range and at CO_2 pressures ≥10 bar.[66,74–76] In this context, it is worth noting that the development of catalysts able to carry out CO_2 fixation under low or atmospheric pressure remains a desirable target;[77–79] it allows the use of simpler reaction setups and the conversion of CO_2 captured after power generation[78] or even the direct use of flue gas[31] without energy-demanding[80] recompression steps. The cycloaddition of CO_2 to epoxides by halide-free homogeneous and heterogeneous *N*-nucleophiles under atmospheric pressure remains underreported; Verpoort *et al.* have very recently reported that nitrogen-rich triazole rings bearing carboxylic acid functionalities were competent halogen-free organocatalysts for atmospheric CO_2 cycloaddition to several epoxides in the 75–100 °C temperature range.[68] However, the most active catalyst of this class was a derivative of highly toxic and environmentally hazardous mesitylene (hazard statements: GHS08: health hazard, GHS09: environmental hazard).[81] Whereas all the above-mentioned halogen-free organocatalysts contain nucleophilic and basic nitrogen atoms to assist in the activation and coordination of CO_2 or of the epoxide, there has been scarce attention at systematically exploring the effect of nitrogen nucleophilicity within a series of comparable compounds with well-known and parameterized nucleophilicity. In this context, 4-aminopyridines are a class of *N*-nucleophilic catalysts whose nucleophilicity can be strongly enhanced by structural modifications[82–84] and conformational fixation.[85,86] Their nucleophilicity can be parameterized by using theoretically calculated and experimental descriptors.[87–89] Therefore, with the aim to discover more efficient single-component, halogen-free organocatalysts for the cycloaddition of CO_2 to epoxides able to operate under atmospheric pressure and to provide useful mechanistic insights for the future design of highly nucleophilic catalysts, we investigated the catalytic performance of a selection of aminopyridines of different nucleophilicity displayed in Scheme 1 (DMAP and compounds **1–4**). To this selection we also added pyridine, DBU and TBD as reference compounds. We show here that the catalytic performance of 4-aminopyridines (**1–4**) under ambient pressure surpasses that of traditional *N*-nucleophiles such as DMAP, DBU and TBD, a result that could be predicted by calculating the carbon basicities of all compounds towards the epoxide substrate.

Additionally, mechanistic experiments and DFT calculations were carried out to gain insight into the possible mechanistic pathways shown in Scheme 2 (each displaying possible reaction intermediates, elementary steps and labels for the expected transition states (TS)) where the nucleophile initially interacts with the epoxide substrate (cycle A) or with CO_2 (cycle B). Finally, the most active aminopyridine catalyst could be readily supported on Merrifield resin (MR) *via* click chemistry leading to a recyclable heterogeneous catalyst able to promote the cycloaddition of CO_2 to epoxides under ambient pressure.

Experimental section

Materials and methods

Pyridine, DMAP, 9-azajulolidine, DBU and TBD were purchased from commercial sources, stored in a nitrogen glovebox and used as received; compounds **2**, **3**, **4** were synthesized according to previously published procedures.[84,90]

For a standard catalytic experiment, the epoxide substrate (16.6 mmol) was charged in a 50 mL round bottom Schlenk flask equipped with a magnetic stirrer. The nucleophilic catalyst (0.332 mmol, 2 mol%) was added. A rubber balloon containing CO_2 was connected to the Schlenk flask and part of the CO_2 was used for flushing the vessel to replace air. The reaction vessel was well-sealed to prevent losses of CO_2 and stirred at 100 °C for 24 h. After this period, the reaction was cooled down and

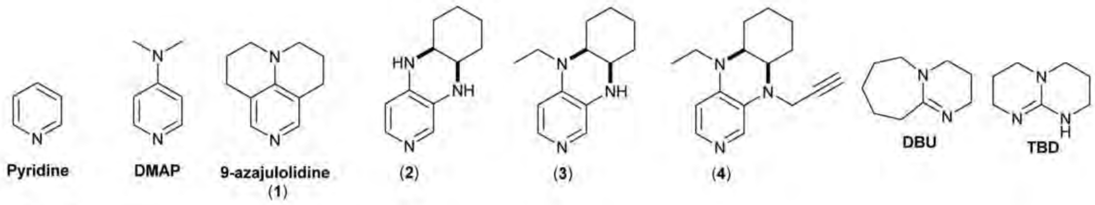

Scheme 1 *N*-Nucleophiles used as catalysts in this study.

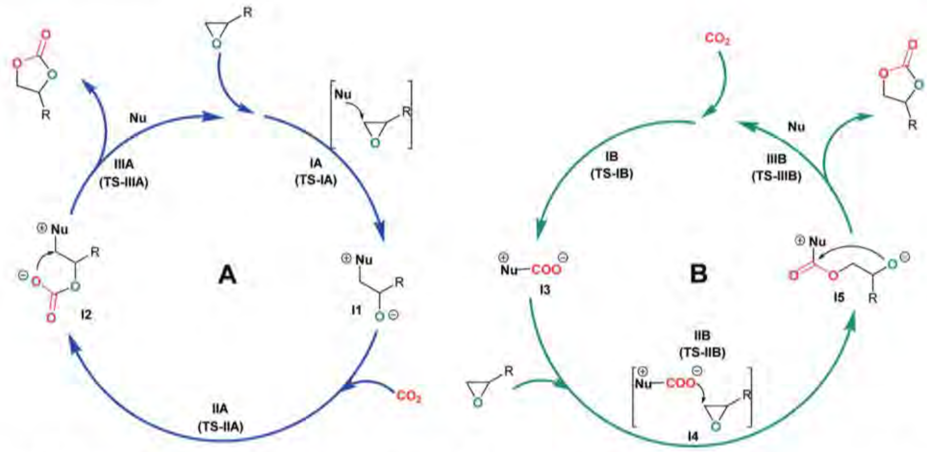

Scheme 2 Possible mechanistic pathways for the cycloaddition of CO_2 to epoxides by single-component nucleophilic catalysts.

the residual pressure in the Schlenk flask was carefully vented out. An aliquot of the reaction mixture was placed into an NMR tube and diluted with *ca.* 0.6 mL $CDCl_3$ to determine substrate conversion and selectivity by ^1H NMR spectroscopy. The crude products were purified by silica-column chromatography using mixtures of ethyl acetate and hexane as eluents.

Further experimental details including computational methods can be found in section S1 of the ESI.†

Results and discussion

For the initial evaluation of the catalytic activity of nucleophilic 4-aminopyridines, and of the dependency of the catalytic performance on nucleophilicity, we selected the compounds in Scheme 1, sorted in order of carbon basicity, according to literature-available MCA (methyl cation affinity) values. The selection includes unfunctionalized pyridine as a reference compound, DMAP and its conformationally fixed analogue 9-aza julolidine (**1**) whose nucleophilicity is higher than DMAP.[86] Additionally, we included three 3,4-diaminopyridines (compounds **2–4**) readily accessible via modular synthesis from the coupling of 3,4-diaminopyridine with 1,2-cyclohexanedione followed by reduction and alkylation of the aliphatic nitrogen atoms.[84,90] Depending also on the pattern of substitution at the latter nitrogen atoms, these compounds generally possess higher nucleophilicity than DMAP due to conformational fixation and inductive effects.[84,88] Finally, for the sake of comparison, we included in the selection of catalysts two well-established *N*-nucleophiles (DBU, TBD) previously used in literature as components of catalytic systems for the cycloaddition of CO_2 to epoxides.[59,91,92] Computationally-derived parameters defining the carbon basicity of several of the *N*-nucleophiles in Scheme 1 are available, such as MCA values[87] or relative acetyl transfer enthalpies.[88] However, in order to make a more meaningful prediction of catalytic performance of the nucleophiles in Scheme 1 in the cycloaddition of CO_2 to epoxides, it would be more helpful to access a scale of carbon basicities relative to the actual electrophilic carbon atoms where the attack of the nucleophilic catalysts takes place during the formation of cyclic carbonates. To this end we have calculated the affinity of all nucleophiles shown in Scheme 1 towards propylene epoxide (PO) as a small unsymmetrical epoxide substrate. As we are interested here in relative Lewis basicities of various catalysts, we express epoxide affinities relative to that of pyridine as a comparatively unreactive catalyst. Relative epoxide affinities at a reaction temperature of 373.15 K ($\Delta H_{373}(epox)$) equate to the reaction enthalpies for the formal propylene epoxide transfer from pyridine adduct **pyr-epox** to other catalysts (Fig. 1). The 4-amino substituted pyridines DMAP and **1** showed significantly higher epoxide affinities as compared to pyridine, as did the 3,4-diaminopyridine catalysts **2–4** (Table 1, entries 1–6). Even higher Lewis basicities were calculated for DBU and TBD (Table 1, entries 7 and 8), the latter of which is predicted to be the most basic catalyst in this set. As shown in Fig. 1, the initially formed zwitterionic epoxide adducts can potentially cyclize to 5-membered ring products, which are unable to propagate the catalytic cycle. The reaction enthalpies for this step ($\Delta H_{373}(cyc)$) thus reflect the propensity of various catalysts to undergo this unimolecular deactivation step. From the results shown graphically in Fig. 1 and numerically in Table 1 we can see that cyclization energies are large for pyridine as a system lacking strong electron donor substituents, but also for DBU and TBD. In contrast, the cyclization is comparatively unattractive in the 3,4-diaminopyridine catalysts **2–4** and in **1**. We may thus speculate that, for this latter group of compounds, the concentration of zwitterionic epoxide adducts formed by the ring-opening of the substrate (Scheme 2, cycle A) may be particularly high at 100 °C due to their intrinsically high Lewis basicity as well as to their low propensity for intramolecular cyclization.

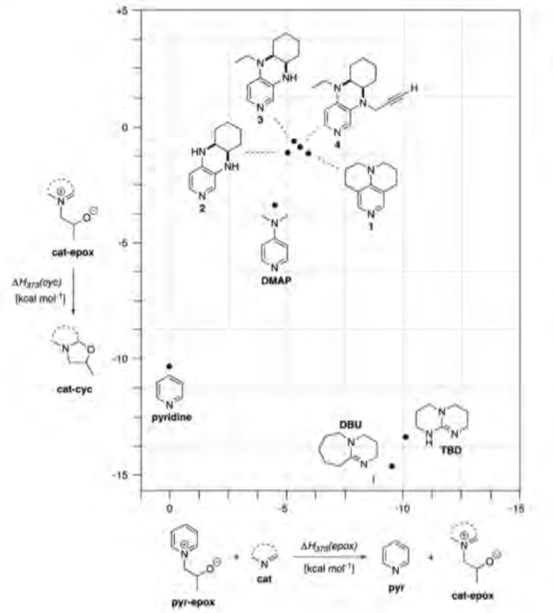

Fig. 1 Relative propylene epoxide (PO) affinities ($\Delta H_{373}(epox)$) using pyridine as the reference, and cyclization energies ($\Delta H_{373}(cyc)$) for the initially formed zwitterionic epoxide adducts. All energies have been calculated for a reaction temperature of T = 373.15 K (in kcal mol^{-1}).

Table 1 Relative propylene epoxide (PO) affinities $\Delta H_{373}(epox)$ and cyclization energies $\Delta H_{373}(cyc)$ shown pictorially in Fig. 1

Entry	Nucleophile	$\Delta H_{373}(epox)^a$ [kcal mol^{-1}]	$\Delta H_{373}(cyc)^a$ [kcal mol^{-1}]
1	Pyridine	0.0	−10.4
2	DMAP	−4.3	−3.3
3	**1**	−5.7	−1.2
4	**2**	−4.9	−1.2
5	**3**	−5.2	−0.6
6	**4**	−5.4	−1.0
7	DBU	−9.5	−14.8
8	TBD	−10.2	−13.2

[a] Calculated at the M06/TZVP PCM(PO) level of theory.

Catalytic testing

The catalytic performance of the 4-aminopyridine nucleophiles and of the reference compounds displayed in Scheme 1 was evaluated *versus* two different terminal epoxide substrates, *i.e.* styrene oxide (**5a**) and 1-hexene oxide (**5b**). The results of the latter catalytic investigation are shown in Table 2. It is possible to observe that use of pyridine (Table 2, entry 1) led to only very low epoxide conversion and no carbonate formation; the only observed products were diols (**7**) formed from the decarboxylation of cyclic carbonates under basic conditions due to the presence of traces of moisture.[93] Conversely, 4-aminopyridines displayed a more remarkable catalytic performance with compound **4** affording nearly quantitative epoxide conversion with very high selectivity for cyclic carbonates **6a** and **6b** (Table 2, entry 6).

Table 2 Catalytic investigation of *N*-nucleophiles from Scheme 1 for the cycloaddition of CO_2 to epoxides **5a** and **5b** under atmospheric CO_2 pressure[a]

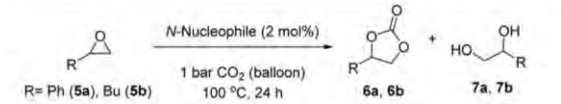

Entry	Nucleophile	Conversion[b] (%) 5a	5b	Selectivity[b,c] (%) 5a	5b
1	Pyridine	26	3	86	—
2	DMAP	50	16	90	84
3	**1**	66	81	85	95
4	**2**	75	69	93	92
5	**3**	87	70	93	93
6	**4**	93	99	95	95
7	**4′**	84	67	88	89
8	DBU	15	12	78	79
9	TBD	38	15	82	82

[a] Epoxide (16.6 mmol), nucleophile (0.332 mmol, 2 mol%) at 100 °C, 1 bar CO_2 (balloon) for 24 h, solventless. [b] Determined by ^1H NMR (see section S4 of the ESI and Fig. S17–S35†). [c] Refers to the selectivity for cyclic carbonates (**6**) *versus* 1,2-diols (**7**).

In general, the catalytic activity of 4-aminopyridines increased in the order DMAP < **2** < **3** < **4**, whereas, the performance of 9-azajulolidine was less predictable and depended on the epoxide substrate used but was generally lower than that of **4** (Table 2, entries 3 and 6). These results are in line with the predicted epoxide-specific carbon basicities of nucleophiles listed in Table 1 (pyridine ≪ DMAP < **2** < **3** < **4**) whereas the catalytic activity of **1** was lower than expected based on its carbon basicity that was slightly higher than that of **4** (*cf.* Table 1, entries 3 and 6). As the propargyl side chain of **4** was specifically introduced in view of its immobilization (*vide infra*), we also tested an analogous compound where the propargyl moiety was replaced by an ethyl group (**4′**, see the ESI†).[84] The performance of **4′** (Table 1, entry 7) was slightly lower than that of **4** and close to that of compound **3** showing that the presence of the propargyl group was not detrimental to the catalytic activity of the 3,4-diaminopyridino scaffold and had, instead, a beneficial effect likely by tuning the electronic properties of the nucleophile.

Finally, nucleophiles DBU and TBD (Table 2, entries 8 and 9) did not perform well under the applied reaction conditions when compared to most 4-aminopyridine species with low epoxide conversions and relatively low carbonate selectivities. This result is in agreement with the trend displayed in Fig. 1, where unimolecular deactivation of the nucleophiles might occur and with previous experimental results where low to moderate epoxide conversions were observed using higher nucleophile loading under identical conditions.[94] Nevertheless, it should also be considered that compounds such as TBD and DBU, known for interacting directly with CO$_2$,[95] might act as catalysts through a different mechanistic pathway (cycle B of Scheme 2, vide infra).[94] Prompted by the promising catalytic activity displayed by **4** in Table 2, we explored the scope of this nucleophile for the conversion of several terminal epoxide substrates under atmospheric pressure (Table 3). In general, quantitative conversions of the epoxide substrates were observed with high selectivities for carbonate products **6a–g** that could be isolated by column chromatography (see ^{1}H NMR spectra in Fig. S57–S70 of the ESI†). In the case of epoxide **5h**, despite complete epoxide conversion, the target carbonate **6h** could be isolated in only moderate yields (Table 3, entry 8) because of the formation of several by-products, possibly due to the nucleophilic attack of diol **7h** on carbonate **6h** with formation of glycerol carbonate (GC) and other by-products (Scheme S3 of the ESI†). This observation is supported by the compounds and molecular fragments identified by mass spectrometry (Fig. S44†) and by the presence of a second cyclic carbonate signal at 155.4 ppm in the ^{13}C NMR of the reaction mixture (Fig. S43†) attributed to the C═O carbon of GC.[96] Such reaction is very likely to be accelerated by the presence of **4** as this kind of aminopyridines are excellent esterification catalysts.[90] Slightly higher **6h** selectivity could be obtained at 60 °C, 5 bar CO$_2$ pressure, however, under such conditions, incomplete epoxide selectivity was observed further limiting the isolated yield of **6h**.

Table 3 Catalytic performance of nucleophilic catalyst **4** for the conversion of several terminal epoxides under atmospheric pressure[a]

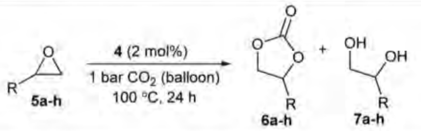

Entry	Substrate	Conversion[b] (%)/ Selectivity for **6**[b] (%)	Yield[c] (%)
1	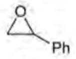 **5a**	93/95	80
2	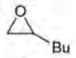 **5b**	99/95	93
3	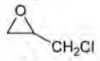 **5c**	99/93	86
4	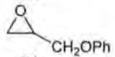 **5d**	>99/97	89
5	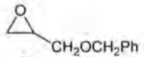 **5e**	>99/93	78
6	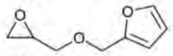 **5f**	>99/97	83
7	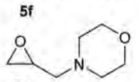 **5g**	>99/96	87
8	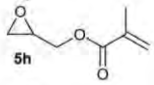 **5h**	>99/n.d.[d] 69/54[e]	39 27[e]

[a] Epoxide (16.6 mmol), **4** (0.332 mmol, 2 mol%) at 100 °C, 1 bar CO$_2$ (balloon) for 24 h, solventless. [b] Conversion and selectivity determined by ^{1}H NMR. [c] Isolated yields of carbonate products after column chromatography. [d] The selectivity for **6h** *versus* **7h** could not be determined because of the presence of additional by-products. [e] At 60 °C, 5 bar CO$_2$.

The ability of nucleophile **4** to promote the cycloaddition of CO$_2$ to epoxides **5b** and **5d** under several reaction conditions was explored by studying the dependence of epoxide conversion and selectivity on the reaction temperature (Fig. 2). It is possible to observe that, at ambient pressure, more reactive epoxide **5d** was partially converted to the target carbonate already at 70–80 °C whereas 1-hexene oxide (**5b**) was not reactive under identical conditions. In both cases a temperature of 100 °C was necessary to achieve quantitative and selective epoxide conversion to the carbonate products. Similarly, when studying the dependence of epoxide conversion at 100 °C and atmospheric CO$_2$ pressure on reaction time (Fig. 3), epoxide **5d** displayed a good degree (77%) of conversion to **6d** after just 6 h, whereas **5b** afforded just moderate conversion in the same period. In both cases, a reaction time of 24 h was necessary to afford complete conversion of the epoxide with the selectivity for the carbonate product being only marginally affected by the reaction time.

As a further crucial parameter, we studied the dependency of the catalytic performance of **4** on CO$_2$ pressure. In Table 4, entries 1 and 2 it is possible to observe that by increasing the CO$_2$ pressure from atmospheric to 5 bar the conversion of **5d** in 6 h increased from 77% to 98% with no change in selectivity for **6d**. However, a further increase in pressure did not lead to a complete disappearance of the substrate (Table 4, entries 3 and 4). To note, when using 5 bar CO$_2$ pressure, complete conversion of **5d** could be achieved at 80 °C in 24 h (Table 4, entry 5). As the catalyst comparison in Table 2 was carried out under atmospheric pressure, and could be potentially affected by low

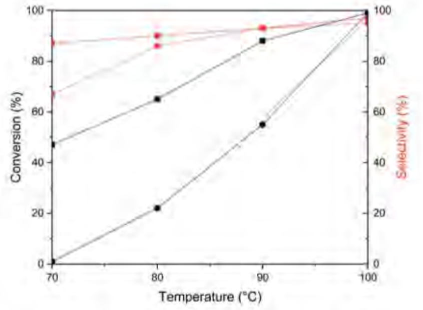

Fig. 2 Conversion (black) and selectivity (red) of the cycloaddition reaction of CO$_2$ to 1-hexene oxide (**5b**, ●) and glycidyl phenyl ether (**5d**, ■) at different temperatures (catalyst: **4** (2 mol%); P_{CO_2} = 1 bar; 24 h).

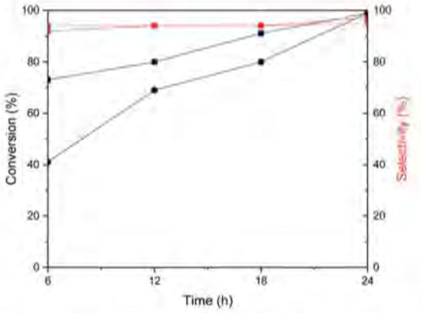

Fig. 3 Conversion (black) and selectivity (red) of the cycloaddition of CO_2 to 1-hexene oxide (**5b**, ●) and glycidyl phenyl ether (**5d**, ■) for different reaction times (catalyst: **4** (2 mol%); P_{CO2} = 1 bar; 100 °C).

Table 4 Effect of CO_2 pressure on the cycloaddition reaction of CO_2 to **5d** catalyzed by 4-aminopyridine catalysts[a]

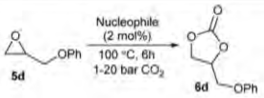

Entry	Nucleophile	P_{CO_2} (bar)	Conversion[b] (%)	Selectivity[b] (%)
1	**4**	1	77	92
2	**4**	5	98	92
3	**4**	10	97	92
4	**4**	20	96	93
5[c]	**4**	5	99	94
6	DMAP	5	91	94
7	**1**	5	90	94
8	**2**	5	90	89
9	**3**	5	89	89

[a] Epoxide (16.6 mmol), nucleophile (0.332 mmol, 2 mol%) at 100 °C, CO_2 pressure as indicated for 6 h, solventless. [b] Conversion and selectivity determined by ^{1}H NMR. [c] At 80 °C, 5 bar CO_2 for 24 h.

CO_2 solubility and diffusion into the initial epoxide medium, we carried out a new comparison of catalysts at 5 bar (Table 4, entries 2 and 6–9). Whereas all aminopyridine catalysts (DMAP, **1–3**) performed well, the highest **5d** conversion was still observed for compound **4**.

In order to further explore the potential of catalyst **4** we attempted the carbonation of internal epoxides such as cyclohexene oxide and epoxidized methyl oleate (EMO, Table S2†). In the case of cyclohexene oxide we observed low conversion (<20%) of the starting material to the carbonate at 100° C under atmospheric CO_2 pressure (Table S2, entry 1†). Increasing the CO_2 pressure to 20 bar led to moderate epoxide conversion but the ^{1}H NMR of the reaction mixture displayed the presence of several products (Fig. S45†) possibly including polymeric material and the desired carbonate was isolated in low yields (Table S2, entry 2†). In the case of methyl oleate (Table S2, entries 3 and 4†), we did not observe any formation of carbonates at atmospheric pressure or at 20 bar. Overall, these data confirm the difficulty of producing internal cyclic carbonates from internal epoxides by using halogen-free single-component organocatalysts.[62–64,68]

Nevertheless, nucleophile **4** could catalyze the synthesis of internal cyclic carbonates from hydroxyl-functionalized internal epoxides and from amino functionalized epoxides (Scheme 3). For instance, the cycloaddition of CO_2 to **5k**[97] using 2 mol% **4** in acetonitrile (Scheme 3A) proceeded with quantitative epoxide conversion (Fig. S46†) to afford exclusively cyclic carbonates **6ka** and **6kb** under relatively mild conditions (60 °C, 20 bar CO_2). The higher selectivity for **6kb**, that could be isolated in good yields after column chromatography, indicates the occurrence of a Payne-type rearrangement in which **4** had, principally, the role of a base in shuttling the proton of the initial epoxy alcohol to the product.[72] To the best of our knowledge, a single previous metal- and halogen-free attempt to carry out the synthesis of **6ka** and **6kb** from **5k** and CO_2 was reported. Kleij *et al.* showed that 10 mol% DMAP provided only moderate conversions of **5k** at similar reaction temperature as in our case (45 °C) but higher CO_2 pressure (30 bar) in methyl ethyl ketone albeit with high selectivity for **6kb**.[72] Under identical conditions as DMAP, 10 mol% DBU and TBD provided quantitative conversion of **5k** with TBD being the most selective for **6kb** (**6ka**/**6kb**, 1 : 9) but with lower overall carbonate selectivity than observed in our case using 2 mol% **4**. As a different epoxy alcohol we considered epoxidized methyl ricinoleate (**5l**, Scheme 3B). Using 2 mol% **4** at 100 °C in a solventless reaction under atmospheric pressure, **5l** could be efficiently converted to carbonate **6la** with the formation of minor amounts of cyclic ether **6lb** from intramolecular cyclization (Fig. S47†). Importantly, **6la** was obtained mainly as the *trans*-isomer indicating inversion of configuration at one of the epoxide carbon atoms. Given the lack of activity of **4** for the carbonation of hydroxyl-free fatty acid EMO, it is expected that the formation of **6la** might proceed with a mechanism comparable to that discussed for the formation of **6kb** with **4** shuttling the proton from the hydroxyl moiety to the product; such process involves a single inversion of configuration by an S_N2 mechanism leading to the trans-isomer.[28] Whereas this process should lead to a 6-membered cyclic carbonate, it is expected that such compound might rearrange into the final 5-membered carbonate **6la** by an intramolecular rearrangement as proposed by Kleij *et al.* when using an aluminum triphenolate complex for the synthesis of **6a**.[28] Interestingly, to the best of our knowledge, our approach to the synthesis of **6la** in Scheme 3B is the first to take place under atmospheric CO_2 pressure and by using halogen- and metal-free catalysts. Overall, the reactions in Scheme 3A and B show that **4** is a competent catalyst for the synthesis of cyclic carbonates from epoxy alcohols, albeit through a "non-traditional" mechanism of proton shuttling rather than by the usually observed epoxide ring opening.[72] Finally, we turned our attention to the use of epoxy amines **5m** and **5n** that, in the cycloaddition reaction with CO_2 (Scheme 3C), could respectively afford either carbonates **6ma** and **6na** (by the "traditional" cycloaddition mechanism), or carbonates **6mb** and **6nb** by initial coordination of CO_2 to the nitrogen atom and H-transfer to **4**.[97,98] As

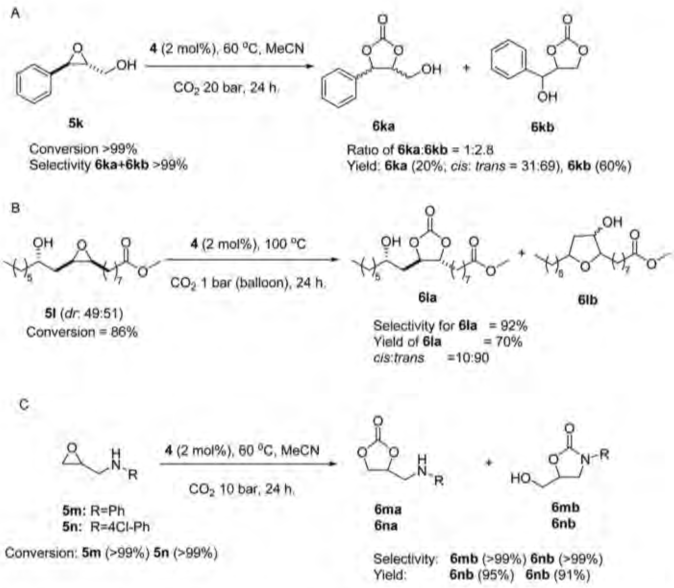

Scheme 3 Cycloaddition of CO_2 to hydroxyl-functionalized internal epoxides and to amino-functionalized epoxides catalyzed by **4**.

in the case of epoxy alcohols **5k** and **5l**, we selectively obtained carbonates **6mb** and **6nb** (Fig. S48 and S49†) under mild conditions (60 °C, 10 bar CO_2 in MeCN) that were isolated in very high yields by using just 2 mol% **4**. As far as we are aware, this was the first organocatalytic (and halogen-free) approach to the reaction in Scheme 3C.

Mechanistic experiments

^{13}C NMR and *in situ* IR experiments were carried out to clarify the reaction mechanism of the cycloaddition reaction catalyzed by **4** with respect to the possible catalytic cycles displayed in Scheme 2. We initially looked into the ^{13}C NMR spectra of reaction mixtures generated by the addition of atmospheric CO_2 to $CDCl_3$ solutions of nucleophiles such as DMAP and **4** along with TBD and DBU as reference compounds (section S7†). When CO_2 was added to solutions of DBU or TBD the formation of white precipitates was observed in both cases in line with the previously reported formation of insoluble DBU-CO_2 and TBD-CO_2 adducts.[95] However, when the same experiments were carried out by using DMAP or **4** no precipitates were observed as well as no new signals in the ^{13}C NMR of the solutions apart for a peak at 125 ppm relative to CO_2 dissolved in $CDCl_3$ (Fig. S54 and S55†). These experiments indicate that, differently from the cases of DBU and TBD, there was no strong detectable interaction between pyridine nucleophiles and CO_2 in the solution phase at atmospheric pressure. To gain further insight, *in situ* IR studies were carried out using solutions of **4** in epoxide **5b** at 100 °C (section S8 of the ESI†). The *in situ* IR spectrum of the solution in 1545–1600 cm^{-1} (Fig. S56a†) initially displayed only a signal at 1585 cm^{-1} attributed to one of the C=C stretching modes of the pyridine ring and also observed in the FT-IR spectrum of pure **4** (Fig. S56b†).[99] Within 1 h, we observed the appearance of a new strong signal at 1645 cm^{-1} attributed to the C=C ring stretching of a pyridinium moiety[100] as expected for the formation of the adduct of ring-opening of the epoxide by the nucleophilic nitrogen atom (Scheme 1, cycle A and Fig. S56c†).[101,102] Additionally, the peak initially centered at 1585 cm^{-1} was replaced by a new signal centered at 1577 cm^{-1}. By the addition of CO_2, the formation of cyclic carbonate was observed by a peak at 1814 cm^{-1} (Fig. S56d†) along with the appearance of a new signal at 1680 cm^{-1} analogous to that observed for the $\nu_{C=O}$ stretching in metal-coordinated hemicarbonates formed by the reaction of ring-opened epoxides (*i.e.* alkoxides) with CO_2 as expected for step **IIA** of cycle A in Scheme 1.[102] Taken together these observations corroborate a mechanistic picture where **4** acts in carbonation of terminal epoxides according to cycle A of Scheme 1 and not by the initial coordination of CO_2.

Heterogenization of compound 4

Based on the promising catalytic activity of nucleophile **4** in the cycloaddition of CO_2 to terminal epoxides, we immobilized this compound on azide-functionalized MR using the copper-catalyzed alkyne–azide click reaction to afford **4@MR** (see section S2 of the ESI† for heterogenization procedure and Fig. S1–S4† for characterization of **4@MR**) following a previously developed protocol.[90] The click reaction between **4** and azide-functionalized MR (MR-N_3) led to the complete disappearance of the azide-related IR stretching band at 2093 cm^{-1} in Fig. S1† as expected for the formation of a triazole moiety. The presence of the scaffold of **4** in **4@MR** was confirmed by the presence of peaks at 1586, 1516, 1201, 1076 cm^{-1} also found in the FT-IR spectrum of **4**. A peak at 2095 cm^{-1}, relative to the C≡C stretching of **4**, was obviously not found in **4@MR** confirming that the heterogenization of **4** took place *via* click reaction. Elemental analysis showed the presence of 6.47% nitrogen (**4** loading 0.77 mmol g^{-1}) in **4@MR** that was higher than 5.66% nitrogen observed for MR-N$_3$ as an effect of the additional nitrogen atoms in the 3,4-diaminopyridine scaffold. SEM investigation of the morphology of the polystyrene beads of MR (Fig. S3†) showed that the reaction with NaN$_3$ to prepare MR-N$_3$, preserved the spherical morphology of the material whereas it slightly increased the rugosity of the beads surface. The morphologies of MR-N$_3$ and **4@MR** were very similar. Finally, SEM-EDS analysis of **4@MR** showed a homogeneous distribution of nitrogen on the surface of the material (Fig. S4†). The thus synthesized heterogeneous catalyst was tested for the cycloaddition of CO$_2$ to several epoxides (**5a–5f**) as shown in Table 5. Importantly, by comparing the results in Table 3, entries 1–6 with those in the corresponding entries of Table 5, it is possible to observe that the heterogenization of **4** did not generally lead to a significant drop in catalytic performance when compared to its homogeneous counterpart.

Table 5 Application of heterogeneous **4@MR** for the cycloaddition of CO$_2$ to epoxide under atmospheric CO$_2$ pressure[a]

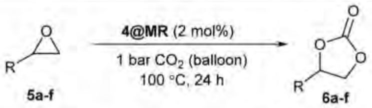

Entry	Substrate	Conversion[b] (%)/Selectivity for **6**[b] (%)
1	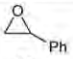 **5a**	85/94
2	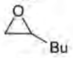 **5b**	Run 1: 64/>99 Run 2: 64/>99 Run 3: 63/>99 Run 4: 63/>99
2b		Run 1: 97/>99[c] Run 2: >99/98[c] Run 3: >99/99[c] Run 4: >99/98[c]
3	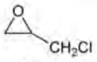 **5c**	>99/95
4	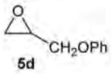 **5d**	Run 1: >99/96 Run 2: >99/96 Run 3: >99/95 Run 4: >99/96
5	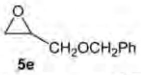 **5e**	95/93
6	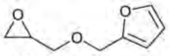 **5f**	97/96

[a] Epoxide (4.2 mmol), **4@MR** (107.8 mg, 0.084 mmol **4**, 2 mol%) at 100 °C, 1 bar CO$_2$ (balloon) for 24 h, solventless. [b] Conversion and selectivity determined by ^{1}H NMR. [c] Using 215.6 mg **4@MR** (4 mol% **4**).

Indeed, for almost all epoxides, except **5b** (Table 5, entry 2), the observed conversions obtained for **4@MR** were only slightly lower, if not identical, to those obtained for **4**. In the case of **5b**, quantitative epoxide conversion to carbonate **6b** could be achieved when increasing the catalyst loading to 4 mol% (Table 5, entry 2b). To note, **4@MR** could be easily recovered from the reaction mixture by filtration and recycled for the cycloaddition of CO$_2$ to **5b** maintaining almost unchanged catalytic performance at the fourth reaction cycle (Table 5, entry 2). The recyclability of **4@MR** was not affected when using a higher loading of catalyst (Table 5, entry 2b) or a different epoxide (**5d**, Table 3, entry 4). Overall, these data show that the immobilization of **4** on MR affords a rare example of metal and halogen-free catalyst with the ability to promote the cycloaddition of CO$_2$ to several epoxides under atmospheric pressure.[103] In this context, the performance of **4@MR** is comparable to that of other excellent, but halogen-based, single-component heterogeneous organocatalysts recently reported in the literature operating at around 80 °C and in the 1–10 bar pressure range.[104–106] Nevertheless, it should be noted that the preparation of **4** and its functionalization for immobilization on MR to afford **4@MR** involved multiple synthetic steps. In comparison, Kleij, Pericàs *et al.* reported a halide-based heterogeneous catalyst for the cycloaddition of CO$_2$ to epoxides under mild conditions (45 °C, 10 bar, 18 h) that could be afforded in just four synthetic steps from commercially available 3,4,5-trimethoxyphenylacetic acid.[107] Therefore, future efforts on the synthesis of halide-free aminopyridine-based heterogeneous catalysts should focus on minimizing the number of synthetic steps to afford more readily available and cost-competitive designs.

DFT Investigation of the mechanism of CO$_2$ cycloaddition to epoxides

Two possible catalytic pathways for single component nucleophilic catalysts (**Nu**), along with expected reaction intermediates (**I1–I5**), are shown in Scheme 2. Each step is expected to proceed through the corresponding transition state (**TS**). In cycle **A**, that is analogous to the cycloaddition mechanism catalyzed by halide anions in the absence of Lewis acids or HBDs,[108,109] the use of strong nucleophiles could facilitate the often crucial step of epoxide ring opening (**IA**) leading to faster reaction rates under the *caveat* that the leaving group ability of the nucleophilic catalyst would allow the final step of carbonate ring-closure (**IIIA**), located after CO$_2$ insertion (**IIA**), to proceed with reasonable energy barriers. On the other hand, based on the ability of nucleophilic compounds such as DBU,[110] TBD (triazabicyclodecene),[95] and N-heterocyclic carbenes[111] to activate and coordinate CO$_2$, an alternative mechanism pathway could be proposed for single-component nucleophilic catalysts involving the initial formation of an adduct between the nucleophile and CO$_2$ (step **IB**). The latter intermediate would subsequently open the epoxide substrate (step **IIB**) and lead to the final product after cyclization (step **IIIB**).[91,112–115] Also in the latter pathway, the use of a strong nucleophile could improve the efficiency of the step of CO$_2$

capture or increase the electron density of the Nu-CO_2 adduct for the attack on the epoxide. In the case of aminopyridines, but limited to the case of DMAP, the mechanism in cycle **A** was found to be favored in the presence of phenols[58] or metal-based Lewis acids.[36,102,116] Nevertheless, CO_2 activation by the pyridine nitrogen has also been proposed in some cases.[117] Therefore, DFT Calculations (B3LYP-D3/TZVP(smd)//BP86-D3/TZVP level) were performed on selected nucleophiles to gain further insight into the reaction mechanism of CO_2 cycloaddition and to investigate the reaction barriers for the different nucleophiles.

For the sake of simplicity, we used propylene oxide (PO) as the substrate (Fig. 4). Calculations on styrene oxide (**5a**, Fig. S85†) for the step of epoxide ring-opening (**IA**) at the same carbon atom showed no significant differences between PO and **5a**. Our calculations show that the reaction of PO with CO_2 to give the corresponding cyclic carbonate was exergonic by 1.2 kcal mol^{-1}. The reaction barriers for the mechanistic pathway relative to cycle A of Scheme 2 starting with epoxide ring opening by the nucleophile are reported in Fig. 4. The reaction barriers for the pathway initiated by the interaction of the nucleophile and CO_2 prior to the epoxide opening (cycle B in Scheme 2) are shown in the ESI (section S11†) and compared with the results for cycle A for each nucleophile (Fig. S86–S89†).

The comparison of both pathways shows that the reaction barriers in cycle B were always more energy demanding than in cycle A. It was also possible to observe that for all pyridine-based nucleophiles the formation of the adduct of coordination of CO_2 (**I3**) was thermodynamically disfavored (by 6.9 kcal mol^{-1} for the case of **4**) whereas it was strongly favored by 23.8 kcal mol^{-1} for the case of TBD (Fig. S89†). Structurally, for the case of TBD, we observed the formation of a N–C bond (1.603 Å), whereas for **4** the N⋯C interaction had a non-covalent character (2.655 Å). These results agree with the fact that a CO_2 adduct of **4** and DMAP could not be observed by NMR under atmospheric CO_2 pressure whereas, in the case of TBD, direct precipitation of the TBD-CO_2 adduct was observed. Based on these data, it is proposed that pyridine and aminopyridines follow the less energy-demanding mechanistic pathway highlighted in cycle A of Scheme 2 whereas TBD, despite milder calculated reaction barriers when acting as a catalyst through cycle A, would form a strong adduct with CO_2 and proceed through the less kinetically favored cycle B leading to lower catalytic performance (Table 2, entries 6 and 8).

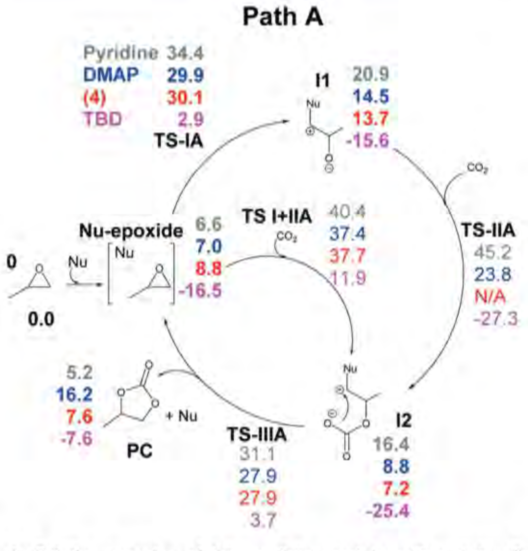

Fig. 4 Relative energies of intermediates and transition states (kcal mol^{-1}) for the cycloaddition of CO_2 to PO catalyzed by several nucleophiles; color code: pyridine grey; DMAP blue; **4** red; TBD pink. Energies shown in kcal mol^{-1}. PC: propylene carbonate.

Focusing on the mechanism of the cycloaddition reactions according to cycle A of Scheme 2 for pyridine derivatives in Fig. 4 (pyridine, DMAP and **4**), the step of epoxide ring-opening (**IA**) resulted as the rate determining step for DMAP and **4** whereas the step of CO_2 activation (**IIA**) by the alkoxide was the most energy demanding for pyridine (45.2 kcal mol^{-1}). This result is substantially in agreement with the low catalytic performance of this nucleophile in the cycloaddition of CO_2 to epoxides (Table 2). Independent of the epoxide (Fig. 2 and Fig. S85†), pyridine also displayed the highest reaction barrier (34.4 kcal mol^{-1} for PO) for epoxide ring-opening that is in line with its lower carbon basicity (Fig. 1 and Table 1). When comparing DMAP and **4**, nearly identical barriers were found for the rate-determining step of epoxide ring opening using PO as the substrate (29.9 kcal mol^{-1} for DMAP *versus* 30.1 kcal mol^{-1} for **4**) whereas the ring opening of **5a** (Fig. S85†) implied a slightly higher barrier for DMAP (32.6 kcal mol^{-1} *versus* 31.9 kcal mol^{-1} for **4**); indeed **4** was a more efficient catalyst than DMAP when using **5a** as the substrate (Table 2, entries 2 and 6) although the difference in the ring-opening barriers was smaller than expected. To note, the latter nucleophiles displayed moderate reaction barriers for the other steps of the mechanism in Fig. 2 with the step of CO_2 activation requiring a barrier of 9.3 kcal mol^{-1} for DMAP. The analogous transition state (**TS-IIA**) could not be located for **4**, however, the decreasing trend for this barrier with increasing catalyst nucleophilicity (24.3 for pyridine *versus* 9.3 for DMAP) suggests a moderate CO_2 activation barrier for **4**. The final ring closure barrier (step **IIIA**) was 19.1 kcal mol^{-1} for DMAP and 20.7 kcal mol^{-1} for **4**. We have also analyzed a trimolecular step through transition state **TS-I + IIA** where epoxide ring-opening takes place along with the activation of CO_2. However, this process was found to be disfavored by at least 6.0 kcal mol^{-1} for all nucleophiles tested and ruled out. Overall, the DFT calculations displayed in Fig. 4 support a cycloaddition mechanism as that represented in cycle A of Scheme 2 for aminopyridine catalysts, in agreement with experimental evidence, however, they do not capture the difference of performance observed between **4** and DMAP in Table 2. Considering that the results in Table 2 were carried out at low CO_2 concentrations and that the results in Table 4 show that, at a higher pressure, the performance of the other aminopyridine catalysts was closer to that of **4**, it could be assumed that CO_2 concentration plays a role in the different catalytic performance observed at atmospheric pressure. In this context, a limitation of the DFT approach is that it treats CO_2 as a highly available liquid reagent in solution and, therefore, it provides results that are more comparable with experiments carried out at higher pressure. Nevertheless, besides the carbon basicity calculations reported in Fig. 1 and Table 1, the different performance for the pyridine-based nucleophiles could also be rationalized from an electronic point of view. Accordingly, DFT calculations show that pyridine is much less nucleophilic according to the Parr electrophilicity[118,119] than **4** (0.051 *vs.* 0.030 h), with DMAP having an intermediate electrophilicity (0.034 h). Chemical hardness[120,121] can also justify the different catalytic behavior, with values of 0.200, 0.216, and 0.247 h, for **4**, DMAP, and pyridine, respectively, that are in a good qualitative agreement with the experimental conversions reported in Table 2,[122] since of the three nucleophiles the pyridine is the one that has less tendency to react.[123]

Conclusions

In the search for single-component and halogen-free organocatalysts for the cycloaddition of CO_2 to epoxides under ambient pressure, we focused on highly nucleophilic 3,4-diaminopyridines that were not previously explored for this reaction. The application of the latter class of catalysts was supported by predictive carbon basicity calculations suggesting higher tendency to ring-open the epoxide substrate than standard pyridine-based nucleophiles such as DMAP. Therefore, we tested 3,4-diaminopyridines, along with other reference *N*-nucleophiles, in the cycloaddition of CO_2 to terminal epoxides **5a** and **5b** reporting high catalytic conversions and carbonate selectivities for 3,4-diaminopyridine **4**. The latter compound could be successfully applied to the cycloaddition of CO_2 to several other terminal epoxides under atmospheric pressure and also to the selective conversion of hydroxyl- and amino-functionalized internal epoxides to the corresponding carbonates. Importantly, **4** could be readily heterogenized on modified Merrifield resin (**4@MR**) and applied as a recoverable and recyclable catalyst for the carbonation of epoxides with no apparent loss of catalytic performance that was comparable to that of its molecular counterpart. The catalytic mechanism of the cycloaddition reaction of CO_2 to epoxides was studied by a combination of mechanistic experiments and DFT calculations; our results support a pathway where pyridine-based nucleophiles initially interact with the epoxide rather than with CO_2 being this conclusion at variance with what observed for other widely applied *N*-nucleophiles such as DBU and TBD that strongly interact with CO_2. Overall, this work demonstrates that highly nucleophilic aminopyridines hold significant potential as new, efficient halogen-free organocatalysts for the cycloaddition of CO_2 to epoxides and we expect that this work will inspire the design of new homogeneous and heterogeneous halogen-free organocatalysts. In this context, the application of even more nucleophilic,[82,83] recently developed aminopyridines appears highly promising and is currently under investigation.

Conflicts of interest

There are no conflicts to declare.

Acknowledgements

V. D. E. thanks the Thailand Research Fund (Grant No. RSA6080059) for funding this research. C. P. acknowledges financial support through a postdoctoral fellowship from the Vidyasirimedhi Institute of Science and Technology. J. A. L. U. thanks Universitat de Girona for an IFUdG2017 Ph.D. fellowship. A. P. is a Serra Húnter Fellow. A. P. and M. S. thank the Ministerio de Economía y Competitividad (MINECO) of Spain for projects CTQ2014-59832-JIN, PGC2018-097722-B-I00 and CTQ2017-85341-P; Generalitat de Catalunya for project 2017SGR39, Xarxa de Referència en Química Teòrica i Computacional, and ICREA Academia prize 2014 to M. S. and 2019 to A. P.

Notes and references

1 C. Yan, Y.-X. Yao, X. Chen, X.-B. Cheng, X.-Q. Zhang, J.-Q. Huang and Q. Zhang, Lithium Nitrate Solvation Chemistry in Carbonate Electrolyte Sustains High-Voltage Lithium Metal Batteries, *Angew. Chem., Int. Ed.*, 2018, **57**, 14055–14059.
2 M. Sathish, K. J. Sreeram, J. Raghava Rao and B. Unni Nair, Cyclic Carbonate: A Recyclable Medium for Zero Discharge Tanning, *ACS Sustainable Chem. Eng.*, 2016, **4**, 1032–1040.
3 S. B. Lawrenson, R. Arav and M. North, The greening of peptide synthesis, *Green Chem.*, 2017, **19**, 1685–1691.
4 M. North and P. Villuendas, A Chiral Solvent Effect in Asymmetric Organocatalysis, *Org. Lett.*, 2010, **12**, 2378–2381.
5 J. E. Gómez, À. Cristòfol and A. W. Kleij, Copper-Catalyzed Enantioselective Construction of Tertiary Propargylic Sulfones, *Angew. Chem., Int. Ed.*, 2019, **58**, 3903–3907.
6 K. Guo and A. W. Kleij, Cu-Catalyzed Synthesis of Tetrasubstituted 2,3-Allenols through Decarboxylative Silylation of Alkyne-Substituted Cyclic Carbonates, *Org. Lett.*, 2020, **22**, 3942–3945.
7 W. Guo, J. E. Gómez, À. Cristòfol, J. Xie and A. W. Kleij, Catalytic Transformations of Functionalized Cyclic Organic Carbonates, *Angew. Chem., Int. Ed.*, 2018, **57**, 13735–13747.
8 B. Grignard, S. Gennen, C. Jérôme, A. W. Kleij and C. Detrembleur, Advances in the use of CO_2 as a renew-

able feedstock for the synthesis of polymers, *Chem. Soc. Rev.*, 2019, **48**, 4466–4514.

9 N. Yadav, F. Seidi, D. Crespy and V. D'Elia, Polymers Based on Cyclic Carbonates as Trait d'Union Between Polymer Chemistry and Sustainable CO_2 Utilization, *ChemSusChem*, 2019, **12**, 724–754.

10 F. D. Bobbink, A. P. van Muyden and P. J. Dyson, En route to CO_2-containing renewable materials: catalytic synthesis of polycarbonates and non-isocyanate polyhydroxyurethanes derived from cyclic carbonates, *Chem. Commun.*, 2019, **55**, 1360–1373.

11 N. Yadav, F. Seidi, S. Del Gobbo, V. D'Elia and D. Crespy, Versatile functionalization of polymer nanoparticles with carbonate groups via hydroxyurethane linkages, *Polym. Chem.*, 2019, **10**, 3571–3584.

12 F. Monie, B. Grignard, J.-M. Thomassin, R. Mereau, T. Tassaing, C. Jerome and C. Detrembleur, Chemo– and regio–selective additions of nucleophiles to cyclic carbonates for the preparation of self–blowing non–isocyanate polyurethane foams, *Angew. Chem.*, 2020, **59**, 17033–17041.

13 J. Artz, T. E. Müller, K. Thenert, J. Kleinekorte, R. Meys, A. Sternberg, A. Bardow and W. Leitner, Sustainable Conversion of Carbon Dioxide: An Integrated Review of Catalysis and Life Cycle Assessment, *Chem. Rev.*, 2017, **118**, 434–504.

14 N. A. Tappe, R. M. Reich, V. D'Elia and F. E. Kühn, Current advances in the catalytic conversion of carbon dioxide by molecular catalysts: an update, *Dalton Trans.*, 2018, **47**, 13281–13313.

15 S. Dabral and T. Schaub, The Use of Carbon Dioxide (CO_2) as a Building Block in Organic Synthesis from an Industrial Perspective, *Adv. Synth. Catal.*, 2019, **361**, 223–246.

16 Q.-W. Song, Z.-H. Zhou and L.-N. He, Efficient, selective and sustainable catalysis of carbon dioxide, *Green Chem.*, 2017, **19**, 3707–3728.

17 L. Song, Y.-X. Jiang, Z. Zhang, Y.-Y. Gui, X.-Y. Zhou and D.-G. Yu, CO_2=CO+[O]: recent advances in carbonylation of C–H bonds with CO_2, *Chem. Commun.*, 2020, **56**, 8355–8367.

18 C.-K. Ran, X.-W. Chen, Y.-Y. Gui, J. Liu, L. Song, K. Ren and D.-G. Yu, Recent advances in asymmetric synthesis with CO_2, *Sci. China: Chem.*, 2020, **63**, 1336–1351.

19 C. C. Truong and D. K. Mishra, Catalyst-free fixation of carbon dioxide into value-added chemicals: a review, *Environ. Chem. Lett.*, 2020, DOI: 10.1007/s10311-020-01121-7.

20 C. Martín, G. Fiorani and A. W. Kleij, Recent Advances in the Catalytic Preparation of Cyclic Organic Carbonates, *ACS Catal.*, 2015, **5**, 1353–1370.

21 H. Büttner, L. Longwitz, J. Steinbauer, C. Wulf and T. Werner, Recent Developments in the Synthesis of Cyclic Carbonates from Epoxides and CO_2, *Top. Curr. Chem.*, 2017, **375**, 50.

22 J. W. Comerford, I. D. V. Ingram, M. North and X. Wu, Sustainable metal-based catalysts for the synthesis of cyclic carbonates containing five-membered rings, *Green Chem.*, 2015, **17**, 1966–1987.

23 R. R. Shaikh, S. Pornpraprom and V. D'Elia, Catalytic Strategies for the Cycloaddition of Pure, Diluted, and Waste CO_2 to Epoxides under Ambient Conditions, *ACS Catal.*, 2018, **8**, 419–450.

24 X.-D. Lang and L.-N. He, Green Catalytic Process for Cyclic Carbonate Synthesis from Carbon Dioxide under Mild Conditions, *Chem. Rec.*, 2016, **16**, 1337–1352.

25 M. Cokoja, M. E. Wilhelm, M. H. Anthofer, W. A. Herrmann and F. E. Kühn, Synthesis of Cyclic Carbonates from Epoxides and Carbon Dioxide by Using Organocatalysts, *ChemSusChem*, 2015, **8**, 2436–2454.

26 A. J. Kamphuis, F. Picchioni and P. P. Pescarmona, CO_2-fixation into cyclic and polymeric carbonates: principles and applications, *Green Chem.*, 2019, **21**, 406–448.

27 L. Longwitz, J. Steinbauer, A. Spannenberg and T. Werner, Calcium-Based Catalytic System for the Synthesis of Bio-Derived Cyclic Carbonates under Mild Conditions, *ACS Catal.*, 2017, **8**, 665–672.

28 L. Peña Carrodeguas, À. Cristòfol, J. M. Fraile, J. A. Mayoral, V. Dorado, C. I. Herrerías and A. W. Kleij, Fatty acid based biocarbonates: Al-mediated stereoselective preparation of mono-, di- and tricarbonates under mild and solvent-less conditions, *Green Chem.*, 2017, **19**, 3535–3541.

29 W. Natongchai, S. Pornpraprom and V. D'Elia, Synthesis of Bio–Based Cyclic Carbonates Using a Bio–Based Hydrogen Bond Donor: Application of Ascorbic Acid to the Cycloaddition of CO_2 to Oleochemicals, *Asian J. Org. Chem.*, 2020, **9**, 801–810.

30 F. De la Cruz-Martínez, M. Martínez de Sarasa Buchaca, J. Martínez, J. Fernández-Baeza, L. F. Sánchez-Barba, A. Rodríguez-Diéguez, J. A. Castro-Osma and A. Lara-Sánchez, Synthesis of Bio-Derived Cyclic Carbonates from Renewable Resources, *ACS Sustainable Chem. Eng.*, 2019, **7**, 20126–20138.

31 A. Barthel, Y. Saih, M. Gimenez, J. D. A. Pelletier, F. E. Kühn, V. D'Elia and J.-M. Basset, Highly integrated CO_2 capture and conversion: direct synthesis of cyclic carbonates from industrial flue gas, *Green Chem.*, 2016, **18**, 3116–3123.

32 M. J. Kelly, A. Barthel, C. Maheu, O. Sodpiban, F.-B. Dega, S. V. C. Vummaleti, E. Abou-Hamad, J. D. A. Pelletier, L. Cavallo, V. D'Elia and J.-M. Basset, Conversion of actual flue gas CO_2 via cycloaddition to propylene oxide catalyzed by a single-site, recyclable zirconium catalyst, *J. CO_2 Util.*, 2017, **20**, 243–252.

33 W. Zhang, F. Ma, L. Ma, Y. Zhou and J. Wang, Imidazolium–Functionalized Ionic Hypercrosslinked Porous Polymers for Efficient Synthesis of Cyclic Carbonates from Simulated Flue Gas, *ChemSusChem*, 2019, **13**, 341–350.

34 J. Steinbauer, A. Spannenberg and T. Werner, An in situ formed Ca^{2+}–crown ether complex and its use in CO_2-fixation reactions with terminal and internal epoxides, *Green Chem.*, 2017, **19**, 3769–3779.

35 M. A. Gaona, F. de la Cruz-Martínez, J. Fernández-Baeza, L. F. Sánchez-Barba, C. Alonso-Moreno, A. M. Rodríguez, A. Rodríguez-Diéguez, J. A. Castro-Osma, A. Otero and A. Lara-Sánchez, Synthesis of helical aluminium catalysts for cyclic carbonate formation, *Dalton Trans.*, 2019, **48**, 4218–4227.

36 A. Monassier, V. D'Elia, M. Cokoja, H. Dong, J. D. A. Pelletier, J.-M. Basset and F. E. Kühn, Synthesis of Cyclic Carbonates from Epoxides and CO$_2$ under Mild Conditions Using a Simple, Highly Efficient Niobium-Based Catalyst, *ChemCatChem*, 2013, **5**, 1321–1324.

37 C. Maeda, K. Ogawa, K. Sadanaga, K. Takaishi and T. Ema, Chiroptical and catalytic properties of doubly binaphthyl-strapped chiral porphyrins, *Chem. Commun.*, 2019, **55**, 1064–1067.

38 C. Maeda, S. Sasaki, K. Takaishi and T. Ema, Calix[4]pyrroles as macrocyclic organocatalysts for the synthesis of cyclic carbonates from epoxides and carbon dioxide, *Catal. Sci. Technol.*, 2018, **8**, 4193–4198.

39 P. Yingcharoen, C. Kongtes, S. Arayachukiat, K. Suvarnapunya, S. V. C. Vummaleti, S. Wannakao, L. Cavallo, A. Poater and V. D'Elia, Assessing the pKa-Dependent Activity of Hydroxyl Hydrogen Bond Donors in the Organocatalyzed Cycloaddition of Carbon Dioxide to Epoxides: Experimental and Theoretical Study, *Adv. Synth. Catal.*, 2019, **361**, 366–373.

40 S. Sopeña, E. Martin, E. C. Escudero-Adán and A. W. Kleij, Pushing the Limits with Squaramide-Based Organocatalysts in Cyclic Carbonate Synthesis, *ACS Catal.*, 2017, **7**, 3532–3539.

41 M. Alves, B. Grignard, R. Mereau, C. Jerome, T. Tassaing and C. Detrembleur, Organocatalyzed coupling of carbon dioxide with epoxides for the synthesis of cyclic carbonates: catalyst design and mechanistic studies, *Catal. Sci. Technol.*, 2017, **7**, 2651–2684.

42 Y. A. Alassmy and P. P. Pescarmona, The Role of Water Revisited and Enhanced: A Sustainable Catalytic System for the Conversion of CO$_2$ into Cyclic Carbonates under Mild Conditions, *ChemSusChem*, 2019, **12**, 3856–3863.

43 N. Liu, Y.-F. Xie, C. Wang, S.-J. Li, D. Wei, M. Li and B. Dai, Cooperative Multifunctional Organocatalysts for Ambient Conversion of Carbon Dioxide into Cyclic Carbonates, *ACS Catal.*, 2018, **8**, 9945–9957.

44 A. Kilic, E. Yasar and E. Aytar, Neutral boron [(L1-3)BPh$_2$] and cationic charged boron [(L1a-3a)BPh$_2$] complexes for chemical CO$_2$ conversion to obtain cyclic carbonates under ambient conditions, *Sustainable Energy Fuels*, 2019, **3**, 1066–1077.

45 X. Wang, L. Wang, Y. Zhao, K. Kodama and T. Hirose, Efficient and practical organocatalytic system for the synthesis of cyclic carbonates from carbon dioxide and epoxides: 3-hydroxypyridine/tetra-n-butylammonium iodide, *Tetrahedron*, 2017, **73**, 1190–1195.

46 A. W. Kleij, Advancing Halide-Free Catalytic Synthesis of CO$_2$ based Heterocycles, *Curr. Opin. Green Sustainable Chem.*, 2020, **24**, 72–81.

47 J. A. Castro-Osma, M. North and X. Wu, Development of a Halide-Free Aluminium-Based Catalyst for the Synthesis of Cyclic Carbonates from Epoxides and Carbon Dioxide, *Chem. – Eur. J.*, 2014, **20**, 15005–15008.

48 S. M. Sadeghzadeh, Heteropolyacid-based ionic liquid immobilized onto fibrous nano-silica as an efficient catalyst for the synthesis of cyclic carbonate from carbon dioxide and epoxides, *Green Chem.*, 2015, **17**, 3059–3066.

49 S. Liang, H. Liu, T. Jiang, J. Song, G. Yang and B. Han, Highly efficient synthesis of cyclic carbonates from CO$_2$ and epoxides over cellulose/KI, *Chem. Commun.*, 2011, **47**, 2131–2133.

50 M. E. Wilhelm, M. H. Anthofer, M. Cokoja, I. I. E. Markovits, W. A. Herrmann and F. E. Kühn, Cycloaddition of Carbon Dioxide and Epoxides using Pentaerythritol and Halides as Dual Catalyst System, *ChemSusChem*, 2014, **7**, 1357–1360.

51 S. Arayachukiat, C. Kongtes, A. Barthel, S. V. C. Vummaleti, A. Poater, S. Wannakao, L. Cavallo and V. D'Elia, Ascorbic Acid as a Bifunctional Hydrogen Bond Donor for the Synthesis of Cyclic Carbonates from CO$_2$ under Ambient Conditions, *ACS Sustainable Chem. Eng.*, 2017, **5**, 6392–6397.

52 S. Sopeña, G. Fiorani, C. Martín and A. W. Kleij, Highly Efficient Organocatalyzed Conversion of Oxiranes and CO$_2$ into Organic Carbonates, *ChemSusChem*, 2015, **8**, 3248–3254.

53 C. J. Whiteoak, A. Nova, F. Maseras and A. W. Kleij, Merging Sustainability with Organocatalysis in the Formation of Organic Carbonates by Using CO$_2$ as a Feedstock, *ChemSusChem*, 2012, **5**, 2032–2038.

54 O. Sodpiban, S. Del Gobbo, S. Barman, V. Aomchad, P. Kidkhunthod, S. Ould-Chikh, A. Poater, V. D'Elia and J.-M. Basset, Synthesis of well-defined yttrium-based Lewis acids by capturing a reaction intermediate and catalytic application for cycloaddition of CO$_2$ to epoxides under atmospheric pressure, *Catal. Sci. Technol.*, 2019, **9**, 6152–6165.

55 B. Zou and C. Hu, Halogen-free processes for organic carbonate synthesis from CO$_2$, *Curr. Opin. Green Sustainable Chem.*, 2017, **3**, 11–16.

56 I. D. V. Ingram, M. North and X. Wu, *Halide-Free Synthesis of Cyclic and Polycarbonates in Chemistry Beyond Chlorine*, ed. P. Tundo, L.-N. He, E. Lokteva and C. Mota, Springer International Publishing, Switzerland, 2016, pp. 413–434.

57 H. Zhou, G.-X. Wang, W.-Z. Zhang and X.-B. Lu, CO$_2$ Adducts of Phosphorus Ylides: Highly Active Organocatalysts for Carbon Dioxide Transformation, *ACS Catal.*, 2015, **5**, 6773–6779.

58 Y.-M. Shen, W.-L. Duan and M. Shi, Chemical Fixation of Carbon Dioxide Co-Catalyzed by a Combination of Schiff Bases or Phenols and Organic Bases, *Eur. J. Org. Chem.*, 2004, 3080–3089.

59 J. Sun, W. Cheng, Z. Yang, J. Wang, T. Xu, J. Xin and S. Zhang, Superbase/cellulose: an environmentally benign

catalyst for chemical fixation of carbon dioxide into cyclic carbonates, *Green Chem.*, 2014, **16**, 3071–3078.

60 Y. Qi, W. Cheng, F. Xu, S. Chen and S. Zhang, Amino acids/superbases as eco-friendly catalyst system for the synthesis of cyclic carbonates under metal-free and halide-free conditions, *Synth. Commun.*, 2018, **48**, 876–886.

61 R. A. Shiels and C. W. Jones, Homogeneous and heterogeneous 4-(N,N-dialkylamino)pyridines as effective single component catalysts in the synthesis of propylene carbonate, *J. Mol. Catal. A: Chem.*, 2007, **261**, 160–166.

62 Z. Yue, M. Pudukudy, S. Chen, Y. Liu, W. Zhao, J. Wang, S. Shan and Q. Jia, A non-metal Acen-H catalyst for the chemical fixation of CO_2 into cyclic carbonates under solvent- and halide-free mild reaction conditions, *Appl. Catal., A*, 2020, **601**, 117646.

63 X. Wu, C. Chen, Z. Guo, M. North and A. C. Whitwood, Metal- and Halide-Free Catalyst for the Synthesis of Cyclic Carbonates from Epoxides and Carbon Dioxide, *ACS Catal.*, 2019, **9**, 1895–1906.

64 W. Cho, M. S. Shin, S. Hwang, H. Kim, M. Kim, J. G. Kim and Y. Kim, Tertiary amines: A new class of highly efficient organocatalysts for CO_2 fixations, *J. Ind. Eng. Chem.*, 2016, **44**, 210–215.

65 K. R. Roshan, B. M. Kim, A. C. Kathalikkattil, J. Tharun, Y. S. Won and D. W. Park, The unprecedented catalytic activity of alkanolamine CO_2 scrubbers in the cycloaddition of CO_2 and oxiranes: a DFT endorsed study, *Chem. Commun.*, 2014, **50**, 13664–13667.

66 H.-G. Kim, B. Seo and C.-S. Lim, Metal- and halide-free catalysts supported on silica and their applications to CO_2 cycloaddition reactions, *J. Ind. Eng. Chem.*, 2019, **75**, 202–210.

67 T. Ema, K. Fukuhara, T. Sakai, M. Ohbo, F.-Q. Bai and J.-y. Hasegawa, Quaternary ammonium hydroxide as a metal-free and halogen-free catalyst for the synthesis of cyclic carbonates from epoxides and carbon dioxide, *Catal. Sci. Technol.*, 2015, **5**, 2314–2321.

68 S. Suleman, H. A. Younus, Z. A. K. Khattak, H. Ullah, M. Elkadi and F. Verpoort, Co-catalyst and solvent free nitrogen rich triazole based organocatalysts for cycloaddition of CO_2 into epoxide, *Mol. Catal.*, 2020, **493**, 111071.

69 Y. Hao, D. Yuan and Y. Yao, Metal–Free Cycloaddition of Epoxides and Carbon Dioxide Catalyzed by Triazole–Bridged Bisphenol, *ChemCatChem*, 2020, **12**, 4346–4351.

70 Y.-B. Wang, D.-S. Sun, H. Zhou, W.-Z. Zhang and X.-B. Lu, CO_2, COS and CS_2 adducts of N-heterocyclic olefins and their application as organocatalysts for carbon dioxide fixation, *Green Chem.*, 2015, **17**, 4009–4015.

71 P. Goodrich, H. Q. N. Gunaratne, J. Jacquemin, L. Jin, Y. Lei and K. R. Seddon, Sustainable Cyclic Carbonate Production, Utilizing Carbon Dioxide and Azolate Ionic Liquids, *ACS Sustainable Chem. Eng.*, 2017, **5**, 5635–5641.

72 S. Sopeña, M. Cozzolino, C. Maquilón, E. C. Escudero-Adán, M. Martínez-Belmonte and A. W. Kleij, Organocatalyzed Domino [3+2] Cycloaddition/Payne-Type Rearrangement using Carbon Dioxide and Epoxy Alcohols, *Angew. Chem., Int. Ed.*, 2018, **57**, 11203–11207.

73 S. García-Argüelles, M. Ferrer, M. Iglesias, F. Del Monte and M. Gutiérrez, Study of Superbase-Based Deep Eutectic Solvents as the Catalyst in the Chemical Fixation of CO_2 into Cyclic Carbonates under Mild Conditions, *Materials*, 2017, **10**, 759.

74 M. Faisal, Z. U. Rehman, Q. u. Aein and A. Saeed, Terpyridine-Pr-Fe_3O_4@boehmite nanoparticles; a novel and highly effective magnetic nanocatalyst for preparation of cyclic carbonates from carbon dioxide and epoxides under solventless conditions, *Mater. Chem. Phys.*, 2019, **231**, 272–280.

75 X. Wang, Q. Dong, Z. Xu, Y. Wu, D. Gao, Y. Xu, C. Ye, Y. Wen, A. Liu, Z. Long and G. Chen, Hierarchically nanoporous copolymer with built-in carbene-CO_2 adducts as halogen-free heterogeneous organocatalyst towards cycloaddition of carbon dioxide into carbonates, *Chem. Eng. J.*, 2021, **403**, 126460.

76 T. Q. Bui, L. J. Konwar, A. Samikannu, D. Nikjoo and J.-P. Mikkola, Mesoporous Melamine-Formaldehyde Resins as Efficient Heterogeneous Catalysts for Continuous Synthesis of Cyclic Carbonates from Epoxides and Gaseous CO_2, *ACS Sustainable Chem. Eng.*, 2020, **8**, 12852–12869.

77 C. J. Whiteoak, E. Martin, M. M. Belmonte, J. Benet-Buchholz and A. W. Kleij, An Efficient Iron Catalyst for the Synthesis of Five- and Six-Membered Organic Carbonates under Mild Condition, *Adv. Synth. Catal.*, 2012, **354**, 469–476.

78 A. M. Chapman, C. Keyworth, M. R. Kember, A. J. J. Lennox and C. K. Williams, Adding Value to Power Station Captured CO_2: Tolerant Zn and Mg Homogeneous Catalysts for Polycarbonate, *ACS Catal.*, 2015, **5**, 1581–1588.

79 J. Meléndez, M. North and R. Pasquale, Synthesis of Cyclic Carbonates from Atmospheric Pressure Carbon Dioxide Using Exceptionally Active Aluminium(salen) Complexes as Catalysts, *Eur. J. Inorg. Chem.*, 2007, 3323–3326.

80 A. Aspelund and K. Jordal, Gas conditioning—The interface between CO_2 capture and transport, *Int. J. Greenhouse Gas Control*, 2007, **1**, 343–354.

81 Mesitylene, https://www.sigmaaldrich.com/catalog/product/sial/m7200?lang=en&region=TH, (accessed October, 21st 2020).

82 J. Helberg, T. Ampßler and H. Zipse, Pyridinyl Amide Ion Pairs as Lewis Base Organocatalysts, *J. Org. Chem.*, 2020, **85**, 5390–5402.

83 M. Kleoff, S. Suhr, B. Sarkar, R. Zimmer, H. U. Reissig, M. Marin-Luna and H. Zipse, Efficient Syntheses of New Super Lewis Basic Tris(dialkylamino)-Substituted Terpyridines and Comparison of Their Methyl Cation Affinities, *Chem. – Eur. J.*, 2019, **25**, 7526–7533.

84 H. Zipse, I. Held and S. Xu, Modular Design of Pyridine-Based Acyl-Transfer Catalysts, *Synthesis*, 2007, 1185–1196.

85 M. R. Heinrich, H. S. Klisa, H. Mayr, W. Steglich and H. Zipse, Enhancing the Catalytic Activity of 4-(Dialkylamino)pyridines by Conformational Fixation, *Angew. Chem., Int. Ed.*, 2003, **42**, 4826–4828.

86 R. Tandon, T. Unzner, T. A. Nigst, N. De Rycke, P. Mayer, B. Wendt, O. R. P. David and H. Zipse, Annelated Pyridines as Highly Nucleophilic and Lewis Basic Catalysts for Acylation Reactions, *Chem. – Eur. J.*, 2013, **19**, 6435–6442.

87 C. Lindner, R. Tandon, B. Maryasin, E. Larionov and H. Zipse, Cation affinity numbers of Lewis bases, *Beilstein J. Org. Chem.*, 2012, **8**, 1406–1442.

88 E. Larionov, F. Achrainer, J. Humin and H. Zipse, The Catalytic Potential of Substituted Pyridines in Acylation Reactions: Theoretical Prediction and Experimental Validation, *ChemCatChem*, 2012, **4**, 559–566.

89 N. D. Rycke, G. Berionni, F. o. Couty, H. Mayr, R. Goumont and O. R. P. David, Synthesis and Reactivity of Highly Nucleophilic Pyridines, *Org. Lett.*, 2011, **13**, 530–533.

90 V. D'Elia, Y. Liu and H. Zipse, Immobilized DMAP Derivatives Rivaling Homogeneous DMAP, *Eur. J. Org. Chem.*, 2011, 1527–1533.

91 O. Coulembier, S. Moins, V. Lemaur, R. Lazzaroni and P. Dubois, Efficiency of DBU/iodine cooperative dual catalysis for the solvent-free synthesis of five-membered cyclic carbonates under atmospheric CO_2 pressure, *J. CO_2 Util.*, 2015, **10**, 7–11.

92 S. Foltran, J. Alsarraf, F. Robert, Y. Landais, E. Cloutet, H. Cramail and T. Tassaing, On the chemical fixation of supercritical carbon dioxide with epoxides catalyzed by ionic salts: an in situ FTIR and Raman study, *Catal. Sci. Technol.*, 2013, **3**, 1046–1055.

93 M. North, R. Pasquale and C. Young, Synthesis of cyclic carbonates from epoxides and CO_2, *Green Chem.*, 2010, **12**, 1514–1539.

94 X. Liu, S. Zhang, Q.-W. Song, X.-F. Liu, R. Ma and L.-N. He, Cooperative calcium-based catalysis with 1,8-diazabicyclo[5.4.0]-undec-7-ene for the cycloaddition of epoxides with CO_2 at atmospheric pressure, *Green Chem.*, 2016, **18**, 2871–2876.

95 C. Villiers, J.-P. Dognon, R. Pollet, P. Thuéry and M. Ephritikhine, An Isolated CO_2 Adduct of a Nitrogen Base: Crystal and Electronic Structures, *Angew. Chem., Int. Ed.*, 2010, **49**, 3465–3468.

96 T. Tabanelli, E. Monti, F. Cavani and M. Selva, The design of efficient carbonate interchange reactions with catechol carbonate, *Green Chem.*, 2017, **19**, 1519–1528.

97 J. Rintjema, R. Epping, G. Fiorani, E. Martín, E. C. Escudero-Adán and A. W. Kleij, Substrate-Controlled Product Divergence: Conversion of CO_2 into Heterocyclic Products, *Angew. Chem., Int. Ed.*, 2016, **55**, 3972–3976.

98 Y. Lee, J. Choi and H. Kim, Stereocontrolled, Divergent, Al(III)-Catalyzed Coupling of Chiral N-Aryl Epoxy Amines and CO_2, *Org. Lett.*, 2018, **20**, 5036–5039.

99 L. J. Cao, A. Y. Li, L. Xu and Y. Zhang, A computational study on the ring stretching modes of halogen-substituted pyridine involved in H-bonding, *Int. J. Quantum Chem.*, 2012, **112**, 498–508.

100 D. Cook, Vibrational Spectra of Pyridinium Salt, *Can. J. Chem.*, 1961, **39**, 2009–2024.

101 V. D'Elia, A. A. Ghani, A. Monassier, J. Sofack-Kreutzer, J. D. A. Pelletier, M. Drees, S. V. C. Vummaleti, A. Poater, L. Cavallo, M. Cokoja, J.-M. Basset and F. E. Kühn, Dynamics of the $NbCl_5$-Catalyzed Cycloaddition of Propylene Oxide and CO_2: Assessing the Dual Role of the Nucleophilic Co-Catalysts, *Chem. – Eur. J.*, 2014, **20**, 11870–11882.

102 B. Dutta, J. Sofack-Kreutzer, A. A. Ghani, V. D'Elia, J. D. A. Pelletier, M. Cokoja, F. E. Kühn and J.-M. Basset, Nucleophile-directed selectivity towards linear carbonates in the niobium pentaethoxide-catalysed cycloaddition of CO_2 and propylene oxide, *Catal. Sci. Technol.*, 2014, **4**, 1534–1538.

103 S. Subramanian, J. Park, J. Byun, Y. Jung and C. T. Yavuz, Highly Efficient Catalytic Cyclic Carbonate Formation by Pyridyl Salicylimines, *ACS Appl. Mater. Interfaces*, 2018, **10**, 9478–9484.

104 T. Jose, S. Cañellas, M. A. Pericàs and A. W. Kleij, Polystyrene-supported bifunctional resorcinarenes as cheap, metal-free and recyclable catalysts for epoxide/CO_2 coupling reactions, *Green Chem.*, 2017, **19**, 5488–5493.

105 Y. Chen, R. Luo, J. Bao, Q. Xu, J. Jiang, X. Zhou and H. Ji, Function-oriented ionic polymers having high-density active sites for sustainable carbon dioxide conversion, *J. Mater. Chem. A*, 2018, **6**, 9172–9182.

106 Y. Zhang, G. Chen, L. Wu, K. Liu, H. Zhong, Z. Long, M. Tong, Z. Yang and S. Dai, Two-in-one: construction of hydroxyl and imidazolium-bifunctionalized ionic networks in one-pot toward synergistic catalytic CO_2 fixation, *Chem. Commun.*, 2020, **56**, 3309–3312.

107 C. J. Whiteoak, A. H. Henseler, C. Ayats, A. W. Kleij and M. A. Pericàs, Conversion of oxiranes and CO_2 to organic cyclic carbonates using a recyclable, bifunctional polystyrene-supported organocatalyst, *Green Chem.*, 2014, **16**, 1552–1559.

108 J.-Q. Wang, K. Dong, W.-G. Cheng, J. Sun and S.-J. Zhang, Insights into quaternary ammonium salts-catalyzed fixation carbon dioxide with epoxides, *Catal. Sci. Technol.*, 2012, **2**, 1480–1484.

109 V. Caló, A. Nacci, A. Monopoli and A. Fanizzi, Cyclic Carbonate Formation from Carbon Dioxide and Oxiranes in Tetrabutylammonium Halides as Solvents and Catalysts, *Org. Lett.*, 2002, **4**, 2561–2563.

110 E. R. Pérez, R. H. A. Santos, M. T. P. Gambardella, L. G. M. de Macedo, U. P. Rodrigues-Filho, J.-C. Launay and D. W. Franco, Activation of Carbon Dioxide by Bicyclic Amidines, *J. Org. Chem.*, 2004, **69**, 8005–8011.

111 H. A. Duong, T. N. Tekavec, A. M. Arif and J. Louie, Reversible carboxylation of N-heterocyclic carbenes, *Chem. Commun.*, 2004, 112–113.

112 X. Zhang, N. Zhao, W. Wei and Y. Sun, Chemical fixation of carbon dioxide to propylene carbonate over amine-functionalized silica catalysts, *Catal. Today*, 2006, **115**, 102–106.

113 H. Zhou, Y.-M. Wang, W.-Z. Zhang, J.-P. Qu and X.-B. Lu, N-Heterocyclic carbene functionalized MCM-41 as an efficient catalyst for chemical fixation of carbon dioxide, *Green Chem.*, 2011, **13**, 644–650.

114 Y. Kayaki, M. Yamamoto and T. Ikariya, N-Heterocyclic Carbenes as Efficient Organocatalysts for CO_2 Fixation Reactions, *Angew. Chem., Int. Ed.*, 2009, **48**, 4194–4197.

115 N. Fanjul-Mosteirín, C. Jehanno, F. Ruipérez, H. Sardon and A. P. Dove, Rational Study of DBU Salts for the CO_2 Insertion into Epoxides for the Synthesis of Cyclic Carbonates, *ACS Sustainable Chem. Eng.*, 2019, **7**, 10633–10640.

116 D. J. Darensbourg and R. M. Mackiewicz, Role of the Cocatalyst in the Copolymerization of CO_2 and Cyclohexene Oxide Utilizing Chromium Salen Complexes, *J. Am. Chem. Soc.*, 2005, **127**, 14026–14038.

117 L. Wang, G. Zhang, K. Kodama and T. Hirose, An efficient metal- and solvent-free organocatalytic system for chemical fixation of CO_2 into cyclic carbonates under mild conditions, *Green Chem.*, 2016, **18**, 1229–1233.

118 R. G. Parr, S. v. Szentpály and S. Liu, Electrophilicity Index, *J. Am. Chem. Soc.*, 1999, **121**, 1922–1924.

119 Y. D. Bidal, C. A. Urbina-Blanco, A. Poater, D. B. Cordes, A. M. Z. Slawin, L. Cavallo and C. S. J. Cazin, Electronic effects in mixed N-heterocyclic carbene/phosphite indenylidene ruthenium metathesis catalysts, *Dalton Trans.*, 2019, **48**, 11326–11337.

120 J. Masdemont, J. A. Luque-Urrutia, M. Gimferrer, D. Milstein and A. Poater, Mechanism of Coupling of Alcohols and Amines To Generate Aldimines and H_2 by a Pincer Manganese Catalyst, *ACS Catal.*, 2019, **9**, 1662–1669.

121 C. Seck, M. Diagne Mbaye, S. Coufourier, A. Lator, J.-F. Lohier, A. Poater, T. R. Ward, S. Gaillard and J.-L. Renaud, Alkylation of Ketones Catalyzed by Bifunctional Iron Complexes: From Mechanistic Understanding to Application, *ChemCatChem*, 2017, **9**, 4410–4416.

122 A. Poater, A. Gallegos Saliner, M. Solà, L. Cavallo and A. P. Worth, Computational Methods to Predict the Reactivity of Nanoparticles Through Structure-Property Relationships, *Expert Opin. Drug Deliv.*, 2010, **7**, 295–305.

123 M. Costas, X. Ribas, A. Poater, J. M. López-Valbuena, R. Xifra, A. Company, M. Duran, M. Solà, A. Llobet, M. Corbella, M. A. Usón, J. Mahía, X. Solans, X. Shan and J. Benet-Buchholz, Copper(II) Hexaaza Macrocyclic Binuclear Complexes Obtained from the Reaction of Their Copper(I) Derivates and Molecular Dioxygen, *Inorg. Chem.*, 2006, **45**, 3569–3581.

Chapter 6. Clean energy production through solar cells

6.1. Do Carbon Nano-onions Behave as Nanoscopic Faraday Cages? A Comparison of the Reactivity of C_{60}, C_{240}, $C_{60}@C_{240}$, $Li^+@C_{60}$, $Li^+@C_{240}$, and $Li^+@C_{60}@C_{240}$

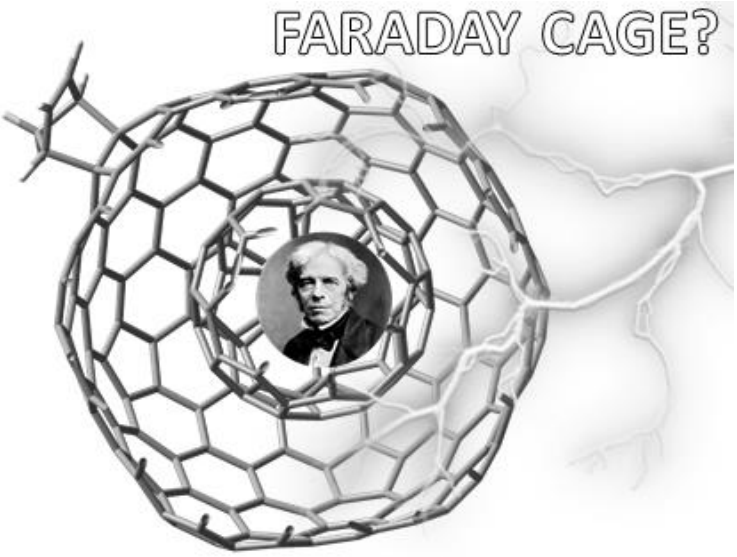
FARADAY CAGE?

Luque-Urrutia, J. A.; Poater, A.; Solà, M. **Do Carbon Nano-onions Behave as Nanoscopic Faraday Cages? A Comparison of the Reactivity of C_{60}, C_{240}, $C_{60}@C_{240}$, $Li^+@C_{60}$, $Li^+@C_{240}$, and $Li^+@C_{60}@C_{240}$.** *Chem. Eur. J.* **2020**, *26*, 804-808. DOI: 10.1002/chem.201904650.

This thesis author has contributed to the DFT calculations, data analysis, writing, and revisions of the article.

Reproduced with permission from:

Luque-Urrutia, J. A.; Poater, A.; Solà, M. **Do Carbon Nano-onions Behave as Nanoscopic Faraday Cages? A Comparison of the Reactivity of C_{60}, C_{240}, $C_{60}@C_{240}$, $Li^{+}@C_{60}$, $Li^{+}@C_{240}$, and $Li^{+}@C_{60}@C_{240}$.** *Chem. Eur. J.* **2020**, *26*, 804-808.

https://doi.org/10.1002/chem.201904650

Copyright © 2020, John Wiley and Sons.

ChemPubSoc
Europe

DOI: 10.1002/chem.201904650

CHEMISTRY
A European Journal
Communicatio

Check for updates

Fullerenes |*Hot Paper*|

Do Carbon Nano-onions Behave as Nanoscopic Faraday Cages? A Comparison of the Reactivity of C_{60}, C_{240}, C_{60}@C_{240}, Li^+@C_{60}, Li^+@C_{240}, and Li^+@C_{60}@C_{240}

Jesús Antonio Luque-Urrutia, Albert Poater,* and Miquel Solà*[a]

Abstract: From the analysis of the polarizability of carbon nano-onions (CNOs), it was concluded that CNOs behave as near perfect nanoscopic Faraday cages. If CNOs behave as ideal Faraday cages, the reactivity of the C_{240} cage should be the same in Li^+@C_{240} and Li^+@C_{60}@C_{240}. In this work, the Diels–Alder reaction of cyclopentadiene to the free C_{240} cage and the C_{60}@C_{240} CNO together with their Li^+-doped counterparts were analyzed using DFT. It was found that in all cases the preferred cycloaddition is on bond [6,6] of type B of C_{240}. Encapsulation of Li^+ results in lower enthalpy barriers due to the decrease of the energy of the LUMO orbital of the C_{240} cage. When the Li^+ is placed inside the CNO C_{60}@C_{240}, the decrease in enthalpy barrier is similar to that of Li^+@C_{240}. However, the location of Li^+ in Li^+@C_{240} (off-centered) and Li^+@C_{60}@C_{240} (centered) is quite different. When Li^+ was placed in the center of the C_{240} cage in Li^+@C_{240}, the barriers increased significantly. Taking into account this effect, the barriers in Li^+@C_{240} and Li^+@C_{60}@C_{240} differ by about 4 kcal mol^{-1}. This result can be attributed to the shielding effect of C_{60} in Li^+@C_{60}@C_{240}. As a result, we conclude that this CNO does not act as a perfect Faraday cage.

Carbon nano-onions (CNOs) were observed for the first time in vacuum-deposited amorphous carbon films by Iijima,[1] five years before the discovery of C_{60} in 1985.[2] CNOs are spherical or polyhedral nanoparticles of carbon formed by several concentric shells of fullerenes in a structure resembling that of an onion.[3] Interestingly, CNOs have been detected in the interstellar medium.[4] Since the synthesis of CNOs by Ugarte in 1992,[5] several methods have been developed to produce them in relatively large scale.[3a,c,6] Mordkovich reported in 2000, the generation of the double-shell C_{60}@C_{240} and C_{240}@C_{560} and triple-shell C_{60}@C_{240}@C_{560} CNOs in the products of the high-temperature laser pyrolysis.[7] CNOs have been recently proposed as acceptors in donor–acceptor dyads for organic photovoltaics.[8] In fact, the photoinduced lowest charge-transfer (CT) excitation in CNOs takes place at lower energy than any transition of the individual fullerenes that form the CNO.[9] Apart from its prospective use in solar cells, the number of potential applications of CNOs have grown in the last decades. Among them, we can mention their application in gas storage processes,[10] solid lubrication,[11] or heterogeneous catalysis,[12] and also as electrode materials in capacitors,[13] anode materials in lithium-ion batteries,[6a] catalyst support in fuel cells,[14] or electro-optical devices.[15] Zope et al.[16] reported in a computational study that when an external electric field is applied, the outer C_{240} or C_{180} fullerene cage almost completely shields the inner C_{60} cage in C_{60}@C_{240} or C_{60}@C_{180}. Indeed, the polarizability of the CNOs is essentially that of the outer fullerene cage and has an insignificant contribution from the encapsulated unit. The outer fullerene cages effectively shield the encapsulated cluster and, therefore, these CNOs can be considered near perfect Faraday cages.

Similar to the case of fullerenes,[17] an enhancement of the applicability of CNOs (in particular, improved solubility) can be achieved through chemical functionalization. Various functionalization reactions of CNOs have been developed. The first covalent functionalized CNO was obtained in 2003 by a 1,3-dipolar addition of azomethine ylide.[18] Later on, the same reaction,[19] as well as the [2+1] Bingel–Hirsch cyclopropanation reaction,[20] the [2+1] cycloaddition of nitrenes,[21] the amidation coupling reactions[19,20] or the combination of diazonium and 1,3-dipolar additions[22] have been used to prepare a variety of CNOs derivatives.

Quite recently, ion-encapsulated fullerenes, that is, fullerenes having an endohedral ion, have emerged as a new family of endohedral fullerenes.[23] A significant enhancement of the Diels–Alder (DA) reactivity was found for those systems having an endohedral cation. Thus, the DA reactions between cyclopentadiene and Li^+@C_{60} were reported to be significantly faster than the analogous processes involving the parent C_{60} fullerene.[24]

The effect of Li^+-encapsulated double-shell CNOs has been recently studied in CT processes.[9c] It has been found that depending on the size of the inner and outer-shells two types of CT states can be generated, namely, one with alternating charges like Li^+@C_{60}^-@C_{240}^+ and another with a positive charge on the outer shell as in Li@C_{240}@C_{540}^-. To our knowl-

---

[a] J. A. Luque-Urrutia, Dr. A. Poater, Prof. Dr. M. Solà
Institut de Química Computacional i Catàlisi (IQCC)
Facultat de Ciències, Universitat de Girona
C/ M. Aurèlia Capmany, 69, 17003 Girona, Catalonia (Spain)
E-mail: albert.poater@udg.edu
miquel.sola@udg.edu

Supporting information and the ORCID identification number(s) for the author(s) of this article can be found under: https://doi.org/10.1002/chem.201904650. It contains Cartesian coordinates of all optimized species, benchmark calculations, electrostatic map, and noncovalent interactions plot.

© 2019 Wiley-VCH Verlag GmbH & Co. KGaA, Weinheim

edge, the effect of Li$^+$-encapsulated double-shell CNOs in their reactivity has not been studied to date. To fill this void, herein, we analyze and compare the reactivity of all different bonds of C$_{60}$, C$_{240}$, C$_{60}$@C$_{240}$, Li$^+$@C$_{60}$, Li$^+$@C$_{240}$, and Li$^+$@C$_{60}$@C$_{240}$ for the DA reaction with cyclopentadiene (Cp). It is known that I_h-C$_{60}$ has two different bonds, the [6,6] pyracylenic A type bond and the [5,6] corannulenic D type bond. For the studied I_h-C$_{240}$, one finds five different bonds (one [5,6] D type bond and four [6,6] bonds, one of them of type B and three pyrenic of type C) depicted in Figures 1 and 2. If C$_{60}$@C$_{240}$ behaves as a perfect Faraday cage, the effect of encapsulated Li$^+$ in the reactivity of the outer cage should not be affected by the inner cage. Consequently, we should have the same reactivity in Li$^+$@C$_{240}$ and Li$^+$@C$_{60}$@C$_{240}$. Our investigation shows that Li$^+$@C$_{240}$ has almost the same reactivity as Li$^+$@C$_{60}$@C$_{240}$. However, this is the result of a cancellation of effects due to the different Li$^+$ position in Li$^+$@C$_{240}$ and Li$^+$@C$_{60}$@C$_{240}$. Our results with the Li$^+$ placed in the center of C$_{240}$ in Li$^+$@C$_{240}$ and Li$^+$@C$_{60}$@C$_{240}$ prove that C$_{60}$@C$_{240}$ does not behave as an ideal nanoscopic Faraday cage.

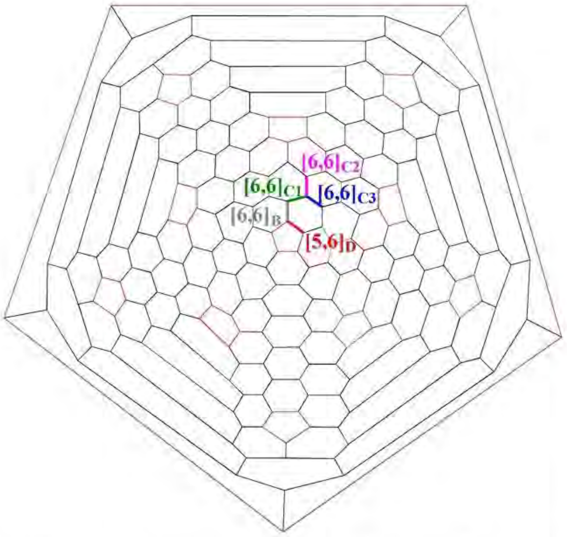

Figure 1. Schlegel diagram for a C$_{240}$ fullerene with the five different bonds highlighted, [5,6]$_D$ in red, [6,6]$_B$ in grey, [6,6]$_{C1}$ in green, [6,6]$_{C2}$ in pink, and [6,6]$_{C3}$ in blue. The 12 pentagons of the fullerene are also marked in red.

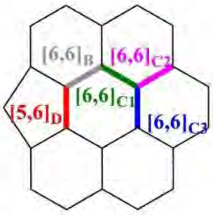

Figure 2. Representation of the different bonds found in a C$_{240}$ cage.

The reaction profiles of the DA reaction between the different species analyzed and Cp involve first the formation of a reactant complex (RC) stabilized through van der Waals interactions that evolve to the transition state (TS) to generate the products (P). Table 1 lists the reaction enthalpy and enthalpy barriers of the DA cycloaddition of Cp to all studied species. In the case of the addition to the [5,6]$_D$ bond, there are two possible adducts that correspond to the usual *endo* and *exo* attacks in DA cycloadditions. Previous works[25] have shown that differences in these two attacks are small and, accordingly, we have analyzed only the addition that has the four carbon atoms of the cyclopentadiene most involved in the reaction facing the six-membered ring of C$_{60}$ or C$_{240}$.

Table 1. Reaction enthalpies (ΔH_r, enthalpy difference between adduct and reactants) and enthalpies barriers ($\Delta H^{\ddagger}$, enthalpy difference between transition state and reactant complex) in kcal mol^{-1} of the Diels–Alder reaction between fullerenes and Cp, with toluene as solvent.

Fullerene	Bond type	$\Delta H^{\ddagger}$	ΔH_r
C$_{60}$	[5-6]$_D$	22.3	−1.9
	[6-6]$_A$	5.4	−22.1
Li$^+$@C$_{60}$	[5-6]$_D$	17.3	−5.8
	[6-6]$_A$	−0.8	−25.9
C$_{240}$	[5-6]$_D$	25.1	4.8
	[6-6]$_B$	19.0	−2.0
	[6-6]$_{C1}$	36.0	25.3
	[6-6]$_{C2}$	34.0	18.4
	[6-6]$_{C3}$	31.6	14.6
Li$^+$@C$_{240}$	[5-6]$_D$	21.1 (16.7)[a]	0.7 (2.2)[a]
	[6-6]$_B$	17.9 (13.4)[a]	−4.3 (−3.1)[a]
	[6-6]$_{C1}$	33.8 (31.2)[a]	23.2 (24.2)[a]
	[6-6]$_{C2}$	30.6 (28.0)[a]	18.2 (18.6)[a]
	[6-6]$_{C3}$	27.2 (23.8)[a]	9.9 (13.9)[a]
C$_{60}$@C$_{240}$	[5-6]$_D$	24.8	4.8
	[6-6]$_B$	18.9	−1.1
	[6-6]$_{C1}$	38.2	26.7
	[6-6]$_{C2}$	33.9	20.6
	[6-6]$_{C3}$	31.2	15.1
Li$^+$@C$_{60}$@C$_{240}$	[5-6]$_D$	22.1	1.7
	[6-6]$_B$	17.2	−3.8
	[6-6]$_{C1}$	35.1	23.6
	[6-6]$_{C2}$	33.9	16.1
	[6-6]$_{C3}$	33.2	12.1

[a] Enthalpies in parentheses are from single-point calculations with the Li$^+$ placed in the center of the C$_{240}$ cage. Thermal corrections were taken from the PBEPBE-D3/3-21G(d) optimized systems.

In the case of C$_{60}$, our calculated M06/6-31G(p,d)//PBEPBE-D3/3-21G(d) enthalpies in toluene are in good agreement with the available experimental data,[26] which show that this DA occurs exclusively over the [6,6]-bond with an activation energy of 6.9 kcal mol^{-1} (compared to our 5.4 kcal mol^{-1} for the enthalpy difference between the reactant complex and the transition state) and a reaction enthalpy of −19.8 ± 2.2 kcal mol^{-1} (compared to our −22.1 kcal mol^{-1} in Table 1). The preference for the DA to the [6,6] bond in C$_{60}$ was attributed to the more effective <HOMO(cyclopentadiene)|LUMO(C$_{60}$)> overlap, which is higher in the [6,6] attack along the entire reaction coordinate.[27] For the Li$^+$ doped C$_{60}$ species, both the [5,6] and the [6,6] additions are faster and the reaction becomes more exothermic. In fact, the [6,6] attack becomes barrierless at this level of theory. This reactivity enhancement was found to be mainly the result of a stronger π(Cp)→π*(C_{60}) molecular orbital interaction due to the stabilization of the LUMO in cation-encapsulated fullerenes (see Table 2).[28] To our knowledge, the reactivity of icosahedral C_{240} has not been studied yet. I_h-C_{240} contains three pyrene C type [6,6] bonds that are unreactive (barriers higher than 30 kcal mol^{-1} and endothermic additions). Moreover, the corannulenic [5,6] D type bond has also a relatively large enthalpy barrier and the reaction is endothermic. Only the [6,6] bond of type B is reactive with an enthalpy barrier of 19.0 kcal mol^{-1} and a reaction enthalpy of only −2.0 kcal mol^{-1}, corresponding to a slightly exothermic cycloaddition. Not unexpectedly, the [6,6] bond of type A of C_{60} is more reactive than the [6,6] bond of type B of C_{240}. This behavior is attributed to the higher pyramidalization angles of the C atoms in [6,6] bonds of type A than in [6,6] bonds of type B. By encapsulating Li^+ inside C_{240}, all bonds become more reactive with a reduction in the enthalpy barriers in the range of 1 to 4 kcal mol^{-1}. This is attributed to the LUMO stabilization due to the presence of the cation (Table 2). If we now compare the reactivity of C_{240} and $C_{60}@C_{240}$, we find that the two systems have almost the same reactivity, the latter being slightly more reactive (smaller enthalpy barriers) for all bonds except the $[6\text{-}6]_{C1}$. Finally, for $Li^+@C_{60}@C_{240}$, we observe the expected increase in the reactivity of the different bonds with the only exception of bond $[6\text{-}6]_{C3}$. However, the reduction in enthalpy barriers due to Li^+ is smaller in $Li^+@C_{240}$ and $Li^+@C_{60}@C_{240}$ than in $Li^+@C_{60}$. Encapsulation of Li^+ cation lowers the enthalpy barrier of the C_{60} $[6,6]_A$, C_{240} $[6,6]_B$, and $C_{60}@C_{240}$ $[6,6]_B$ by 6.2, 1.1, and 1.7 kcal mol^{-1}, respectively. Further, it is worth noting that the enthalpy barrier of the $[6,6]_B$ attack is only 0.7 kcal mol^{-1} lower for $Li^+@C_{60}@C_{240}$ than for $Li^+@C_{240}$. This seems to indicate that $Li^+@C_{240}$ and $Li^+@C_{60}@C_{240}$ have almost the same reactivity, and, consequently, $C_{60}@C_{240}$ acts as an almost perfect Faraday cage. However, the location of Li^+ in $Li^+@C_{240}$ (off center) and $Li^+@C_{60}@C_{240}$ (center) is quite different. When we place Li^+ in the center of the C_{240} cage in $Li^+@C_{240}$, the barriers decrease significantly by about 2–5 kcal mol^{-1} (Table 1). The reason for this reduction is that the RC is more destabilized by moving the Li^+ to the center (by 6.8 kcal mol^{-1}) than the TS (only by 2.3 kcal mol^{-1}). We attribute this effect to the fact that Li^+ interacts more favorably with the rings having the largest π charge and this charge is larger in the RC than in the TS.[29] Taking into account this effect, the barriers in $Li^+@C_{240}$ and $Li^+@C_{60}@C_{240}$ differ by about 4 kcal mol^{-1}, those of $Li^+@C_{240}$ being lower. This means that C_{60} in $Li^+@C_{60}@C_{240}$ partially shields the positive charge of the Li^+, showing that $C_{60}@C_{240}$ is not a perfect Faraday cage. This result is reinforced by two findings: first, the energy of the LUMO of $Li^+@C_{240}$ (−0.158 a.u.) is slightly smaller than that of $Li^+@C_{60}@C_{240}$ (−0.155 a.u.), indicating that the C_{60} cage has a shielding effect that reduces the reactivity of the C_{240} cage in $Li^+@C_{60}@C_{240}$; and, second, the map of electrostatic potential of $Li^+@C_{60}@C_{240}$ (Figure S2 in the Supporting Information) shows that the electrostatic potential is similar in the inner and outer faces of C_{60} (a perfect Faraday cage should have different electrostatic potentials in the inner and outer faces).

Table 2. Energy of the LUMO for the different fullerenes studied in this work.

Reactant	LUMO (a.u.)
C_{60}	−0.114
$Li^+@C_{60}$[a]	−0.179
C_{240}	−0.124
$Li^+@C_{240}$	−0.158
$C_{60}@C_{240}$	−0.124
$Li^+@C_{60}@C_{240}$[b]	−0.155

[a] For $Li^+@C_{60}$, we report the energy of LUMO+1 (LUMO is located on the Li cation). [b] For $Li^+@C_{60}@C_{240}$, we provide the energy of the LUMO+5 (LUMO is located in the Li cation and the LUMO+1, +2, +3, +4 orbitals are located in the C_{60} cage).

Figure 3 contains the bond lengths of the two formed bonds in the RC, TS, and products of C_{240} and $C_{60}@C_{240}$ and their Li^+ doped derivatives. The data show that both C_{240} and $C_{60}@C_{240}$ have nearly the same bond distances. The TS is concerted but asynchronous, the bond formed with the C atom shared with the [5,6] bond being somewhat shorter. However, when we introduce the lithium cation inside the cages, the bond lengths of the bonds formed in the TSs are slightly elongated as expected from the Hammond postulate[30] for more exothermic reactions. Finally, the non-covalent interaction (NCI)[31] plot of the $Li^+@C_{60}@C_{240}$ displays the expected green surface between C_{60} and C_{240} as a result of the presence of attractive van der Waals interactions (see Figure S3 in the Supporting Information).

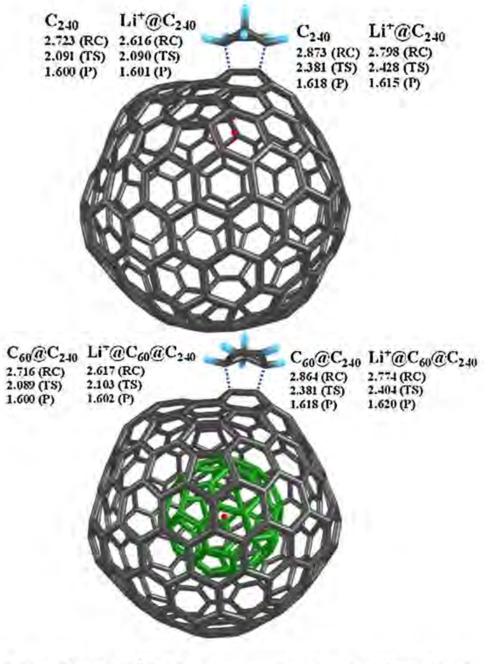

Figure 3. Bond lengths [Å] of the two new bonds being formed in the reactant complex (RC), transition state (TS), and product (P) for C_{240} and $Li^+@C_{240}$ (top) and for $C_{60}@C_{240}$ and $Li^+@C_{60}@C_{240}$ (bottom) for the most reactive $[6,6]_B$ bond. Inner fullerene colored in green for the sake of clarity. Li^+ is represented as a red dot.

In conclusion, we have studied the reactivity of the different bonds for the DA reaction of cyclopentadiene to C_{60}, C_{240}, and $C_{60}@C_{240}$ as well as their Li$^+$-doped counterparts. In all species, the preferred attack is on bond [6,6] either of type A (for C_{60} cages) or type B (for C_{240} cages). The most favored attack in C_{240} is slightly exothermic, the rest being endothermic. Encapsulation of Li$^+$ results in a decrease of the energy of the LUMO orbital of the outer cage that results in lower enthalpy barriers for all attacks. When the Li$^+$ is placed inside the CNO $C_{60}@C_{240}$, the decrease is smaller. We attribute this result to the shielding effect of C_{60}. Because no shielding is expected in a perfect Faraday cage, we conclude that this CNO does not act as an ideal Faraday cage.

Computational Details

All density functional theory calculations were performed with the Gaussian 16 set of programs.[32] A benchmark of different functionals and basis sets was done for the DA to C_{60} and the results were compared to experimental data (see Table S1 in the Supporting Information). The electronic configuration of the molecular systems was described with the pure functional of Perdew, Burke, and Ernzerhof (PBEPBE keyword in Gaussian 16) using the small split-valence basis set 3-21G(d)[33] due to the size of the target species (Figure S1 of the Supporting Information shows that the geometries obtained with a larger basis set such as the 6-311G(d,p) are almost indistinguishable from those obtained with the 3-21G(d) basis set). Since corrections due to dispersion are essential to study the reactivity in carbon nanostructures,[34] we have included them through the Grimme's method with Becke–Johnson damping[35] (GD3BJ keyword in Gaussian). The geometry optimizations were performed without symmetry constraints and the characterization of the local stationary points was carried out by analytical frequency calculations. These frequencies were used to calculate unscaled zero-point energies (ZPEs) as well as thermal corrections and entropy effects at 298.15 K and 1 atm. We obtained the energies by single-point calculations on the optimized geometries with the M06 functional[36] and the double-zeta polarized basis set 6-31G(d,p)[37] for increased accuracy. Solvent effects were included with the polarizable continuous solvation model (PCM)[38] using toluene as a solvent. The reported enthalpies in this work are electronic energies (including solvent effects) obtained at the M06/6-31G(d,p)//PBEPBE-D3/3-21G(d) level of theory corrected with zero-point energies, thermal corrections and entropy effects evaluated at 298.15 K and 1 atm with the PBEPBE-D3/3-21G(d) method.

Acknowledgements

J.A.L.U. thanks Universitat de Girona for an IFUdG2017 Ph.D. fellowship. A.P. is a Serra Húnter fellow. A.P. and M.S. thank the Spanish MINECO for projects PGC2018-097722-B-I00 and CTQ2017-85341-P, respectively. M.S. thanks the Generalitat de Catalunya for project 2017SGR39, the Xarxa de Referència en Química Teòrica i Computacional, and ICREA Academia 2014 prize. Excellent service provided by the CSUC supercomputer center is acknowledged.

Conflict of interest

The authors declare no conflict of interest.

Keywords: buckyonions · carbon nano-onions · Diels–Alder · Faraday cages · fullerenes

[1] S. Iijima, *J. Cryst. Growth* **1980**, *50*, 675–683.
[2] H. W. Kroto, J. R. Heath, S. C. O'Brien, R. F. Curl, R. E. Smalley, *Nature* **1985**, *318*, 162–163.
[3] a) B.-s. Xu, *New Carbon Mater.* **2008**, *23*, 289–301; b) L. Echegoyen, A. L. Ortiz, M. N. Chaur, A. J. Palkar in *Chemistry of Nanocarbons* (Eds.: T. Akasaka, F. Wudl, S. Nagase), Wiley, Chichester, **2010**; c) J. Bartelmess, S. Giordani, *Beilstein J. Nanotechnol.* **2014**, *5*, 1980–1998.
[4] a) W. A. de Heer, D. Ugarte, *Chem. Phys. Lett.* **1993**, *207*, 480–486; b) S. Iglesias-Groth, *Astrophys. J.* **2004**, *608*, L37–L40.
[5] D. Ugarte, *Nature* **1992**, *359*, 707–709.
[6] a) F.-D. Han, B. Yao, Y.-J. Bai, *J. Phys. Chem. C* **2011**, *115*, 8923–8927; b) V. Z. Mordkovich, Y. Shiratori, H. Hiraoka, Y. Takeuchi, *Phys. Solid State* **2002**, *44*, 603–606.
[7] V. Z. Mordkovich, *Chem. Mater.* **2000**, *12*, 2813–2818.
[8] D. M. Bobrowska, H. Zubyk, E. Regulska, E. Romero, L. Echegoyen, M. E. Plonska-Brzezinska, *Nano Adv.* **2019**, *1*, 3164–3176.
[9] a) A. A. Voityuk, M. Solà, *J. Phys. Chem. A* **2016**, *120*, 5798–5804; b) M. A. Hashmi, M. Lein, *J. Phys. Chem. C* **2018**, *122*, 2422–2431; c) A. J. Stasyuk, O. A. Stasyuk, M. Solà, A. A. Voityuk, *J. Phys. Chem. C* **2019**, *123*, 16525–16532.
[10] N. Sano, H. Wang, I. Alexandrou, M. Chhowalla, K. B. K. Teo, G. A. J. Amaratunga, K. Iimura, *J. Appl. Phys.* **2002**, *92*, 2783–2788.
[11] A. Hirata, M. Igarashi, T. Kaito, *Tribol. Int.* **2004**, *37*, 899–905.
[12] N. Keller, N. I. Maksimova, V. V. Roddatis, M. Schur, G. Mestl, Y. V. Butenko, V. L. Kuznetsov, R. Schlögl, *Angew. Chem. Int. Ed.* **2002**, *41*, 1885–1888; *Angew. Chem.* **2002**, *114*, 1962–1966.
[13] D. Pech, M. Brunet, H. Durou, P. Huang, V. Mochalin, Y. Gogotsi, P.-L. Taberna, P. Simon, *Nat. Nanotechnol.* **2010**, *5*, 651–654.
[14] B. Xu, X. Yang, X. Wang, J. Guo, X. Liu, *J. Power Sources* **2006**, *162*, 160–164.
[15] E. Koudoumas, O. Kokkinaki, M. Konstantaki, S. Couris, S. Korovin, P. Detkov, V. Kuznetsov, S. Pimenov, V. Pustovoi, *Chem. Phys. Lett.* **2002**, *357*, 336–340.
[16] a) R. R. Zope, *J. Phys. B* **2008**, *41*, 085101; b) R. R. Zope, S. Bhusal, L. Basurto, T. Baruah, K. Jackson, *J. Chem. Phys.* **2015**, *143*, 084306.
[17] a) A. Hirsch, *The Chemistry of Fullerenes*, Thieme, Stuttgart, **1994**; b) A. Hirsch, M. Brettreich, *Fullerenes: Chemistry and Reactivity*, John Wiley & Sons, Weinheim, **2004**.
[18] V. Georgakilas, D. M. Guldi, R. Signorini, R. Bozio, M. Prato, *J. Am. Chem. Soc.* **2003**, *125*, 14268–14269.
[19] A. S. Rettenbacher, B. Elliott, J. S. Hudson, A. Amirkhanian, L. Echegoyen, *Chem. Eur. J.* **2006**, *12*, 376–387.
[20] A. Palkar, F. Melin, C. M. Cardona, B. Elliott, A. K. Naskar, D. D. Edie, A. Kumbhar, L. Echegoyen, *Chem. Asian J.* **2007**, *2*, 625–633.
[21] L. Zhou, C. Gao, D. Zhu, W. Xu, F. F. Chen, A. Palkar, L. Echegoyen, E. S.-W. Kong, *Chem. Eur. J.* **2009**, *15*, 1389–1396.
[22] K. Flavin, M. N. Chaur, L. Echegoyen, S. Giordani, *Org. Lett.* **2010**, *12*, 840–843.
[23] a) S. Aoyagi, E. Nishibori, H. Sawa, K. Sugimoto, M. Takata, Y. Miyata, R. Kitaura, H. Shinohara, H. Okada, T. Sakai, Y. Ono, K. Kawachi, K. Yokoo, S. Ono, K. Omote, Y. Kasama, S. Ishikawa, T. Komuro, H. Tobita, *Nat. Chem.* **2010**, *2*, 678–683; b) S. Fukuzumi, K. Ohkubo, Y. Kawashima, D. S. Kim, J. S. Park, A. Jana, V. M. Lynch, D. Kim, J. L. Sessler, *J. Am. Chem. Soc.* **2011**, *133*, 15938–15941; c) S. Aoyagi, Y. Sado, E. Nishibori, H. Sawa, H. Okada, H. Tobita, Y. Kasama, R. Kitaura, H. Shinohara, *Angew. Chem. Int. Ed.* **2012**, *51*, 3377–3381; *Angew. Chem.* **2012**, *124*, 3433–3437; d) H.

© 2019 Wiley-VCH Verlag GmbH & Co. KGaA, Weinheim

Ueno, K. Kokubo, Y. Nakamura, K. Ohkubo, N. Ikuma, H. Moriyama, S. Fukuzumi, T. Oshima, *Chem. Commun.* **2013**, *49*, 7376–7378.

[24] a) H. Kawakami, H. Okada, Y. Matsuo, *Org. Lett.* **2013**, *15*, 4466–4469; b) H. Ueno, H. Kawakami, K. Nakagawa, H. Okada, N. Ikuma, S. Aoyagi, K. Kokubo, Y. Matsuo, T. Oshima, *J. Am. Chem. Soc.* **2014**, *136*, 11162–11167.

[25] a) M. Solá, J. Mestres, J. Martí, M. Duran, *Chem. Phys. Lett.* **1994**, *231*, 325–330; b) M. Cases, M. Duran, J. Mestres, N. Martín, M. Solà in *Fullerenes for the New Millennium, Vol. 11* (Eds.: P. V. Kamat, D. M. Guldi, K. M. Kadish), The Electrochemical Society, Pennington, **2001**, pp. 244–269.

[26] a) L. M. Giovane, J. W. Barco, T. Yadav, A. L. Lafleur, J. A. Marr, J. B. Howard, V. M. Rotello, *J. Phys. Chem.* **1993**, *97*, 8560–8561; b) L. S. K. Pang, M. A. Wilson, *J. Phys. Chem.* **1993**, *97*, 6761–6763.

[27] I. Fernández, M. Solà, F. M. Bickelhaupt, *Chem. Eur. J.* **2013**, *19*, 7416–7422.

[28] Y. García-Rodeja, M. Solà, F. M. Bickelhaupt, I. Fernández, *Chem. Eur. J.* **2017**, *23*, 11030–11036.

[29] M. Güell, J. Poater, J. M. Luis, O. Mó, M. Yáñez, M. Solà, *ChemPhysChem* **2005**, *6*, 2552–2561.

[30] G. S. Hammond, *J. Am. Chem. Soc.* **1955**, *77*, 334–338.

[31] J. Contreras-García, E. R. Johnson, S. Keinan, R. Chaudret, J.-P. Piquemal, D. N. Beratan, W. Yang, *J. Chem. Theory Comput.* **2011**, *7*, 625–632.

[32] Gaussian 16, Revision B.01, M. J. Frisch, G. W. Trucks, H. B. Schlegel, G. E. Scuseria, M. A. Robb, J. R. Cheeseman, G. Scalmani, V. Barone, G. A. Petersson, H. Nakatsuji, X. Li, M. Caricato, A. V. Marenich, J. Bloino, B. G. Janesko, R. Gomperts, B. Mennucci, H. P. Hratchian, J. V. Ortiz, A. F. Izmaylov, J. L. Sonnenberg, D. Williams-Young, F. Ding, F. Lipparini, F. Egidi, J. Goings, B. Peng, A. Petrone, T. Henderson, D. Ranasinghe, V. G. Zakrzewski, J. Gao, N. Rega, G. Zheng, W. Liang, M. Hada, M. Ehara, K. Toyota, R. Fukuda, J. Hasegawa, M. Ishida, T. Nakajima, Y. Honda, O. Kitao, H. Nakai, T. Vreven, K. Throssell, J. A. Montgomery, Jr., J. E. Peralta, F. Ogliaro, M. J. Bearpark, J. J. Heyd, E. N. Brothers, K. N. Kudin, V. N. Staroverov, T. A. Keith, R. Kobayashi, J. Normand, K. Raghavachari, A. P. Rendell, J. C. Burant, S. S. Iyengar, J. Tomasi, M. Cossi, J. M. Millam, M. Klene, C. Adamo, R. Cammi, J. W. Ochterski, R. L. Martin, K. Morokuma, O. Farkas, J. B. Foresman, D. J. Fox, Gaussian Inc., Wallingford CT, **2016**.

[33] a) J. S. Binkley, J. A. Pople, W. J. Hehre, *J. Am. Chem. Soc.* **1980**, *102*, 939–947; b) M. S. Gordon, J. S. Binkley, J. A. Pople, W. J. Pietro, W. J. Hehre, *J. Am. Chem. Soc.* **1982**, *104*, 2797–2803.

[34] S. Osuna, M. Swart, M. Solà, *J. Phys. Chem. A* **2011**, *115*, 3491–3496.

[35] a) S. Grimme, S. Ehrlich, L. Goerigk, *J. Comput. Chem.* **2011**, *32*, 1456–1465; b) A. D. Becke, E. R. Johnson, *J. Chem. Phys.* **2005**, *122*, 154104.

[36] Y. Zhao, D. G. Truhlar, *Theor. Chem. Acc.* **2008**, *120*, 215–241.

[37] a) R. Ditchfield, W. J. Hehre, J. A. Pople, *J. Chem. Phys.* **1971**, *54*, 724–728; b) W. J. Hehre, R. Ditchfield, J. A. Pople, *J. Chem. Phys.* **1972**, *56*, 2257–2261.

[38] a) G. Scalmani, M. J. Frisch, *J. Chem. Phys.* **2010**, *132*, 114110; b) J. Tomasi, B. Mennucci, R. Cammi, *Chem. Rev.* **2005**, *105*, 2999–3094.

Manuscript received: October 10, 2019
Accepted manuscript online: November 18, 2019
Version of record online: December 27, 2019

Chapter 7. Results and discussion

In this chapter, we will discuss the achievements of this thesis based on the research published papers shown in the previous chapters. We highly recommend reading them beforehand.

As stated in the introduction, this thesis focuses on the idea of green chemistry. We have presented several works towards clean energy production, waste recycling, and industrial refining. These projects separate into three: hydrogen production as a clean energy source (Section 1.2.1), atmospheric gas recycling (Section 1.2.2), and clean energy production through solar cells (Section 1.3). Accordingly, we will analyze them in the category they are in, followed by a more global view.

7.1. Highlights of hydrogen production for a clean energy source

We divide the thesis projects within this category into WOC (Sections 4.1 and 4.2) and PNP ligand catalysis (Sections 4.3, 4.4). Despite the different topics, all of them produce hydrogen, and each article provides a deep understanding of their respective processes.

7.1.1. Water Oxidation Catalysis: carboxylates, phosphonates, and pH

This section is based on the manuscripts' contents by Luque-Urrutia *et al*. *Catal. Today*, **2020**, *358*, 278-283, and Luque-Urrutia *et al*. *Dalton Trans.* **2020**, *49*, 14052-14060, which can be found in sections 4.1 and 4.2 of this thesis.

The most renowned catalyst for WOC up to date is the Ru(bda) catalyst. The reason is believed to be the opening angle of this bda ligand, and more accurately, the angle between its carboxylates with the metal center O-Ru-O. Most of the studies reported[215-217] that the reaction mechanism goes through WNA or I2M, depending on the performed experiments. Nevertheless, we found out one that stood out from the rest because it did not follow the typical I2M or WNA; instead, it created a sort of intramolecular I2M based on two monomers bonding, generating the almost rhomboid bis-μ-oxo structure ***E*** as represented in ***Figure 53***.

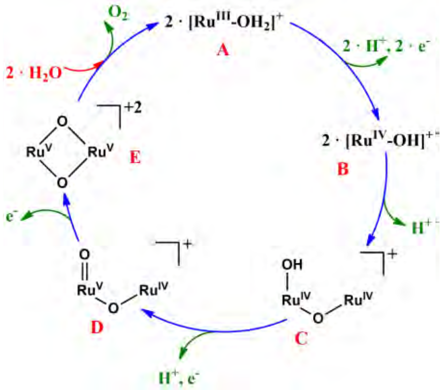

Figure 53. Proposed water oxidation mechanism for $[Ru(bda)(pic)_2]$ at pH = 8.

Before the publication of Concepcion et al., all reported studies discussing I2M considered intermolecular I2M processes. For this reason, the proposal of a possible intramolecular I2M was particularly interesting. In this new case, the monomers would interact, forming a metal-oxo-metal bond followed by a second bond like the first one, and then, the oxygen would be released. This statement already raised many eyebrows since the catalyst particularity is that the angle formed through the bda and the Ru center enabled a water molecule to bind, forming a very reactive hepta-coordinated Ru, yet if they bind like ***Figure 53***, one should reach an octa-coordinated Ru at least. It could mean that the bda could allow further bonding in particular cases, which could improve the performance of the catalyst, or at least, it could enable further research on this topic. There was still another reason to delve into this mechanism: the pH. This new proposal was made at pH = 8, which differs from other authors' usual neutral or acidic pHs. Given the Ru(bda) catalyst structure, where there are no acidic protons or weak bonds that could deprotonate, we wondered why the pH mattered. Those inquiries about the mechanism derived into the following results:

Figure 54 shows the conclusions of a thorough structure scan that considered all possible pathways, step by step (oxidations and deprotonations) or concerted single-steps (PCETs). The data at pH = 1 show the most common procedure reported in most papers that analyzed this catalyst; the catalyst ($^{1}\mathbf{0}^{+0}$) binds to water ($^{1}\mathbf{0}^{+0} \rightarrow {}^{1}\mathbf{3}^{+0}$), oxidizes ($^{1}\mathbf{3}^{+0} \rightarrow {}^{2}\mathbf{4}^{+1}$), makes a couple of PCETs ($^{2}\mathbf{4}^{+1} \rightarrow {}^{1}\mathbf{8}^{+1}$ and $^{1}\mathbf{8}^{+1} \rightarrow {}^{2}\mathbf{12}^{+1}$), and reaches the Ru^V=O complex. From here onwards, we tried to locate the rhomboid structure ***E*** of ***Figure 53***, but we were not successful. All trials derived into an O-O bonding, which denotes a clear intermolecular I2M.

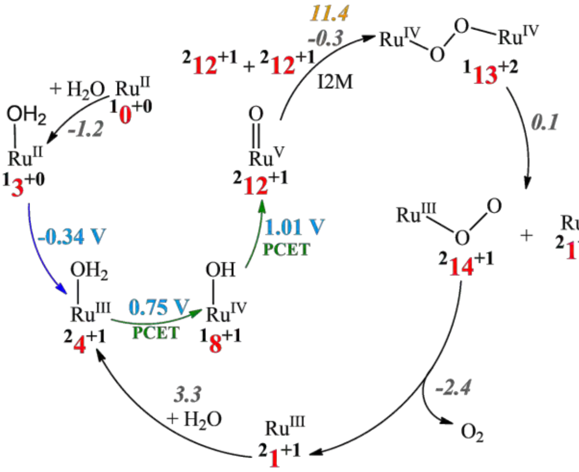

Figure 54. Mechanism for the Ru-bda catalyst at pH = 1; PCETs in green; Gibbs energy barriers in orange; reduction potentials in light blue; Gibbs reaction energies in grey. Energies are given in kcal/mol and oxidation potentials in V. Arrows in blue denote oxidation processes and in green proton-coupled electron transfers.

As this is done at pH = 1 and the experiment at pH = 8, it is not a fair comparison; thus, we also studied the mechanism at pH = 8, as shown in ***Figure 55***. Even at first glance, it is clear that changing the pH enables far more possibilities than at pH = 1. The key differences are compounds **7** and **11** that appear at pH = 8 instead of compound **8** at pH = 1. These molecules enable the suggested path of ***Figure 53***, represented as either compound **A** or **A'**. The issue with these molecules is that, as expected, an octa-coordinated metal center was not possible. Despite several trials, we found out that to reach such a dimer, one of the carboxylates bonded to the Ru had to break its bond and rotate 90 º so that the oxygen may bond. This opening has an affordable energy cost of 17.0 kcal/mol. However, adding this opening with the dimerization, we can see the reasoning behind the high TSs energy of 32.7 kcal/mol for **A** and 26.7 kcal/mol for **A'**.

Despite this change in the pathway, we can still reach the Ru^V=O state and perform the common I2M pathway. If we compare the three possible pathways, it is clear that the already known I2M TS, with a barrier of 11.4 kcal/mol, is the most favored one. With everything said, the results are quite simple: the preferred pathway is the same at both acid and basic pH. Nevertheless, the intermediate species that go towards the reactive Ru^V monomer differ slightly, but the catalysis proceeds through the same r.d.s.

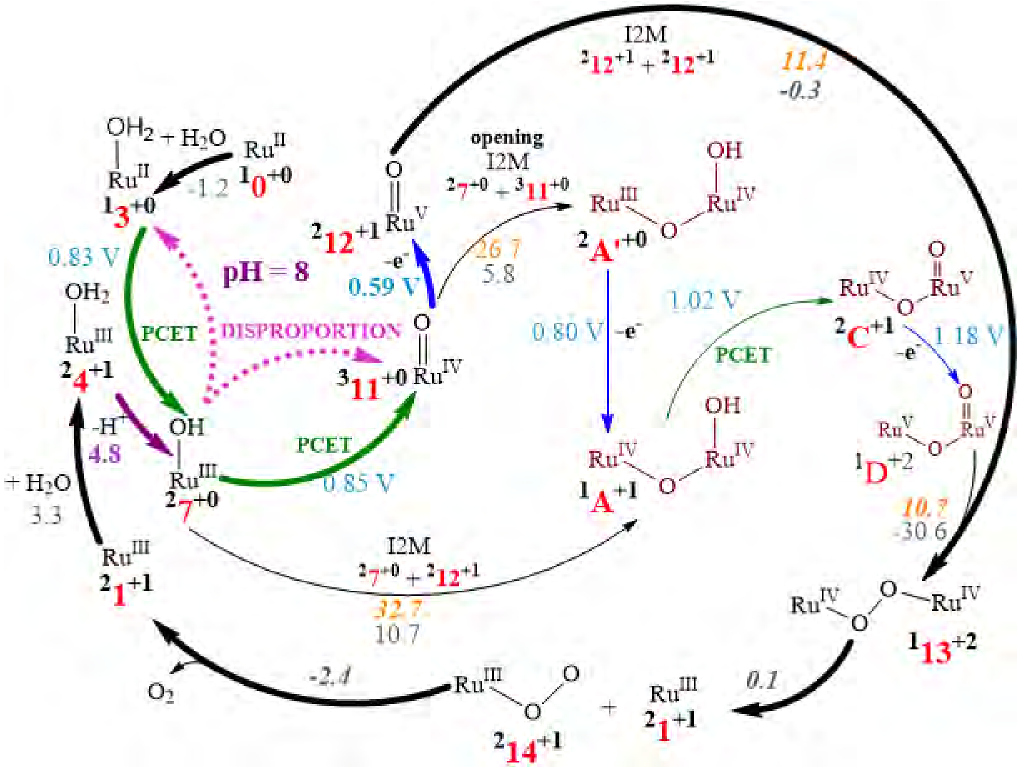

Figure 55. The carboxylate catalyst mechanism at pH = 8; Gibbs energy barriers in orange; reduction potentials in light blue; pK_a in purple; Gibbs reaction energies in grey. Energies are given in kcal/mol and reduction potentials in V. Main path represented with bold arrows. Arrows in blue denote oxidation processes, in purple proton transfers, in green proton-coupled electron transfers, and pink for dashed disproportion processes.

After unraveling the Ru(bda) catalyst's whole mechanism, we noticed that the pH had a small and imperceptible impact since it affects non-stationary complexes; thus, we looked into similar catalysts with broader pH effects. Accordingly, we found a promising target for our inquiries: a Ru(bpa) catalyst, which is equivalent to the previous Ru(bda) but instead of having carboxylates as ligands, it has phosphonates. This new catalyst, Ru(bpa), where the “p” stands for phosphonates, not only is similar enough to the Ru(bda) catalyst, but since it has a hydroxyl ligand bound to the phosphonate, it is a pH-responsive catalyst as it could deprotonate according to the pH.

As stated in the article, there are already many studies regarding this catalyst, and the main conclusion is that the Ru(bpa) performs worse than the Ru(bda). The phosphonated catalyst has lower TOFs and needs higher potentials than the carboxylated one, and even more, it requires the presence of a specific oxidant: Cerium Ammonium Nitrate (CAN). To make things worse, CAN provides protons to the media. Thus, it works only under acidic conditions (near pH = 1), but in more basic media, it precipitates, disabling the possibility of working at pH = 8 like its predecessor. Nevertheless, we decided to check all possible paths and pHs to know the reasoning behind this reactivity disparity. The results of the analysis at pH = 8 appear in ***Figure 56***.

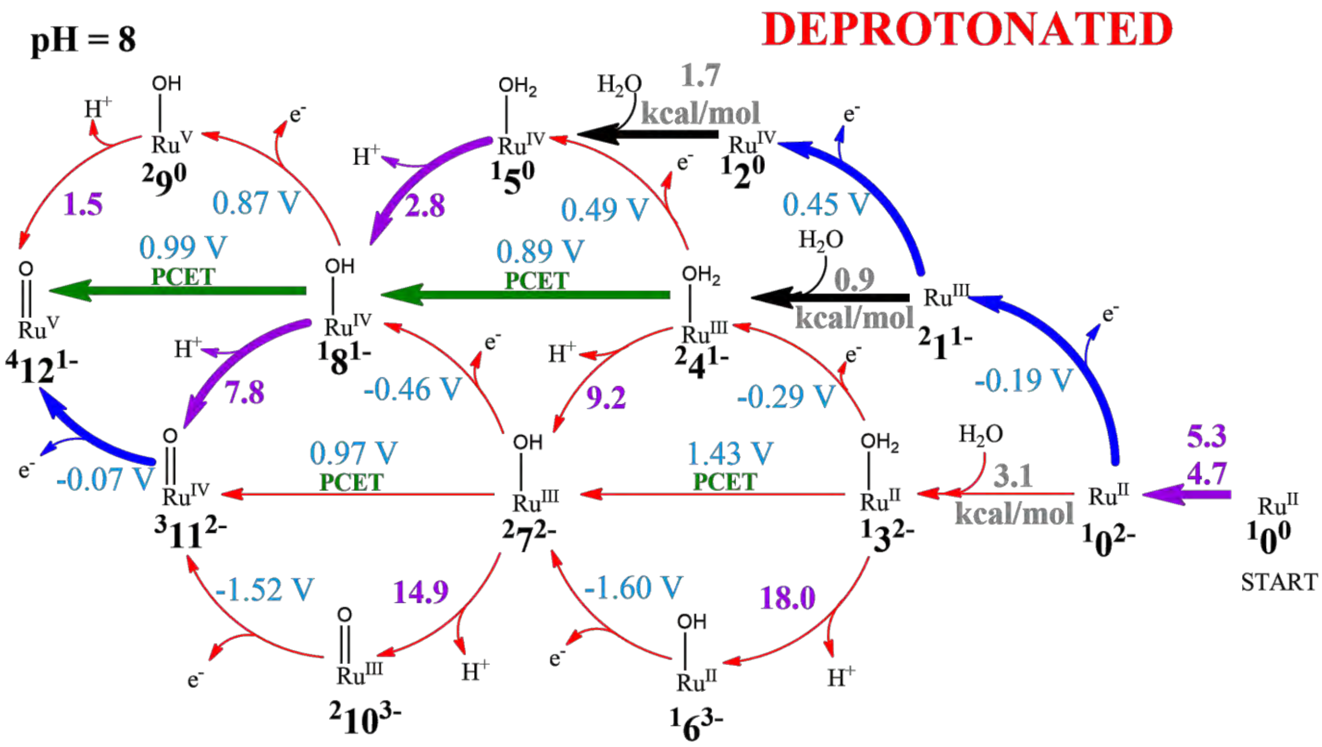
pH = 8
DEPROTONATED
OH
H+
e-
RuV
29^0
1.5
0.87 V
OH2
RuIV
15^0
H+
2.8
H2O
1.7
kcal/mol
e-
RuIV
12^0
e-
0.49 V
0.45 V
0.99 V
PCET
0.89 V
PCET
O
RuV
412^1-
OH
RuIV
18^1-
OH2
RuIII
24^1-
H2O
0.9
kcal/mol
RuIII
21^1-
e-
H+
7.8
e-
-0.46 V
H+
9.2
e-
-0.29 V
-0.19 V
O
e-
-0.07 V
RuIV
311^2-
0.97 V
PCET
OH
RuIII
27^2-
1.43 V
PCET
OH2
RuII
13^2-
H2O
3.1
kcal/mol
RuII
10^2-
5.3
4.7
RuII
10^0
START
-1.52 V
14.9
-1.60 V
18.0
O
RuIII
210^3-
e-
H+
e-
OH
RuII
16^3-
H+

Figure 56. Electrochemical reaction mechanism catalyzed by **Ru(bpa)** (= $^{1}\mathbf{0}^{+0}$) at pH = 8. Favored pathways highlighted with thick arrows. Green = PCET, blue = oxidation, purple = deprotonation. Species are labeled $^{\mathbf{X}}\mathbf{Y}^{\mathbf{q}}$, where **X** indicates a spin state, and q is the total charge of species **Y**.

First of all, we assume that the resting state of the catalyst ($^{1}\mathbf{0}^{0}$) has both hydroxyl ligands protonated. When we drive the reaction towards basic pHs (higher than 5.3), it deprotonates, as shown in ***Figure 56***. There are many possible outcomes of the mechanism, and we show all of them with the data we obtained. Following this logic, and considering the available potential in the media, we can choose one path or another. Starting from the deprotonated Ru^{II}, we chose water oxidation instead of water coordination due to two factors. First, Sun *et al*. stated[69-70, 218] that it must oxidize before the water binds, and second, the O-Ru-O opening angle, the one that enables the hepta-coordination, varies in width depending on the OS of the metal. Comparing the Ru^{III} and the Ru^{II} compounds, the angle is wider for Ru^{III}, meaning that it is easier for water to bind to the metal. Additionally, despite picturing a 3.1 kcal/mol step ($^{1}\mathbf{0}^{2-} \rightarrow {}^{1}\mathbf{3}^{2-}$), complex $^{1}\mathbf{3}^{2-}$ is an adduct since we could not locate the complex with the water bonded. Furthermore, the Ru^{III} angle is 5 º narrower than the equivalent at Ru(bda) while the Ru^{II} is almost 12 º, which could mean that the water cannot bind with such a narrow-angle. We could argue that according to the redox potential of Ru^{III} to Ru^{IV}, it could also oxidize and then bond with the water molecule, as the energy difference is almost negligible (0.8 kcal/mol between Ru^{III} and Ru^{IV} water bonding). According to our calculations alone, we cannot distinguish which is preferred; thus, we highlight both paths. A similar problem arises from compound **8**; the pH is higher than the pK_a, but they are almost equal. If we think on a pH = pK_a situation, we cannot distinguish whether it will be a PCET or deprotonation since we could also have method related errors that may change the pK_a slightly enough to set the balance off. Once again, we highlight both paths.

This reasoning is only one half of the solution, as it is only based on computational results, and shows clear doubts about which path to take in each case; therefore, we require the experimental data to help us solve this riddle. Analysis of the voltammograms provided by one of the authors included in the article's annexes in section 10.2 demonstrates the paths the mechanism follows. First, there is no peak at 0.45 V. This indicates that the Ru^{III}/Ru^{IV} oxidation does not occur. We believe it does not occur due to the molecule destabilization since it goes from a Ru^{III} with a -1 charge that could help stabilize the OS to an even higher OS but with now an overall +0 charge, which does not help to stabilize it. The second important thing we found out through the experimental data is that the PCET prevails over the deprotonation simply because the experiments were done at pH = 7, while in the diagram, we considered a pH = 8 to compare the data of this catalyst with the Ru(bda) catalyst. If we consider pH = 7, the PCET predominates. It also coincides with the 2H$^+$/2e$^-$ step that other authors reported. Before going further into whether the mechanism proceeds *via* I2M or WNA, let us discuss the mechanism at pH = 1 shown in ***Figure 57***.

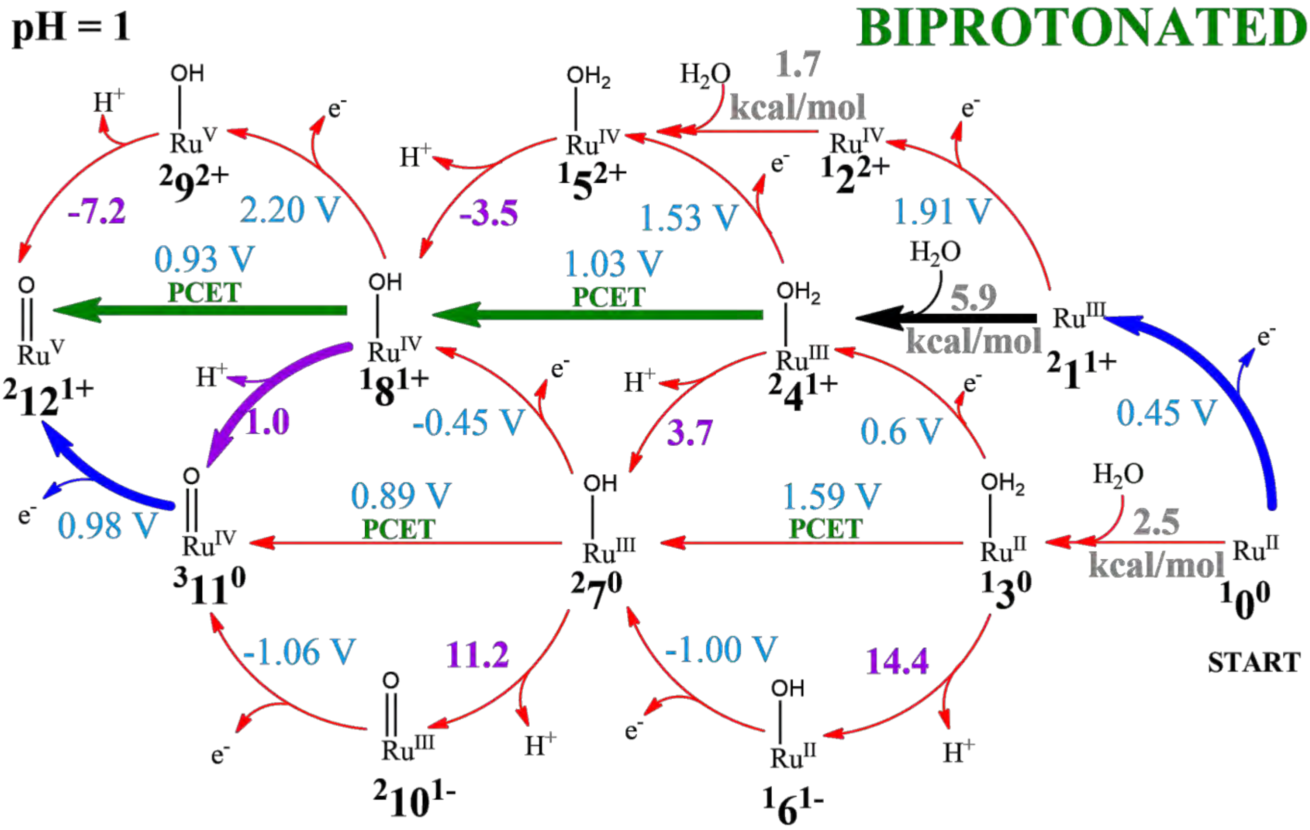

Figure 57. General mechanism for **Ru(bpa)** at pH = 1. Green arrows for PCETs, blue for OSs, and purple for pK$_a$. Species are labeled $^{\mathbf{X}}\mathbf{Y}^{\mathbf{q}}$, where **X** indicates the spin state, and **q** is the total charge of species **Y**.

In this case, the pathway is a bit clearer since the previous oxidation from Ru^{III} to Ru^{IV} is not possible as it has an electropotential of 1.91 V, and the CAN only provides an oxidative media from 1.6 V to 1.7 V. Despite this, the same issue at compound **8** occurs at pH = 1 and pH = 8, which is that pH = pK$_a$. Following the previous statements and experimental data analysis, considering that there is a 2H$^+$/2e$^-$ step, we believe that the same procedure happens again; thus, the PCET is preferred over the deprotonation plus oxidation. This explanation would be perfect except for one detail found in the experimental data: the 2H$^+$/2e$^-$ voltammogram shows a peak at 1.40 V, far from the 1.03 V shown here. For reference, in the mechanism at pH = 8, the computational PCET was at 0.99 V and the experimental peak at 1.25 V, a 0.26 V difference at pH = 8 and a 0.37

V at pH = 1. We know that the computational predictions are the ideal case, but the experiments require overpotentials to progress the product's reaction.

Nevertheless, a difference of almost 0.4 V seems too much for an overpotential, and since the same method applies to both pHs, the difference between them should be minimal. The solution to this problem is within the deprotonation of the phosphonate ligands. Each compound can deprotonate and re-protonate according to the pK_a and pH; thus, we checked which compounds should deprotonate at pH = 1. By doing so, we found the source of our problems: compounds **4**, **8**, and **12**, the ones involved in the PCETs, vary their protonation states. With a pK_a for the deprotonation of the bpa ligand of 0.2 for molecule **4**, a pK_a of 0.8 for molecule **8**, and a pK_a of 1.1 for molecule **12**, it means that the PCETs do not occur while both phosphonated ligands are protonated; instead, they occur when only one of them is deprotonated, as shown in ***Figure 58***.

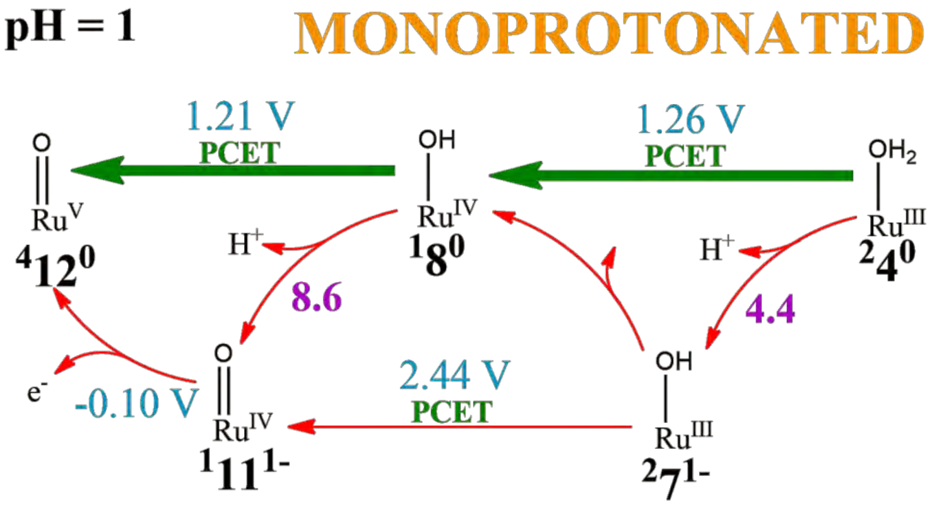

Figure 58. Monoprotonated phosphonate mechanism for **Ru(bpa)** at pH = 1. Species are labeled $^{\mathbf{X}}\mathbf{Y}^{\mathbf{q}}$, where **X** indicates the spin state, and **q** is the total charge of species **Y**.

Going back to the potential problem explained before, we see that the highest potential of the PCETs is 1.26 V. Compared to the experimental 1.4 V, we observe a difference of 0.14 V; thus, there is less absolute error concerning the experimental value. Not only the PCETs are closer in potential now, but they are also explained through deprotonation that, despite having acidic pH = 1, occurs due to their lower pK_a (0.2). We must remark that despite this deprotonation, compound **12** has a pK_a of 1.1, and thus it should re-protonate to the biprotonated phosphonate, leaving this monoprotonated reaction hidden between biprotonated phosphonates.

This should cover the H_2 formation since the free protons would later combine with the electrons and form the gas, which is the focus of the thesis; however, since we were unfolding new parts of the WOC catalyst, we wanted to finish the cycle by regenerating the catalyst. As stated in the introduction, there are two known ways of creating the O_2 molecule: WNA and I2M. We display the results of the kinetic barriers in ***Figure 59***. At pH = 8, we have the deprotonated bpa ligand. Experimentally, there was no catalytic activity, if any, and looking into the computational data, we see an I2M barrier of 19.7 kcal/mol and a WNA barrier of 28.8 kcal/mol. Given the experimental conditions, the former energy barrier could be feasible; but it is still 7.3 kcal/mol higher than the Ru(bda) counterpart, explaining the catalyst's lower performance. Since the WNA is too high in energy (28.8 kcal/mol), this could explain the almost none (if any) catalytic activity at pH

= 8 through an I2M mechanism. Looking into the pH = 1 path, we observe an I2M barrier of 18.4 kcal/mol, which is lower than the one at pH = 8, and a WNA barrier of 14.3 kcal/mol, way much lower than at pH = 8. This WNA supports the experimental information that this catalyst has first-order kinetics since only one monomer is involved, and the barrier is reasonable given the experimental conditions. Considering all the above, the WNA should be preferred at pH = 1, as many authors already suggested.

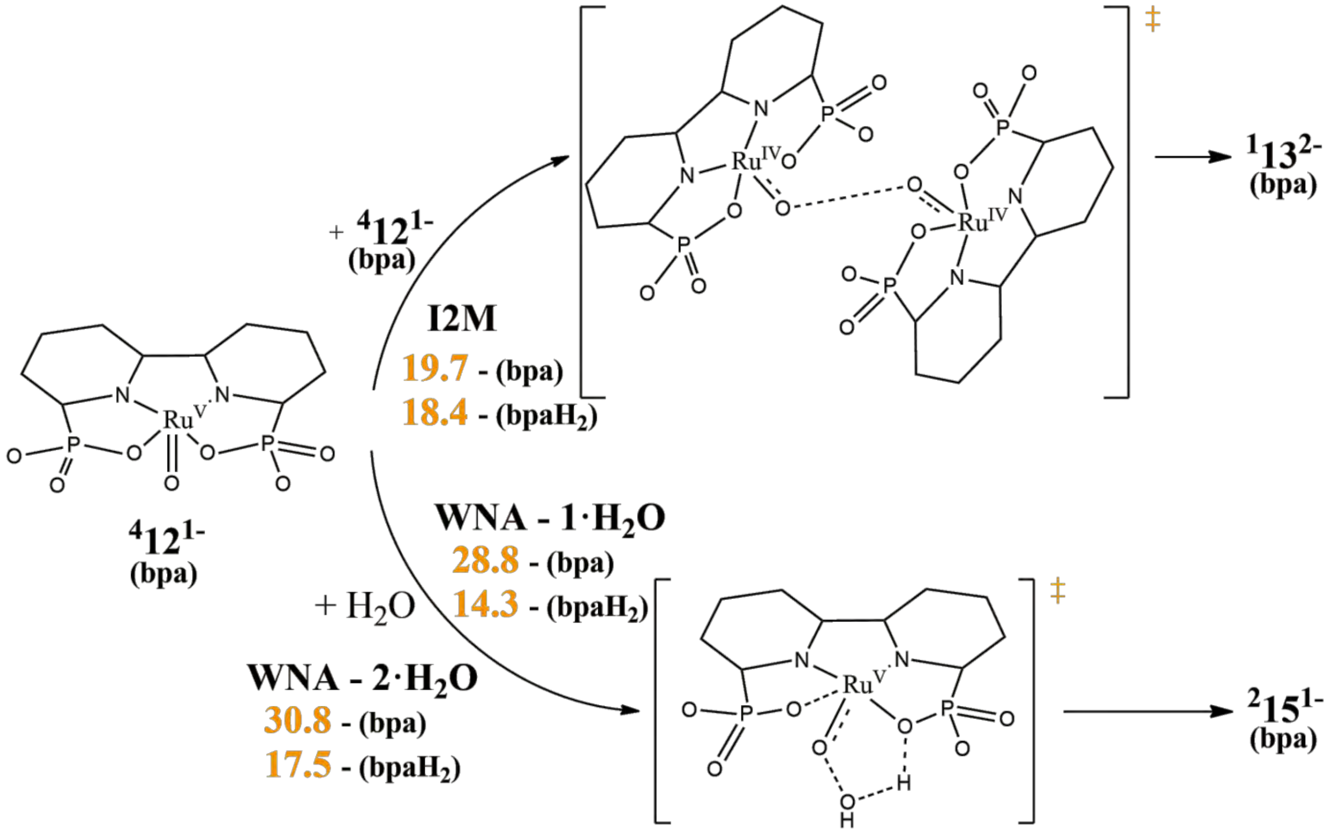

$^{4}12^{1-}$
(bpa)
+ $^{4}12^{1-}$
(bpa)
I2M
19.7 - (bpa)
18.4 - ($bpaH_2$)
‡
$^{1}13^{2-}$
(bpa)
WNA - $1\cdot H_2O$
28.8 - (bpa)
14.3 - ($bpaH_2$)
+ H_2O
WNA - $2\cdot H_2O$
30.8 - (bpa)
17.5 - ($bpaH_2$)
‡
$^{2}15^{1-}$
(bpa)

Figure 59. I2M and WNA mechanisms pathways (with 1 or 2 assisting water molecules) for the deprotonated (bpa at pH = 8) and protonated ($bpaH_2$ at pH = 1) phosphonate catalyst (axial ligands and non-interacting hydrogens removed for clarity). Gibbs energy barriers (kcal/mol) in orange.

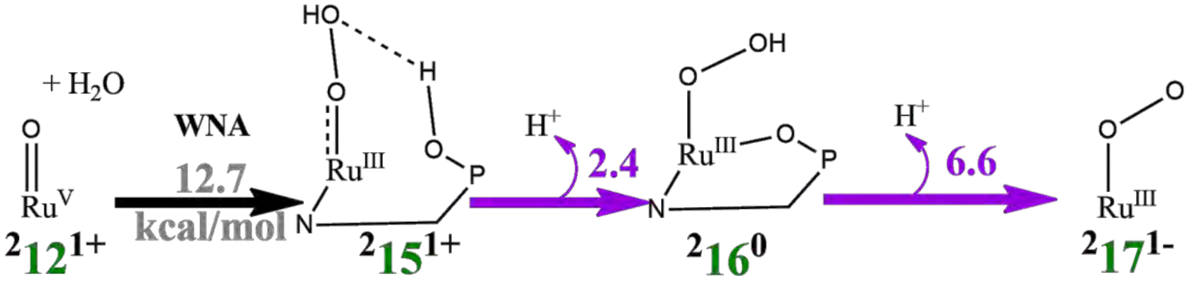

+ H_2O
$^{2}12^{1+}$
WNA
12.7
kcal/mol
$^{2}15^{1+}$
H^+
2.4
$^{2}16^{0}$
H^+
6.6
$^{2}17^{1-}$

Figure 60. Liberation of O_2 through WNA for the $bpaH_2$ catalyst at pH = 1. Gibbs reaction energy (kcal/mol) in grey, pK_a for deprotonations in purple.

The next steps are simple; now that we consider a WNA mechanism, we must deprotonate twice the water molecule and liberate the oxygen while having appropriate OSs for the metal center. Deprotonation seems the most reasonable since it will not change the OS (Ru^{III}), but the charge will become -1, as shown in ***Figure 60*** ($^{2}\mathbf{15}^{1+} \rightarrow {}^{2}\mathbf{17}^{1-}$). As one can see, the water pK_a is too high given the pH = 1 of the media. Furthermore, the result would be a Ru^{III} with an overall charge of -1, which is not within the mechanism in ***Figure 57*** and adds the negative charge problem. The high pK_a indicates that even if water binds to the Ru^{V} through a WNA, it could never deprotonate, staying stuck in that step and showing no catalytic activity. PCETs are not possible even though when the water binds to the oxygen, the OS of the Ru^{V} shifts to Ru^{III} ($^{2}\mathbf{12}^{1+} \rightarrow {}^{2}\mathbf{15}^{1+}$), which we tested using Salvador's EOS program.[205] These two PCETs would mean increasing the Ru^{III} to Ru^{V} again but without a water molecule attached, creating a Ru^{V} complex ($^{2}\mathbf{17'}^{1+}$) not able to regenerate the catalyst (***Figure 61***). This phenomenon also happens experimentally: there is no catalytic activity under external voltage, except if we include CAN into the media.

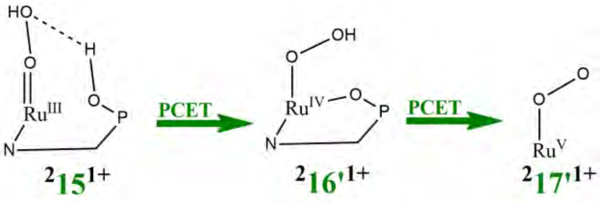

Figure 61. PCET test showing the formation of a Ru^{V}-OO complex that could not regenerate the catalyst.

Let us review for a moment the data that we have. This WOC catalyst does not work without a sacrificial oxidant (CAN). With external potential alone, there is no catalytic activity. Computationally, we observe that WNA is possible, but the attached water will never deprotonate; thus, the catalyst's regeneration will not occur. Finally, experimental results show the first-order kinetics of the reaction. With everything said, there is only one possible explanation of this catalyst's reactivity: the CAN added into the media as oxidant plays a direct role as cocatalyst in this WOC. We demonstrated that neither WNA nor I2M occur; thus, there must be another pathway.

Additionally, the reaction does not progress unless there is this specific oxidant; other common oxidants do not work either. If the oxidant formed an I2M with the Ru catalyst, it would still fulfill the first-order kinetics because we would still use one monomer of catalyst, and since the CAN is usually in excess, it would not hinder the I2M pathway. There is one thing left to try, the CAN-Ru pathway.

There is, however, a problem with CAN: we do not know its structure in aqueous media. We know that CAN precipitates if the pH is not low enough and that it can provide between 1.6 V to 1.7 V of redox potential, but that is all. To try the Ru-CAN pathway, we attempted to develop a systematic CAN transformation shown in ***Figure 62***. The starting point was $[Ce^{IV}(NO_3)_6]^{2-}$. We analyzed all species resulting from the substitution of NO_3^- by H_2O until four substitutions are done, and we look at the reduction potentials of all species involved.

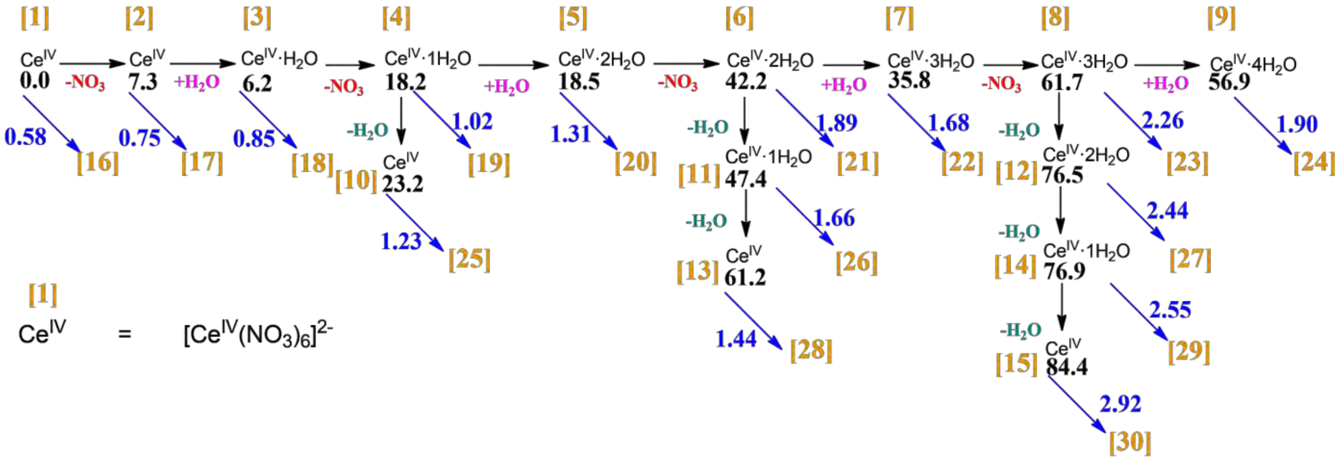
[1]
Ce^{IV} 0.0
-NO$_3$
[2]
Ce^{IV} 7.3
+H$_2$O
[3]
Ce^{IV}·H$_2$O 6.2
-NO$_3$
[4]
Ce^{IV}·1H$_2$O 18.2
+H$_2$O
[5]
Ce^{IV}·2H$_2$O 18.5
-NO$_3$
[6]
Ce^{IV}·2H$_2$O 42.2
+H$_2$O
[7]
Ce^{IV}·3H$_2$O 35.8
-NO$_3$
[8]
Ce^{IV}·3H$_2$O 61.7
+H$_2$O
[9]
Ce^{IV}·4H$_2$O 56.9
0.58
[16]
0.75
[17]
0.85
[18]
-H$_2$O
[10] Ce^{IV} 23.2
1.02
[19]
1.31
[20]
-H$_2$O
[11] Ce^{IV}·1H$_2$O 47.4
1.89
[21]
1.68
[22]
-H$_2$O
[12] Ce^{IV}·2H$_2$O 76.5
2.26
[23]
1.90
[24]
1.23
[25]
-H$_2$O
[13] Ce^{IV} 61.2
1.66
[26]
-H$_2$O
[14] Ce^{IV}·1H$_2$O 76.9
2.44
[27]
1.44
[28]
-H$_2$O
[15] Ce^{IV} 84.4
2.55
[29]
2.92
[30]
[1]
Ce^{IV} = [Ce^{IV}(NO$_3$)$_6$]$^{2-}$

Figure 62. Cerium Ammonium Nitrate electropotential study (in blue, the reduction potentials; in black, the Gibbs energies of the successive substitution of NO_3^- by H_2O in the CAN structure).

By developing the above mechanism, we expected to find a structure that we can reach at room temperature that is also able to provide the 1.6-1.7 V. Looking at ***Figure 62***, the last structure we could reach is **[5]** since the next step would increase the energy by 23.7 kcal/mol, without taking into account possible TSs; therefore, we could not reach it at room temperature. This compound **[5]** has a potential of 1.31 V, far from the experimental minimum of 1.6 V. Even taking into account that just like the computation *vs*. experiments, the computational results ranged from 0.2 V to 0.3 V lower potentials than the experimental results, indicating that this structure could reach the 1.6 V threshold, we could not verify that this structure is the one present in aqueous media. With this information and results, we thought it would be wise to stop delving into this topic, as a wrong reactant could lead to a bad result. Nevertheless, the Ru-Ce dimer's hypothesis was already present in some papers like that of Costas, Lloret-Fillol *et al.*,[219] and it makes sense as a possible outcome, but this lack of certainty to its structure is detrimental to the study.

Overall, the final mechanism at both pHs appears in ***Figure 63***. We managed to discover the different pathways according to the pH while also understanding why there is no I2M between two Ru monomers due to the high energy barriers, nor WNA due to the high pK_a compared to the low pH, which would not allow further deprotonations. The final path we hypothesize is an I2M with a Ru monomer and a CAN molecule, and since the structure of CAN is unknown in aqueous media, we could not delve further into the final steps of the mechanism.

Turning back towards green chemistry, not only we understand better a H_2 generator catalyst, but we also found out that one of the components in the media, CAN, should be part of the catalysis, which indicates that lower quantities of CAN could be used for the same results, reducing the reagents considerably, and thus the waste produced in the process.

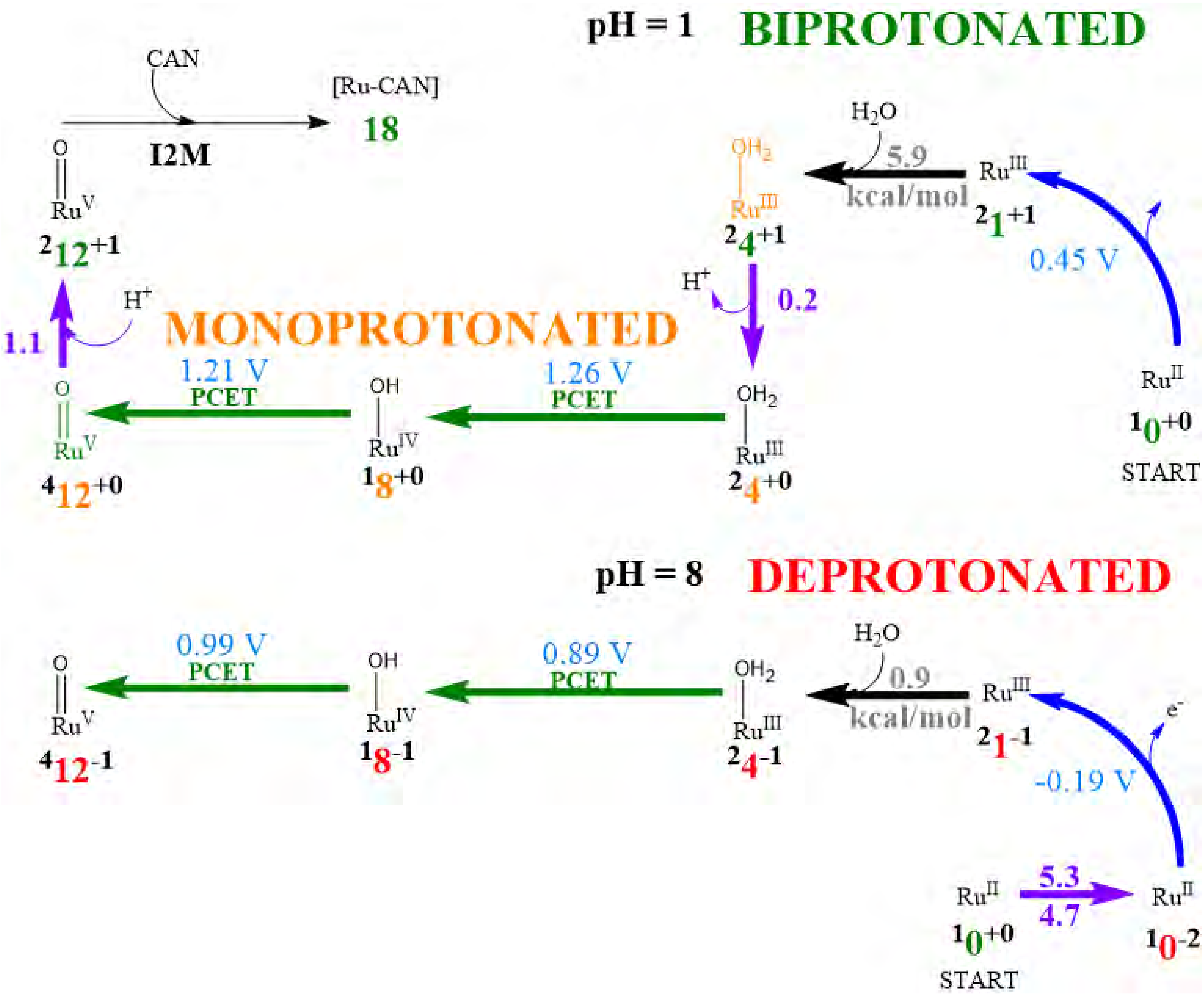
pH = 1
BIPROTONATED
CAN
[Ru-CAN]
18
I2M
H2O
5.9
kcal/mol
OH2
RuIII
RuIII
2 1 +1
0.45 V
RuV
2 12 +1
2 4 +1
H+
0.2
1.1
H+
MONOPROTONATED
1.21 V
PCET
1.26 V
PCET
OH
RuIV
OH2
RuIII
RuII
1 0 +0
START
RuV
4 12 +0
1 8 +0
2 4 +0
pH = 8
DEPROTONATED
H2O
0.99 V
PCET
0.89 V
PCET
OH2
0.9
kcal/mol
RuIII
e-
RuV
4 12 -1
RuIV
1 8 -1
RuIII
2 4 -1
2 1 -1
-0.19 V
RuII
5.3
4.7
RuII
1 0 +0
1 0 -2
START

Figure 63. Proposed final mechanisms at both pH for bpaH_2/bpaH and bpa catalysts. Green arrows for PCETs, and purple for pKa. Species are labeled $^{X}Y^{q}$**,** where **X** indicates the spin state, and **q** is the total charge of species **Y**. Blue values represent redox potentials, grey values represent Gibbs reaction energies and purple values represent pK_a.

7.1.2. Acceptorless Dehydrogenative Coupling: industrial processes refining

This section is based on the contents of the manuscripts by Luque-Urrutia *et al. J. Am. Chem. Soc.* **2019**, *141*, 2398-2403, Masdemont *et al. ACS Catal.* **2019**, *9*, 1662-1669, which can be found in sections 4.3 and 4.4 of this thesis.

After revising the most recent catalysis in clean hydrogen production through WOC, we wanted to check other Green Chemistry options such as industrial processes and toxic gases they emit. We could have chosen any possible chemical reaction, but we wanted to continue in the H_2 production for energy usage while also studying the latest catalysts available to be relevant to the field. We found the solution to our inquiries by looking into PNP catalysts that are a hot topic in research, and they also have broad reactivity in different fields, including processes involved in H_2 production.

The first reaction that piqued our interest was the recent alcohol and nitrile coupling developments for acrylonitrile production. On the one hand, we had the target product: acrylonitriles, widely used in synthesis as precursors as necessary as malaria treatment drugs and others. On the other hand, the most exciting part is the recent development in catalysts for this process. Until recently, this reaction proceeded like ***Figure 64***.

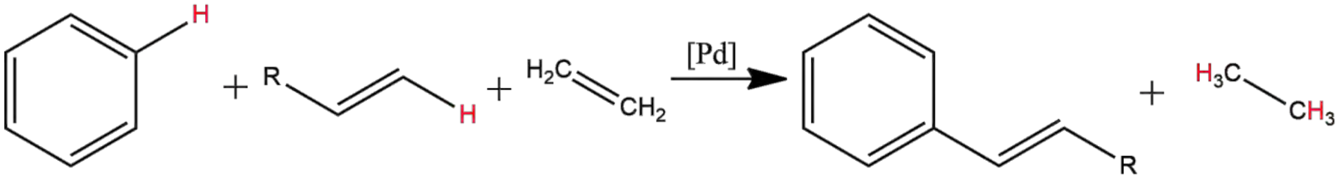

Figure 64. Dehydrogenative coupling of arenes and alkenes with the aid of a hydrogen acceptor in a palladium-catalyzed reaction.

The dehydrogenative coupling is a known reaction for "extracting" two hydrogen atoms from two molecules that we want to bond. Besides a heavy metal catalyst such as palladium, the main requirement with this reaction is the need for a hydrogen acceptor. A hydrogen acceptor is any given alkene that can hydrogenate to retain the hydrogen atoms from the reactants, but there is no particular interest to produce them, so they are considered waste or a by-product in the best scenario. Though needed, their presence is not optimal for waste management and, having more steps in a reaction leads to slower/higher energy consuming procedures. With everything said, a new manganese catalyst developed by Milstein *et al*.[86, 98] showed good catalytic activity in this field (see ***Figure 65***).

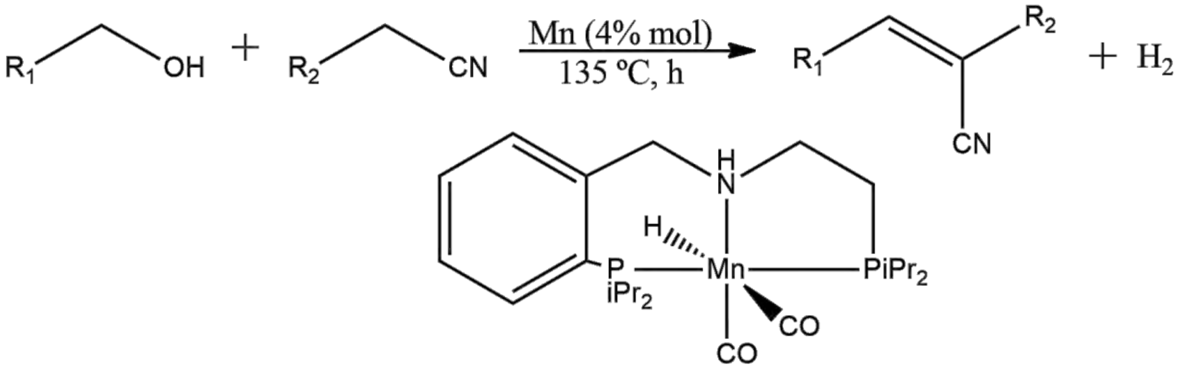

Figure 65. Catalytic ADC reported by Milstein *et al*.[87] with the catalyst structure.

Their paper reports a mechanism that combines experimental results and hypotheses, leading to apparent holes in the pathway. After some research, we found the full mechanism for this catalyst, including the answers to their experimental questions. The full mechanism appears in ***Figure 66***, which will be discussed in various sections since it could be challenging to fully understand the whole reaction mechanism at the beginning.

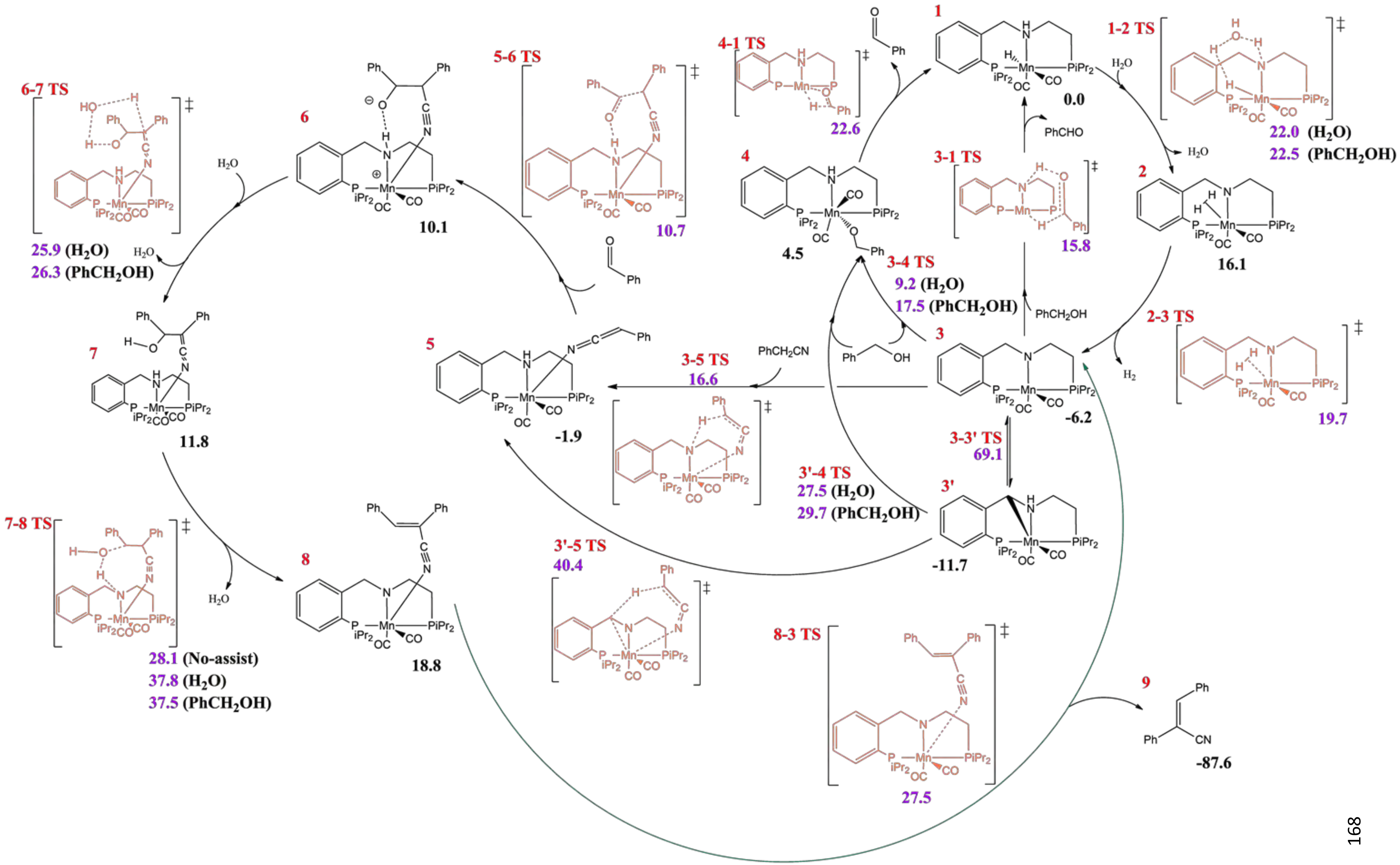
1
0.0
1-2 TS
22.0 (H₂O)
22.5 (PhCH₂OH)
2
16.1
2-3 TS
19.7
H₂
3
-6.2
3-1 TS
15.8
PhCH₂OH
PhCHO
H₂O
4-1 TS
22.6
4
4.5
3-4 TS
9.2 (H₂O)
17.5 (PhCH₂OH)
3-3' TS
69.1
3'
-11.7
3'-4 TS
27.5 (H₂O)
29.7 (PhCH₂OH)
3-5 TS
16.6
PhCH₂CN
5
-1.9
3'-5 TS
40.4
5-6 TS
10.7
6
10.1
6-7 TS
25.9 (H₂O)
26.3 (PhCH₂OH)
7
11.8
7-8 TS
28.1 (No-assist)
37.8 (H₂O)
37.5 (PhCH₂OH)
8
18.8
8-3 TS
27.5
9
-87.6

Figure 66. Full mechanism of the manganese catalyzed ADC for the synthesis of acrylonitriles starting from alcohols and nitriles. All values shown are Gibbs energies in kcal/mol. TS highlighted in purple.

Let us start from the right side of the mechanism that involves producing an aldehyde from alcohol, shown in ***Figure 67***.

Comparing this mechanism to the one reported in the original experimental article[87] is relatively easy. Everything is the same except for compound **2**. The pathway, however, is very different for compounds **3** and **3'**. Both are experimental intermediates: while **3** is the kinetic intermediate (the one formed first), **3'** is the thermodynamic one (the most stable one). Now, the difficulties arose from the experimental data. This experiment was performed at 25 ºC and **3'** completely formed in 12h.

On the other hand, **3'** appeared in just 30 min at 135 ºC. This particularity means that the energy barrier should be relatively low since the formation of the thermodynamic isomer needs 12 h at room temperature, yet the direct interconversion between **3** and **3'** demonstrated a barrier of almost 70 kcal/mol. This barrier is outrageously high, given the experimental conditions, and it is the result of the hydrogen swap between the C and N atoms and the C-M bond formed. We could obtain the next water/alcohol assisted pathways with relatively low barriers, which meant that it would be even more challenging to compete with this isomerization. The experiments, however, were there to prove that such a pathway was more than possible. The solution we found was hiding in plain sight, not through **3** nor **3'**, but within the next step, **4**.

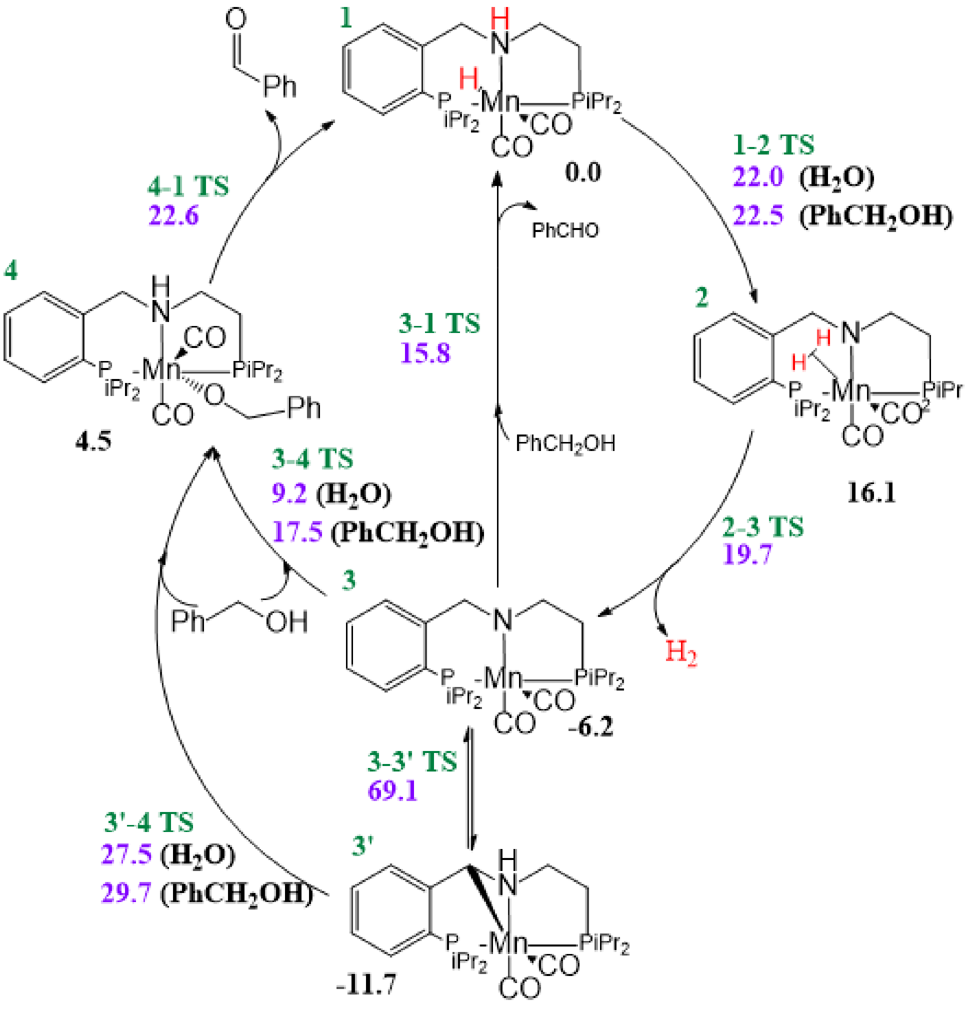

Figure 67. First cycle of the ADC catalysis for aldehyde formation (energies in kcal/mol).

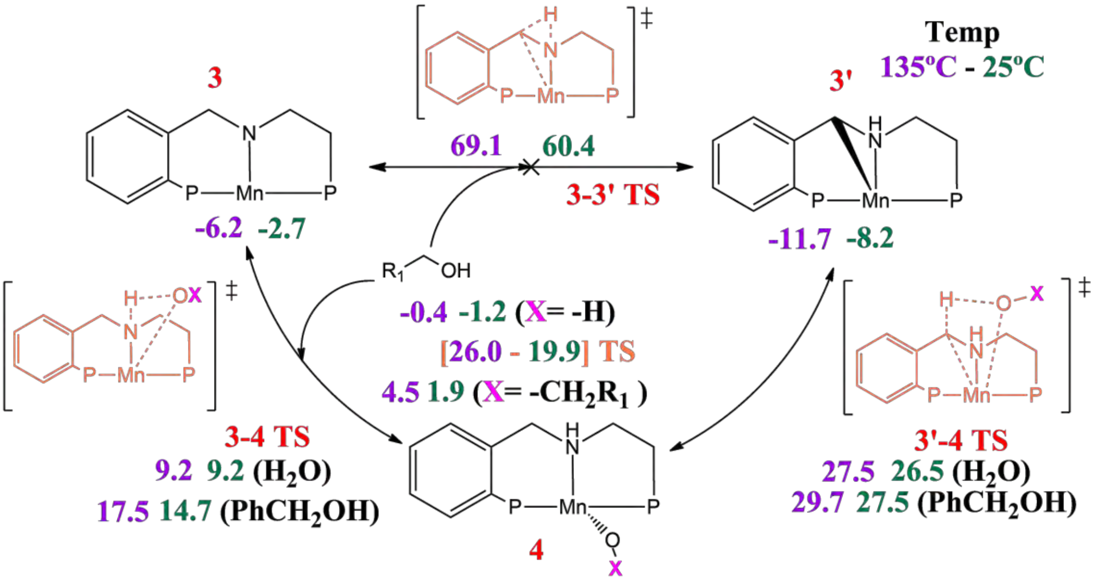
Temp
135ºC - 25ºC
3
3'
69.1 60.4
3-3' TS
-6.2 -2.7
-11.7 -8.2
R1 OH
-0.4 -1.2 (X= -H)
[26.0 - 19.9] TS
4.5 1.9 (X= -CH2R1)
H---OX
H----O-X
3-4 TS
9.2 9.2 (H2O)
17.5 14.7 (PhCH2OH)
3'-4 TS
27.5 26.5 (H2O)
29.7 27.5 (PhCH2OH)
4
P—Mn—P
N
H
O
X

Figure 68. Isomerization assisted by explicit water or alcohol molecules (energies in kcal/mol).

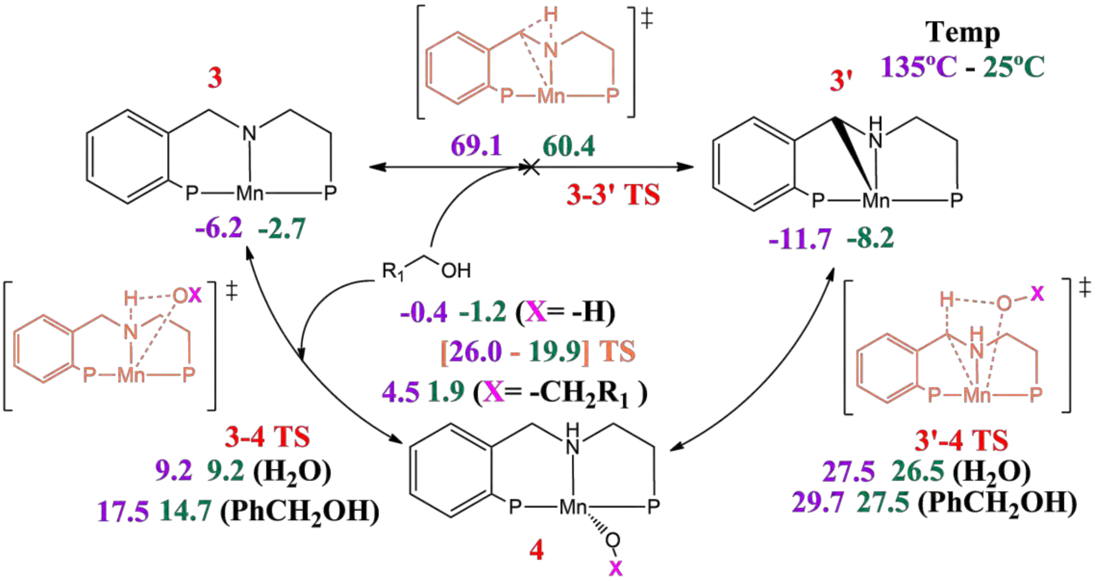

Temp
135ºC - 25ºC
3
3'
69.1 60.4
3-3' TS
-6.2 -2.7
-11.7 -8.2
R1 OH
-0.4 -1.2 (X= -H)
[26.0 - 19.9] TS
4.5 1.9 (X= -CH2R1)
3-4 TS
9.2 9.2 (H2O)
17.5 14.7 (PhCH2OH)
3'-4 TS
27.5 26.5 (H2O)
29.7 27.5 (PhCH2OH)
4

As *Figure 68* shows, the key was to introduce the assistance of water. To find the intermediates **3** and **3’**, no alcohol was needed experimentally; thus, we assumed that water could also play a role here. If we reach **4** with a water molecule, the barrier from **3** is only 9.7 kcal/mol at 25 ºC. Since the next step would mean converting the alcohol into aldehyde, we cannot progress further with just a water molecule. According to this, we thought about using **4** as a bridge between **3** and **3’**, and interestingly, that is indeed what occurs. Thanks to the use of this compound **4**, we can obtain the thermodynamic isomer with a barrier as high as 28.1 kcal/mol, ideal for the experimental results. At 25 ºC, the reaction would be possible but slow (12 h) since the barrier is a little too high given the temperature, and at 135 ºC, it would be quite fast, thus only needing 30 min to do so.

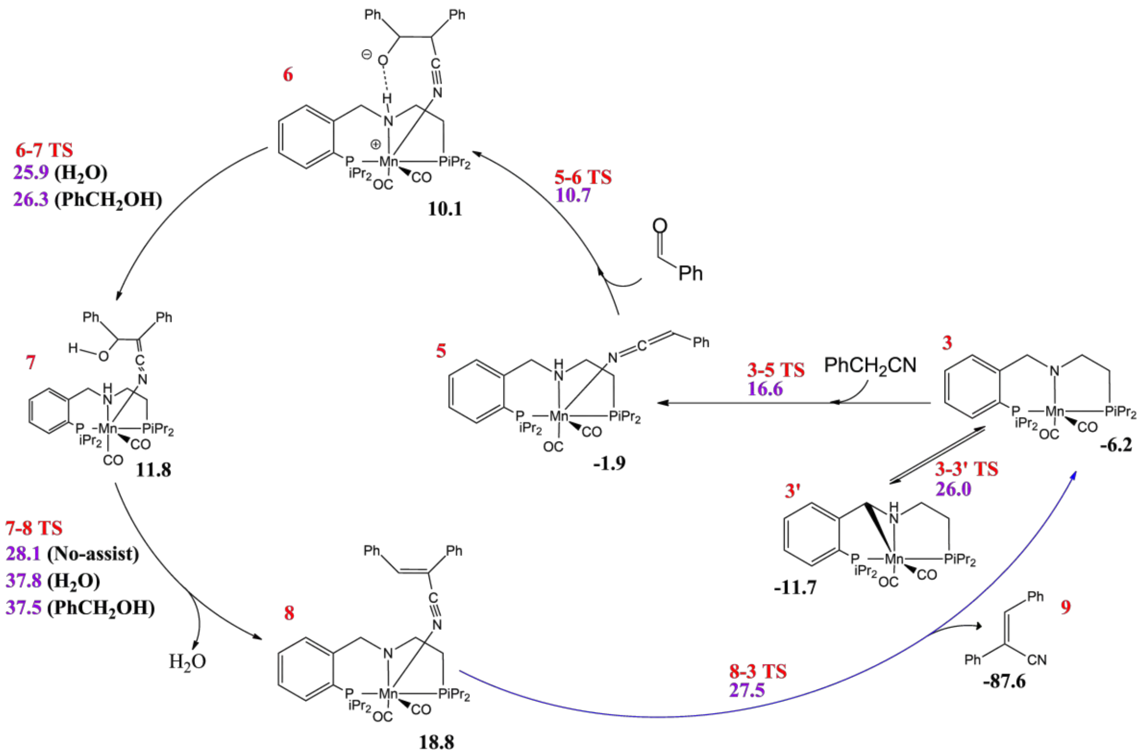

Figure 69. Second cycle for ADC catalysis showing acrylonitrile formation (energies in kcal/mol).

Now, let us look into the second part of the mechanism, the acrylonitrile synthesis in ***Figure 69***. Starting from **3**, we denote a clear difference to the previously reported mechanism. In Milstein's report, they stated a possible ionic combination without a clear structure (compound **5** in ***Figure 48***, Chapter 3). We located this in compound **6** through a Mn-N(C) bond that joins both molecules. We also kept considering either water or alcohol assistance because due to the Knovenagel condensation in step **7**-**8**, water will keep producing as the process continues. This condensation step is the r.d.s. of the whole mechanism, with a barrier of 28.1 kcal/mol. Overall, we found out that most steps, except the condensation, are assisted by either a water or an alcohol molecule, depending on which is present at the moment, but if we had to choose, it would prefer water as it has lower energy barriers in most steps, probably due to its smaller size. After obtaining the acrylonitrile, the catalyst regenerates in compound **3**, reinforcing both **3** and **3'** experimental findings since they are the connection between aldehyde formation and acrylonitrile production.

The high temperature involved in the reaction is something we should try to reduce if we want to go towards greener chemistry since more temperature means we need to use more energy to maintain it. We could try to make small changes in the catalyst and test whether it improves or not; however, as stated in the introduction, these PNP pincer ligand catalysts have quite broad reactivity. Knowing this, we looked for a similar reaction that could give us other insights to deepen the research. Out of all the reaction mechanisms we looked at, alcohols and amines coupling to produce aldimines took our attention. This reaction looked similar to the acrylonitrile synthesis for several reasons. First, the reactants are alcohol and amines, compared to alcohols and nitriles in the acrylonitrile synthesis. The proximity in functional groups (alcohol + nitrogenized ligand) is different enough to explore another pathway but close enough to relate both. Second, the experimental temperature is the same, 135 ºC, but the reaction time is very different, 60 h *vs*. 1 h. We wanted to see why the temperature could be the same, but the time was so different. The energy barrier must be higher, but perhaps we could find a clue on the PNP catalyst reactivity since the reactants were similar. When one compares the acrylonitrile with the aldimine synthesis, we find two important changes: 1) the aldimine synthesis changes the phosphonated ligands: *tert*-butyls instead of isopropyls, and 2) the equatorial PNP ligand is bulkier in the acrylonitrile synthesis while it is smaller for the aldimine synthesis. Here, we would like to discuss the similarities and differences between the two mechanisms. We studied this new procedure with everything considered and obtained the following results shown in ***Figure 70***.

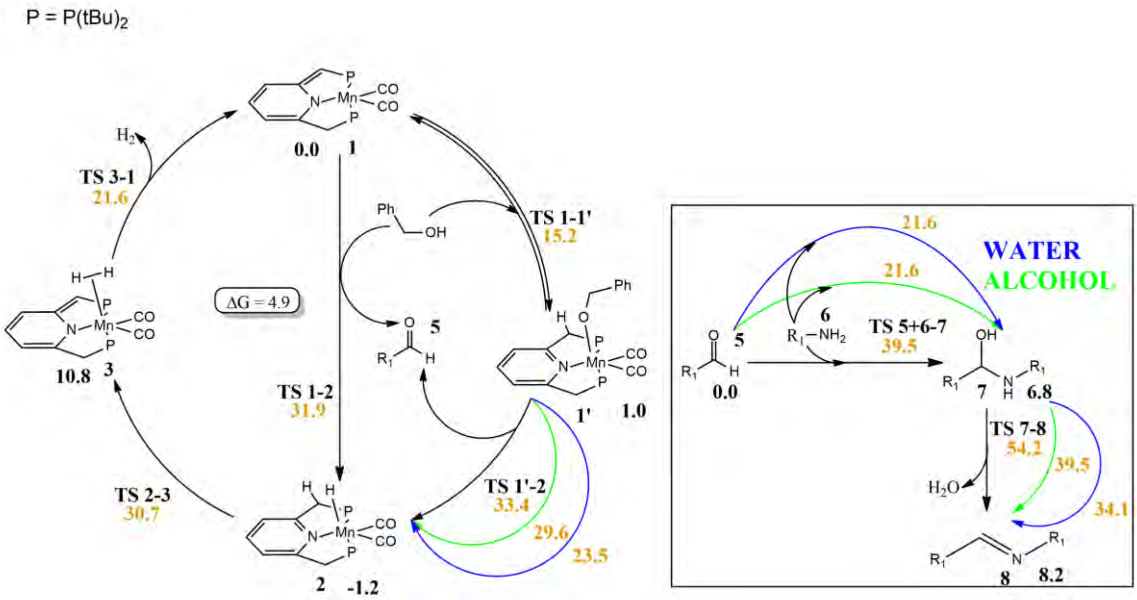

Figure 70. The full reaction mechanism for the ADC of benzyl alcohols with benzyl amines (in blue the steps assisted by water and in green by the alcohol; R$_1$ = CH_2-Ph; in black (minima) and in orange (TSs). Solvent Gibbs energies in kcal/mol and referred to catalyst **1**, except for the metal-free reaction pathway included in the box that refers to aldehyde **5**).

Comparing this mechanism to the previous one, there is a clear difference: the catalyst does not intervene in all the steps. Here we can see condensation like earlier (**TS 7-8** in ***Figure 70***), but the catalyst does not assist here. Nevertheless, let us see the catalyst intervention first. The mechanism for aldehyde formation is almost the same. The first step (**1** → **1'**) gives the hydrogen from the alcohol ligand to the double bond located next to the phosphorous atom. Here the TS is lower than the acrylonitrile (15.2 kcal/mol *vs*. 17.5 kcal/mol). While the phosphorous based ligands are bulkier and impede the alcohol binding, the hydrogen in the PNP structure's double bond restores its pyridine ring's aromaticity, lowering the energy. Considering that the aromaticity restoration should decrease the energy, but the overall step is 2.3 kcal/mol higher for the aldimine with the same computational methodology, it is clear to us that the phosphorous ligands bulkiness affects the reactivity of this catalyst negatively.

In the next step, we also observed the aldehyde formation, where the aldimine catalyst has a barrier of 23.5 kcal/mol (water assisted), and the acrylonitrile one has a barrier of 22.6 kcal/mol. Here the energy barrier difference is smaller, but only because a water molecule assists the mechanism that leads to the aldimine formation. If we compare

both in the same conditions, without an additional assistant molecule, the energy of the aldimine catalyst skyrockets to 33.4 kcal/mol. This factor is present in the rest of the hydrogen formation, as the energy barriers are always higher for the aldimine catalyst.
From here onwards, the comparison between both mechanisms becomes a challenging task. The nitrile ligand involved in the acrylonitrile synthesis allowed it to bond to the manganese metal center, facilitating the hydroxyl deprotonation. In this catalyst for aldimine synthesis, the reactant is not a nitrile but an amine; thus, this bonding does not occur. Instead, once the aldehyde forms, the catalyst stops its function. Consequently, we can say that the sole job of the catalyst is to convert alcohols into aldehydes. Considering this, the reaction between aldehyde and amine becomes the r.d.s., with a barrier of 34.1 kcal/mol for the assisted condensation reaction (**7** → **8**). This energy barrier justifies the experimental conditions of 135 ºC and 60 h and makes sense compared to the 28.1 kcal/mol for the acrylonitrile catalyst since the latter occurred in 1 h.
Even though the comparison of both types of catalyzed reactions ends here, the aldimine one had some interesting experimental data that we wanted to study as well. In the experiments, using an aryl amine with a methoxy group (OMe), they obtained a 99% yield yet, with the same aryl amine, but instead of a methoxy group, a fluoride ligand (F), the yield dropped to 55%. We invite the readers to check the article in section 4.4 to see the study; however, since it does not relate to green chemistry catalysis, it will not be further discussed.

7.2. Atmospheric gas recycling

This section is based on the contents of the manuscripts by Luque-Urrutia *et al. Inorg. Chem.* **2017**, *56*, 14383-14387, and Natongchai *et al. Org. Chem. Front.* **2021**, Advance Article, which can be found in sections 5.1 and 5.2 of this thesis.

Making better green chemistry is producing less waste material and finding ways of reusing such waste. In many cases, this waste is related to the invisible atmospheric gases that we may overlook, but there are increasing rapidly every second. This section will focus on how to reuse two of these gases, N_2O and CO_2. Furthermore, section 7.2.1 can also be included in the previous PNP catalysis block, as it also uses this type of catalyst, but since we could not include it within the H_2 production section, we moved it into this one.

7.2.1. Energy production through N_2O recycling

The last studied PNP pincer ligand catalyst involves the hydrogenation of N_2O to convert it into inert nitrogen and water gas molecules. The original scheme, the source of the project, appears in ***Figure 71***.

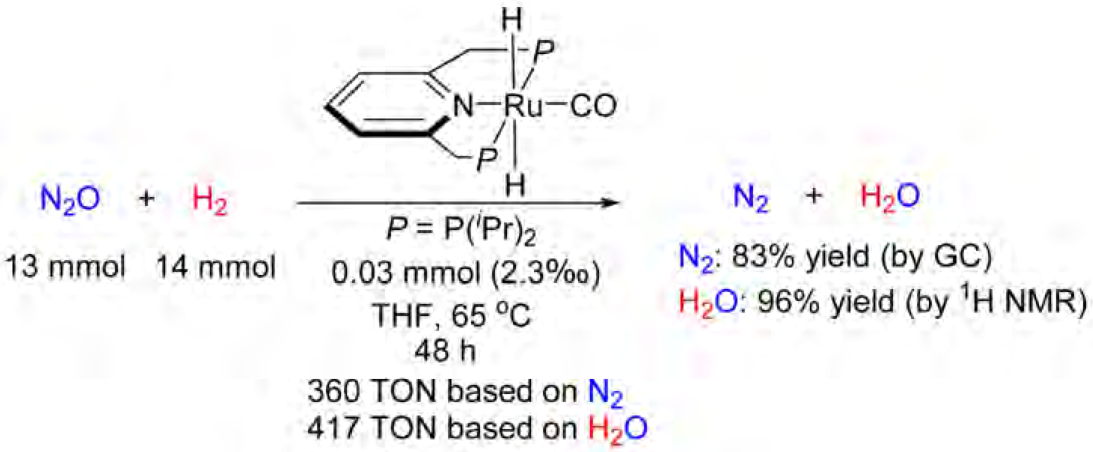
N₂O + H₂
13 mmol
14 mmol
H
P
N–Ru–CO
P
H
P = P(ⁱPr)₂
0.03 mmol (2.3‰)
THF, 65 °C
48 h
360 TON based on N₂
417 TON based on H₂O
N₂ + H₂O
N₂: 83% yield (by GC)
H₂O: 96% yield (by ¹H NMR)

Figure 71. Hydrogenation of N_2O by the PNP-pincer Ru-based catalyst **1** (P = P(*i*Pr)₂).

The experiments are straightforward; it is possible to deactivate N_2O catalytically in 48 h, at 65 ºC in THF solvent. However, we believe that the optimization of the reaction mechanism is possible. To do so, we decided to study computationally all the steps involved in this process, and the results we obtained appear in ***Figure 72***.

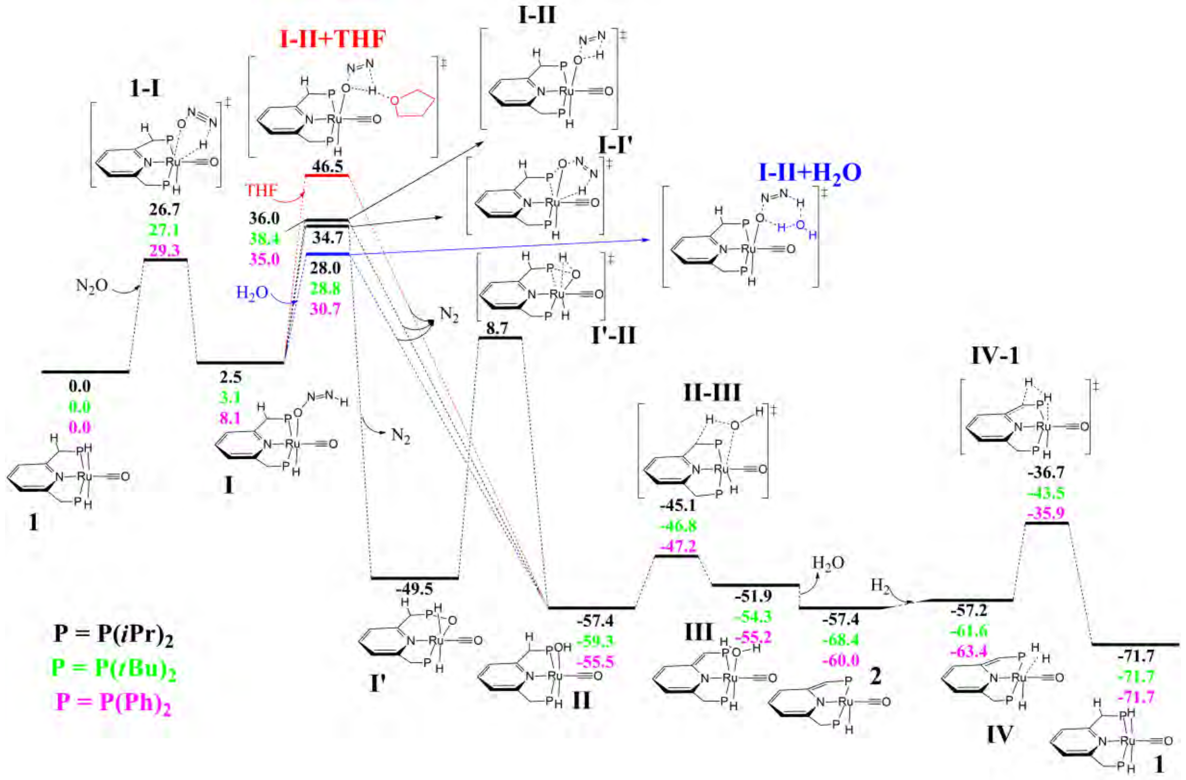

Figure 72. Full mechanism for the hydrogenation of N_2O. Isopropyl ligand represented. *Tert*-butyl and phenyl ligands energy shown as well (green and pink energies respectively). (Gibbs energies in kcal/mol, and referred to the catalyst **1**).

While testing the mechanism, we noticed that there was a high TS located in step I-II. This step relates to the conversion of N_2O into N_2 and a hydroxo ligand attached to the catalyst. Without an assisting molecule, the energy barrier is 34.7 kcal/mol. This barrier is already high in energy, and we would need high temperatures to surpass it, yet, the temperature needed in this process (65 ºC) is half of the previous PNP catalysts explained in this work (135 ºC). The experimental temperature would not be enough to proceed through this TS; thus, we tried it with an assisting molecule such as THF. The reason for using THF is that it was used as a solvent in the experiments. To our surprise, instead of lowering the barrier, it increased up to 46.5 kcal/mol, so we decided to try with water. Now, water is produced in the catalysis, but it is also present in the media since the THF is not dehydrated. The barrier decreases to 28.0 kcal/mol using water, which is still a bit high, but it is now possible. Since it is within the limit, it explains why it needs 48 h to complete the reaction.

According to the previous analysis in PNP pincer ligands, we knew that the phosphonate ligands bulkiness could directly affect the system's energy barriers. To analyze this issue, we decided to study the mechanism with the different P-R groups in the PNP pincer, namely, isopropyl (*i*Pr), *tert*-butyl (*t*Bu), and phenyl (Ph) ligands. Looking at the differences between them, the results are almost expected. On the r.d.s. of the system, step **I**-**II** assisted with water, the *i*Pr has the lowest energy barrier of the three, but it is not the less bulky. For the other two, size analysis (***Figure 73***)[220-222] demonstrated that *t*Bu is bulkier than *i*Pr, yet, the *t*Bu's energy barrier is smaller than the Ph's barrier. We attribute this difference to the C-P bond's strength within the PNP ligand, located between the pyridine of the PNP ligand and the Ru metal. Searching for the MBOs of this specific bond, we found that the C-P MBO for the Ph ligand is 0.052 larger than the same bond for the *i*Pr ligand. Once the carbon is later hydrogenated, the catalyst with the Ph ligand C-P MBO is again 0.013 larger than the *i*Pr one. This phenomenon hints towards a stronger bond character owing to the Ph ligand, lowering the catalyst reactivity, and explains why even though the Ph is less bulky than the *i*Pr, the r.d.s. is more energetically demanding.

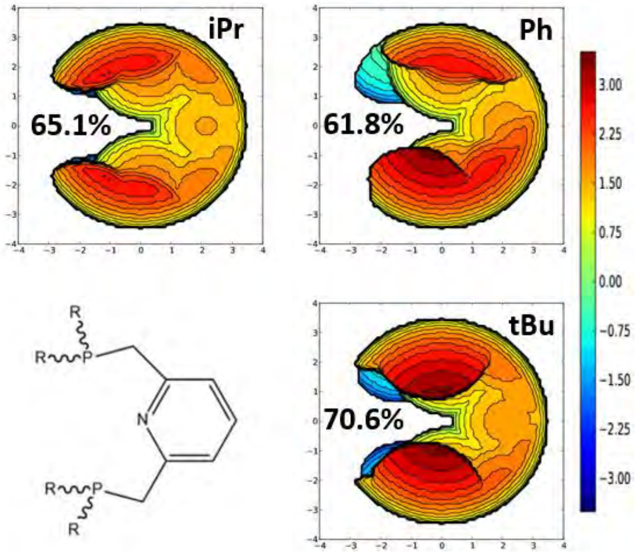

Figure 73. Percentage of the occupied volume of the ligands in respect to the metal center (%V_{bur}) and steric maps (XY plane) for the PNP pincer ligands, including *i*Pr, Ph, and *t*Bu substituents on the phosphorous atoms of catalyst **1** (Mn is placed in the center and the closest N atom is on the x-axis, while both hydrides are on the z-axis, curves are given in Å).

As a final remark to close this PNP ligand catalysis section, let us mention that we found some similarities between them to use towards an efficient and greener production. First, the catalysts can generate aldehydes from alcohols. Second, all of them had hydrogen close to the metal center that can react to form or break H-H bonds, and third, the highest energy barrier for the three studied processes is 28.1 kcal/mol. Therefore, one could combine the best aspects of each of them. If we take the catalyst from ***Figure 70***, we can see that it is almost the same as the catalyst in ***Figure 71***. We could use this catalyst with alcoholic media to produce aldehyde and hydrogen. Once it transforms the alcohol into aldehyde, we could add nitriles to form acrylonitriles (same as ***Figure 66***, but with the other catalyst) while at the same time, pump N_2O from another industrial process and the H_2 produced previously with the alcohol to convert N_2O into the inert N_2. We wanted to test this hypothesis with some tweaks to the catalyst, like using methyls (Me) instead of isopropyls since they are smaller ligands than *i*Pr, see whether the energy barriers are within the expected values, and think how could this be done experimentally (***Figure 74***). Nevertheless, the time required exceeded the thesis scope; thus, we could not do it.

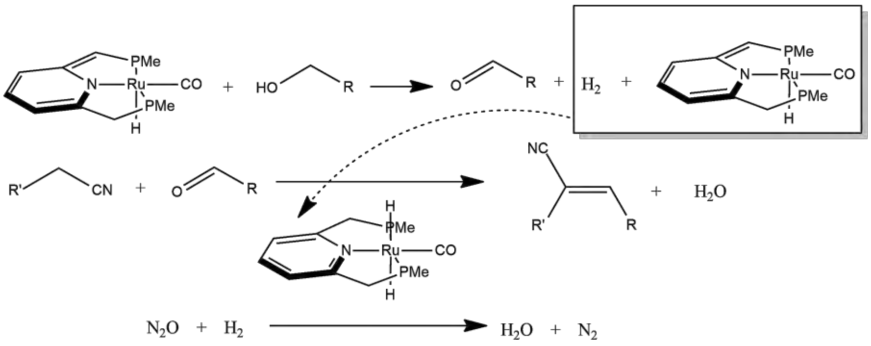

Figure 74. A hypothesis of the PNP catalysis for greener chemistry.

7.2.2. CO_2 recycling as a building block for other carbon-based compounds

We have investigated the cyclization of CO_2 and propylene epoxide with the help of several different nucleophiles. In order to study this process, we looked at the mechanism proposal included in ***Figure 75***.

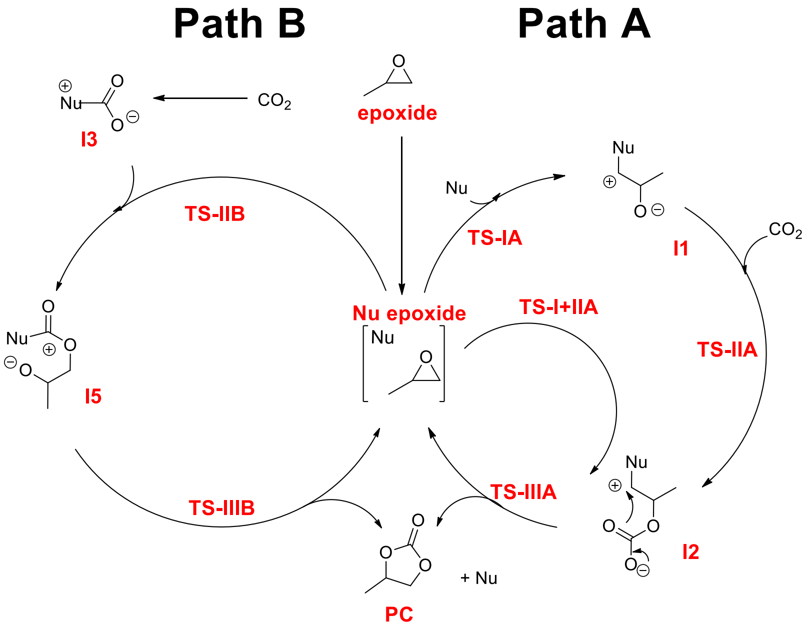

Figure 75. Mechanism of the epoxide cyclization. Path A depicted on the right side mechanism, and Path B is depicted on the left side.

There are two possible paths, A and B, that have the adduct between the nucleophile and the epoxide in common, but Path A goes through the epoxide opening by direct attack of the nucleophile, while Path B starts with the attack of the nucleophile to CO_2. Let us review first Path A for the sake of clarity in ***Figure 76***.

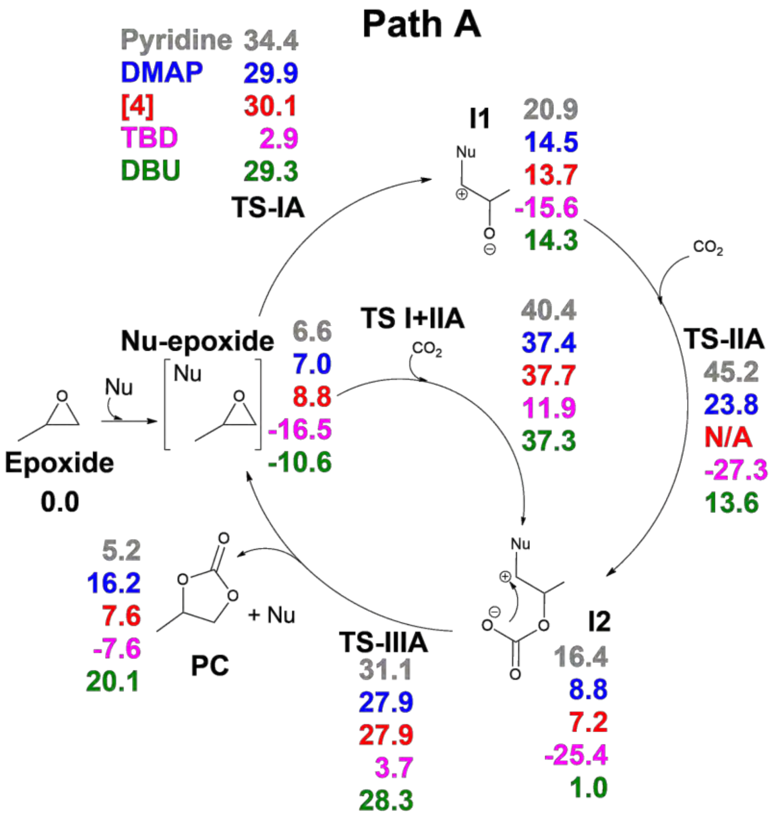

Figure 76. Path A of CO_2 cyclization

Here we observe all the steps undergone in Path A with all the nucleophiles studied in this project. First, let us enumerate the r.d.s. for each nucleophile: **TS-IA** for DMAP (29.9 kcal/mol), [4] (30.1 kcal/mol) and DBU (39.9 kcal/mol [29.3 – (-10.6) from **Nu-epoxide**]), **TS-IIA** for pyridine (45.2 kcal/mol), and **TS-IIIA** for TBD (29.1 kcal/mol [3.7 – (-25.4) from **I2**). As we can see, different limiting steps depend on the nucleophile, but we can determine a couple of things from these data. First, the pyridine has a TS energy so high that in our current experimental conditions (100 ºC, 1 atm), which are also the usual conditions used with this kind of nucleophiles, the barrier cannot be overcome. This means that pyridine cannot produce the cyclic carbonate, as reflected in the experiments, since the epoxide conversion is low, and the carbonate did not appear (see section 5.2 for more details). Looking into the rest of the nucleophiles, we could say that TBD should be the best out of them, that DBU also has a very high energy barrier as pyridine; thus, it should show similar results, and that DMAP and [4] are both viable and close in energy to produce the cyclic carbonate.

We found that the CO_2 binding (**I1** to **I2**) is barrierless for all paths except for pyridine, which coincidentally is its r.d.s., and DMAP (9.3 kcal/mol). Overall, since the CO_2 binding is not an issue, it proves that by tuning the epoxide opening, and in some cases, the closing, we can improve this reaction. We have also tested the trimolecular TS **TS I+IIA** which combines the epoxide opening with the CO_2 binding. As expected, its energy is higher than **TS-IA**; thus, we can discard this step.

Moving on, we must compare Path B to Path A and decide which path is better (***Figure 77***). The first thing that we noticed is that in all cases, Path B is more energetically demanding than Path A, *i.e.*, the r.d.s. of Path B is **TS-IIB** for pyridine (59.1 kcal/mol),

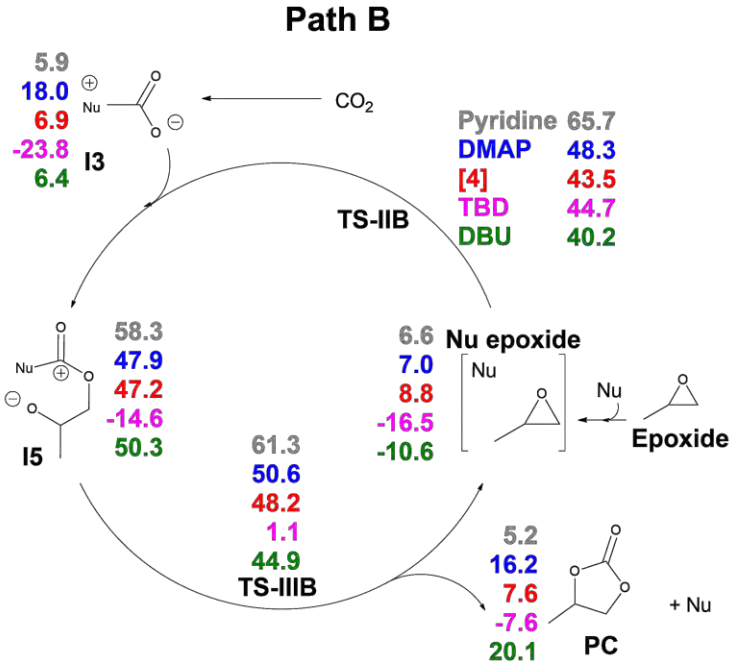
Path B
5.9
18.0
6.9
-23.8
6.4
I3
Nu
CO2
Pyridine 65.7
DMAP 48.3
[4] 43.5
TBD 44.7
DBU 40.2
TS-IIB
58.3
47.9
47.2
-14.6
50.3
I5
6.6
7.0
8.8
-16.5
-10.6
Nu epoxide
Epoxide
61.3
50.6
48.2
1.1
44.9
TS-IIIB
5.2
16.2
7.6
-7.6
20.1
PC
+ Nu

Figure 77. Path B of CO_2 cyclization

DMAP (41.3 kcal/mol), [4] (34.7 kcal/mol), TBD (61.2 kcal/mol) and DBU (50.8 kcal/mol). Since it is the first step of the mechanism, we can assume that Path B does not occur. However, there is a most crucial intermediate found in this Path B, the intermediate **I3**. It represents the union of the nucleophile with the CO_2, and we can see that for TBD, it is very stable (-23.8 kcal/mol), even more than the adduct between the TBD and the propylene epoxide (-16.5 kcal/mol). Forming this intermediate is way more comfortable for TBD than proceeding through Path A, and this, in turn, has been observed experimentally. The experiments have shown that both TBD and DBU, when in contact with the CO_2, precipitate. While we could not find the intermediate **I3** for DBU computationally, since we could only find the adduct, we did locate it for TBD. The energy shows higher preference towards this intermediate than Path A; thus, we believe that TBD forms this intermediate and then precipitates. Furthermore, while we did not locate a DBU-CO_2 intermediate, there have been reports of both DBU and TBD that found them experimentally,[223] and computationally;[224-225] thus, we believe it also occurs for DBU. Now, having looked at Paths A and B, let us revise the mechanism with the best nucleophiles for a long list of reasons: Path B is more energetically demanding than Path A; TBD and DBU precipitate in contact with CO_2, and pyridine will not go through the cyclization since the CO_2 binding step barrier is too high in energy.

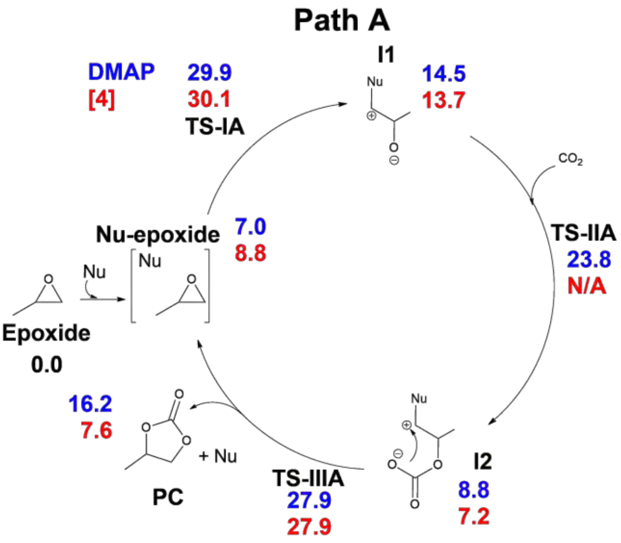
Path A
DMAP 29.9
[4] 30.1
TS-IA
I1
Nu
14.5
13.7
CO2
TS-IIA
23.8
N/A
Nu-epoxide
7.0
8.8
Nu
Epoxide
0.0
16.2
7.6
PC
+ Nu
TS-IIIA
27.9
27.9
I2
8.8
7.2

Figure 78. The optimized mechanism for CO_2 and epoxide cyclization. Values shown represent Gibbs energies in kcal/mol. In blue, with DMAP, and in red, with [4].

Once filtered, the mechanism is now clear. Both DMAP and [4] share the r.d.s. with energy so similar that discerning which one of them is better than the other, falls within the expected methodological error; therefore, we can only rely on the experiments and the nucleophilicity of the nucleophiles (DMAP<<[4]) to understand which one is better:

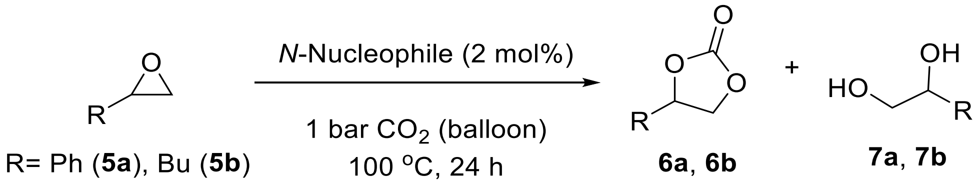

Figure 79. Experimental conditions for the epoxide cyclization.

Table 2. Catalytic investigation of N-nucleophiles for the cycloaddition of CO_2 to epoxides **5a** and **5b** under atmospheric CO_2 pressure.[a]

Nucleophile	**Conversion (%)**		**Selectivity (%)**[b]	
	5a	**5b**	**5a**	**5b**
DMAP	50	16	90	84
[4]	93	99	95	95

[a] Epoxide (16.6 mmol), nucleophile (0.332 mmol, 2 mol%) at 100 °C, 1 bar CO_2 (balloon) for 24 h, solventless. [b] Refers to the selectivity for cyclic carbonates (**6**) versus 1,2-diols (**7**).

From the experimental results, we see that DMAP has less conversion of epoxide than [4], and it is less selective as well, forming more diols in the process (derived from ambient moisture). Therefore, we can conclude that [4] is better than DMAP, and from all the data collected, it is possible to theorize that the more nucleophilic, the better (if it does not precipitate).

Overall, we determined the mechanism in which these nucleophiles react, determined a possible nucleophilic poisoning (DBU-CO_2 and TBD-CO_2), located the r.d.s. and found the best of the studied nucleophiles.

7.3. Highlights of clean energy production through solar cells

In this category, we include one project. Solar cells are a broad topic of research, and while there are many possibilities, the size of this project, more precisely the CNOs, required most of our time to develop it. To be used in solar cells, CNOs must be functionalized. Therefore, in this section, we discuss a CNO reactivity (see section 6.1) for its functionalization and use as electron donor-acceptor dyes.

7.3.1. Third-generation solar cells: are nano onions a future possibility?

This section is based on the contents of the manuscripts by Luque-Urrutia *et al*. *Chem. Eur. J.* **2020**, *26*, 804-808, which can be found in section 6.1 of this thesis.

Aiming for greener chemistry through other means than catalytic reactions, we delved into the world of solar cells. We decided to study organic-based solar cells; in this case, CNO based solar cells. Considering the size of the CNOs, and the computational limits, we chose the smallest CNO possible, *i.e.*, C_{60}@C_{240} and its Li^+ doped endohedral CNO. While the C_{60} is widely studied, the regioselectivity of C_{240} is unknown; thus, we include the first bond analysis for the C_{240} in ***Figure 80*** and ***Figure 81***.

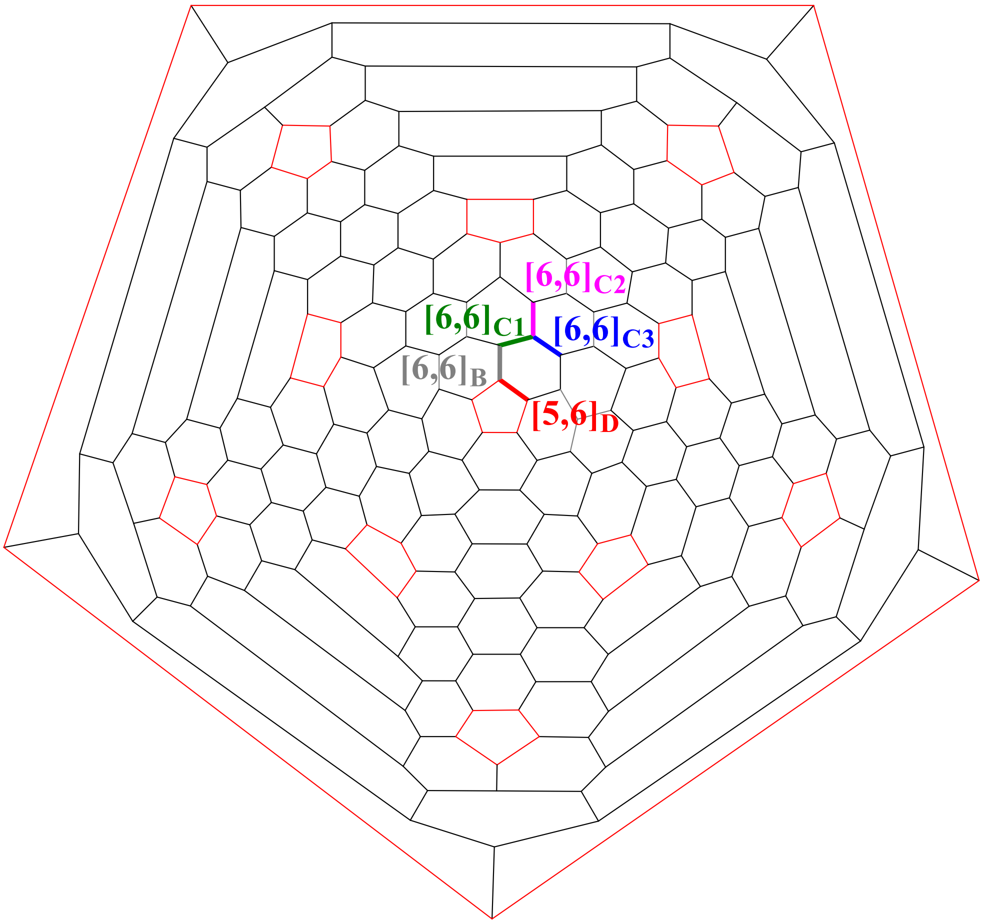

Figure 80. Schlegel diagram for a C_{240} fullerene with the five different bonds highlighted, $[5,6]_D$ in red, $[6,6]_B$ in grey, $[6,6]_{C1}$ in green, $[6,6]_{C2}$ in pink, and $[6,6]_{C3}$ in blue. The 12 pentagons of the fullerene are also marked in red.

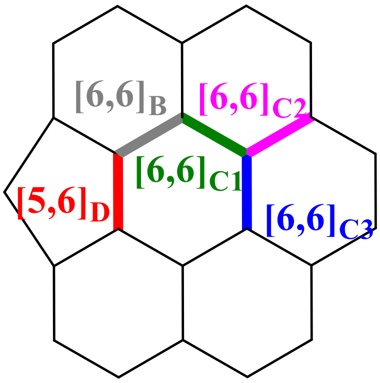

Figure 81. Representation of the different bonds found in a C_{240} cage.

Once we located the different bonds, we test their reactivity with a simple Diels-Alder reaction between the fullerene and cyclopentadiene. To ensure that our results are consistent with the bibliography, we performed a benchmark with several combinations of functionals and basis sets and chose not only the closest in energy to the available experimental data,[226-227] but the less time-consuming method out of the best ones. The reasoning behind this was the >300 atoms that the system would have; thus, a fast and accurate methodology is a must-have. Having settled the methodology and the study's object, we obtained in ***Table 3*** the data on bond reactivity.

Table 3. Reaction enthalpies (ΔH_r, enthalpy difference between adduct and reactants) and enthalpies barriers ($\Delta H^{\ddagger}$, enthalpy difference between TS and reactant complex) in kcal/mol of the Diels-Alder reaction between fullerenes and Cp, with toluene as solvent.

Fullerene	Bond type	$\Delta H^{\ddagger}$	ΔH_r
C_{60}	$[5\text{-}6]_D$	22.3	-1.9
	$[6\text{-}6]_A$	5.4	-22.1
$Li^+@C_{60}$	$[5\text{-}6]_D$	17.3	-5.8
	$[6\text{-}6]_A$	-0.8	-25.9
C_{240}	$[5\text{-}6]_D$	25.1	4.8
	$[6\text{-}6]_B$	19.0	-2.0
	$[6\text{-}6]_{C1}$	36.0	25.3
	$[6\text{-}6]_{C2}$	34.0	18.4
	$[6\text{-}6]_{C3}$	31.6	14.6
$Li^+@C_{240}$	$[5\text{-}6]_D$	21.1 (16.7)[a]	0.7 (2.2)[a]
	$[6\text{-}6]_B$	17.9 (13.4)[a]	-4.3 (-3.1)[a]
	$[6\text{-}6]_{C1}$	33.8 (31.2)[a]	23.2 (24.2)[a]
	$[6\text{-}6]_{C2}$	30.6 (28.0)[a]	18.2 (18.6)[a]
	$[6\text{-}6]_{C3}$	27.2 (23.8)[a]	9.9 (13.9)[a]
$C_{60}@C_{240}$	$[5\text{-}6]_D$	24.8	4.8
	$[6\text{-}6]_B$	18.9	-1.1
	$[6\text{-}6]_{C1}$	38.2	26.7
	$[6\text{-}6]_{C2}$	33.9	20.6
	$[6\text{-}6]_{C3}$	31.2	15.1
$Li^+@C_{60}@C_{240}$	$[5\text{-}6]_D$	22.1	1.7
	$[6\text{-}6]_B$	17.2	-3.8
	$[6\text{-}6]_{C1}$	35.1	23.6
	$[6\text{-}6]_{C2}$	33.9	16.1
	$[6\text{-}6]_{C3}$	33.2	12.1

[a] Enthalpies in parenthesis are from single-point calculations with the Li^+ placed in the C_{240} cage center. Thermal corrections were taken from the PBEPBE-D3/3-21G(d) optimized systems.

Before going further, we see that the rest of the bonds are higher in energy than $[6\text{-}6]_{A/B}$, meaning that to functionalize them, we must functionalize first the $[6\text{-}6]_{A/B}$ bond. With this in mind, we summarize the above data in a shorter and more readable ***Table 4***.

Table 4. Summarized [6-6] bond energies (in kcal/mol) extracted from Table 3.

Fullerene	Bond type	$\Delta H^{\ddagger}$	ΔH_r
C_{60}	$[6\text{-}6]_A$	5.4	-22.1
$Li^+@C_{60}$	$[6\text{-}6]_A$	-0.8	-25.9
C_{240}	$[6\text{-}6]_B$	19.0	-2.0
$Li^+@C_{240}$	$[6\text{-}6]_B$	17.9	-4.3
$C_{60}@C_{240}$	$[6\text{-}6]_B$	18.9	-1.1
$Li^+@C_{60}@C_{240}$	$[6\text{-}6]_B$	17.2	-3.8

Let us start with the C_{60} and Li^+/C_{60} results. First, the C_{60} reflects the aforementioned experimental data available.[226-227] Second, the bond reactivity shows a clear preference towards the $[6\text{-}6]_A$ bond as expected. The inclusion of the Li^+ cation made the reaction barrierless. To understand this result, we analyzed the LUMO of the fullerenes related to the Li^+ cation shown in ***Table 5***.

Table 5. The energy of the LUMO for the different fullerenes studied in this work (in a.u.).

Reactant	LUMO
C_{60}	-0.114
$Li^+@C_{60}$[a]	-0.179
C_{240}	-0.124
$Li^+@C_{240}$	-0.158
$C_{60}@C_{240}$	-0.124
$Li^+@C_{60}@C_{240}$[b]	-0.155

[a] For $Li^+@C_{60}$, we report the energy of LUMO +1 (the LUMO is located on the Li cation). [b] For $Li^+@C_{60}@C_{240}$, we provide the energy of the LUMO +5 (LUMO located in the Li cation and the LUMO +1, +2, +3, +4 orbitals located on the C_{60} cage).

We see that the cation stabilizes the LUMO of the fullerene. Thus, the bond between cyclopentadiene and C_{60} is stronger and translates into better kinetics. This step becomes barrierless. Following the smallest fullerene, it is the C_{240} turn. From the bond information we gathered, we observe that the reaction enthalpies are higher than that of the C_{60}. This is within expectations as the higher number of atoms implies a flatter surface than with the C_{60}; thus, the required deformation to form the bonds should be higher in energy for the C_{240}. Besides, the $[6\text{-}6]_B$ bond is the most reactive one, which is coincidentally the equivalent of the $[6\text{-}6]_A$ bond for the C_{60}. Overall, the bond reactivity is located in the same bond in both fullerenes.

Let us consider now the $C_{60}@C_{240}$ fullerene. The reactivity is approximately the same as the C_{240} since the principal bonds' energy reduces a maximum of 0.2 kcal/mol due to the C_{60}, but this change is barely remarkable.

With the cation-doped fullerenes, there is an apparent decrease in energy barriers once the Li^+ is present. The C_{60} reduces 6.2 kcal/mol, the C_{240} 1.1 kcal/mol, and the $C_{60}@C_{240}$ 1.7 kcal/mol. There is, however, a difference in the position of Li^+ between $Li^+@C_{60}$ and $Li^+@C_{240}$. In the C_{60}, the Li^+ is centered, while in the C_{240}, it is located near the reactive site. Due to the large size of the fullerene and the cation's small size, we believe that the cation approaches the fullerene wall to stabilize itself, but it does not occur in C_{60} since they are closer than in C_{240}. Therefore, to compare the energies of C_{240} properly, we did a single point calculation with the Li^+ in the fullerene's geometrical center, and the results are the ones shown in parenthesis in ***Table 3***. This means that the energy decrease with the Li^+ in the center of the C_{240} is 5.6 kcal/mol compared to the 1.1 kcal/mol off-center. Without the Li^+ movement, the C_{60} TS barriers decrease (6.2 kcal/mol), and C_{240} (5.6 kcal/mol) are more related. This Li^+ movement does not occur in the larger $Li^+@C_{60}@C_{240}$ since it is encapsulated within the C_{60}, and the C_{60} cannot displace itself due to the lack of space.

We used these results to determine if the $Li^+@C_{60}@C_{240}$ is a Faraday cage or not. Considering the Li^+ at the center, we can see that the energy barrier for the $Li^+@C_{60}@C_{240}$

is 17.2 kcal/mol, while for the $Li^+@C_{240}$ (centered) is 13.4 kcal/mol. This means that the addition of the C_{60} partially shields the cation's effect. If it shielded it completely, as in an ideal Faraday cage (***Figure 82***), the energy should have been closer to the 17.9 kcal/mol of the $Li^+@C_{240}$.

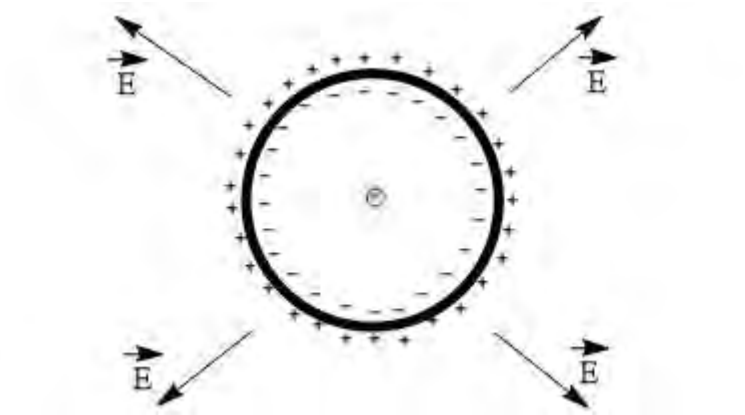

Figure 82. Effect of a charge inside a Faraday cage. The charge (cation) polarizes the cage (fullerene) and can polarize the outside in the same intensity while being unaffected by external fields.

Overall, the CNOs are not perfect Faraday cages, but it is apparent that there is some shielding. Since it is not perfect, we still can dope fullerenes to facilitate CNO functionalization in solar cells, but the charge inside it will have a lesser influence than if it had perfect shielding. This fact would mean that larger cations could be involved in the process to compensate for this effect. Still, there is room for research in this field since we have only researched this shielding with a small cation, thus larger cations and anions could lead to different outcomes to consider in CNO based solar cell production.

Chapter 8. Conclusions

We collect the main conclusions for this thesis in this chapter and display them according to the objectives (Chapter 3).

8.1. Hydrogen production as a clean energy source

8.1.1. Water Oxidation Catalysis

First:

We have been able to determine the full mechanism for the Ru(2,2’-bipyridine-6,6’-dicarboxylate)(4-picoline)$_2$ WOC catalyst at acid (1) and basic (8) pH. We revealed that at different pH, the intermediates of the mechanism are not the same. The lower pH enables some species' deprotonation, but the final monomer previous to the r.d.s. is the same at both pH. We ruled out the previous mechanistic proposal *via* rhomboidal intermediate since the energy barriers were much higher than the most known path.

Second:

We found the mechanism of the Ru(2,2’-bipyridine-6,6’-diphosphonate)(4-picoline)$_2$ WOC catalyst, which is the phosphonated analogous of the previous catalyst. There are three possible biphosphonate conformations according to the pH: biprotonated, monoprotonated, and deprotonated. At pH = 1, the two PCET of the mechanism occurs through the monoprotonated state, but the rest of the species involved are biprotonated. At pH = 8, the deprotonated state predominates over the mechanism. The pH is critical in r.d.s. determination since the media's oxidant, Cerium Ammonium Nitrate (CAN), only works under acidic conditions. In the absence of CAN, at pH = 8, the r.d.s. goes through an I2M path. The high energy barrier combined with the catalyst's dimerization correlates with the poor to inexistent experimental catalytic activity. In the presence of CAN in excess, the mechanism does not undergo WNA despite its low energy barrier since the water would not be able to deprotonate afterward. We hypothesize an I2M between CAN-catalyst that could explain the need of CAN to increase the catalytic activity and fulfilling all experimental evidence. Since CAN could be part of the catalysis, lower amounts could reduce the reaction's chemical waste.

8.1.2. Acceptorless Dehydrogenative Coupling

Third:

We demonstrated the full mechanism for the first PNP-pincer ADC Mn catalyst found by Milstein and coworkers. We divide the mechanism into aldehyde and acrylonitrile formation, but both mechanisms entwine through the thermodynamic resting state. We found that the experimental equilibrium between thermodynamic and kinetic isomers is not direct; it proceeds with an assisting molecule, either water or alcohol, through an intermediate. All steps where a proton transfer is needed, an assisting molecule, preferably water, lowers the energy barriers except for the r.d.s. The r.d.s. consists of a Knoevenagel condensation that releases a water molecule to form the final product. We discard Milstein's hypothesis for the nitrile addition to the catalyst through an ionic intermediate. Instead, nitrile addition creates a covalent bond between the N from the nitrile and the Mn of the catalyst. The catalyst framework operates both as an alcohol deprotonator and as a template for the Knoevenagel condensation.

Fourth:

We determined the full process of aldimine synthesis with a second PNP-pincer ADC Mn catalyst, published by Milstein and coworkers. We only need the aldehyde synthesis catalyst since the aldimines form from the aldehyde and the amine in the media; thus, they do not require assistance. The catalytic r.d.s. lies within the H_2 formation. The catalyst needs an assisting molecule for the proton transfers, being water the one that lowers the most the energy barriers. Some catalytic species in equilibrium may reduce the quantity of catalyst present since they reach dead ends, and the TS are lower than the catalytic r.d.s.

8.2. Atmospheric gas recycling

Fifth:

We developed the whole mechanism of an N_2O PNP-pincer Ru catalyst that transforms it into N_2 and H_2O. To lower the TS, we need assisting molecules like water in the initial steps. Since it is one of the main products, it could also lead to lower catalytic rates as time progresses. The Ru-P bonds opening in the absence of water leads to a poisoned catalyst, a highly stable Ru-O-P structure, which cannot progress any further since the energy barriers are too high. According to ligand bulkiness between *i*Pr, *t*Bu, and Ph, the Ph should be the best to improve catalytic activity; however, Ph induces conjugation with the pyridine, increasing the energy barriers and, consequently, *i*Pr becomes the most favored ligand.

Sixth:

We studied the mechanism for epoxide cyclization using different nucleophiles to search for a substitute for the halides. The mechanism starts by opening the epoxide assisted by the nucleophile agent, followed by the CO_2 binding, and then closes the cycle into the cyclic carbonate. Out of all the nucleophile candidates, DMAP and [4] were the most efficient according to our calculations. The CO_2 binding step is not the r.d.s. of the mechanism, with very low or non-existent energy barriers. The experiments showed that [4] is better than DMAP, but this difference could not be found on the calculations as differences in energy barriers are within the method’s error. This research has shown the possible substitution of halides into N-labile nucleophiles.

8.3. Clean energy production through solar cells

Seventh:

We studied the reactivity of C_{60}, C_{240}, and $C_{60}@C_{240}$ fullerenes and their Li^+ doped counterparts through a Diels-Alder reaction. The most reactive bond in all cases is the [6,6] closest to the [5,6] bond. Encapsulation of Li^+ shows an energy decrease of the LUMO orbital of the outer fullerene that results in lower barriers for all attacks. When placed inside the $C_{60}@C_{240}$, this energy decrease is lower, meaning that the C_{60} shields the Li^+ charge partially. This means that the CNO is not a perfect Faraday cage. We must take this effect into account for the development of fullerene-based solar cells.

Chapter 9. Bibliography

1. Somepics https://commons.wikimedia.org/w/index.php?curid=38088695
2. Gregg, J. S.; Andres, R. J.; Marland, G., China: Emissions pattern of the world leader in CO_2 emissions from fossil fuel consumption and cement production. *Geophys. Res. Lett.* **2008,** *35* (8), L08806.
3. Sushil, S.; Batra, V. S., Catalytic applications of red mud, an aluminium industry waste: A review. *Appl. Catal. B-Environ.* **2008,** *81* (1-2), 64-77.
4. Husain, T., Extinguishing of Kuwaiti oil fires — Challenges, technology, and success. *Atmos. Environ.* **1994,** *28* (13), 2139-2147.
5. Lebreton, L.; Slat, B.; Ferrari, F.; Sainte-Rose, B.; Aitken, J.; Marthouse, R.; Hajbane, S.; Cunsolo, S.; Schwarz, A.; Levivier, A.; Noble, K.; Debeljak, P.; Maral, H.; Schoeneich-Argent, R.; Brambini, R.; Reisser, J., Evidence that the Great Pacific Garbage Patch is rapidly accumulating plastic. *Sci. Rep.* **2018,** *8* (1), 4666.
6. Jackson, R. B.; Friedlingstein, P.; Andrew, R. M.; Canadell, J. G.; Le Quéré, C.; Peters, G. P., Persistent fossil fuel growth threatens the Paris Agreement and planetary health. *Environ. Res. Lett.* **2019,** *14* (12), 121001.
7. Feng, C.; Zheng, C.-J.; Shan, M.-L., The clarification for the features, temporal variations, and potential factors of global carbon dioxide emissions. *J. Clean. Prod.* **2020,** *255*, 120250.
8. Yang, S.; Lei, L.; Zeng, Z.; He, Z.; Zhong, H., An Assessment of Anthropogenic CO(2) Emissions by Satellite-Based Observations in China. *Sensors (Basel)* **2019,** *19* (5), 1118.
9. Charlock, T. P., CO_2 induced climatic change and spectral variations in the outgoing terrestrial infrared radiation. *Tellus B* **2017,** *36* (3), 139-148.
10. Thacker, I.; Sinatra, G., Visualizing the Greenhouse Effect: Restructuring Mental Models of Climate Change Through a Guided Online Simulation. *Educ. Sci.* **2019,** *9* (1), 14.
11. Administration, N. O. a. A. Climate at a glance: Global Mapping. https://www.ncdc.noaa.gov/cag/.
12. Zanna, L.; Khatiwala, S.; Gregory, J. M.; Ison, J.; Heimbach, P., Global reconstruction of historical ocean heat storage and transport. *Proc. Natl. Acad. Sci. U.S.A.* **2019,** *116* (4), 1126-1131.
13. Carrington, D. Global warming of oceans equivalent to an atomic bomb per second. https://www.theguardian.com/environment/2019/jan/07/global-warming-of-oceans-equivalent-to-an-atomic-bomb-per-second.
14. Collins, M., R. Knutti, J. Arblaster, J.-L. Dufresne, T. Fichefet, P. Friedlingstein, X. Gao, W.J. Gutowski, T. Johns, G. Krinner, M. Shongwe, C. Tebaldi, A.J. Weaver, and M. Wehner, Long-term Climate Change projections, commitments and irreversibility. *Climate Change 2013: The Physical Science Basis* **2013**, 1029-1136.
15. Shultz, J. M.; Sands, D. E.; Kossin, J. P.; Galea, S., Double Environmental Injustice - Climate Change, Hurricane Dorian, and the Bahamas. *N. Engl. J. Med.* **2020,** *382* (1), 1-3.
16. Moon, T.; Ahlstrom, A.; Goelzer, H.; Lipscomb, W.; Nowicki, S., Rising Oceans Guaranteed: Arctic Land Ice Loss and Sea Level Rise. *Curr. Clim. Change Rep.* **2018,** *4* (3), 211-222.

17. Cole, S.; Jacobs, P. NASA, NOAA Analyses Reveal 2019 Second Warmest Year on Record. https://www.giss.nasa.gov/research/news/20200115/.
18. Prather, M. J.; Hsu, J.; DeLuca, N. M.; Jackman, C. H.; Oman, L. D.; Douglass, A. R.; Fleming, E. L.; Strahan, S. E.; Steenrod, S. D.; Sovde, O. A.; Isaksen, I. S.; Froidevaux, L.; Funke, B., Measuring and modeling the lifetime of nitrous oxide including its variability. *J. Geophys. Res. Atmos.* **2015,** *120* (11), 5693-5705.
19. Agency, U. S. E. P. Methane and Nitrous Oxide Emissions from Natural Sources https://nepis.epa.gov/Exe/ZyNET.exe/P100717T.TXT?ZyActionD=ZyDocument&Client=EPA&Index=2006+Thru+2010&Docs=&Query=&Time=&EndTime=&SearchMethod=1&TocRestrict=n&Toc=&TocEntry=&QField=&QFieldYear=&QFieldMonth=&QFieldDay=&IntQFieldOp=0&ExtQFieldOp=0&XmlQuery=&File=D%3A%5Czyfiles%5CIndex%20Data%5C06thru10%5CTxt%5C00000017%5CP100717T.txt&User=ANONYMOUS&Password=anonymous&SortMethod=h%7C-&MaximumDocuments=1&FuzzyDegree=0&ImageQuality=r75g8/r75g8/x150y150g16/i425&Display=hpfr&DefSeekPage=x&SearchBack=ZyActionL&Back=ZyActionS&BackDesc=Results%20page&MaximumPages=1&ZyEntry=1&SeekPage=x&ZyPURL.
20. Cassia, R.; Nocioni, M.; Correa-Aragunde, N.; Lamattina, L., Climate Change and the Impact of Greenhouse Gasses: CO_2 and NO, Friends and Foes of Plant Oxidative Stress. *Front. Plant. Sci.* **2018,** *9*, 273.
21. Lee, C.; Martin, R. V.; van Donkelaar, A.; Lee, H.; Dickerson, R. R.; Hains, J. C.; Krotkov, N.; Richter, A.; Vinnikov, K.; Schwab, J. J., SO_2 emissions and lifetimes: Estimates from inverse modeling using in situ and global, space-based (SCIAMACHY and OMI) observations. *J. Geophys. Res.* **2011,** *116* (D6), D06304.
22. Mehmood, A.; Alhasani, H.; Alamoodi, N.; AlWahedi, Y. F.; Ibrahim, S.; Raj, A., An evaluation of kinetic models for the simulation of Claus reaction furnaces in sulfur recovery units under different feed conditions. *J. Nat. Gas Sci. Eng.* **2020,** *74*, 103106.
23. Marsh, D. W.; Ulrichson, D. L., Rate and diffusional study of the reaction of calcium oxide with sulfur dioxide. *Chem. Eng. Sci.* **1985,** *40* (3), 423-433.
24. Center, C. A. T., Nitrogen oxides (NOx), why and how they are controlled. Division, I. T. a. P. I., Ed. Environmental Protection Agency: 1999; p 24.
25. Brantley, S. L.; Borgiatt, A.; Rowe, G.; Fernandez, J. F.; Reynolds, J. R., Poás volcano crater lake acts as a condenser for acid metal-rich brine. *Nature* **1987,** *330* (6147), 470-472.
26. Nachbar-Hapai, M.; Siegel, B. Z.; Russell, C.; Siegel, S. M.; Siy, M. L.; Priestley, D., Acid rain in the kilauea Volcano area (Hawaii). *Arch. Environ. Con. Tox.* **1989,** *18* (1-2), 65-73.
27. Grennfelt, P.; Engleryd, A.; Forsius, M.; Hov, O.; Rodhe, H.; Cowling, E., Acid rain and air pollution: 50 years of progress in environmental science and policy. *Ambio* **2020,** *49* (4), 849-864.
28. Singh, A.; Agrawal, M., Acid rain and its ecological consequences. *J. Environ. Biol.* **2008,** *29* (1), 15-24.
29. Busenberg, E.; Plummer, L. N., Use of chlorofluorocarbons (CCl_3F and CCl_2F_2) as hydrologic tracers and age-dating tools: The alluvium and terrace system of central Oklahoma. *Water Resour. Res.* **1992,** *28* (9), 2257-2283.
30. Buis, A. The atmosphere: tracking the ongoing recovery of Earth's ozone hole. https://climate.nasa.gov/news/2916/the-atmosphere-tracking-the-ongoing-recovery-of-earths-ozone-hole/.
31. Soni, P. The Year That Was. https://secondsguru.com/top-environmental-news-2019/.
32. Shafiee, S.; Topal, E., When will fossil fuel reserves be diminished? *Energy Policy* **2009,** *37* (1), 181-189.
33. BP *BP statistical review of world energy*; BP website, 2019; p 64.
34. Smil, V., *Energy transitions: global and national perspectives*. 2nd ed.; Praeger: 2016.
35. Ritchie, H.; Roser, M. Fossil fuels 2017. https://ourworldindata.org/fossil-fuels.

36. Nagatani, K.; Kiribayashi, S.; Okada, Y.; Otake, K.; Yoshida, K.; Tadokoro, S.; Nishimura, T.; Yoshida, T.; Koyanagi, E.; Fukushima, M.; Kawatsuma, S., Emergency response to the nuclear accident at the Fukushima Daiichi Nuclear Power Plants using mobile rescue robots. *J. Field Robot.* **2013,** *30* (1), 44-63.
37. Cardis, E.; Hatch, M., The Chernobyl accident--an epidemiological perspective. *Clin. Oncol. (R. Coll. Radiol.)* **2011,** *23* (4), 251-260.
38. Lee, H. K. H.; Telford, A. M.; Röhr, J. A.; Wyatt, M. F.; Rice, B.; Wu, J.; de Castro Maciel, A.; Tuladhar, S. M.; Speller, E.; McGettrick, J.; Searle, J. R.; Pont, S.; Watson, T.; Kirchartz, T.; Durrant, J. R.; Tsoi, W. C.; Nelson, J.; Li, Z., The role of fullerenes in the environmental stability of polymer:fullerene solar cells. *Energy Environ. Sci.* **2018,** *11* (2), 417-428.
39. Zhang, F.; Inganäs, O.; Zhou, Y.; Vandewal, K., Development of polymer–fullerene solar cells. *Natl. Sci. Rev.* **2016,** *3* (2), 222-239.
40. Thompson, B. C.; Frechet, J. M., Polymer-fullerene composite solar cells. *Angew. Chem. Int. Ed. Engl.* **2008,** *47* (1), 58-77.
41. Center, A. F. D. Alternative Fuels Data Center - Fuel Properties Comparison. https://afdc.energy.gov/fuels/fuel_comparison_chart.pdf.
42. Andersson, J.; Grönkvist, S., Large-scale storage of hydrogen. *Int. J. Hydrog. Energy* **2019,** *44* (23), 11901-11919.
43. Takeno, K.; Okabayashi, K.; Kouchi, A.; Nonaka, T.; Hashiguchi, K.; Chitose, K., Dispersion and explosion field tests for 40MPa pressurized hydrogen. *Int. J. Hydrog. Energy* **2007,** *32* (13), 2144-2153.
44. Zuttel, A., Hydrogen storage methods. *Naturwissenschaften* **2004,** *91* (4), 157-72.
45. Rödl, A.; Wulf, C.; Kaltschmitt, M., Assessment of selected hydrogen supply chains - factors determining the overall GHG emissions. Hydrogen supply chains. **2019**.
46. Crowl, D. A.; Jo, Y.-D., The hazards and risks of hydrogen. *J. Loss Prev. Process Ind.* **2007,** *20* (2), 158-164.
47. Cheng, H.-M.; Yang, Q.-H.; Liu, C., Hydrogen storage in carbon nanotubes. *Carbon* **2001,** *39* (10), 1447-1454.
48. Zhevago, N. K.; Denisov, E. I.; Glebov, V. I., Experimental investigation of hydrogen storage in capillary arrays. *Int. J. Hydrog. Energy* **2010,** *35* (1), 169-175.
49. Jordá-Beneyto, M.; Suárez-García, F.; Lozano-Castelló, D.; Cazorla-Amorós, D.; Linares-Solano, A., Hydrogen storage on chemically activated carbons and carbon nanomaterials at high pressures. *Carbon* **2007,** *45* (2), 293-303.
50. McEvoy, J. P.; Brudvig, G. W., Water-splitting chemistry of photosystem II. *Chem. Rev.* **2006,** *106* (11), 4455-4483.
51. Srinivasan, N. K.; Michael, J. V., The thermal decomposition of water. *Int. J. Chem. Kinet.* **2006,** *38* (3), 211-219.
52. Baykara, S., Hydrogen production by direct solar thermal decomposition of water, possibilities for improvement of process efficiency. *Int. J. Hydrog. Energy* **2004,** *29* (14), 1451-1458.
53. Fester, J.; Garcia-Melchor, M.; Walton, A. S.; Bajdich, M.; Li, Z.; Lammich, L.; Vojvodic, A.; Lauritsen, J. V., Edge reactivity and water-assisted dissociation on cobalt oxide nanoislands. *Nat. Commun.* **2017,** *8*, 14169.
54. Le Caër, S., Water Radiolysis: Influence of Oxide Surfaces on H2 Production under Ionizing Radiation. *Water* **2011,** *3* (1), 235-253.
55. Werner, Z. R., W.; Ludwig, B., Advantages and disadvantages of hydrogen. Hydrogen in the energy sector. *Systemtechnik Gmbitt* **1996**.
56. Soriano-López, J.; Schmitt, W.; García-Melchor, M., Computational modelling of water oxidation catalysts. *Curr. Opin. Electrochem.* **2018,** *7*, 22-30.
57. Hetterscheid, D. G.; Reek, J. N., Mononuclear water oxidation catalysts. *Angew. Chem. Int. Ed. Engl.* **2012,** *51* (39), 9740-9747.

58. Sameera, W. M.; McKenzie, C. J.; McGrady, J. E., On the mechanism of water oxidation by a bimetallic manganese catalyst: a density functional study. *Dalton Trans.* **2011,** *40* (15), 3859-3870.
59. Gilbert, J. A.; Eggleston, D. S.; Murphy, W. R.; Geselowitz, D. A.; Gersten, S. W.; Hodgson, D. J.; Meyer, T. J., Structure and redox properties of the water-oxidation catalyst [(bpy)2(OH2)RuORu(OH2)(bpy)2]4+. *J. Am. Chem. Soc.* **1985,** *107* (13), 3855-3864.
60. Gersten, S. W.; Samuels, G. J.; Meyer, T. J., Catalytic oxidation of water by an oxo-bridged ruthenium dimer. *J. Am. Chem. Soc.* **1982,** *104*, 4029-4030.
61. Zhang, B.; Sun, L., Ru-bda: Unique Molecular Water-Oxidation Catalysts with Distortion Induced Open Site and Negatively Charged Ligands. *J. Am. Chem. Soc.* **2019,** *141* (14), 5565-5580.
62. Najafpour, M. M.; Rahimi, F.; Aro, E. M.; Lee, C. H.; Allakhverdiev, S. I., Nano-sized manganese oxides as biomimetic catalysts for water oxidation in artificial photosynthesis: a review. *J. R. Soc. Interface* **2012,** *9* (75), 2383-2395.
63. Yagi, M.; Kaneko, M., Molecular catalysts for water oxidation. *Chem. Rev.* **2001,** *101* (1), 21-35.
64. Grotjahn, D. B.; Brown, D. B.; Martin, J. K.; Marelius, D. C.; Abadjian, M. C.; Tran, H. N.; Kalyuzhny, G.; Vecchio, K. S.; Specht, Z. G.; Cortes-Llamas, S. A.; Miranda-Soto, V.; van Niekerk, C.; Moore, C. E.; Rheingold, A. L., Evolution of iridium-based molecular catalysts during water oxidation with ceric ammonium nitrate. *J. Am. Chem. Soc.* **2011,** *133* (47), 19024-19027.
65. Zong, R.; Thummel, R. P., 2,9-Di-(2'-pyridyl)-1,10-phenanthroline: a tetradentate ligand for Ru(II). *J. Am. Chem. Soc.* **2004,** *126* (35), 10800-10801.
66. Sens, C.; Romero, I.; Rodriguez, M.; Llobet, A.; Parella, T.; Benet-Buchholz, J., A new Ru complex capable of catalytically oxidizing water to molecular dioxygen. *J. Am. Chem. Soc.* **2004,** *126* (25), 7798-9.
67. Zong, R.; Thummel, R. P., A new family of Ru complexes for water oxidation. *J. Am. Chem. Soc.* **2005,** *127* (37), 12802-12803.
68. Xu, Y.; Akermark, T.; Gyollai, V.; Zou, D.; Eriksson, L.; Duan, L.; Zhang, R.; Akermark, B.; Sun, L., A new dinuclear ruthenium complex as an efficient water oxidation catalyst. *Inorg. Chem.* **2009,** *48* (7), 2717-2719.
69. Duan, L.; Fischer, A.; Xu, Y.; Sun, L., Isolated seven-coordinate Ru(IV) dimer complex with [HOHOH](-) bridging ligand as an intermediate for catalytic water oxidation. *J. Am. Chem. Soc.* **2009,** *131* (30), 10397-10399.
70. Duan, L.; Bozoglian, F.; Mandal, S.; Stewart, B.; Privalov, T.; Llobet, A.; Sun, L., A molecular ruthenium catalyst with water-oxidation activity comparable to that of photosystem II. *Nat. Chem.* **2012,** *4* (5), 418-423.
71. Ezhov, R.; Karbakhsh Ravari, A.; Page, A.; Pushkar, Y., Water Oxidation Catalyst cis-[Ru(bpy)(5,5′-dcbpy)(H2O)$_2$]$^{2+}$ and Its Stabilization in Metal–Organic Framework. *ACS Catal.* **2020,** *10* (9), 5299-5308.
72. de Palo, A.; La Ganga, G.; Nastasi, F.; Guelfi, M.; Bortoluzzi, M.; Pampaloni, G.; Puntoriero, F.; Campagna, S.; Marchetti, F., Ru(ii) water oxidation catalysts with 2,3-bis(2-pyridyl)pyrazine and tris(pyrazolyl)methane ligands: assembly of photo-active and catalytically active subunits in a dinuclear structure. *Dalton Trans.* **2020,** *49* (10), 3341-3352.
73. Masllorens, E.; Rodriguez, M.; Romero, I.; Roglans, A.; Parella, T.; Benet-Buchholz, J.; Poyatos, M.; Llobet, A., Can the disproportion of oxidation state III be favored in Ru^{II}-OH$_2$/Ru^{IV}=O systems? *J. Am. Chem. Soc.* **2006,** *128* (16), 5306-5307.
74. Vereshchuk, N.; Matheu, R.; Benet-Buchholz, J.; Pipelier, M.; Lebreton, J.; Dubreuil, D.; Tessier, A.; Gimbert-Surinach, C.; Ertem, M. Z.; Llobet, A., Second Coordination Sphere Effects in an Evolved Ru Complex Based on Highly Adaptable Ligand Results in Rapid Water Oxidation Catalysis. *J. Am. Chem. Soc.* **2020,** *142* (11), 5068-5077.

75. Shaffer, D. W.; Xie, Y.; Szalda, D. J.; Concepcion, J. J., Lability and Basicity of Bipyridine-Carboxylate-Phosphonate Ligand Accelerate Single-Site Water Oxidation by Ruthenium-Based Molecular Catalysts. *J. Am. Chem. Soc.* **2017,** *139* (43), 15347-15355.

76. Xie, Y.; Shaffer, D. W.; Lewandowska-Andralojc, A.; Szalda, D. J.; Concepcion, J. J., Water Oxidation by Ruthenium Complexes Incorporating Multifunctional Bipyridyl Diphosphonate Ligands. *Angew. Chem. Int. Ed. Engl.* **2016,** *55* (28), 8067-8071.

77. Kamdar, J. M.; Marelius, D. C.; Moore, C. E.; Rheingold, A. L.; Smith, D. K.; Grotjahn, D. B., Ruthenium Complexes of 2,2′-Bipyridine-6,6′-diphosphonate Ligands for Water Oxidation. *ChemCatChem* **2016,** *8* (19), 3045-3049.

78. Matheu, R.; Ertem, M. Z.; Benet-Buchholz, J.; Coronado, E.; Batista, V. S.; Sala, X.; Llobet, A., Intramolecular Proton Transfer Boosts Water Oxidation Catalyzed by a Ru Complex. *J. Am. Chem. Soc.* **2015,** *137* (33), 10786-10795.

79. Hoque, M. A.; Gil-Sepulcre, M.; de Aguirre, A.; Elemans, J.; Moonshiram, D.; Matheu, R.; Shi, Y.; Benet-Buchholz, J.; Sala, X.; Malfois, M.; Solano, E.; Lim, J.; Garzon-Manjon, A.; Scheu, C.; Lanza, M.; Maseras, F.; Gimbert-Surinach, C.; Llobet, A., Water oxidation electrocatalysis using ruthenium coordination oligomers adsorbed on multiwalled carbon nanotubes. *Nat. Chem.* **2020,** *12* (11), 1060-1066.

80. Li, C.-J.; Li, Z., Green chemistry: The development of cross-dehydrogenative coupling (CDC) for chemical synthesis. *Pure Appl. Chem.* **2006,** *78* (5), 935-945.

81. Fuse, H.; Mitsunuma, H.; Kanai, M., Catalytic Acceptorless Dehydrogenation of Aliphatic Alcohols. *J. Am. Chem. Soc.* **2020,** *142* (9), 4493-4499.

82. He, X.; Li, Y.; Fu, H.; Zheng, X.; Chen, H.; Li, R.; Yu, X., Synthesis of Unsymmetrical N-Heterocyclic Carbene–Nitrogen–Phosphine Chelated Ruthenium(II) Complexes and Their Reactivity in Acceptorless Dehydrogenative Coupling of Alcohols to Esters. *Organometallics* **2019,** *38* (8), 1750-1760.

83. Cheng, J.; Zhu, M.; Wang, C.; Li, J.; Jiang, X.; Wei, Y.; Tang, W.; Xue, D.; Xiao, J., Chemoselective dehydrogenative esterification of aldehydes and alcohols with a dimeric rhodium(ii) catalyst. *Chem. Sci.* **2016,** *7* (7), 4428-4434.

84. Musa, S.; Ackermann, L.; Gelman, D., Dehydrogenative Cross-Coupling of Primary and Secondary Alcohols. *Adv. Synth. Catal.* **2013,** *355* (14-15), 3077-3080.

85. Taniguchi, K.; Jin, X.; Yamaguchi, K.; Nozaki, K.; Mizuno, N., Versatile routes for synthesis of diarylamines through acceptorless dehydrogenative aromatization catalysis over supported gold-palladium bimetallic nanoparticles. *Chem. Sci.* **2017,** *8* (3), 2131-2142.

86. Chakraborty, S.; Gellrich, U.; Diskin-Posner, Y.; Leitus, G.; Avram, L.; Milstein, D., Manganese-Catalyzed N-Formylation of Amines by Methanol Liberating H_2 : A Catalytic and Mechanistic Study. *Angew. Chem. Int. Ed. Engl.* **2017,** *56* (15), 4229-4233.

87. Chakraborty, S.; Das, U. K.; Ben-David, Y.; Milstein, D., Manganese Catalyzed alpha-Olefination of Nitriles by Primary Alcohols. *J. Am. Chem. Soc.* **2017,** *139* (34), 11710-11713.

88. Guchhait, S. K.; Sisodiya, S.; Saini, M.; Shah, Y. V.; Kumar, G.; Daniel, D. P.; Hura, N.; Chaudhary, V., Synthesis of Polyfunctionalized Pyrroles via a Tandem Reaction of Michael Addition and Intramolecular Cyanide-Mediated Nitrile-to-Nitrile Condensation. *J. Org. Chem.* **2018,** *83* (10), 5807-5815.

89. Zhu, C.-Z.; Wei, Y.; Shi, M., Base-Promoted Tandem Cyclization for the Synthesis of Benzonitriles by C−C Bond Construction. *Adv. Synth. Catal.* **2018,** *360* (4), 808-813.

90. Sharma, K.; Shrivastava, A.; Mehra, R. N.; Deora, G. S.; Alam, M. M.; Zaman, M. S.; Akhter, M., Synthesis of novel benzimidazole acrylonitriles for inhibition of Plasmodium falciparum growth by dual target inhibition. *Arch. Pharm.* **2018,** *351* (1).

91. Garbe, M.; Junge, K.; Walker, S.; Wei, Z.; Jiao, H.; Spannenberg, A.; Bachmann, S.; Scalone, M.; Beller, M., Manganese(I)-Catalyzed Enantioselective Hydrogenation of Ketones Using a Defined Chiral PNP Pincer Ligand. *Angew. Chem. Int. Ed. Engl.* **2017,** *56* (37), 11237-11241.

92. Kuriyama, S.; Arashiba, K.; Nakajima, K.; Tanaka, H.; Kamaru, N.; Yoshizawa, K.; Nishibayashi, Y., Catalytic formation of ammonia from molecular dinitrogen by use of dinitrogen-bridged dimolybdenum-dinitrogen complexes bearing PNP-pincer ligands: remarkable effect of substituent at PNP-pincer ligand. *J. Am. Chem. Soc.* **2014,** *136* (27), 9719-9731.
93. Weng, W.; Guo, C.; Celenligil-Cetin, R.; Foxman, B. M.; Ozerov, O. V., Skeletal change in the PNP pincer ligand leads to a highly regioselective alkyne dimerization catalyst. *Chem. Commun.* **2006,** (2), 197-199.
94. Fan, L.; Foxman, B. M.; Ozerov, O. V., N−H Cleavage as a Route to Palladium Complexes of a New PNP Pincer Ligand. *Organometallics* **2004,** *23* (3), 326-328.
95. Masdemont, J.; Luque-Urrutia, J. A.; Gimferrer, M.; Milstein, D.; Poater, A., Mechanism of Coupling of Alcohols and Amines To Generate Aldimines and H2 by a Pincer Manganese Catalyst. *ACS Catal.* **2019,** *9* (3), 1662-1669.
96. Thomas, G., *Medicinal Chemistry: An Introduction, 2nd Edition*. 2008.
97. Leigh, G. J., *Haber-Bosch and Other Industrial Processes*. 2004.
98. Zeng, R.; Feller, M.; Ben-David, Y.; Milstein, D., Hydrogenation and Hydrosilylation of Nitrous Oxide Homogeneously Catalyzed by a Metal Complex. *J. Am. Chem. Soc.* **2017,** *139* (16), 5720-5723.
99. Dabral, S.; Schaub, T., The Use of Carbon Dioxide (CO_2) as a Building Block in Organic Synthesis from an Industrial Perspective. *Adv. Synth. Catal.* **2019,** *361* (2), 223-246.
100. Tappe, N. A.; Reich, R. M.; D'Elia, V.; Kuhn, F. E., Current advances in the catalytic conversion of carbon dioxide by molecular catalysts: an update. *Dalton Trans.* **2018,** *47* (38), 13281-13313.
101. Artz, J.; Muller, T. E.; Thenert, K.; Kleinekorte, J.; Meys, R.; Sternberg, A.; Bardow, A.; Leitner, W., Sustainable Conversion of Carbon Dioxide: An Integrated Review of Catalysis and Life Cycle Assessment. *Chem. Rev.* **2018,** *118* (2), 434-504.
102. Song, Q.-W.; Zhou, Z.-H.; He, L.-N., Efficient, selective and sustainable catalysis of carbon dioxide. *Green Chem.* **2017,** *19* (16), 3707-3728.
103. Gaona, M. A.; de la Cruz-Martinez, F.; Fernandez-Baeza, J.; Sanchez-Barba, L. F.; Alonso-Moreno, C.; Rodriguez, A. M.; Rodriguez-Dieguez, A.; Castro-Osma, J. A.; Otero, A.; Lara-Sanchez, A., Synthesis of helical aluminium catalysts for cyclic carbonate formation. *Dalton Trans.* **2019,** *48* (13), 4218-4227.
104. Steinbauer, J.; Spannenberg, A.; Werner, T., An in situ formed Ca^{2+}–crown ether complex and its use in CO_2-fixation reactions with terminal and internal epoxides. *Green Chem.* **2017,** *19* (16), 3769-3779.
105. Shaikh, R. R.; Pornpraprom, S.; D’Elia, V., Catalytic Strategies for the Cycloaddition of Pure, Diluted, and Waste CO_2 to Epoxides under Ambient Conditions. *ACS Catal.* **2017,** *8* (1), 419-450.
106. Monassier, A.; D'Elia, V.; Cokoja, M.; Dong, H.; Pelletier, J. D. A.; Basset, J.-M.; Kühn, F. E., Synthesis of Cyclic Carbonates from Epoxides and CO_2 under Mild Conditions Using a Simple, Highly Efficient Niobium-Based Catalyst. *ChemCatChem* **2013,** *5* (6), 1321-1324.
107. Kleij, A. W., Advancing halide-free catalytic synthesis of CO_2-based heterocycles. *Curr. Opin. Green Sustain. Chem.* **2020,** *24*, 72-81.
108. Zou, B.; Hu, C., Halogen-free processes for organic carbonate synthesis from CO 2. *Curr. Opin. Green Sustain. Chem.* **2017,** *3*, 11-16.
109. Tundo, P.; He, L.-N.; Lokteva, E.; Mota, C., *Chemistry Beyond Chlorine*. 2016; p 608.
110. Tandon, R.; Unzner, T.; Nigst, T. A.; De Rycke, N.; Mayer, P.; Wendt, B.; David, O. R.; Zipse, H., Annelated pyridines as highly nucleophilic and Lewis basic catalysts for acylation reactions. *Chemistry* **2013,** *19* (20), 6435-6442.
111. Heinrich, M. R.; Klisa, H. S.; Mayr, H.; Steglich, W.; Zipse, H., Enhancing the catalytic activity of 4-(dialkylamino)pyridines by conformational fixation. *Angew. Chem. Int. Ed. Engl.* **2003,** *42* (39), 4826-4828.

112. Zipse, H.; Held, I.; Xu, S., Modular Design of Pyridine-Based Acyl-Transfer Catalysts. *Synthesis* **2007,** *2007* (8), 1185-1196.
113. Kleoff, M.; Suhr, S.; Sarkar, B.; Zimmer, R.; Reissig, H. U.; Marin-Luna, M.; Zipse, H., Efficient Syntheses of New Super Lewis Basic Tris(dialkylamino)-Substituted Terpyridines and Comparison of Their Methyl Cation Affinities. *Chemistry* **2019,** *25* (31), 7526-7533.
114. Helberg, J.; Ampssler, T.; Zipse, H., Pyridinyl Amide Ion Pairs as Lewis Base Organocatalysts. *J. Org. Chem.* **2020,** *85* (8), 5390-5402.
115. Bard, A. J.; Faulkner, L. R., *Electrochemical Methods: Fundamentals and Applications*. 2000.
116. Gonzalez, T.; Diaz-Herrera, J.; Tucker, A., *Computing Handbook, Third Edition: Computer Science and Software Engineering*. CRC Press: 2014.
117. Flexer, V.; Baspineiro, C. F.; Galli, C. I., Lithium recovery from brines: A vital raw material for green energies with a potential environmental impact in its mining and processing. *Sci. Total Environ.* **2018,** *639*, 1188-1204.
118. Kesler, S. E.; Gruber, P. W.; Medina, P. A.; Keoleian, G. A.; Everson, M. P.; Wallington, T. J., Global lithium resources: Relative importance of pegmatite, brine and other deposits. *Ore Geol. Rev.* **2012,** *48*, 55-69.
119. Sharma, S.; Jain, K. K.; Sharma, A., Solar Cells: In Research and Applications—A Review. *Mater. Sci. Appl.* **2015,** *06* (12), 1145-1155.
120. Kibria, M. T.; Ahammed, A.; Sony, S. M.; Hossain, F.; Shams-Ul-Islam, A Review: Comparative studies on different generation solar cells technology. In *5th International Conference on Environmental Aspects of Bangladesh*, 2014; pp 51-53.
121. Vigil-Galán, O.; Courel, M.; Andrade-Arvizu, J. A.; Sánchez, Y.; Espíndola-Rodríguez, M.; Saucedo, E.; Seuret-Jiménez, D.; Titsworth, M., Route towards low cost-high efficiency second generation solar cells: current status and perspectives. *J. Mater. Sci.: Mater. Electron.* **2014,** *26* (8), 5562-5573.
122. Yan, J.; Saunders, B. R., Third-generation solar cells: a review and comparison of polymer:fullerene, hybrid polymer and perovskite solar cells. *RSC Adv.* **2014,** *4* (82), 43286-43314.
123. Gómez-Ortíz, N. M.; Vázquez-Maldonado, I. A.; Pérez-Espadas, A. R.; Mena-Rejón, G. J.; Azamar-Barrios, J. A.; Oskam, G., Dye-sensitized solar cells with natural dyes extracted from achiote seeds. *Sol. Energy Mater. Sol. Cells* **2010,** *94* (1), 40-44.
124. Beiley, Z. M.; Christoforo, M. G.; Gratia, P.; Bowring, A. R.; Eberspacher, P.; Margulis, G. Y.; Cabanetos, C.; Beaujuge, P. M.; Salleo, A.; McGehee, M. D., Semi-transparent polymer solar cells with excellent sub-bandgap transmission for third generation photovoltaics. *Adv. Mater.* **2013,** *25* (48), 7020-7026.
125. Nozik, A. J.; Beard, M. C.; Luther, J. M.; Law, M.; Ellingson, R. J.; Johnson, J. C., Semiconductor quantum dots and quantum dot arrays and applications of multiple exciton generation to third-generation photovoltaic solar cells. *Chem. Rev.* **2010,** *110* (11), 6873-6890.
126. Geisz, J. F.; France, R. M.; Schulte, K. L.; Steiner, M. A.; Norman, A. G.; Guthrey, H. L.; Young, M. R.; Song, T.; Moriarty, T., Six-junction III–V solar cells with 47.1% conversion efficiency under 143 Suns concentration. *Nat. Energy* **2020,** *5* (4), 326-335.
127. Arjunan, T. V.; Senthil, T. S., Review: Dye sensitised solar cells. *Mater. Technol.* **2013,** *28* (1-2), 9-14.
128. Bomben, P. G.; Robson, K. C. D.; Koivisto, B. D.; Berlinguette, C. P., Cyclometalated ruthenium chromophores for the dye-sensitized solar cell. *Coord. Chem. Rev.* **2012,** *256* (15-16), 1438-1450.
129. Kroto, H. W.; Allaf, A. W.; Balm, S. P., C_{60}: Buckminsterfullerene. *Chem. Rev.* **1991,** *91* (6), 1213-1235.

130. Erten-Ela, S.; Chen, H.; Kratzer, A.; Hirsch, A.; Brabec, C. J., Perovskite solar cells fabricated using dicarboxylic fullerene derivatives. *New J. Chem.* **2016,** *40* (3), 2829-2834.
131. Ooyama, Y.; Uenaka, K.; Kamimura, T.; Ozako, S.; Kanda, M.; Koide, T.; Tani, F., Dye-sensitized solar cell based on an inclusion complex of a cyclic porphyrin dimer bearing four 4-pyridyl groups and fullerene C_{60}. *RSC Adv.* **2016,** *6* (20), 16150-16158.
132. Liu, X.; Jiao, W.; Lei, M.; Zhou, Y.; Song, B.; Li, Y., Crown-ether functionalized fullerene as a solution-processable cathode buffer layer for high performance perovskite and polymer solar cells. *J. Mater. Chem. A* **2015,** *3* (17), 9278-9284.
133. Bai, Y.; Dong, Q.; Shao, Y.; Deng, Y.; Wang, Q.; Shen, L.; Wang, D.; Wei, W.; Huang, J., Enhancing stability and efficiency of perovskite solar cells with crosslinkable silane-functionalized and doped fullerene. *Nat. Commun.* **2016,** *7*, 12806.
134. Hino, T.; Ogawa, Y.; Kuramoto, N., Preparation of functionalized and non-functionalized fullerene thin films on ITO glasses and the application to a counter electrode in a dye-sensitized solar cell. *Carbon* **2006,** *44* (5), 880-887.
135. Wang, Y.; Cheng, L. T., Nonlinear optical properties of fullerenes and charge-transfer complexes of fullerenes. *J. Phys. Chem.* **1992,** *96* (4), 1530-1532.
136. Lappas, A.; Prassides, K.; Vavekis, K.; Arcon, D.; Blinc, R.; Cevc, P.; Amato, A.; Feyerherm, R.; Gygax, F. N.; Schenck, A., Spontaneous Magnetic Ordering in the Fullerene Charge-Transfer Salt (TDAE)C60. *Science* **1995,** *267* (5205), 1799-1802.
137. Borgohain, R.; Li, J.; Selegue, J. P.; Cheng, Y. T., Electrochemical Study of Functionalized Carbon Nano-Onions for High-Performance Supercapacitor Electrodes. *J. Phys. Chem. C* **2012,** *116* (28), 15068-15075.
138. Francesco Fringuelli, A. T., *The Diels-Alder reaction: Selected practical methods*. John Wiley & Sons: 2002; p 358.
139. Delaney, P.; Greer, J. C., C_{60} as a Faraday cage. *Appl. Phys. Lett.* **2004,** *84* (3), 431-433.
140. Descartes, R., *Discourse on Method and Meditations*. Bobbs-Merril Educational Publications: 1960.
141. Newton, I., A letter of Mr. Isaac Newton, Professor of the Mathematicks in the University of Cambridge; containing his new theory about light and colors: sent by the author to the publisher from Cambridge, Febr. 6. 1671/72; in order to be communicated to the R. Society. *Philos. Trans. R. Soc.* **1997,** *6* (80), 3075-3087.
142. Hooke, R., Robert Hooke's Critique of Newton's Theory of Light and Colors. *His. R. Soc.* **1672,** *3*, 10-15.
143. Huygens, C., Traité de la lumière. *Les maîtres de la pensée scientifique* **1678,** *1*, 174.
144. Young, T., I. The Bakerian Lecture. Experiments and calculations relative to physical optics. *Philos. Trans. R. Soc.* **1997,** *94*, 1-16.
145. Fresnel, A.-J., *Memoir upon the colours produced in homogeneous fluids by polarized light*. London, 1818; Vol. 5.
146. Loudon, R., *The quantum theory of light*. 3 ed.; 2000; p 448.
147. Kuhn, T. S., *Black-body theory and the quantum discontinuity, 1984-1912*. 1987; p 378.
148. Planck, M., On the Law of Distribution of Energy in the Normal Spectrum. *Ann. Phys.* **1901,** *4*.
149. Einstein, A., On a Heuristic Point of View about the Creatidn and Conversion of Light. *Ann. Phys.* **1905,** *17*.
150. 2020, N. M. A. The Nobel Prize in physics 1921. https://www.nobelprize.org/prizes/physics/1921/summary/.
151. Broglie, L. d. Recherches sur la théorie des Quanta. University of Paris, St. Germain, Paris, 1924.
152. Davisson, C. J.; Germer, L. H., Reflection of Electrons by a Crystal of Nickel. *Proc. Natl. Acad. Sci. U.S.A.* **1928,** *14* (4), 317-322.

153. Thomson, G. P.; Reid, A., Diffraction of Cathode Rays by a Thin Film. *Nature* **1927,** *119* (3007), 890-890.
154. Schrödinger, E., An Undulatory Theory of the Mechanics of Atoms and Molecules. *Phys. Rev.* **1926,** *28* (6), 1049-1070.
155. Born, M.; Oppenheimer, R., Zur Quantentheorie der Molekeln. *Ann. Phys.* **1927,** *389* (20), 457-484.
156. Jensen, F., *Introduction to computational chemistry*. Wiley: 2013.
157. Cramer, C. J., *Essentials of Computational Chemistry Theories and Models*. 2004.
158. Hartree, D. R., The Wave Mechanics of an Atom with a non-Coulomb Central Field. Part III. Term Values and Intensities in Series in Optical Spectra. *Math. Proc. Cambridge Philos. Soc.* **2008,** *24* (3), 426-437.
159. Hartree, D. R., The Wave Mechanics of an Atom with a Non-Coulomb Central Field. Part II. Some Results and Discussion. *Math. Proc. Cambridge Philos. Soc.* **2008,** *24* (1), 111-132.
160. Hartree, D. R., The Wave Mechanics of an Atom with a Non-Coulomb Central Field. Part I. Theory and Methods. *Math. Proc. Cambridge Philos. Soc.* **2008,** *24* (1), 89-110.
161. Lanczos, C., *The Variational Principles of Mechanics*. University of Toronto Press: Toronto, 1974.
162. Pauli, W., Über den Zusammenhang des Abschlusses der Elektronengruppen im Atom mit der Komplexstruktur der Spektren. *Z. Phys.* **1925,** *31* (1), 765-783.
163. Slater, J. C., Note on Hartree's Method. *Phys. Rev.* **1930,** *35* (2), 210-211.
164. Fock, V., Näherungsmethode zur Lösung des quantenmechanischen Mehrkörperproblems. *Z. Phys.* **1930,** *61* (1-2), 126-148.
165. Hartree, D. R.; Hartree, W., Self-consistent field, with exchange, for beryllium. *Proc. R. Soc. A* **1997,** *150* (869), 9-33.
166. Hall, G. G., The growth of computational quantum chemistry from 1950 to 1971. *Chem. Soc. Rev.* **1973,** *2* (1), 21-28.
167. Liverpool, U. o., Chemtube3D, pp https://www.chemtube3d.com/orbitals-p/.
168. Gerlach, W.; Stern, O., Der experimentelle Nachweis des magnetischen Moments des Silberatoms. *Z. Phys.* **1922,** *8* (1), 110-111.
169. Gerlach, W.; Stern, O., Der experimentelle Nachweis der Richtungsquantelung im Magnetfeld. *Z. Phys.* **1922,** *9* (1), 349-352.
170. Dirac, P. A., The quantum theory of the electron. *Proc. R. Soc. A* **1997,** *117* (778), 610-624.
171. Solà, M.; Ugalde, J. M., Quantum Chemistry Methods:II Density Functional Theory. In *Theoretical and Computational Chemistry: Foundations, Methods and Techniques*, Universitat Jaume I, Castelló de la Plana: 2007; pp 221-277.
172. Hohenberg, P.; Kohn, W., Inhomogeneous Electron Gas. *Phys. Rev.* **1964,** *136* (3B), B864-B871.
173. Kohn, W.; Sham, L. J., Self-Consistent Equations Including Exchange and Correlation Effects. *Phys. Rev.* **1965,** *140* (4A), A1133-A1138.
174. Vega, L.; Ruvireta, J.; Vines, F.; Illas, F., Jacob's Ladder as Sketched by Escher: Assessing the Performance of Broadly Used Density Functionals on Transition Metal Surface Properties. *J. Chem. Theory Comput.* **2018,** *14* (1), 395-403.
175. Negele, J. W., Structure of Finite Nuclei in the Local-Density Approximation. *Phys. Rev. C* **1970,** *1* (4), 1260-1321.
176. Perdew, J. P.; Burke, K.; Ernzerhof, M., Generalized Gradient Approximation Made Simple. *Phys. Rev. Lett.* **1996,** *77* (18), 3865-3868.
177. Perdew, J. P.; Tao, J.; Staroverov, V. N.; Scuseria, G. E., Meta-generalized gradient approximation: explanation of a realistic nonempirical density functional. *J. Chem. Phys.* **2004,** *120* (15), 6898-6911.

178. Simon, L.; Goodman, J. M., How reliable are DFT transition structures? Comparison of GGA, hybrid-meta-GGA and meta-GGA functionals. *Org. Biomol. Chem.* **2011,** *9* (3), 689-700.
179. Rontani, M.; Cavazzoni, C.; Bellucci, D.; Goldoni, G., Full configuration interaction approach to the few-electron problem in artificial atoms. *J. Chem. Phys.* **2006,** *124* (12), 124102.
180. Korenblum, D., Newton-Raphson visualization. Online, 2015.
181. Raphson, J. Analysis Æequationum Universalis seu ad Æequationes Algebraicas Resolvendas Methodus Generalis, & Expedita, Ex nova Infinitarum Serierum Methodo, Deducta ac Demonstrata 1697.
182. Cashwell, J.; Wallis, J. A Treatise of Algebra, both Historical and Practical. Shewing the Original, Progress, and Advancement thereof, from time to time, and by what Steps it hath attained to the Heighth at which it now is 1685.
183. Lemaréchal, C., Cauchy and the gradient method. *Doc. Math.* **2012,** *Extra volume*, 251-254.
184. Curry, H. B., The method of steepest descent for non-linear minimization problems. *Q. Appl. Math.* **1944,** *2* (3), 258-261.
185. Gibbs, J. W., On the equilibrium of heterogeneous substances. *Trans. Conn. Acad. Arts Sci.* **1874-1878,** *3*.
186. Parr, R. G., Quantum Chemistry: Classic Scientific Papers Quantum Chemistry: Classic Scientific Papers Hinne Hettema World Scientific, River Edge, N.J., 2000. ISBN 981-02-2771-X. *Phys. Today* **2001,** *54* (6), 63-64.
187. Parsegian, V. A., *Van der Waals Forces: A Handbook for biologists, chemists, engineers and physicists*. Cambridge University Press: 2005.
188. Grimme, S.; Antony, J.; Ehrlich, S.; Krieg, H., A consistent and accurate ab initio parametrization of density functional dispersion correction (DFT-D) for the 94 elements H-Pu. *J. Chem. Phys.* **2010,** *132* (15), 154104.
189. Becke, A. D.; Johnson, E. R., A simple effective potential for exchange. *J. Chem. Phys.* **2006,** *124* (22), 221101.
190. Sharp, R. T.; Horton, G. K., A Variational Approach to the Unipotential Many-Electron Problem. *Phys. Rev.* **1953,** *90* (2), 317-317.
191. Talman, J. D.; Shadwick, W. F., Optimized effective atomic central potential. *Phys. Rev. A* **1976,** *14* (1), 36-40.
192. Grimme, S.; Ehrlich, S.; Goerigk, L., Effect of the damping function in dispersion corrected density functional theory. *J. Comput. Chem.* **2011,** *32* (7), 1456-1465.
193. Tomasi, J.; Mennucci, B.; Cammi, R., Quantum mechanical continuum solvation models. *Chem. Rev.* **2005,** *105* (8), 2999-3093.
194. Cossi, M.; Rega, N.; Scalmani, G.; Barone, V., Energies, structures, and electronic properties of molecules in solution with the C-PCM solvation model. *J. Comput. Chem.* **2003,** *24* (6), 669-681.
195. Marenich, A. V.; Cramer, C. J.; Truhlar, D. G., Universal solvation model based on solute electron density and on a continuum model of the solvent defined by the bulk dielectric constant and atomic surface tensions. *J. Phys. Chem. B* **2009,** *113* (18), 6378-96.
196. Goerigk, L., Treating London-Dispersion Effects with the Latest Minnesota Density Functionals: Problems and Possible Solutions. *J. Phys. Chem. Lett.* **2015,** *6* (19), 3891-3896.
197. Mardirossian, N.; Head-Gordon, M., Characterizing and Understanding the Remarkably Slow Basis Set Convergence of Several Minnesota Density Functionals for Intermolecular Interaction Energies. *J. Chem. Theory Comput.* **2013,** *9* (10), 4453-4461.
198. Wheeler, S.; Bootsma, A.; N, Popular Integration Grids Can Result in Large Errors in DFT-Computed Free Energies. *ChemRxiv* **2019,** *Preprint*.

199. Gilson, R.; Durrant, M. C., Estimation of the pKa values of water ligands in transition metal complexes using density functional theory with polarized continuum model solvent corrections. *Dalton Trans.* **2009,** (46), 10223-10230.
200. Kelly, C. P.; Cramer, C. J.; Truhlar, D. G., Single-ion solvation free energies and the normal hydrogen electrode potential in methanol, acetonitrile, and dimethyl sulfoxide. *J. Phys. Chem. B* **2007,** *111* (2), 408-22.
201. Liao, R. Z.; Siegbahn, P. E. M., Quantum Chemical Modeling of Homogeneous Water Oxidation Catalysis. *ChemSusChem* **2017,** *10* (22), 4236-4263.
202. Binstead, R. A.; Meyer, T. J., Hydrogen-atom transfer between metal complex ions in solution. *J. Am. Chem. Soc.* **1987,** *109* (11), 3287-3297.
203. Huynh, M. H.; Meyer, T. J., Proton-coupled electron transfer. *Chem. Rev.* **2007,** *107* (11), 5004-5064.
204. Mayer, I., Bond order and valence indices: a personal account. *J. Comput. Chem.* **2007,** *28* (1), 204-221.
205. Postils, V.; Delgado-Alonso, C.; Luis, J. M.; Salvador, P., An Objective Alternative to IUPAC's Approach To Assign Oxidation States. *Angew. Chem. Int. Ed. Engl.* **2018,** *57* (33), 10525-10529.
206. Karen, P.; McArdle, P.; Takats, J., Comprehensive definition of oxidation state (IUPAC Recommendations 2016). *Pure Appl. Chem.* **2016,** *88* (8), 831-839.
207. Frisch, M. J.; Trucks, G. W.; Schlegel, H. B.; Scuseria, G. E.; Robb, M. A.; Cheeseman, J. R.; Scalmani, G.; Barone, V.; Mennucci, B.; Petersson, G. A.; Nakatsuji, H.; Caricato, M.; Li, X.; Hratchian, H. P.; Izmaylov, A. F.; Bloino, J.; Zheng, G.; Sonnenberg, J. L.; Hada, M.; Ehara, M.; Toyota, K.; Fukuda, R.; Hasegawa, J.; Ishida, M.; Nakajima, T.; Honda, Y.; Kitao, O.; Nakai, H.; Vreven, T.; Montgomery, J. A.; Peralta, J. E.; Ogliaro, F.; Bearpark, M.; Heyd, J. J.; Brothers, E.; Kudin, K. N.; Staroverov, V. N.; Kobayashi, R.; Normand, J.; Raghavachari, K.; Rendell, A.; Burant, J. C.; Iyengar, S. S.; Tomasi, J.; Cossi, M.; Rega, N.; Millam, J. M.; Klene, M.; Knox, J. E.; Cross, J. B.; Bakken, V.; Adamo, C.; Jaramillo, J.; Gomperts, R.; Stratmann, R. E.; Yazyev, O.; Austin, A. J.; Cammi, R.; Pomelli, C.; Ochterski, J. W.; Martin, R. L.; Morokuma, K.; Zakrzewski, V. G.; Voth, G. A.; Salvador, P.; Dannenberg, J. J.; Dapprich, S.; Daniels, A. D.; Farkas, Ö.; Foresman, J. B.; Ortiz, J. V.; Cioslowski, J.; Fox, D. J. *Gaussian 09 Rev. E.01*, Wallingford, CT, 2009.
208. Frisch, M. J.; Trucks, G. W.; Schlegel, H. B.; Scuseria, G. E.; Robb, M. A.; Cheeseman, J. R.; Scalmani, G.; Barone, V.; Petersson, G. A.; Nakatsuji, H.; Li, X.; Caricato, M.; Marenich, A. V.; Bloino, J.; Janesko, B. G.; Gomperts, R.; Mennucci, B.; Hratchian, H. P.; Ortiz, J. V.; Izmaylov, A. F.; Sonnenberg, J. L.; Williams; Ding, F.; Lipparini, F.; Egidi, F.; Goings, J.; Peng, B.; Petrone, A.; Henderson, T.; Ranasinghe, D.; Zakrzewski, V. G.; Gao, J.; Rega, N.; Zheng, G.; Liang, W.; Hada, M.; Ehara, M.; Toyota, K.; Fukuda, R.; Hasegawa, J.; Ishida, M.; Nakajima, T.; Honda, Y.; Kitao, O.; Nakai, H.; Vreven, T.; Throssell, K.; Montgomery Jr., J. A.; Peralta, J. E.; Ogliaro, F.; Bearpark, M. J.; Heyd, J. J.; Brothers, E. N.; Kudin, K. N.; Staroverov, V. N.; Keith, T. A.; Kobayashi, R.; Normand, J.; Raghavachari, K.; Rendell, A. P.; Burant, J. C.; Iyengar, S. S.; Tomasi, J.; Cossi, M.; Millam, J. M.; Klene, M.; Adamo, C.; Cammi, R.; Ochterski, J. W.; Martin, R. L.; Morokuma, K.; Farkas, O.; Foresman, J. B.; Fox, D. J. *Gaussian 16 Rev. C.01*, Wallingford, CT, 2016.
209. *Chemcraft - graphical software for visualization of quantum chemistry computations*.
210. Dennington, R.; Keith, T. A.; Millam, J. M. *GaussView, Version 6.1*, Semichem Inc., Shawnee Mission, KS: 2016.
211. Informatics, P. *ChemDraw Ultra 12.0*, 2010.
212. Stasyuk, A. J.; Stasyuk, O. A.; Solà, M.; Voityuk, A. A., Photoinduced Charge Shift in Li+-Doped Giant Nested Fullerenes. *J. Phys. Chem. C* **2019,** *123* (27), 16525-16532.
213. Hashmi, M. A.; Lein, M., Carbon Nano-onions as Photosensitizers: Stacking-Induced Red-Shift. *J. Phys. Chem. C* **2018,** *122* (4), 2422-2431.

214. Voityuk, A. A.; Sola, M., Photoinduced Charge Separation in the Carbon Nano-Onion $C_{60}@C_{240}$. *J. Phys. Chem. A* **2016,** *120* (29), 5798-5804.
215. Tong, L.; Duan, L.; Xu, Y.; Privalov, T.; Sun, L., Structural modifications of mononuclear ruthenium complexes: a combined experimental and theoretical study on the kinetics of ruthenium-catalyzed water oxidation. *Angew. Chem. Int. Ed. Engl.* **2011,** *50* (2), 445-449.
216. Scherrer, D.; Schilling, M.; Luber, S.; Fox, T.; Spingler, B.; Alberto, R.; Richmond, C. J., Ruthenium water oxidation catalysts containing the non-planar tetradentate ligand, biisoquinoline dicarboxylic acid (biqaH_2). *Dalton Trans.* **2016,** *45* (48), 19361-19367.
217. Kang, R.; Chen, K.; Yao, J.; Shaik, S.; Chen, H., Probing ligand effects on O-O bond formation of Ru-catalyzed water oxidation: a computational survey. *Inorg. Chem.* **2014,** *53* (14), 7130-6.
218. Nyhlen, J.; Duan, L.; Akermark, B.; Sun, L.; Privalov, T., Evolution of O_2 in a seven-coordinate Ru(IV) dimer complex with a $[HOHOH]^-$ bridge: a computational study. *Angew. Chem. Int. Ed. Engl.* **2010,** *49* (10), 1773-7.
219. Codola, Z.; Gamba, I.; Acuna-Pares, F.; Casadevall, C.; Clemancey, M.; Latour, J. M.; Luis, J. M.; Lloret-Fillol, J.; Costas, M., Design of Iron Coordination Complexes as Highly Active Homogenous Water Oxidation Catalysts by Deuteration of Oxidation-Sensitive Sites. *J. Am. Chem. Soc.* **2019,** *141* (1), 323-333.
220. Falivene, L.; Credendino, R.; Poater, A.; Petta, A.; Serra, L.; Oliva, R.; Scarano, V.; Cavallo, L., SambVca 2. A Web Tool for Analyzing Catalytic Pockets with Topographic Steric Maps. *Organometallics* **2016,** *35* (13), 2286-2293.
221. Falivene, L.; Cao, Z.; Petta, A.; Serra, L.; Poater, A.; Oliva, R.; Scarano, V.; Cavallo, L., Towards the online computer-aided design of catalytic pockets. *Nat. Chem.* **2019,** *11* (10), 872-879.
222. Poater, A.; Cosenza, B.; Correa, A.; Giudice, S.; Ragone, F.; Scarano, V.; Cavallo, L., SambVca: A Web Application for the Calculation of the Buried Volume of N-Heterocyclic Carbene Ligands. *Eur. J. Inorg. Chem.* **2009,** *2009* (13), 1759-1766.
223. Villiers, C.; Dognon, J. P.; Pollet, R.; Thuery, P.; Ephritikhine, M., An isolated CO_2 adduct of a nitrogen base: crystal and electronic structures. *Angew. Chem. Int. Ed. Engl.* **2010,** *49* (20), 3465-3468.
224. Buchard, A., DFT study of the reaction between DBU, CO_2 and (R)-1,3-butanediol to form cyclic carbonate (R)-4-Methyl-[1,3]-dioxan-2-one. 2015.
225. von Wolff, N.; Villiers, C.; Thuéry, P.; Lefèvre, G.; Ephritikhine, M.; Cantat, T., Reactivity and Structural Diversity in the Reaction of Guanidine 1,5,7-Triazabicyclo[4.4.0]dec-5-ene with CO_2, CS2, and Other Heterocumulenes. *Eur. J. Org. Chem.* **2017,** *2017* (3), 676-686.
226. Pang, L. S. K.; Wilson, M. A., Reactions of fullerenes C_{60} and C_{70} with cyclopentadiene. *J. Phys. Chem.* **1993,** *97* (26), 6761-6763.
227. Giovane, L. M.; Barco, J. W.; Yadav, T.; Lafleur, A. L.; Marr, J. A.; Howard, J. B.; Rotello, V. M., Kinetic stability of the fullerene C_{60}-cyclopentadiene Diels-Alder adduct. *J. Phys. Chem.* **1993,** *97* (33), 8560-8561.
228. Becke, A. D., Density-functional thermochemistry. III. The role of exact exchange. *J. Chem. Phys.* **1993,** *98* (7), 5648-5652.
229. Perdew, J. P., Density-functional approximation for the correlation energy of the inhomogeneous electron gas. *Phys. Rev. B* **1986,** *33* (12), 8822-8824.
230. Grimme, S.; Antony, J.; Ehrlich, S.; Krieg, H., A consistent and accurate ab initio parametrization of density functional dispersion correction (DFT-D) for the 94 elements H-Pu. *J. Chem. Phys.* **2010,** *132* (15), 154104.
231. Grimme, S.; Ehrlich, S.; Goerigk, L., Effect of the damping function in dispersion corrected density functional theory. *J. Comp. Chem.* **2011,** *32* (7), 1456-1465.

232. Schäfer, A.; Horn, H.; Ahlrichs, R., Fully optimized contracted Gaussian basis sets for atoms Li to Kr. *J. Chem. Phys.* **1992,** *97* (4), 2571-2577.

233. Zhao, Y.; Truhlar, D. G., The M06 suite of density functionals for main group thermochemistry, thermochemical kinetics, noncovalent interactions, excited states, and transition elements: two new functionals and systematic testing of four M06-class functionals and 12 other functionals. *Theor. Chem. Acc.* **2007,** *120* (1-3), 215-241.

234. Tomasi, J.; Mennucci, B.; Cammi, R., Quantum Mechanical Continuum Solvation Models. *Chem. Rev.* **2005,** *105* (8), 2999-3094.

235. M. J. Frisch, G. W. T., H. B. Schlegel, G. E. Scuseria, M. A. Robb, J. R. Cheeseman, G. Scalmani, V. Barone, G. A. Petersson, H. Nakatsuji, X. Li, M. Caricato, A. Marenich, J. Bloino, B. G. Janesko, R. Gomperts, B. Mennucci, H. P. Hratchian, J. V. Ortiz, A. F. Izmaylov, J. L. Sonnenberg, D. Williams-Young, F. Ding, F. Lipparini, F. Egidi, J. Goings, B. Peng, A. Petrone, T. Henderson, D. Ranasinghe, V. G. Zakrzewski, J. Gao, N. Rega, G. Zheng, W. Liang, M. Hada, M. Ehara, K. Toyota, R. Fukuda, J. Hasegawa, M. Ishida, T. Nakajima, Y. Honda, O. Kitao, H. Nakai, T. Vreven, K. Throssell, J. A. Montgomery, Jr., J. E. Peralta, F. Ogliaro, M. Bearpark, J. J. Heyd, E. Brothers, K. N. Kudin, V. N. Staroverov, T. Keith, R. Kobayashi, J. Normand, K. Raghavachari, A. Rendell, J. C. Burant, S. S. Iyengar, J. Tomasi, M. Cossi, J. M. Millam, M. Klene, C. Adamo, R. Cammi, J. W. Ochterski, R. L. Martin, K. Morokuma, O. Farkas, J. B. Foresman, and D. J. Fox *Gaussian 09, Revision D.01*, Gaussian, Inc.: Wallingford CT, 2009.

236. Becke, A. D., Density-functional exchange-energy approximation with correct asymptotic behavior. *Phys. Rev. A* **1988,** *38* (6), 3098-3100.

237. Perdew, J. P., Erratum: Density-functional approximation for the correlation energy of the inhomogeneous electron gas. *Phys. Rev. B Condens. Matter.* **1986,** *34* (10), 7406.

238. Grimme, S., Semiempirical hybrid density functional with perturbative second-order correlation. *J. Chem. Phys.* **2006,** *124* (3).

239. Weigend, F.; Ahlrichs, R., Balanced basis sets of split valence, triple zeta valence and quadruple zeta valence quality for H to Rn: Design and assessment of accuracy. *Phys. Chem. Chem. Phys.* **2005,** *7* (18), 3297-3305.

240. Lee, C.; Yang, W.; Parr, R. G., Development of the Colle-Salvetti correlation-energy formula into a functional of the electron density. *Phys. Rev. B* **1988,** *37* (2), 785-789.

241. Stephens, P. J.; Devlin, F. J.; Chabalowski, C. F.; Frisch, M. J., Ab Initio Calculation of Vibrational Absorption and Circular Dichroism Spectra Using Density Functional Force Fields. *J. Phys. Chem.* **1994,** *98* (45), 11623-11627.

242. Barone, V.; Cossi, M., Quantum Calculation of Molecular Energies and Energy Gradients in Solution by a Conductor Solvent Model. *J. Phys. Chem. A* **1998,** *102* (11), 1995-2001.

243. Tomasi, J.; Persico, M., Molecular Interactions in Solution: An Overview of Methods Based on Continuous Distributions of the Solvent. *Chem. Rev.* **1994,** *94* (7), 2027-2094.

Chapter 10. Annex

Here we report the SI for all the articles present. For the sake of clarity, we have removed the computational geometries, and we encourage the reader to check the online articles for them.

10.1. Section 4.1 SI

Supporting Information

for

The Influence of the pH on the Reaction Mechanism of Water Oxidation by a Ru(bda) catalyst

Jesús A. Luque-Urrutia,[‡] Miquel Solà*,[‡] and Albert Poater*,[‡]

[‡]Institut de Química Computacional i Catàlisi and Departament de Química, Universitat de Girona, C/ Maria Aurèlia Capmany, 69, 17003 Girona, Catalonia, Spain

Further computational details

Reduction potentials. Equations and explanation

Starting from the reduction potential formula explained in the article:

$$\varepsilon^{o}{}_{red} = -\frac{\Delta G_{reaction}}{-nF} - SHE \tag{S1}$$

We can specify our ΔG according to a PCET reaction:

$$Ru^{III}OH + H^{+} + e^{-} \rightarrow Ru^{II}OH_2 \tag{S2}$$

Therefore, we obtain the following ΔG:

$$\Delta G_{reaction} = \Delta G_{Ru^{II}OH_2} - \Delta G_{Ru^{III}OH} - \Delta G_{H^+} \tag{S3}$$

In order to address the new proton term concerning a redox reaction where does not appear, we can observe the SHE reaction:

$$H^{+}{}_{solv} + e^{-} \rightarrow \frac{1}{2} \cdot H_{2_{gas}} \tag{S4}$$

Which we can obtain the ΔG_{SHE}:

$$\Delta G_{SHE} = \frac{1}{2}\Delta G_{H_2} - \Delta G_{H^+} \tag{S5}$$

Where we can obtain the ΔG_{H^+} which we can translate into our $\Delta G_{reaction}$:

$$\varepsilon^{o}{}_{red} = -\frac{\Delta G_{Ru^{II}OH_2} - \Delta G_{Ru^{III}OH} - \frac{1}{2}\Delta G_{H_2} + \Delta G_{SHE}}{-nF} - SHE \tag{S6}$$

$$\varepsilon^{o}{}_{red} = -\frac{\Delta G_{Ru^{II}OH_2} - \Delta G_{Ru^{III}OH} - \frac{1}{2}\Delta G_{H_2}}{-nF} + SHE - SHE \tag{S7}$$

Thus, we obtain the proposed reaction for the reduction potential for PCETs reactions.

$$\varepsilon^{o}{}_{red} = -\frac{\Delta G_{Ru^{II}OH_2} - \Delta G_{Ru^{III}OH} - \frac{1}{2}\Delta G_{H_2}}{-nF} \tag{S8}$$

In order to compare it with the more used methodology of using the $\Delta G_{reaction}$ with an experimental $\Delta G_{H^+} = 262.4\frac{kcal}{mol}$; we performed both and obtained the same potentials in both cases, using any of them. However, due to not requiring experimental values and addressing the potentials from a computational perspective, we used the methodology explained above.

Finally, in order to predict the involvement of protons in the redox potentials, we use the Nernst equation correction:

$$\varepsilon_{red} = \varepsilon^{o}{}_{red} + 0.059 \cdot (pH - pKa) \tag{S9}$$

Given the following pK$_a$:

$$RuOH_2{}^{3+}: pKa^{I} \quad \& \quad RuOH_2{}^{2+}: pKa^{II} \tag{S10}$$

If $pH < pKa^{I}$ we consider a 0H$^+$/1e$^-$ pH independent reaction:

$$Ru^{III}OH_2{}^{3+} + e^- \rightarrow Ru^{II}OH_2{}^{2+} \tag{S11}$$

Thus, no correction is applied.

If $pKa^{I} < pH < pKa^{II}$we consider a 1H$^+$/1e$^-$ pH dependent reaction:

$$Ru^{III}OH^{2+} + e^- + H^+ \rightarrow Ru^{II}OH_2{}^{2+} \tag{S12}$$

Thus, we use the Nernst equation.

If $pKa^{II} < pH$ then we consider a 0H$^+$/1e$^-$ pH independent reaction:

$$Ru^{III}OH^{2+} + e^- \rightarrow Ru^{II}OH^{+} \tag{S13}$$

Thus, no correction is applied.

10.2. Section 4.2 SI

Supporting information for

Understanding the Performance of a Bisphosphonate Ru catalyst for Water Oxidation Catalysis

Jesús A. Luque-Urrutia,[‡] Jayneil M. Kamdar,[§] Douglas B. Grotjahn,[§,*] Miquel Solà,[‡,*] and Albert Poater[‡,*]

[‡]Institut de Química Computacional i Catàlisi and Departament de Química, Universitat de Girona, C/ Maria Aurèlia Capmany 69, 17003 Girona, Catalonia, Spain.

[§]Department of Chemistry and Biochemistry, San Diego State University, 5500 Campanile Drive, San Diego, CA, US 92182-1030.

Table of Contents

1. **pK_a calculation (*Table S1*, *Figure S*1).** 205
2. **Full reaction mechanisms at pH 1 and 8 (*Figure S2*, *Figure S3*, and *Figure S4*).** 207
3. **pK_a for the conversion of the two phosphonates in the catalyst: biprotonated, monoprotonated, and deprotonated (*Table S2*, *Figure S5*).** 209
4. **Multiplicity and Spin density for all the relevant structures (*Table S3*).** 210
5. **Experimental voltammetries (*Figure S6*, *Figure S7*, *Figure S8*, *Figure S9*).** 211
6. **Cerium Ammonium Nitrate study (*Figure S10*).** 212

pK$_a$ calculation. Equations and explanation.

We begin with a general reaction:

$$AOH \rightarrow AO^{-} + H^{+} \tag{S14}$$

Which will give us a ΔG. This term can be used in the pK$_a$ calculation as follows:

$$\Delta G = -R \cdot T \cdot \ln(K_a) \tag{S15}$$

$$pK_a = \log\left(e^{\frac{\Delta G}{RT}}\right) \tag{S16}$$

This procedure is how we obtain our calculated pK$_a$. In order to have a better approximation, we follow the same procedure as Concepcion *et al*. have presented in their SI by calculating different pK$_a$ and comparing them with known experimental values in order to adjust our results:

Table S1. Experimental, DFT, and corrected pK$_a$ values for different acids.

Acid	pK$_a$		
	Experimental	Calculated	Corrected
CF_3-COOH	0.23	3.1	0.17
CHF_2-COOH	1.34	5.3	1.08
CH_2F-COOH	2.60	9.1	2.56
CH_3-COOH	4.76	14.2	4.61
H-PO(OH)$_2$	1.30	6.4	1.52
H_3C-PO(OH)$_2$	2.38	9.3	2.66

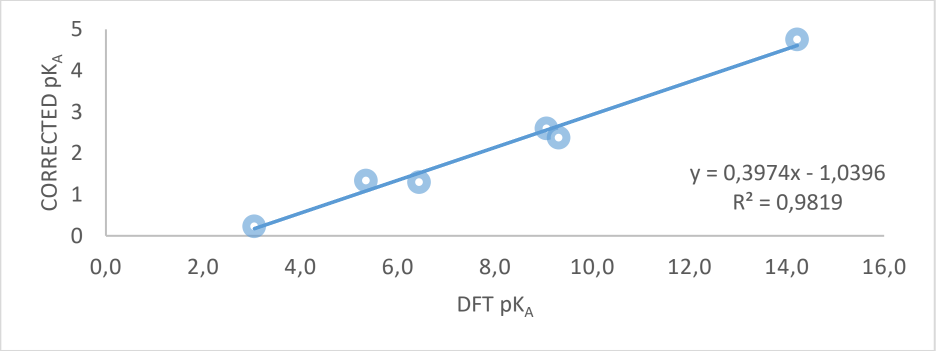

Figure S1. Plot of the DFT (x-axis) and experimental (y-axis) pK$_a$ of the different acids.

Using the formula obtained in the linear regression, we can adjust our DFT pK$_a$ to be closer to the experimental ones.

Reduction potentials. Equations and explanation

Starting from the reduction potential formula explained in the article:

$$\varepsilon^{o}{}_{red} = -\frac{\Delta G_{reaction}}{-nF} - SHE \tag{S17}$$

We can specify our ΔG according to a PCET reaction:

$$Ru^{III}OH + H^{+} + e^{-} \rightarrow Ru^{II}OH_2 \tag{S18}$$

Therefore, we obtain the following ΔG:

$$\Delta G_{reaction} = \Delta G_{Ru^{II}OH_2} - \Delta G_{Ru^{III}OH} - \Delta G_{H^+} \tag{S19}$$

In order to address the new proton term concerning a redox reaction where does not appear, we can observe the SHE reaction:

$$H^{+}{}_{solv} + e^{-} \rightarrow \frac{1}{2} \cdot H_{2_{gas}} \tag{S20}$$

Which we can obtain the ΔG_{SHE}:

$$\Delta G_{SHE} = \frac{1}{2}\Delta G_{H_2} - \Delta G_{H^+} \tag{S21}$$

Where we can obtain the ΔG_{H^+} which we can translate into our $\Delta G_{reaction}$:

$$\varepsilon^{o}{}_{red} = -\frac{\Delta G_{Ru^{II}OH_2} - \Delta G_{Ru^{III}OH} - \frac{1}{2}\Delta G_{H_2} + \Delta G_{SHE}}{-nF} - SHE \tag{S22}$$

$$\varepsilon^{o}{}_{red} = -\frac{\Delta G_{Ru^{II}OH_2} - \Delta G_{Ru^{III}OH} - \frac{1}{2}\Delta G_{H_2}}{-nF} + SHE - SHE \tag{S23}$$

Thus, we obtain the proposed reaction for the reduction potential for PCETs reactions.

$$\varepsilon^{o}{}_{red} = -\frac{\Delta G_{Ru^{II}OH_2} - \Delta G_{Ru^{III}OH} - \frac{1}{2}\Delta G_{H_2}}{-nF} \tag{S24}$$

In order to compare it with the more used methodology of using the $\Delta G_{reaction}$ with an experimental $\Delta G_{H^+} = 270.3\frac{kcal}{mol}$; we performed both and obtained the same potentials in both cases, using any of them. However, due to not requiring experimental values and addressing the potentials from a computational perspective, we used the methodology explained above.

Finally, in order to predict the involvement of protons in the redox potentials, we use the Nernst equation correction:

$$\varepsilon_{red} = \varepsilon^{o}{}_{red} + 0.059 \cdot (pH - pKa) \tag{S25}$$

Given the following pK_a:

$$RuOH_2{}^{3+}: pKa^{I} \quad \& \quad RuOH_2{}^{2+}: pKa^{II} \tag{S26}$$

If $pH < pKa^{I}$ we consider a 0H⁺/1e⁻ pH independent reaction:

$$Ru^{III}OH_2{}^{3+} + e^{-} \rightarrow Ru^{II}OH_2{}^{2+} \qquad (S27)$$

Thus, no correction is applied.

If $pKa^{I} < pH < pKa^{II}$ we consider a 1H⁺/1e⁻ pH dependent reaction:

$$Ru^{III}OH^{2+} + e^{-} + H^{+} \rightarrow Ru^{II}OH_2{}^{2+} \qquad (S28)$$

Thus, we use the Nernst equation.

If $pKa^{II} < pH$ then we consider a 0H⁺/1e⁻ pH independent reaction:

$$Ru^{III}OH^{2+} + e^{-} \rightarrow Ru^{II}OH^{+} \qquad (S29)$$

Thus, no correction is applied.

Full figures at pH=8 and pH=1.

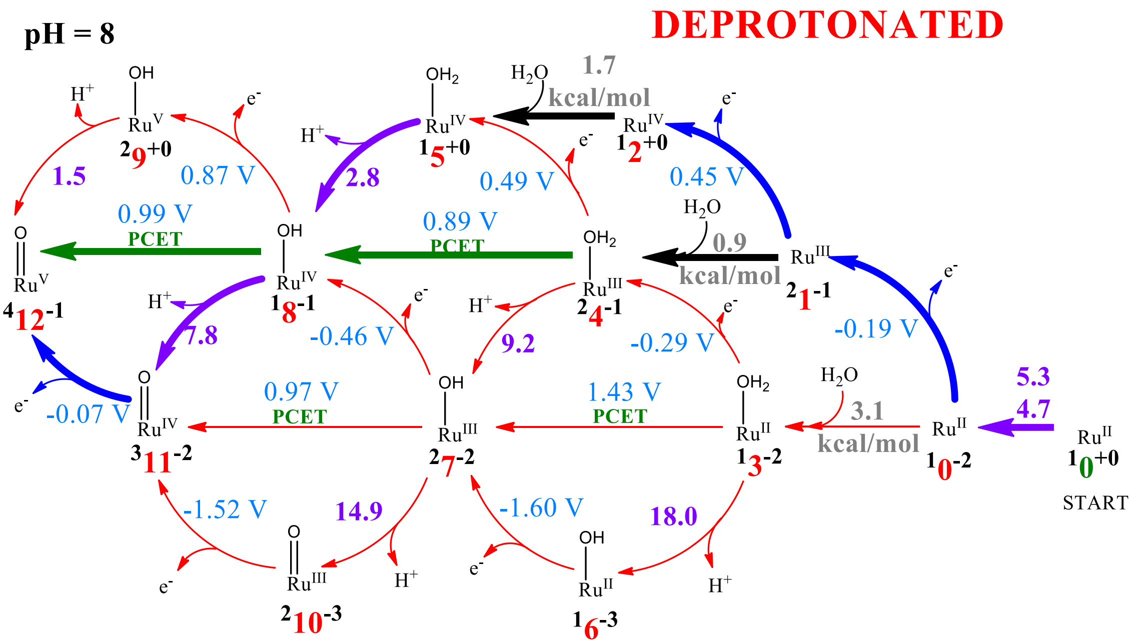
pH = 8
DEPROTONATED
1.7 kcal/mol
0.9 kcal/mol
3.1 kcal/mol
H₂O
0.87 V
0.49 V
0.45 V
0.99 V PCET
0.89 V PCET
0.97 V PCET
1.43 V PCET
-0.46 V
-0.29 V
-0.19 V
-0.07 V
-1.52 V
-1.60 V
1.5
2.8
7.8
9.2
14.9
18.0
5.3
4.7
H⁺
e⁻
2 9 +0
1 5 +0
1 2 +0
4 12 -1
1 8 -1
2 4 -1
2 1 -1
3 11 -2
2 7 -2
1 3 -2
1 0 -2
1 0 +0
2 10 -3
1 6 -3
START

Figure S2. The bisphosphonate Ru catalyst B's mechanism according to the two phosphonate ligands' protonation at pH = 8. Species $^{1}\mathbf{0}^{-2}$ is **B** deprotonated twice at pH 8; the superscripts left and right signify spin multiplicity (here, singlet) and overall charge, respectively. For reaction arrows, red = less favorable, blue = oxidation, green = PCET, and purple = deprotonation. For numbered species, green indicates deprotonated diphosphonate ligand, whereas red indicates doubly deprotonated ligand. Numbers near arrows in blue indicate the reduction potential in V; purple numbers indicate pKₐ, and grey numbers (minima) indicate Gibbs free energy in kcal/mol.

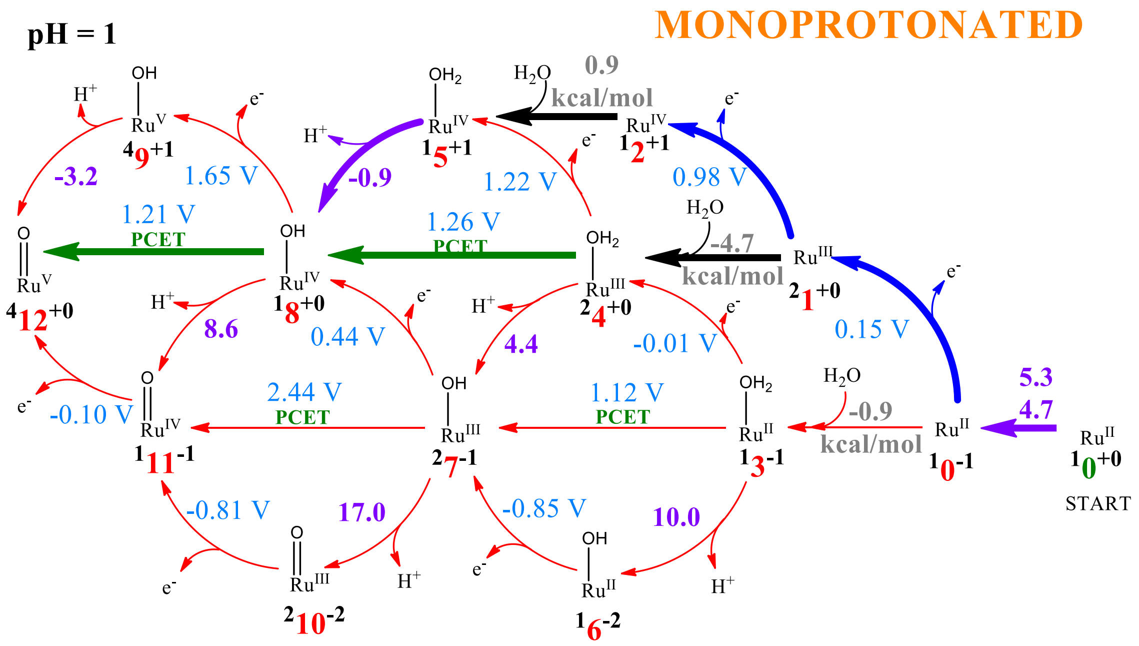
pH = 1
MONOPROTONATED
OH RuV 49+1
H+
e-
-3.2
1.65 V
OH2 RuIV 15+1
H+
-0.9
H2O
0.9 kcal/mol
RuIV 12+1
e-
1.22 V
0.98 V
O RuV 412+0
1.21 V PCET
OH RuIV 18+0
1.26 V PCET
OH2 RuIII 24+0
H2O
-4.7 kcal/mol
RuIII 21+0
e-
H+
8.6
0.44 V
4.4
-0.01 V
0.15 V
e-
-0.10 V
O RuIV 111-1
2.44 V PCET
OH RuIII 27-1
1.12 V PCET
OH2 RuII 13-1
H2O
-0.9 kcal/mol
RuII 10-1
5.3
4.7
RuII 10+0
START
-0.81 V
17.0
-0.85 V
10.0
O RuIII 210-2
OH RuII 16-2

Figure S3. The mechanism for the bisphosphonate Ru catalyst **B** with retention of ligand protons at pH 1. For reaction arrows, red = less favorable, blue = oxidation, green = PCET, and purple = deprotonation. For numbered species, green indicates deprotonated diphosphonate ligand, whereas red indicates doubly deprotonated ligand. Numbers near arrows indicate the reduction potential in V; purple numbers indicate pKa, and grey numbers (minima) indicate Gibbs free energy in kcal/mol.

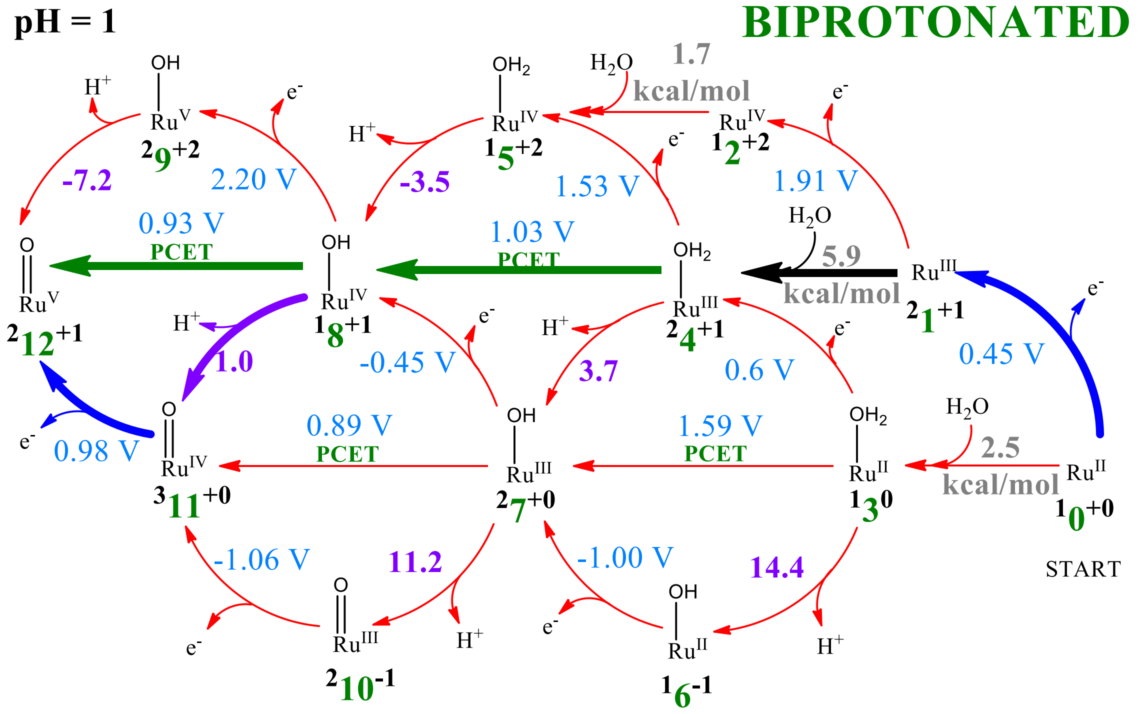
pH = 1
BIPROTONATED
OH RuV 29+2
H+
e-
-7.2
2.20 V
OH2 RuIV 15+2
H+
-3.5
H2O
1.7 kcal/mol
RuIV 12+2
1.53 V
1.91 V
O RuV 212+1
0.93 V PCET
OH RuIV 18+1
1.03 V PCET
OH2 RuIII 24+1
H2O
5.9 kcal/mol
RuIII 21+1
e-
0.45 V
1.0
-0.45 V
3.7
0.6 V
e-
0.98 V
O RuIV 311+0
0.89 V PCET
OH RuIII 27+0
1.59 V PCET
OH2 RuII 130
H2O
2.5 kcal/mol
RuII 10+0
START
-1.06 V
11.2
-1.00 V
14.4
O RuIII 210-1
OH RuII 16-1

Figure S4. The mechanism for the bisphosphonate Ru catalyst **B** with retention of ligand protons at pH 1. For reaction arrows, red = less favorable, blue = oxidation, green = PCET, and purple = deprotonation. For numbered species, green indicates deprotonated diphosphonate ligand, whereas red indicates doubly deprotonated ligand. Numbers near arrows indicate the reduction potential in V; purple numbers indicate pKa, and grey numbers (minima) indicate Gibbs free energy in kcal/mol.

Table S2. pK_a for the conversion of the two phosphonates in the catalyst: biprotonated, monoprotonated, and deprotonated.

Biprotonated to Monoprotonated	pK_a	Monoprotonated to Deprotonated	pK_a
Bi-0 to Mono-0	5.3	Mono-0 to Dep-0	4.7
Bi-1 to Mono-1	3.3	Mono-1 to Dep-1	2.3
Bi-2 to Mono-2	-2.9	Mono-2 to Dep-2	-1.2
Bi-3 to Mono-3	4.3	Mono-3 to Dep-3	5.8
Bi-4 to Mono-4	0.2	Mono-4 to Dep-4	4.0
Bi-5 to Mono-5	-1.8	Mono-5 to Dep-5	-1.0
Bi-6 to Mono-6	-0.1	Mono-6 to Dep-6	13.9
Bi-7 to Mono-7	0.9	Mono-7 to Dep-7	8.8
Bi-8 to Mono-8	0.8	Mono-8 to Dep-8	2.8
Bi-9 to Mono-9	-2.9	Mono-9 to Dep-9	-2.5
Bi-10 to Mono-10	6.7	Mono-10 to Dep-10	6.7
Bi-11 to Mono-11	8.3	Mono-11 to Dep-11	2.0
Bi-12 to Mono-12	1.1	Mono-12 to Dep-12	2.2

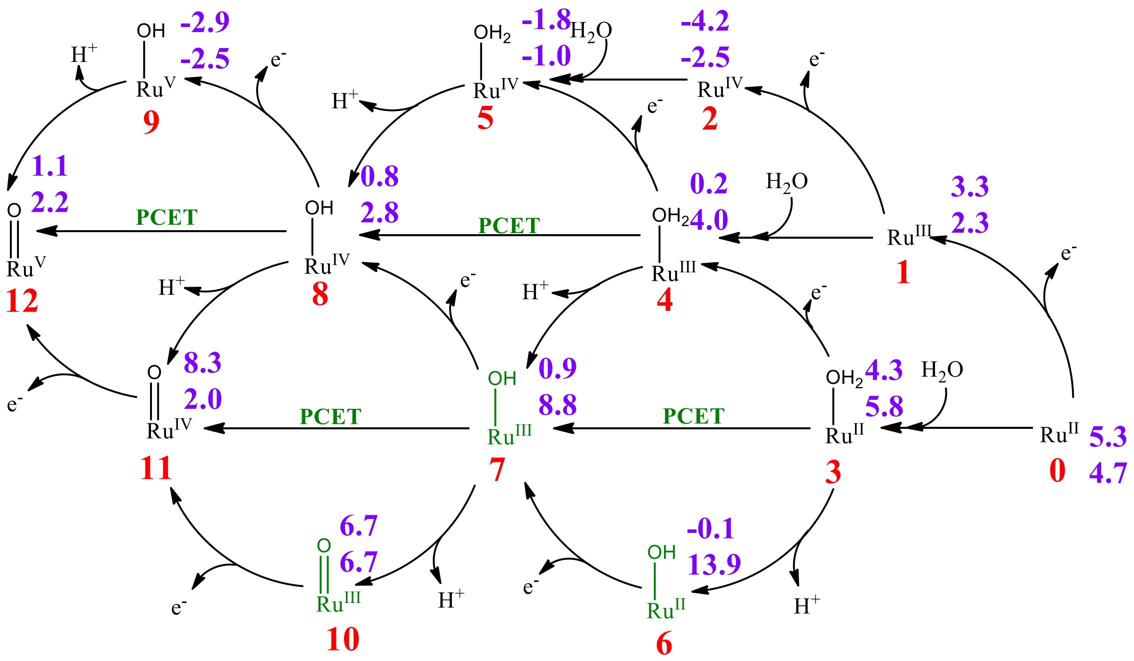
Ru^V 9 OH -2.9 -2.5
Ru^IV 5 OH2 -1.8 -1.0
Ru^IV 2 -4.2 -2.5
O=Ru^V 12 1.1 2.2
Ru^IV 8 OH 0.8 2.8
Ru^III 4 OH2 0.2 4.0
Ru^III 1 3.3 2.3
O=Ru^IV 11 8.3 2.0
Ru^III 7 OH 0.9 8.8
Ru^II 3 OH2 4.3 5.8
Ru^II 0 5.3 4.7
O=Ru^III 10 6.7 6.7
Ru^II 6 OH -0.1 13.9
PCET
PCET
PCET
PCET
H2O
H2O
H2O
H+
e-

Figure S5. pK_a for each molecule going from Biprotonated to Monoprotonated and Deprotonated phosphonates.

Table S3. Multiplicity and Spin density for all the relevant structures.

	0		1		2		3		4		5		6		7	
	M	S^2	M	S^2	M	S^2	M	S^2	M	S^2	M	S^2	M	S^2	M	S^2
Bip.	R.S	0	D	0.76	R.S	0	R.S	0	D	0.76	R.S	0	R.S	0	D	0.76
Monop.	R.S	0	D	0.76	R.S	0	R.S	0	D	0.76	R.S	0	R.S	0	D	0.76
Dep.	R.S	0	D	0.76	R.S	0	R.S	0	D	0.76	R.S	0	R.S	0	D	0.76
	8		9		10		11		12		Adduct		TS I2M		TS WNA	
	M	S^2	M	S^2	M	S^2	M	S^2	M	S^2	M	S^2	M	S^2	M	S^2
Bip.	R.S	0	D	0.76	D	0.76	T	2	D	0.76	U.S	1.04	R.S	0	D	0.76
Monop.	R.S	0	Q	3.77	D	0.76	R.S	0	Q	3.76	-	-	-	-	-	-
Dep.	R.S	0	D	0.76	D	0.76	T	2	Q	3.76	U.S	1.02	R.S	0	D	0.76

Experimental voltammetries

The following are taken from Grotjahn *et al*. *ChemCatChem* **2016**, *8*, 3045-3049:

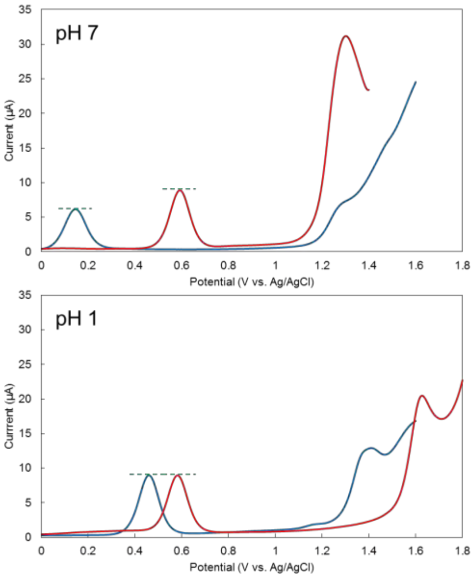

Figure S8. Differential pulse voltammetry comparing **2** (blue) and **3** (red). [Note: **2** is the bpa catalyst subject of our computational studies] Top: pH 7 (0.1 M potassium phosphate buffer). Bottom: pH 1 (0.1 M CF3SO3H). Dashed lines highlight relative peak heights. Catalyst concentration: 0.5 mM.

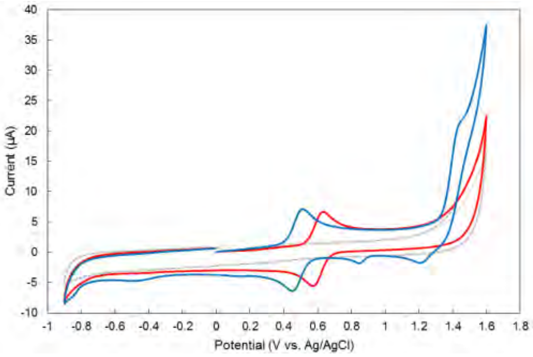

Figure S6. Cyclic voltammetry of Ru(bpa) at pH=1 (Blue).

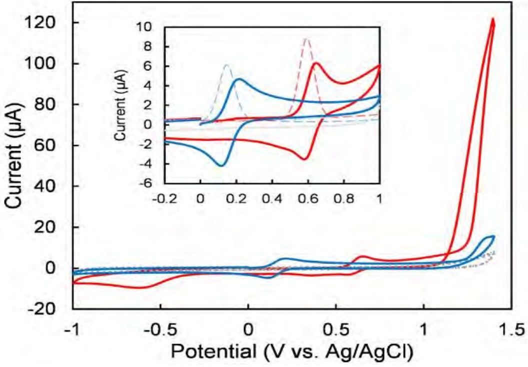

Figure S7. Cyclic voltammetry of Ru(bpa) at pH=7 (blue).

The following is taken from Xie *et al*. *Angew. Chem. Int. Ed.* **2016**, *55*, 8067:

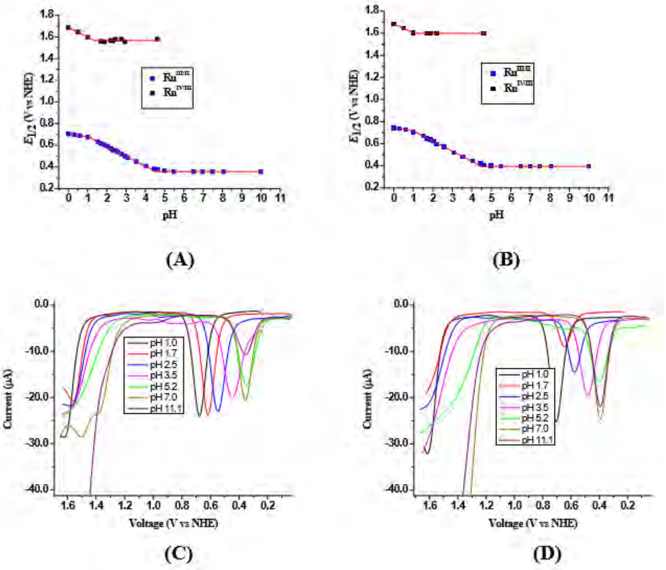

(A) (B)

(C) (D)

Figure S9. Pourbaix diagrams and square wave voltammograms for [Ru^{II}(bpaH$_2$)(pic)$_2$] **(A,C)**; [Ru^{II}(bpaH$_2$)(isq)$_2$] **(B,D)**.

CERIUM AMMONIUM NITRATE STUDY

Currently, there is no known structure for Cerium Ammonium Nitrate in an aqueous solution. We did try to develop a robust guess of CAN by trying to emulate a redox reaction of 1.6~1.7V in order to evaluate possible dimerizations between the Ru catalyst and the Ce in CAN, as there are other articles like Costas and Lloret-Fillol[1] that propose such coordination. Nevertheless, after several trials and exchanges between other researchers in the field, we concluded that we do not hold solid ground in our CAN structure hypothesis to use it for the mechanism. Rather than proposing a theoretical mechanism with Ru-Ce that might or might not be correct, we decided not to include it in the report. Here we show a sample of the tests done for CAN, and they will be included in the SI as well. Calculations for CAN have been performed with 6-31++G** to include diffuse functions and NO_3^- leaves through the following formula:

$$(Ce(NO_3)_6)^{-2} + 3 \cdot H_2O \rightarrow Ce(NO_3)_5{}^{-} + (NO_3 \cdot 3H_2O)^{-}$$

---

[1] Design of Iron Coordination Complexes as Highly Active Homogenous Water Oxidation Catalysts by Deuteration of Oxidation-Sensitive Sites *J. Am. Chem. Soc.* 2019, *141*, 1, 323-333

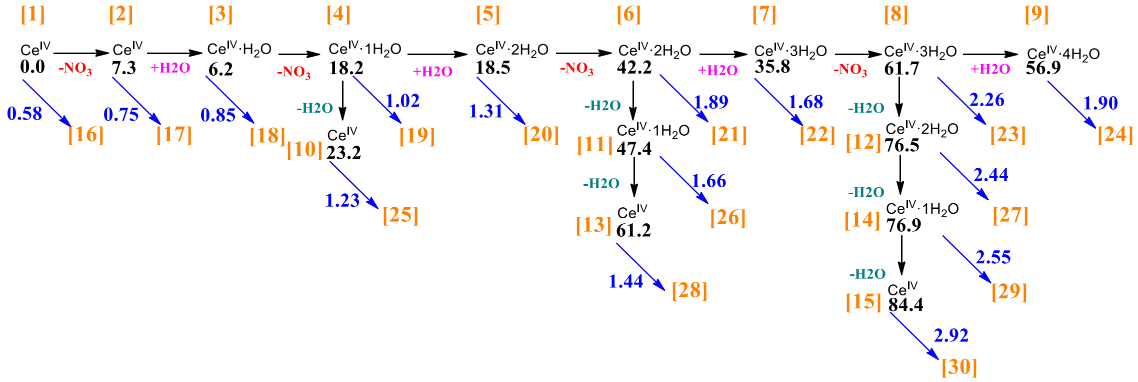
[1]
Ce^{IV}
0.0
-NO$_3$
[2]
Ce^{IV}
7.3
+H2O
[3]
Ce^{IV}·H$_2$O
6.2
-NO$_3$
[4]
Ce^{IV}·1H$_2$O
18.2
+H2O
[5]
Ce^{IV}·2H$_2$O
18.5
-NO$_3$
[6]
Ce^{IV}·2H$_2$O
42.2
+H2O
[7]
Ce^{IV}·3H$_2$O
35.8
-NO$_3$
[8]
Ce^{IV}·3H$_2$O
61.7
+H2O
[9]
Ce^{IV}·4H$_2$O
56.9
0.58
[16]
0.75
[17]
0.85
[18]
-H2O
[10]
Ce^{IV}
23.2
1.02
[19]
1.23
[25]
1.31
[20]
-H2O
[11]
Ce^{IV}·1H$_2$O
47.4
1.89
[21]
-H2O
[13]
Ce^{IV}
61.2
1.66
[26]
1.44
[28]
1.68
[22]
-H2O
[12]
Ce^{IV}·2H$_2$O
76.5
2.26
[23]
-H2O
[14]
Ce^{IV}·1H$_2$O
76.9
2.44
[27]
-H2O
[15]
Ce^{IV}
84.4
2.55
[29]
2.92
[30]
1.90
[24]

Figure S10. Cerium Ammonium Nitrate electropotential study.

In blue are the reduction potentials and in black the Gibbs free energies.

10.3. Section 4.4 SI

Supporting Information

for

Mechanism of Coupling of Alcohols and Amines to Generate Aldimines and H_2 by a Pincer Manganese Catalyst.

Judit Masdemont,[‡] Jesús A. Luque-Urrutia,[‡] Martí Gimferrer,[‡] David Milstein,[§] and Albert Poater[‡,*]

[‡]Institut de Química Computacional i Catàlisi and Departament de Química, Universitat de Girona, Campus Montilivi, 17003 Girona, Catalonia, Spain

[§]Department of Organic Chemistry, The Weizmann Institute of Science, Rehovot, 76100, Israel

Table S4. Benchmark study of all the computed species included in Figure 2 and Scheme 2 (Gibbs free energies in the solvent, in kcal/mol), using the optimized geometries at the BP86-D3BJ/SVP~sdd level.

Geometry Optimization	BP86D3BJ/SVP	BP86-D3BJ/SVP	BP86-D3BJ/SVP	BP86-D3BJ/SVP	BP86-D3BJ/SVP	BP86-D3BJ/SVP	BP86-D3BJ/SVP
Single point Energy Calculation in Solvent (SMD)	M06 /cc-pVTZ	M06 /6-31++G(d,p)	B3LYP-D3 /cc-pVTZ	PBE0-D3 /cc-pVTZ	M062X-D3 /cc-pVTZ	M062X /cc-pVTZ	M06-D3 /cc-pVTZ
1	0.0	0.0	0.0	0.0	0.0	0.0	0.0
1-1'	15.2	14.4	12.7	12.6	10.2	12.3	10.7
1'	1.0	0.1	4.2	4.2	-2.1	-0.1	-3.1
1'-2	33.4	33.1	32.6	33.1	30.9	33.1	28.8
1'-2+H2O	30.2	30.8	27.2	28.5	26.4	29.2	24.2
1,-2+2H2O	23.5	25.1	19.4	21.7	18.6	22.0	16.2
1'-2+ALCOHOL	30.9	30.9	27.2	29.4	25.2	29.6	21.4
1'-2+2ALCOHOL	29.6	29.8	21.9	26.2	21.6	28.7	14.8
1-2	31.9	31.1	29.3	28.7	29.2	31.5	27.2
2	-1.2	-2.4	3.5	3.2	11.2	11.3	-1.2
2-3	30.7	31.1	30.4	32.1	36.9	37.2	30.1
3	10.8	11.5	15.6	14.8	18.5	18.6	10.8
3-1	21.6	22.4	20.1	25.7	25.2	25.4	21.2
1-4	18.9	19.2	17.4	18.2	16.4	18.3	14.7
4	12.3	12.3	14.0	12.7	7.2	9.0	8.8
4-4'	19.1	19.0	20.7	18.6	14.4	16.1	15.5
4'	9.9	8.0	9.8	4.5	1.6	3.6	5.7
5	8.1	8.7	6.4	12.1	11.5	11.4	8.3
5+6-7	39.5	39.3	39.1	33.4	35.2	36.0	38.0
5+6-7+H2O	24.7	25.9	22.0	15.8	17.8	18.8	22.6
5+6-7+2H2O	21.6	23.1	16.0	9.7	12.7	14.0	18.9
5+6-7+ALCOHOL	32.7	33.7	28.8	23.4	24.1	26.1	28.1
5+6-7+2ALCOHOL	21.6	23.9	15.3	10.4	12.6	16.7	14.5
7	6.8	4.6	8.3	2.3	1.4	2.2	5.4
7-8	54.2	50.9	52.2	49.8	52.8	53.7	52.8
7-8+2H2O	34.1	31.1	24.5	23.8	27.3	28.7	31.1
7-8+2ALCOHOL	39.5	28.2	29.1	28.8	30.6	34.4	30.2
7-8+3ALCOHOL	43.6	44.7	28.6	29.5	31.8	38.0	29.9
8	3.0	3.3	3.0	1.6	0.3	0.9	2.4
With the *p*-F amine:							
6F	0.0	0.0	0.0	0.0	0.0	0.0	0.0
5+6-7F+H2O	25.2	26.5	22.6	16.4	18.4	19.2	23.1
5+6-7+2H2OF	22.5	24.1	16.9	10.7	13.7	14.8	19.7
5+6-7F+alcohol	32.6	33.8	28.8	23.4	24.1	25.9	28.1
5+6-7+2ALCOHOLF	24.5	24.6	15.9	11.0	13.2	17.1	15.2
7F	6.7	4.6	8.3	2.3	1.4	1.9	5.3
7-8F+H2O	34.5	31.4	24.9	24.2	27.8	28.9	31.4
7-8F+ALCOHOL	38.8	27.3	28.7	28.9	30.7	34.4	29.3
8F	3.0	3.4	2.8	1.6	0.4	0.7	2.5
With the *p*-OMe amine:							
6OMe	0.0	0.0	0.0	0.0	0.0	0.0	0.0
5+6-7OMe+H2O	24.4	26.0	21.7	15.4	17.4	18.2	22.2
5+6-7+2H2OOMe	20.5	22.5	15.0	8.7	11.7	12.8	17.9
5+6-7OMe+alcohol	31.8	33.3	27.9	22.5	23.3	25.1	27.3
5+6-7+2ALCOHOL-OMe	22.4	22.9	13.8	9.0	11.1	15.1	13.1
7OMe	6.4	4.3	7.9	2.0	1.0	1.6	5.0
7-8OMe+H2O	33.9	30.8	24.3	23.6	27.1	28.3	30.9
7-8OMe+ALCOHOL	39.1	27.2	29.1	29.4	31.0	34.9	29.3

8OMe	2.7	3.5	2.5	1.3	0.1	0.4	2.2

Table S5. Benchmark study of all the computed species included in Figure 2 and Scheme 2 (Gibbs free energies in the solvent, in kcal/mol).

Geometry Optimization	BP86-D3BJ/SVP	B3LYP-D3/SVP	PBE0-D3/SVP	PBE0-D3/6-31G(d,p)
Single point Energy Calculation in Solvent (SMD)	M06/cc-pVTZ	M06/cc-pVTZ	M06/cc-pVTZ	M06/cc-pVTZ
1	0.0	0.0	0.0	0.0
1-1'	15.2	14.9	14.8	13.6
1'	1.0	1.1	1.1	-0.6
1'-2	33.4	33.2	34.7	32.9
1'-2+H2O	30.2	29.0	29.0	27.9
1,-2+2H2O	23.5	23.2	24.4	22.8
1'-2+ALCOHOL	30.9	30.4	30.4	30.8
1'-2+2ALCOHOL	29.6	30.0	30.1	29.0
1-2	31.9	29.8	30.8	29.0
2	-1.2	-0.9	-1.0	-2.7
2-3	30.7	28.8	30.1	28.3
3	10.8	11.3	10.9	10.5
3-1	21.6	20.8	20.8	19.1
1-4	18.9	19.9	20.2	19.2
4	12.3	11.8	13.0	12.0
4-4'	19.1	18.7	19.6	18.0
4'	9.9	11.1	9.5	7.8
5	8.1	7.1	6.4	6.1
5+6-7	39.5	41.7	41.8	41.6
5+6-7+H2O	24.7	26.8	27.2	27.1
5+6-7+2H2O	21.6	23.4	24.0	24.4
5+6-7+ALCOHOL	32.7	28.4	31.6	28.7
5+6-7+2ALCOHOL	21.6	27.3	25.2	25.3
7	6.8	6.3	6.3	6.4
7-8	54.2	52.8	53.6	53.7
7-8+2H2O	34.1	31.0	31.1	31.2
7-8+2ALCOHOL	39.5	30.2	24.7	25.4
7-8+3ALCOHOL	43.6	39.4	-	36.9
8	3.0	2.7	2.8	1.3
With the *p*-F amine:				
6F	0.0	0.0	0.0	0.0
5+6-7F+H2O	25.2	26.8	27.0	27.1
5+6-7+2H2OF	22.5	25.1	24.4	24.6
5+6-7F+alcohol	32.6	28.5	32.0	28.0
5+6-7+2ALCOHOLF	24.5	27.2	25.5	25.6
7F	6.7	6.1	6.1	6.2
7-8F+H2O	34.5	31.1	30.9	31.0
7-8F+ALCOHOL	38.8	25.8	24.2	23.7
8F	3.0	2.5	2.4	2.6
With the *p*-OMe amine:				
6OMe	0.0	0.0	0.0	0.0
5+6-7OMe+H2O	24.4	26.7	26.9	27.1
5+6-7+2H2OOMe	20.5	24.3	23.7	24.1
5+6-7OMe+alcohol	31.8	28.5	28.2	28.3
5+6-7+2ALCOHOLOMe	22.4	26.7	24.9	26.0
7OMe	6.4	6.0	5.9	6.2
7-8OMe+H2O	33.9	30.4	30.1	30.7
7-8OMe+ALCOHOL	39.1	26.3	25.9	25.2
8OMe	2.7	3.2	2.9	2.7

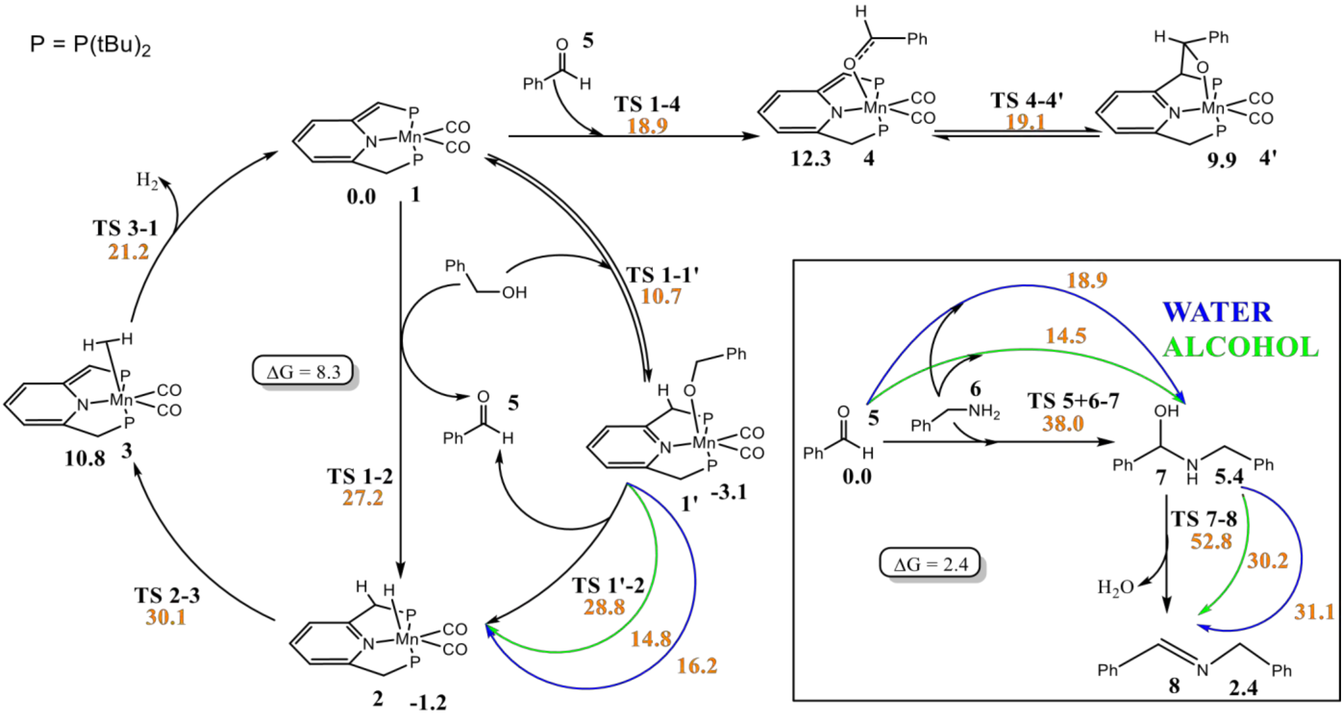
P = P(tBu)2
0.0 1
5
TS 1-4
18.9
12.3 4
TS 4-4'
19.1
9.9 4'
TS 3-1
21.2
H2
10.8 3
ΔG = 8.3
TS 1-1'
10.7
5
TS 1-2
27.2
1' -3.1
TS 2-3
30.1
TS 1'-2
28.8
14.8
16.2
2 -1.2
18.9
WATER
ALCOHOL
14.5
5
6
TS 5+6-7
38.0
0.0
7 5.4
TS 7-8
52.8
30.2
31.1
H2O
ΔG = 2.4
8 2.4

Figure S11. Full reaction mechanism at the level M06-D3/cc-pVTZ~sdd//BP86-D3BJ/SVP~sdd for the ADC of benzyl alcohols with benzyl amines (in blue the steps assisted by water and in green by the alcohol; in black (minima) and in orange (TSs) Gibbs free energies in the solvent in kcal/mol and referred to catalyst **1**, whereas to the aldehyde **5** in the metal-free reaction pathway included in the box).

10.4. Section 5.1 SI

The Fundamental Noninnocent Role of Water for the Hydrogenation of Nitrous Oxide by PNP Pincer Ru-based Catalysts.

Jesús A. Luque-Urrutia[‡] and Albert Poater[‡,*]

[‡]Institut de Química Computacional i Catàlisi and Departament de Química, Universitat de Girona, Campus Montilivi, 17003 Girona, Catalonia, Spain

Computational Details

All the DFT static calculations were performed with the Gaussian09 set of programs, using the BP86 functional of Becke and Perdew, together with the Grimme D3BJ correction term to the electronic energy. The molecular systems' electronic configuration was described with the triple-ζ basis set of Weigend and Ahlrichs for main-group atoms (TZVP keyword in Gaussian), whereas for ruthenium, the SDD basis set was employed. The small-core described ruthenium; quasi-relativistic Stuttgart/Dresden effective core potential, with an associated valence basis set (standard SDD keywords in gaussian09). The geometry optimizations were performed without symmetry constraints, and analytical frequency calculations performed the characterization of the located stationary points. These frequencies were used to calculate unscaled zero-point energies (ZPEs), and thermal corrections and entropy effects at 298 K. Energies were obtained by single-point calculations on the optimized geometries with the M06 functional and the aug-cc-PVTZ basis set. Solvent effects were included with the PCM using THF as a solvent. The reported free energies in this work include energies obtained at the M06/aug-cc-PVTZ~sdd level of theory corrected with zero-point energies, thermal corrections, and entropy effects evaluated at 298 K, achieved at the M06/TZVP~sdd level. The buried volume calculations were performed with the SambVca package developed by Cavallo *et al*. The radius of the sphere around the origin placed two Å below the metal center was set to 3.5 Å, while for the atoms, we adopted the Bondi radii scaled by 1.17, and a mesh of 0.1 Å was used to scan the sphere for buried voxels. The steric maps were evaluated with a development version of the SambVca package.

10.5. Section 5.2 SI

Electronic Supplementary Information for

Cycloaddition of CO_2 to epoxides by highly nucleophilic 4-aminopyridines: establishing a relationship between carbon basicity and catalytic performance by experimental and DFT investigations

Wuttichai Natongchai,[a] Jesús Antonio Luque-Urrutia,[b] Chalida Phungpanya,[a] Miquel Solà,[b] Valerio D' Elia,[a] Albert Poater,[b]* Hendrik Zipse[c]*

[a] Department of Materials Science and Engineering, School of Molecular Science and Engineering, Vidyasirimedhi Institute of Science and Technology (VISTEC), 555 Moo 1, 21210, Payupnai, WangChan, Rayong, Thailand. E-mail: valerio.delia@vistec.ac.th

[b] Institut de Química Computacional i Catàlisi and Department de Química, Universitat de Girona, c/ Mª Aurèlia Capmany 69, 17003 Girona, Catalonia, Spain. E-mail: albert.poater@udg.edu

[c] Department Chemie, Ludwig-Maximilians-Universität München, Butenandtstraße 5–13, Haus F, 81377 München, Germany.

Summary

S1. General Information …………………………………………………………………………………………..219

S2. Computational data…………………………………………………………………………………………….220

S1. General Information

Experimental details

All chemicals and solvents were obtained commercially and used as received without further purification. All air and water sensitive manipulations were carried out under a nitrogen atmosphere using standard Schlenk techniques. Merrifield resin was purchased from Sigma-Aldrich (Mesh: 100-200, loading: 1.0 to 1.6 mmol/g Cl^-, cross-linked with 1% DVB). NMR spectra were measured on an automated “Bruker” 600 MHz for ^1H (150 MHz for ^{13}C). Chemical shifts are reported in ppm (δ, relative to TMS) using $CHCl_3$ residual peak (δ = 7.26 ppm for ^1H and 77.16 ppm for ^{13}C) in $CDCl_3$ as an internal standard or 2.05 ppm for ^1H and 29.84 ppm for ^{13}C of acetone-d_6 ($(CD_3)_2CO$) or 4.79 ppm for ^1H of D_2O. Mass spectrometry data were collected by using Bruker data analysis Esquire-LC mass spectrometer (APCI mode). FT-IR spectra were recorded on a Frontier FT-IR, Universal-ATR, PerkinElmer (ATR mode). Thermogravimetric analysis was measured on a Rigaku model TG-DTA 8122 with smart loader, 30-800 ℃, 10 ℃/min under N_2 atmosphere. Elemental analysis was measured on CHNS analyzer, Leco model TruSpec Micro and *in situ* IR was performed on a METTLER TOLEDO, ReactIR^{TM} 15.

Computational methods

Epoxide affinity calculations: Geometry optimizations have been performed using the BP86 hybrid functional[228-229] complemented by the D3 dispersion correction.[230-231] The TZVP all-electron basis set[232] has been used for all elements. Thermal corrections to enthalpies at 373.15 K have been calculated at the same level using the rigid rotor/harmonic oscillator model. This level of theory will in the following be designated "BP86-D3/TZVP".

Single point energies have subsequently been calculated with the hybrid M06 functional[233] combined with the TZVP basis set,[232] the ultrafine integration grid, and the PCM continuum solvation model[234] for propylene oxide (PO) as the reaction medium. Estimated values for this latter solvent are eps=13.9 and rsolv=4.26. Enthalpies and free energies at this level of theory are calculated using thermal corrections from the previous gas-phase geometry optimizations. This level of theory will in the following be designated "PCM(PO)/M06/TZVP(SP)".

Finally, geometry optimizations have been repeated at the PCM(PO)/M06/TZVP level of theory, again using the ultrafine integration grid. Enthalpies and free energies at 373.15 K are obtained through combination with thermal corrections calculated at this same level. This level of theory will in the following be designated "PCM(PO)/M06/TZVP".

All calculations have been performed with *Gaussian 09, rev. D.01*.[235]

__Mechanistic pathways calculations__: DFT static calculations were performed with the Gausian09 set of programs,[235] using the BP86 functional of Becke and Perdew,[229, 236-237] including corrections due to dispersion through the Grimme's method (GD3 keyword in Gaussian).[230, 238] The electronic configuration of the molecular systems was described with the triple-ζ basis set with the polarization of Ahlrichs for main-group atoms (TZVP keyword in Gaussian).[239] The geometry optimizations were performed without symmetry constraints, and analytical frequency calculations confirmed the character of the located stationary points. These frequencies were used to calculate unscaled zero-point energies (ZPEs) as well. Single-point calculations energies obtained on the optimized geometries with the B3LYP-D3 functional[228, 240-241] and the triple-ζ basis set TZVP and by estimating solvent effects with the PCM as implemented in Gaussian09 for the epoxide.[242-243] The reported free Gibbs free energies in this work include electronic energies obtained at the B3LYP-D3/TZVP//BP86-D3/TZ2P level of theory corrected with zero-point energies, thermal corrections and entropy effects computed with the BP86-D3/TZVP level (see SI for further details).

S2. Computational data

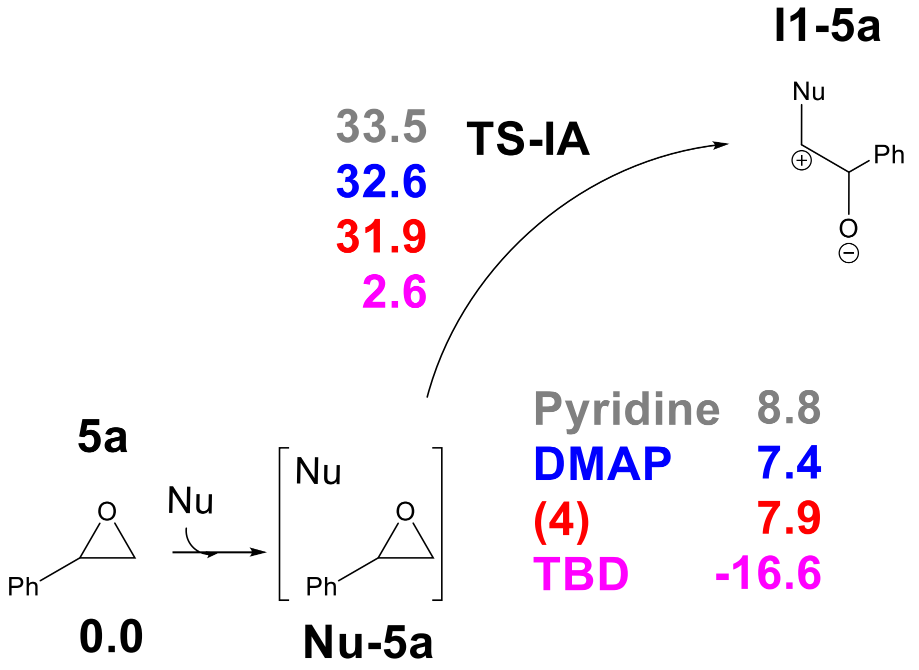

Figure S12. Reaction barriers (kcal/mol) for the ring-opening of epoxide **5a** by several nucleophiles.

PYRIDINE

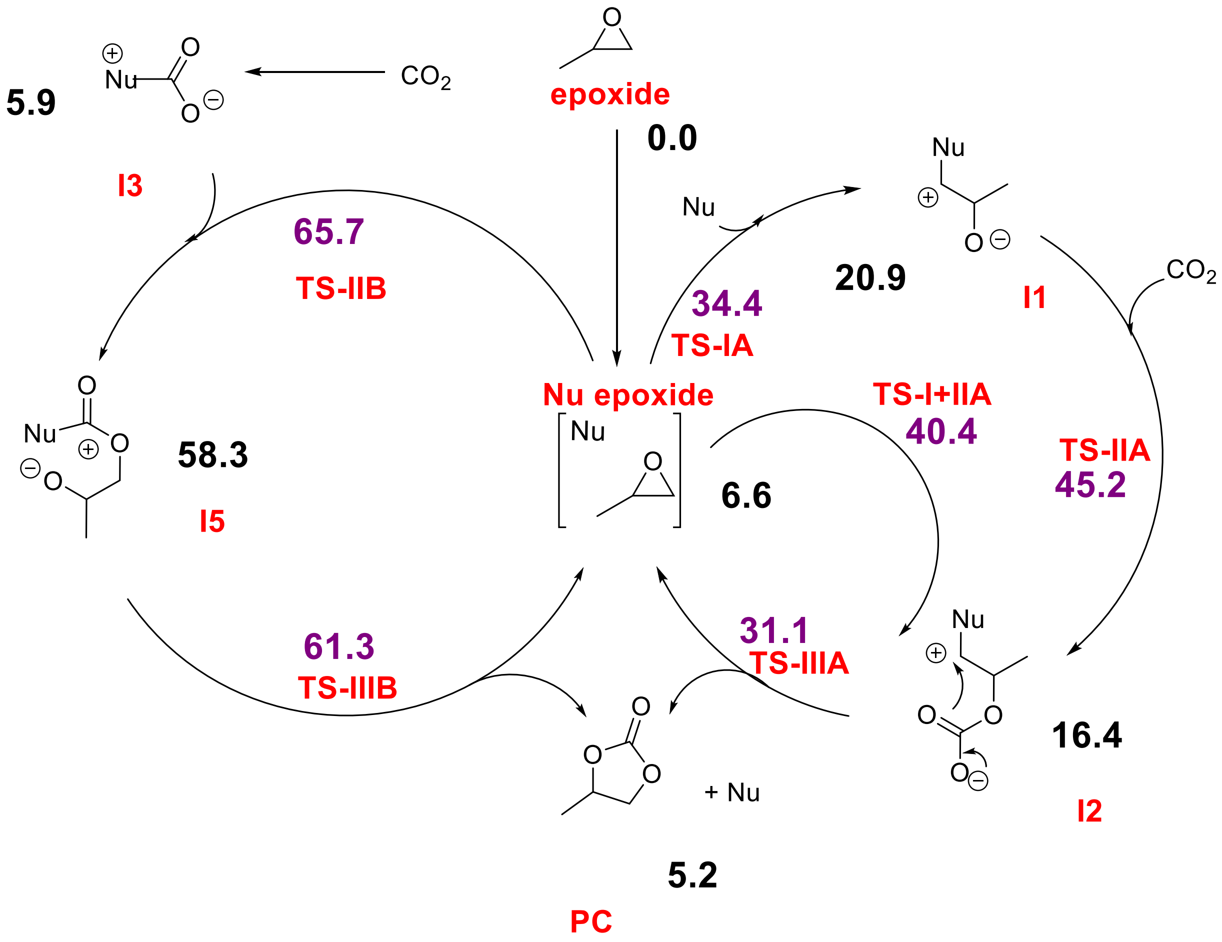
5.9
Nu
O
O
CO2
I3
65.7
TS-IIB
O
epoxide
0.0
Nu
Nu
O
20.9
I1
CO2
34.4
TS-IA
Nu epoxide
Nu
O
6.6
TS-I+IIA
40.4
TS-IIA
45.2
O
Nu
O
58.3
I5
61.3
TS-IIIB
31.1
TS-IIIA
Nu
O
O
O
16.4
I2
O
O
O
+ Nu
5.2
PC

Figure S13. Reaction barriers (kcal/mol) for the cycloaddition of CO_2 to propylene oxide catalyzed by pyridine according to two different pathways.

DMAP

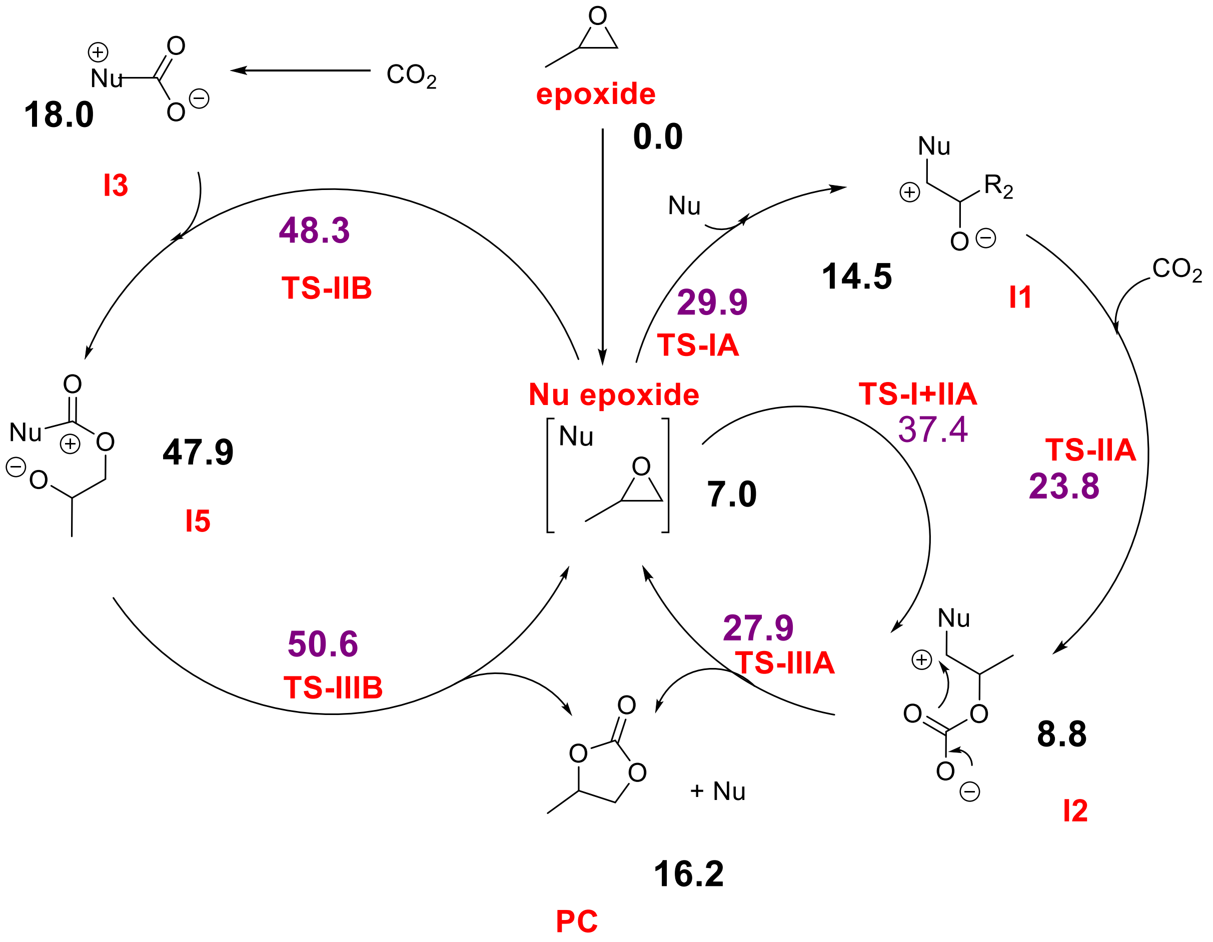
Nu
O
O
CO2
18.0
I3
O
epoxide
0.0
Nu
Nu
R2
O
29.9
TS-IA
14.5
I1
CO2
48.3
TS-IIB
O
Nu
O
O
47.9
I5
Nu epoxide
Nu
O
7.0
TS-I+IIA
37.4
TS-IIA
23.8
27.9
TS-IIIA
Nu
O
O
O
8.8
I2
50.6
TS-IIIB
O
O
O
+ Nu
16.2
PC

Figure S14. According to two different pathways, reaction barriers (kcal/mol) for the cycloaddition of CO_2 to propylene oxide are catalyzed by DMAP.

(4)

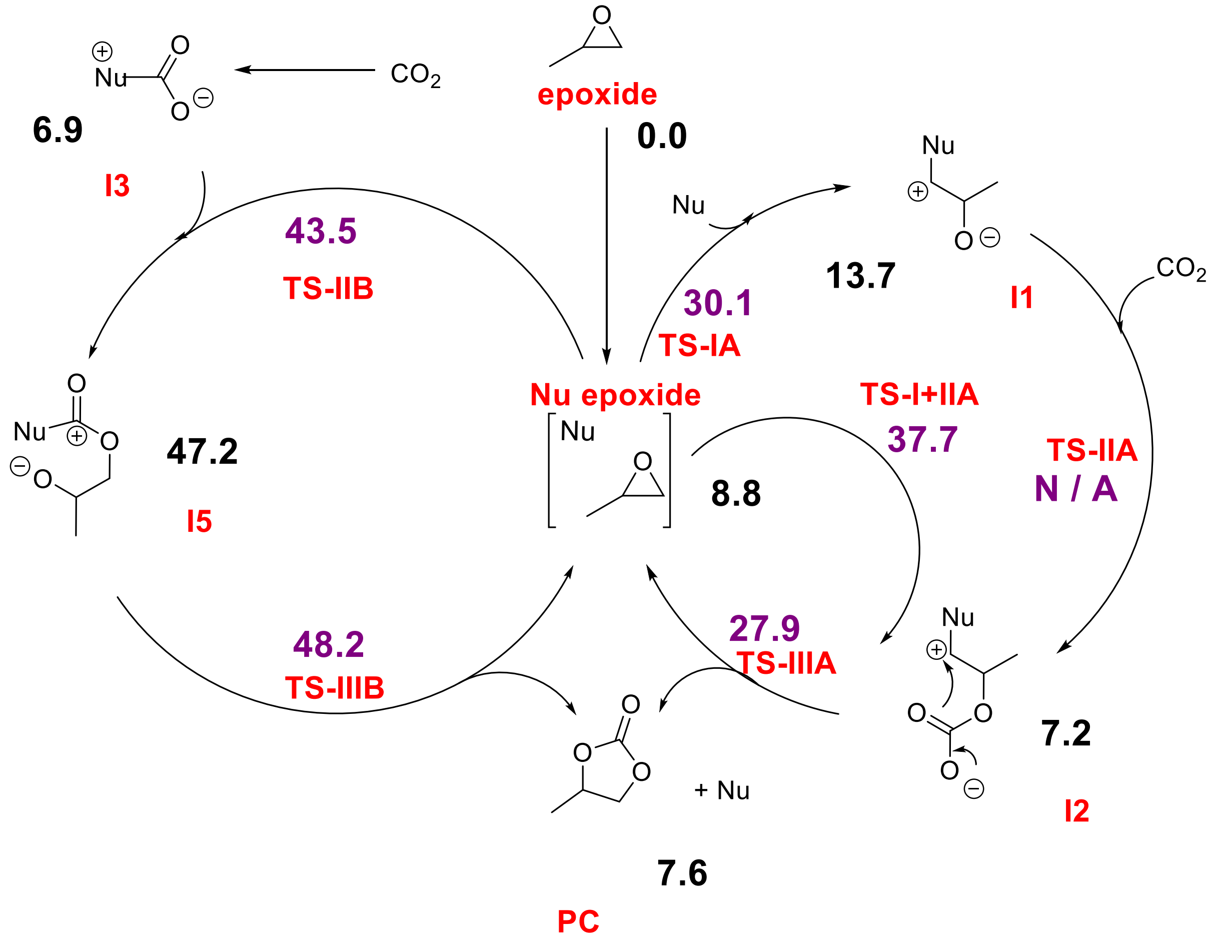

CO$_2$
epoxide
0.0
6.9
I3
43.5
TS-IIB
Nu
30.1
TS-IA
13.7
I1
CO$_2$
47.2
I5
Nu epoxide
8.8
TS-I+IIA
37.7
TS-IIA
N / A
48.2
TS-IIIB
27.9
TS-IIIA
+ Nu
7.2
I2
7.6
PC

Figure S15. Reaction barriers (kcal/mol) for the cycloaddition of CO$_2$ to propylene oxide catalyzed by nucleophile **4** according to two different pathways.

TBD

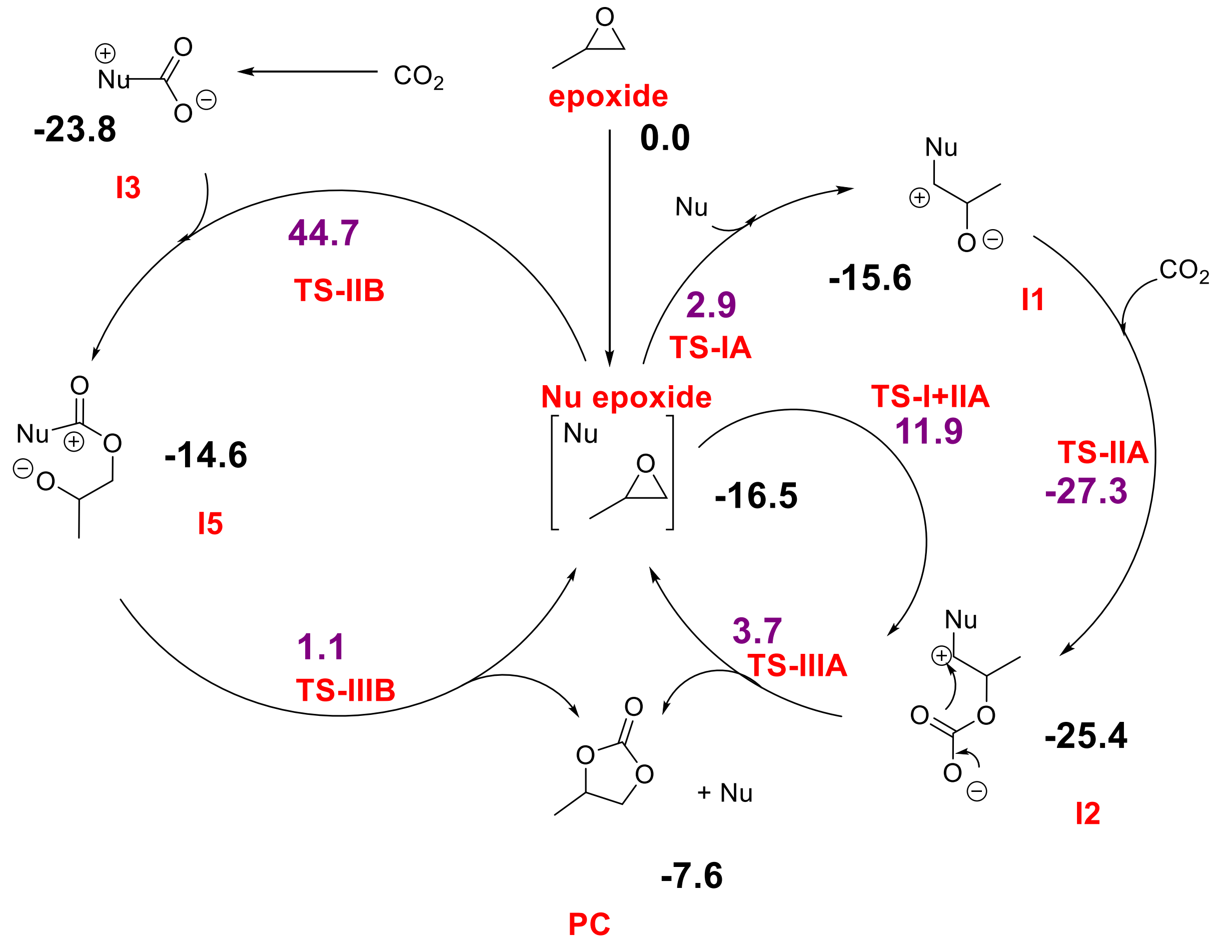
CO$_2$
-23.8
I3
epoxide
0.0
Nu
-15.6
I1
CO$_2$
44.7
TS-IIB
2.9
TS-IA
Nu epoxide
Nu
TS-I+IIA
11.9
TS-IIA
-27.3
Nu
-14.6
I5
-16.5
1.1
TS-IIIB
3.7
TS-IIIA
Nu
-25.4
I2
+ Nu
-7.6
PC

Figure S16. Reaction barriers (kcal/mol) for the cycloaddition of CO$_2$ to propylene oxide catalyzed by TBD according to two different pathways.

10.6. Section 6.1 SI

CHEMISTRY
A European Journal

Supporting Information

Do Carbon Nano-onions Behave as Nanoscopic Faraday Cages?

A Comparison of the Reactivity of C_{60}, C_{240}, C_{60}@C_{240}, Li^+@C_{60}, Li^+@C_{240}, and Li^+@C_{60}@C_{240}

Jesús Antonio Luque-Urrutia, Albert Poater,* and Miquel Solà*[a]

chem_201904650_sm_miscellaneous_information.pdf

Author Contributions

J.A.L.-U. Formal analysis: Equal; Investigation; Writing - Review & Editing: Equal.

A.P. Formal analysis: Equal; Investigation: Supporting; Writing - Review & Editing: Supporting.

M.S. Conceptualization; Formal analysis: Equal; Investigation: Supporting; Writing - Review & Editing: Equal.

SUPPORTING INFORMATION FOR

Do carbon nano-onions behave as nanoscopic Faraday cages? A comparison of the reactivity of C_{60}, C_{240}, C_{60}@C_{240}, Li^+@C_{60}, Li^+@C_{240}, and Li^+@C_{60}@C_{240}.

Jesús Antonio Luque-Urrutia, Albert Poater* and Miquel Solà*

Table of contents

Figure S17. Structure comparison between PBEPBE/3-21G(d) and PBEPBE/6-311G(d,p) with the root-mean-square deviation of atomic positions (RMSD). 227

Figure S18. Electrostatic potential surface for Li^+@C_{240} optimized (top left) and non-optimized with the Li at the center and Li^+@C_{60}@C_{240} 227

Figure S19. Non-covalent interactions in Li^+@C_{60}@C_{240} 228

Table S6. Benchmarking for the fullerene calculations..228

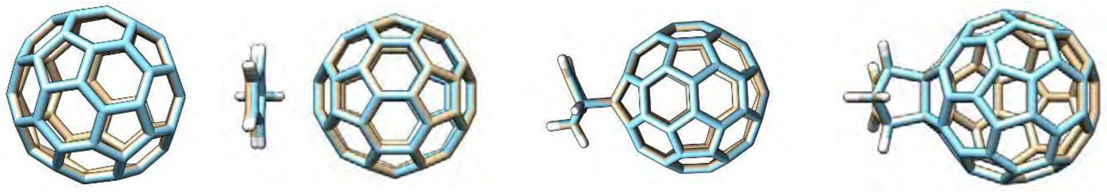

C60
RMSD=0.0108

C60-RC
RMSD=0.0946

C60-66
RMSD=0.0183

C60-56
RMSD=0.0178

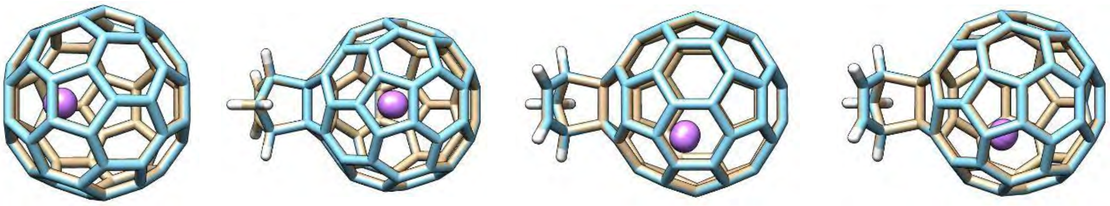

C61
RMSD=0.0199

C61-RC
RMSD=0.0256

C61-66
RMSD=0.0240

C61-56
RMSD=0.0259

Figure S17. Structure comparison between PBEPBE/3-21G(d) and PBEPBE/6-311G(d,p) with the root-mean-square deviation of atomic positions (RMSD).

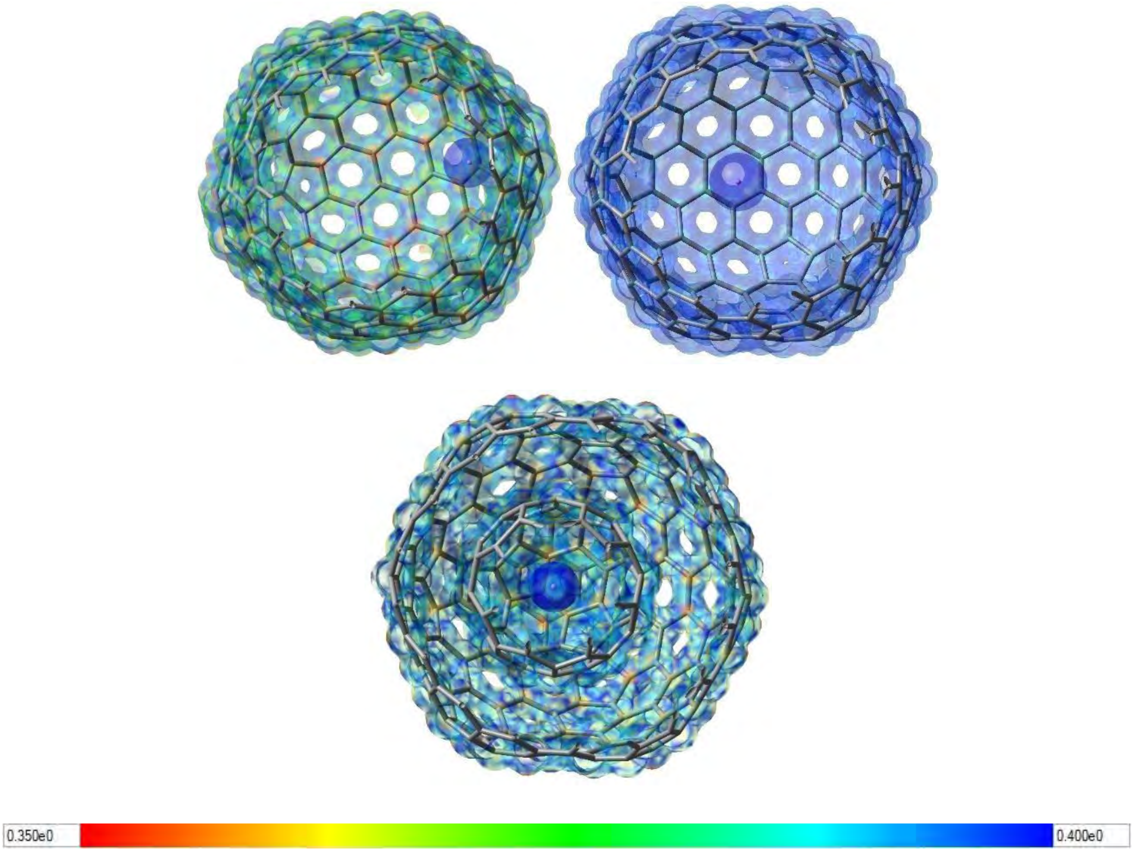

Figure S18. Electrostatic potential surface for $Li^+@C_{240}$ optimized (top left) and non-optimized with the Li^+ at the center (top right) and $Li^+@C_{60}@C_{240}$ (bottom).

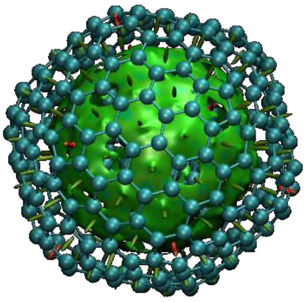

Figure S19. Non-covalent interactions in the $Li^+@C_{60}@C_{240}$.

Table S6. Benchmarking for the fullerene calculations.

Benchmarking	$\Delta H^‡$	ΔH_R
B3LYP-D/6-31G* [1]	2.3	-23.3
BLYP/6-31G**//BLYP-D/3-21G*	3.5	-19.3
B3LYP/6-31G**//B3LYP-D/3-21G*	4.1	-25.8
BP86/6-31G**//BP86-D/3-21G*	1.9	-28.6
M06/6-31G**//M06/3-21G*	5.4	-22.1

M06-2X/6-31G**//M06-2X/3-21G*	5.1	-30.1
M06/6-31G**//M06-D3/3-21G*	5.4	-29.9
PBEPBE/6-31G**//PBEPBE-D/3-21G*	2.4	-27.1
MN15/6-31G**//MN15/3-21G*	5.0	-28.8
O3LYP/6-31G**//O3LYP/3-21G*	5.9	-9.4
wB97XD/6-31G**//wB97XD/3-21G*	5.8	-34.1
TPSSh/6-31G**//TPSSh/3-21G*	3.9	-17.9
Experimental [2]	6.9	-19.8

[1] S. Osuna, M. Swart and M. Solà *J. Phys. Chem. A* **2011**, *115*, 3491-3496.

[2] [a] L. M. Giovane, J. W. Barco, T. Yadav, A. L. Lafleur, J. A. Marr, J. B. Howard, V. M. Rotello, *J. Phys. Chem.* **1993**, *97*, 8560-8561; [b] L. S. K. Pang, M. A. Wilson, *J. Phys. Chem.* **1993**, *97*, 6761-6763.